Manganese Coordination Complexes: From Magnetism to Water Oxidation

Swetanshu Tandon

Trinity College Dublin
Coláiste na Tríonóide, Baile Átha Cliath
The University of Dublin

A thesis submitted in partial fulfilment of the requirements

for the degree of Doctor of Philosophy

at the

School of Chemistry and CRANN

University of Dublin, Trinity College

Supervisors: Prof. Graeme W. Watson and Prof. Wolfgang Schmitt

2020

Declaration of Authorship

I declare that this thesis has not been submitted as an exercise for a degree at this or any other university and it is entirely my own work, except where otherwise cited.

I agree to deposit this thesis in the University's open access institutional repository or allow the Library to do so on my behalf, subject to Irish Copyright Legislation and Trinity College Library conditions of use and acknowledgement.

_____

Swetanshu Tandon.

2020

University of Dublin, Trinity College.

Summary

Ever increasing energy demands and the closely related issue of global warming derived from fossil fuel combustion have encouraged the development of renewable energy sources and energy storage concepts as one of the most important scientific challenges today. H_2 serves as a clean alternative to fossil fuels, and the electrolysis of water is promising for H_2 generation and hence the development of the H_2 economy. Catalysing the oxidation-half reaction of water splitting represents the key obstacle for the utilisation of H_2 as an alternative clean fuel. Since H_2O is diamagnetic and O_2 is paramagnetic, the electronic structure and hence the magnetic nature of the catalyst affects this half-reaction. In plants, this highly endergonic reaction is facilitated in photosystem-II by the oxygen evolving complex which comprises of a Mn based coordination complex. Since Mn contains a large number of unpaired electrons, it provides the possibility of tuning the electronic structure to facilitate the oxidation of water. In addition, the presence of unpaired electrons also gives rise to interesting magnetic properties in Mn coordination complexes.

Considering the diversity in applications of Mn coordination complexes, this work focusses on investigating Mn coordination complexes for these applications using a combined computational and experimental approach. In this thesis, we report the development of a computational methodology for investigating the magnetic properties of coordination complexes, and a synthetic approach for the synthesis of Mn based high nuclearity coordination complexes. The synthesised complexes have been characterised using various analytical techniques. The magnetic properties of some of the synthesised complexes have been studied both experimentally and using the developed computational approach. Furthermore, we have investigated the oxidation-half reaction of water splitting with selected complexes under electrochemical conditions in aqueous media using carbon paste electrodes.

Chapter 1 provides a brief summary of the available literature illustrating the recent developments in the field of water oxidation and magnetism with a focus on Mn coordination complexes. Chapter 2 describes the basic principles of Hartree-Fock and density functional theory and their application along with the details of the developed computational methodology and the concepts that have been used to develop it. Chapter 3 reports the development of the synthetic approach and introduces the various coordination complexes synthesised using this approach.

In chapter 4, the application of the computational methodology using a hexanuclear Mn complex is demonstrated. In this chapter, a novel methodology for determining the mechanism of coupling *via* each ligand bridge in instances where multiple ligand groups bridge a given pair of metal centres is also described. Chapter 5 further explores the use of the computational methodology to understand the electronic structure of a tridecanuclear Mn complex. The potential and limitations of the novel methodology are also discussed in this chapter.

The coordination complexes introduced in chapter 3 are described in detail in chapters 6, 7 and 8. These chapters illustrate the versatility of the synthetic approach in terms of modifying previously known structures, accessing rare geometrical arrangements and structurally mimicking the oxygen evolving complex. Chapter 6 describes the carboxylate based complexes, chapter 7 covers the mixed carboxylate-phosphonate complexes and in chapter 8, the phosphonate based complexes are described. The magnetic properties and electrochemical behaviour of selected complexes are also discussed in these chapters.

In chapter 9, a summary of this work is provided and possible future work based on the results described here is considered.

Chapter 10 describes the experimental details of the work carried out. This is followed by the bibliography of this thesis and an appendix covering some additional information. Crystallographic information files for each structure, optimised coordinates for the structures modelled and the FORTRAN codes developed in this work are provided on the attached compact disc. The codes are also available on github (https://github.com/WatsonGroupTCD).

Dedicated to Dadimaa and Baba. You'll always be missed.

Acknowledgements

This work was impossible for me to complete by myself. So, I want to take this opportunity to thank everyone who have not only helped me complete this work but have made me who I am today.

First and foremost, I would like to express my sincere gratitude towards Prof. Graeme Watson and Prof. Wolfgang Schmitt for providing me the opportunity to conduct this research and their much needed guidance throughout the course of this project. I also thank Dr. Abhinav Kumar and Dr. Rishikesh Shukla who made me love chemistry enough that I decided to pursue a Ph.D. in chemistry, and their guidance throughout this journey. I consider myself extremely lucky to have met these four geniuses.

A sincere thanks to Dr. Brendan Twamley for not only ploughing through my never ending samples of bad crystals and refining the data, but also for teaching me crystal structure refinement. I also thank Dr. Amal Cherian Kathalikkattil, Paul Wix and Friedrich Steuber for tolerating my infinite batches of polymorphs and for teaching me so much about crystallography. A big thank you to Dr. Joaquín Soriano-López for helping me with electrochemistry, Dr. Munuswamy Venkatesan for the magnetic measurements, Dr. Guanghua Jin and Éadaoin Whelan for the SEM and EDX measurements, and Dr. Ross Lundy for the XPS measurements. Thanks are also due to Dr. Colm Healy, Éadaoin Whelan, Mariah O'Doherty and Luana Martins for taking care of the chemical orders. I thank Dr. Manuel Rüther for training me on various instruments, Dr. Martin Feeney and Dr. Gary Hessman for the mass spectroscopy analysis, and Dr. Ann Connolly and Dr. Rónán Crowley for the elemental analysis. I also thank Patsy Greene and Thomas Conroy for their help with the labs and Frederick Cowzer and Maura Boland for their help in stores. I also thank Dr. Noelle Scully, Dr. Sinead Boyce, Teresa McDonnell, Anne Marie Farrell, Jennifer McHugh and Ben Power for administrative help. A big thank you to Dr. Niamh McGoldrick for the much needed support throughout this work. I also thank ICHEC and Research IT for the compute time and the Irish Research Council for the financial support without which this research would not have been possible.

A large number of personal acknowledgements are also due. I thank all the past and present members of the Watson and the Schmitt group for their help throughout the years and for making the office a fun place to work: Ailbhe, Ako, Amal bhai, Aneela, the three Aoifes, Aviral, Colm, Debo, Douglas, Éadaoin, Friedrich, Greg, Guanghua, Joaquín (Ximo), Joe, Jom, Julia, Kevin, Lauren, Luana, Mariah, Muhamed, Paul, Rory, Sébastien, Uma didi, Xiao-Ping and Zubair. Special thanks to Ailbhe and Aoife for organising all the ice skating sessions; Amal, Guanghua and Uma who have always treated me like their younger brother; Colm and Paul for all the amazing discussions on chemistry and life; Debo for the 'shuddh Hindi' discussions in the lab; Friedrich for sharing his encyclopaedic

knowledge of animes and for keeping me up to date with all the SNIAM gossip that I would have otherwise missed; Sébastien for teaching me how to compose music on a computer.

I am grateful to my friends Rajeev and Rishabh who have always been there for me since school days; Gauri, Nitheen, Shourjya and Sriram for helping me throughout my time in Dublin, and Geeta for all those skype 'panchaayat' sessions without which I don't think I would have come this far.

I am indebted to my brothers Abhiroop and Anant who made sure that my sanity remains intact with all the jamming sessions, the laughs and the delicious food that we cooked together. I thank you both for forcing me to travel which, I admit, was refreshing, and for tolerating my forced Naruto binge watch sessions. Lastly and most importantly, I thank Maa and Pitaji for always being there for me, for believing in me even in times when I did not believe in myself and for making me what I am today.

I personally don't think that I can ever thank you guys enough but to slightly lessen this guilt of mine, I want to dedicate this piece (link below) to you. I hope you guys like it!

Link: https://drive.google.com/file/d/11OJ3ZbR27BbZqgWiF_duUhJEy0N3rmoB/view?usp=sharing

Table of Contents

Abbreviations

1-D	One-Dimensional
ATR	Attenuated Total Reflectance
BVS	Bond Valence Sum
CA	Chronoamperometry
CP	Carbon Paste
CV	Cyclic Voltammetry
DFT	Density Functional Theory
DMF	*N*,*N*-Dimethylformamide
DMSO	Dimethyl Sulfoxide
EDX	Energy Dispersive X-ray
GGA	Generalised Gradient Approximation
GTO	Gaussian Type Orbital
HF	Hartree-Fock
IR	Infrared
LDA	Local Density Approximation
LSDA	Local Spin Density Approximation
LSV	Linear Sweep Voltammetry
NHE	Normal Hydrogen Electrode
OEC	Oxygen Evolving Complex
OER	Oxygen Evolution Reaction
PAW	Projector Augmented Wave
PS-II	Photosystem-II
PXRD	Powder X-ray Diffraction
RHE	Reversible Hydrogen Electrode
SCF	Self-Consistent Field
SEM	Scanning Electron Microscopy
SMM	Single Molecule Magnet
STO	Slater Type Orbital
TGA	Thermogravimetric Analysis
TOF	Turnover Frequency
TON	Turnover Number
VASP	Vienna Ab-initio Simulation Package
XPS	X-ray Photoelectron Spectroscopy
XRD	X-ray Diffraction

1 Introduction

Global energy demands are increasing at a rapid rate with 2018 having witnessed a consumption of 11.2 billion tonnes of oil equivalents, 2.1% greater than 2017. This rise in the global energy consumption has led to an increase of 1.7% in global CO_2 emissions between 2017 and 2018 to 27 billion tonnes.[1] These increasing energy demands and the closely related issue of global warming derived from increased CO_2 emissions have led to the development of alternative clean energy sources become one of the most important scientific challenges today.[2, 3]

1.1 Alternatives to Fossil Fuels

Nuclear energy and renewable energy serve as the two most promising options for clean energy. The former is quite attractive owing to its high energy density, and provides a near-term scalable alternative.[4-6] The CO_2 emissions associated with nuclear energy are predicted to be 400 times less than that for energy generated by fossil fuels.[7] Although the risk associated with the use of nuclear power is extremely low,[8] and the waste generated by nuclear power plants compared to that generated by fossil fuel based power plants is small, the disposal of the waste product generated by nuclear power plants is a matter of concern in its sustainable use.[9] The current disposal method involves geological disposal whereby the waste is stored in deep-mined repositories and this method has been accepted as a safe and reliable method for radioactive waste disposal.[10] Despite the low volumes of the nuclear waste generated and the reliability of the geological disposal method, the radioactive character of this waste necessitates its lifelong active monitoring and surveillance. The life span of this waste however, makes guaranteeing of this requirement impossible which is concerning.[11, 12]

Renewable energy sources, in comparison, provide a relatively safer and hence, a more appealing alternative. A variety of options are available under the umbrella of renewable energy sources but they can be broadly grouped into five categories – (a) wind, (b) hydropower, (c) geothermal power, (d) biomass and (e) solar power. Each of these sources have their own benefits and limitations. For example, wind and hydropower are relatively simple to exploit and require low maintenance but at the same time, there is a large capital cost to set up these technologies as they require the use of magnets which are generally made using rare-earth metals which are expensive.[9, 13] Additionally, installation of a wind farm can adversely affect human health[14] and can lead to increased bird mortality rates.[9] Similarly, hydropower plants result in loss of agricultural land and displacement of population.[15] Geothermal energy generation is also associated with expensive set up and the cost of maintenance is also high. Biomass can serve as an inexpensive and cleaner alternative to fossil fuels but at the same time, increased biomass use requires more land and leads to higher demands for fertilisers and pesticides and hence increased air and soil pollution.[16]

Solar energy, among other renewable energy sources, is considered to be more ecologically sustainable and of higher economic impact due to its ubiquity. The amount of solar energy intercepted by earth in a year is 7500 times greater than the annual global consumption which suggests that efficient exploitation of solar energy can end our reliance on fossil fuels.[17, 18] Compared to nuclear power plants, larger quantities of land is required for developing solar farms[9] but at the same time, unlike other renewable energy resources, harnessing of solar energy does not necessarily require a dedicated space. Solar panels can easily be accommodated in the current infrastructure without adversely affecting the surrounding ecology making the use of solar energy more appealing compared to other renewable energy resources. The intermittent supply of solar energy however, is a major limitation in the direct use of solar energy because of the mismatch between peak supply and demand periods and hence, the implementation of solar energy as an alternative, sustainable energy source requires the development of better energy storage concepts.[19]

1.2 Energy Storage Technologies

There are a few potential options available for energy storage that includes batteries and chemical fuels. A number of battery based technologies have been developed for different applications. Lead-acid battery technology is quite mature and has a huge market in automotive applications and battery-based uninterrupted power supplies.[19-21] These batteries are quite cheap and robust but at the same time, they have a short cycle-lifetime, are unsuitable for charging at partial state-of-charge and have a limited charging power capability.[19-23] There are advanced versions of these batteries that are currently under development which overcome some of these drawbacks[21-23] but Li-ion batteries have emerged as a more appealing alternative.[21] Due to their high gravimetric and volumetric energy density (75-200 Wh/kg and 200-500 Wh/L respectively), high efficiency and long cycle lifetimes they are currently being used in various electronic devices.[19-21, 24-26] The impact of Li-ion batteries on the society has recently been recognized by the Nobel committee and the 2019 Nobel prize for chemistry was awarded to Akira Yoshino, M. Stanley Whittingham, and John B. Goodenough for their contribution towards the development of Li-ion batteries.[27]

The low abundance of Li (18 ppm in earth's crust)[28] and consequently, the relatively higher costs of these batteries is a deterrent for the wider use of Li-ion batteries.[19] Flow batteries represent another segment of battery technology with the unique advantage of having their power and energy capability decoupled. The energy capability in these batteries depends on the volume and concentration of electrolytes while the power capability depends upon the size of the cell stack allowing for flexible design and easy scale up. There are a number of electrolyte materials used for these batteries – V/H_2SO_4, ZnBr, Br/polysulphide and Fe/Cr couple – and these technologies are at various stages of development.[19, 29, 30]

Chemical fuels provide another means for energy storage and a number of chemicals like NH_3, CH_3OH and H_2 can be used for this purpose. Chemical fuels have the added advantage of decoupled power and energy capabilities when compared with most of the current battery technology. Among these fuels, the use of H_2 as a source of energy storage is quite promising because of high specific energy density of H_2 (33 kWh/kg).[31] It has been argued that the use of batteries is more efficient when compared to the production of H_2 using renewable energy sources.[32] It must be noted however that this study assumed that the final energy is needed at the time of production which prevents a wider applicability of this conclusion. Marchenko and Solomin have argued that to compare the economic efficiency of both technologies in a broader fashion, three key costs need to be taken into account– production, transport and storage costs. They have shown that the electricity based system are indeed more economical when the storage time is short (< 50-110 hours depending upon the source of energy generation) but when the energy needs to be stored for longer periods, the use of H_2 is more economical.[33] Based on this study and the fact that there is only limited amount of Li available on earth (18 ppm in earth's crust)[28], it can be inferred that both technologies need to co-exist. It must be noted that this study assumes that the generated H_2 is being compressed for storage purposes and concerns have been raised about the safety associated with compressed H_2.[34] In this respect, ammonia boranes, metal hydrides and metal borohydrides are currently being investigated as potential materials for safe and economical hydrogen storage.[31, 35-37]

1.3 Hydrogen Generation

For the development of the hydrogen economy (**Figure 1.1**),[38] the problem of H_2 generation also needs to be addressed in addition to the problem of H_2 storage. Current H_2 generation methods rely on the water gas shift reaction and steam reforming reaction both of which rely on fossil fuels.[39-42] For the development of an environment friendly hydrogen economy, electrolysis of water serves as a promising candidate as nuclear/renewable energy can be used to split water photochemically or electrochemically to obtain H_2. This process however, is currently not as economically efficient as the water gas shift reaction. Electrochemically, at pH = 0, water splitting occurs at 1.23 V (vs. reversible hydrogen electrode, RHE) *via* the half-reactions shown below:[43]

$$2H_2O \longrightarrow O_2 + 4H^+ + 4e^- \qquad E_{anodic} = 1.23 \text{ V vs. RHE}$$

$$4H^+ + 4e^- \longrightarrow 2H_2 \qquad E_{cathodic} = 0 \text{ V vs. RHE}$$

$$2H_2O \longrightarrow 2H_2 + O_2 \qquad E_{total} = 1.23 \text{ V}$$

Due to the kinetics of the reaction (which includes transfer of reactants and products towards and away from the electrodes) and the efficiency of the catalyst, there is always an overpotential (η)

associated with both the reactions which means that in practice, the water splitting reaction will occur at a potential higher than 1.23V.[38] Energetically, the bottleneck of water splitting reaction is associated with the oxidation half-reaction or the oxygen evolution reaction (OER) and a significant amount of scientific effort has been directed towards optimising this half-reaction.[44-47]

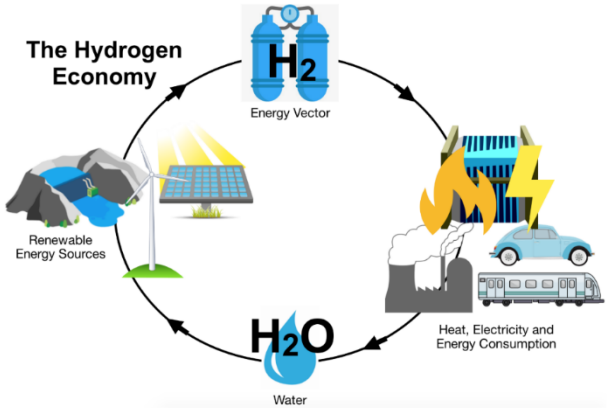

Figure 1.1: A simplified representation of the hydrogen economy.[37]

1.4 PS-II and The Oxygen Evolving Complex (OEC)

One approach for optimising the OER is to study and develop an understanding of how Nature achieves this reaction and mimic it. It has been found that the OER occurs in plants in photosystem-II (PS-II), as part of photosynthesis.[38, 46-52] A significant amount of effort has therefore been dedicated to understanding the mechanism of water oxidation in the PS-II unit.

The PS-II unit, which is located in the thylakoid membrane of green plants, cyanobacterias and algae, can catalyse water oxidation with turnover frequencies (TOFs) of 10^2 sec^{-1}.[53, 54] It is a large membrane-protein complex with a molecular mass of 350 kDa (**Figure 1.2 (a)**). Numerous successful attempts towards crystallizing PS-II have greatly aided our understanding of its complex structure.[27, 55-58] The oxygen evolving complex (OEC) is the active site for water oxidation in PS-II. It is comprised of a distorted $\{Mn_3Ca\}$ cubane unit that has a dangling Mn atom attached to it (**Figure 1.2 (b)**). The Mn centres resides in an octahedral environment while Ca resides in a seven coordinate environment. This core structure is stabilised by oxo-groups and the metal centres are additionally coordinated to O- and N-donors from amino acids. The dangling Mn centre and Ca are further bound to two water molecules each.

The basic mechanism of water oxidation by the OEC can be described by the Kok cycle in which the system cycles between 5 states called the S states (**Figure 1.3**).[59] The OEC resides in its dark stable $\{Mn^{III}_2Mn^{IV}_2\}$ form, which is commonly referred to as the S_1 state. During photosynthesis, the complex oxidises and undergoes structural changes cycling through different intermediate (S_2, S_3 and S_4) states, each of which differs from the others in the number of charge equivalents stored. The structure of the OEC core and the oxidation state of the Mn centres in the various S states is

shown in **Figure 1.3**.[60-63] The removal of protons and electrons throughout the cycle follows a strictly alternating pattern, with all transitions involving a proton loss except the S_1 to S_2 transition.[64-66] In the last metastable state, S_3, all Mn centres are in +IV oxidation state and the transition to the S_4 state is followed by rapid decomposition to the $\{Mn^{III}_3Mn^{IV}\}$ S_0 state and simultaneous evolution of O_2.[49] The structure of the S_4 state and the exact mechanism of the O-O bond formation are still under extensive investigation.[67-70]

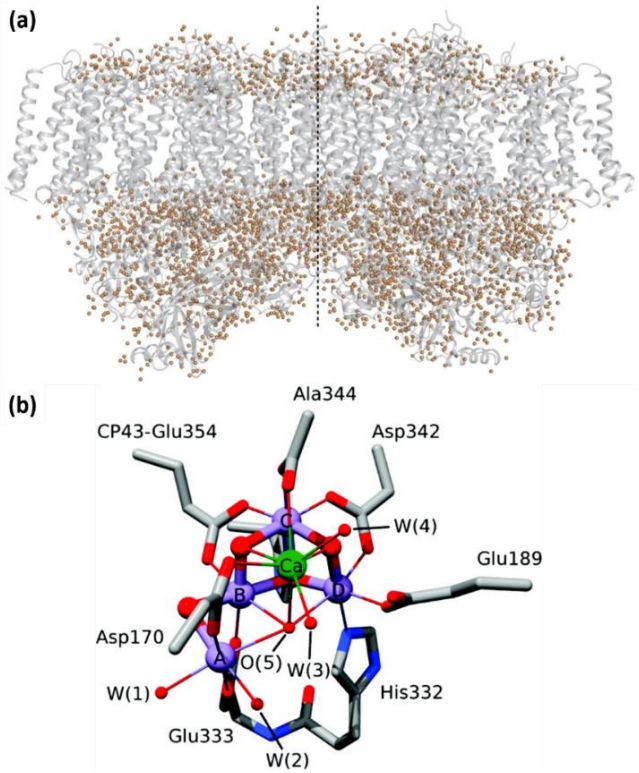

Figure 1.2: (a) Crystal structure of the PS-II unit[27] and **(b)** the active OEC centre[63] within the PS-II unit. Colour scheme: Mn (purple), Ca(green), N(blue), C (grey) and O (red).

The water oxidation half-reaction occurs at neutral pH[71-73] but the harsh oxidising conditions damage the OEC and deactivate it during H_2O oxidation within approximately 30 minutes[74] but owing to self-healing mechanisms, it reconstitutes to catalyse H_2O oxidation for extended periods.[46, 75]

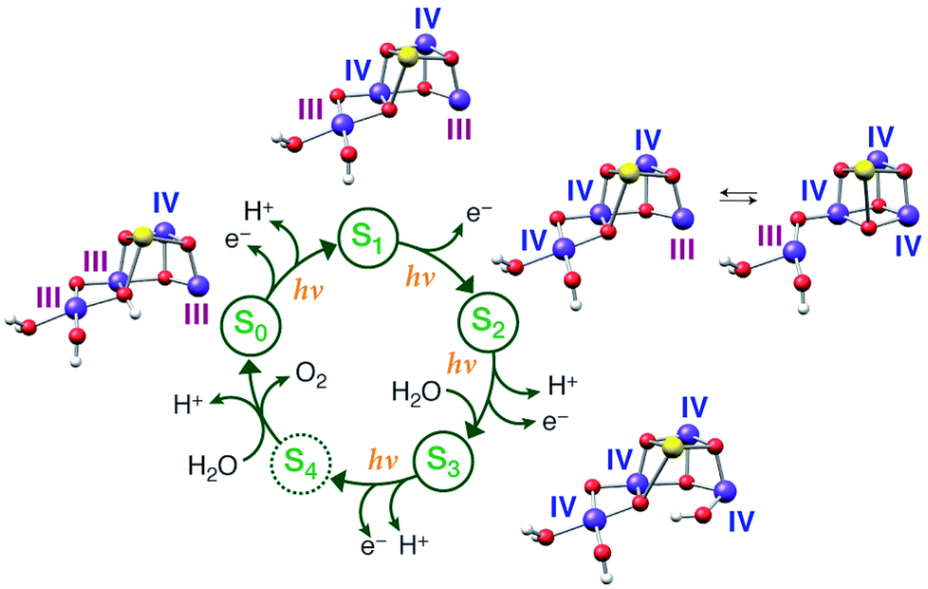

Figure 1.3: The Kok cycle indicating the electron and proton release at each transition and the oxidation state of the Mn centres in the various S states.[62]

1.4.1 Role of Ca

The Ca^{2+} ion forms an integral part of the distorted cubane unit of the OEC and plays a key role in the water oxidation reaction. Its exact role depends upon which stage of the Kok cycle and hence which S state the OEC is in. Dy^{3+} and Cd^{2+} analogues of the OEC do not evolve oxygen but these are able to advance from the S_1 to S_2 state.[76] This suggests that for the S_1 and S_2 state the Ca^{2+} centre primarily contributes in maintaining the structural integrity of the OEC. Additionally, its participation in maintaining a hydrogen bond network and in the delivery of water to Mn has also been suggested.[77, 78]

The Ca^{2+} centre has also been found to be responsible for controlling the hydration environment and the redox potential of the redox active tyrosine (Tyr161 or Y_z, **Figure 1.4**) which is responsible for the oxidation of the Mn centres of the OEC and thus driving the water-oxidation half reaction.[79] The substitution of Ca with metals besides Dy and Cd has been investigated and among these, the Sr analogue serves as the closest OEC mimic.[76, 80-83] Even the Sr analogue however, has been observed to be significantly less active compared to the OEC indicating that Ca is important for achieving water oxidation in the OEC.[81, 84-86] Model complexes with different heteroatoms other than Ca have higher redox potential which suggests that Ca may aid in tuning the redox properties of the OEC and this is also supported by computational investigations.[61, 87-89]

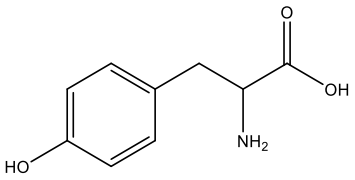

Figure 1.4: Structure of the tyrosine molecule.

1.5 Mimicking the OEC – The Journey So Far

Considerable effort has been dedicated towards mimicking the OEC in the hope of developing efficient catalysts for water oxidation. Early works in this area were focussed on dinuclear complexes[44, 90-94] but a number of {Mn_4} cubane type complexes have now been synthesised.[95-105] Dismukes *et al.* was the first to report a {Mn_4O_4} cubane complex, $[Mn_4O_4(O_2P(C_6H_5)_2)_6]$, that was active for water oxidation (**Figure 1.5 (a)**). This complex is stabilised by phosphinate based ligands and was found to promote water oxidation heterogeneously on application of a voltage of 0.8-1.2 V in the presence of UV-light for 3 days. [97-99, 101] Later however, it was shown that the compound decomposes during the preparation of the electrode and the activity observed was due to Mn based oxides.[106, 107] This does suggest that the identification of the active species can be quite challenging. Two tetranuclear square planar Mn complexes with heptadentate ligands bound by N- and O-donors (**Figure 1.5 (b)**) were reported by Berggren *et al.* that were found to be active for chemical and electrochemical water oxidation.[108] Brudvig and co-workers reported a tetranuclear Mn complex $[\{(H_2O)(terpyridine)Mn^{IV}(\mu\text{-}O)_2Mn^{IV}(terpy)\}_2(\mu\text{-}O)](ClO_4)_6$, that does not have a cubane unit but is essentially a dimer of dimers with the dimers being perpendicular to each other (**Figure 1.5 (c)**).[109, 110] This complex was found to catalyse water oxidation chemically and electrochemically but the active species in this case was found to decompose quite rapidly resulting in the formation of Mn oxide species.[110]

Bonchio and co-workers recently reported a {Mn_4O_3} unit stabilised by acetate bridges and tungstosililcate platforms, $[Mn_4O_3(CH_3COO)_3(A\text{-}\alpha\text{-}SiW_9O_{34})]^{6-}$, that corresponds to the S_0 state of the OEC based on the oxidation state of the Mn centres (**Figure 1.5 (d)**). This complex has been found to be active for photochemical water oxidation achieving TOFs around $5X10^{-4}$ sec^{-1}.[102] A vanadate based {Mn_4O_4} complex reported by Schwarz *et al*., $[Mn_4V_4O_{17}(CH_3COO)_3]^{3+}$, that corresponds to the S_2 state of the OEC has also been found to catalyse water oxidation under visible light conditions (**Figure 1.5 (e)**). The TOF for this complex was found to be 1.75 sec^{-1} which is a significant improvement over the tungstate analogue but this complex also degrades rapidly.[103]

The catalysts described thus far are heterogeneous catalysts and it is only recently that a water soluble Mn based cubane type complex has been reported for homogeneous water oxidation.[104, 105] The complex $[Mn_{12}O_{12}(dhb_{16})(H_2O)_4]$ (dhb=3,5-dihydroxybenzoate) contains a $\{Mn^{IV}{}_4O_4\}$ cubane unit encapsulated in an $\{Mn^{III}{}_8\}$ ring (**Figure 1.5 (f)**). The core structure has been known for a long time[111-113] and a series of structural analogues of this complex have been previously shown to be heterogeneous catalysts for electrochemical water oxidation which can achieve OER at varying overpotentials (640-820 mV) in neutral pH conditions. These systems however, were found to be quite unstable decomposing within minutes.[114] The dodecanuclear complex $[Mn_{12}O_{12}(dhb_{16})(H_2O)_4]$ on the other hand, has been reported to be active for electrochemical water oxidation at pH 6 with an onset overpotential (η_{onset}) of 334 mV. It was found to oxidise water for 3 hours at 91 % efficiency

after which the efficiency decreases.[104] Furthermore, the addition of an extra –OH group at the para- position of the 3,5-dihydroxybenzoate group has been shown to shift the onset overpotential down to a mere 74 mV.[105]

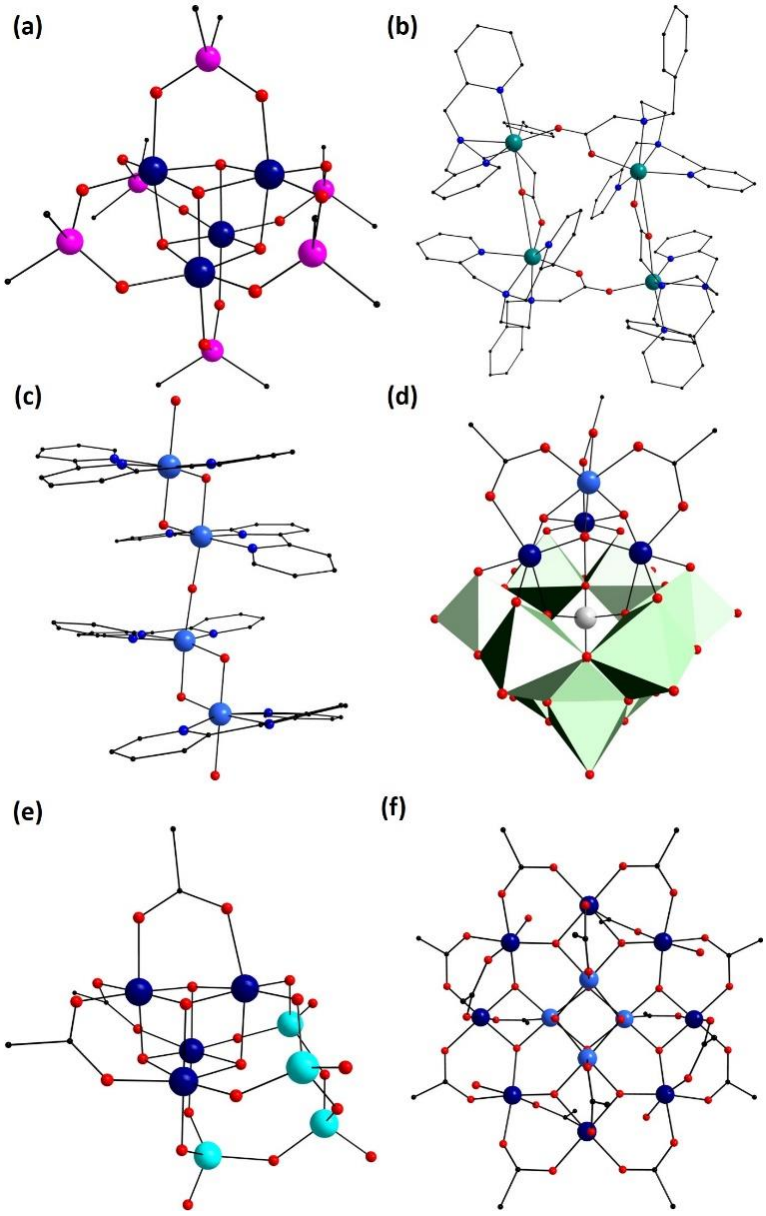

Figure 1.5: Core structure of **(a)** $[Mn_4O_4(O_2P(C_6H_5)_2)_6]$,[97] **(b)** $[L_4Mn_4](ClO_4)_4$ (L=2-((2-(bis(pyridin-2-ylmethyl)amino)ethyl)(methyl)amino)acetic acid),[108] **(c)** $[\{(H_2O)(terpyridine)Mn^{IV}(O)_2Mn^{IV}(terpy)\}_2(O)]$,[109, 110] **(d)** $[Mn_4O_3(CH_3COO)_3(A\text{-}\alpha\text{-}SiW_9O_{34})]^{6-}$,[102] **(e)** $[Mn_4V_4O_{17}(CH_3COO)_3]^{3+}$ and[103] **(f)** $[Mn_{12}O_{12}(dhb_{16})(H_2O)_4]$.[104, 105] Colour scheme: Mn^{II} (teal), Mn^{III} (deep blue), Mn^{IV} (light blue), V (turquoise), Si (grey), P (pink), O (red) and C (black). W octahedra are shown in green.

The decrease in the overpotential for the $\{Mn_{12}\}$ complex has been attributed to the presence of additional –OH groups bound to the aryl substituent which aid in the proton-coupled electron transfers necessary to drive the O_2 formation. This is further supported by an investigation of a series of dinuclear Mn complexes for which the incorporation of a distal carboxyl group was found to promote proton-coupled electron transfers.[115] In both these examples, the presence of proton

acceptors essentially drives the removal of the proton thus facilitating efficient oxidation of water and this idea has been explored previously by others too.[116-119] A very recent study has revealed high activity for electrochemical water oxidation by carbon nanomaterials containing quinone type moieties with an onset potential of 1.50 V *vs.* RHE (i.e. η_{onset} = 270 mV) under basic pH conditions. These have also been shown to achieve current densities as high as 10 mA cm^{-2} at η = 350 mV illustrating their high OER activity.[120] A study employing a Ru based complex has also reported an enhancement in activity in presence of quinone type moieties.[121] This does suggest that the activity observed for the homogeneous $\{Mn_{12}\}$ systems may be enhanced by the inherently active hydroquinone type groups available in close proximity. The activity cannot be completely attributed to the organic moieties however, as the $\{Mn_{12}\}$ core without these groups has been shown to be active for water oxidation.[114]

Considering the important role played by Ca, the development of mixed-metal cubane complexes may be essential for closely mimicking the OEC. Early reports of incorporating Ca^{2+} included a Ca salt of a carboxylate based tetranuclear Mn complex[122] and a mixed Mn-Ca polymer system comprising of octahedrally coordinated Mn(II) species and stabilised by malonate groups and water molecules.[123] Since then, there have been reports illustrating the incorporation of Ca^{2+} in high nuclearity Mn molecular complexes in different geometric arrangements.[124-130] A noteworthy system among these is the tridecanuclear complex $[Mn_{13}Ca_2O_{10}(OH)_2(OMe)_2(O_2CPh)_{18}(H_2O)_4$ reported by Christou *et al.* (**Figure 1.6 (a)**) that contains a cubane core although the overall nuclearity of this complex is still too high to be directly comparable with the OEC unit.[124]

The incorporation of a hetero-metal in cubane geometries has been found to be synthetically difficult and its only recently that a few such complexes have been reported.[87, 89, 131-137] Such a feat was first reported by Agapie and co-workers using a 'rational' synthesis approach where a trinuclear Mn coordination complex was oxidised with superoxide in presence of Ca(trifluoromethanesulphonate)$_2$. This resulted in the formation of $LMn_3CaO_4(OAc)_3$ (H_3L=1,3,5-tris(2-(di(2-pyridyl)hydroxymethyl)phenyl)benzene) (**Figure 1.6 (b)**) that contains the desired $\{Mn_3CaO_4\}$ core with each Mn centre in oxidation state IV.[131] Substitution of Ca^{2+} with Sr^{2+} in this complex reveals that the redox potentials in both complexes are quite similar[87] which is consistent with the observation that OEC is active only when Ca^{2+} or Sr^{2+} are incorporated in the cubane unit.[76, 80-83] Analogues of this complex containing Na^+, Zn^{2+}, Y^{3+}, Sc^{3+} and Mn^{3+} show that the Lewis acidity of the hetero-metal affects the redox potentials of the system with an increase of 90-100 mV per unit increase in the pK_a.[87-89] The presence of Ca in the cubane unit has also been found to allow the incorporation of a dangling Ag centre to the core.[133] The $\{Mn^{IV}_3Ca\}$ core with a dangling Ca centre has also been reported by Mukherjee *et al.* in which the structure is stabilised by *tert*-butyl carboxylate (pivalate) groups (**Figure 1.6 (c)**).[132] The synthesis of this complex relies more on serendipity and is based on self-assembly in contrast to the more rational approach adopted by

Agapie and co-workers.[87, 131, 133] The self-assembly approach has also been demonstrated to drive the synthesis of $[Mn^{IV}_6Ca_2O_9((CH_3)_3CCO_2)_{10}(H_2O)_4]$ which essentially contains three cubane units that share an edge comprised of the Ca centres (**Figure 1.6 (d)**). OER activity with any of these complexes has not been reported.

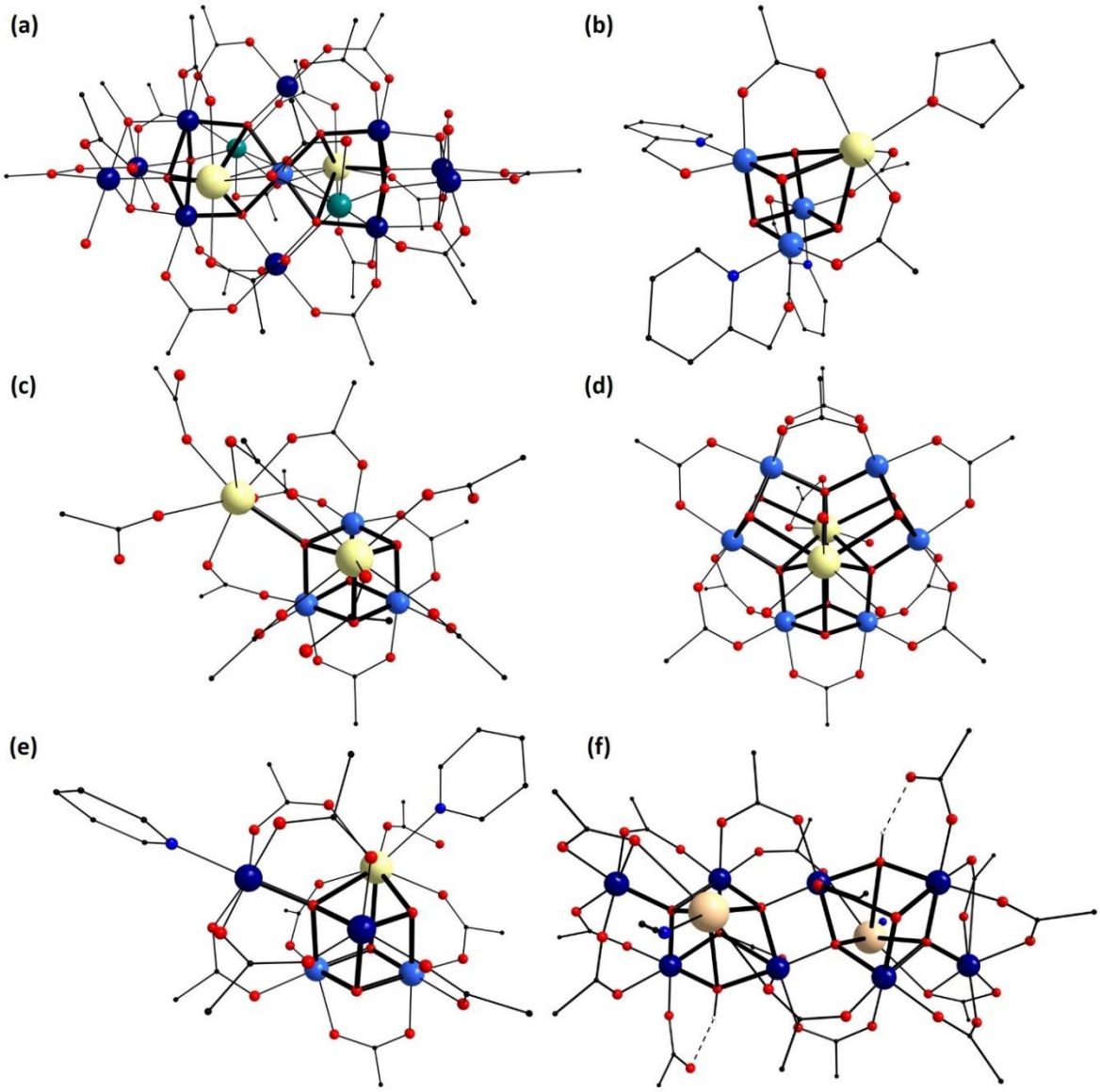

Figure 1.6: Structure of **(a)** $[Mn_{13}Ca_2O_{10}(OH)_2(OMe)_2(O_2CPh)_{18}(H_2O)_4]$,[124] **(b)** $LMn_3CaO_4(OAc)_3$ (H_3L=1,3,5-tris(2-(di(2-pyridyl)hydroxymethyl)phenyl)benzene),[131] **(c)** $[Mn_3Ca_2O_4(O_2CBu^t)_8(Bu^tCO_2H)_4]$,[132] **(d)** $[Mn_6Ca_2O_9(Bu^tCO_2)_{10}(H_2O)_4]$,[134] **(e)** $[Mn_4CaO_4((CH_3)_3CCO_2)_8((CH_3)_3CCO_2H)_2(C_5H_5N)]$[135] and **(f)** $[Mn_8K_2O_4(OH)_2((CH_3)_3CCO_2)_{16}((CH_3)_3CCO_2H)(CH_3CN)]$.[136] Colour scheme: Mn^{II} (teal), Mn^{III} (deep blue), Mn^{IV} (light blue), Ca (light yellow), O (red) and C (black).

Very recently a series of ligand free $Ca_nMn_{4-n}O_4^+$ (n=0–4) cluster ions with varying Ca content have been synthesised by sputtering Mn oxides and binary Ca-Mn oxides with Xe ions. It was observed that $CaMn_3O_4^+$ facilitates partial water oxidation leading to the formation of H_2O_2 and the reaction does not proceed further towards the formation of O_2. The other cluster ions with higher Ca content were found to be capable of only dissociating water. The differences observed in the behaviour of these cluster ions was found to be related to the varying Lewis acidity of these species.[138] Higher

Ca content lead to decreased Lewis acidity and hence, increased redox potentials[138] which is consistent with previous reports.[87-89]

Incorporation of the key features of the OEC namely the mixed-metal distorted cubane unit with a dangling Mn centre attached to it is even more difficult. It is only recently that a complex that captures all these key structural characteristics has been synthesised.[135, 137] The complex $[Mn_4CaO_4((CH_3)_3CCO_2)_8((CH_3)_3CCO_2H)_2(C_5H_5N)]$ (**Figure 1.6 (e)**) contains a $\{Mn_3Ca\}$ distorted cubane unit which has a dangling Mn centre attached to it. This complex has also been synthesised using the serendipitous self-assembly approach and is stabilised by pivalate and pyridine ligands.[135] It has also been demonstrated that the pyridine molecules bound to the Mn centres can be replaced with CH_3CN and $(CH_3)_2NCH$ (dimethylformamide, DMF) molecules.[137] Based on the oxidation states of the Mn centres, this complex can be formally compared with the S_1 state of the OEC. An extensive DFT study using B3LYP functional investigated the analogous S_1 – S_3 states of this synthetic $\{CaMn_4O_4\}$ system and confirms the oxidation states of the metal centres.[139] This complex has been suggested to be able to access the analogous S-states in non-aqueous solvent electrochemically. Catalytic water oxidation however, has not been reported for this distorted, mixed-metal cubane complex.[135] This system is topologically different from the OEC as the dangling Mn atom is attached to the cubane unit by one oxo-bridge in this complex, while in the OEC, it is linked by two oxo-bridges.[140] The possible lack of activity *via* this complex has been attributed to the absence of the additional oxo-bridge as it may allow the dangling Mn to completely detach from the cubane and hence render the system inactive.[141]

A dimeric mixed-metal distorted cubane system containing dangling Mn centres $[Mn_8K_2O_4(OH)_2((CH_3)_3CCO_2)_{16}((CH_3)_3CCO_2H)(CH_3CN)]$ (**Figure 1.6 (f)**), has also been reported recently and investigation of its electrochemical behaviour in aqueous media reveals that Mn based oxides, and not the complex, serve as the active species for water oxidation.[136]

From the above discussion, it can be seen that a lot of progress has been made with regards to developing structural mimics of the OEC. However, a structural mimic of the OEC capable of catalysing the water oxidation half-reaction of water splitting is yet to be developed.

1.6 Accomplishing Water Oxidation – Other Explored Avenues

Considering that Nature uses a Mn based molecular catalyst to accomplish water oxidation, the obvious path to pursue seems to be the development of molecular Mn based complexes. Other approaches however, have also been implemented and these include the use of other transition metal based coordination complexes[44] and metal oxides[45] some of which show reasonable catalytic activity. Since the OER can be achieved chemically, photochemically and electrochemically, different materials have been investigated using different conditions which makes it impossible to compare the activity of all materials relative to each other. It is still possible to compare activity of

materials investigated for OER activity using the same mode of operation and under similar conditions, and the following discussion briefly reviews some of the key highlights in this area.

1.6.1 Water oxidation using metal oxides and the influence of the pH

The pH of the solution affects the activity and stability of catalysts and thus, the catalytic activity of materials is generally investigated in three pH regimes – acidic (pH ~0 – 6), neutral (pH ~6 – 7.5) and basic (pH > ~7.5). In acidic media, hydrogen production is easier since the proton concentration is higher.[142, 143] The Ir based oxides serves as best catalyst for the OER achieving current densities of 10 mA cm^{-2} at overpotentials of 270-290 mV in acidic media[144, 145] and the activity of these material surpasses that of Ru based oxides which are also less stable than the former.[146, 147] The activity of Ir and Ru based oxides is reasonable and these materials can be implemented in devices but the scarcity of these materials prevent large scale applications. These materials are therefore used as benchmarks for assessing activity of the other catalytic materials.[148] Thus, most studies focussing on the OER activity of metal oxides aim to achieve a current density of 10 mA cm^{-2}. For studies investigating coordination complexes however, the target current density is generally 1 mA cm^{-2}. This is primarily because most coordination complexes are structurally less robust compared to metal oxides.

OER in basic media is quite attractive as it is relatively easier to achieve under these conditions and because 3d-transition metal oxides generally show high activity in basic media.[149-151] OER in basic media however, suffers from one major drawback – carbonation. The excess hydroxyl ions can react with the atmospheric CO_2 or the CO_2 dissolved in the electrolyte solution to form carbonate salts resulting in the decrease of the pH of the solution.[142, 152]

Considering that OER occurs in Nature at neutral pH, water splitting at neutral pH has also gained a lot of attention. Additionally, durability and regulatory issues make the use of neutral aqueous media more attractive from an application point of view.[153]

1.6.1.1 Mn oxides

Since Nature uses Mn to catalyse water oxidation, it is only natural to investigate Mn based materials for achieving OER and hence Mn oxides have been studied quite extensively. Among the various Mn oxides, MnO_2 has been found to be inactive while the activity of the other Mn oxides has been found to vary significantly depending upon the polymorph under investigation.[154] Additionally, the activity of Mn oxides has been found to be dependent on the choice of method employed for investigating the OER activity – chemical, photochemical or electrochemical.[155] Mn oxides have been found to be quite stable under acidic conditions but the OER activity for these is quite low and above an overpotential of ~300 mV, the Tafel slope obtained was found to vary between 365-851 mV/decade which suggests poor catalytic activity.[156] The low activity can be

attributed to the instability of Mn(III) sites below pH 9.[157] This has been further supported by a 25 fold increase in the turnover frequency (TOF, number of catalytic cycles occurring per catalyst site per unit time) under chemical oxidation conditions at pH 1 when the Mn(III) sites are stabilised.[158] This is also supported by the increase in activity (at pH 8) observed when Mn(III) sites residing in tetrahedral environments are introduced in electrodeposited MnO_2 which suppresses the disproportionation of Mn(III) to Mn(II) and Mn(IV).[159] Additionally, cycling the potential of MnO_2 polymorphs has been found to introduce Mn(III) sites which enhances the OER activity.[160, 161] Formation of nanolayered Mn oxide using Li^+ electrolyte has also been shown to be a strategy to stabilise Mn(III) sites.[162]

Mn based oxides have also been explored for OER catalysis under neutral pH conditions and they show some promise.[163] The stabilisation of Mn(III) sites in defective layered MnO_2 allows for reasonable OER activity (8.2 mA cm^{-2} at η = 580 mV) for over 20 hours at neutral pH.[164] The addition of carbon nanotubes to MnO_2 has also been reported to enhance the OER activity at pH 5.6 under photocatalytic conditions achieving TOFs of 5.4 X 10^{-4} sec^{-1} per Mn site.[165] The synthesis conditions for MnO_x have been found to affect the activity and stability significantly.[160, 166-169] Doping with Mo and W has also been found to significantly enhance the OER activity.[170, 171]

In basic media Mn_2O_3 has been shown to display OER activity achieving 10 mA cm^{-2} of current density at overpotentials as low as 340 mV by tuning the thickness of the films.[172] Reasonable photoelectrochemical activity with MnO_x has also been demonstrated although in this case, the formation of H_2O_2 is also observed.[173]

1.6.1.2 Co oxides

Nanostructured Co_3O_4 have been shown to exhibit reasonable activity under acidic conditions achieving 10 mA/cm^{-2} at η = 570 mV but they tend to dissolve and degrade after 12 hours.[174] The OER activity of fluorine doped CoO_x has been investigated in the pH range 0-14 and it has been found to behave as a homogeneous catalyst at low pH (< 3.5) producing H_2O_2 and a heterogeneous one yielding O_2 at higher pH.[175] CoO_x in a phosphate buffer has been found to be an active self-healing catalyst for water oxidation under neutral pH conditions achieving a current density 1 mA cm^{-2} at η = 410 mV .[176, 177] The catalyst essentially comprises of CoO(OH) species stabilised by phosphate ions and is often referred to as "CoP_i".[178] The phosphate ions facilitate the seal-healing process by capturing the Co ions in solution and immobilising them on the electrode surface. The role of phosphate ions has been shown to be mainly structural although they have been observed to aid the proton transfer steps thereby improving the kinetics of the process.[179-181] A similar material prepared using methyl phosphonate has also been shown to achieve a current density of 100 mA cm^{-2} at η = 363 mV and 442 mV in borate (pH 9.2) and phosphate (pH 7) buffer solutions respectively.[182]

In basic media, defective Co_3O_4 has been reported to display OER activity achieving 10 mA cm^{-2} current density at 268 mV of overpotential.[183] The activity of Co based oxides and hydroxides is enhanced in presence of Fe impurities[184] and more so in the presence of a third metal.[185]

1.6.1.3 Fe oxides

Fe oxides are quite attractive for OER application because they are cheap.[186] Recently, mixed polymorph films of α- and γ-Fe_2O_3 (hematite) with high activity in acidic media have been reported. These films can achieve a current density of 10 mA cm^{-2} at η = 650 mV and have been found to be stable under the OER conditions for more than 24 hours.[187] OER activity has also been observed with thin films of iron oxide (1 mA cm^{-2} at η = 480 mV) and iron oxyhydroxide (10 mA cm^{-2} at η = 600 mV) at neutral pH.[188, 189]

FeO_x films have also been found to be active in basic media and the kinetics of this reaction have been investigated extensively.[190-192] Due to the smaller band gap of Fe_2O_3 (2.1 eV), photoelectrochemical water oxidation using Fe_2O_3 has also been investigated under alkaline conditions (pH > 10).[193, 194] The maximum photocurrent obtained however, has found to be < 20% of the theoretical value.[195-197] The photoelectrochemical and photocatalytic activity of Fe_2O_3 can be enhanced by decreasing the particle size to the nanoscale.[198-200]

1.6.1.4 Ni oxides

Ni oxides are stable in basic medium and hence their OER activity is generally investigated in alkaline media although a few studies at near-neutral pH have been conducted.[201-203] Ni oxides have been found to be quite active for water oxidation under basic conditions (1 mA cm^{-2} at η = 425 mV)[204, 205] and the activity is heavily dependent on the preparative method.[206-208] The OER activity of Ni based oxides and hydroxides is particularly enhanced in presence of Fe impurities.[184, 209-211] Like Co, the presence of a third metal was found to increase the activity even further.[185]

1.6.1.5 Mixed metal oxides

The synergistic effects of additional metals have already been highlighted for Co and Ni oxides and similar behaviour is observed for other metals as well. The presence of Mn and Ca in the OEC has focussed a lot of attention on mixed Mn-Ca oxides. A study conducted on layered Mn oxides with various alkali and alkaline earth metals incorporated between the layers reveals that the highest activity is observed for Mn-Ca oxides with the second best being Mn-Sr oxides which is consistent with what has been observed for the OEC[212] and is in agreement with another study comparing Mn_2O_3 and $CaMn_2O_4$.[213] Mixed Mn-Ca oxides have also been shown to be quite stable in acidic conditions and the observed activity (1 mA/cm^{-2} at η > 700 mV) has been found to be better compared to that observed in neutral and basic media.[214] Additionally the OER activity of calcium

manganese oxide has been found to be dependent on how the oxide material was prepared.[215, 216] Mn-Ca oxide has also been incorporated into a peptide matrix[217, 218] which has been found to influence the redox properties of the oxide[218] and also results in the initiation of the OER at low overpotential (240 mV).[219]

Mixed CoMn and CoFePb oxides have been shown to be stable catalysts under acidic conditions with the latter being more stable (> 50 hours) and approaching relatively higher activities (1 mA cm^{-2} at η > 700 mV) compared to CoMn oxide. Interestingly, the CoMn oxide has been found to be more active than MnO_x and more stable that CoO_x towards water oxidation thereby illustrating the synergistic effect of mixed metal oxides.[220] Recently, nickel-manganese-antimonate ($Ni_xMn_{1-x}Sb_{1.6-1.8}O_y$) has also been shown to be quite stable (168 hours) under acidic conditions but the overpotentials required to achieve reasonable activity (10 mA cm^{-2}) is still quite high (735 ± 10 mV).[221]

A double perovskite containing Ba, Sr, Co and Fe in the stoichiometry 0.5:0.5:0.8:0.2 has been found to be more active for OER in alkaline media than IrO_2 (10 A g^{-1} at η ~ 300 mV).[150] This double perovskite however, is not as stable as IrO_2. The stability problem has been tackled using rare-earth based double perovskites, $(Ln_{0.5}Ba_{0.5})CoO_x$ that are as active as their transition metal analogue (10 mA cm^{-2} at η ~ 330 mV) but are more resistant to degradation under the harsh OER conditions (stable for > 2hrs at 5 mA cm^{-2}).[151] Ca containing FeO_x have also been shown to exhibit OER activity (10 mA cm^{-2} at η ~ 650 mV) although it tends to decompose gradually.[222] Doped $SrTiO_3$ has also been found to be quite active for photocatalytic OER at neutral pH (pH = 6.8) achieving solar energy to hydrogen conversion efficiency > 1%.[223] Al doped $SrTiO_3$ with rhodium chromium oxide as a co-catalyst has recently been shown to be active for photocatalytic OER at neutral pH (solar energy to hydrogen conversion efficiency > 0.3%) and continues to be active for more than 1000 hours.[224]

1.6.2 Water oxidation using molecular catalysts

Metal oxides show promising catalytic OER activity but due to lack of exact structural and electronic information, it is difficult to optimise these materials.[45] In this respect, molecular catalysts provide a platform to investigate the mechanistic aspects of the OER and to systematically improve upon the current catalytic materials. In addition, they provide the opportunity to tune the electronic environment of the active site to enhance selectivity. Since molecular complexes can potentially be used as homogeneous catalysts, they also provide a 100% metal utilisation which is unachievable by heterogeneous catalyst making them quite appealing for catalytic applications.[225] Additionally, since the natural OEC is comprised of a molecular catalyst, a lot of attention has been directed towards the synthesis of molecular catalysts for water oxidation.[44, 226] The following discussion briefly reviews some of the noble metal and earth abundant metal based complexes reported in recent years.

1.6.2.1 Ru and Ir based molecular catalysts

The first example of a molecular water oxidation catalyst was a Ru based complex $[Ru^{III}_2(\mu\text{-}O)(H_2O)_2(bpy)_4]^{4+}$ (**Figure 1.7 (a)**), reported in 1982 and often referred to as the 'blue dimer' due to its distinctive blue colour. This complex can split water at low pH in presence of ceric ammonium nitrate as an oxidant and is comprised of a Ru dimer bridged by an oxo-group and stabilised by bipyridine ligands and water molecules.[227, 228] The turnover number (TON, maximum number of catalytic cycles occurred per catalyst site) and turnover frequency (TOF) for this complex were found to be 13.2 and 4.2 X 10^{-3} s^{-1} respectively for chemically assisted water oxidation. Structural, kinetic and computational studies reveal that the OER occurs via four proton coupled electron transfer steps that facilitate the formation of $Ru^{V,V}$ intermediate which is attacked by an additional H_2O molecule generating hydroperoxide species which is subsequently oxidised to O_2 by the second Ru centre.[229-242] Furthermore, phosphonate derivatives of this complex and a terpyridine analogue of this complex have also been investigated although their activity has been found to be inferior to that of the blue dimer.[243-247]

Another dinuclear Ru complex $[Ru_2(OH_2)_2(bpp)(tpy)_2]^{2+}$ (Hbpp = bis(2-pyridyl)pyrazole, tpy = 2,2':6',2"-terpyridine) (**Figure 1.7 (b)**), has been reported to be a better catalyst than the blue dimer in acidic media with a TON and TOF of 18.6 and 1.4 X 10^{-2} s^{-1} respectively.[248] This has been followed by a series of dinuclear Ru complexes that have also been found to be more active than the blue dimer in acidic media achieving turnover numbers as high as 3200 although the TOFs are relatively lower.[249, 250] Another series of dinuclear Ru complexes and their corresponding tetranuclear analogues that are essentially dimer of dimers have also been reported. These systems have been found to be active for water oxidation in acidic conditions with some of them being more active than the blue dimer. The higher nuclearity of the tetranuclear complexes does not enhance the OER activity.[251] The use of neutral ligands instead of anionic ligands on the other hand, has been found to decrease the overpotential required for the OER.[252, 253]

In addition to dinuclear Ru complexes, mononuclear complexes have also been shown to be quite active for water oxidation. The first series of these complexes comprised of tridentate polypyridyl type ligand, 2,6-di(1,8-naphthyridin-2-yl)pyridine, with uncoordinated napthyrine nitrogen atoms and an example of these is trans-$[Ru(L)(4\text{-Methyl-pyridine})_2(H_2O)]^{2+}$ (L=4-tert-Butyl-2,6-di([1',8']-naphthyrid-2'-yl)pyridine) (**Figure 1.7 (c)**). The water molecule bound to the Ru centre is further involved in hydrogen bonding with the free N-donors and this complex can catalyse water oxidation achieving a TON and TOF of 580 and 3.5 X 10^{-4} s^{-1}.[249] Synthesis of similar complexes with modified ligand backbones has shown that complexes with ligands that tend to stabilise Ru(III) show higher catalytic activity but lower TONs.[254] Mechanistic studies confirm that for these systems, water oxidation occurs *via* single-site catalysis.[255] Using analogues of 2,2'-bipyridine and 2,2':6',2''-terpyridine type ligands, further insight into the dependence of catalytic activity on the electronic

structure has been obtained. The presence of electron withdrawing group was shown to decrease the catalytic activity but increase TONs and hence the stability, and the effects were found to be more pronounced when the bipyridine ligand was modified.[256]

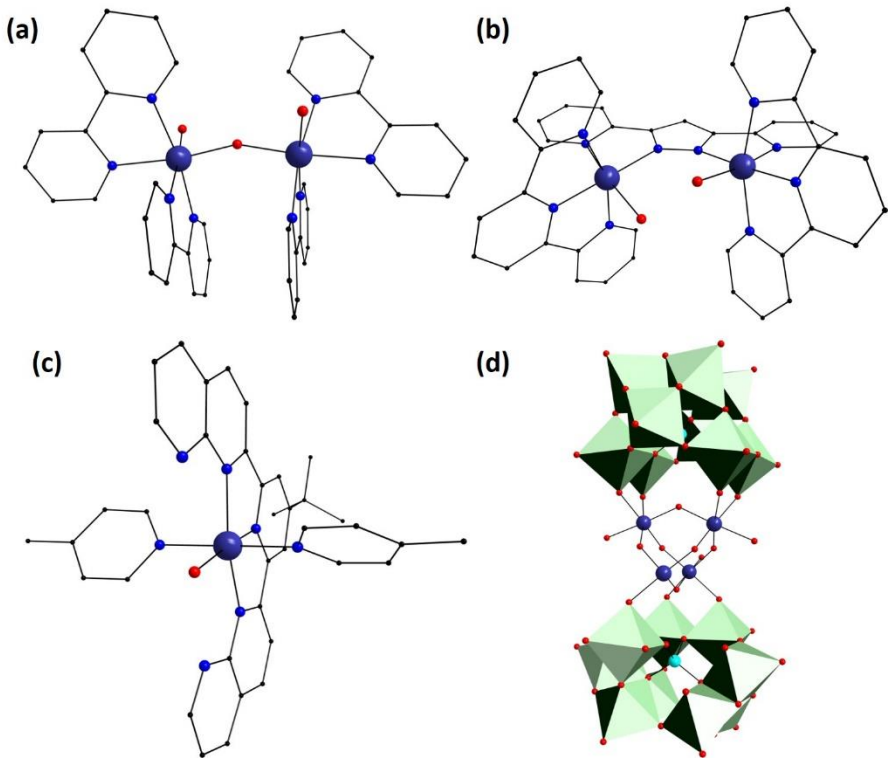

Figure 1.7: (a) Structure of $[Ru^{III}_2(\mu\text{-}O)(H_2O)_2(bpy)_4]^{4+}$,[44, 227] **(b)** $[Ru_2(OH_2)_2(bpp)(tpy)_2]^{2+}$,[44, 248] **(c)** trans-$[Ru(L)(4\text{-Methyl-pyridine})_2(H_2O)]^{2+}$ [249] and **(d)** $[\{Ru_4O_4(OH)_2(H_2O)_4\}(\gamma\text{-}SiW_{10}O_{36})_2]^{10-}$.[226, 257] Colour scheme: Ru (indigo), Si (turquoise), O (red), N (blue) and C (black). W octahedra are shown in green.

As the organic ligands can potentially decompose under the harsh OER conditions, Ru complexes stabilised by polyoxometalates have also been reported for homogeneous water oxidation.[257-263] Among these, $[\{Ru_4O_4(OH)_2(H_2O)_4\}(\gamma\text{-}SiW_{10}O_{36})_2]^{10-}$ (**Figure 1.7 (d)**), has been found to be the most active achieving TON of 500 and TOF > 450 $hour^{-1}$ under chemical oxidation conditions using ceric ammonium nitrate at pH = 0.6.[258] This complex has also been attached to conductive surfaces by immobilising it on carbon based materials bound to the surfaces and has been found to show OER activity in neutral pH solutions above η_{onset} = 300-350 mV depending upon the carbon material used.[264-266]

Mononuclear Ir complexes with N-donor based ligands and pentamethylcyclopentadienyl ligands (Cp*) have been extensively investigated for catalysing the OER[267-271] although decomposition to Ir based oxide nanoparticles has been observed with some complexes.[272] This is especially highlighted in the case of Ir complexes with Cp* and functionalised 2,2'-bipyridine ligands where Ir hydroxide nanoparticles were observed particularly in case of the –OH functionalised complexes.[273, 274] The decomposition of these complexes to oxide nanoparticles makes it challenging to identify the true catalyst.

1.6.2.2 Co based molecular catalysts

A few mononuclear Co complexes stabilised by pthalocyanine,[275] corrole[276, 277] porphyrin[278, 279] and other polydentate N-donor based ligands[280] have been found to be active for water oxidation. The pthalocyanine complex has been found to be active in basic media (pH = 11) under photocatalytic conditions (using a bias potential of 0.3 V) [275] while the corrole complexes have been studied at neutral pH under electrochemical conditions for OER activity (η_{onset} > 530[277]/600[276] mV). The porphyrin based complexes have been identified as active catalyst under both photochemical (pH = 11, TOF = 0.17 s^{-1})[279] and electrochemical conditions (pH = 7, η_{onset} ~ 1 V) [278] although decomposition of such systems to form the corresponding oxide species has also been reported.[281] Furthermore, dinuclear complexes structurally similar to the Ru systems have also been synthesised and demonstrated to be active for electrochemical water oxidation in acidic media (pH = 2.1) η_{onset} > 735 mV.[282] Other dinuclear complexes active for electrochemical water oxidation in basic media have also been investigated.[283] Additionally, Co based polyoxometalates have been investigated for their water oxidation properties in the recent years.[284-293] Essentially, a $\{Co_4\}$[284, 287, 292] and a $\{Co_9\}$[285, 286, 288-293] moiety sandwiched between polyoxometalate units have been employed (**Figure 1.8 (a)** and **(b)**) for this purpose and the latter has been shown to be exhibit activity similar to that of IrO_2 in acidic media (1 mA cm^{-2} at η = 189 mV).[290]

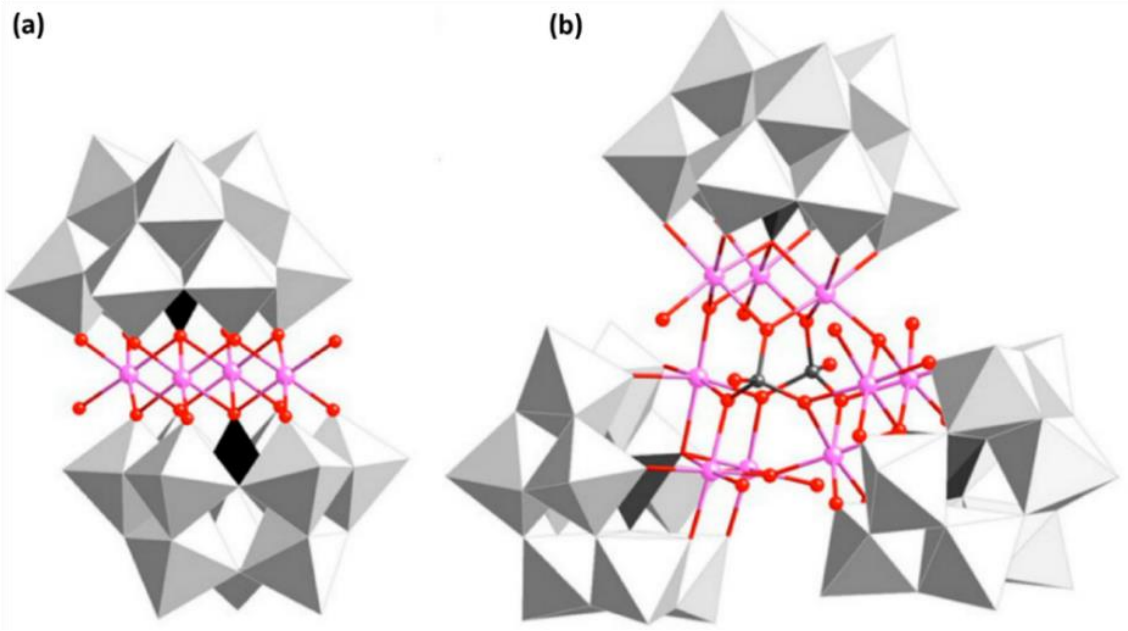

Figure 1.8: Representation of the **(a)** $\{Co_4\}$ and **(b)** $\{Co_9\}$ units of the Co based polyoxometalates.[285] Co is shown in pink and O is shown in red. The grey polyhedra represent the $\{WO_6\}$ units and the black polyhedra represent the $\{PO_4\}$ unit.

1.6.2.3 Fe based molecular catalysts

Fe based complexes capable of oxidising water are rare and it was only in 2010 that the first such complex was reported. This complex comprises of a macrocyclic tetraamido that encapsulates a Fe centre which is bound to a water perpendicular to the plane of the tetraamido ligand (**Figure 1.9 (a)**) and it can catalyse water oxidation in acidic media using chemical oxidants (ceric ammonium nitrate). A series of such complexes was made by changing the functional groups at the periphery of the tetraamido group and the complex shown in **Figure 1.9 (a)** was found to be the most active oxidising water with TOFs > 1.3 s^{-1}.[294, 295] This report was followed by another series of mononuclear Fe complexes with tetradentate and pentadentate ligands that show OER activity in acidic media under chemical oxidation conditions reaching TONs > 1000 and TOFs > 800 h^{-1}.[296] With polydentate N-donor based ligands, other mononuclear Fe complexes have also been reported to be active for water oxidation.[297-299] It has been observed that for this type of complexes, water oxidation is derived from the molecular species at lower pH while at higher pH the Fe oxide nanoparticles are responsible for the OER activity.[300] A dinuclear Fe complex comprising of Fe centres bridged by an oxo-group and further stabilised by pentadentate N-donor based ligand has also been reported as a homogeneous water oxidation catalyst under electrochemical conditions (η_{onset} = 300-400 mV).[301] A highly active pentanuclear Fe complex stabilised by tetradentate N-donor groups (**Figure 1.9 (b)**) has also been reported that is active in the pH range of 2-9 (TOF > 1900 sec^{-1}) albeit at high overpotentials of 500-900 mV.[302] It has been observed that for this complex, the introduction of electron donating groups leads to a decrease in the onset overpotential.[303]

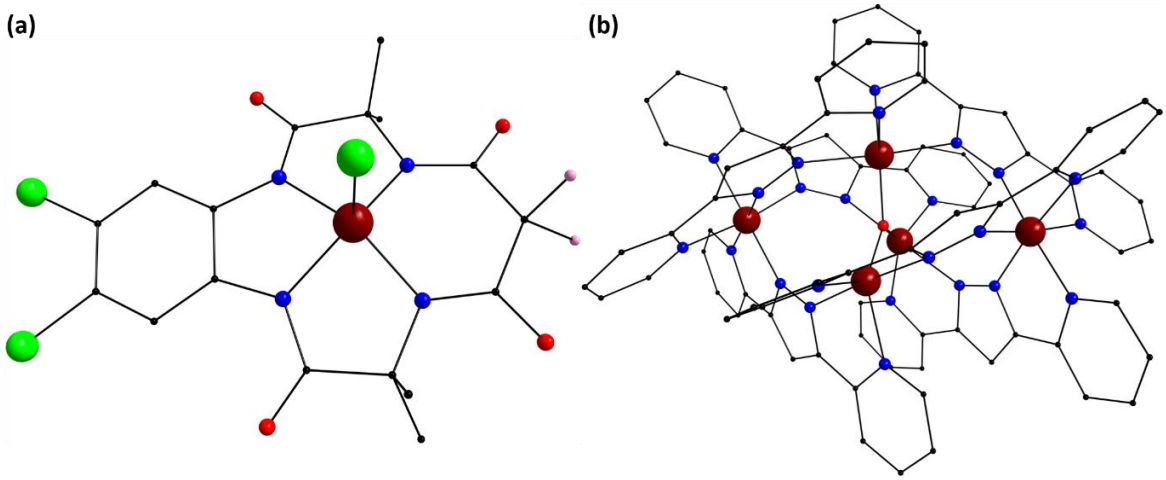

Figure 1.9: Core structure of **(a)** the first Fe based water oxidation catalyst[294, 295] and **(b)** the pentanuclear Fe catalyst.[302] Colour scheme: Fe (dark red), Cl (green), F (rose), O (red), N (blue) and C (black).

1.6.2.4 Ni and Cu based molecular catalysts

All reported Ni water oxidation complexes are mononuclear and based on polydentate nitrogen ligands[304-313] and except for two complexes which achieve water oxidation at η_{onset} ~180 mV (pH = 7),[304, 305] the overpotential to achieve water oxidation in each case is quite high (η_{onset} = 450-750 mV).

Cu complexes of varying nuclearity have been reported for being active for OER.[314] Salts of $[Cu(OH)_2(2,2'\text{-bipyridine})]_2^{2+}$ have been shown to be active for water oxidation in basic media with high a TOF of 100 s^{-1} although the overpotential required is also quite high (750 mV).[315] Incorporating the bipyridine group into a peptoid type ligand also allows the formation of a similar complex and the catalytic properties are not affected much by such a change (overpotential of 800 mV at pH 11.5).[316] In slightly basic media (pH 8), a mononuclear Cu complex stabilised by [Cu(*N*,*N*-bis(2-(2-pyridyl)ethyl)pyridine-2,6-dicarboxamidate)] (**Figure 1.10 (a)**) has been shown to be an active catalyst although the overpotential is still quite high (~650 mV).[317] Cu based porphyrin complex have been shown to be active for water oxidation at relatively low overpotentials in alkaline (350 mV for 1 mA cm^{-2} and 450 mV for 10 mA cm^{-2})[318] and neutral media (310 mV for 0.1 mA cm^{-2}).[319] Other mononuclear Cu complexes with polydentate N-donor based ligand have also been shown to be active for water oxidation.[320, 321] Two structurally similar trinuclear complex stabilised by 6-pyridinecarboxylate groups and phosphonate groups have also been reported for water oxidation at neutral pH at η_{onset} ~800 mV.[322] A tetranuclear cubane type Cu complex $[Cu_4(\text{pyridine-2,6-dimethoxy})_4(\text{acetate})_2]^{2+}$, with a $\{Cu_4O_4\}$ core has also been described (**Figure 1.10 (b)**). The Cu centres are coordinated to acetate and pyridine-2,6-dimethanol groups and can catalyse water oxidation at η_{onset} ~400-665 mV in basic media.[322]

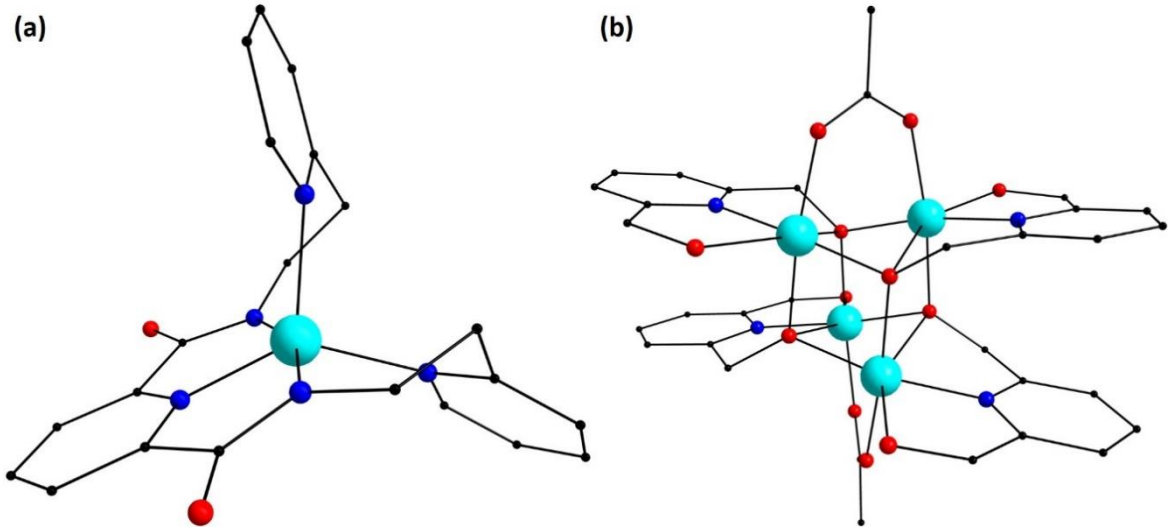

Figure 1.10: Structure of **(a)** [Cu(*N*,*N*-bis(2-(2-pyridyl)ethyl)pyridine-2,6-dicarboxamidate)][317] and **(b)** $[Cu_4(\text{pyridine-2,6-dimethoxy})_4(\text{acetate})_2]^{2+}$.[322] Colour scheme: Cu (turquoise), O (red), N (blue) and C (black).

1.7 Magnetism

The magnetic properties of materials arise from the inherent nature of the electron and how the electrons interact with each other and with the external environment. An electron is a moving charged particle with an associated spin and orbital angular momentum due to which it produces a magnetic field (magnetic moment).[323] If there are two electrons present, then they can spin either parallel or anti-parallel to each other. If they align parallel to each other in presence of a magnetic field, they are attracted by the magnetic field giving rise to what is referred to as paramagnetism. If the electrons spin anti-parallel to each other, they tend to weakly repel the applied magnetic field and this phenomenon is known as diamagnetism. Paramagnetic materials therefore, possess unpaired electrons which is not the case for diamagnetic materials. Paramagnetic materials can be further divided into different categories depending upon how the spins on the constituent units of the material interact with each other (**Figure 1.11**). The parallel or anti-parallel alignment of spins gives rise to ferromagnetism and antiferromagnetism respectively. Ferrimagnetism is a special case of antiferromagnetism where there is a net magnetic moment due to unequal magnitude of the individual magnetic moment of the interacting units.[324]

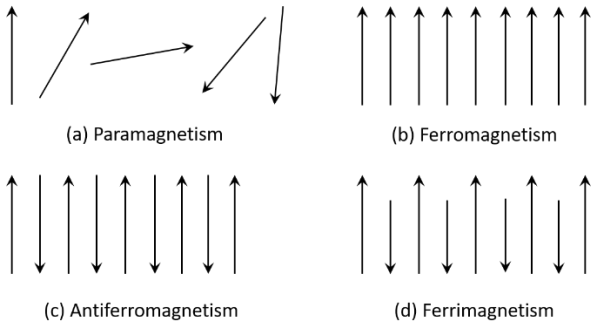

Figure 1.11: Different categories of paramagnetism.[324]

To investigate the magnetic properties of a material, its response to an external magnetic field is determined. In the presence of a homogeneous magnetic field H, one mole of the material under consideration gets magnetised and acquires a molar magnetisation or molar magnetic moment M which is related to H as:[325]

$$\frac{\partial M}{\partial H} = \chi \tag{1.1}$$

Where χ is the molar magnetic susceptibility. χ is comprised of two components – the diamagnetic component χ^D, which is negative, and the paramagnetic component χ^P, which is positive – and is related to them as:

$$\chi = \chi^D + \chi^P \tag{1.2}$$

χ^P is independent of the applied field but varies with temperature while χ^D is independent of both. χ is a measurable quantity and is generally determined using a superconducting quantum

interference device (SQUID) magnetometer in which the movement of the sample induces a current which is measured and then related to the magnetic susceptibility of the material.

Once χ is determined, it can be used to investigate the electronic structure of the material. For this purpose, the diamagnetic part (χ^D) is subtracted from χ to determine χ^P(denoted as χ from here on). Using the Boltzmann distribution law and noting that the magnetisation is related to the variation of the energy with the applied field, the magnetisation can be described as:[325]

$$M = \frac{N\sum_n(-\frac{\partial E_n}{\partial H})\exp(-\frac{E_n}{kT})}{\sum_n \exp(-\frac{E_n}{kT})} \quad (1.3)$$

Where N is the Avogadro number, E_n is the energy of the nth energy level among the various M_S states where M_S is the magnetic quantum number, n is the number of M_S states in the system, T is the temperature and k is the Boltzmann constant (= 0.69504 cm^{-1}K^{-1}). Using equations 1.1 and 1.3 and simplifying gives the following description of χ:

$$\chi = NkT(\frac{\partial^2 \ln Z}{\partial H^2}) \quad (1.4)$$

where $Z = \sum_n \exp(-\frac{E_n}{kT})$. Since this equation requires a knowledge of all E_n energy levels and all $\frac{\partial E_n}{\partial H}$ derivatives, it has no practical use. Van Vleck proposed a simplification to the above equation using the approximation $\frac{H}{kT} \ll 1$ in which case χ can be given as:[325, 326]

$$\chi = \frac{N\sum_n(\frac{E_n^{(1)2}}{kT} - 2E_n^{(2)})\exp(-\frac{E_n^{(0)}}{kT})}{\sum_n \exp(-\frac{E_n^{(0)}}{kT})} \quad (1.5)$$

Where $E_n^{(x)}$ is the x^{th} derivative of the energy level E_n with respect to the magnetic field H. The above formula is known as the Van Vleck formula. Using this formula, the electronic picture can be related to the molar magnetic susceptibility of the material.

The observed magnetic properties are a collective representation of different effects which further depend upon the nuclearity of the system under investigation. It must be noted that in this discussion, the nuclearity is defined as the number of paramagnetic centres in a molecule. For mononuclear complexes, the contributing effects in the decreasing order of their strength are interelectronic repulsion in the valence shell, ligand field effects, spin-orbit coupling and the Zeeman effect. The first two effects are mainly related to how the electrons interact with each other in presence of a ligand field and these effects can be of similar magnitudes. The presence of spin and orbital angular momentum of electrons gives rise to a total angular momentum which also influences the magnetic properties of the material. Whenever a material has more than one unpaired electrons (i.e., the multiplicity S > ½), the combined effects of ligand field and spin-orbit coupling can partly remove the degeneracy of the states denoted by the magnetic quantum number M_s. Such a removal can occur even in the absence of a magnetic field which is why this phenomenon

is known as zero-field splitting.[327] Zero-field splitting gives rise to anisotropy in the system which is quite important for the study of single molecule magnetism.[328-332] The Zeeman effect essentially takes into account the variation of the magnetic properties with the magnetic field and is the smallest of all the effects.[327]

In polynuclear complexes, the paramagnetic centres interact with each other which also affects the magnetic behaviour of the material and this interaction is known as the exchange interaction. This interaction tends to align the spins parallel (ferromagnetic coupling) or anti-parallel (antiferromagnetic coupling) to each other and its strength is generally denoted by the exchange coupling constant J. For two centres with one unpaired electron each, J essentially represents the difference in the energy between the singlet and the triplet state. The stabilisation of the singlet state leads to antiferromagnetic coupling while stabilising the triplet state results in ferromagnetic coupling.[333]

The exchange coupling can be facilitated by the direct interaction of orbitals of the paramagnetic centres or by the orbitals of the diamagnetic ligand bridging the paramagnetic centres. In the former case, the coupling interaction is said to be facilitated by 'direct-exchange' while in the latter case, it occurs via what is known as 'superexchange'. In case of direct-exchange, the strength of coupling is dependent upon the extent of overlap and the nature of coupling depends upon the interelectronic repulsion and the exchange energy which tend to stabilise the singlet and triplet state respectively. In the case of superexchange the same principles apply but the coupling is *via* a bridge and hence, the coupling strength depends upon the strength of the bonds between the ligand and the paramagnetic centres. The strength of the superexchange also depends upon the ionicity of these bonds and decreases with the increase in the ionic nature of the bonds.[325, 327, 333, 334]

1.7.1 Single molecule magnetism

Magnetic properties can be used for a variety of applications like magnetic refrigeration,[335-337] data storage[338] and medical uses (like magnetic resonance imaging).[339] These applications are a result of various phenomena like magnetic cooling,[335-337] magnetoresistance[340, 341] and single molecule magnetism[328-332] that arise from the combination of the various electronic effects, most importantly the zero-field splitting and the exchange coupling, outlined in the previous section. Among these phenomena, single molecule magnetism has attracted a lot of interest owing to its potential use in numerous fields like high density data storage, quantum computing and spintronics.[342-347] Single molecule magnets (SMMs) are, as the name suggests, materials where each molecule is a magnet by itself. For a molecule to function as an SMM, it must display slow magnetisation relaxation. SMMs display such a behaviour below a characteristic blocking temperature T_B, which is generally quite low and the record T_B has recently been pushed to liquid N_2 temperatures.[348-350] Below T_B,

SMMs are magnetically bi-stable and exhibit an energy barrier (referred to as U_{eff}) to spin reversal from $+M_S$ to $-M_S$. The nature of this energy barrier depends upon two factors – the zero-field splitting parameter that depends upon the structure of the complex, and the square of the number of unpaired electrons in the ground state, although the latter dependence has recently been argued to be not true.[351-353]

Considering the supposed dependence of U_{eff} on the multiplicity of the ground spin state, Mn serves as the ideal candidate among the 3d metals for SMM materials since it has the highest number of unpaired electrons. The past few decades have consequently witnessed immense development in the field of Mn based coordination complexes[338, 354-356] and the key Mn based homometallic complexes displaying SMM properties are summarised in **Table 1.1**. The first reported SMM, was a Mn based polynuclear complex, $[Mn_{12}O_{12}(O_2CR)_{16}(H_2O)_4]$[357] (**Figure 1.12 (a)**) and since this complex is easy to synthesise, it has served as a playground to understand the effects of structural and electronic modifications on the SMM behaviour.[338, 358-361]

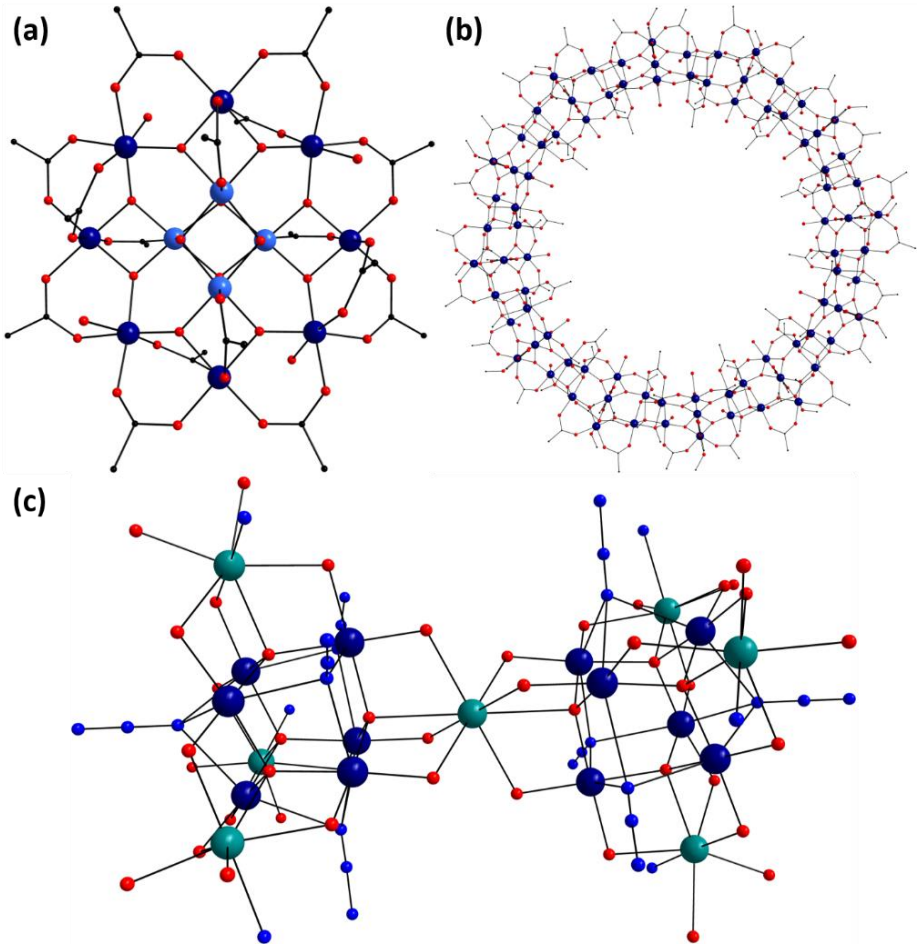

Figure 1.12: Core structure of **(a)** $[Mn_{12}O_{12}(O_2CR)_{16}(H_2O)_4]$,[357] **(b)** $([Mn_{84}O_{72}(CH_3CO_2)_{78}(CH_3O)_{24}(CH_3OH)_{12}(H_2O)_{42}(OH)_6]$[362] and **(c)** $[Mn_{19}O_8(N_3)_8(HL)_{12}(CH_3CN)_6]^{2+}$.[363] Colour scheme: Mn^{II} (teal), Mn^{III} (deep blue), Mn^{IV} (light blue), V (turquoise), N (blue), O (red) and C (black).

To increase the multiplicity of the ground spin state, there has also been a drive to increase the nuclearity of the complexes[364] and Mn complexes with nuclearity as high as 84

($[Mn_{84}O_{72}(CH_3CO_2)_{78}(CH_3O)_{24}(CH_3OH)_{12}(H_2O)_{42}(OH)_6]$, **Figure 1.12 (b)**) have been reported.[362] Unfortunately, increasing the nuclearity is not sufficient and to stabilise high spin ground states the coupling between the metal centres must also be tuned such that the metal centres are ferromagnetically coupled. A large number of Mn complexes with high spin ground states have been reported[363, 365-368] and for a long time the record for the highest spin ground state among 3d transition metal complexes was held by the complex $[Mn_{19}O_8(N_3)_8(HL)_{12}(CH_3CN)_6]^{2+}$ (H_3L=2,6-bis(hydroxymethyl)-4-methylphenol) (**Figure 1.12 (c)**). This complex has a ground spin state of S = 81/2 and all the Mn centres are ferromagnetically coupled, however this complex does not exhibit SMM behaviour.[363] This complex has recently been surpassed by a $\{Fe_{42}\}$ complex which has a ground spin state S = 90/2.[369]

Table 1.1: Compilation of some of the key Mn coordination complexes displaying SMM behaviour.

Chemical Formula	$S_{ground\ state}$	U_{eff} (K)	T_B (K)
$[Mn_6(O)_2(5\text{-Me-salox})_6(C_6H_5CH(OH)CO_2)_2(CH_3CH_2OH)_6]$[370]	2	35	< 3
$[Mn_{12}O_4(salox)_{12}(N_3)_4(CH_3OH)_6(H_2O)_2]$[371]	4	70	< 2.5
$[Mn_6O_2(H_2N\text{-sao})_6(C_6H_5CO_2)_2(EtOH)_4(H_2O)_2]$[372]	4	24/86[a]	< 1.8
$[Mn_4(O)_3(Cl)(OAc)_3\{N(^iPr_2PO)_2\}_3]$[373]	9/2	14	< 1.2
$[Mn_{30}O_{24}(OH)_8((CH_3)_3CCH_2CO_2)_{32}(H_2O)_2(CH_3NO_2)_4]$[374]	5	15	< 3
$[Mn_{12}O_7(OH)_2(CH_3O)_2(dmhmp)_4(C_6H_5CO_2)_{11}(H_2O)]$[375]	11/2	9	< 1.9
$[Mn_{84}O_{72}(OAc)_{78}(CH_3O)_{24}(CH_3OH)_{12}(H_2O)_{42}(OH)_6]$ [362]	6	18	< 1.5
$[Mn_3O(Et_3\text{-sao})_3(ClO_4)(NH_3)_3]$[376]	6	47	<1.8
$[Mn_3O(Et\text{-sao})_3(ClO_4)(CH_3OH)_3]$[377]	6	58	<5
$[Mn_{12}O_7(OH)(OMe)_2(O_2CPh)_{12}(dmhmp)_4(H_2O)]$[378]	13/2	11	< 3
$[Mn_{12}O_4(OH)_2(C_6H_5COO)_{12}(thme)_4(py)_2]$[379]	7	18	< 3
$[Mn_{12}O_8Cl_4(C_6H_5CO_2)_8(hmp)_6]$[380]	7	21/20[a]	< 4
$[Mn_{16}O_8(OH)_2(C_6H_5CO_2)_{12}(hmp)_{10}(H_2O)_2](C_6H_5CO_2)_2$[381]	8	8.1	< 1.8
$[Mn_{12}(O)_4(salox)_{12}(N_3)_4(MeOH)_4(H_2O)_2]$[382]	8	51	< 4
$[Mn_{21}O_{14}(OH)_2(OAc)_{16}(hmp)_8(pic)_2(py)(H_2O)](ClO_4)_4$[383]	17/2	13	< 2.5
$[Mn_{15}O_8Cl_2(CH_3O)_4(CH_3OH)_2((CH_3)_3CPO_3H)_2((CH_3)_3CPO_3)_{10}]$[384]	17/2	17	< 4
$[Mn_{17}NaO_{10}(OH)_2(N_3)_3(CH_3)_3CCO_2)_{13}(tea)_3(teaH)(DMF)]$[385]	17/2	19	< 3
$[Mn_9O_7(OAc)_{11}(thme)(py)_3(H_2O)_2]$[386, 387]	17/2	30	< 4
$[Mn_4(hmp)_6Br_2(H_2O)_2]Br_2$[388]	9	16	< 2
$[Mn_4(OAc)_2(pdmH)_6](ClO_4)_2$[389]	9	17	< 2
$[Mn_{12}O_{12}(O_2CCHCl_2)_{16}(H_2O)_4]^{z-}$ (z = 0–3)[338, 360, 361]	19/2 – 10	25-65	< 2-8
$[Mn_{22}O_6(CH_3O)_{14}(OAc)_{16}(tmp)_8(HIm)_2]$[390]	10	14	< 3
$[Mn_{12}O_{12}(OAc)_{16}(H_2O)_4]$[357]	10	60	< 4
$[Mn_{12}O_{12}(OAc)_8((C_6H_5)_2PO_2)_8(H_2O)_4]$[359]	10	60	< 3
$[Mn_{18}O_{11}(OH)(OMe)(N_3)_{12}(tea)_3(teaH)_3(MeOH)]$[385]	21/2	8.8	< 3
$[Mn_6O_2(H_2N\text{-sao})_6(C_6H_5CO_2)_2(EtOH)_6]$[372]	11	68/86[a]	< 2
$[Mn_6O_2(Et\text{-sao})_6(O_2C_{11}H_{15})_2(CH_3CH_2OH)_6]$[391]	12	80	< 6
$[Mn_{25}O_{18}(OH)_2(N_3)_{12}(pdm)_6(pdmH)_6](Cl)_2$[367]	51/2	12	< 0.6
$[Mn_{25}O_{18}(OH)(CH_3O)(hmp)_6(pdm)_6(pdmH)_6](N_3)_2(ClO_4)_6$[368]	61/2	16	< 1

[a]variation is due to degree of solvation. (5-Me-salox = 5-methyl-salicylaldoxime, salox = salicylaldoxime, H_2N-sao = salicylamidoxime, OAc = $CH_3CO_2^-$, $N(^iPr_2PO)_2$ = bis(diisopropylphosphinyl)imide, dmhmpH = dimethylhydroxy methylpyridine, Et-sao = 2'-hydroxypropiophenone oxime, H_3thme = 1,1,1-tris(hydroxymethyl)ethane, py = pyridine, hmpH = 2-(hydroxymethyl)pyridine, picH = pyridine-2-carboxylic acid, $teaH_3$ = triethanolamine, DMF = dimethyl- formamide, $pdmH_2$ = 2,6-pyridine-dimethanol, H_3tmp = 1,1,1-tris(hydroxymethyl)propane, HIm = imidazole)

Table 1.1 clearly highlights that higher nuclearity or spin ground state do not necessarily result in higher U_{eff} which is consistent with recent arguments about the dependence of U_{eff} on the ground state spin multiplicity.[351-353] Understanding that the increase in the nuclearity does not necessarily enhance the SMM properties of the system, the field has steadily started moving towards the development of mononuclear complexes.[331, 346] These mononuclear complexes are generally classified as single ion magnets (SIMs) instead of SMMs. Dy based SIMs have significantly advanced the field by pushing T_B to 80 K.[348-350] Compared to lanthanide based SIMs, the chemistry of 3d metals based SIMs is still in its infancy but is growing at a rapid rate.[346]

1.8 Water Oxidation and Magnetism – Are They Related?

The effect of the electron donating and electron withdrawing ligands on the OER activity of molecular catalysts has been investigated for numerous molecular water oxidation catalyst and the insights gained are described in the previous section. The effect of the electronic structure on the OER activity however, especially for polynuclear metal complexes and metal oxides, has largely been neglected. Since two (diamagnetic) water molecules are needed during the OER to produce O_2 which is paramagnetic, how the spins on the interacting metal centres and the water molecules are aligned can potentially affect the kinetics of the reaction. It has been observed that the antiferromagnetic coupling between the Mn centres is more favourable for the formation of the O-O σ bond while ferromagnetic coupling is more favourable for the formation of the O-O π bond. The nature of coupling between metal centres thus affects the kinetic barrier to bond formation/cleavage.[392] The kinetics of this reaction can therefore be modified if one can have antiferromagnetically coupled metal centres for the formation of O-O σ bond which can switch to being ferromagnetically coupled for the formation of the O-O π bond. Additionally, it has been observed that the ground spin state of the OEC varies with the S state[393-399] which suggests that the efficiency of the OEC can in part be attributed to how it tackles this spin conservation problem.[67, 68, 400]

In addition to the enhancing effects of spin conservation in the OEC, similar results have been observed in artificial systems too. The positive effects of spin polarisation induced by chiral molecules have been demonstrated for TiO_2 photoanodes which on coating with chiral molecules showed a significant decrease in the overpotential required for H_2 production. The chiral molecules have been suggested to act as spin filters which aid in reducing the overpotential.[401] In presence of chiral molecules, Fe_3O_4 nanoparticles have been found to perform better than TiO_2 photoanodes achieving a high current density of 10 mA cm^{-2} albeit still at high overpotentials (> 550 mV).[402] It has also been observed that the presence of chiral molecules can aid the reduction of formation of H_2O_2 which is a side product generated during the OER.[402, 403] These observations are consistent with theoretical works which also highlight the importance of spin control.[404-407]

Co oxide nanosheets have recently been shown to be more active than the bulk material and the enhancement in activity has been attributed to a transition from the low spin to the high spin state for Co ions occupying the edge sites.[408] Furthermore, the application of magnetic field to a highly magnetic material ($NiZnFe_4O_x$) has been demonstrated to enhance its OER activity by > 100%.[409] Tuning the magnetic environment, or more specifically, the exchange coupling between the metal centres can thus provide a way to enhance the efficiency of the OER.

1.9 Aims and Thesis Outline

The key conclusions that can be drawn from the above discussion are as follows:

1. The OER is quite hard to achieve and forms the bottleneck for the overall water splitting reaction and hence the development of the hydrogen economy.
2. Numerous pathways are available that have the potential to tackle this problem. Among these, the one employed by Nature involves the use of a Mn based mixed-metal molecular complex.
3. There is an urgent need to develop strategies to improve the stability of the catalysts.
4. In addition to the structural characteristics of the catalyst, the magnetic properties of the material under consideration can significantly impact the catalytic activity again exemplifying the complexity of the problem.
5. Besides influencing the OER activity, the magnetic properties also lead to a plethora of other applications like magnetic refrigeration, data storage and magnetic resonance imaging.

This work aims towards exploring the OER problem from both the structural and the electronic perspective. The path adopted in this work is inspired by Nature and hence focusses on Mn based coordination complexes – their synthesis, magnetic properties and electrochemical behaviour. The key aims of this work include:

1. Development of a synthetic strategy to synthesise novel high nuclearity Mn coordination complexes.
2. Structural characterisation of the synthesised Mn complexes.
3. Employing the developed synthetic strategy for the synthesis and structural characterisation of Mn based mixed-metal coordination complexes for capturing key structural characteristics of the OEC.
4. Computational methodology development for investigating the electronic structure and understanding the magnetic properties of materials.
5. Investigation of the OER activity of selected Mn complexes.

The first part of this thesis focusses on the experimental and computational strategy employed to synthesise novel complexes and develop an understanding of their electronic structure. In chapter **2**, the basic principles of quantum chemistry are introduced which is followed by a description of Hartree-Fock theory, Density functional theory (DFT), DFT+U and hybrid DFT. Furthermore, the description and analysis of the wavefunction and a brief description of how the magnetic properties are evaluated are discussed which is followed by a description of the computational methodology adopted in this work. In chapter **3** the development of the synthetic strategy employed in this work is described. We have investigated the use of phosphonate and carboxylate based ligands for the synthesis of novel high nuclearity Mn complexes.

In the second part of this thesis, the magnetic properties of high nuclearity Mn complexes are investigated. Not only do we determine the strength of exchange coupling between the Mn centre, we also describe a novel methodology that allows to study the nature of coupling via different pathways in cases where the Mn centres are coupled to each other via multiple bridges. Additionally, we provide evidence in support of the validity of the use of this methodology. This part of the work is described in chapters **4** and **5**.

In the third part of the thesis, we further illustrate the use of our synthetic strategy for the synthesis of novel polynuclear complexes that are stabilised by carboxylate and/or phosphonate groups. Additionally, we investigate the magnetic properties and the electrochemical behaviour of these complexes in aqueous media for electrocatalytic water oxidation. This part of the work is described in chapter **6-8**.

In the final part of this thesis, a summary of this work is provided and possible future work based on the results described here is considered.

2 Computational Theory and Methodology

Quantum chemistry primarily aims at understanding the interaction of the nucleus/nuclei and the electron(s) with each other and with the surrounding environment for the system under consideration. Such a system can be described using a wavefunction that contains all the information about it, and with the use of quantum mechanical operators, the properties of interest can be determined. This wavefunction can be determined by solving the Schrödinger wave equation[410] but the wavefunction becomes increasingly complicated with the increasing size of the system and thus, obtaining analytical solutions are not possible for any classical or quantum three body system and beyond. Additionally, due to the associated charge, the electrons interact with each other and thus their movement is correlated which means that the movement of one electron affects the movement of all the others. This added complexity creates the need for approximations to obtain even a numerical solution. This chapter describes the Schrödinger wave equation and how the solutions to this equation are approximated.

2.1 Schrödinger Wave Equation

The Schrödinger wave equation in its time-independent form is given as:

$$\hat{H}\varphi = E\varphi \tag{2.1}$$

Here φ is the wavefunction describing the system under consideration, E is the energy and $\hat{H}$, known as the Hamiltonian operator, is the sum of kinetic and potential energy operators, is given as:

$$\hat{H} = T_e + T_N + V_{N-N} + V_{e-e} + V_{e-N} \tag{2.2}$$

Here the first two terms represent the kinetic energy of the electrons (T_e) and the nuclei (T_N) while the other three terms represent the coulombic repulsion between nuclei and between electrons, and the coulombic attraction between electrons and nuclei. The concise form of $\hat{H}$ (in atomic units) is given as:

$$\hat{H} = -\frac{1}{2}\sum_i \frac{1}{m_i}\nabla^2 + V \tag{2.3}$$

Here m_i is the mass of the particle i, ∇^2 is the laplacian operator ($\nabla_i^2 = \frac{\partial^2}{\partial x_i^2} + \frac{\partial^2}{\partial y_i^2} + \frac{\partial^2}{\partial z_i^2}$) and V is the potential energy operator of the system.

The Schrödinger wave equation is thus, a partial differential eigenvalue equation where the Hamiltonian operates on the wavefunction to return the energy of the system and the wavefunction. The wavefunction itself has no physical meaning as it is not an observable, but the squared modulus of the wavefunction gives the probability of finding the electrons. This deceivingly simple equation can be exactly solved only for systems with only two independent particles like He^+, Li^{2+} and H_2^+ (by the H-H distance fixed) and hence, approximations need to be made.

Additionally, the wavefunction describing the system that is required to solve the Schrödinger wave equation is also unknown and has to be approximated. The following sections describe methods employed for determining the wavefunction and approximations made to the Hamiltonian.

2.2 Variational Principle

The wavefunction contains all information about the system under consideration but unfortunately, there is no direct way to obtain the ground state wavefunction. We can try to guess the wavefunction but we also need a way to ascertain that the guessed wavefunction corresponds to the ground state. This can be achieved by using the variational principle according to which the expectation value E of the Hamiltonian $\hat{H}$ for any given wavefunction φ cannot be lower than that obtained using the true wavefunction φ_0, i.e.:

$$\langle\varphi|\hat{H}|\varphi\rangle = E \geq E_0 = \langle\varphi_0|\hat{H}|\varphi_0\rangle \tag{2.4}$$

Thus, any trial wavefunction will correspond to higher energy than that of the true ground state. We can, therefore, systematically modify the trial wavefunction until the lowest energy is obtained.

2.3 Born-Oppenheimer Approximation

One of the approximations made to the Schrödinger wave equation is the Born-Oppenheimer approximation.[411] The nuclei, being much heavier than the electrons, move slowly compared to the electrons and thus, the electrons are always at the lowest energy configuration for the given atomic arrangement. It is therefore reasonable to treat nuclei as stationary objects. This approximation implies that for a fixed set of atomic coordinates the kinetic energy of the nuclei (T_N) can be neglected while the internuclear coulombic interaction (V_{N-N}) can be considered to be constant. Therefore, equation 2.2, under this approximation, changes to:

$$\hat{H} = T_e + V_{e-N} + V_{e-e} \tag{2.5}$$

The internuclear repulsion term, V_{N-N}, has also been completely neglected above since it will merely shift the total energy of the system by a constant value. It does get calculated however, for comparing the energy of different structural arrangements and optimising the geometric structure. The Hamiltonian in equation 2.5 is also known as the electronic Hamiltonian the first term of which can explicitly be represented (in atomic units) as:

$$T_e = -\frac{1}{2}\sum_{i=1}^{N}\nabla_i^2 \tag{2.6}$$

where the summation is over the N electrons. The coulombic attraction between nuclei and electrons (V_{e-N}) is given as:

$$V_{e-N} = -\sum_{i=1}^{N}\sum_{A=1}^{M}\frac{Z_A}{r_{iA}} \tag{2.7}$$

where Z_A is the mass of the A^{th} nuclei and r_{iA} is the distance of the i^{th} electron from the A^{th} nuclei. The interelectronic repulsion is formally described as:

$$V_{e-e} = \sum_{i=1}^{N} \sum_{j>i}^{N} \frac{1}{r_{ij}} \tag{2.8}$$

Since the movement of electrons is correlated, the calculation of the exact interelectronic repulsion is not possible and thus has to be approximated. The two key theories to employed for this purpose are the Hartree-Fock theory and the density functional theory and these are described in the discussion that follows.

2.4 The Hartree Model and Hartree-Fock Theory

The Hartree model[412] condenses the multielectron problem to a single electron problem. This is achieved by transforming the wavefunction into a collection of one-electron orbitals the Hamiltonian for which is given as follows:

$$\widehat{H} = \sum_{i=1}^{N} \hat{h}_i \tag{2.9}$$

In this model, the electron-electron repulsion is completely ignored and the one-electron Hamiltonian can therefore be presented as:

$$\hat{h}_i = -\frac{1}{2}\nabla_i^2 - \sum_{A=1}^{M} \frac{Z_A}{r_{iA}} \tag{2.10}$$

The total wavefunction φ, in this case, is defined as the product of the one-electron orbitals χ_i (Hartree product):

$$\varphi = \prod_{i=1}^{N} \chi_i \tag{2.11}$$

The total energy of the system can thus be given as:

$$E = \langle \varphi | \widehat{\mathrm{H}} | \varphi \rangle = \sum_{\mathrm{i}=1}^{\mathrm{N}} \langle \chi_{\mathrm{i}} | \widehat{\mathrm{h}}_{\mathrm{i}} | \chi_{\mathrm{i}} \rangle = \sum_{\mathrm{i}=1}^{\mathrm{N}} \varepsilon_{\mathrm{i}} \tag{2.12}$$

In this approach, the interelectronic repulsion has been completely neglected so far. Hartree proposed a way to include it using a self-consistent field (SCF) model (often referred to as the Hartree SCF model)[413-415] where each electron is assumed to move in a field created by the nuclei and all the other electrons. The Hartree SCF approach begins with a trial wavefunction. The Schrödinger wave equation is then solved with this guess wavefunction which leads to a set of energies for different orbitals and a new wavefunction. The new wavefunction obtained is then used as the guess for solving the Schrödinger wave equation and the procedure is repeated until the wavefunction converges.

Molecular systems modelled with the Hartree SCF approach tend to fall apart and thus it is still not applicable to real systems. This is because the wavefunction used does not satisfy Pauli's exclusion principle according to which the wavefunction should be antisymmetric, i.e. an interchange of any two electrons should result in the wavefunction changing its sign.[412] This issue was realized by Fock[416] who proposed the use of determinants based on the work of Slater[417] to overcome this. For an N-electron system, the N one-electron orbitals are arranged in a determinant in such a way that allows each electron to occupy any of the N orbitals and thus restoring the electrons indistinguishability. For example, the wavefunction for a 2-electron system, with the electrons occupying the spin orbitals χ_1 and χ_2, can be given as:[412]

$$\varphi = \frac{1}{\sqrt{2!}}\begin{vmatrix}\chi_1(x_1) & \chi_2(x_1)\\ \chi_1(x_2) & \chi_2(x_2)\end{vmatrix} = \frac{1}{\sqrt{2!}}[\chi_1(x_1)\chi_2(x_2) - \chi_1(x_2)\chi_2(x_1)] \tag{2.13}$$

where the pre-factor is the normalization factor.

For an n-electron system with a wavefunction represented by a Slater determinant, the solution of the Schrödinger wave equation can be approximated using the Hamiltonian given by equation 2.10 along with the interelectronic repulsion which can be included by using the following additional terms:[412]

$$J_{ij} = \iint \chi_i(x_1)\chi_j^*(x_2)\frac{1}{r_{ij}}\chi_i(x_1)\chi_j^*(x_2)\partial\tau_i\partial\tau_j \tag{2.14}$$

$$K_{ij} = \iint \chi_i(x_1)\chi_j^*(x_2)\frac{1}{r_{ij}}\chi_i(x_2)\chi_j^*(x_1)\partial\tau_i\partial\tau_j \tag{2.15}$$

where $\chi_i(x_1)$ represents the ith spin orbital containing electron 1. J_{ij} here is known as the Coulomb term and gives the electrostatic repulsion between the electrons in the orbitals *i* and *j*. K_{ij} is called the exchange term and is a direct result of the antisymmetry of the wavefunction. This term reflects the reduction in the repulsion as electrons possessing the same spin cannot occupy the same space and thus tend to avoid each other. Equations 2.10, 2.14 and 2.15 together with the use of Slater determinants constitute the Hartree-Fock (HF) model. Within the HF model, the total energy is given as:[412]

$$E_{Total} = 2\sum_{i=1}^{N/2}\hat{h}_i + \sum_{i=1}^{N/2}\sum_{j=1}^{N/2}\left(2J_{ij} - K_{ij}\right) \tag{2.16}$$

The HF model describes the electronic systems well but it suffers from a few limitations. First of all, the correlated motion of the electrons is not fully captured due to the use of an inadequate representation of the wavefunction. A single Slater determinant captures the instantaneous correlation of electrons only in an average manner because of which the tendency of the electrons to avoid each other is only partially described by the HF model. Electrons close to each other, thus, repel each other more than what they would in reality which also means that the energy of the system predicted by this model will be higher than the true energy. The same can be concluded

from the variational principle as well which states that only the true wavefunction for a system will give the lowest energy and since, in the HF model, the wavefunction used is an approximate one, the energy obtained using this model will be higher than the true energy. The difference between the true (non-relativistic) energy and that obtained from the HF model has been defined by Lowdin as the correlation energy.[418]

As the electron correlation in the HF model is only partially included, it is ineffective for systems with significant electron delocalisation. There are many different schemes to recover the missing correlation and these are collectively termed as post-HF methods which include configuration interaction (CI) methods, multi-configurational SCF, Møller Plesset (MP) perturbation theory, quantum Monte Carlo method and coupled cluster method. Among these, the coupled cluster method is generally used for benchmarking purposes. All post-HF methods make use of multi-determinant wavefunctions to take into account the missing correlation energy which makes them quite expensive even for small systems and their routine use is highly restricted. Unlike the HF model which scales as N^4, the use of multi-determinant makes these methods formally scale as >= N^5, where N is the size of the basis set.[419] A solution to tackle the computational cost can be to compute the electron correlation in a completely different way instead of trying to recover the correlation by adding corrections to the HF model. This is achieved by density functional theory (DFT) which computes the electron correlation with little or no additional computational cost compared to the HF model.

2.5 Density Functional Theory

DFT, in principle, relates the energy of the system to its electron density unlike HF theory which relies on the wavefunction.[420] DFT is based on the two theorems put forward by Hohenberg and Kohn[421] which state that (a) the ground state energy of a many-body system can be uniquely defined by electron density and (b) the exact total energy of a system can be determined by applying the variational principle to the exact ground state density. This enables the description of any system using just 3 variables representing its electron density which is significantly advantageous over the use of the wavefunction which is defined using 3N variables for an N-particle system. The total energy of a system is a function of the electron density, $[\rho(r)]$, and can be represented as:

$$E[\rho(r)] = \int V(r)\rho(r)dr + F[\rho(r)]dr \qquad (2.17)$$

The first term takes into account the nuclear-electron attraction while the second term, also known as the universal functional, takes into account the inter-electronic repulsion and the kinetic energy. The exact form of the latter is unknown which prevents one from obtaining the exact energy for

any system using this approach. One can, however, divide $F[\rho(r)]$ into different interactions as follows:[420]

$$F[\rho(r)] = T[\rho(r)] + J[\rho(r)] + E_{nc}[\rho(r)] \quad (2.18)$$

The first term in the above equation represents the kinetic energy. The second term denotes the inter-electronic interactions and the coulombic energy of the electrons moving in an external field. The third term in the non-classical electron-electron interaction which essentially takes into account the exchange and correlation energy. The issue with using the above equation for practical purpose is that only the coulombic term is known. The exact form of E_{nc} is completely unknown and the errors associated with the approximations that have been developed to calculate T are significant.

Kohn and Sham proposed the re-introduction of the wavefunction formalism to address the issues associated with DFT.[422] In this scheme the kinetic energy $T[\rho(r)]$ is split into the energy associated with the non-interacting electrons (T_s) and a correction term due to electron-electron interactions (T_c). The former can be calculated using the HF approach and the latter is included in the E_{nc} term. Equation 2.18 can thus be represented as:[420]

$$F[\rho(r)] = T_s[\rho(r)] + J[\rho(r)] + E_{xc}[\rho(r)] \quad (2.19)$$

where E_{xc} is the sum of E_{nc} and T_c. Similar to HF theory, one can describe a system using one-electron orbitals, χ_i, although these orbitals are different from the one-electrons orbitals in HF theory in that these are related to the ground state electron density, $\rho(r)$, as:[420]

$$\rho(r) = \sum_{i=1}^{N} |\chi_i(r)|^2 \quad (2.20)$$

It must be noted at this stage that the advantage of DFT of only being dependent on the electron density is lost by introducing a wavefunction. Within the wavefunction formalism, the coulombic attraction between electrons and nuclei, $E_{Ne}[\rho r]$, can be given as:[420]

$$E_{Ne}[\rho r] = -\sum_{i=1}^{N}\sum_{A=1}^{M} \int \frac{Z_A}{r_{iA}} |\chi_i|^2 dr \quad (2.21)$$

The kinetic energy of the non-interacting electrons can be exactly calculated as:

$$T_s[\rho(r)] = -\frac{1}{2}\sum_{i=1}^{N} \int \chi_i^*(r) \nabla^2 \chi_i(r) dr \quad (2.22)$$

The coulombic repulsion between electrons can be calculated as follows:

$$J[\rho(r)] = \frac{1}{2}\iint \frac{\rho(r_1)\rho(r_2)}{r_{12}} dr_1 dr_2 = \frac{1}{2}\sum_{i=1}^{N}\sum_{j=1}^{N} \iint |\chi_i|^2 \frac{1}{r_{12}} |\chi_i|^2 dr_1 dr_2 \quad (2.23)$$

For a non-interacting system, one can now apply the variational principle to the one-particle equations to determine the exact ground state wavefunction and energy. If the true form of

$E_{xc}[\rho(r)]$ is known, the energy of any system can be exactly determined. This makes it superior to HF theory because compared to HF theory which only accounts for the exchange effects, all exchange and correlation effects are included in $E_{xc}[\rho(r)]$. Since the functional form of $E_{xc}[\rho(r)]$ is unknown, it has to be approximated which leads to the approximation of both the exchange and correlation energy unlike HF theory where the correlation energy is neglected although the exact exchange energy is known.

Many approximations made to $E_{xc}[\rho(r)]$ are based on the idea of a uniform electron gas which is a hypothetical system with infinite electrons that move in an infinitely large space with a positive background charge such that the electron density is constant everywhere.[423, 424] This resembles the situation of the valence electrons in an ideal metallic system. The advantage of using this approximation is that the form of the exchange functional for this system is exactly known and the correlation energy as a function of density is known to a very high accuracy from accurate quantum Monte-Carlo simulations.[425, 426] Functionals can therefore be fitted to this data.

Local density approximation (LDA) employs the uniform electron gas approach and under this approximation, $E_{xc}[\rho(r)]$ depends only on the electron density and at each point, the energy is the same as for a uniform electron gas of the same density. The exchange energy is given as a function of the electron density using the equation of Bloch and Dirac.[427, 428] The application of this approach is limited only to closed-shell systems. To extend its use to open-shell systems, the spin up and spin down densities are treated separately and the total density is given as the sum of spin up and spin down densities. This extended form of LDA approach is sometimes referred to as the local spin density approximation (LSDA). LDA and LSDA work reasonably well for systems where the electron density does not vary rapidly (e.g. metals). Generally, however, these approaches tend to overestimate the binding energy of electrons which leads to the underestimation of bond lengths and overestimation of binding and atomisation energies.[429]

The logical way to improve on LDA methods is to take into account the dependence of correlation energy not only on the electron density but also on its gradient (first derivative) and this forms the basis of the generalised gradient approximation (GGA) methods. The inclusion of the gradient of the electron density makes these methods more flexible and allows one to partially account for the non-homogeneous nature of the electron density making it superior to the LDA/LSDA approach. The GGA functionals can be divided into two categories – parameterised/semi-empirical and non-parameterised/ab-initio functionals. The parameterised functionals are derived by fitting to experimental data and examples of these include the Becke's exchange and correlation functionals[430] and Lee-Yang-Parr correlation functional.[431] Since the fitting procedure for these functionals uses a limited set of (light) elements and only small molecules,[430, 431] their indiscriminate use needs to be avoided especially when heavy elements are involved. The non-parameterized functionals, on the other hand, are based on the physics of electrons and thus can be applied more

generally. Examples of such functionals are the ones proposed by Perdew and Wang(PW91),[432] and Perdew, Burke and Ernzerhof (PBE).[433] GGA functionals, in general, perform better than LDA/LSDA functionals but they tend to underestimate the binding energies of the electrons leading to the overestimation of bond lengths.[429]

Further improvement to GGA functionals can, in principle, be achieved by including higher order derivatives of the electron density. Functionals employing this approach are known as meta-GGA functionals. These functionals generally suffer from numerical instabilities and it is only recently that a robust meta-GGA functional, the SCAN functional,[434] has been reported and it has been found to be, in general, better than GGA functionals.[435] This functional is still quite new and further investigation is required to conclusively understand its behaviour.

DFT in practice, suffers from two major limitations because of the approximate nature of the exchange-correlation functional E_{xc}. First of all, unlike the HF model, where the solution can be systematically improved (post-HF methods), there is no prescription to improve the DFT solution or more specifically E_{xc}. The progression from LDA/LSDA functionals to GGA and meta-GGA functionals does seem to improve the solutions but the use of derivatives of electron density to E_{xc} is accompanied with the simultaneous addition of more constraints to avoid functional instabilities which makes further progression quite difficult. The other major problem associated with DFT is the self-interaction error (SIE). Similar to the HF model, the coulomb term $J[\rho(r)]$ (eq. 2.23), contains the terms associated with the artificial interaction of each electron with itself. In the HF model, the exchange term exactly cancels this spurious interaction. In DFT, however, the exchange term is approximated and therefore, electrons partially interact with themselves. This leads to the SIE which results in larger delocalisation of electrons. SIE can be addressed in two ways, the use of a correction (DFT+U) or combining HF and DFT models together (hybrid DFT).

2.5.1 DFT+U approach

In this approach, additional parameters are added to the Hamiltonian such that the partial orbital occupation is penalised. Here, a Hubbard U parameter is included for specific orbitals (azimuthal quantum numbers) and an additional exchange parameter J is introduced. These terms, are then included in the Hamiltonian as separate terms as proposed by Liechtenstein et al.[436] Dudarev et al. has proposed the generation of a U_{eff} term ($U_{eff} = U - J$) which is then included in the Hamiltonian.[437] This correction is zero for integer occupation (i.e. zero or one) and non-zero for partial occupation thereby encouraging integer occupation of the orbitals.

The inclusion of this correction does not increase the computational cost and thus, the accuracy of the calculation can be increased without additional expense. A shortcoming of this approach is that the U and J terms depend on the atoms being modelled and their chemical environment and hence are specific for the system under consideration. The selection of these parameters can be done by

comparing the computed results with experimental data and the comparable properties can include magnetic properties and band structure.[438, 439] The U values can be derived in an ab-initio fashion as well using approaches based on constrained DFT[440, 441] (linear response method based on Koopmans' theorem)[442-444] and density functional perturbation theory.[445]

2.5.2 Hybrid DFT approach

This approach to deal with SIE makes use of the fact that the HF exchange term nullifies SIE exactly which implies that using the HF exchange with the correlation part of the DFT E_{xc} term will remove the SIE and hence increase the quality of the solution.[446] Implementation of this approach however, yields results inferior to those obtained with pure GGA functionals which is because HF exchange and DFT exchange are different. DFT exchange and correlation are local while HF exchange is non-local. To overcome this, a linear combination of the HF exchange and the E_{xc} term is employed as follows:[446]

$$E_{XC}^{HDFT} = \alpha E_X^{HF} + (1-\alpha)E_{XC}^{DFT} \tag{2.24}$$

Here α is a factor that can be varied depending upon the amount of exact exchange needed. Functionals often employ more parameters to reproduce experimental data and B3LYP is a good example of such functionals. B3LYP[447] is a three parameter functional which includes 20% HF exchange and can be given as:

$$E_{XC}^{B3LYP} = aE_X^{HF} + (1-a)E_X^{LSDA} + bE_X^{B88} + cE_C^{LYP} + (1-c)E_C^{LSDA} \tag{2.25}$$

Here a = 0.2, b = 0.72 and c = 0.81 and these parameters have been obtained by fitting to a well-known set of energetic data called the G2 data set.[448] This functional makes use of the B88 exchange functional, the LYP correlation functional and the LSDA exchange and correlation functionals.

The problem with this parameterised approach is that the parameters need to be empirically fitted which means that it requires experimental assistance. Additionally, the performance of these functionals depend on how well the systems under study resembles the test set that was used to fit the parameters. Hence, such functionals may prove good for certain systems but not necessarily for all. For example, B3LYP has been found to perform poorly for metals and semiconductors.[449] Although the amount of exchange required seems to vary with the properties under investigation and the elements modelled,[450] non-empirical hybrid functionals have been developed and a prime example of these is PBE0.[451] This functional uses 25% of exact exchange which has been argued to be the correct amount on theoretical grounds by Burke et al.[452] This functional employs 100% PBE correlation and 75% PBE exchange[433] along with 25% HF exchange:

$$E_{XC}^{PBE0} = 0.25E_X^{HF} + 0.75E_X^{PBE} + E_C^{PBE} \tag{2.26}$$

PBE0 has been found to be more robust than B3LYP especially for modelling metals and semiconductors.[449] Additionally, it has been shown that PBE0 outperforms most GGA and hybrid functionals when it comes to reproducing the correct electron density. In this study, the electron

densities were determined from the radial distribution functions and the performance of all functionals were compared with the values obtained using the coupled cluster approach.[453]

Other modifications to the use of hybrid functionals for making calculations fast and accurate have also been explored. These generally involve separating the components based on long and short range parts and an example of such functionals is the HSE06 functional.[454]

2.6 Describing the Wavefunction – Basis Sets

To investigate the properties of a material, one can model the repeating unit (e.g. molecule) or model the whole crystal. The former is simplistic and neglects the interactions between the adjacent repeating units but, depending upon the properties of interest, may be sufficient. The latter is prohibitively expensive but can be achieved if one uses the repeating unit (the unit cell) and define the periodicity of the system using some boundary conditions. This will allow one to take into account the interaction of the repeating unit with its periodic images. This is achieved by making use of the Bloch's theorem according to which the wavefunction for a periodic system can be represented as:

$$\varphi(r) = e^{ikr}u(r) \tag{2.27}$$

Where r is the spatial direction, k is the wavevector, the term e^{ikr} is the phase factor which describes the interactions between repeating unit cells and $u(r)$ is the periodic Bloch function which describes the repeating unit in the wavefunction. The electron density can be calculated by integrating the square of the Kohn-Sham wavefunction over the Brillouin zone which is the region in reciprocal space of a unit cell where all values of k or k-points are unique. The modelling of periodic systems, in principle, requires the integration over all k-points in the Brillouin zone. The Brillouin zone contains an infinite number of k-points but, for the calculation to be feasible, only a discrete number of k-points are used and the integration is done numerically.

For both periodic and non-periodic systems, the wavefunction can be represented by a linear combination of one-electron orbitals. The coefficients associated with each of these orbitals can then be varied to obtain the wavefunction with the lowest energy (linear combination of atomic orbitals, LCAO). The problem at hand now is that how does one define these one-electron orbitals, and this is addressed by using basis sets. Basis sets are essentially a mathematical way of representing the wavefunction. These functions need not represent the atomic orbitals accurately because one uses a linear combination of these functions to produce the wavefunction. This flexibility allows one to shift the focus towards making their computation efficient instead of trying to obtain the accurate representation of atomic orbitals. Basis sets can broadly be classified into two categories – atom centred basis sets and plane wave basis sets. The former is generally employed in non-periodic type calculations while the latter is used in periodic calculations.

2.6.1 Atom centred basis sets

In this approach, the basis sets describing each orbital are localised on each nucleus. Such basis sets can adopt different forms and the two key ones are the Slater type orbitals (STOs) and the Gaussian type orbitals (GTOs). The functional form of STOs is similar to that of the orbitals of a hydrogen atom:

$$\varphi^{STO}(\zeta, r) = Ae^{-\zeta r} \tag{2.28}$$

Here ζ and r are the orbital exponent and the distance from the nucleus. The advantage of STOs is that at $r = 0$, these reproduce the correct cusp and they also display the correct exponential decay. STOs do not have any nodes and hence the orbitals with higher principal quantum numbers are not properly represented but it does not matter since one uses a linear combination of a number of STOs.[455]

GTOs have the following general form:

$$\varphi^{GTO}(\zeta, r) = Ae^{-\zeta r^2} \tag{2.29}$$

Unlike STOs, GTOs do not produce the correct cusp at $r = 0$ or the correct exponential decay. The advantage of using GTOs, however, is that these are easy to work with computationally. This is because the product of two GTOs is a GTO centred between the two and this property makes computing the complicated two-electron multi-centre integrals analytical. With STOs the computation of multi-centre integrals is numerical and thus, even though fewer STOs will be required for representing the wavefunction, their computation will still be costlier.[455]

As GTOs are functionally quite different from hydrogenic atomic orbitals, a large number of GTOs are required for the proper description of the wavefunction of a given system. The SCF procedure to determine the wavefunction requires varying the coefficients associated with the orbitals and hence the coefficients of the basis functions. Since a large number of GTOs are in use, there are a large number of coefficients that have to be varied and optimised due to which obtaining solutions will still require significant computational resources. For example, for a {Mn_6} system (containing 2407 basis functions), a single SCF cycle took approximately 25 minutes on a machine with 16 Intel(R) Xeon(R) CPU E5-2470 0 @ 2.30GHz cores. To solve this problem, one can couple some GTOs together to obtain the desired functional/orbital form and fix the coefficient associated with each individual GTO. This coupled set of GTOs with fixed coefficients is known as a contracted GTO and each constituent GTO is called a primitive GTO. This approach decreases the number of variable coefficients drastically making the use of GTOs computationally cost-effective.

To allow for flexibility, one must use more than one contracted GTOs although the use of more contracted GTOs increases the computational cost. There are mainly two types of basis sets developed using primitive GTOs – n-zeta and split valence basis sets. The n-zeta basis sets, as the name suggests, make use of n contracted GTOs to represent each orbital. The split valence basis sets, on the other hand, treat the core and valence electrons differently. The core orbitals are

essentially unaffected by changes in the external environment and thus, are represented by a few contracted GTOs each with a large number of primitive GTOs to ensure a good representation. The valence orbitals change more and thus, are represented by a larger number of contracted GTOs so that they can accurately describe the effects of the external environment on the electronic structure. An example of such basis sets is a 3-21G basis set where the core orbitals are represented by a single contracted GTO comprising of three primitive GTOs. Hence, only one variable needs to be varied instead of three. The valence orbitals, in this case, are represented using two contracted GTOs – one with two primitive GTOs and the other with one primitive GTO.[456-461]

When two atoms bond, their electron clouds are polarised and to describe this polarisation, further flexibility in the basis set is required which is accomplished by adding polarisation functions to the basis set. Polarisation functions are essentially functions with higher angular momentum. Generally, functions with angular momentum a unit higher than that of the highest occupied angular momentum in the given atom is introduced for describing the polarisation.[455] For example, for H, in which the valence electron resides in an s-orbital, p-orbital type functions are introduced as polarisation functions.

In instances like modelling of excited states or for describing long-range interaction like hydrogen bonding, where electron density that needs to be modelled is very diffuse, additional functions are required for an accurate description. This class of additional functions are known as diffuse functions. Diffuse functions are functions with small orbital exponent (ζ) so that they decay slowly over distance thereby allowing the proper description of diffuse electron density.[455]

For making calculations computationally more efficient, especially for heavier elements, instead of representing all electrons with basis functions, one can take advantage of the fact that the core electrons are not much affected by the external environment. This allows one to simply introduce a potential known as the effective core potential to represent the effect of the core electrons on the valence electrons. For this purpose, a core radius is defined and the effect of all electrons within this cut-off radius is defined using a function which represents the effect of the core electrons on the valence electrons. At the cut-off radius and beyond, the core potential matches the all-electron potential.[455]

The exact representation of a system will require the use of an infinite number of basis functions. Since the use of such a basis set is practically not possible, one chooses a basis set that is incomplete but describes the system reasonably well. The consequence of the use of an incomplete basis set is basis set superposition error (BSSE). If one investigates the interaction of two species, A and B, the individual species are represented by their own basis sets but the adduct A-B is represented by a larger basis set – the combined basis set of A and B. This allows A to make use of the basis set of B and vice-versa which can lead to spurious lowering of the total energy of the A-B adduct with respect to the individual constituents which is referred to as BSSE. This problem can be mitigated

by performing counterpoise correction calculations in which A and B are individually modelled in the presence of the basis set of each other.[462]

2.6.2 Plane wave basis sets

In periodic systems, especially with a large number of atoms in a unit cell, the use of atom centred basis sets may prove quite expensive due to the increasing number of integrals and k-points. In this respect, plane wave basis sets provide a much simpler and efficient alternative especially in cases where HF exchange is not required. These basis sets comprise of just plane waves of the form e^{ikx} and the wavefunction is described as a linear combination of these waves.[463] The basis set is independent of the number of atoms but depends on the size of the simulation cell.

The plane waves are less flexible because of which a linear combination of a number of these is required for the proper description of a system. In principle, an infinite number of plane waves will be required to describe the system exactly but this cannot be realised practically. To obtain a finite basis, a plane wave energy cut-off is introduced as each plane wave has an associated kinetic energy term (frequency). High frequency plane waves are required to model rapid changes in the wavefunction. The cut-off is therefore chosen such that these changes in the wavefunction are described accurately and the problem is computationally efficient.

The variation in the wavefunction due to the core orbitals is quite high and capturing this effect on the valence orbitals accurately requires a higher plane wave energy cut-off which makes the computations expensive. Since the effect of the external environment on the core electrons is negligible, similar to the use of effective core potential with atom centred basis sets, the potential of the nucleus and the core electrons is replaced by a pseudopotential. The pseudopotential mimics the interaction of core electrons with the valence electrons and allows the use of lower plane wave cut-offs to accurately describe the system under consideration. A slightly different approach proposed by Blöchl involves the use of the so-called projector augmented wave (PAW) pseudopotentials. In this approach, the core electrons are represented by localised basis sets the effect of which is projected onto the valence electrons, that are described by plane waves.[464] Essentially, an all-electron calculation with lower plane wave cut-offs can thus be performed with this approach.

An advantage of using plane wave basis sets over atom centred basis sets is that the optimisation of the basis set requires the variation of only the plane wave energy cut-off. Additionally, if two species A and B, and the adduct A-B are modelled with the same cut-off, the number of basis functions representing each species is the same and thus, there is no BSSE.

The problem of Pulay stress, however, does arise due to the use of an incomplete basis set. Pulay stress[465] is the stress on the simulation cell resulting from the derivative of the basis set with respect to the volume of the cell and results in underestimation of the equilibrium volume of the simulation

cell. This problem can be decreased by either increasing the plane wave cut-off or by calculating the energy for different lattice volumes with a fixed energy cut-off and fitting the energy-volume curve to an equation of state like the Murnaghan equation of state.[466]

2.7 Electronic and Geometric Optimisation

One can investigate the properties of interest for the system under consideration by modelling it using the basis set and functional of choice. Irrespective of whether one is dealing with a periodic system or an isolated species, the basic optimisation procedure for the geometric and electronic structure is the same.

With the knowledge of the elementary composition and the atomic coordinates of the system, a trial wavefunction, using the basis set of choice, and charge density, based on the number of electrons in the system, can be generated. The Hamiltonian is then set up as the sum of equations 2.22 (T), 2.23 (J) and E_{xc} where the form of E_{xc} is dependent on the functional used. The Kohn-Sham equations are then solved and the matrix of solutions thus obtained is diagonalised either partially (for periodic systems) or completely (for molecules), to obtain the eigenvalues.[446] These Kohn-Sham matrices can be quite large making the diagonalisation procedure the bottleneck of the calculation. The exact diagonalisation method can become very resource intensive in which case iterative diagonalisation schemes are employed which are used to solve only the lowest eigenvalues thereby allowing for faster convergence.[467] The diagonalisation procedure provides a set of modified coefficients which is then used as a guess for the next set of solutions. This procedure is repeated until the difference in the energy between consecutive solutions is less than a particular threshold i.e., self-consistency is achieved, in which case the electronic structure is considered to be converged.

Once the electronic structure is converged, the forces on each atom are calculated to determine whether the geometry is optimised or not. The force on an atom is the derivative of the energy with respect to the atom position and can be determined analytically.[468] It can also be calculated using the Hellmann-Feynman theorem which states that in a system with fixed nuclei, the force on a nucleus is the classical electrostatic interaction of the nucleus with electrons and other nuclei.[469] Hence, if the wavefunction is known, the forces can be calculated directly from it. With plane wave basis sets, the Hellmann-Feynman theorem can be employed but in case of atom centred basis sets, the former method of calculating forces needs to be resorted to. This is because the plane wave basis sets are fixed while atom centred basis sets move with the nuclei. For the application of Hellman-Feynman theorem, each parameter entering the wavefunction must either be variationally determined or must remain unaffected by nuclear distortions. As the nuclear centred basis sets move with the nuclei, their positions are neither variationally determined nor fixed and thus Hellman-Feynman theorem cannot be directly applied.[470]

The calculation of forces allows one to determine the movement of the nuclei so that the forces can be minimised. A variety of ways can be used to treat this – steepest descent, conjugate gradient, Newton-Raphson and quasi Newton-Raphson methods being the key ones.[471] Steepest descent method moves the atoms along the gradient direction. Conjugate gradient method involves moving them in a direction conjugate to all previous directions traversed. Newton-Raphson and quasi Newton-Raphson methods involve the determination of the hessian or the derivative of forces (or the second derivative of energy) to determine the distance and direction of movement. While the former requires the calculation of the hessian, which is computationally expensive, the latter works with an estimated hessian which is constantly updated.[471]

Once the forces are determined and the atoms are moved accordingly, the electronic structure and forces are re-determined. This cycle is repeated until the forces on all atoms are zero or below a certain threshold and at this stage the structure is considered to be optimised.

2.8 Wavefunction Analyses

In this work, the wavefunction is mainly analysed to determine the electron densities on different elements. A number of electron density population analysis schemes are available. The ones employed in this work are described below.

2.8.1 Mulliken population analysis[472-475]

This is the simplest population analysis scheme that is based on the partition of the basis functions. The total electron density of the system (i.e. the total number of electrons) can be related to the molecular orbitals (φ_i) and hence the basis functions (χ_α) as follows:

$$\rho(r) = \sum_i \int \varphi_i^2 dr = \sum_i \sum_{\alpha\beta} c_{\alpha i} c_{\beta i} \int \chi_\alpha \chi_\beta dr \qquad (2.30)$$

Where $c_{\alpha i}$ is the coefficient associated with the basis function α in the molecular orbital i. The matrix of the product of these coefficients is known as the density matrix D while the matrix of the integral of products of the basis functions χ_α is called the overlap matrix. The diagonal elements of D represent the number of electrons associated with each basis function while the off-diagonal elements represent the electrons being shared by two basis functions. Electrons belonging to basis functions completely localised on a single nucleus are associated solely with the given nucleus while those belonging to basis functions shared between nuclei are divided equally between the sharing nuclei. The electrons associated with a given nucleus can easily be calculated from D. Such a simplistic approach proves unrealistic at times and depends significantly on the basis functions used.[476]

2.8.2 Hirshfeld population analysis[477-479]

In the Hirshfeld population analysis scheme, one begins by assuming that the given molecule comprises of isolated atoms positioned as in the real molecule. The atomic densities of isolated atoms are then used to define the 'promolecular' density for the given molecule. The contribution of each atom to the promolecular density is then used to determine the weight of each atom. The Hirshfeld populations are then defined by integrating the actual molecular density over space with each point weighted according to the weighting scheme obtained using promolecular density.

This approach provides a relatively basis set independent approach to partitioning the electron density. The only issue with this approach, however, is that there is no strict definition of the atomic or the promolecular density. Spherically averaged ground state densities for neutral atoms are generally used for this purpose. Iterative or self-consistent Hirshfeld charges, where the promolecular densities are derived using a self-consistent approach have been found to be a promising alternative for defining the atomic densities. In this approach, one begins with a trial electron density associated with each atom that is used to determine the promolecular density. This promolecular density is then used to define the weight of each atom. The weights are used to obtain the electron density associated with each atom in the molecule which is then used to define a new promolecular density and this cycle is repeated until self-consistency is achieved.[480, 481]

2.8.3 Bader population analysis[482]

The Bader population analysis involves partitioning the electron density into atomic basins based on the topology of the electron density. For any molecular system, the electrons density is a maximum near the nuclei and rapidly decays away from these positions. Between any two such maxima lies a zero-flux surface, known as the interatomic surface, which is a surface with zero charge density normal to the surface. If ρ is the density and n is a unit vector perpendicular to the surface then

$$\nabla\rho \cdot n = 0 \tag{2.31}$$

On these surfaces lies a point at which $\nabla\rho = 0$ and these points are known as bond critical points. These points are used to determine whether there is a bond between the two atoms or not. The volume of space associated with each atom within the molecule can be defined as the region of space surrounding the nucleus bound by the interatomic surfaces. The electron density associated with any nuclei n, can then be given as:

$$\rho_n = \int \rho(r)\, dr \tag{2.32}$$

Here the integration is over the volume enclosed by the interatomic surfaces surrounding the nuclei n. The Bader charge associated with each atom can thus be defined as the difference between the

nuclear charge and the number of electrons within the region of space bound by the interatomic surfaces.

The key principle of this scheme is to identify the stationary points in the electron density where the gradient of the electron density is zero, and characterise them as nuclei or critical points and partition the electron density accordingly. At any point, the gradient of electron density will point towards the maximum i.e., the nuclei, and the negative of the gradient will point towards a critical point (minima). Once the positions of critical points are known, the interatomic surface can be determined which will allow the identification of the volume occupied by each atomic basin.

2.9 Magnetic Properties

The presence of a paramagnetic centre in a system results in the display of magnetic properties. If many such centres are present in the same molecule, they can interact with each other which leads to the modification of the magnetic properties of the molecule. The magnetic behaviour of a molecule is generally investigated using the spin-Hamiltonian approach which provides a way to parameterise the magnetic properties without being explicitly dependent on the geometric and electronic structure of the system under consideration.[483-485] This approach involves the exclusive use of spin operators and operates on the states that span the ground state electronic configuration. It provides a means to identify the relationship between the magnetic properties of the system under study and its geometric and electronic structure. The spin-Hamiltonian for a system containing more than one paramagnetic centre is given as:[333]

$$\widehat{H} = -2\sum_{i>j} J_{ij}\hat{S}_i\,\hat{S}_j + \sum_i g\mu_B\vec{B}\hat{S}_i + \sum_i \hat{S}_i D_i \hat{S}_i + \sum_i \hat{S}_i D_{ij}\hat{S}_j + \sum_{i>j}\vec{d}_{ij}\hat{S}_i \otimes \hat{S}_j \qquad (2.33)$$

Here $\widehat{S_\iota}$ and $\widehat{S_j}$ are the spin operators for the centres i and j, μ_B is the Bohr magneton, g is gyromagnetic tensor, B is the applied magnetic field, J_{ij} is the exchange coupling constant and D_i, D_{ij} and $\vec{d}_{ij}$ are operators associated with the anisotropy of the complex. The first term in the above equation is the isotropic exchange coupling term that accounts for the interaction between centres with unpaired electrons which leads to these electrons being parallel or antiparallel to each other. The second term is known as the Zeeman term and takes into account the splitting of the energy levels in the presence of a magnetic field. The third and the fourth terms describe the single-ion anisotropy and the anisotropic dipolar contributions to the system under investigation which align the spins along a specific spatial orientation. The final term, also known as the Dzyaloshinskii-Moriya term, describes the antisymmetric contribution to the exchange coupling.[327, 333, 486] Since the first term in the above equation has the largest contribution and has a direct impact on the O-O bond formation,[392] the focus of this work has been on the evaluation of this term which is described below.

2.10 Calculation of Coupling Constants (Theory)

The isotropic interaction of local spins of a set of magnetic centres can be described using the Heisenberg-Dirac-van Vleck (HDVV) Hamiltonian:[487-489]

$$\widehat{H} = -2\sum_{i>j} J_{ij}\widehat{S}_i.\widehat{S}_j \tag{2.34}$$

where J_{ij}represents the coupling strength between the magnetic centres i and j.

DFT involves the use of single determinant but the spin symmetry of the non-ferromagnetic states can only be represented by the use of multiple determinants. To overcome this, the broken symmetry approach, developed by Ginsberg[490] and Noodleman,[491, 492] is employed. This involves defining a fictitious mixed spin state which is not a true state but can be represented by a single determinant. For a system with two centres with equal number of unpaired electrons, the broken symmetry state has a total spin of zero with one centre that has unpaired electrons with up spin while the other with down spin. The energy of this state, in principle, can be described as the average of the pure spin states, i.e., the high-spin state (where the paramagnetic centres coupled ferromagnetically) and the low-spin state (where the paramagnetic centres coupled antiferromagnetically):

$$E_{Broken\ symmetry} = \frac{1}{2}(E_{high-spin} + E_{low-spin}) \tag{2.35}$$

Calculation of coupling constants involves mapping of the DFT energies computed by broken symmetry wavefunctions to the energies of the Ising Hamiltonian, i.e. the diagonal elements of the HDVV Hamiltonian.[493] For a dimeric system, if each centre contains $S/2$ unpaired electrons (such that there are a total of S unpaired electrons) and the energy of the high-spin state and the low-spin states are determined, the coupling strength between the centres can be given as:

$$J = \frac{E_{high-spin} + E_{Broken\ symmetry}}{S^2} \tag{2.36}$$

The broken symmetry state suffers from spin contamination which needs to be taken into account for J to make sense. Modification of equation 2.36 for limiting cases of strong and weak coupling have been developed but a more generalized adaptation has been given by Yamaguchi et. al:[494-496]

$$J = \frac{E_{high-spin} + E_{Broken\ symmetry}}{\langle S^2\rangle_{high-spin} - \langle S^2\rangle_{Broken\ symmetry}} \tag{2.37}$$

Here $\langle S^2\rangle = S(S+1)$ is the expectation value of the spin for a given spin configuration. This procedure can be extended to systems with larger number of paramagnetic centres using the generalized spin projection approach.[497] Another way to extend the above approach involves the pairwise consideration of the paramagnetic centres such that equation 2.37 can be used for each pair.[498] A slightly different approach for tackling the spin contamination problem has been proposed

by Paul and Misra which involves the use of spin density to define the spin operator in equation 2.34.[499]

Once the coupling constants are determined, one can determine their accuracy by calculating the magnetic susceptibility at different temperatures and compare with the experimental data.

2.11 Computational Methodology

In vacuo calculations for systems in a non-periodic environment have been carried out using the codes gaussian09[500] and ORCA,[501] and the periodic calculations have been performed using the code VASP (Vienna Ab-initio Simulation Package).[502-504] The calculations with gaussian09 have been performed using hybrid-GGA functionals while those with VASP have been performed using the DFT+U approach. These calculations have been followed by the analysis of the electronic structure to understand the magnetic properties the details of which have been described in the following discussion.

2.11.1 Structural optimisation with gaussian09 and ORCA

For each system investigated, the crystal structure was used to obtain the initial set of atomic coordinates. To determine the appropriate functional and basis set, an initial search for the appropriate basis set and functional was carried out by modelling $[Mn(H_2O)_6]^{2+}$ and $[Mn(H_2O)_6]^{3+}$ ions and comparing with the experimental data[505, 506]. The investigation indicated that the hybrid PBE0[433, 451] functional gives accurate results when used in conjunction with the SDDALL[507] (a double zeta) basis set having an effective core potential for the Mn atoms (replacing the 10 core electrons – $1s^2 2s^2 2p^6$ – of Mn with fully relativistic pseudopotentials), the 6-31G(d)[508] basis set for O and 6-31G(p)[508] basis set for H. A difference of ~1.5% in the bond lengths between the experimental structure and the model has been observed. Based on previous experience, the 6-31G(d)[508] basis set for C and N and 6-31G(2d)[508] basis set for P, Cl and Br, SDDALL[509] basis set with Binning-Curtiss (df) polarisation functions[510, 511] for As and 6-311G(2d)[512] basis set for I have been used in this work. For the calculation of the ferromagnetic configurations of the various systems investigated in this work, the SCF convergence criteria was chosen to be the default one which is 10^{-8} atomic units (Hartrees/atom). Once the electronic structure was converged, the geometry optimisation was performed using berny optimiser[513] as implemented in gaussian09. This optimiser, at its core, uses a modified conjugate gradient algorithm and has been shown to achieve rapid convergence.[513] The optimisation was performed using a large grid containing 225 radial shells with each shell containing 974 angular points and the default convergence criteria defined in gaussian09 (root mean square forces < 0.0003 Hartrees/Bohr, the maximum force on any atom < 0.00045 Hartrees/Bohr, root mean square displacement < 0.0018 Bohr and maximum displacement of any atom < 0.0012 Bohr).

For modelling the non-ferromagnetic configurations, broken symmetry calculations were performed.[492, 514] For these calculations, the corresponding ferromagnetic state was used as the initial guess. It was ensured that in each case the overall multiplicity of the system was positive. A guess wavefunction with the appropriate spin multiplicity was generated, analysed to look for instabilities[515] and optimised until a stable wavefunction was found. This wavefunction was then employed for the final geometry optimisation using the berny optimiser[513]. After the optimisation was completed, a few more geometry optimisation steps were performed using the 'verytight' convergence criteria and a smaller step size. This was followed by switching back to the default criteria. This additional step was included to ensure that the minimum obtained was a well-defined minimum. The visualization was carried out using gaussview.[516]

The calculations with ORCA were carried out for calculating the gyromagnetic-tensor. These calculations were performed using the same basis set and functional as used in the calculations with gaussian09. The integration grid used in these calculations was grid 7 as implemented in ORCA.

2.11.2 Structural optimisation with VASP

For these calculations, the optimised coordinates of the ferromagnetic state obtained from the hybrid DFT calculations were used as the starting point. To ensure that there is no interaction between the periodic images, a gap of 15 Å was introduced in each direction. DFT+U calculations were performed using the Γ point with the PBEsol[517] functional. The U value was defined using both Dudarev[437] and Liechtenstein[436] approaches. Plane wave basis set with a 400 eV plane wave cut off was used. The interaction between the core electrons and valence electrons was specified using projector augmented wave (PAW) method[464]. For Mn, the 3d and 4s electrons were treated explicitly, while for P, O, C, N and Cl, the valence s- and p- electrons were modelled explicitly. For optimisation, the electronic and ionic convergence criteria of 10^{-6} eV and 0.01 eV/Å respectively were selected. The optimisation was carried out using the conjugate gradient optimiser developed by the Henkelman group as the other optimisers implemented in VASP had difficulties converging the strutcture. The visualization was carried out using VESTA[518].

2.11.3 Wavefunction/Population analysis

Mulliken and Hirshfeld population analysis were performed using gaussian09. Bader population analysis scheme was performed using a grid based code developed by Henkelman group.[519] In this code, the steepest descent method is employed to explore the electron density space, which is in the form of a 3-dimensional grid, to identify the nuclei. Each point on the grid is considered only once and all paths are terminated once they intersect with points that have already been accounted for. The whole grid can thus be mapped in an efficient manner that scales linearly with system size.

2.12 Calculation of Coupling Constants in Polynuclear Complexes

The energy obtained from the DFT calculations includes the energy associated with interactions other than the exchange coupling. In order to extract the coupling constants, one needs to determine the energy associated with the exchange coupling. For this purpose, one of the states is used as a reference and it is assumed that the energy of each configuration differs only by the amount associated with the coupling of the paramagnetic centres. To obtain n coupling constants, at least (n+1) spin configurations need to be modelled.[520-522] For x centres with unpaired electrons, there can be a maximum of x(x-1)/2 coupling constants and a total of 2^x different spin configurations, although the number of unique coupling constants and spin configurations may be less due to the symmetry of the system. For a system with 6 Mn(III) centres one can have a maximum of (6(6-1)/2 =) 15 coupling constants while the total number of spin configurations for this system will be (2^6 =) 64. Out of these 64 configurations, 32 are mirror images of the other 32 configurations based on the spin orientation. For example, the configuration with all unpaired electrons spin up will be identical to the one where all unpaired electrons are spin down. Thus, the total number of unique configurations will be 2^5 (= 32).

For any system with more than 3 paramagnetic centres, the number of configurations that are available are more than that required to calculate all coupling constants. Although to obtain n coupling constants, a minimum of n+1 states need to be modelled, to remove any dependence of the coupling constants on the choice of the spin states modelled, recent works have explored the option of modelling extra states.[523-526] This work has used a similar approach and more unique states than the required minimum have been modelled and this implies that more than one set of coupling constants exists, i.e. the solution is overspecified. Since one ends up with more than one set of coupling constants, they have to be averaged in some sensible way. To address this, a FORTRAN code ej_calc has been developed (code available in the attached disc and on github[527]).

When calculating r coupling constants using n (where $n > r$) spin states, then after using one of the configurations as a reference for all the other states, the remaining $(n-1)$ configurations yield $\left[{}^{(n-1)!}\Big/_{r!\,(n-1-r)!}\right]$ (i.e. ${}^{n-1}C_r$) sets of solutions (i.e. coupling constants). Since any of the n modelled spin states can be used as a reference, a total of $n({}^{n-1}C_r)$ sets of solutions are obtained. The code ej_calc calculates all $n({}^{n-1}C_r)$ sets of coupling constants and the sets which turn out to be singular are discarded. The valid solutions are averaged and the standard deviation is calculated. The solutions that deviate by more than three standard deviations are discarded and the standard deviation is calculated again and this cycle is repeated until self-consistency is obtained.

The coupling constants obtained this way are then used to further determine the energy of all the possible electronic states ($2^{x/2}$ for x paramagnetic centres) using the Heisenberg Dirac van Vleck

Hamiltonian (eq. 2.34). The spin operator for each paramagnetic centre is determined by taking an average of the spin value in the different electronic states.

2.13 Simulation of Magnetic Susceptibility

Once the coupling constants have been determined, they can also be used to calculate the variation of magnetic susceptibility with temperature for comparison with the experimental data. The relationship between coupling constants and magnetic susceptibility is well understood and described in detail in the literature.[486, 528] The simulation of magnetic susceptibility has been carried out using the code PHI[529] along with a FORTRAN code suscep developed in this work (code available in the attached disc and on github[530]). The approach adopted for the development of the code for simulation of magnetic susceptibility is described in the following discussion.

The basic working of this code involves setting up a matrix of all possible M_S (the magnetic spin quantum number) states for the given system. This is followed by operating each term of this matrix with eq. 2.33. In this code we have only used the first two terms, the isotropic exchange and the Zeeman term, for the evaluation of the temperature dependence of magnetic susceptibility. Once this operation is complete, the matrix is diagonalised to obtain the eigenvalues which are then used to determine the magnetic susceptibility at different temperatures using the van Vleck equation.[528] The details of the implementation of this procedure are given below.

Matrix Elements: The matrix elements are constructed using an uncoupled basis comprising of spin elements (the magnetic spin quantum number, M_s, value) for each magnetic centre. If a magnetic centre has N unpaired electron, then the magnetic spin quantum number values for that particular magnetic centre range from N/2 to –N/2; the consecutive values differing from each other by unity (total (N+1) values).

Hamiltonian: Only the two major contributors – the isotropic exchange term and the Zeeman term – to the Hamiltonian have been taken into consideration.

Isotropic Exchange term:[531]

$$-2\sum_{A=1,B=1}^{N,N} J_{AB} < I|\hat{S}_A.\hat{S}_B|J > \qquad (2.38)$$

where J_{AB} is the coupling constant between the magnetic centres A and B, I and J represent the particular M_s terms in the basis elements that $\hat{S}_A.\hat{S}_B$ operate on and

$$\hat{S}_A.\hat{S}_B = \frac{1}{2}\left(\hat{S}_{A,+}\hat{S}_{B,-} + \hat{S}_{A,-}\hat{S}_{B,+}\right) + \hat{S}_{A,z}.\hat{S}_{B,z} \qquad (2.39)$$

where $\hat{S}_{A,+}$ and $\hat{S}_{B,-}$ are increment and decrement operators that are defined as follows:[531]

$$\hat{S}_{A,+}|M_A\rangle = [(S_A(S_A+1) - M_A(M_A+1)]^{0.5}|S_A, M_A+1\rangle \quad (2.40)$$

$$\hat{S}_{A,-}|M_A\rangle = [(S_A(S_A+1) - M_A(M_A-1)]^{0.5}|S_A, M_A-1\rangle \quad (2.41)$$

$$\hat{S}_{A,z}|M_A\rangle = M_A|S_A, M_A\rangle \quad (2.42)$$

Zeeman term:[531]

$$\mu_B \vec{B}. \sum_{A=1}^{N} g_A \langle I|\hat{S}_A|J\rangle \quad (2.43)$$

Here $\vec{B}$ represents the applied magnetic field, g_A is the gyromagnetic tensor and μ_B is the unit Bohr Magneton.

$$\begin{aligned}\langle S_A M_A|\vec{B}.g_A.\hat{S}_A|S_A M'_A\rangle = \\ +0.5\left[\left(B_x g_{Ax} + iB_y g_{Ay}\right)\{(S_A - M_A + 1)(S_A + M_A)\}^{0.5}\delta_{M'_A M_{A-1}}\right] \\ +0.5\left[\left(B_x g_{Ax} - iB_y g_{Ay}\right)\{(S_A + M_A + 1)(S_A - M_A)\}^{0.5}\delta_{M'_A M_{A+1}}\right] \\ +B_z g_{Az} M_A \delta_{M'_A M_A}\end{aligned} \quad (2.44)$$

where δ_{AB} is the kroenecker delta operator which is equal to 1 if A=B. Otherwise its value is 0. B_i and g_{Ai} represent the value of the magnetic field and the gyromagnetic tensor along a given direction.[531]

The effective Hamiltonian is thus given as:[531]

$$H_{E+Z} = -2\sum_{A=1,B=1}^{N,N} J_{AB} < I|\hat{S}_A.\hat{S}_B|J > + \mu_B \vec{B}. \sum_{A=1}^{N} g_A \langle I|\hat{S}_A|J\rangle \quad (2.45)$$

The Hamiltonian matrix can thus be represented as:[531]

$$\sum_{I=1}^{N}\sum_{J=1}^{N}\langle A_I|H_{E+Z}|A_J\rangle \quad (2.46)$$

where A_I and A_J represent the elements of the basis and N is the total number of elements in the basis.

The eigenvalues ε_i and hence the energy levels of the various magnetic states are obtained by the diagonalisation of the Hamiltonian matrix. Once the eigenvalues are obtained, it can be used to plot the magnetic susceptibility with respect to temperature. To calculate the magnetic susceptibility, the Van Vleck equation[528] is used which is:

$$\chi = \mu_0 N_A \frac{\sum_i [\frac{(-\epsilon_i^{(1)})^2}{kT} - 2\epsilon_i^{(2)}] exp(-\epsilon_i^{(0)}/kT)}{\sum_i exp(-\epsilon_i^{(0)}/kT)} \quad (2.47)$$

where $\epsilon_i^{(1)}$ and $\epsilon_i^{(2)}$ are the first and second derivative of energy with respect to the magnetic induction, μ_0 is the permeability of free space, N_A is the Avogadro's number, k is the Boltzmann constant and T is the temperature.

By Taylor expansion, the eigenvalues can be represented as:[486]

$$\varepsilon_i = \epsilon_i^{(0)} + \epsilon_i^1 \Delta B + \epsilon_i^{(2)} \Delta B^2 + \epsilon_i^{(3)} \Delta B^3 + \cdots \quad (2.48)$$

with

$$\epsilon_i^{(n)} = \frac{1}{n!}\left(\frac{\partial^n \epsilon_i}{\partial B^n}\right) = C_i^{(n)} \quad (2.49)$$

being the coefficients to be determined. To obtain these coefficients, 3 sets of eigenvalues, $\varepsilon_{i,m}$ are generated using 5 different magnetic fields B_m, where

$$B_m = B_0 \pm N\delta \quad (2.50)$$

where N = 0, 1 and 2, and δ has been chosen to be equal $B_0/10$

Therefore,[486]

$$\varepsilon_{i,m} = c_i^{(0)} + c_i^{(1)} \Delta B_m + \cdots + c_i^{(n)} (\Delta B_m)^n \quad (2.51)$$

for

$$\Delta B_m = B_m - B_0 \quad (2.52)$$

In matrix form,[486]

$$\left(\varepsilon_{i,1}, \varepsilon_{i,2}, \ldots, \varepsilon_{i,m}\right) = \left(c_i^1, c_i^2, \ldots, c_i^n\right) \begin{pmatrix} 1 & 1 & \ldots & 1 \\ \Delta B_1 & \Delta B_2 & \ldots & \Delta B_m \\ \ldots & \ldots & \ldots & \ldots \\ \Delta B_1^n & \Delta B_2^n & \ldots & \Delta B_m^n \end{pmatrix} \quad (2.53)$$

or

$$e = cB \quad (2.54)$$

The matrix of coefficients can be calculated, provided the inverse of B exists, as follows:[486]

$$c = eB^{-1} \quad (2.55)$$

By assembling the rows together, we obtain,

$$\begin{pmatrix} \varepsilon_{1,1} & \varepsilon_{1,2} & \ldots & \varepsilon_{1,m} \\ \varepsilon_{2,1} & \varepsilon_{2,2} & \ldots & \varepsilon_{2,m} \\ \ldots & \ldots & \ldots & \ldots \\ \varepsilon_{n,1} & \varepsilon_{n,2} & \ldots & \varepsilon_{n,m} \end{pmatrix} = \begin{pmatrix} c_1^0 & c_1^1 & \ldots & c_1^n \\ c_2^0 & c_2^1 & \ldots & c_2^n \\ \ldots & \ldots & \ldots & \ldots \\ c_m^0 & c_m^1 & \ldots & c_m^n \end{pmatrix} \begin{pmatrix} 1 & 1 & \ldots & 1 \\ \Delta B_1 & \Delta B_2 & \ldots & \Delta B_m \\ \ldots & \ldots & \ldots & \ldots \\ \Delta B_1^n & \Delta B_2^n & \ldots & \Delta B_m^n \end{pmatrix} \quad (2.56)$$

i.e.,

$$E = CB \quad (2.57)$$

Thus all the coefficients can be determined by the following equation:

$$C = EB^{-1} \quad (2.58)$$

These coefficients can then be used to calculate the magnetic susceptibility using the Van Vleck equation which can now be given as:[486]

$$\chi = \mu_0 N_A \frac{\sum_i [\frac{(-c_i^{(1)})^2}{kT} - 2c_i^{(2)}] exp(-c_i^{(0)}/kT)}{\sum_i exp(-c_i^{(0)}/kT)} \quad (2.59)$$

3 Synthetic Approach

There are two general strategies adopted for the synthesis of polynuclear Mn coordination complexes. The first involves the use of chelating ligands and preformed oligonuclear complexes.[532-537] The other approach relies mostly on serendipity and is based on self-assembly where potentially bridging ligands are mixed with Mn salts to give rise to high nuclearity coordination complexes.[112, 113, 384, 538-547] This approach often makes use of comproportionation reaction whereby two Mn salts in different oxidation states (generally +II and +VII) are mixed together to give rise to species with Mn in an intermediate oxidation state.[113, 384, 538, 540-545] The success rate with the latter approach is quite low but what makes it appealing is the possibility of obtaining structural arrangements that would be extremely hard to obtain from a rational approach. An example of this is the first characterised SMM, $\{Mn_{12}\}$,[112, 113] which has a $\{Mn_4\}$ cubane moiety encapsulated in a $\{Mn_8\}$ ring. A rational synthesis for such a complex is inconceivable due to the low symmetry of this system. This serendipitous self-assembly approach has been adopted for most part of this work.

Comproportionation reactions, in combination with the various attributes of the reaction mixture like the ligands used, the solvent used and the pK_a of the solution, provide an opportunity to stabilise different oxidation states. These conditions, however, also introduce an extra layer of complexity from the viewpoint of understanding how self-assembly proceeds in such reactions. First of all, the counterion in the Mn^{II} salt in use may not be the same as the potentially bridging ligands present in the reaction mixture which means that it can affect the self-assembly behaviour. Secondly, Mn in MnO_4^- ion resides in a tetrahedral coordination environment[548] while in Mn(II) salts, it generally resides in an octahedral coordination environment.[549-554] Thus, Mn centres with two different coordination environments are present in the reaction mixture. Predicting which coordination environment favours the formation of the major product and how the electron transfer process takes place becomes quite complicated. This problem has been briefly highlighted in this work.

This project builds upon the previous work conducted in the Schmitt group on phosphonate based polynuclear Mn complexes.[384, 542-545] To this end, the choice of bridging ligands has been kept largely limited to the use of phosphonate and carboxylate ligands. Although phosphonate based ligands are not present in the OEC, they have been previously shown to give rise to cubane type complexes.[555-560] Furthermore, their versatile binding capabilities make them highly suitable for stabilising high nuclearity molecular species[536, 561-563] because of which they have also been included in this work.

In this chapter, we describe the synthetic approach that we have adopted in this work and how slight modifications to this approach can yield high nuclearity Mn coordination complexes. The coordination complexes reported here can broadly be divided into three classes – phosphonate based, mixed carboxylate-phosphonate based and carboxylate based. *tert*-Butyl phosphonic acid

(**Figure 3.1 (a)**) has been mainly used for the synthesis of phosphonate based complexes while for the mixed complexes, phenylphosphonic acid (**Figure 3.1 (b)**) and pivalic acid (**Figure 3.1 (c)**) have been employed. For the carboxylate based complexes, pivalic acid has been utilised as the primary ligand.

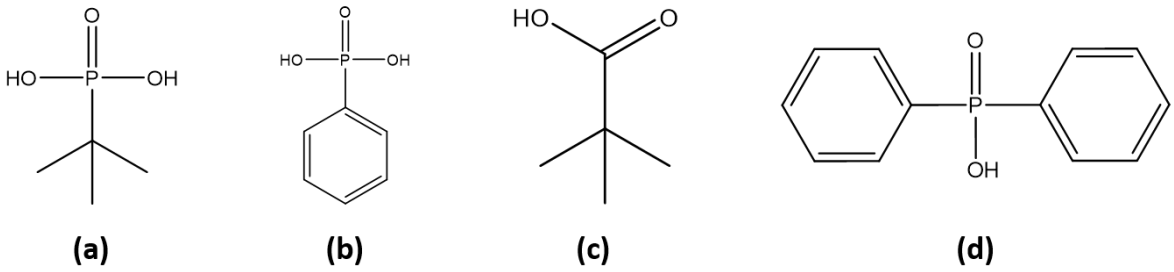

Figure 3.1: Structure of **(a)** *tert*-butyl phosphonic acid, **(b)** phenylphosphonic acid, **(c)** pivalic acid and **(d)** diphenylphosphinic acid.

3.1 Phosphonate based complexes

Previously the group has reported a {Mn_6} cage, [Cl⊂Mn_6(*tert*-butyl-PO_3)$_8$(4-picoline)$_6$],[545] (**Figure 3.2 (a)**) and a symmetric {Mn_{13}} complex, [Mn_{13}(μ_4-O)$_8$(μ_4-Cl)$_6$(*tert*-butyl-PO_3)$_8$],[384, 543] (**Figure 3.2 (b)**) both of which contain *tert*-butyl phosphonate bridging groups. Additionally, a less symmetric form of the {Mn_{13}} complex, Mn_{13}(μ_4-O)$_6$(μ-OH)$_2$(μ-CH_3O)$_4$(CH_3OH)$_2$(*tert*-butyl-PO_3)$_{10}$(4-picoline)$_4$], (**Figure 3.2 (c)**) that contains labile 4-methylpyridine (or 4-picoline) ligands, which can be replaced with bridging ligands to form one-dimensional chains, has also been previously reported.[542] In this work, the {Mn_6} cage and the symmetric {Mn_{13}} complex have been used as model compounds for developing the computational methodology to investigate the electronic structure and understand the magnetic properties. Details of this work are provided in chapter **4** and **5**.

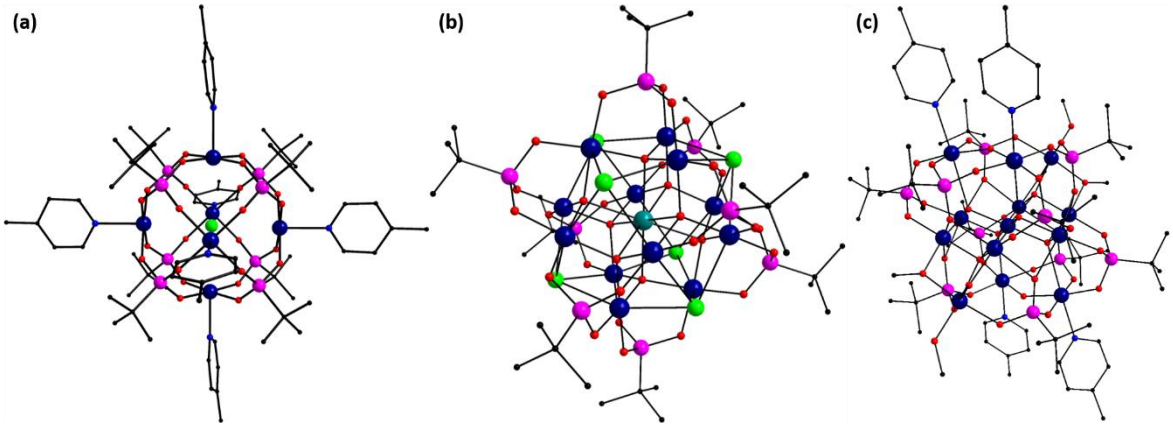

Figure 3.2: Structure of **(a)** the {Mn_6} complex [Cl⊂Mn_6(*tert*-butyl-PO_3)$_8$(4-picoline)$_6$],[545] **(b)** the symmetric complex [Mn_{13}(μ_4-O)$_8$(μ_4-Cl)$_6$(*tert*-butyl-PO_3)$_8$][384, 543] and **(c)** the asymmetric complex Mn_{13}(μ_4-O)$_6$(μ-OH)$_2$(μ-CH_3O)$_4$(CH_3OH)$_2$(*tert*-butyl-PO_3)$_{10}$(4-picoline)$_4$][542] Colour scheme: Mn^{III} (dark blue), Mn^{II} (teal), Cl (green), P (pink), C (black), N (blue) and O (red). All hydrogen atoms have been removed for clarity.

For the synthesis of the {Mn_6} and the {Mn_{13}} complexes, in essence, the comproportionation reaction between $MnCl_2{\cdot}2H_2O$ and $KMnO_4$ is carried out in presence of *tert*-butyl phosphonic acid. The striking similarity in the synthetic protocol for these complexes – especially {Mn_6} and the asymmetric {Mn_{13}} – lead us to believe that these complexes must be structurally related. To verify this hypothesis, the counterion of the Mn^{II} salt was varied and under similar reaction conditions, the {Mn_6} cage was obtained with $MnCl_2$ and the less symmetric {Mn_{13}} complex was obtained with MnI_2. With $MnBr_2{\cdot}4H_2O$ as the source of Mn^{II} ions however, $[Mn^{II}_4Mn^{III}_8Br_2(\mu\text{-}O)_4((CH_3)_3CPO_3)_{10}((CH_3)_3CPO_3H)_2(4\text{-picoline})_6(H_2O)_{10}]{\cdot}2CH_3CN$ (compound **8.1**) (4-picoline = $(CH_3)C_5H_4N$) was synthesised. The formation of three different complexes under similar reaction conditions by simply varying the Mn(II) salt highlights the importance of the counterion associated with Mn^{II} ions. The structural and physicochemical properties of the dodecanuclear complex are described in chapter **8**.

To obtain high nuclearity mixed-metal complexes, comproportionation reaction between $Mn(CH_3COO)_2{\cdot}4H_2O$ and $KMnO_4$ in presence of *tert*-butyl phosphonic acid and an alkali/alkaline earth metal salt was carried out under different reaction conditions. This resulted in the formation of four compounds that are structurally related to the less symmetric {Mn_{13}} complex. In presence of NaI and 4-picoline, $Na[Na_{0.4}(Mn^{II}_{0.5}Mn^{III}_{0.5})Mn^{III}_{12}(\mu_4\text{-}O)_2(\mu_3\text{-}O)_4(\mu\text{-}O)_{0.4}(\mu\text{-}OH)_{1.6}((CH_3)_3CPO_3)_{10}(4\text{-picoline})_4(\mu\text{-}CH_3O)_4(CH_3OH)_2][(Mn^{II}_{0.5}Mn^{III}_{0.5})Mn^{III}_{12}(\mu_4\text{-}O)_2(\mu_3\text{-}O)_4(\mu\text{-}OH)_2((CH_3)_3CPO_3)_{10}((CH_3)_3CPO_3H)_2(4\text{-picoline})_4(\mu\text{-}CH_3O)_4]{\cdot}5CH_3OH$ (compound **8.2**) was formed. Refluxing $KMnO_4$ and $Mn(CH_3COO)_2{\cdot}4H_2O$ with *tert*-butyl phosphonic acid and pivalic acid in the ratio 1:4:5:10 lead to the formation of $K[K_2(Mn^{II}_{0.5}Mn^{III}_{0.5})Mn^{III}_{12}(\mu_4\text{-}O)_2(\mu_3\text{-}O)_4(\mu\text{-}OH)_2((CH_3)_3CPO_3)_{10}((CH_3)_3CO_2)_2(\mu\text{-}CH_3O)_4(CH_3OH)_6][(Mn^{II}_{0.5}Mn^{III}_{0.5})Mn^{III}_{12}(\mu_4\text{-}O)_2(\mu_3\text{-}O)_4(\mu\text{-}OH)_2((CH_3)_3CPO_3)_{10}((CH_3)_3CPO_3H)_2(\mu\text{-}CH_3O)_4(CH_3OH)_4]{\cdot}2CH_3OH$ (compound **8.3**).

Refluxing $KMnO_4$ with $Mn(CH_3COO)_2{\cdot}4H_2O$ and $Ca(CH_3COO)_2$ with diphenylphosphinic acid (**Figure 3.1 (d)**) and *tert*-butyl phosphonic acid in the ratio 1:4:5:5:5 in presence of excess of pivalic acid lead to the formation of $[Mn^{II}Mn^{III}_{12}Ca_2(\mu_4\text{-}O)_2(\mu_3\text{-}O)_6((CH_3)_3CPO_3)_{10}((C_6H_5)_2PO_2)_2((CH_3)_3CCO_2H)_2(\mu\text{-}CH_3O)_4(CH_3OH)_{5.15}(CH_3CN)_{0.85}]{\cdot}CH_3OH{\cdot}CH_3CN$ (compound **8.4**). By increasing the ratio of $KMnO_4$ and $Mn(CH_3COO)_2{\cdot}4H_2O$ from 1:4 to 5:1, $[Mn^{II}_3Mn^{III}_{12}Ca_2(\mu_4\text{-}O)_4(\mu_3\text{-}O)_2(\mu_3\text{-}OH)_2((CH_3)_3CPO_3)_8((C_6H_5)_2PO_2)_2((CH_3)_3CCO_2)_4(CH_3CO_2)_2(\mu\text{-}CH_3O)_8(CH_3OH)_2]{\cdot}2CH_3OH{\cdot}2CH_3CN$ (compound **8.5**) was obtained. The structural characteristics and the physicochemical behaviour of all four complexes are discussed in chapter **8**.

There are a few key points to take away from the synthesis of these mixed-metal complexes. First of all, except for the compounds **8.1** and **8.2**, the synthesis of these complexes requires the use of large amounts of pivalic acid. This was done to suppress the formation of the less symmetric {Mn_{13}} complex which highlights the strong binding capabilities of the phosphonate group. Additionally, it can be seen from the molecular formulae that the pivalic acid forms an integral part of the structure

and it was observed that it aids in stabilising the hetero-metal. Secondly, the synthesis of the Ca containing complexes shows how varying the ratio of the Mn^{II} and Mn^{VII} salts can lead to stabilisation of different species. Additionally, the incorporation of $CH_3CO_2^-$ ions in the $\{Mn_{15}\}$ complex (compound **8.5**) again points towards the non-innocent behaviour of the counterions.

3.2 Mixed phosphonate-carboxylate based complexes

Considering that both phosphonate and carboxylate ligands can give rise to structures similar to the OEC,[555-560] we have also investigated the simultaneous use of both ligands. We have primarily made use of pivalic acid and phenylphosphonic acid for this purpose. The reason behind the choice of these specific ligands is that they provide a balanced mix of structural and electronic features. It was observed in the phosphonate based complexes that the use of bulky and strongly binding *tert*-butyl phosphonic acid lead to the formation of complexes that belonged to the same family of $\{Mn_{13}\}$ complexes.[542] Here we have tried to isolate the steric and the electronic features by using sterically less hindered but strongly binding phenylphosphonic acid along with a sterically demanding pivalic acid. The idea behind this is to form low nuclearity units stabilised by pivalate groups that can be then linked together by the phosphonate groups. This idea has witnessed some success in the past[536, 562, 564] although separation of steric and electronic features remains largely unexplored.

Based on the observations with the phosphonate compounds, an excess of carboxylic acid was used to suppress the formation of complexes that exclusively contain phosphonate ligands. The solvent has been also found to play an important role in stabilising different species. It was observed that if the comproportionation reaction between $Mn(CH_3COO)_2{\cdot}4H_2O$ and $KMnO_4$ in presence of phenylphosphonic acid, pivalic acid and L(-)-proline in the ratio 1:4:2:40:2 was carried out in CH_3CN and dimethyl sulfoxide (DMSO), a dodecanuclear Mn complex, $[Mn^{II}_{12}(\mu_3\text{-}OH)_4((C_6H_5)PO_3)_4((CH_3)_3CCO_2)_{12}((CH_3)_2CSO)_6]{\cdot}DMSO{\cdot}34CH_3CN$ (compound **7.1**) was formed. When DMSO was replaced with *N*,*N*-dimethylformamide (DMF), a mixed-valance hexanuclear complex, $[Mn^{II}_2Mn^{III}_4(\mu_3\text{-}O)_2((CH_3)_3CCO_2)_{10}(DMF)_4]{\cdot}(DMF)$ (compound **6.1**), with only pivalate ligands crystallised. Refluxing $KMnO_4$, $Mn(CH_3COO)_2{\cdot}4H_2O$, phenylphosphonic acid, pivalic acid and L(-)-proline in the ratio 1:4:2.5:20:1, in a mixture of CH_3CN and CH_3OH leads to the formation of a highly symmetric pentadecanuclear coordination complex, $[Mn^{II}_6Mn^{III}_9(\mu_3\text{-}O)_4((CH_3)_3CCO_2)_{11}((CH_3)_3CCO_2H)(C_6H_5PO_3)_6(\mu\text{-}CH_3O)_6(\mu_3\text{-}CH_3O)_2(CH_3OH)_5]$ (compound **7.2**). By changing the ratio of Mn^{II} and Mn^{VII} salts to 5:1, replacing L(-)-proline with 2, 6-pyridinedimethanol and by addition of acetic acid, an asymmetric form of this pentadecanuclear complex, $[Mn^{II}_5Mn^{III}_{10}(\mu_3\text{-}O)_4((CH_3)_3CCO_2)_{7.15}(CH_3CO_2)_{4.85}(C_6H_5PO_3)_6(\mu\text{-}CH_3O)_6(\mu_3\text{-}CH_3O)_2(CH_3OH)_5]{\cdot}2CH_3CN{\cdot}CH_3OH$ (compound **7.3**), was also obtained.

By varying the amount of pivalic acid used, comproportionation reaction between $KMnO_4$ and $Mn(CH_3COO)_2{\cdot}4H_2O$ in presence of phenylphosphonic acid and 2,6-pyridinedimethanol in the ratio

1:5:2.5:1 in a CH_3CN/CH_3OH mixture, results in the formation of two compounds. With a 20 fold excess of pivalic acid (with respect to $KMnO_4$), a tetradecanuclear complex, $[Mn^{II}_4Mn^{III}_{10}(\mu_3\text{-}O)_4(\mu_3\text{-}OH)_2(\mu\text{-}CH_3O)_9(CH_3OH)_2(H_2O)_2((C_6H_5)PO_3)_3((CH_3)_3CCO_2)_{10}(CH_3CO_2)_3]$ (compound **7.4**), is formed while a 20 fold excess results in the formation of a tridecanuclear complex, $[(Mn^{II}_{0.5}Mn^{III}_{0.5})_2 Mn^{III}_{11}(\mu_3\text{-}O)_8((C_6H_5)PO_3)_4((CH_3)_3CCO_2)_{10}(\mu\text{-}CH_3O)_4(\mu\text{-}CH_3OH)_4]\cdot CH_3OH\cdot CH_3CN$ (compound **7.5**). For the former, acetate ions form an integral part of the structure which again shows the non-innocent behaviour of the counterion.

This class of complexes also points out the importance of other attributes of the reaction mixture in a comproportionation reaction like the solvent system used. All these mixed phosphonate-carboxylate complexes have also been found to be structurally related and the structural characteristics and the physicochemical behaviour of these complexes are discussed in detail in chapter **7**.

3.3 Carboxylate based complexes

The previous sections highlighted the effect that the counterion of the Mn^{II} salt can have on stabilisation of different species in the reaction mixture. To address this, we have completely avoided the use of Mn^{II} salts for the synthesis of carboxylate only complexes.

To this end it was observed that the reaction of $KMnO_4$ with excess of pivalic acid in CH_3CN leads to the formation of a polymorph of the hexanuclear complex, $[Mn^{II}_2Mn^{III}_4(\mu_3\text{-}O)_2((CH_3)_3CCO_2)_{10}(DMF)_4]\cdot(DMF)$ (compound **6.1**), that was briefly mentioned in the previous section. The crystal quality of this polymorph however, was poor because of which $[Mn^{II}_2Mn^{III}_4(\mu_3\text{-}O)_2((CH_3)_3CCO_2)_{10}(DMF)_4]\cdot(DMF)$ has been used for characterisation purposes. Using a mixture of CH_3CN and $CHCl_3$ as the solvent for the reaction between $KMnO_4$ and excess of pivalic acid results in the formation of $[K_2Mn^{III}_8(\mu_3\text{-}O)_4(\mu\text{-}OH)_2((CH_3)_3CCOO)_{16}(CH_3CN)_2]\cdot CHCl_3$ (compound **6.2**). It is thus clear that the solvent can significantly affect the stabilisation of different species in the reaction mixture.

To investigate the structure directing effects of the ligand, pivalic acid was replaced with 4-phenylbenzoic acid (4-biphenylcarboxylic acid). Such a replacement lead to the formation of a dodecanuclear complex, $[Mn^{IV}_4Mn^{III}_8(\mu_3\text{-}O)_{12}(C_6H_5C_6H_4CO_2)_{16}(H_2O)_4]\cdot 3CH_3CN\cdot 13CHCl_3$ (compound **6.3**), which is structurally related to the first reported single molecule magnet.[113] The structural characteristics and the physicochemical behaviour of these three complexes are discussed in chapter **6**. Based on the synthesis of these carboxylate only complexes, it is clear that by tuning the steric properties of the ligand and with proper choice of solvent systems, one can obtain complexes with varying nuclearities and geometries.

3.4 Conclusion

For the synthesis of high nuclearity Mn coordination complexes, a facile synthetic self-assembly approach based on the comproportionation reaction between Mn^{II} and Mn^{VII} salts in presence of carboxylate and/or phosphonate based ligands has been developed. With tert-butyl phosphonic acid, a dodecanuclear complex was obtained which may be regarded as a structural intermediate between the $\{Mn_6\}$ and the $\{Mn_{13}\}$ complexes based on the synthesis. Four high nuclearity mixed-metal coordination complexes were also obtained with *tert*-butyl phosphonic acid by introducing subtle changes to the synthetic protocol.

To obtain mixed phosphonate-carboxylate based coordination complexes, sterically less hindered but strongly binding phenylphosphonic acid and a sterically demanding pivalic acid were used. This combination of ligands was used as an attempt to isolate the steric and the electronic features of the ligand groups and harness them individually. A series of high nuclearity complexes were obtained using this approach. For carboxylate based complexes the synthetic approach was modified and only $KMnO_4$ was used as the source for Mn ions. By varying the ligands and the solvent, three coordination complexes of different nuclearities were obtained.

The synthesis of all complexes discussed in this chapter highlights a few key points:

1. The ratio of the Mn^{II} and Mn^{VII} salts also affects the stabilisation of different species which indicates that the use of two Mn salts not only facilitates the stabilisation of intermediate oxidation state but it also has a direct structural effect on the species formed during the reaction.
2. The counterion of the Mn^{II} salt is not inert. It can lead to the stabilisation of different end products and may even get incorporated into the structure of the end product.
3. Compared to the carboxylate groups, the phosphonates have stronger affinity towards metal ions. Thus, for obtaining complexes that contain both carboxylate and phosphonate groups, an excess of carboxylic acid is required.
4. The choice of solvent can affect the stability of intermediate species in the reaction mixture and thus can lead to different end products.
5. The steric nature of the ligands participating in the reaction can direct the reaction towards the formation of different end products.

We have thus described a synthetic approach which involves the modification of the comproportionation reaction and have illustrated the versatility of this approach.

4 Magnetic Properties of $[Cl\subset Mn^{III}_6(tert\text{-}butyl\text{-}PO_3)_8(4\text{-}picoline)_6]Cl$ (4.1)

The influence of magnetic properties on the catalytic activity has been highlighted in the past.[67, 392, 393, 404-407] It is therefore, important to have an understanding of the magnetic properties of the system under consideration. The exchange coupling between the metal centres is the most important among the various interactions affecting the magnetic behaviour of the system and hence influencing the OER.[67, 68]

In polynuclear complexes, metal centres are generally bridged together by multiple ligands. This implies that the observed magnetic coupling strength between the metal centres is a sum of coupling via all the bridges. To fully understand the coupling in a polynuclear complex, one therefore needs to identify the effect of each ligand bridge on the coupling. There has been some work towards understanding the mechanism of coupling via various bridges in polynuclear complexes.[524, 565-570] These investigations have either varied the geometrical parameters of the system under study or made use of the overlap matrix both of which become increasingly complicated with larger systems.

In this chapter the magnetic properties of a hexanuclear Mn cage complex $[Cl\subset Mn^{III}_6(tert\text{-butyl-}PO_3)_8(4\text{-picoline})_6]Cl$[545] (compound **4.1**) are described. This complex was made in the Schmitt group by a former postdoctoral fellow Lei Zhang. The synthetic protocol adopted for this complex is based on comproportionation reaction involving the reaction of $MnCl_2{\cdot}2H_2O$, $KMnO_4$, *tert*-butyl phosphonic acid and 4-picoline in presence of 1,4-phenylenediacetic acid. The calculations were primarily carried out using the PBE0 functional[451] along with a SDDALL[507] basis set for Mn, 6-31G(2d)[508] basis set for P and Cl, 6-31G(d)[508] basis set for O and 6-31G(p)[508] basis set for H. The aim of this chapter is investigate the electronic structure of this complex in five oxidation states using hybrid density functional theory. Additionally, we aim to understand the nature of coupling between the Mn centres in the different oxidation states and examine the possibility of switching the coupling during the oxidation process. To investigate the mechanism of exchange coupling between Mn centres via different bridges a novel methodology has been developed and described in this chapter.

Note: A large portion of this work has been pulished as a journal article (ref. 571).

4.1 Crystal Structure and DFT Model

Compound **4.1** ([Cl⊂Mn^{III}_6(*tert*-butyl-PO_3)$_8$(4-picoline)$_6$]Cl) contains a positively charged hexanuclear Mn complex where the 6 Mn(III) centres reside at the vertices of an octahedron centred around a Cl^- ion (**Figure 4.1**).[545] This complex is stabilised by 8 *tert*-butyl phosphonate groups which fulfil 4 out of the 6 coordination sites for each Mn(III) centre and any two Mn centres *cis*- to each other are connected to each other by two phosphonate groups. The Mn centres are additionally coordinated to the N-donor of the 4-picoline ligands. The Jahn-Teller axis of all the Mn(III) atoms is along the Mn(III)-Cl bond.

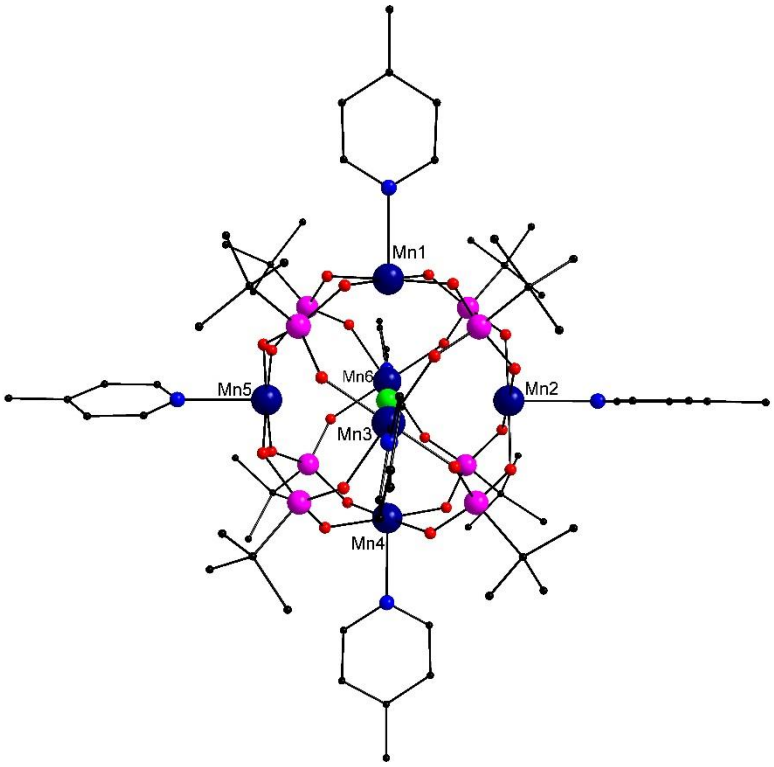

Figure 4.1: Structure of the hexanuclear compound **4.1**. Colour scheme: Mn^{III} (dark blue), P(pink), Cl (green), C (black) O (red). Hydrogens have been removed for clarity.

For investigating the magnetic properties, the reported crystal structure was used to build the initial model and the whole complex was modelled without simplifying the structure. The ferromagnetic state of this complex was modelled and the differences in the key Mn-Mn and Mn-ligand bond lengths were found to be < 2 % in comparison to the experimental crystal structure (**Table 4.1**). The distance between the Mn centres *trans*- to each other was always found to be 6.217 Å but a slight variation in the distances between the *cis*-Mn centres was observed (**Table 4.2**). Among the other possible (2^6-1 =)63 spin states, five unique spin configurations were identified (assuming that the difference in the cis-Mn distances are not important) and all of them were modelled. The ferromagnetic state was found to be the highest in energy and the state Mn123 (the configuration in which the Mn centres Mn1, Mn2 and Mn3 have down spin) with spin multiplicity S = 0 was found to be the most stable (**Figure 4.2**). The impact of lowering of spin symmetry on the structural

features in the non-ferromagnetic states was found to be small as is evident from the bond distances (**Table 4.1**).

Table 4.1: Comparison of the average distances (Å) in the crystal structure and the DFT model in the different spin states for compound **4.1**. The numbers after 'Mn' specify which Mn centres have a down spin. For example, Mn124 corresponds to a state where Mn1, Mn2 and Mn4 have a spin down while others have a spin up configuration.

Configuration\Parameter	Mn-Mn (*trans*)	Mn-Mn (*cis*)	Mn-Cl	Mn-N	Mn-O	P-O
Experimental[545]	6.217	4.396	3.109	2.228	1.866	1.485
Ferromagnetic	6.192	4.378	3.096	2.279	1.896	1.543
Mn1	6.190	4.377	3.095	2.279	1.895	1.543
Mn12	6.189	4.376	3.095	2.279	1.893	1.543
Mn14	6.192	4.378	3.096	2.279	1.895	1.543
Mn123	6.188	4.376	3.094	2.279	1.895	1.543
Mn124	6.190	4.377	3.095	2.279	1.895	1.543

Table 4.2: Mn-Mn distances for compound **4.1** in the ferromagnetic state.

Mn centres	Distance (Å)	Mn centres	Distance (Å)	Mn centres	Distance (Å)
Mn1Mn2	4.386	Mn2Mn4	4.406	Mn4Mn6	4.386
Mn1Mn3	4.386	Mn2Mn6	4.406	Mn5Mn6	4.386
Mn1Mn5	4.406	Mn3Mn4	4.406	Mn1Mn4	6.217
Mn1Mn6	4.406	Mn3Mn5	4.406	Mn2Mn5	6.217
Mn2Mn3	4.386	Mn4Mn5	4.386	Mn3Mn6	6.217

4.2 Exchange Coupling Constants (*J*-Values)

There are (6*5/2 =)15 possible coupling interactions between the Mn centres in compound **4.1** and by taking into account the geometrical arrangement in the system, these interactions can be divided into 2 sets. These sets take into account the coupling between the Mn centres *cis*- to each other (J_{cis}) and the Mn centre *trans*- to each other (J_{trans}). The coupling between the Mn centres *cis*- to each other is facilitated by both the phosphonate groups and the central Cl^- while the Mn centres *trans*- to each other are bridged only *via* the central Cl. This division can be represented by the following Hamiltonian:

$$\begin{aligned} H = & -2J_{trans}[\langle s_1.s_4\rangle + \langle s_2.s_5\rangle + \langle s_3.s_6\rangle] \\ & - 2J_{cis}[\langle s_1.s_2\rangle + \langle s_1.s_3\rangle + \langle s_1.s_5\rangle + \langle s_1.s_6\rangle \\ & + \langle s_2.s_3\rangle + \langle s_2.s_4\rangle + \langle s_2.s_6\rangle + \langle s_3.s_4\rangle \\ & + \langle s_3.s_5\rangle + \langle s_4.s_5\rangle + \langle s_4.s_6\rangle + \langle s_5.s_6\rangle] \end{aligned} \quad (4.1)$$

Considering the large distance between the *trans*-Mn centres, the possibility that one coupling constant (J_{cis}) may prove sufficient cannot be ignored. Additionally, since Mn centres *cis*- to each other can also be divided into two groups based on the Mn-Mn distances (4.41 and 4.39 Å), there is a possibility that 3 coupling constants will be needed. The reason for using Mn-Mn distance as a parameter to determine the number of coupling constants here is because differences in the Mn-

Mn distances correspond to different Mn-ligand bond lengths which will ultimately affect the strength of coupling.

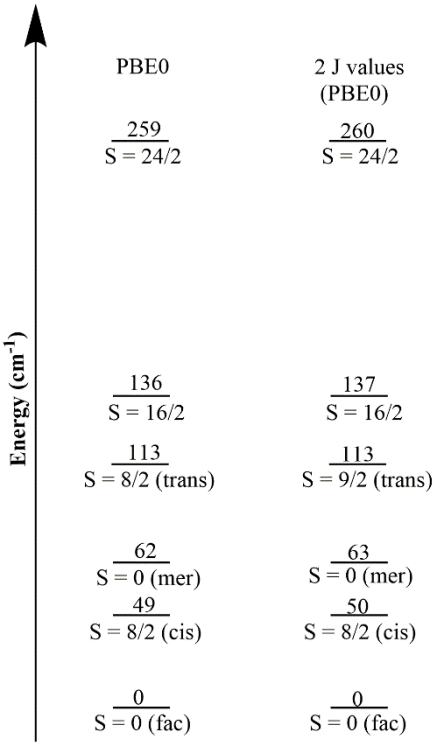

Figure 4.2: Relative energies of the 6 spin states of compound **4.1** obtained using DFT (PBE0), and the calculated J-values.

For defining the spin operators in eq. 4.1, the spin density on each Mn centre in the different spin states was determined using Bader charge analysis.[519] Bader analysis predicts that the spin density on each Mn centre is approximately 3.8 (**Table 4.3**) indicating strong localisation.

Table 4.3: Bader spin density on Mn centres in the different electronic configurations truncated to three decimal places. The states Mn16, Mn156 and Mn146 are symmetry equivalent to the Mn12, Mn123 and Mn124 states respectively.

Configuration	Mn1	Mn2	Mn3	Mn4	Mn5	Mn6
Ferromagnetic	3.789	3.789	3.789	3.790	3.790	3.789
Mn1	-3.786	3.789	3.789	3.787	3.789	3.789
Mn16	-3.786	3.789	3.787	3.787	3.789	-3.786
Mn14	-3.788	3.788	3.789	-3.788	3.789	3.789
Mn156	-3.786	3.786	3.786	3.787	-3.786	-3.786
Mn146	-3.789	3.789	3.787	-3.789	3.789	-3.787

A 1 J-value model was investigated by removing the J_{trans} term from eq. 4.1 but consistent solutions were not obtained implying that the J_{trans} term is required. With the 2 J-value model, the average coupling constants obtained using Bader spin densities are provided in **Table 4.4**. The relative energies of the 6 states have been calculated using these J-values and have been found to

be in agreement with the DFT results (**Figure 4.2**). On dividing the J_{cis} term into two based on the Mn-Mn distance, the spin Hamiltonian in eq. 4.1 changes to the following:

$$\begin{aligned} H = &-2J_1[\langle s_1.s_4\rangle + \langle s_2.s_5\rangle + \langle s_3.s_6\rangle] \\ &- 2J_2[\langle s_1.s_2\rangle + \langle s_1.s_3\rangle + \langle s_2.s_3\rangle + \langle s_4.s_5\rangle + \langle s_4.s_6\rangle + \langle s_5.s_6\rangle] \\ &- 2J_3[\langle s_1.s_5\rangle + \langle s_1.s_6\rangle + \langle s_2.s_4\rangle + \langle s_2.s_6\rangle + \langle s_3.s_4\rangle + \langle s_3.s_5\rangle] \end{aligned} \quad (4.2)$$

The three J-values obtained are within the standard deviation for the 2 J-values (**Table 4.4**) which implies that defining the Hamiltonian with 2 J-values can be considered optimal.

Table 4.4: Calculated J values (cm^{-1}) and the standard deviations obtained using a 2 J-value and a 3 J-value Hamiltonian for compound **4.1**.

Number of J-values	J_{trans}/J_1 (cm^{-1})	J_{cis}/J_2 (cm^{-1})	J_3 (cm^{-1})
2	-3.48 ± 0.05	-1.28 ± 0.04	-
3	-3.46 ± 0.06	-1.29 ± 0.06	-1.26 ± 0.06

4.2.1 Effect of the spin operator definition of J-values

To investigate the dependence of the coupling constants on the definition of spin operator, the spin operators were defined using formal spin values, spin densities obtained using Mulliken[472-475] and Hirshfeld population analysis,[461, 477, 478] and the generalized spin projection approach.[497] The formal spin approach essentially assumes that the unpaired electrons are completely localised on the Mn centre. The other charge analysis schemes have been discussed in chapter **2**. Mulliken charge analysis predicts higher localisation of the electrons compared to Hirshfeld and Bader charge analysis schemes (**Table 4.5**). The equations associated with the spin projection approach are provided in the appendix. Since the 2 J-value model was found to be optimal, it was used for calculating the coupling constants with the different spin operator definitions and the values obtained are provided in **Table 4.6**.

It can be seen that the coupling constants obtained by the spin projection approach are identical to those obtained by the formal spin approach and are similar to those obtained using the Mulliken spin values. The coupling constants obtained by Bader and Hirshfeld spin values are also close to each other but different from those obtained by the other three approaches.

To understand the effect of the changes in the coupling constants on the magnetic susceptibility, the temperature dependence of magnetic susceptibility was plotted using the different pairs of coupling constants (**Figure 4.3**). The value of the g-tensor was determined to be 1.998 for this complex which was used for the calculation of the magnetic susceptibility.

Table 4.5: Spin density on Mn centres (truncated to three decimal places) in the different electronic configurations obtained using Mulliken and Hirshfeld charge analyses. The states Mn16, Mn156 and Mn146 are symmetry equivalent to the Mn12, Mn123 and Mn124 states respectively.

Configuration	Mn1	Mn2	Mn3	Mn4	Mn5	Mn6
			Mulliken charge analysis			
Ferromagnetic	3.946	3.946	3.946	3.946	3.946	3.946
Mn1	-3.918	3.940	3.941	3.939	3.940	3.939
Mn16	-3.924	3.935	3.934	3.933	3.935	-3.923
Mn14	-3.925	3.934	3.936	-3.925	3.934	3.936
Mn156	-3.929	3.929	3.929	3.929	-3.929	-3.929
Mn146	-3.930	3.929	3.930	-3.930	3.929	-3.927
			HIrshfeld charge analysis			
Ferromagnetic	3.744	3.744	3.744	3.744	3.744	3.744
Mn1	-3.728	3.741	3.741	3.741	3.741	3.741
Mn16	-3.731	3.738	3.738	3.738	3.738	-3.731
Mn14	-3.732	3.738	3.738	-3.732	3.738	3.738
Mn156	-3.735	3.734	3.734	3.734	-3.735	-3.734
Mn146	-3.735	3.735	3.735	-3.735	3.735	-3.735

Table 4.6: J-values obtained using different definitions of spin densities on the Mn centres.

Approach	J_{trans} (cm^{-1})	J_{cis} (cm^{-1})
Formal Spin	-3.12 ± 0.05	-1.15 ± 0.04
Spin Projection	-3.12 ± 0.05	-1.15 ± 0.04
Mulliken	-3.22 ± 0.05	-1.18 ± 0.04
Bader	-3.48 ± 0.05	-1.28 ± 0.04
Hirshfeld	-3.57 ± 0.05	-1.31 ± 0.04

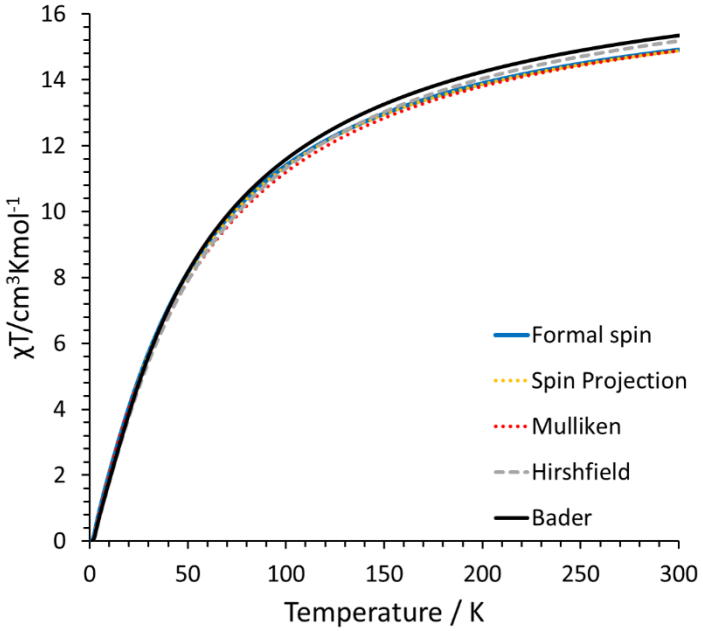

Figure 4.3: Temperature dependence of magnetic susceptibility for the {Mn_6} cage calculated using the coupling constants obtained using PBE0 functional and different definitions of spin operators.

It can be seen that the susceptibility plots obtained from the J-values of formal spin, spin projection approach and Mulliken analysis are almost coincident. The plot obtained using Bader and Hirshfeld analyses are quite similar. Since the Bader charge analysis provides a basis set independent description of the electron density and is not dependent on any arbitrary promolecular density, it has been used for further investigations.

4.2.2 Functional dependence of coupling constants

PBE0 has been previously shown to provide good estimates of magnetic properties[572, 573] and since, we are using calculated spin densities to define the spin operators, PBE0 is better suited than most other DFT functionals since it has been shown to reproduce the electron density quite accurately.[453] The functional dependence has still been tested using B3LYP[426, 431, 447, 574] which has also been shown to give reasonable results for the calculation of exchange coupling constants.[514, 521, 575] For this purpose, the Mn123, Mn12 and Mn124 states were modelled with B3LYP and eq. 4.1 in conjunction with the Bader spin densities (**Table 4.7**) was used for the calculation of the coupling constants. In this case, J_{trans} and J_{cis} were calculated to be -3.86 and -1.48 cm^{-1} respectively in reasonable agreement with the values obtained with PBE0 (**Table 4.6**). The susceptibility plot obtained using B3LYP also looks similar to that obtained using PBE0 (**Figure 4.4**).

Table 4.7: Bader spin density on Mn centres in the different electronic configurations using B3LYP (truncated to three decimal places). The state Mn126 is symmetry equivalent to the Mn123 state.

Configuration	Mn1	Mn2	Mn3	Mn4	Mn5	Mn6
Mn12	-3.740	-3.740	3.743	3.743	3.741	3.741
Mn126	-3.743	-3.741	3.743	3.743	3.741	-3.743
Mn124	-3.741	-3.740	3.740	-3.740	3.740	3.740

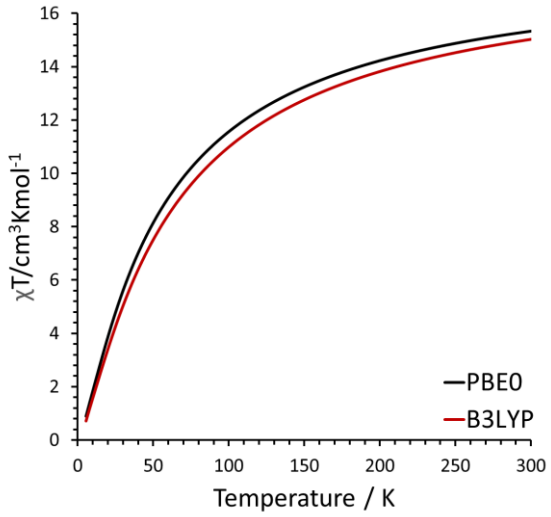

Figure 4.4: Calculated χT vs T plot for the {Mn_6} cage and the same plot obtained using the coupling constants obtained using PBE0 and B3LYP.

4.2.3 Effect of *tert*-butyl group

To determine the impact, the *tert*-butyl group has on the coupling strength, it was replaced with a methyl group and the six spin configurations were modelled again. The coupling constants were obtained using the Hamiltonian given in eq. 4.1 in conjunction with the Bader spin densities (**Table 4.8**). For this system, the value of J_{cis} and J_{trans} were calculated to be -1.15 ± 0.02 and -3.47 ± 0.05 cm^{-1} respectively. It can thus be seen that there is a reasonable effect of the *tert*-butyl group on the exchange coupling strength.

Table 4.8: Bader spin density (truncated to three decimal places) on each Mn centre and the relative energy of each spin state for compound **4.1** with the *tert*-butyl groups replaced with methyl groups.

Mn1	Mn2	Mn3	Mn4	Mn5	Mn6	Energy (cm^{-1})
3.781	3.781	3.781	3.781	3.781	3.781	0.00
-3.777	3.780	3.780	3.778	3.780	3.780	-115.71
-3.777	-3.777	3.780	3.778	3.778	3.780	-197.55
-3.779	3.780	3.780	-3.779	3.780	3.780	-130.62
-3.777	-3.778	-3.777	3.777	3.777	3.778	-246.65
-3.779	-3.777	3.779	-3.779	3.777	3.779	-181.12

4.2.4 Effect of replacement of 4-picoline groups with solvent molecules

The labile 4-picoline groups of compound **4.1** can potentially be replaced with solvent molecules from the reaction mixture and this has been previously observed.[545] To explore this possibility, the 4-picoline group on Mn1 was replaced with CH_3CN (**4.1.CH_3CN**) and with H_2O (**4.1.H_2O**) (**Figure 4.5 (a)** and **(b)** respectively). Such a replacement was found to be energetically unfavourable by ~34 kJ/mol in the former case and ~4 kJ/mol in the latter under vacuum conditions but it suggests that such replacement may be feasible under reaction conditions.

The introduction of a solvent molecule in the complex reduces the symmetry of the complex and this reduction is more pronounced in case of **4.1.H_2O** which is possibly because in this case the donor has been changed from N to O. For **4.1.CH_3CN**, six spin configurations were modelled and Bader spin densities on the Mn centres and the relative energy of each state are provided in **Table 4.9**. The Hamiltonian used for the calculation of the coupling constants is given as:

$$\begin{aligned} H = & -2J_1[\langle s_1.s_4\rangle] - 2J_2[\langle s_2.s_5\rangle + \langle s_3.s_6\rangle] \\ & - 2J_3[\langle s_1.s_2\rangle + \langle s_1.s_3\rangle + \langle s_1.s_5\rangle + \langle s_1.s_6\rangle] \\ & - 2J_4[\langle s_2.s_3\rangle + \langle s_2.s_4\rangle + \langle s_2.s_6\rangle + \langle s_3.s_4\rangle + \langle s_3.s_5\rangle \\ & + \langle s_4.s_5\rangle + \langle s_4.s_6\rangle + \langle s_5.s_6\rangle] \end{aligned} \quad (4.3)$$

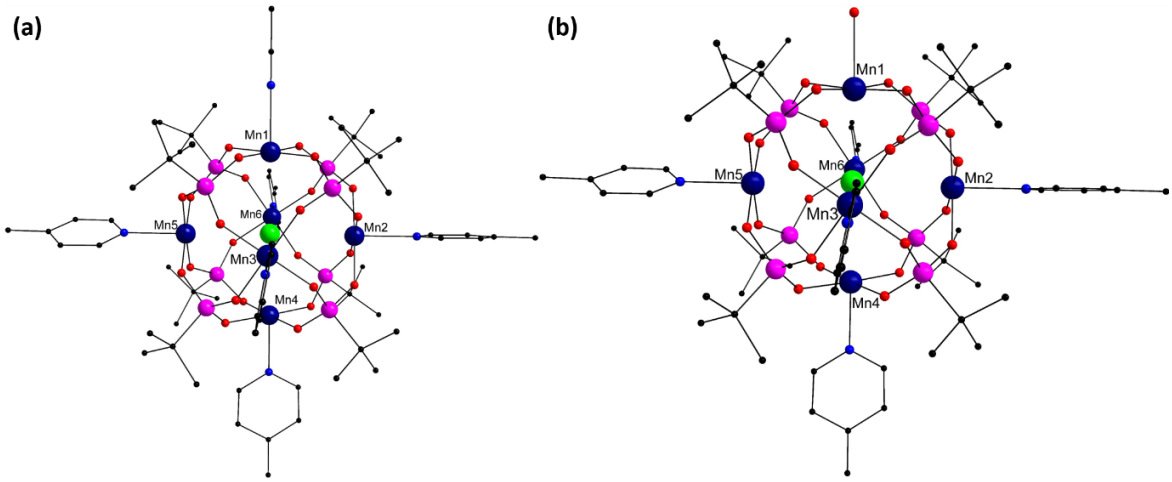

Figure 4.5: Optimised model of **(a) 4.1.CH_3CN** and **(b) 4.1.H_2O**. Colour scheme: Mn^{III} (dark blue), P(pink), Cl (green), C (black) O (red). Hydrogens have been removed for clarity.

Due to lower symmetry, three additional states were modelled in case of **4.1.H_2O** and the spin density of Mn centres and the energy of these states are provided in **Table 4.10**. The Hamiltonian for this system is given as:

$$\begin{aligned} H = & -2J_1[\langle s_1.s_4\rangle] - 2J_2[\langle s_2.s_5\rangle + \langle s_3.s_6\rangle] \\ & - 2J_3[\langle s_1.s_2\rangle + \langle s_1.s_3\rangle + \langle s_1.s_5\rangle + \langle s_1.s_6\rangle] \\ & - 2J_4[\langle s_2.s_3\rangle + \langle s_2.s_6\rangle + \langle s_3.s_5\rangle + \langle s_5.s_6\rangle] \\ & - 2J_5[\langle s_2.s_4\rangle + \langle s_3.s_4\rangle + \langle s_4.s_5\rangle + \langle s_4.s_6\rangle] \end{aligned} \quad (4.4)$$

Table 4.9: Bader spin density on each Mn centre (truncated to three decimal places) and the relative energy of each spin state for **4.1.CH_3CN**.

Mn1	Mn2	Mn3	Mn4	Mn5	Mn6	Energy (cm^{-1})
3.813	3.789	3.791	3.789	3.789	3.791	0.00
-3.809	3.789	3.790	3.786	3.789	3.790	-131.79
-3.809	-3.786	3.790	3.786	3.786	3.790	-215.44
-3.813	3.788	3.790	-3.789	3.788	3.790	-148.75
-3.809	-3.786	-3.787	3.786	3.786	3.787	-262.76
-3.812	-3.786	3.790	-3.789	3.786	3.789	-196.62

The coupling constants obtained for both systems are provided in **Table 4.11**. It is clear that the substitution of the 4-picoline ligands with solvent molecules does affect the coupling strength. The coupling between the Mn centres *trans*- to each other is more significantly affected compared to the coupling between *cis*-Mn centres. These changes however are not reflected in the temperature dependence of magnetic susceptibility (**Figure 4.6**) and this can be due to two possible reasons. It is possible that the susceptibility curve is not too sensitive to the changes in coupling strength. The other possible reason is that as the average coupling strength for the Mn centres *cis*- and *trans*- to each other for both **4.1.CH_3CN** and **4.1.H_2O**, is very similar to that observed for **4.1**, it results in similar susceptibility behaviour.

Table 4.10: Bader spin density on each Mn centre (truncated to three decimal places) and the relative energy of each spin state for **4.1.H₂O**.

Mn1	Mn2	Mn3	Mn4	Mn5	Mn6	Energy (cm^{-1})
3.812	3.788	3.788	3.787	3.787	3.789	0.00
3.812	-3.784	3.788	3.787	3.785	3.789	-119.13
3.809	3.787	3.788	-3.784	3.787	3.789	-136.58
-3.808	3.788	3.788	3.784	3.787	3.789	-137.64
-3.809	3.787	-3.785	3.784	3.787	3.787	-216.86
-3.808	-3.784	3.787	3.784	3.785	3.788	-220.00
-3.811	3.787	3.788	-3.787	3.787	3.789	-149.40
-3.809	-3.785	-3.785	3.784	3.784	3.786	-260.60
-3.812	-3.785	3.787	-3.787	3.784	3.788	-195.47

Table 4.11: Coupling constants (cm^{-1}) obtained for **4.1.CH₃CN** and **4.1.H₂O**.

	J_1 (cm^{-1})	J_2 (cm^{-1})	J_3 (cm^{-1})	J_4 (cm^{-1})	J_5 (cm^{-1})
4.1.CH₃CN	-3.79 ± 0.06	-3.40 ± 0.05	-1.33 ± 0.01	-1.25 ± 0.02	-
4.1.H₂O	-4.23 ± 0.17	-2.95 ± 0.14	-1.31 ± 0.05	-1.38 ± 0.11	-1.30 ± 0.05

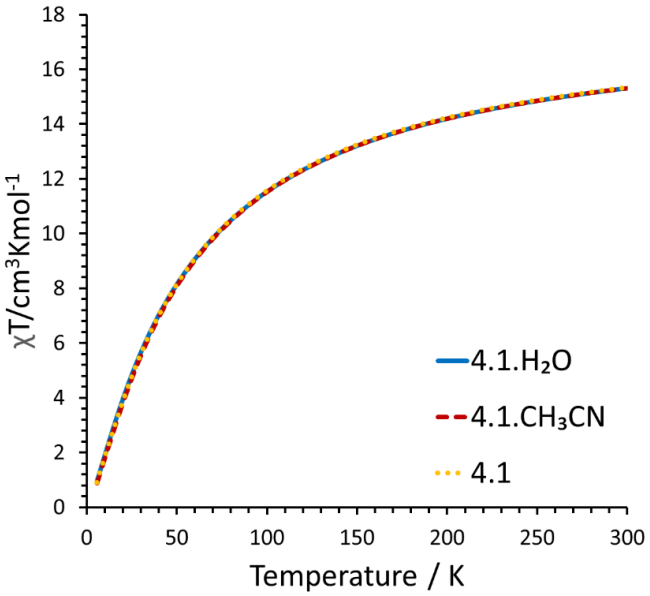

Figure 4.6: Calculated χT vs T plot for the {Mn_6} cage and the calculated plots for compound **4.1**, **4.1.CH₃CN** and **4.1.H₂O** using the PBE0 functional.

4.2.5 Comparison with the experiment

To assess the validity of the coupling constants obtained using DFT, the effect of temperature on the magnetic susceptibility has been determined experimentally and compared with the calculated plots. For this purpose, we synthesized the cage using the published procedure[545] and measured the magnetic susceptibility. The complex was characterised using powder X-ray diffraction and infrared spectroscopy (**Figure 4.7**). The temperature dependence of magnetic susceptibility obtained for this complex is shown in **Figure 4.8**.

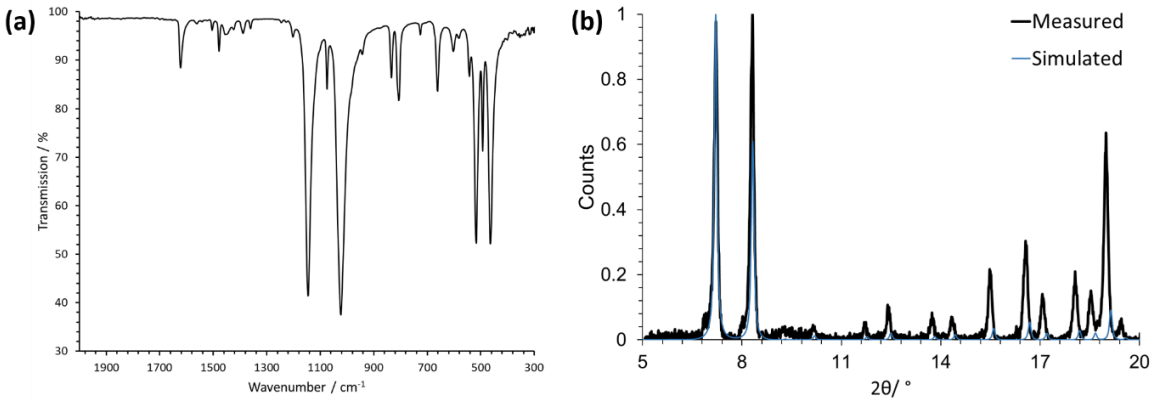

Figure 4.7: (a) The infrared spectrum and **(b)** simulated and measured PXRD pattern for compound **4.1**.

The comparison of the calculated χT plots with the experimental one reveals that the plot obtained using the coupling constants determined with PBE0 functional and Bader spin densities was the closest fit although it did not exactly reproduce the experimental plot. Due to this, a fit using two J-values was performed and the values corresponding to the best fit are given in **Table 4.12**. J_{cis} has been found to be identical to that calculated while J_{trans} differs from the calculated one by ~1 cm^{-1}. For comparison, only 1 coupling constant (J_{cis}) was also fitted to the experimental curve and it can be seen that it reproduces the experimental curve reasonably (**Figure 4.8**). The residual error, as calculated using phi,[529] for the one and two fitted coupling constants were found to be 19.4 and 12.2 respectively which shows that the curve obtained from 1 J-value is inferior to that obtained using 2 J-values as was expected.

Table 4.12: Calculated (Bader spin density) and fitted J-values for the {Mn_6} cage.

Approach\J value	J_{trans} (cm^{-1})	J_{cis} (cm^{-1})
Calculated (PBE0)	-3.48 ± 0.05	-1.28 ± 0.04
Fit to Experiment (2 J-values)	-2.53	-1.28
Fit to Experiment (1 J-value)	-	-1.88

To understand the effect of using one and two J-values on the electronic picture of the cage, the relative energies of the 6 states was calculated using the coupling constants obtained from the fit to experiment. For this purpose, eq. 4.1 was used and the s_i values were defined using average Bader spin densities. **Figure 4.9** shows the energy levels calculated from the 2 J-values fit, in line with the DFT results. The states quite close in energy, S = 4/2 (*cis*) and S = 0 (mer), are calculated to be almost degenerate with the 2 J-values fit. When J_{trans} is ignored, i.e. when only one J-value is used, the ground state is incorrectly predicted even though the susceptibility curve is reasonably reproduced. This confirms the previous idea that the susceptibility curve is not very sensitive to the details of the coupling constants. Thus one needs to be cautious when trying to fit coupling constants to magnetic susceptibility curves and ensure that the complete electronic picture is captured.

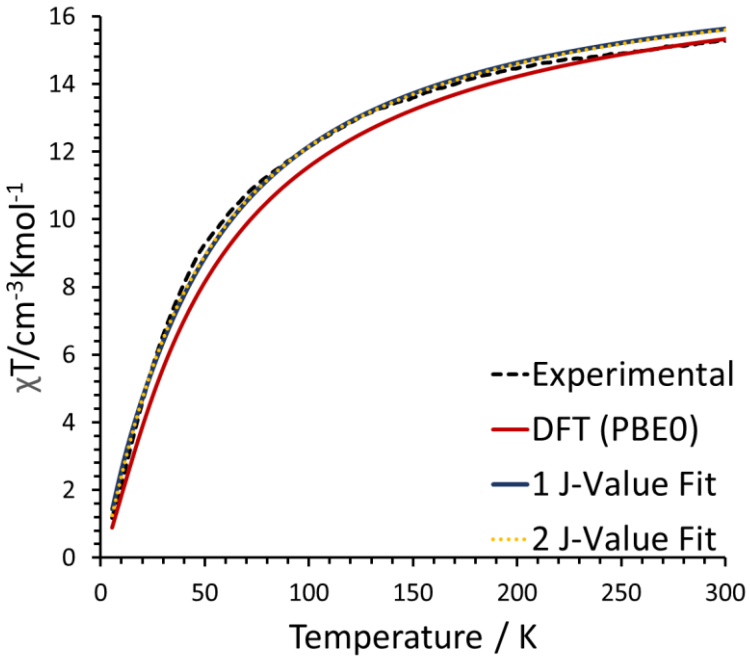

Figure 4.8: Experimental χT vs T plot for the {Mn_6} cage and the same plot obtained using the calculated (PBE0) and fitted coupling constants.

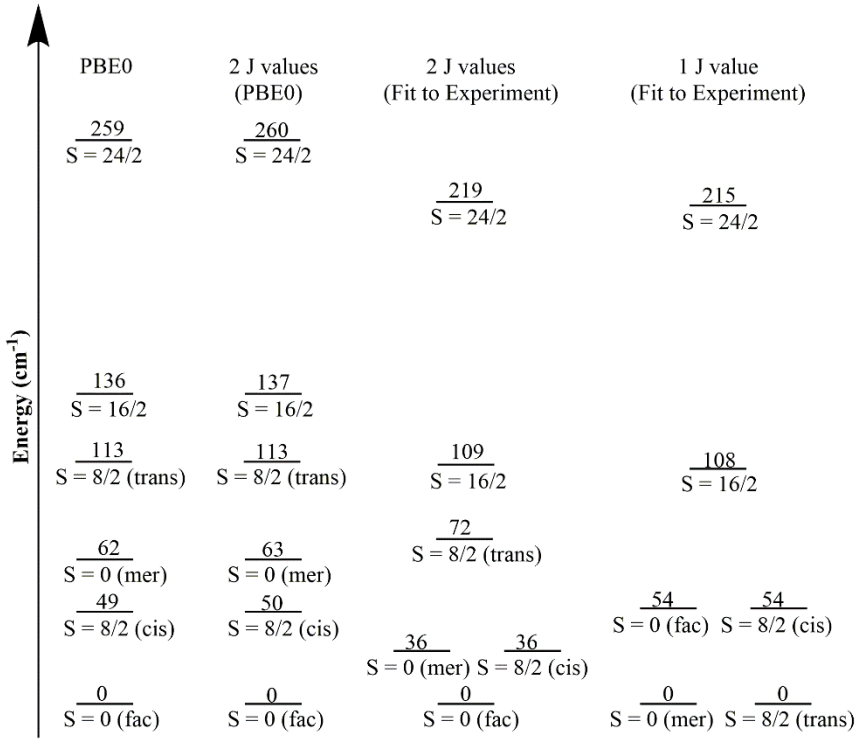

Figure 4.9: Relative energies of the 6 spin states of the {Mn_6} cage obtained using DFT (PBE0), and the calculated and fitted *J*-values.

4.3 The Nature of the Coupling Pathways

The Mn centres *trans*- to each other can only be coupled *via* the Cl^- and the negative J_{trans} value indicates that the coupling pathway between the *trans*-Mn centres is antiferromagnetic. The Mn centres *cis*- to each other, on the other hand, can be coupled by the phosphonate and the Cl^- bridge. In this case, both pathways may be antiferromagnetic or only the dominant one may be antiferromagnetic.

In order to investigate the coupling mechanism between the *cis*-Mn centres *via* the different bridges, an innovative approach that involves perturbing the system while retaining the symmetry and analysing the effect on the coupling strength due to the perturbation was employed. The perturbation can be introduced in two ways – by changing the electronegativity of the bridge or by changing the Mn-bridge bond distance. In general, a decrease in the electronegativity of the ligand bridge and/or a decrease in the Mn-bridge distance increase the coupling strength. The nature of coupling *via* a given bridge can thus be identified by determining how the coupling changes with the change in these factors.

To investigate the effect of the change in electronegativity, the central Cl^- in the parent model (compound **4.1**) was replaced with Br^- and I^- (**Mn_6Br** and **Mn_6I** respectively), and all 6 spin configurations were modelled. The coupling constants were obtained using the 2 J -value Hamiltonian (eq. 4.1) and are given in **Table 4.13**. For both models, the J_{trans} value increases rapidly with the decrease in the electronegativity of the central halide which confirms that the coupling between the *trans*-Mn centres is antiferromagnetic. The changes in the J_{cis} value however, were found to be too small to reach any conclusions. This is possibly due to the effect of the substitution with Br and I on the Mn-bridge distances.

For investigating the effect of changing only the Mn-Cl distance and hence the Mn-Cl bond strength, Br^- and I^- centres in **Mn_6Br** and **Mn_6I** were replaced with Cl^- and constrained geometry optimisation calculations were performed for the six spin configurations with the position of the Mn centres kept fixed (**Mn_6Br'** and **Mn_6I'** respectively). The coupling constants obtained are presented in **Table 4.13**. For both **Mn_6Br'** and **Mn_6I'**, the J_{trans} term was found to be negligible which indicates that there is negligible direct coupling between the Mn centres. In these models, although the Mn-Cl bridge is weaker, an increase in the J_{cis} value is observed which suggests that the coupling *via* this bridge may be ferromagnetic and that via the phosphonate bridge may be antiferromagnetic.

To exclusively identify the nature of the phosphonate pathway, the Cl^- in the parent model (compound **4.1**) was removed and the six spin configurations model were optimised keeping the position of the Mn centres fixed (**Mn_6**). Additionally, the constrain on the Mn centres was removed and the structure was allowed to fully optimise (**Mn_6'**). The Cl^- was later added to **Mn_6'** and this new system was optimised keeping the position of the Mn centres fixed (**Mn_6'Cl**). The coupling constants obtained for each model are presented in **Table 4.13**.

A negligible J_{trans} value observed in case of **Mn_6** and **Mn_6'** confirms the absence of direct coupling. The negative J_{cis} value for **Mn_6** and **Mn_6'** confirms the antiferromagnetic nature of the phosphonate pathway since the coupling between the *cis*-Mn centres is only *via* the phosphonate bridge in these models. Furthermore, the re-introduction of Cl^- in **Mn_6'** (**Mn_6'Cl**) leads to a decrease in J_{cis} value which in only possible if the Cl^- bridge is ferromagnetic in nature. As the change in the J_{cis} value is small, it implies that the Cl^- bridge is only weakly antiferromagnetic. Thus, it can be concluded that the phosphonate pathway is antiferromagnetic while the Cl^- bridge is antiferromagnetic for the *trans*-Mn centres and ferromagnetic for the *cis*-Mn centres.

Table 4.13: Average (*cis*-) Mn-Mn distances (Å) and coupling constants (cm^{-1}) for the different models of the {Mn_6} cage.

Model	*cis*-Mn-Mn distance (Å)	J_{trans} (cm^{-1})	J_{cis} (cm^{-1})
Compound **4.1**	4.378	-3.48 ± 0.05	-1.28 ± 0.04
Mn_6Br	4.391	-6.80 ± 0.07	-1.30 ± 0.06
Mn_6I	4.438	-14.78 ± 0.25	-1.55 ± 0.13
Mn_6Br'	4.391	-0.04 ± 0.02	-1.46 ± 0.01
Mn_6I'	4.438	-0.04 ± 0.01	-1.38 ± 0.01
Mn_6	4.378	-0.06 ± 0.02	-1.48 ± 0.02
Mn_6'	4.542	-0.03 ± 0.02	-1.40 ± 0.01
Mn_6'Cl	4.542	-1.86 ± 0.02	-1.12 ± 0.01

4.3.1 Overlap analysis

To further ensure the validity of the novel methodology, the overlaps between the d-orbitals of the Mn centres and the p-orbitals of Cl^- were determined and are shown in **Table 4.14**. It can be seen that d-orbitals of Mn1 and Mn4 mainly interact with the p_z orbital of Cl, while that of Mn2 and Mn5 overlap with the p_x orbital of Cl^- and the d-orbitals of Mn3 and Mn6 overlap with the p_y orbital. The coupling between these pairs must be antiferromagnetic based on Goodenough-Kanamori rules.[334, 576, 577] For Mn1 and Mn2 however, and similarly for all other *cis*-Mn pairs, the coupling is facilitated by p-orbitals that are orthogonal to each other. Since electron transfer is, in principle, forbidden, the Goodenough-Kanamori-Anderson rules suggest that this coupling should thus be ferromagnetic.[334, 576, 577] These insights are in line with what was proposed using the novel methodology which further supports the reliability of the methodology.

Table 4.14: Overlap matrix ($\times$ 100) for the d-orbitals of the Mn centres and the p-orbitals of Cl.

Cl\Mn	D	D+1	D-1	D+2	D-2
			Mn1		
P_X	0.00	0.04	0.00	0.00	0.00
P_Y	0.00	0.00	0.04	0.00	0.00
P_Z	1.40	0.00	0.00	0.00	0.00
			Mn2		
P_X	0.36	0.00	0.00	1.04	0.00
P_Y	0.00	0.00	0.00	0.00	0.04
P_Z	0.00	0.04	0.00	0.00	0.00
			Mn3		
P_X	0.00	0.00	0.00	0.00	0.04
P_Y	0.34	0.00	0.00	1.06	0.00
P_Z	0.00	0.00	0.04	0.00	0.00
			Mn4		
P_X	0.00	0.04	0.00	0.00	0.00
P_Y	0.00	0.00	0.04	0.00	0.00
P_Z	1.40	0.00	0.00	0.00	0.00
			Mn5		
P_X	0.36	0.00	0.00	1.04	0.00
P_Y	0.00	0.00	0.00	0.00	0.04
P_Z	0.00	0.04	0.00	0.00	0.00
			Mn6		
P_X	0.00	0.00	0.00	0.00	0.04
P_Y	0.34	0.00	0.00	1.06	0.00
P_Z	0.00	0.00	0.04	0.00	0.00

4.4 DFT+U Approach and the Possibility of Non-Collinear Spins

Considering the presence of multiple {Mn_3} triangular units in compound **4.1**, the possibility of spin frustration[325, 578] and hence non-collinear spins cannot be ignored. Since non-collinearity cannot be investigated using gaussian09, the calculations were performed using VASP. To simulate in vacuo non-periodic conditions, only the isolated molecule was modelled. Modelling the whole unit cell was not possible due to the computational cost. The calculations were performed using the DFT+U approach employing the PBEsol functional.[517] Here DFT+U was chosen over the use of PBE0 due to the computational cost of hybrid DFT calculations with plane wave basis sets. A number of U and J values have been suggested for Mn in the literature.[579-586] Previous work in the Watson group has shown that the Dudarev approach[437] with a U-J value of 4.5 eV for Mn is most appropriate.[587-589] Hence, in this work, we have used the Dudarev approach[437] with a U-J value of 4.5 eV. We have however, also tested the Liechtenstein approach[436] with U and J values chosen such that U-J = 4.5 eV. These approaches have been employed to determine the energy of all 6 states which, in combination with eq. 4.1, have been used to calculate the coupling constants that are summarised in **Table 4.15**. The J-values obtained in this case are slightly overestimated compared to those obtained using PBE0.

Table 4.15: The coupling constants obtained using DFT+U approach.

Approach	U	J	J_{trans} (cm^{-1})	J_{cis} (cm^{-1})
Dudarev	4.5	0.0	-3.40 ± 0.03	-1.67 ± 0.02
Liechtenstein	5.5	1.0	-3.60 ± 0.03	-1.45 ± 0.02
Liechtenstein	6.4	1.9	-3.83 ± 0.05	-1.25 ± 0.03

To investigate the non-collinear behaviour, we have employed the Dudarev approach, and the Liechtenstein approach with a U and J value of 5.5 and 1 respectively as the J-values obtained with this combination are relatively closer to those obtained using PBE0. Two extreme cases have been investigated – one where the spins on Mn centres point towards the Cl^- centre (state 1) and the other where they point away from the Cl^- (state 2). The relative energy of all the collinear state and the two non-collinear states are presented in **Table 4.16**. It can be observed that with both approaches, state 2 is more stable than state 1. Since the states 1 and 2 were modelled by taking the spin-orbit coupling into account while the other states were modelled without it, a direct comparison between them is not possible. Future work will include accounting for the spin-orbit coupling in the calculation of the other states.

Table 4.16: Energy (cm^{-1}) of the various states relative to the Mn123 state calculated using the Dudarev (U = 4.5 eV, J = 0.0 eV) and Liechtenstein (U = 5.5 eV, J = 1 eV) approaches.

State	Dudarev Approach Relative Energy (cm^{-1})	Liechtenstein approach Relative Energy (cm^{-1})
Ferromagnetic	289.3	271.0
Mn1	145.3	140.7
Mn12	49.2	50.7
Mn14	98.7	109.9
Mn123	0.0	0.0
Mn124	49.3	59.6
State 1	206.4	186.2
State 2	131.2	123.9

4.5 Higher Charged States

The four successive charged states of compound **4.1** were investigated to understand the effect of oxidation on the magnetic properties. In these states, the oxidation has been achieved by introducing Mn(IV) sites and in cases where the Mn(IV) centres can be *cis*- or *trans*- to each other, both have been analysed. Oxidation to the first charged state was achieved by removing an electron from Mn2. This oxidation gives rise to the **2 - Mn25** (S = 9/2) ground state in which Mn2 is in oxidation state IV and Mn2 and Mn5 have down spin (**Figure 4.10 (b)**). An S = 1/2 state does not form the ground state as may have been expected. This indicates that the oxidation of the system leads to a change in not only the strength but also the nature of interactions between Mn centres. Further oxidation presents two possibilities as the additional charge can be accommodated by the cage such that the two Mn(IV) centres are *cis*- or *trans*- to each other. The *cis*- isomer has been found to be more stable by ~19 kJ/mol. The ground electronic state for the two isomers has been found to be different with *cis* **- 24 - Mn235** having a S = 0 ground state and *trans* **- 25- Mn25** having a S = 10/2 ground state, where the prefix *cis*- and *trans*- highlights the fact that the Mn(IV) centres are *cis*- or *trans*- to each other (**Figure 4.10 (c)** and **(d)**). The oxidation to the third and fourth charged state also leads to two isomers each. The *fac*/*cis*- isomer for the third and fourth charged state (**Figure 4.10 (e)** and **(g)**) is more stable (~3 and ~9 kJ/mol respectively) although the stabilisation energy is lower compared to the second charged state. For both *fac*- and *mer*- isomers of the third charged state a S = 1/2 state forms the ground state. Similarly, for the *cis*- and *trans*- isomer of the fourth charged states, the lowest spin states (S = 0) are the most stable (**Figure 4.10 (e)**-**(h)**).

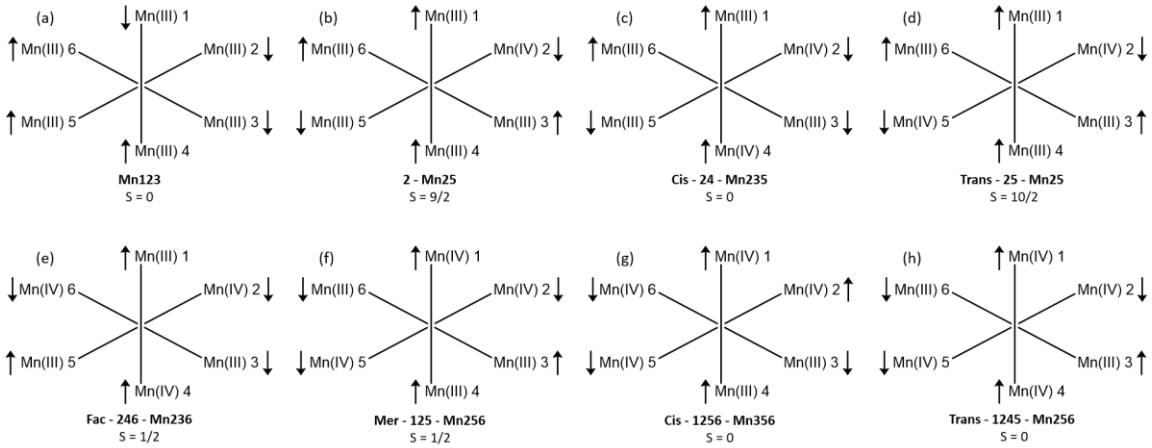

Figure 4.10: Arrangement of Mn atoms and their spins in the $\{Mn_6\}$ cage in the ground electronic state of the various charged states and their multiplicity. The numbers before 'Mn' in the labels below each state specify which Mn centres are in +IV oxidation state while the numbers after 'Mn' specify which Mn centres have a spin down configuration. The prefix (*cis*/*trans* or *fac*/mer) specifies the arrangement of Mn(IV) centres in the model for the 2nd and 3rd charged states and that of Mn(III) atoms in the 4th charged state. e.g. *cis***– 24 – Mn235** state represents the state where Mn2 and Mn4, which are *cis*- to each other, are in oxidation state IV and Mn2, Mn3 and Mn5 have down spin.

To understand these changes in the electronic configuration on oxidation, we need to understand how the Mn centres couple and this has been described in the following discussion. All bond distances reported (irrespective of the charged state under consideration) correspond to those of the ferromagnetic configuration because like the fully reduced state, the bond distances of other spin configurations do not vary significantly (< 0.1 Å). The Mn-Mn distances and the Mn-ligand distances in the different charged states are summarised in **Table 4.17** and **Table 4.18** respectively. For defining the spin operators in the higher charged states only Bader spin densities have been used and the spin densities reported in the following discussion are the ones for the ferromagnetic state. The Bader spin densities on the ligands are summarised in **Table 4.19**. The sum of overlaps between the d- and p- orbitals of Mn and Cl^- respectively are provided in **Table 4.20**. The value of the g-tensor for these states was found to be 1.997 ± 0.001, decreasing with increasing charge (**Table 4.21**). This data will be used to rationalise the results described in the forthcoming discussion.

Table 4.17: Mn-Mn distances (Å) in different charged states.

	Charged States							
	Fully reduced	**1st**	**2nd (*cis*)**	**2nd (*trans*)**	**3rd (Fac)**	**3rd (Mer)**	**4th (*cis*)**	**4th (*trans*)**
Mn1Mn2	4.386	4.328	4.455	4.325	4.488	4.156	4.374	4.162
Mn1Mn3	4.386	4.473	4.532	5.506	4.539	4.405	4.503	4.425
Mn1Mn5	4.406	4.487	4.488	5.482	4.539	4.389	4.334	4.411
Mn1Mn6	4.406	4.482	4.534	4.509	4.462	4.415	4.215	4.434
Mn2Mn3	4.386	4.322	4.387	4.324	4.462	4.409	4.514	4.425
Mn2Mn4	4.406	4.328	4.107	4.325	4.228	4.461	4.513	4.415
Mn2Mn6	4.406	4.322	4.382	4.320	4.228	4.413	4.384	4.427
Mn3Mn4	4.406	4.482	4.407	4.509	4.487	4.566	4.575	4.542
Mn3Mn5	4.406	4.493	4.534	4.480	4.539	4.512	4.505	4.545
Mn4Mn5	4.386	4.487	4.441	4.482	4.462	4.485	4.524	4.470
Mn4Mn6	4.386	4.473	4.379	4.504	4.229	4.568	4.487	4.549
Mn5Mn6	4.386	4.493	4.549	4.478	4.488	4.505	4.334	4.538
Mn1Mn4	6.217	6.332	6.183	6.377	6.262	6.223	6.286	6.177
Mn2Mn5	6.217	6.130	6.182	6.072	6.262	6.140	6.259	6.165
Mn3Mn6	6.217	3.332	6.436	6.369	6.262	6.468	6.281	6.510

Table 4.18: Mn-ligand bond distances (Å) for all their coordinating atoms in all oxidation states (ferromagnetic configuration). The number next to each O represents the Mn centres which are linked together by the corresponding phosphonate group. For example, O123 denotes that this oxygen belongs to a phosphonate that links Mn1, Mn2 and Mn3.

	Charged State							
	Fully reduced	**1st**	**2nd (*cis*)**	**2nd (*trans*)**	**3rd (Fac)**	**3rd (Mer)**	**4th (*cis*)**	**4th (*trans*)**
Mn1								
Cl	3.096	3.219	3.692	3.227	3.626	2.506	2.661	2.648
N	2.279	2.242	2.213	2.226	2.196	1.997	1.979	1.982
O126	1.892	1.895	1.895	1.881	1.922	1.851	1.864	1.845
O123	1.899	1.906	1.909	1.890	1.897	1.849	1.846	1.844
O135	1.892	1.882	1.875	1.896	1.864	1.864	1.842	1.861
O156	1.899	1.889	1.880	1.909	1.894	1.866	1.864	1.863
Mn2								
Cl	3.096	2.369	2.551	2.425	2.712	2.742	3.245	2.652
N	2.279	2.027	1.991	2.012	1.971	1.970	1.942	1.980
O126	1.892	1.865	1.846	1.862	1.847	1.862	1.873	1.849
O123	1.899	1.862	1.844	1.859	1.826	1.859	1.839	1.847
O234	1.892	1.865	1.868	1.862	1.852	1.839	1.812	1.868
O246	1.899	1.862	1.865	1.859	1.880	1.837	1.842	1.859
Mn3								
Cl	3.095	3.218	3.299	3.225	3.624	3.279	3.665	3.292
N	2.279	2.240	2.218	2.223	2.196	2.201	2.179	2.186
O123	1.899	1.906	1.892	1.892	1.894	1.914	1.910	1.902
O234	1.892	1.902	1.925	1.887	1.922	1.880	1.888	1.890
O135	1.892	1.881	1.872	1.905	1.864	1.900	1.904	1.892
O345	1.899	1.889	1.893	1.906	1.897	1.897	1.886	1.913
Mn4								
Cl	3.095	3.219	2.552	3.227	2.712	3.741	3.669	3.566
N	2.279	2.242	1.990	2.226	1.971	2.196	2.180	1.936
O234	1.892	1.895	1.864	1.881	1.847	1.882	1.879	1.827
O345	1.899	1.888	1.843	1.909	1.826	1.901	1.889	1.846
O456	1.892	1.882	1.847	1.896	1.852	1.888	1.904	1.837
O246	1.899	1.907	1.862	1.890	1.880	3.578	1.911	1.836
Mn5								
Cl	3.096	3.760	3.689	3.648	3.626	3.472	3.111	3.552
N	2.279	2.228	2.210	1.932	2.196	1.934	1.946	1.933
O135	1.892	1.885	1.874	1.831	1.864	1.851	1.843	1.835
O345	1.899	1.893	1.908	1.834	1.894	1.824	1.816	1.842
O456	1.892	1.885	1.906	1.831	1.922	1.821	1.837	1.846
O156	1.899	1.893	1.882	1.834	1.897	1.850	1.877	1.834
Mn6								
Cl	3.097	3.217	3.268	3.225	2.713	3.293	2.663	3.302
N	2.279	2.240	2.217	2.223	1.971	2.201	1.978	2.186
O126	1.892	1.902	1.890	1.887	1.852	1.908	1.866	1.897
O456	1.892	1.881	1.881	1.905	1.847	1.896	1.848	1.907
O156	1.899	1.889	1.879	1.906	1.826	1.905	1.862	1.895
O246	1.899	1.906	1.933	1.892	1.880	1.883	1.843	1.899

Table 4.19: Bader spin density on the coordinating atoms in ferromagnetic configuration of all oxidation states (truncated to three decimal places). The number next to each N represents the Mn centre to which it is linked. For the O centres, the sum of spin density on the four oxygens centre linked to and lying in between the corresponding Mn centres is provided. The number next to O represents the Mn centres being taken into account.

	Charged States							
	Fully reduced	**1st**	**2nd (*cis*)**	**2nd (*trans*)**	**3rd (Fac)**	**3rd (Mer)**	**4th (*cis*)**	**4th (*trans*)**
Cl	0.116	0.012	-0.022	0.016	-0.027	-0.019	-0.019	-0.014
N1	0.056	0.062	0.068	0.067	0.072	-0.117	-0.150	-0.149
N2	0.056	-0.075	-0.112	-0.095	-0.139	-0.142	-0.165	-0.150
N3	0.056	0.062	0.067	0.067	0.072	0.072	0.078	0.077
N4	0.056	0.062	-0.112	0.067	-0.139	0.073	0.078	-0.163
N5	0.056	0.063	0.068	-0.134	0.072	-0.147	-0.165	-0.164
N6	0.056	0.062	0.067	0.067	-0.139	0.072	-0.150	0.077
O12	0.085	0.091	0.130	0.102	0.137	0.105	0.137	0.118
O13	0.084	0.100	0.111	0.096	0.117	0.100	0.123	0.112
O15	0.084	0.107	0.119	0.135	0.116	0.139	0.132	0.152
O16	0.086	0.100	0.110	0.096	0.127	0.102	0.100	0.113
O23	0.084	0.089	0.106	0.100	0.127	0.123	0.144	0.109
O24	0.084	0.091	0.087	0.102	0.113	0.140	0.136	0.151
O26	0.084	0.089	0.111	0.100	0.113	0.118	0.140	0.111
O34	0.084	0.100	0.113	0.096	0.137	0.104	0.107	0.129
O35	0.084	0.107	0.108	0.134	0.116	0.133	0.135	0.134
O45	0.084	0.107	0.128	0.136	0.126	0.147	0.148	0.164
O46	0.084	0.099	0.106	0.096	0.112	0.104	0.121	0.134
O56	0.085	0.106	0.111	0.133	0.135	0.137	0.133	0.127

Table 4.20: Sum of overlaps ($\times$ 100) between the d-orbitals of Mn and p-orbitals of Cl^- in the various charged states.

	Charged State							
	Fully reduced	**1st**	**2nd (*cis*)**	**2nd (*trans*)**	**3rd (Fac)**	**3rd (Mer)**	**4th (*cis*)**	**4th (*trans*)**
Mn1-Cl	1.4800	1.0630	0.2960	1.1890	0.3970	5.9630	3.9200	4.7310
Mn2-Cl	1.4800	6.7060	4.9670	5.9670	3.9230	3.6810	1.5120	4.3330
Mn3-Cl	1.4800	0.8340	0.8310	1.0260	0.4440	0.9610	0.3120	1.0500
Mn4-Cl	1.4800	1.0640	5.8710	1.1960	4.0150	0.3650	0.2360	1.0630
Mn5-Cl	1.4800	0.6040	0.2590	1.0800	0.3840	1.0180	2.0060	0.9760
Mn6-Cl	1.4800	0.8310	0.9190	1.0300	3.8310	0.9310	4.1890	1.0250

Table 4.21: g-tensor for the $\{Mn_6\}$ cage in the different charged states.

Charged state	**g-tensor**	**Charged state**	**g-tensor**	**Charged state**	**g-tensor**
1st	1.998	2nd (*cis*)	1.997	2nd (*trans*)	1.997
3rd (Fac)	1.997	3rd (Mer)	1.997	4th (*cis*)	1.996
4th (*trans*)	1.996				

4.5.1 1st charged state

In this charged state Mn2 is in oxidation state IV **(Figure 4.11**). The Mn1-Mn4 and Mn3-Mn6 distances have been found to be 6.332 Å while the Mn2-Mn5 distance has been found to be 6.129 Å which means that the cage expands on oxidation. Cl^- shifts towards Mn2, because of its higher oxidation state (**Table 4.18**).

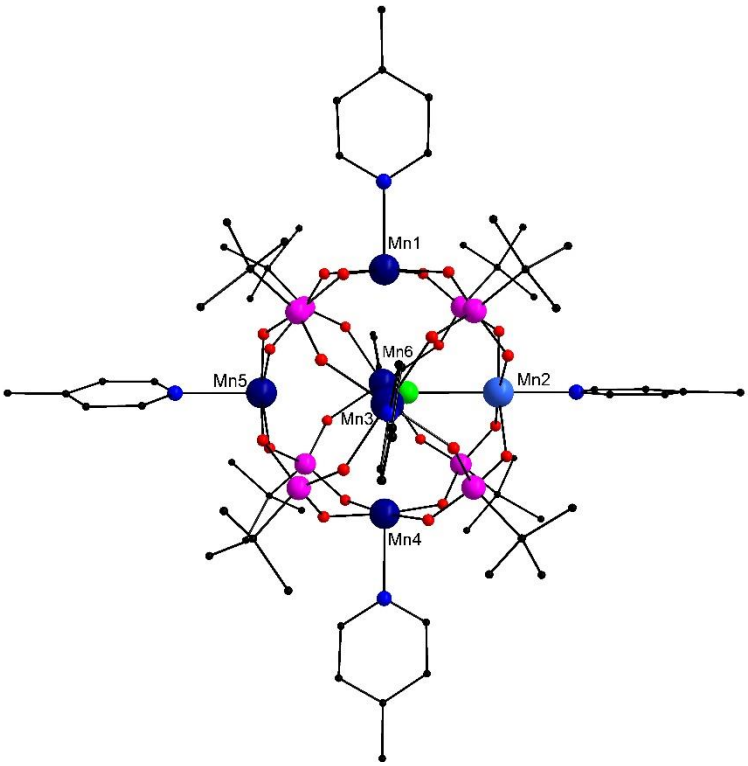

Figure 4.11: Optimised model of the 1st charged state for the {Mn_6} cage. Colour scheme: Mn^{III} (dark blue), Mn^{IV} (light blue), P(pink), Cl (green), C (black) O (red). Hydrogens have been removed for clarity.

The electronic environment of Mn5(III) can be considered different from all other Mn(III) centres since it is *trans*- to Mn2(IV) which itself resides in a unique electronic environment owing to its oxidation state. Keeping this in mind and ignoring small variations in the Mn-Mn distances, the coupling behaviour can be captured using 5 coupling constants *via* the following Hamiltonian:

$$\begin{aligned} H = \; & -2J_1[\langle s_2.s_5\rangle] - 2J_2[\langle s_1.s_4\rangle + \langle s_3.s_6\rangle] \\ & -2J_3[\langle s_1.s_2\rangle + \langle s_2.s_3\rangle + \langle s_2.s_4\rangle + \langle s_2.s_6\rangle] \\ & -2J_4[\langle s_1.s_3\rangle + \langle s_1.s_6\rangle + \langle s_3.s_4\rangle + \langle s_4.s_6\rangle] \\ & -2J_5[\langle s_1.s_5\rangle + \langle s_3.s_5\rangle + \langle s_4.s_5\rangle + \langle s_5.s_6\rangle] \end{aligned} \tag{4.5}$$

To calculate these J-values, 16 electronic configurations were modelled (**Table 4.22**) and the J-values thus obtained (**Table 4.23**) were found to reproduce the relative energies of all 15 states well with less than 3% error. The coupling between Mn2(IV) and Mn5(III) (J_1), which are *trans*- to each other, is ferromagnetic. In the fully reduced state, Mn2(III) and Mn5(III) were found to be

antiferromagnetically coupled. Oxidation of this system from the fully reduced state, thus leads to a switch in the nature of coupling from antiferromagnetic to ferromagnetic. All the other J-values in this charged state are negative suggesting antiferromagnetic coupling. There is, thus, a competition between ferromagnetic and anti-ferromagnetic coupling which affects the energy of the different spin configurations and enables the **2 – Mn25** (S = 9/2) state to be the lowest in energy and the ferromagnetic state to be the highest.

Table 4.22: Bader spin density on each Mn centre (truncated to three decimal places) and the relative energy of each spin state with respect to the ferromagnetic state for the 1st charged state.

Mn1	Mn2	Mn3	Mn4	Mn5	Mn6	Energy (cm^{-1})
3.773	3.036	3.775	3.773	3.765	3.775	0.00
3.773	3.032	3.774	3.773	-3.765	3.774	-60.69
3.772	3.036	3.774	3.772	3.765	-3.772	-109.21
-3.770	3.036	3.774	3.772	3.765	3.775	-109.34
3.772	-3.030	3.774	3.772	3.766	3.774	-132.38
3.772	-3.034	3.774	3.772	-3.764	3.774	-237.25
-3.771	3.036	3.774	3.772	3.765	-3.773	-183.72
3.772	-3.031	3.773	3.772	3.765	-3.773	-165.47
3.772	3.035	-3.773	3.772	3.764	-3.773	-189.45
3.772	3.032	3.774	3.772	-3.765	-3.773	-128.00
3.771	-3.034	-3.773	3.771	-3.764	3.773	-228.74
3.771	-3.031	-3.773	-3.771	3.765	3.773	-161.38
3.771	-3.035	3.773	3.771	-3.764	-3.773	-228.72
-3.772	-3.031	3.773	-3.772	3.765	3.773	-166.63
-3.771	-3.030	3.773	3.771	3.765	-3.773	-161.39
3.771	-3.031	-3.774	3.771	3.765	-3.774	-169.45

The Cl^- is closer to Mn2 than Mn5 and hence, the overlap between the p-orbitals of Cl^- and d-orbitals of Mn is greater for Mn2 than for Mn5 (**Table 4.20**). Cl^-, however, serves as the only bridge between Mn2 and Mn5 and hence the ferromagnetic coupling between Mn2 and Mn5 must be facilitated by Cl^-. To confirm this, the same system was modelled without the Cl^- in the centre. 10 states were modelled for this system (**Table 4.24**) and the coupling constants were determined using the same Hamiltonian (eq. 4.5). This model gives a negligible value for J_1 (**Table 4.23**) confirming that the coupling between Mn2 and Mn5 is *via* the Cl^- bridge.

The coupling between the Mn(III) centres *trans*- to each other (J_2) is antiferromagnetic and is significantly weaker compared to that in the fully reduced state. This is also a consequence of the movement of Cl^- away from the centre which results in weaker Mn(III)-Cl overlaps (**Table 4.20**) and hence weaker couplings.

The spin density on Mn2 and the N of 4-picoline ligands bound to it (**Table 4.19**) have been found to be opposite to each other (3.036 and -0.075 respectively) which suggests the presence of spin polarisation mechanism.[330] The presence of the spin polarisation mechanism explains the ferromagnetic interaction between Mn2 and Mn5. The spin density on the Mn(III) centres and the N of 4-picoline groups bound to them are found to have the same sign (3.77 and 0.06 respectively).

The same has been found to be true for the spin density on the Mn centres and Cl. This suggests that both the spin delocalisation mechanism introduced by Mn(III) centres, and spin polarisation mechanism introduced by Mn2(IV) are active.[330] This is further confirmed by the spin density plot which shows that Cl^- accommodates spin density associated with both up and down spin (**Figure 4.12**). There is thus a competition between spin delocalisation and spin polarisation mechanism which dictates the overall sign of the spin density on Cl.

Table 4.23: Magnitude of J-values (cm^{-1}) and the Mn-Mn interactions that constitute each J-value for the 1st charged state in presence and absence of the central Cl^-.

J-value	Interacting Mn centres	With Cl	Without Cl
J_1	*trans*-Mn2(IV)-Mn5(III)	1.94 ± 0.10	0.04 ± 0.05
J_2	*trans*-Mn1(III)-Mn4(III)	-1.03 ± 0.04	-0.09 ± 0.02
	trans-Mn3(III)-Mn6(III)		
J_3	*cis*-Mn1(III)-Mn2(IV)	-3.40 ± 0.04	-1.63 ± 0.02
	cis-Mn2(IV)-Mn3(III)		
	cis-Mn2(IV)-Mn4(III)		
	cis-Mn2(IV)-Mn6(III)		
J_4	*cis*-Mn1(III)-Mn3(III)	-1.25 ± 0.04	-1.28 ± 0.02
	cis-Mn1(III)-Mn6(III)		
	cis-Mn3(III)-Mn4(III)		
	cis-Mn4(III)-Mn6(III)		
J_5	*cis*-Mn1(III)-Mn5(III)	-1.45 ± 0.03	-1.67 ± 0.02
	cis-Mn3(III)-Mn5(III)		
	cis-Mn4(III)-Mn5(III)		
	cis-Mn5(III)-Mn6(III)		

Table 4.24: Bader spin density on each Mn centre (truncated to three decimal places) and the relative energy of each spin state with respect to the ferromagnetic state for the 1st charged state without the central Cl^-.

Mn1	Mn2	Mn3	Mn4	Mn5	Mn6	Energy (cm^{-1})
3.750	2.926	3.752	3.750	3.749	3.752	0.00
-3.748	2.925	3.751	3.750	3.749	3.751	-79.18
3.750	-2.921	3.751	3.750	3.749	3.751	-70.55
3.750	2.926	3.751	3.750	-3.748	3.751	-93.42
3.750	2.925	3.751	3.749	3.749	-3.749	-78.40
-3.748	2.924	3.751	3.749	3.748	-3.750	-121.21
3.749	2.925	-3.750	3.749	3.748	-3.750	-154.39
3.749	2.925	3.751	3.749	-3.747	-3.750	-125.34
-3.749	-2.924	3.751	3.749	3.748	-3.750	-120.89
3.748	-2.922	3.750	3.748	-3.748	-3.750	-161.63

Unlike the fully reduced state, the spin density on the O-donors of the phosphonate groups varies depending on the Mn centres they are attached to (**Table 4.19**). Between any two Mn centres lie four phosphonate O-donors that are directly attached to these Mn centres. The spin density on these O-donors and the strength of the exchange coupling between the Mn centres they link are correlated and increased spin densities correspond to stronger coupling. This can be illustrated by comparing the coupling between the *cis*-Mn(III) centres where it can be seen that $J_5 > J_4$ (**Table**

4.23). The sum of the spin densities on the oxygens bound to Mn centres associated with J_5 is greater than those associated with J_4 which is consistent with our proposal (**Table 4.19**). In addition, both J_4 and J_5 are greater than J_{cis} in the fully reduced state for which the sum of spin densities on the O-donors of the phosphonate groups is even smaller (**Table 4.19**). The magnitude of spin density on the phosphonate O-donors thus provides an indication of the coupling strength between the Mn centres that they are attached to.

Despite the lower spin density on the oxygens attached to Mn2(IV) compared to those attached to Mn(III) centres, the coupling between Mn2 and its *cis*-neighbours (J_3) is stronger. This is most likely due to the higher electronegativity of Mn(IV) and the interactions *via* the Cl^- bridge. The latter is confirmed by the model without the Cl^- in the centre for which J_3 decreased to -1.63 cm^{-1} (**Table 4.23**) suggesting strong antiferromagnetic coupling *via* the Cl^- bridge. Hence, for understanding the coupling strength between Mn centres one needs to take into account the oxidation state of the interacting Mn centres, the spin density on oxygens and the overlap between the orbitals of Mn and Cl.

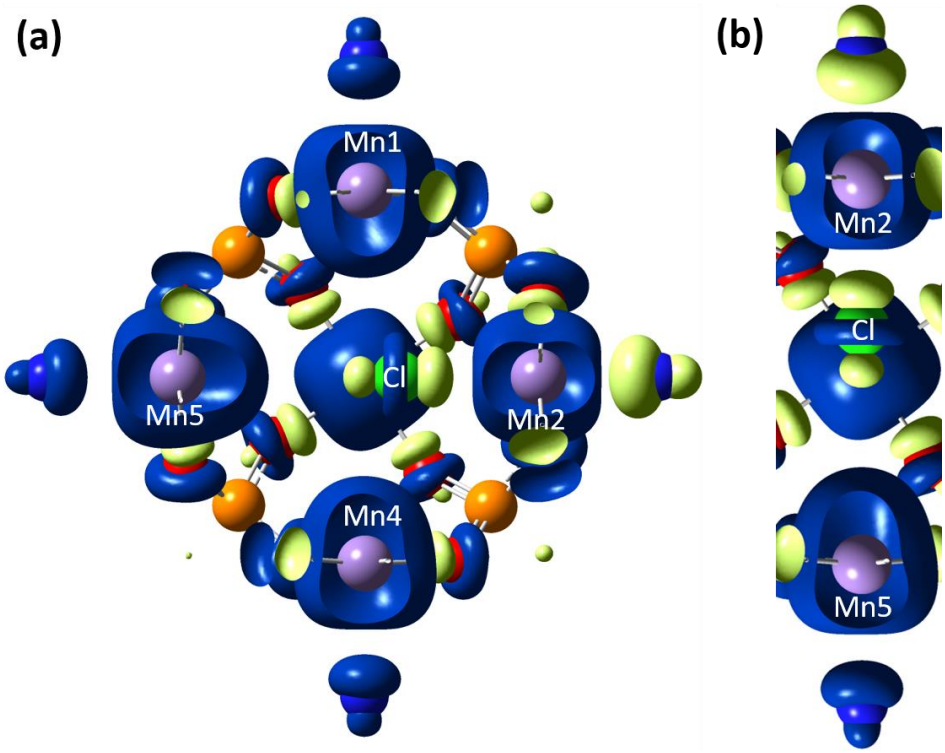

Figure 4.12: (a) Plot of the spin density distribution in the high spin configuration of the 1st charged state of the $\{Mn_6\}$ cage and **(b)** plot highlighting the spin density on Mn2 and Mn5, the N-donor bound to these Mn centres, and Cl. Blue and green regions represent the spin density associated with up and down spin respectively. Spin density associated with Mn3 and the ligands coordinated to it has been removed for clarity. Cl can be clearly seen to be accommodating spin density associated with both up and down spin confirming the presence of both spin delocalisation and polarisation.

4.5.2 2nd charged state (*cis*-isomer)

There are two possibilities to consider in modelling the 2nd charged state – the two Mn centres in +IV oxiation state can either be *cis*- to each other or *trans*- to each other both of which were investigated. For the *cis*-isomer, Mn2 and Mn4 are in oxidation state IV (**Figure 4.13 (a)**). The *trans*-Mn(IV)-Mn(III) and Mn(III)-Mn(III) distances have been found to be ~6.182 Å and ~6.436 Å respectively. The central space containing Cl^- is larger compared to that in the fully reduced and the first oxidised state. Cl^- is shifted towards Mn2(IV) and Mn4(IV) again owing to the higher oxidation state of these Mn centres.

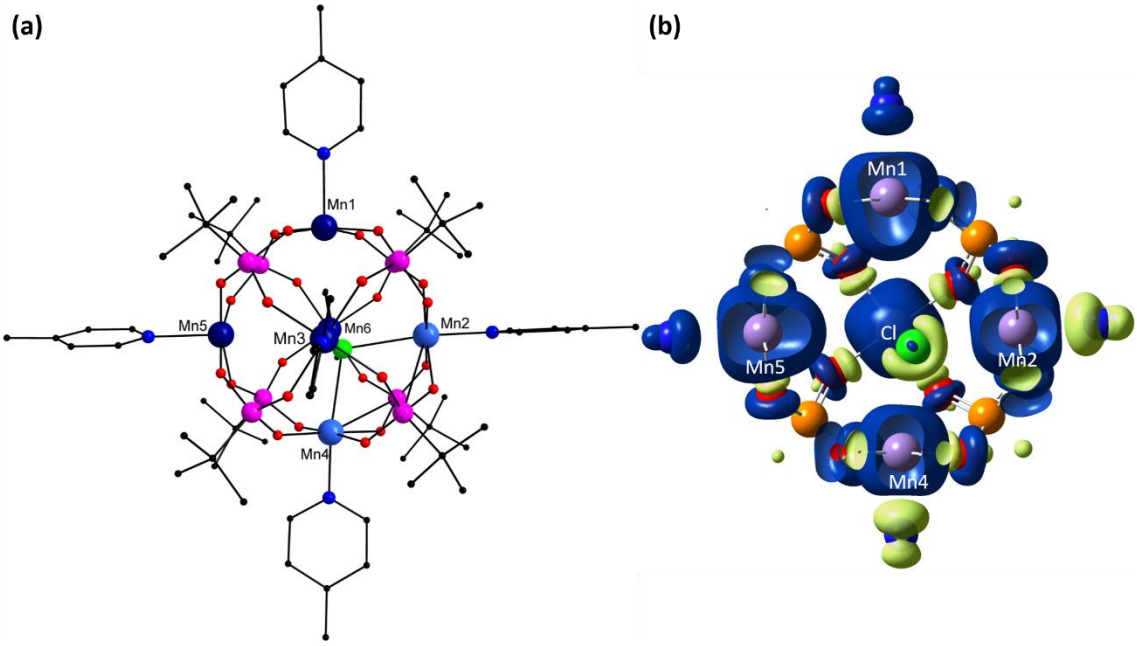

Figure 4.13: (a) Optimized model of the *cis*-isomer of the 2nd charged state for the $\{Mn_6\}$ cage. Colour scheme: Mn^{III} (dark blue), Mn^{IV} (light blue), P(pink), Cl (green), C (black) O (red). Hydrogens have been removed for clarity. **(b)** The distribution of the spin density in this state. Blue and green regions in the spin density plots represent the spin density associated with up and down spin respectively. Spin density associated with Mn3 and the ligands coordinated to it has been removed for clarity. Cl can be clearly seen to be accommodating both up and down spin density confirming the presence of spin delocalisation and polarisation with the latter being dominant.

19 electronic configurations were modelled (**Table 4.25**) and the spin Hamiltonian was found to require 12 J-values for the proper description of the electronic structure and can be given as:

$$\begin{aligned} H = &-2J_1[\langle s_1.s_4\rangle + \langle s_2.s_5\rangle] - 2J_2[\langle s_3.s_6\rangle] - 2J_3[\langle s_2.s_4\rangle] - 2J_4[\langle s_1.s_2\rangle] \\ &- 2J_5[\langle s_2.s_3\rangle] - 2J_6[\langle s_2.s_6\rangle] - 2J_7[\langle s_3.s_4\rangle] - 2J_8[\langle s_4.s_5\rangle] \\ &- 2J_9[\langle s_4.s_6\rangle] - 2J_{10}[\langle s_1.s_5\rangle] - 2J_{11}[\langle s_1.s_3\rangle + \langle s_5.s_6\rangle] \\ &- 2J_{12}[\langle s_1.s_6\rangle + \langle s_3.s_5\rangle] \end{aligned} \quad (4.6)$$

Table 4.25: Bader spin density on each Mn centre (truncated to three decimal places) and the relative energy of each spin state with respect to the ferromagnetic state for the *cis*-isomer of the 2nd charged state.

Mn1	Mn2	Mn3	Mn4	Mn5	Mn6	Energy (cm^{-1})
3.755	3.031	3.764	3.026	3.759	3.764	0.00
3.755	3.027	3.764	3.025	-3.758	3.763	-76.69
3.755	3.030	3.764	3.025	3.758	-3.761	-106.06
3.755	-3.019	3.764	3.022	3.759	3.763	-87.38
-3.755	3.026	3.764	3.022	-3.758	3.763	-107.23
3.755	-3.023	3.763	-3.019	3.759	3.763	-136.81
3.755	-3.022	3.764	3.021	-3.757	3.763	-191.56
3.755	-3.020	3.763	3.021	3.759	-3.762	-133.51
3.755	3.028	-3.763	3.024	3.758	-3.762	-195.24
3.756	3.023	3.764	-3.017	-3.758	3.763	-117.78
3.755	3.026	3.763	3.023	-3.758	-3.762	-140.06
-3.754	3.021	3.763	-3.020	-3.759	3.762	-175.60
3.755	-3.025	-3.763	-3.020	3.759	3.762	-131.37
3.755	-3.026	3.763	-3.021	-3.758	3.762	-193.94
3.755	-3.024	3.763	-3.020	3.759	-3.762	-128.31
3.755	-3.023	3.763	3.019	-3.758	-3.762	-195.00
3.755	3.024	-3.763	-3.017	3.758	-3.763	-165.84
-3.755	-3.025	3.763	-3.022	3.758	3.762	-188.72
3.756	3.022	3.763	-3.018	-3.759	-3.762	-126.40

The coupling constants obtained using this Hamiltonian are provided in **Table 4.26**. The relative energies of the different spin states are well reproduced using 12 J-values (< 1.5% error). All 15 coupling constants were also calculated for this isomer (**Table 4.27**) and the values obtained were found to be similar to those obtained using the 12 J-value Hamiltonian implying that the 12 J-values are sufficient.

The coupling between Mn(IV) centres and their *trans*- Mn(III) counterpart is again ferromagnetic (J_8) as observed for the 1st charged state. This is due to spin polarisation mechanism which is evident not only from the spin density on the N-donor of the 4-picoline bound to Mn(IV) but also the central Cl. Unlike the 1st charged state, the spin density on Cl^- here is opposite to that on the Mn(IV) centres because there is a strong overlap between the p-orbitals of Cl^- and the d-orbitals of the Mn(IV) centres (Mn2 and Mn4) but much weaker overlap between the p-orbitals of Cl^- and the d-orbitals of Mn(III) centres (**Table 4.20**). This is evident from the spin density plot as well (**Figure 4.13 (b)**). The spin density on Cl^- is thus primarily the spin density induced by the Mn(IV) centres confirming that the spin polarisation mechanism is active. Like the 1st charged state, even though the overlap is negligible, Mn3 and Mn6 are coupled *via* the Cl^- bridge albeit weakly. Additionally, the weaker coupling between Mn(IV) centres and their *cis*-Mn(III) neighbours ($J_4 - J_9$) compared to the first charged state can be attributed to weaker contribution to the coupling *via* the Cl^- bridge which is due to negligible Mn(III)-Cl overlaps (**Table 4.20**).

Table 4.26: Magnitude of *J*-values (cm^{-1}) and the Mn-Mn interactions that constitute each *J*-value for the *cis*-isomer of the 2nd charged state.

J-value	Interacting Mn centres	Magnitude (cm^{-1})
J_1	*trans*-Mn1(III)-Mn4(IV)	1.20 ± 0.02
	trans-Mn2(IV)-Mn5(III)	
J_2	*trans*-Mn3(III)-Mn6(III)	-0.52 ± 0.03
J_3	*cis*-Mn2(IV)-Mn4(IV)	-2.13 ± 0.04
J_4	*cis*-Mn1(III)-Mn2(IV)	-2.50 ± 0.03
J_5	*cis*-Mn2(IV)-Mn3(III)	-2.04 ± 0.04
J_6	*cis*-Mn2(IV)-Mn6(III)	-2.64 ± 0.02
J_7	*cis*-Mn3(III)-Mn4(IV)	-2.76 ± 0.03
J_8	*cis*-Mn4(IV)-Mn5(III)	-2.07 ± 0.04
J_9	*cis*-Mn4(IV)-Mn6(III)	-2.40 ± 0.02
J_{10}	*cis*-Mn1(III)-Mn5(III)	-1.79 ± 0.02
J_{11}	*cis*-Mn1(III)-Mn3(III)	-1.51 ± 0.02
	cis-Mn5(III)-Mn6(III)	
J_{12}	*cis*-Mn1(III)-Mn6(III)	-1.42 ± 0.02
	cis-Mn3(III)-Mn5(III)	

For this configuration, the S = 0 state (***cis* - 24 – Mn235**) has been found to be the lowest in energy and the ferromagnetic state is the highest in energy. Unlike the first oxidised state, the presence of ferromagnetic interactions does not lead to a state with higher multiplicity being the ground state.

Table 4.27: *J*-values (cm^{-1}) for the *cis*-isomer of the 2nd oxidised state obtained with the 15 *J*-value and 12 *J*-value Hamiltonians.

Interaction	*J*-value(15 *J*-values)	*J*-value(12 *J*-values)
Mn1Mn2	-2.48 ± 0.01	-2.50 ± 0.03
Mn1Mn3	-1.53 ± 0.00	-1.51 ± 0.02
Mn1Mn4	1.20 ± 0.01	1.20 ± 0.02
Mn1Mn5	-1.79 ± 0.01	-1.79 ± 0.02
Mn1Mn6	-1.39 ± 0.00	-1.42 ± 0.02
Mn2Mn3	-2.07 ± 0.01	-2.04 ± 0.04
Mn2Mn4	-2.12 ± 0.01	-2.13 ± 0.04
Mn2Mn5	1.21 ± 0.00	1.20 ± 0.02
Mn2Mn6	-2.63 ± 0.00	-2.64 ± 0.02
Mn3Mn4	-2.77 ± 0.01	-2.76 ± 0.03
Mn3Mn5	-1.43 ± 0.00	-1.42 ± 0.02
Mn3Mn6	-0.55 ± 0.00	-0.52 ± 0.03
Mn4Mn5	-2.08 ± 0.01	-2.07 ± 0.04
Mn4Mn6	-2.40 ± 0.00	-2.40 ± 0.02
Mn5Mn6	-1.50 ± 0.00	-1.51 ± 0.02

4.5.3 2nd charged state (*trans*-isomer)

For the *trans*-isomer, Mn2 and Mn5 are in oxidation state IV and Cl^- is again closer to Mn2 (**Figure 4.14 (a)**). The Mn(IV)-Mn(IV) and Mn(III)-Mn(III) distances have been found to be 6.073 and 6.376 Å respectively suggesting further expansion of the cage compared to the 1st charged state.

8 coupling constants are required to properly describe the electronic structure and the required Hamiltonian can be given as:

$$\begin{aligned} H = &-2J_1[\langle s_2.s_5\rangle] - 2J_2[\langle s_1.s_4\rangle + \langle s_3.s_6\rangle] - 2J_3[\langle s_1.s_2\rangle + \langle s_2.s_4\rangle] \\ &-2J_4[\langle s_2.s_3\rangle + \langle s_2.s_6\rangle] - 2J_5[\langle s_1.s_5\rangle + \langle s_4.s_5\rangle] \\ &-2J_6[\langle s_3.s_5\rangle + \langle s_5.s_6\rangle] - 2J_7[\langle s_1.s_3\rangle + \langle s_1.s_6\rangle] \\ &-2J_8[\langle s_3.s_4\rangle + \langle s_4.s_6\rangle] \end{aligned} \quad (4.7)$$

11 different configurations were modelled for this state (**Table 4.28**) and the coupling constants thus obtained are given in **Table 4.29**. The relative energies of the different spin states are well reproduced (< 1% error). The symmetry of this state, the spin densities on the phosphonate oxygens and the similar values of J_3 and J_4, J_5 and J_6, and J_7 and J_8 suggest that these interactions can be coupled but doing so leads to a large standard deviation on J_1 and its sign cannot be determined.

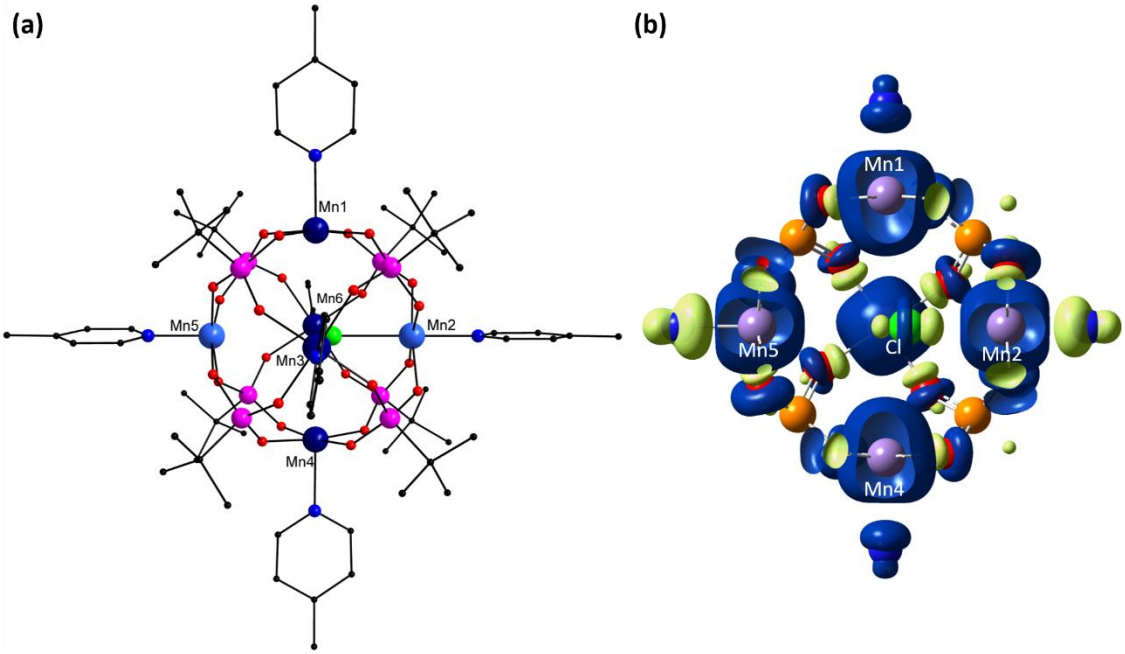

Figure 4.14: Optimised model of the *trans*-isomer of the 2nd charged state for the $\{Mn_6\}$ cage **(a)** and the distribution of the spin density in this state **(b)**. Colour scheme: Mn^{III} (dark blue), Mn^{IV} (light blue), P(pink), Cl (green), C (black) O (red). Hydrogens have been removed for clarity. Blue and green regions in the spin density plots represent the spin density associated with up and down spin respectively. Cl can be clearly seen to be accommodating both up and down spin density confirming the presence of spin delocalisation and polarisation.

Table 4.28: Bader spin density on each Mn centre (truncated to three decimal places) and the relative energy of each spin state with respect to the ferromagnetic state for the *trans*-isomer of the 2nd charged state.

Mn1	Mn2	Mn3	Mn4	Mn5	Mn6	Energy (cm^{-1})
3.765	3.036	3.769	3.765	2.944	3.769	0.00
3.764	3.036	3.768	3.765	2.942	-3.767	-109.57
3.764	-3.035	3.768	3.764	2.942	3.768	-158.35
-3.763	3.036	3.768	3.764	2.940	-3.767	-187.77
3.764	-3.035	3.768	3.764	-2.934	3.768	-241.84
3.764	-3.035	3.768	3.764	2.940	-3.767	-190.25
3.764	3.036	-3.767	3.764	2.940	-3.767	-188.62
-3.763	-3.035	3.767	3.763	2.938	-3.767	-186.61
3.763	-3.035	3.768	-3.763	-2.937	3.768	-231.06
3.764	-3.035	-3.768	3.764	2.938	-3.768	-191.29
3.764	-3.035	3.767	3.764	-2.937	-3.768	-234.93

The coupling between the Mn(IV) centres is weakly ferromagnetic (J_1) and the tendency to switch the nature of coupling in this case is retained. It can be concluded that oxidation of a Mn(III) centre to Mn(IV) leads to ferromagnetic coupling between the Mn(IV) centre and its *trans*-Mn(III)/Mn(IV) counterpart. The ferromagnetic coupling here is also due to spin polarisation as indicated by the spin density on the nitrogen of the 4-picoline ligands bound to the Mn(IV) centres and the spin density plot (**Table 4.19** and **Figure 4.14 (b)** respectively). The spin density on Cl^- is again of the same sign as that on the Mn centres which is due to the relatively larger overlaps between the d-orbitals of Mn(III) centres and the p-orbitals of Cl^- compared to the *cis*-isomer (**Table 4.20**).

Table 4.29: Magnitude of *J*-values (cm^{-1}) and the Mn-Mn interactions that constitute each *J*-value for the *trans*-isomer of the 2nd charged state.

***J*-value**	**Interacting Mn centres**	**Magnitude (cm^{-1})**
J_1	*trans*-Mn2(IV)-Mn5(IV)	0.13 ± 0.01
J_2	*trans*-Mn1(III)-Mn4(III)	-1.09 ± 0.01
	trans-Mn3(III)-Mn6(III)	
J_3	*cis*-Mn1(III)-Mn2(IV)	-3.58 ± 0.01
	cis-Mn2(IV)-Mn4(III)	
J_4	*cis*-Mn2(IV)-Mn3(III)	-3.40 ± 0.01
	cis-Mn2(IV)-Mn6(III)	
J_5	*cis*-Mn1(III)-Mn5(IV)	-1.97 ± 0.01
	cis-Mn4(III)-Mn5(IV)	
J_6	*cis*-Mn3(III)-Mn5(IV)	-1.75 ± 0.01
	cis-Mn5(IV)-Mn6(III)	
J_7	*cis*-Mn1(III)-Mn3(III)	-1.25 ± 0.01
	cis-Mn1(III)-Mn6(III)	
J_8	*cis*-Mn3(III)-Mn4(III)	-1.29 ± 0.01
	cis-Mn4(III)-Mn6(III)	

The coupling between Mn2(IV) and its *cis*-neighbours (J_3 and J_4) is similar to that in the first charged state while the coupling between Mn5(IV) and its *cis*- neighbours (J_5 and J_6) is similar to the coupling between the Mn(IV) centres and their *cis*-neighbours in the *cis*- isomer of this charged

state. This comparison highlights the importance of the Mn(IV)-Cl overlaps which is larger in the former case and smaller in the latter which results in J_3 and J_4 being larger than J_5 and J_6.

For this configuration, the ferromagnetic state is the highest in energy while the S = 10/2 state (***trans* - 25 – Mn25**) has been found to be the lowest in energy with a S = 2/2 state lying close to it. The 2nd charged state thus presents the possibility of two isomers where one (*cis*-isomer) has an S = 0 ground state while the other (*trans*-isomer) has an S = 10/2 ground state. Different ground states can thus be stabilised depending upon the isomer.

4.5.4 3rd charged state (*Fac*-isomer)

To look at whether the tendency to switch the ground state can be retained in even higher oxidation states, the 3rd charged state was modelled. In this state, the Mn(IV) centres can be arranged to form the *fac*- and *mer*- isomer and both these configurations were modelled. In the *fac*-isomer, Mn2, Mn4 and Mn6 are in oxidation state IV, the distance between *trans*-Mn centres is 6.626 Å and Cl^- is shifted towards the Mn(IV) centres (**Figure 4.15 (a)**). A proper description of the electronic picture requires the use of only 5 J-values and the required Hamiltonian can thus be given as:

$$\begin{aligned} H = &-2J_1[\langle s_1.s_4\rangle + \langle s_2.s_5\rangle + \langle s_3.s_6\rangle] - 2J_2[\langle s_2.s_4\rangle + \langle s_2.s_6\rangle + \langle s_4.s_6\rangle] \\ &-2J_3[\langle s_1.s_2\rangle + \langle s_3.s_4\rangle + \langle s_5.s_6\rangle] - 2J_4[\langle s_1.s_6\rangle + \langle s_2.s_3\rangle + \langle s_4.s_5\rangle] \\ &-2J_6[\langle s_1.s_3\rangle + \langle s_1.s_5\rangle + \langle s_3.s_5\rangle] \end{aligned} \quad (4.8)$$

14 electronic configurations were modelled for this state (**Table 4.30**) and the J-values obtained are given in **Table 4.31**. The J_1 term corresponding to the coupling between the *trans*-Mn centres is ferromagnetic although weaker compared to the lower charged states owing to the relatively smaller Mn(IV)-Cl overlaps (**Table 4.20**). The presence of polarised spin density on the Cl^- centre is confirmed by the spin density plot (**Figure 4.15 (b)**). The coupling between the Mn(IV) centres *cis*- to each other (J_2) is stronger compared to that in the *cis*- isomer of the 2nd charged state. This is also due to higher delocalisation of spin density (**Table 4.19**). Each Mn(IV) centre has two *cis*-Mn(III) neighbours out of which one is closer than the other by ~0.03 Å and the impact of this difference seems to be quite large if one compares J_3 and J_4. This is again due to differences in the spin density of the oxygens attached to the Mn centres.

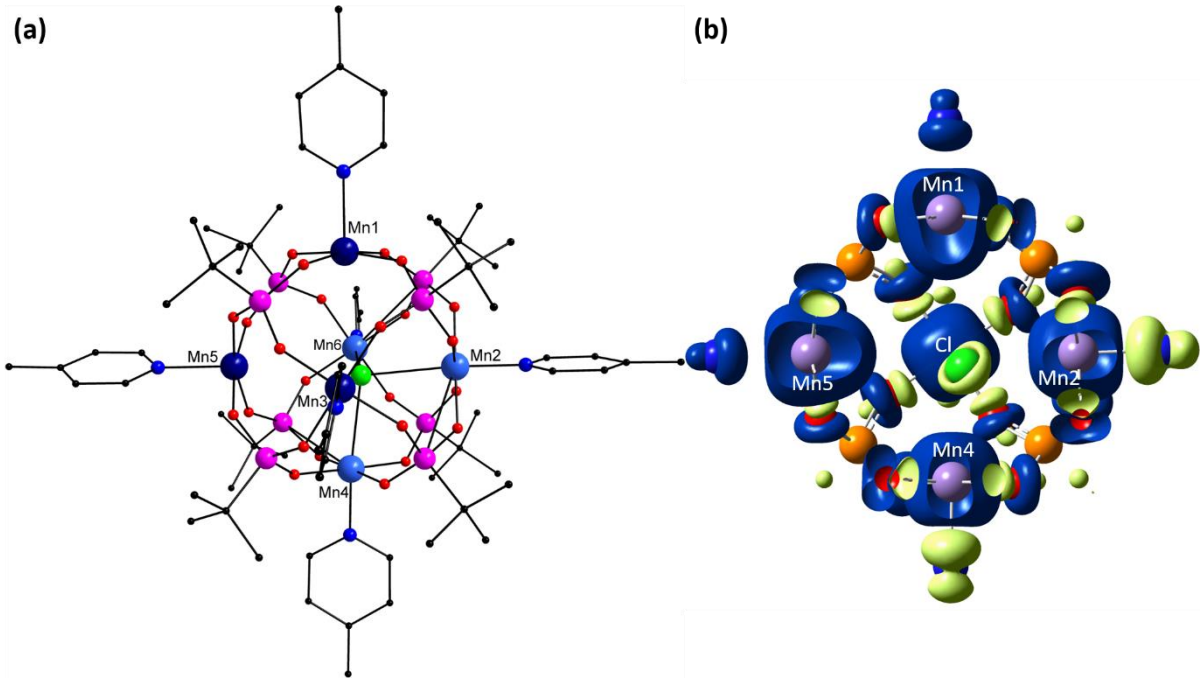

Figure 4.15: Optimised model of the *fac*-isomer of the 3rd charged state for the {Mn_6} cage **(a)** and the distribution of the spin density in this state **(b)**. Colour scheme: Mn^{III} (dark blue), Mn^{IV} (light blue), P(pink), Cl (green), C (black) O (red). Hydrogens have been removed for clarity. Blue and green regions in the spin density plots represent the spin density associated with up and down spin respectively.

Table 4.30: Bader spin density on each Mn centre (truncated to three decimal places) and the relative energy of each spin state with respect to the ferromagnetic state for the *fac*-isomer of the 3rd charged state.

Mn1	Mn2	Mn3	Mn4	Mn5	Mn6	Energy (cm^{-1})
3.750	3.034	3.750	3.034	3.750	3.034	0.00
3.750	-3.023	3.750	3.032	3.751	3.032	-96.22
3.750	3.032	-3.749	3.032	3.750	3.031	-86.23
3.749	-3.026	-3.750	3.030	3.750	3.030	-150.43
3.750	-3.025	3.751	3.030	3.750	-3.024	-132.20
3.749	3.029	-3.750	3.029	-3.750	3.030	-121.30
3.750	3.029	-3.749	3.031	3.749	-3.025	-203.23
3.750	3.028	3.750	-3.027	-3.750	-3.027	-126.31
-3.750	-3.027	3.750	3.027	3.750	-3.027	-125.25
3.750	-3.027	-3.750	-3.027	3.750	3.028	-124.93
-3.749	3.028	3.750	-3.027	3.749	-3.028	-208.14
3.749	-3.028	-3.749	3.028	3.750	-3.027	-208.09
3.750	-3.027	3.750	-3.027	3.750	-3.027	-106.43

For this configuration, the S = 1/2 state (**Fac - 246 - Mn236**) has been found to be the lowest in energy which shows its similarity with the fully reduced state. The ferromagnetic state is the highest in energy.

Table 4.31: Magnitude of J-values (cm^{-1}) and the Mn-Mn interactions that constitute each J-value for the *fac*-isomer of the 3rd charged state.

J-value	Interacting Mn centres	Magnitude (cm^{-1})
J_1	*trans*-Mn1(III)-Mn4(IV)	0.95 ± 0.04
	trans-Mn2(IV)-Mn5(III)	
	trans-Mn3(III)-Mn6(IV)	
J_2	*cis*-Mn2(IV)-Mn4(IV)	-3.32 ± 0.04
	cis-Mn2(IV)-Mn6(IV)	
	cis-Mn4(IV)-Mn6(IV)	
J_3	*cis*-Mn1(III)-Mn2(IV)	-2.69 ± 0.04
	cis-Mn3(III)-Mn4(IV)	
	cis-Mn5(III)-Mn6(IV)	
J_4	*cis*-Mn1(III)-Mn6(IV)	-1.39 ± 0.05
	cis-Mn2(IV)-Mn3(III)	
	cis-Mn4(IV)-Mn5(III)	
J_5	*cis*-Mn1(III)-Mn3(III)	-1.79 ± 0.03
	cis-Mn1(III)-Mn5(III)	
	cis-Mn3(III)-Mn5(III)	

4.5.5 3rd charged state (*Mer*-isomer)

For this isomer, Mn1, Mn2 and Mn5 are in oxidation state IV (**Figure 4.16 (a)**). The Mn1-Mn4, Mn2-Mn5 and Mn3-Mn6 distances are 6.223, 6.141 and 6.468 Å respectively. This configuration is the least symmetric configuration studied. The Mn(IV)-Cl distance follows the order Mn1-Cl (2.506 Å) < Mn2-Cl (2.74 Å) < Mn5-Cl (3.47 Å) which suggests that each Mn(IV) resides in a unique environment. The Hamiltonian used for this charged state is the following:

$$\begin{aligned} H = & -2J_1[< s_2.s_5 >] - 2J_2[< s_1.s_4 >] - 2J_3[< s_3.s_6 >] - 2J_4[< s_1.s_2 >] \\ & -2J_5[< s_1.s_5 >] - 2J_6[< s_1.s_3 >] - 2J_7[< s_1.s_6 >] - 2J_8[< s_2.s_3 >] \\ & -2J_9[< s_2.s_4 >] - 2J_{10}[< s_2.s_6 >] - 2J_{11}[< s_3.s_5 >] - 2J_{12}[< s_4.s_5 >] \\ & -2J_{13}[< s_5.s_6 >] - 2J_{14}[< s_3.s_4 >] - 2J_{15}[< s_4.s_6 >] \end{aligned} \quad (4.9)$$

21 electronic configurations were modelled (**Table 4.32**) and the J-values obtained are given in **Table 4.33**. The coupling strengths between Mn centres are in line with what is expected from the spin density on the phosphonate oxygens. The interaction between Mn2(IV) and Mn5(IV) (J_1) is ferromagnetic but weaker than that between the Mn1(IV) and its *trans*-Mn4(III) (J_2). The ferromagnetic interaction between Mn1(IV) and Mn4(III) is stronger compared to that in the *cis*-isomer of this charged state because of the larger Mn-Cl overlaps (**Table 4.20**). The spin density on

Cl^- and the N-donor of the 4-picoline ligands attached to the Mn(IV) centres is opposite to that on the Mn centres indicating the presence of spin polarisation mechanism which is further confirmed by the spin density plot (**Figure 4.16 (b)**). Mn3 and Mn6 (J_3), both being in oxidation state III, couple antiferromagnetically. The coupling between *cis*-Mn(IV) centres (J_4 and J_5) is quite strong as can be expected due to higher oxidation states of the interacting Mn centres. The similarity in the coupling of Mn3 and Mn6 with their *cis*-neighbours suggests that these Mn centres reside in similar electronic environments.

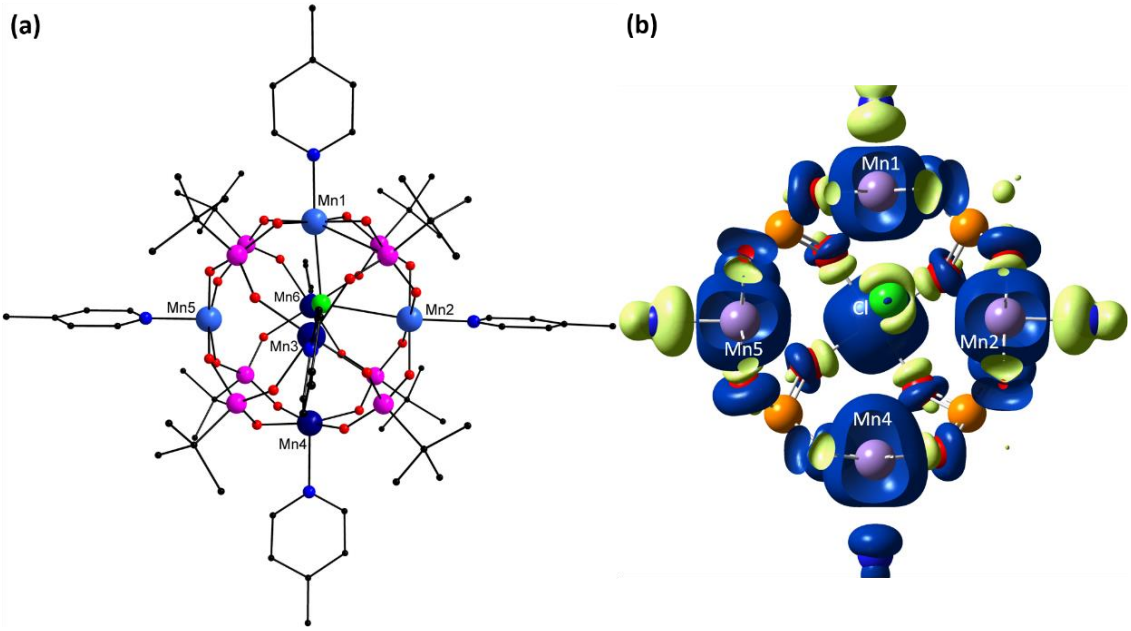

Figure 4.16: Optimised model of the *mer*-isomer of the 3rd charged state for the $\{Mn_6\}$ cage **(a)** and the distribution of the spin density in this state **(b)**. Colour scheme: Mn^{III} (dark blue), Mn^{IV} (light blue), P(pink), Cl (green), C (black) O (red). Hydrogens have been removed for clarity. Blue and green regions in the spin density plots represent the spin density associated with up and down spin respectively.

For this configuration, unlike the *trans*-isomer of the 2nd charged state, the S = 1/2 state (***Mer* - 125 - Mn256**) has been found to be the lowest in energy which indicates that the ability to stabilise intermediate states is lost. The ferromagnetic state is the highest in energy.

Table 4.32: Bader spin density on each Mn centre (truncated to three decimal places) and the relative energy of each spin state with respect to the ferromagnetic state for the *mer*-isomer of the 3rd charged state.

Mn1	Mn2	Mn3	Mn4	Mn5	Mn6	Energy (cm^{-1})
3.049	3.033	3.758	3.747	2.971	3.758	0.00
3.046	3.031	3.758	-3.745	2.968	3.758	-83.33
3.047	3.032	3.758	3.746	-2.960	3.758	-89.31
3.048	3.031	3.757	3.746	2.968	-3.756	-103.45
-3.039	3.029	3.757	3.747	2.970	3.758	-100.60
-3.042	3.027	3.757	-3.745	2.968	3.757	-212.33
-3.041	3.028	3.757	3.747	-2.961	3.757	-136.01
-3.040	3.027	3.757	3.747	2.968	-3.756	-142.84
3.044	-3.024	3.757	3.746	-2.961	3.757	-201.74
3.047	3.029	-3.756	3.746	2.965	-3.757	-187.46
3.044	3.030	3.757	-3.746	-2.963	3.757	-120.86
3.045	3.029	3.757	-3.746	2.966	-3.756	-145.59
3.046	3.030	3.757	3.746	-2.963	-3.756	-147.95
-3.044	-3.027	3.756	3.746	-2.962	3.757	-190.04
-3.044	3.027	3.757	-3.746	-2.964	3.757	-195.42
-3.042	3.027	3.756	3.746	-2.963	-3.757	-133.24
3.043	-3.025	-3.757	3.746	-2.966	3.757	-213.25
3.041	-3.026	3.757	-3.746	-2.964	3.757	-171.40
3.043	-3.026	3.756	3.746	-2.964	-3.757	-218.93
-3.046	-3.028	3.757	-3.746	2.967	3.757	-202.44
-3.043	-3.028	-3.757	3.746	2.965	3.757	-138.30

Table 4.33: Magnitude of J-values (cm^{-1}) and the Mn-Mn interactions that constitute each J-value for the *mer*-isomer of the 3rd charged state.

J-value	Interacting Mn centres	Magnitude (cm^{-1})
J_1	*trans*-Mn2(IV)-Mn5(IV)	0.11 ± 0.01
J_2	*trans*-Mn1(IV)-Mn4(III)	1.23 ± 0.01
J_3	*trans*-Mn3(III)-Mn6(III)	-0.64 ± 0.00
J_4	*cis*-Mn1(IV)-Mn2(IV)	-3.17 ± 0.01
J_5	*cis*-Mn1(IV)-Mn5(IV)	-3.00 ± 0.01
J_6	*cis*-Mn1(IV)-Mn3(III)	-2.43 ± 0.01
J_7	*cis*-Mn1(IV)-Mn6(III)	-2.68 ± 0.00
J_8	*cis*-Mn2(IV)-Mn3(III)	-2.69 ± 0.01
J_9	*cis*-Mn2(IV)-Mn4(III)	-2.73 ± 0.01
J_{10}	*cis*-Mn2(IV)-Mn6(III)	-1.82 ± 0.00
J_{11}	*cis*-Mn3(III)-Mn5(IV)	-1.33 ± 0.01
J_{12}	*cis*-Mn4(III)-Mn5(IV)	-2.34 ± 0.01
J_{13}	*cis*-Mn5(IV)-Mn6(III)	-2.01 ± 0.00
J_{14}	*cis*-Mn3(III)-Mn4(III)	-1.41 ± 0.01
J_{15}	*cis*-Mn4(III)-Mn6(III)	-1.46 ± 0.00

4.5.6 4th charged state (*cis*-isomer)

To ensure that further oxidation does not stabilise the intermediate spin states either, the 4th charged state was modelled. This charged state is very similar to the 2nd charged state and just like the 2nd charged state, there are two possible configurations depending upon whether the Mn(III) centres are *cis*- to each other or *trans*- to each other both of which were modelled.

For the *cis*-isomer, Mn3 and Mn4 are in oxidation state III while the others are in oxidation state IV (**Figure 4.17 (a)**). The *trans*-Mn(IV)-Mn(IV) and Mn(IV)-Mn(III) distances are 6.259 and 6.286 Å respectively. The cage has expanded even further which implies that Cl^- ion can move more freely within the void. The Mn-Cl distance follows the order Mn1(IV)-Cl ~ Mn6(IV)-Cl (2.66Å) < Mn5(IV)-Cl (3.11Å) < Mn2(IV)-Cl (3.24.Å) < Mn3(III)-Cl ~ Mn4(III)-Cl (3.66Å).

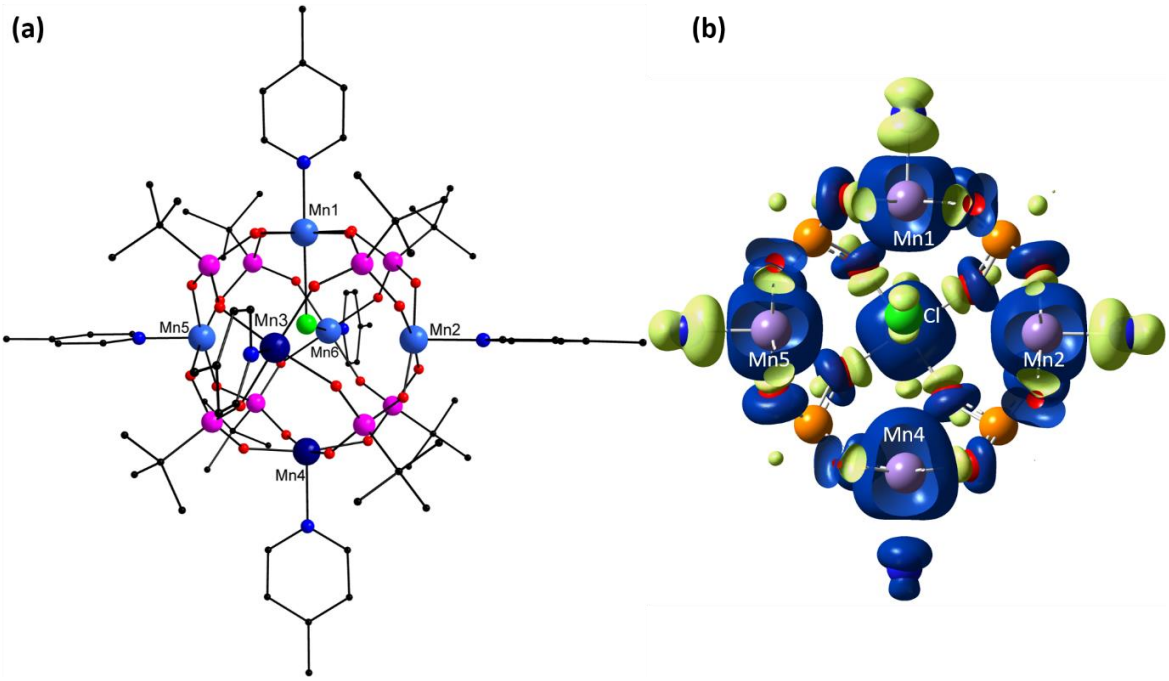

Figure 4.17: Optimised model of the *cis*-isomer of the 4th charged state for the $\{Mn_6\}$ cage **(a)** and the distribution of the spin density in this state **(b)**. Colour scheme: Mn^{III} (dark blue), Mn^{IV} (light blue), P(pink), Cl (green), C (black) O (red). Hydrogens have been removed for clarity. Blue and green regions in the spin density plots represent the spin density associated with up and down spin respectively.

Like the *cis*-isomer of the 2nd charged state, 12 coupling constants are needed to fully describe the spin environment of the system. The Hamiltonian thus used for this charged state is the following:

$$\begin{aligned} H = & -2J_1[\langle s_2.s_5\rangle] - 2J_2[\langle s_1.s_4\rangle + \langle s_3.s_6\rangle] - 2J_3[\langle s_1.s_2\rangle + \langle s_2.s_6\rangle] \\ & -2J_4[\langle s_1.s_5\rangle + \langle s_5.s_6\rangle] - 2J_5[\langle s_1.s_6\rangle] - 2J_6[\langle s_1.s_3\rangle] - 2J_7[\langle s_2.s_3\rangle] \\ & -2J_8[\langle s_2.s_4\rangle] - 2J_9[\langle s_3.s_5\rangle] - 2J_{10}[\langle s_4.s_5\rangle] - 2J_{11}[\langle s_4.s_6\rangle] \\ & -2J_{12}[\langle s_3.s_4\rangle] \end{aligned} \quad (4.10)$$

18 electronic configurations were modelled for this state (**Table 4.34**) and the *J*-values obtained are given in **Table 4.35**. The coupling strengths are in line with the observed trend. The *trans*-Mn centres are ferromagnetically coupled and this is consistent with the presence of polarised spin density on the Cl^- as highlighted by **Figure 4.17 (b)**. The difference in J_7 and J_8, and J_9 and J_{10} is due to differences in the spin density of the oxygens joining Mn2 and Mn5 to Mn3 and Mn4 respectively (**Table 4.19**). The large spin densities on the phosphonate oxygens joining Mn3 and Mn4 make them strongly coupled.

Table 4.34: Bader spin density on each Mn centre (truncated to three decimal places) and the relative energy of each spin state with respect to the ferromagnetic state for the *cis*-isomer of the 4th charged state.

Mn1	Mn2	Mn3	Mn4	Mn5	Mn6	Energy (cm^{-1})
3.064	3.011	3.742	3.741	3.020	3.066	0.00
3.061	3.008	3.742	-3.740	3.018	3.064	-83.10
3.062	3.011	3.743	3.741	3.020	-3.055	-98.54
3.062	-3.004	3.742	3.741	3.019	3.064	-101.62
-3.055	3.011	3.743	3.741	3.019	-3.057	-144.03
3.059	-3.008	3.741	-3.740	3.017	3.061	-149.68
3.060	-3.004	3.742	3.740	-3.012	3.062	-210.51
3.060	-3.004	3.742	3.740	3.019	-3.056	-140.54
3.060	3.005	-3.742	-3.740	3.014	3.061	-115.99
3.060	3.008	-3.741	3.740	3.016	-3.057	-201.69
3.059	3.006	3.743	-3.740	3.019	-3.057	-139.74
-3.057	-3.004	3.742	3.741	3.019	-3.059	-132.83
-3.058	3.006	3.742	-3.739	3.018	-3.060	-206.73
3.058	-3.007	-3.741	3.740	3.015	-3.059	-188.03
3.057	-3.009	3.741	-3.740	-3.015	3.059	-195.44
3.057	-3.008	3.742	-3.740	3.018	-3.059	-146.66
3.058	-3.005	3.742	3.740	-3.013	-3.058	-187.31
3.058	3.009	-3.741	3.739	-3.018	-3.060	-219.03

The coupling between Mn2 and Mn5 (J_1) is greater in this state compared to the same in the *trans*-isomer of the 3rd charged state. At the same time however, the standard deviation is also quite high. To check the reliability of these values, all 15 coupling constants were also calculated which gives a value of 0.02 ± 0.02 for J_1 (**Table 4.36**). The coupling strength between Mn2 and Mn5 is thus in line with the observed trend (i.e. decreasing with increasing Mn-Mn distance).

For this configuration again the antiferromagnetic coupling dominates and like the *cis*-configuration of the 2nd oxidised state, the S = 0 state (***cis* - 1256 – Mn356**) has been found to be the lowest in energy while the ferromagnetic state is the highest in energy.

Table 4.35: Magnitude of J-values (cm^{-1}) and the Mn-Mn interactions that constitute each J-value for the *cis*-isomer of the 4th charged state.

J-value	Interacting Mn centres	Magnitude (cm^{-1})
J_1	*trans*-Mn2(IV)-Mn5(IV)	0.23 ± 0.18
J_2	*trans*-Mn1(IV)-Mn4(III)	1.01 ± 0.08
	trans-Mn3(III)-Mn6(IV)	
J_3	*cis*-Mn1(IV)-Mn2(IV)	-3.06 ± 0.14
	cis-Mn2(IV)-Mn6(IV)	
J_4	*cis*-Mn1(IV)-Mn5(IV)	-3.39 ± 0.12
	cis-Mn5(IV)-Mn6(IV)	
J_5	*cis*-Mn1(IV)-Mn6(IV)	-2.99 ± 0.15
J_6	*cis*-Mn1(IV)-Mn3(III)	-2.31 ± 0.13
J_7	*cis*-Mn2(IV)-Mn3(III)	-2.54 ± 0.11
J_8	*cis*-Mn2(IV)-Mn4(III)	-1.50 ± 0.16
J_9	*cis*-Mn3(III)-Mn5(IV)	-1.14 ± 0.15
J_{10}	*cis*-Mn4(III)-Mn5(IV)	-2.80 ± 0.11
J_{11}	*cis*-Mn4(III)-Mn6(IV)	-1.83 ± 0.16
J_{12}	*cis*-Mn3(III)-Mn4(III)	-1.74 ± 0.10

Table 4.36: A comparison of the J-values (cm^{-1}) for the *cis*-isomer of the 4th oxidised state obtained with the 15 J-value and 12 J-value Hamiltonians.

Interaction	J-values (15 J-values)	J-values (12 J-values)
Mn1Mn2	-2.89 ± 0.01	-3.06 ± 0.14
Mn1Mn3	-2.25 ± 0.01	-2.31 ± 0.13
Mn1Mn4	0.95 ± 0.00	1.01 ± 0.08
Mn1Mn5	-3.43 ± 0.01	-3.39 ± 0.12
Mn1Mn6	-2.98 ± 0.01	-2.99 ± 0.15
Mn2Mn3	-2.47 ± 0.01	-2.54 ± 0.11
Mn2Mn4	-1.56 ± 0.00	-1.50 ± 0.16
Mn2Mn5	0.02 ± 0.02	0.23 ± 0.18
Mn2Mn6	-3.24 ± 0.00	-3.06 ± 0.14
Mn3Mn4	-1.70 ± 0.01	-1.74 ± 0.10
Mn3Mn5	-1.28 ± 0.01	-1.14 ± 0.15
Mn3Mn6	0.98 ± 0.01	1.01 ± 0.08
Mn4Mn5	-2.79 ± 0.01	-2.80 ± 0.11
Mn4Mn6	-1.83 ± 0.00	-1.83 ± 0.16
Mn5Mn6	-3.37 ± 0.01	-3.39 ± 0.12

4.5.7 4th charged state (*trans*-isomer)

In this state, Mn3 and Mn6 are in oxidation state III while the others are in oxidation state IV (**Figure 4.18 (a)**). The *trans*- Mn(IV)-Mn(IV) and Mn(III)-Mn(III) distances are ~6.170 and 6.510 Å respectively. The Mn(IV)-Mn(IV) distance between the *trans*-Mn centres is close to the Mn-Mn distance between the *trans*-Mn centres in the fully reduced state. The Mn-Cl distance follows the order Mn1(IV)-Cl ~ Mn2(IV)-Cl (2.65Å) < Mn3(III)-Cl (3.29Å) ~ Mn6(III)-Cl (3.30.Å) < Mn5(IV)-Cl ((3.55Å)) < Mn4(IV)-Cl (3.57 Å). Cl^- is shifted towards Mn1(IV) and Mn2(IV) just like the *trans*-configuration of the second oxidised state. Surprisingly, the Mn(III)-Cl distance is smaller than Mn-Cl distance for Mn4 and Mn5 which are in oxidation state IV.

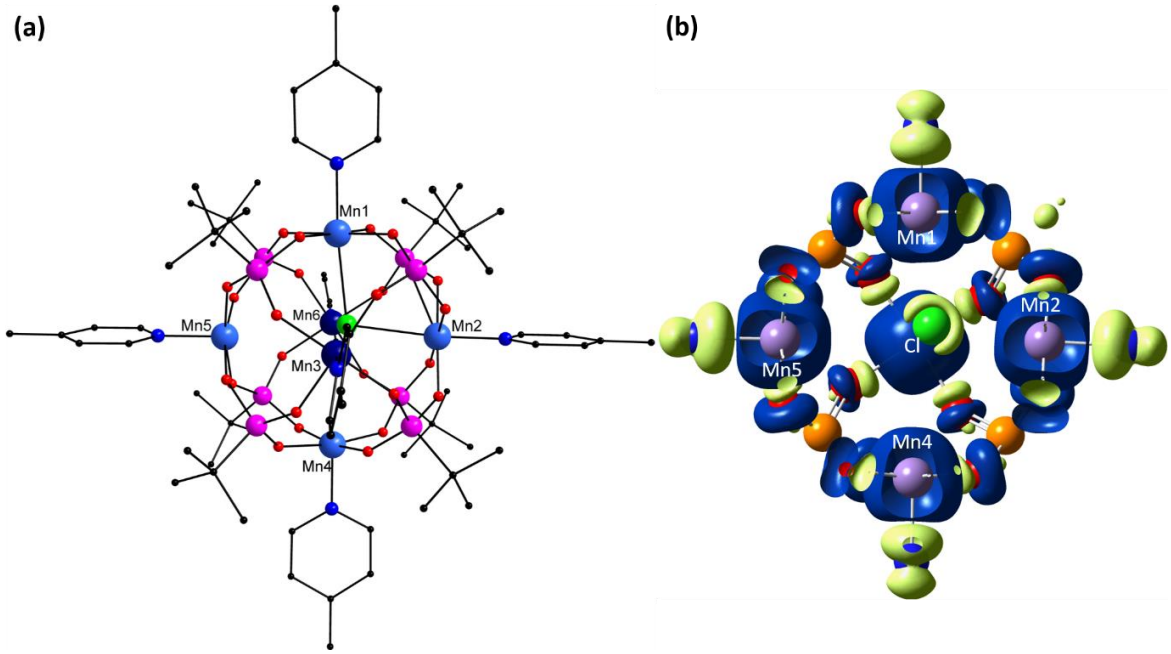

Figure 4.18: Optimised model of the *trans*-isomer of the 4th charged state for the $\{Mn_6\}$ cage **(a)** and the distribution of the spin density in this state **(b)**. Colour scheme: Mn^{III} (dark blue), Mn^{IV} (light blue), P(pink), Cl (green), C (black) O (red). Hydrogens have been removed for clarity. Blue and green regions in the spin density plots represent the spin density associated with up and down spin respectively.

The Hamiltonian used for this charged state is the following:

$$\begin{aligned} H = & -2J_1[\langle s_1.s_4\rangle + \langle s_2.s_5\rangle] - 2J_2[\langle s_3.s_6\rangle] - 2J_3[\langle s_1.s_2\rangle] - 2J_4[\langle s_4.s_5\rangle] \\ & - 2J_5[\langle s_1.s_5\rangle + \langle s_2.s_4\rangle] - 2J_6[\langle s_1.s_3\rangle + \langle s_2.s_3\rangle] - 2J_7[\langle s_1.s_6\rangle] \\ & - 2J_8[\langle s_2.s_6\rangle] - 2J_9[\langle s_3.s_4\rangle + \langle s_3.s_5\rangle] - 2J_{10}[\langle s_4.s_6\rangle + \langle s_5.s_6\rangle] \end{aligned} \quad (4.11)$$

19 electronic configurations were modelled for this state (**Table 4.37**) and the 10 J-values obtained are given in **Table 4.38**. The coupling between *cis*-Mn(IV) centres with each other can be correlated to the Mn-Cl distances and hence the Mn-Cl overlaps (**Table 4.20**). Mn1 and Mn2 also couple strongly to Mn(III) centres compared to the coupling of Mn(III) centres with Mn4 and Mn5. This is due to relatively stronger coupling of Mn1 and Mn2 with the Mn(III) centres via the Cl^- bridge. The

coupling strength between Mn(III) centres is antiferromagnetic and is in line with the observed trends.

Table 4.37: Bader spin density on each Mn centre (truncated to three decimal places) and the relative energy of each spin state with respect to the ferromagnetic state for the *trans*-isomer of the 4th charged state.

Mn1	Mn2	Mn3	Mn4	Mn5	Mn6	Energy (cm^{-1})
3.063	3.070	3.748	2.990	2.997	3.750	0.00
3.060	-3.063	3.748	2.989	2.995	3.749	-125.65
3.062	3.068	-3.746	2.987	2.995	3.749	-100.71
-3.058	-3.065	3.747	2.988	2.995	3.749	-174.33
3.059	-3.064	-3.746	2.986	2.993	3.748	-168.38
3.059	-3.063	3.748	2.989	-2.990	3.749	-219.73
3.061	3.067	-3.746	2.985	2.992	-3.748	-183.35
-3.060	-3.066	-3.747	2.985	2.993	3.748	-163.92
-3.060	-3.066	3.747	2.987	-2.991	3.748	-205.62
3.057	-3.064	-3.746	2.986	-2.993	3.748	-225.95
-3.058	3.065	3.747	-2.984	-2.991	3.748	-203.40
3.062	3.068	3.748	-2.981	2.997	3.749	-97.57
3.062	3.068	3.747	2.987	2.994	-3.747	-100.46
3.060	-3.064	3.748	-2.983	2.995	3.749	-156.41
3.059	-3.064	3.747	2.987	2.993	-3.748	-178.69
-3.060	-3.067	3.746	2.985	2.992	-3.748	-164.60
3.058	-3.065	-3.747	-2.985	2.993	3.748	-164.28
3.057	-3.064	-3.746	2.986	-2.993	3.748	-226.21
3.057	-3.064	3.747	2.986	-2.993	-3.748	-241.01

Table 4.38: Magnitude of *J*-values (cm^{-1}) and the Mn-Mn interactions that constitute each *J*-value for the *trans*-isomer of the 4th charged state.

J-value	Interacting Mn centres	Magnitude (cm^{-1})
J_1	*trans*-Mn1(IV)-Mn4(IV)	0.02 ± 0.15
	trans-Mn2(IV)-Mn5(IV)	
J_2	*trans*-Mn3(III)-Mn6(III)	-0.55 ± 0.12
J_3	*cis*-Mn1(IV)-Mn2(IV)	-4.44 ± 0.27
J_4	*cis*-Mn4(IV)-Mn5(IV)	-3.13 ± 0.26
J_5	*cis*-Mn1(IV)-Mn5(IV)	-3.46 ± 0.15
	cis-Mn2(IV)-Mn4(IV)	
J_6	*cis*-Mn1(IV)-Mn3(III)	-2.40 ± 0.14
	cis-Mn2(IV)-Mn3(III)	
J_7	*cis*-Mn1(IV)-Mn6(III)	-2.86 ± 0.27
J_8	*cis*-Mn2(IV)-Mn6(III)	-1.88 ± 0.24
J_9	*cis*-Mn3(III)-Mn4(IV)	-1.57 ± 0.11
	cis-Mn3(III)-Mn5(IV)	
J_{10}	*cis*-Mn4(IV)-Mn6 (III)	-1.54 ± 0.18
	cis-Mn5(IV)-Mn6(III)	

As J_1 has a standard deviation larger than its value, a set of 14 coupling constants was also determined (**Table 4.39**) using a Hamiltonian in which the only terms that were kept coupled were $\langle s_1 . s_4 \rangle$ and $\langle s_2 . s_5 \rangle$ (since these are the only two terms that should be identical based on the Mn-Mn distances) and the coupling between Mn1 and Mn4, and Mn2 and Mn5 was found to be 0.10 ± 0.01 cm^{-1} which implies that it follows the observed trend. This is also consistent with the presence of polarised spin density on the Cl^- centre (**Figure 4.18 (b)**).

In this configuration unlike the *trans*-configuration of the 2nd oxidised state, the S = 0 state (***trans* - 1245 – Mn256**) has been found to be the lowest in energy while the ferromagnetic state is the highest in energy. This indicates that the ability to stabilise intermediate spin states is lost.

Table 4.39: A comparison of the J-values (cm^{-1}) for the *trans*-isomer of the 4th oxidised state obtained with the 14 J-value and 12 J-value Hamiltonians.

Interaction	J-values (14 J-values)	J-values (10 J-values)
Mn1Mn2	-4.29 ± 0.02	-4.44 ± 0.27
Mn1Mn3	-2.34 ± 0.03	-2.40 ± 0.14
Mn1Mn4	0.10 ± 0.01	0.02 ± 0.15
Mn1Mn5	-3.46 ± 0.03	-3.46 ± 0.15
Mn1Mn6	-2.75 ± 0.02	-2.86 ± 0.27
Mn2Mn3	-2.52 ± 0.01	-2.40 ± 0.14
Mn2Mn4	-3.65 ± 0.02	-3.46 ± 0.15
Mn2Mn5	0.10 ± 0.01	0.02 ± 0.15
Mn2Mn6	-2.06 ± 0.01	-1.88 ± 0.24
Mn3Mn4	-1.56 ± 0.02	-1.57 ± 0.11
Mn3Mn5	-1.64 ± 0.02	-1.57 ± 0.11
Mn3Mn6	-0.64 ± 0.01	-0.55 ± 0.12
Mn4Mn5	-3.07 ± 0.02	-3.13 ± 0.26
Mn4Mn6	-1.80 ± 0.02	-1.54 ± 0.18
Mn5Mn6	-1.43 ± 0.02	-1.54 ± 0.18

4.5.8 Trends observed in the charged states

The oxidation of the complex affects the coupling behaviour between the Mn centres but some general trends can be identified within all the oxidations states modelled. The coupling between Mn centres *trans*- to each other becomes ferromagnetic if one of the Mn centres is in oxidation state IV, and the coupling is *via* the spin polarisation mechanism which is indicated by the spin density on the N of the 4-picoline bound to the Mn centre and, in some cases, by the Cl^- centre. The strength of coupling between *trans*-Mn centres decreases with oxidation due to the expansion of the cage which results in weaker Mn-Cl overlaps. Such a change in the nature of coupling between metal centres however, becomes very important in reactions like the O-O bond formation.[393, 401, 403, 406, 407, 409, 590] Systems similar to this $\{Mn_6\}$ cage with a diamagnetic ion trapped within may provide a way to catalyse such reactions effectively.

The oxidation of the cage leads to its expansion and the central Cl^- moves towards the Mn(IV) centre(s) resulting in different Mn-Cl overlaps. The extent of delocalisation of the spin density from Mn centres to the bound ligand groups increases with the oxidation state and the spin density distribution on the O-donors of the phosphonate groups becomes non-uniform. The spin density on the O-donors was found to be inversely proportional to the Mn-Cl overlaps. Smaller Mn-Cl overlaps lead to greater spin density on the O-donors bound to the corresponding Mn centre. A direct consequence of the increased delocalisation is that the coupling between Mn(IV) centres cis- to each other and Mn(III) centres cis- to each other, in general, increases. When Mn(IV) centres are cis- to Mn(III) centres, some variation is observed in the coupling strength. In the various charged states, the cis-Mn(IV)-Mn(III) coupling is found to vary between -3.6 and -1.5 cm^{-1} and the variation is due to different Mn-Cl overlaps and the consequential non-uniform distribution of spin densities on the O-donors.

4.5.9 Temperature dependence of magnetic susceptibility in higher charged states

The temperature dependence of magnetic susceptibility was calculated for each charged state and has been summarised in **Figure 4.19**. The presence of ferromagnetic coupling is clearly indicated at lower temperatures for the 1st charged state and the *trans*-isomer of the 2nd charged state. The susceptibility plots for *trans*-isomer of each charged state indicates that the ground state in each case has an intermediate spin multiplicity. This may seem unusual for the charge states higher than the 2nd charged state for which an S = 0 (or 1/2) state was predicted to be the ground state. This observation can be explained by noting that the calculation of the magnetic susceptibility requires the diagonalisation of the full Hamiltonian that depends upon all the M_S states and not the S states. The multiplicity of the ground state predicted using the experimental magnetic susceptibility is the multiplicity of the M_s state and not the spin multiplicity.

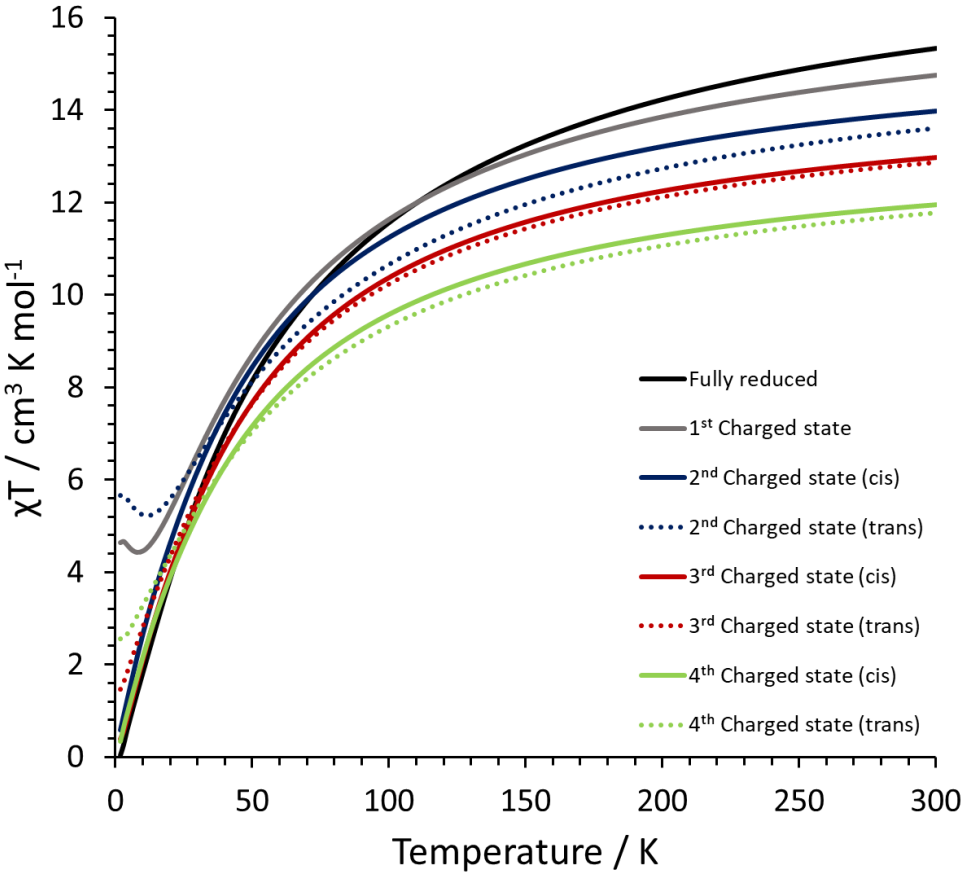

Figure 4.19: χT vs T plots for the different charged states of the {Mn_6} complex.

To determine the most stable M_s state for each charged state, the eigenvectors of the diagonalised Hamiltonian matrix were determined. For the fully reduced state M_s = 0 states were found to form the ground state. For the 1st charged state the exact diagonalisation revealed a degenerate ground state with M_S = 0.5, 1.5 and 2.5 states contributing to it. The **2 – Mn25** state was found to contribute to a level lying above (~5.5 cm^{-1} higher in energy) the ground state. For the *cis*-isomer of the 2nd, 3rd and 4th charged states M_s = 0 states were found to constitute the ground level. The ground level for the *trans*-isomer of the 2nd charged state was found to be degenerate with M_S = 0, 1 and 2 states contributing to it. For the *trans*-isomer of 3rd charged state, M_S = 0.5 and 1.5 states were found to constitute the ground level. The *trans*-isomer of 4th charged state was found to be similar to that of the 2nd charged state with M_S = 0, 1 and 2 states contributing to the ground state.

4.6 Conclusions

To conclude, we have computationally and experimentally probed the magnetic properties of a $\{Mn_6\}$ cage in its ground state. All the Mn centres in this state are coupled to each other and the coupling can be described using two coupling constants – one for the coupling between the Mn centres *cis*- to each other while the other for the one *trans*- to each other. The coupling between the *trans*-Mn centres is antiferromagnetic and occurs via the Cl^- bridge. Mn centres *cis*- to each other are coupled via both the Cl^- bridge and the phosphonate bridge. The coupling constants obtained were found to reproduce the experimental curve reasonably well and the problem of experimentally fitting coupling constants to the magnetic susceptibility was highlighted. The mechanism of coupling via both bridges was explicitly determined using a novel methodology involving perturbing the system in such a way that the symmetry is retained and then analysing the effect of the perturbation on the coupling strength. It was found that the coupling between the *cis*-Mn centres via the Cl^- bridge is ferromagnetic while that via the phosphonate bridge is antiferromagnetic.

The oxidation of this cage was also investigated and it was observed that the $\{Mn_6\}$ cage can potentially accommodate the loss of four electrons which is accompanied by expansion of the cage. The successive oxidation of this system gives rise to some unusual magnetic properties. The oxidation results in the movement of Cl^- towards the Mn(IV) centre(s). The trends in the coupling strength between Mn centres *cis*- to each can be explained by taking into account the oxidation state of the interacting Mn centres, the spin density on the O-donors of phosphonate groups and the Mn-Cl overlaps. The oxidation also leads to switching of the nature of coupling between *trans*-Mn centres from antiferromagnetic to ferromagnetic in addition to stabilisation of intermediate spin states. The latter is retained up to the second charged state but the switching occurs whenever one of the interacting *trans*-Mn centres is in oxidation state IV. Such a change can potentially allow fine tuning of reactions like the O-O bond formation during OER where the nature of coupling between the Mn sites can affect the rate of the reaction.

5 Magnetic Properties of $[Mn^{II}Mn^{III}_{12}(\mu_4\text{-}O)_8(\mu_4\text{-}Cl)_6(\text{tert-butyl-}PO_3)_8]$ (5.1)

In this chapter the magnetic properties of the symmetric tridecanuclear Mn cage complex $[Mn^{II}Mn^{III}_{12}(\mu_4\text{-}O)_8(\mu_4\text{-}Cl)_6(\textit{tert}\text{-butyl-}PO_3)_8]$[384, 543] (compound **5.1**) are described. This complex was synthesised in the Schmitt group by a former postdoctoral fellow Lei Zhang. The synthetic protocol adopted for this complex is based on comproportionation reaction involving the reaction of $MnCl_2$, $KMnO_4$ and *tert*-butyl phosphonic acid in presence of $CuCl_2$, isonicotinic acid and triethylamine.

The aim of this chapter is to develop an understanding of the magnetic properties of this complex and determine the strength of exchange coupling between the Mn centres besides exploring the capabilities of the novel methodology described in the previous chapter. The calculations have been carried out using the PBE0 functional[451] along with a SDDALL[507] basis set for Mn, 6-31G(2d)[508] basis set for P and Cl, 6-31G(d)[508] basis set for O and 6-31G(p)[508] basis set for H. The coupling constants are determined and the nature of the various coupling pathways is determined using the novel methodology. Additionally, the nature of the coupling pathways is further verified by overlap analysis.

5.1 Crystal Structure and DFT Model

Compound **5.1** is a mixed valence tridecanuclear Mn complex containing 12 Mn(III) centres and a Mn(II) centre.[384, 543] The Mn(III) centres reside on the vertices of an cuboctahedra while the Mn(II) centre resides at the centre of the cuboctahedra (**Figure 5.1**). The coordination environment of each Mn(III) centre is fulfilled by two μ_4-Cl^-, two μ_4-O^{2-} and O-donors from two *tert*-butyl phosphonate groups and it is quite distorted owing to the restraints imposed by the ligands. The Cl^- centres cap the square faces of the cuboctahedra and are arranged at the vertices of an octahedron centred around the Mn(II) centre. The Jahn-Teller axis of each Mn(III) centre is directed towards the Cl^- centres as is evident from the Mn-ligand distances (**Table 5.1**). The Mn(II) centre resides in an eight coordinated environment which is fulfilled by eight μ_4-O^{2-} groups.

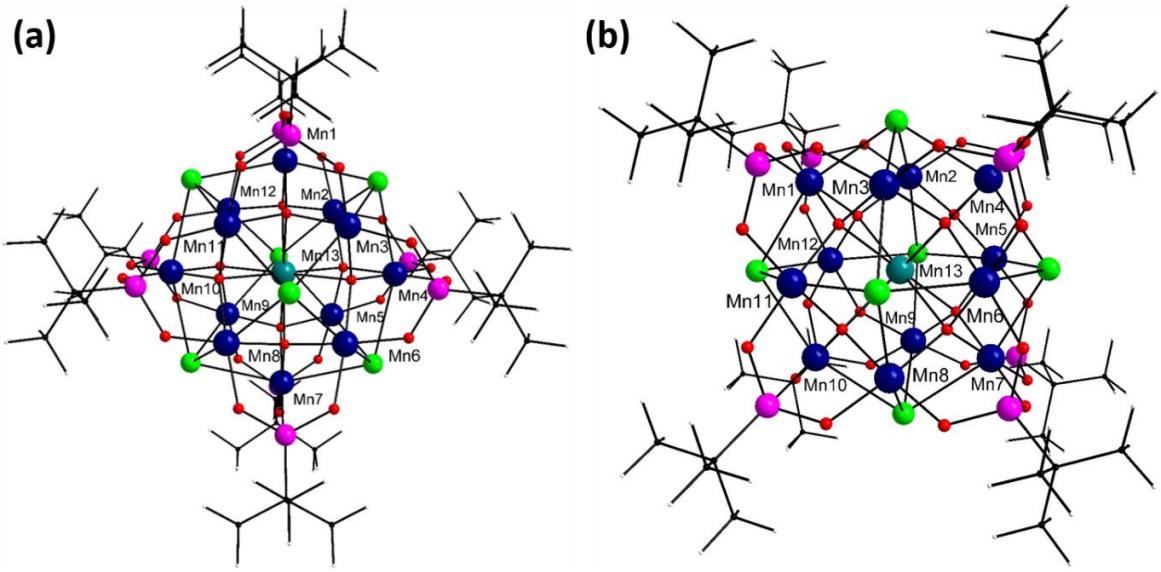

Figure 5.1: Structure of the tridecanuclear compound **5.1** from two different angles **(a)** and **(b)**. Colour scheme: Mn^{II} (teal), Mn^{III} (dark blue), P(pink), Cl (green), C (black) O (red) and H (grey).

For investigating the magnetic properties, the reported crystal structure was used to build the initial model and the whole complex was modelled without simplifying the structure. The methodology adopted is the same as that described in the previous chapter. All calculations have been carried out using the cluster code gaussian09[500]. The model in the ferromagnetic state reproduces the crystal structure well and a comparison of key bond distances is provided in **Table 5.1**. The distances in the non-ferromagnetic states were found to be similar to those in the ferromagnetic state.

Table 5.1: Comparison of key bond distances in the crystal structure and the DFT model in the ferromagnetic state for compound **5.1**. The Mn-Cl and Mn-O distances reported here are the average distances.

	XRD (Å)[384, 543]	DFT (Å)		XRD (Å)[384, 543]	DFT (Å)
Mn1-Mn2	3.26	3.27	Mn1-Mn8	5.64	5.66
Mn1-Mn11	3.26	3.27	Mn1-Mn9	5.65	5.66
Mn1-Mn12	3.26	3.27	Mn1-Mn6	5.65	5.66
Mn1-Mn3	3.26	3.27	Mn1-Mn7	6.52	6.54
Mn1-Mn13	3.26	3.27	Mn(III)-Cl	2.77-2.79	2.75
Mn1-Mn4	4.61	4.62	Mn(III)-O (Phosphonate)	1.90-1.91	1.89
Mn1-Mn10	4.61	4.62	Mn(III)-O (oxo)	1.91-1.92	1.93
Mn1-Mn5	5.64	5.66	Mn(II)-O (oxo)	2.27	2.28

5.2 5.2 Exchange Coupling Pathways and Coupling Constants

There are (13*12/2 =)78 possible coupling interactions between the Mn centres in compound **5.1** and by taking into account the symmetry of the system and the Mn-Mn distances, these interactions can be divided into 5 unique sets (**Table 5.2** and **Table 5.3**). The first set contains interactions between Mn(III) pairs that are coupled *via* phosphonate, μ_4-Cl^- and μ_4-O^{2-} bridges. The second set of pairs includes the coupling interactions of the central Mn(II) with rest of the Mn(III) centres and this coupling is facilitated by the μ_4-O^{2-} and μ_4-Cl^- groups. The third set takes into account the coupling between Mn(III) centres that are coupled only *via* the μ_4-Cl^- bridge. The last two sets contain the interactions between Mn centres that do not interact with each other *via* any bridge and the only possible coupling pathway would be direct coupling. Since these Mn centres are far apart from each other (>5.5 Å), the extent of direct coupling between these pairs should be negligible but to ensure that this is the case, these pairs have been included.

Table 5.2: Mn-Mn distances, oxidation states and ligand bridges for Mn centres associated with different exchange coupling pathways. The value in brackets in the first column is the total number of Mn pairs associated with the particular pathway.

Pathway	Mn-Mn distance (Å)	Oxidation states	Direct ligand bridges
J_1 (24 pairs)	3.27	III-III	μ_4-O^{2-}, μ_4-Cl^-, phosphonate
J_2 (12 pairs)	3.27	II-III	μ_4-O^{2-}, μ_4-Cl^-
J_3 (12 pairs)	4.62	III-III	μ_4-Cl^-
J_4 (24 pairs)	5.66	III-III	None
J_5 (6 pairs)	6.54	III-III	None

This division can be represented by the following Hamiltonian:

$$
\begin{aligned}
H = \; & -2J_1[\langle s_1.s_2\rangle + \langle s_1.s_3\rangle + \langle s_1.s_{11}\rangle + \langle s_1.s_{12}\rangle + \langle s_2.s_4\rangle + \langle s_2.s_5\rangle + \langle s_2.s_{12}\rangle + \langle s_3.s_4\rangle \\
& + \langle s_3.s_6\rangle + \langle s_3.s_{11}\rangle + \langle s_4.s_5\rangle + \langle s_4.s_6\rangle + \langle s_5.s_7\rangle + \langle s_5.s_9\rangle + \langle s_6.s_7\rangle \\
& + \langle s_6.s_8\rangle + \langle s_7.s_8\rangle + \langle s_7.s_9\rangle + \langle s_8.s_{10}\rangle + \langle s_8.s_{11}\rangle + \langle s_9.s_{10}\rangle + \langle s_9.s_{12}\rangle \\
& + \langle s_{10}.s_{11}\rangle + \langle s_{10}.s_{12}\rangle] \\
& - 2J_2[\langle s_1.s_{13}\rangle + \langle s_2.s_{13}\rangle + \langle s_3.s_{13}\rangle + \langle s_4.s_{13}\rangle + \langle s_5.s_{13}\rangle + \langle s_6.s_{13}\rangle + \langle s_7.s_{13}\rangle \\
& + \langle s_8.s_{13}\rangle + \langle s_9.s_{13}\rangle + \langle s_{10}.s_{13}\rangle + \langle s_{11}.s_{13}\rangle + \langle s_{12}.s_{13}\rangle] \\
& - 2J_3[\langle s_1.s_4\rangle + \langle s_1.s_{10}\rangle + \langle s_2.s_3\rangle + \langle s_2.s_9\rangle + \langle s_3.s_8\rangle + \langle s_4.s_7\rangle + \langle s_5.s_6\rangle \\
& + \langle s_5.s_{12}\rangle + \langle s_6.s_{11}\rangle + \langle s_7.s_{10}\rangle + \langle s_8.s_9\rangle + \langle s_{11}.s_{12}\rangle] \\
& - 2J_4[\langle s_1.s_5\rangle + \langle s_1.s_6\rangle + \langle s_1.s_8\rangle + \langle s_1.s_9\rangle + \langle s_2.s_6\rangle + \langle s_2.s_7\rangle + \langle s_2.s_{10}\rangle \\
& + \langle s_2.s_{11}\rangle + \langle s_3.s_5\rangle + \langle s_3.s_7\rangle + \langle s_3.s_{10}\rangle + \langle s_3.s_{12}\rangle + \langle s_4.s_8\rangle + \langle s_4.s_9\rangle \\
& + \langle s_4.s_{11}\rangle + \langle s_4.s_{12}\rangle + \langle s_5.s_8\rangle + \langle s_5.s_{10}\rangle + \langle s_6.s_9\rangle + \langle s_6.s_{10}\rangle + \langle s_7.s_{11}\rangle \\
& + \langle s_7.s_{12}\rangle + \langle s_8.s_{12}\rangle + \langle s_9.s_{11}\rangle] \\
& - 2J_5[\langle s_1.s_7\rangle + \langle s_2.s_8\rangle + \langle s_3.s_9\rangle + \langle s_4.s_{10}\rangle + \langle s_5.s_{11}\rangle + \langle s_6.s_{12}\rangle]
\end{aligned}
$$

Table 5.3: Mn-ligand-Mn angles for Mn centres associated with different exchange coupling pathways. The value in brackets in the first column is the total number of Mn pairs associated with the particular pathway.

Pathway	Mn-O-Mn (˚)	Mn-Cl-Mn (˚)	Mn-P-Mn (˚)
J_1 (24 pairs)	116.0	70.2	66.5
J_2 (12 pairs)	101.7	54.4	-
J_3 (12 pairs)	-	108.8	-

19 electronic configurations have been modelled for this system so that the solution is overspecified. Configurations with different multiplicities were modelled so that solutions are not biased towards a particular spin multiplicity. The Bader spin densities on the Mn centres in each configuration and the energy of each modelled state are given in **Table 5.4**. The difference between the Bader spin and the formal spin value essentially represents the extent of delocalisation of the electron density from the Mn centre. It can be seen that the delocalisation of spin density from the central Mn(II) is greater than that from the Mn(III) centres which is probably due to the lower electronegativity of Mn(II). The J-values obtained (**Table 5.5**) confirm that the coupling strength between Mn centres associated with J_4 and J_5 terms is negligible. Hence, these terms were removed from the Hamiltonian and the coupling constants were recalculated. The coupling constants thus obtained (**Table 5.5**) are similar to the former ones as was expected. In both cases the relative energies of the different electronic states were well reproduced (error < 0.5%).

Table 5.4: Bader spin densities on each Mn centre (truncated to three decimal places) and in each modelled state and the energy (cm^{-1}) of each state relative to the ferromagnetic state.

Mn1	Mn2	Mn3	Mn4	Mn5	Mn6	Mn7	Mn8	Mn9	Mn10	Mn11	Mn12	Mn13	Energy
3.850	3.849	3.849	3.850	3.849	3.849	3.850	3.849	3.849	3.850	3.849	3.849	4.681	0.00
-3.797	3.838	3.838	3.848	3.849	3.849	3.850	3.849	3.849	3.848	3.838	3.839	4.677	560.49
-3.806	-3.806	3.837	3.837	3.840	3.849	3.850	3.850	3.847	3.847	3.840	3.829	4.677	824.26
-3.800	3.826	3.826	-3.800	3.837	3.837	3.848	3.848	3.848	3.848	3.837	3.837	4.679	1216.24
-3.804	3.829	3.829	3.838	3.838	3.838	3.838	3.837	3.837	3.838	3.828	3.828	-4.667	1200.36
-3.815	-3.808	-3.807	3.827	3.838	3.838	3.849	3.847	3.847	3.846	3.828	3.829	4.677	1179.33
-3.808	-3.816	3.827	-3.808	3.829	3.838	3.847	3.849	3.846	3.847	3.838	3.828	4.677	1179.60
-3.806	-3.806	3.837	3.836	3.827	3.838	-3.798	3.838	3.835	3.846	3.838	3.829	4.677	1388.71
-3.813	-3.813	3.827	3.827	3.828	3.839	3.837	3.837	3.836	3.836	3.828	3.821	-4.670	1334.48
-3.805	3.829	3.828	3.835	3.829	3.828	-3.805	3.828	3.828	3.835	3.828	3.828	-4.669	1626.43
-3.816	-3.816	-3.816	-3.816	3.829	3.829	3.847	3.847	3.847	3.846	3.829	3.829	4.677	1244.19
-3.801	3.826	3.826	-3.801	3.826	3.826	-3.801	3.826	3.826	-3.800	3.826	3.826	4.675	2636.17
3.829	3.847	-3.816	3.829	3.847	-3.816	3.829	-3.816	3.847	3.829	-3.816	3.847	4.677	1243.53
-3.816	-3.825	-3.817	-3.825	-3.816	3.827	3.836	3.846	3.836	3.846	3.829	3.827	4.674	1214.60
-3.834	-3.817	-3.818	3.826	3.836	3.836	3.848	3.836	3.836	3.826	-3.818	-3.817	4.673	1215.05
3.817	3.817	3.817	3.818	-3.807	-3.807	3.818	3.818	3.818	3.818	-3.807	-3.806	-4.671	2877.06
-3.817	-3.826	-3.826	-3.835	-3.818	-3.818	3.826	3.836	3.836	3.846	3.826	3.827	4.673	1278.82
-3.817	-3.825	3.817	-3.817	3.809	3.818	-3.807	3.818	3.816	-3.807	3.818	3.809	-4.670	2715.39
3.824	3.836	-3.825	-3.816	3.836	-3.826	3.825	-3.826	3.836	-3.816	-3.825	3.836	4.673	1186.09

Table 5.5: J-values (cm^{-1}) obtained for compound **5.1** using the 5 J-value and 3 J-value Hamiltonian.

	J_1	J_2	J_3	J_4	J_5
J-values (5 J-value Hamiltonian)	10.11 ± 0.16	3.52 ± 0.09	-3.29 ± 0.15	-0.04 ± 0.15	-0.03 ± 0.31
J-values (3 J-value Hamiltonian)	10.08 ± 0.13	3.50 ± 0.07	-3.34 ± 0.15	-	-

The coupling between Mn centres is dominantly ferromagnetic which is in agreement with the observed experimental temperature dependence of magnetic susceptibility.[543] The strongest coupling is between Mn(III) centres that are coupled *via* phosphonate, μ_4-Cl^- and μ_4-O^{2-} bridges (J_1). The coupling between the Mn(II) and Mn(III) centres (J_2) is also ferromagnetic but is significantly weaker compared to J_1. The Mn centres bridged only *via* the Cl^- centres (J_3), on the other hand, are coupled antiferromagnetically.

The temperature dependence of magnetic susceptibility has not been determined using the calculated J-values for this complex for two reasons. First of all, the full Hamiltonian matrix is too big ($6.5^{12} \times 6.5^{12}$) so exact diagonalisation is not possible. There are other methods available that can be used to approximate the eigenvalues and eigenvectors of the full Hamiltonian matrix. One of these methods involves the use of Lanczos algorithm[591, 592] for approximating the eigenvalues while another involves the use of Monte Carlo methods.[593] The latter was attempted but success has not been achieved. Another problem with comparison of calculated and experimentally determined magnetic susceptibility for this complex is that the crystal structure of this compound contains an additional Mn(II) counter-cation in the crystal lattice. Since the complex itself is neutral, the charge of the additional Mn(II) is balanced by two additional Cl^- centres that are trapped in the crystal lattice. The presence of the additional Mn(II) centre can lead to additional interactions that can be accounted for only by modelling the complex in its crystal lattice. Even if those interactions are weak, the presence of an additional paramagnetic centre cannot be directly accounted for, making a direct comparison of the calculated and experimental susceptibility challenging. An approach to resolve this issue can be to crystallise the system such that it packs without additional paramagnetic centres and the intermolecular exchange interactions are negligible.

To approximate the ground spin state however, the calculated J-values have been used to determine the energy of all possible unique 2^{12} (=4096) spin states and the energy of some of the states has been provided in **Table 5.6**. The ferromagnetic state has indeed been found to be the lowest in energy and the state above it is 553 cm^{-1} higher thereby making the former a well-defined minimum.

Table 5.6: The relative energies (cm^{-1}) of all the unique spin states for compound **5.1**.

Configuration	Energy	Configuration	Energy
↑↑↑↑↑↑↑↑↑↑↑↑	0	↑↑↓↑↓↑↑↑↓↓↓↓↓	1756
↑↓↓↓↓↓↓↓↓↓↓↓	553	↑↓↓↑↓↓↓↑↓↓↓↓↓	1763
↑↑↑↑↑↑↑↑↑↑↑↓	751	↑↓↓↑↓↑↑↑↓↓↓↓↓	1790
↑↑↓↓↓↓↓↓↓↓↑↓	779	↑↓↑↑↑↓↓↓↑↑↓↑↓	1818
↑↑↓↓↓↓↓↓↓↓↓↓	814	↑↓↓↑↑↑↑↑↑↑↓↓↑	1825
↑↑↓↓↑↓↓↓↓↓↓↓	1074	↑↓↓↑↑↓↓↓↓↓↓↓↑	1843
↑↓↓↓↑↓↓↓↓↓↓↓	1109	↑↓↓↑↑↑↑↑↓↓↓↓↓	1853
↑↓↑↑↓↑↓↓↓↓↓↓	1137	↑↓↓↑↓↓↑↓↓↓↓↓↓	1861
↑↑↓↓↓↓↓↓↓↓↑↑	1155	↑↑↓↓↓↑↓↑↓↓↓↓↑	1881
↑↑↓↓↑↓↑↓↑↓↓↑↓	1166	↑↓↓↑↑↑↑↓↓↓↓↓↓	1889
↑↑↓↑↓↓↓↓↓↓↓↓	1171	↑↓↓↑↓↑↑↑↓↓↓↓↑	1916
↑↓↓↓↓↓↓↓↓↓↓↑	1179	↑↓↓↑↓↑↓↑↓↓↓↓↑	1978
↑↑↑↑↓↑↓↓↓↓↓↓	1200	↑↓↓↑↑↓↓↑↑↑↑↓↑	1989
↑↓↓↑↓↓↓↓↓↓↓↓	1206	↑↓↓↑↑↓↑↓↑↑↓↑↓	2014
↑↑↑↑↑↑↓↑↑↓↑↑↑	1213	↑↓↓↑↑↑↓↑↑↑↓↑↑	2024
↑↑↑↑↓↓↓↓↓↓↓↓	1235	↑↓↓↓↑↓↓↑↓↓↓↓↑	2042
↑↑↑↑↑↑↓↓↓↓↓↓	1263	↑↓↓↑↑↓↓↓↑↑↑↓↓	2051
↑↑↓↓↓↓↓↓↓↓↓↑	1315	↑↓↓↑↑↑↑↑↑↑↓↓↓	2076
↑↑↑↑↓↑↓↓↓↓↓↑	1326	↑↓↓↑↑↓↓↓↑↑↓↓↓	2086
↑↓↓↓↑↓↑↓↑↓↓↓↓	1335	↑↓↓↑↑↓↓↑↑↑↑↓↓	2114
↑↑↓↓↓↑↓↓↓↓↓↓↓	1370	↑↓↓↑↓↓↑↑↓↓↓↓↓	2122
↑↓↑↑↓↑↓↓↓↓↓↓↑	1388	↑↓↓↑↓↓↓↑↓↓↓↓↑	2139
↑↓↓↓↑↓↑↑↑↑↑↓↑	1398	↑↓↓↑↑↑↓↑↓↓↑↓↓	2150
↑↓↑↑↑↓↓↓↓↓↓↓↓	1432	↑↓↓↑↓↑↑↑↑↓↓↑	2184
↑↑↓↓↑↓↓↓↓↓↓↓↑	1450	↑↓↓↑↑↓↓↓↑↑↓↓↑	2211
↑↓↓↑↑↓↓↓↓↓↓↓↓	1467	↑↓↓↑↓↓↑↓↓↓↓↓↑	2237
↑↑↑↑↓↓↓↓↓↓↓↓↑	1486	↑↓↓↑↑↓↑↓↑↑↓↓↑	2247
↑↓↑↑↑↑↓↓↓↓↓↓↓	1495	↑↓↓↑↑↑↓↑↑↑↓↑↓	2275
↑↓↑↑↑↑↑↓↑↓↓↓↓	1523	↑↓↓↑↑↓↑↑↑↑↓↓↓	2310
↑↑↓↑↓↓↓↓↓↓↓↓↑	1548	↑↑↓↓↑↑↓↑↓↑↓↓↓	2348
↑↓↑↑↓↑↑↑↓↓↓↓↓	1558	↑↓↓↑↓↓↓↑↓↑↓↓↑	2372
↑↓↓↓↑↓↑↓↑↓↓↓↑	1585	↑↓↓↑↑↑↓↑↑↑↓↓↑	2382
↑↑↓↓↓↑↑↑↓↓↓↓↓	1595	↑↓↓↓↑↑↓↓↓↑↓↓↓	2419
↑↓↓↓↑↓↓↓↓↓↓↓↑	1610	↑↓↓↑↑↑↓↑↓↑↓↓↓	2445
↑↓↓↓↑↓↓↓↑↑↓↑↑	1621	↑↓↓↑↑↑↓↓↓↑↓↓↓	2481
↑↑↓↓↓↑↓↑↓↓↓↓↓	1631	↑↓↓↑↑↑↓↑↑↑↓↓↓	2508
↑↑↓↓↑↑↑↑↓↓↓↓↓	1658	↑↓↓↑↓↑↑↓↑↑↓↓↑	2543
↑↓↓↓↑↓↓↑↓↓↓↓↓	1667	↑↓↓↑↓↓↑↓↑↑↓↓↓	2579
↑↓↓↓↑↑↑↑↑↑↓↑↓	1683	↑↓↓↑↓↓↓↑↑↑↓↓↑	2606
↑↑↓↑↓↑↓↑↓↓↓↓↓	1693	↑↓↓↑↓↓↑↓↓↑↓↓↓	2615
↑↓↓↑↓↓↓↓↓↓↓↓↑	1707	↑↓↓↑↓↓↑↑↑↑↓↓↑	2641
↑↑↓↓↓↑↑↑↓↓↓↓↑	1721	↑↓↓↓↑↑↓↓↓↑↓↓↑	2670
↑↓↓↑↓↑↓↑↓↓↓↓↓	1728	↑↓↓↑↓↓↑↓↑↑↓↓↑	2704
↑↑↓↓↓↑↓↓↓↓↓↓↑	1746	↑↓↓↑↓↓↑↓↓↑↓↓↑	2865

5.3 Nature of Coupling Pathways

For Mn pairs whose coupling is described by J_3, the coupling is only *via* the Cl^- bridge. Since this coupling is antiferromagnetic, it means that the Cl^- pathway for these Mn pairs is antiferromagnetic. Since the coupling between Mn(III) centres and the central Mn(II) is ferromagnetic and as these are coupled *via* the μ_4-O^{2-} and μ_4-Cl^- bridge, either both pathways are ferromagnetic or only the dominant one is. The average Mn(II)-Cl distance is quite large (~3.81 Å) which suggests that the

coupling *via* the Cl^- bridge will be significantly weaker compared to the oxo- bridge. It can therefore be assumed that the coupling *via* the μ_4-O^{2-} bridge would be ferromagnetic but nothing can be concluded on the nature of the μ_4-Cl^- bridge. The Mn pairs whose coupling is accounted for by J_1 presents an even greater challenge as there are three coupling pathways and the magnitude of J_1 only provides the combined picture of the individual pathways.

In order to determine the nature of coupling *via* each pathway, we again perturb the system in such a way that the symmetry is retained and determine the changes in the coupling strength due to the perturbation. We can replace each bridge by its heavier/lighter analogue and determine the effect it has on the magnitude and/or nature of the *J*-value. Since *J*-values for Mn pairs that are not coupled *via* any ligand bridge have been ascertained to be negligible, these terms have been neglected in the calculation of coupling constants in further investigation. For each model described in the following discussion, eight states have been modelled for the determination of the three coupling constants and the configurations are chosen such that they cover a range of spin multiplicities ensuring that the electronic picture is properly captured.

5.3.1 Phosphonate pathway

To determine the nature of this pathway, compound **5.1** was initially modelled with the *tert*-butyl groups substituted with phenyl groups ($[Mn_{13}(\mu_4\text{-}O)_8(\mu_4\text{-}Cl)_6(\text{phen-}PO_3)_8]$, **MnP**). Such a replacement was made for computational ease because the rotation of the methyl groups makes it hard to locate a well-defined minimum. This was followed by substitution of the P centres with As to perturb the system ($[Mn_{13}(\mu_4\text{-}O)_8(\mu_4\text{-}Cl)_6(\text{phen-}AsO_3)_8]$, **MnAs**). Such a replacement leads to perturbations that arise from the combined effects of both changes in electronegativity and in the Mn-ligand distance. To decouple the two effects and determine the effect of only the Mn-ligand distance on coupling, **MnAs** was modelled again with the As centres substituted with P and constrained geometry optimisations were performed keeping the position of the P and Mn centres fixed (constrained $[Mn_{13}(\mu_4\text{-}O)_8(\mu_4\text{-}Cl)_6(\text{phen-}PO_3)_8]$, **MnPc**). It was observed that keeping only the Mn centres fixed in the constrained geometry optimisations (constrained $[Mn_{13}(\mu_4\text{-}O)_8(\mu_4\text{-}Cl)_6(\text{phen-}PO_3)_8]$, **MnPc'**) allows the P centres to move back to their equilibrium position and the constrained optimisation fails to serve its purpose making it necessary to constrain both Mn and P centres. The changes in the Mn-ligand distances and the coupling constants resulting from these substitutions are summarised in **Table 5.7** and **Table 5.8** respectively.

In the previous chapter, the correlation between spin density on the ligand groups and the strength of coupling was established and higher spin densities were found to indicate stronger coupling. Thus, the effect of these substitutions on the electronic structure was also determined by calculating the spin density on the donors attached to the Mn centres. Due to the symmetry of the complex, the spin density on the various donors of each type is equally distributed and hence, just

the sum of spin density on each type of donor is enough to investigate the electronic structure and this is presented in **Table 5.9**.

Table 5.7: The various Mn-ligand distances (Å) for the different models. In cases where significant variations were observed in the distances, the range is given.

Model	Mn(III)-O (oxo)	Mn(III)-Cl	Mn(III)-O (phosphonate)	Mn(II)-O (oxo)	Mn(II)-Cl
Compound **5.1**	1.93	2.75	1.89	2.28	3.81
MnP	1.92-1.93	2.75	1.88-1.89	2.28	3.80
MnAs	1.91-1.93	2.75-2.77	1.87-1.88	2.33	3.81
MnPc	1.95	2.76	1.91-1.93	2.30	3.80
MnPc'	1.94-1.95	2.76	1.86-1.88	2.30	3.81

A comparison of the J-values for **MnP** and **MnAs** reveals a significant decrease in the magnitude of J_1. Since As is less electronegative than P, a stronger coupling would be expected *via* the phenyl arsonate group and hence, the decrease in J_1 suggests that the coupling *via* this pathway is antiferromagnetic. Additionally, in **MnPc**, the Mn-O bonds are longer compared to **MnP** suggesting that the coupling *via* the phosphonate bridge will be weaker. The other Mn-ligand distances in **MnPc** are less affected which implies that the effect of the magnitude of J-values is primarily due to changes in the phosphonate pathway. J_1 for **MnPc** is greater than that obtained for **MnP** which is only possible if the coupling *via* this bridge is antiferromagnetic thereby confirming the antiferromagnetic nature of the phosphonate pathway. The spin density on the O-donors of the phosphonate groups is lower in **MnPc** compared to that in **MnP** and since J_1 is greater in **MnP** compared to **MnPc** the coupling *via* the phosphonate bridge is confirmed to be antiferromagnetic.

Table 5.8: J-value for compound **5.1** and its analogues with the *tert*-butyl groups replaced with different groups.

Model	J_1	J_2	J_3
Compound **5.1**	10.08 ± 0.13	3.50 ± 0.07	-3.34 ± 0.15
MnP	9.49 ± 0.16	3.64 ± 0.11	-3.29 ± 0.22
MnAs	8.48 ± 0.04	2.07 ± 0.04	-3.30 ± 0.05
MnPc	10.52 ± 0.11	4.61 ± 0.16	-3.36 ± 0.20
MnPc'	9.79 ± 0.08	4.11 ± 0.03	-3.40 ± 0.10

Table 5.9: Sum of spin densities on the Mn centres and the various donors attached to them in the ferromagnetic state of the different models involving substitution of the phosphonate group.

	Compound 5.1	MnP	MnAs	MnPc	MnPc'
Mn	50.870	50.841	50.812	51.045	51.373
Cl	1.199	1.209	1.170	1.165	1.145
O (μ_4-O)	0.049	0.037	0.166	-0.114	-0.228
O (phosphonate)	0.977	0.976	0.875	0.964	0.769

In all models, the value of J_3 does not change significantly and this is because the replacement of P with As (and vice versa) does not affect the position of Cl^- which is evident from the Mn-Cl distances

which remain constant (**Table 5.7**). It can also be seen that the sum of spin density on Cl^- remains essentially the same and that explains the constant value of J_3 in all models.

The substitution of the P centres affects the coupling *via* the oxo-groups and the effect of such changes are reflected in the magnitude of J_2 (**Table 5.8**). This is a consequence of the simultaneous presence of both spin delocalisation and polarisation mechanism as is evident from the spin density plot for **MnP** (**Figure 5.2**). The spin density on the oxo- groups is quite small for **MnP** but is significantly larger and of opposite nature for **MnPc'** and **MnPc**. This indicates that there may be a competition between spin polarisation and spin delocalisation mechanism and small changes to the structure result in one mechanism dominating the other. This is further confirmed by the higher spin density of the same nature as on Mn on the oxo groups in **MnAs** for which the J_2 value is significantly lower. The spin densities on the oxo- groups in **MnAs** and **MnPc** together reveal the two extremes and establish the presence of the two coupling mechanism. The presence of both mechanisms explains the small value of spin density in the case of compound **5.1** and **MnP**. Additionally, the presence of spin polarisation suggests that the oxo-pathway for the coupling between Mn(II) and Mn(III) centres is ferromagnetic. The dominance of spin polarisation results in higher J_2 values for **MnP** and **MnPc** compared to **MnP**.

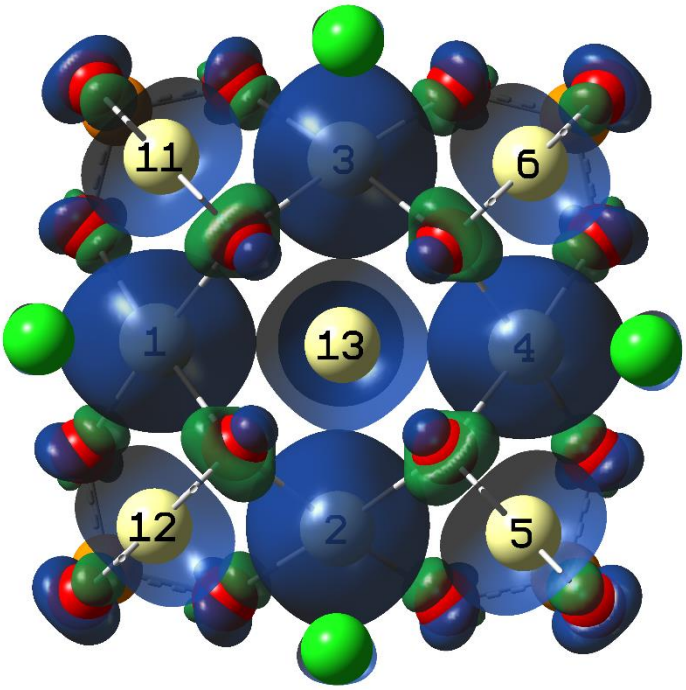

Figure 5.2: Spin density plot for MnP. Purple and green regions in the spin density plots represent the spin density associated with up and down spin respectively. The μ_4-O^{2-} groups can be clearly seen to be accommodating both up and down spin density confirming the presence of spin delocalisation and polarisation. The presence of spin polarisation on the phosphonate O-donors can also be observed.

5.3.2 Chloride pathway

The chloride pathway contributes to all the three coupling constants which means that perturbing the chloride pathway will affect all the three *J*-values. The nature of this pathway for Mn pairs whose coupling is described by J_3 is antiferromagnetic in nature because it is the only coupling pathway available and J_3 is negative. For Mn pairs associated with J_1 and J_2, its nature is unknown and to investigate this, the Cl^- centres in compound **5.1** were initially replaced with Br^- ($[Mn_{13}(\mu_4\text{-}O)_8(\mu_4\text{-}Br)_6(tert\text{-butyl-}PO_3)_8]$, **MnBr**) and I^- ($[Mn_{13}(\mu_4\text{-}O)_8(\mu_4\text{-}I)_6(tert\text{-butyl-}PO_3)_8]$, **MnI**). The Mn-X (X=Cl, Br and I) distance increases with increasing size of X (**Table 5.10**). Again, to decouple the effects of electronegativity and Mn-X distances, constrained geometry calculations were carried out by replacing Br^- and I^- with Cl^- (**MnBrCl** and **MnICl**) and keeping the positions of both Mn and Cl^- fixed. The changes observed in Mn-ligand distances and the coupling constants due to these substitutions are presented in **Table 5.10** and **Table 5.11** respectively. Just like in the investigation of the phosphonate pathway, the spin density on the donors attached to the Mn centres was also determined and the sum of spin density on each type of donor in the different models is summarised in **Table 5.12**.

Table 5.10: The various Mn-ligand distances (Å) for the different models.

Model	Mn(III)-O (oxo)	Mn(III)-X	Mn(III)-O (phosphonate)	Mn(II)-O (oxo)	Mn(II)-X
Compound **5.1**	1.93	2.75	1.89	2.28	3.81
MnBr	1.93	2.85	1.89	2.28	3.97
MnI	1.94	3.04	1.89	2.29	4.28
MnBrCl	1.93	2.85	1.89	2.28	3.97
MnICl	1.94	3.04	1.87	2.28	4.28

The value of J_1 is not affected much between compound **5.1**, **MnBr** and **MnI** making it difficult to obtain any insight. This could be due to the two effects – increasing Mn-X distances which decrease the extent of coupling, and decreasing electronegativity which increases the coupling strength – competing against each other. The clear decrease in the magnitude of J_1 (**Table 5.11**) however, when the Mn-Cl distance increases from **MnBrCl** to **MnICl** (**Table 5.10**) suggests that the coupling *via* this bridge is ferromagnetic for the Mn pairs whose coupling is described by J_1. On moving from compound **5.1** to **MnBrCl** and **MnICl**, the change in spin densities on the oxo-groups and the O-donors of the phosphonate groups is small which suggests that the changes observed in the J_1 value must be dominantly due to the changes introduced in the halide group. As the Mn-Cl distance increases from compound **5.1** to **MnBrCl** and **MnICl**, the sum of spin density on Cl^- centres and the magnitude of J_1 decreases which confirms that the coupling *via* the Cl^- bridge is ferromagnetic for Mn pairs whose coupling is described by J_1.

The increased sum of spin density on the halides in case of **MnBr** and **MnI** without any significant change in the magnitude of J_1 suggests that the size of the halide centres may have an effect on the

coupling behaviour. To investigate this behaviour, an insight into the overlaps between the d-orbitals of the Mn centres and the p-orbitals of the halides is required.

Table 5.11: *J*-value for compound **5.1** and its analogues with Cl replaced with other halides.

Model	J_1	J_2	J_3
Compound **5.1**	10.08 ± 0.13	3.50 ± 0.07	-3.34 ± 0.15
MnBr	10.74 ± 0.07	3.61 ± 0.11	-2.95 ± 0.15
MnI	10.56 ± 0.14	3.75 ± 0.13	-1.17 ± 0.17
MnBrCl	9.13 ± 0.06	3.73 ± 0.07	-1.83 ± 0.12
MnICl	7.35 ± 0.10	3.94 ± 0.14	-0.54 ± 0.16

Among compound **5.1**, **MnBrCl** and **MnICl**, the change in the magnitude of J_2 is small compared to the changes observed in J_1 and J_3. This suggests that the coupling between the Mn(II) centre and the Mn(III) centres is dominated by the oxo bridge and confirms the ferromagnetic nature of the oxo bridge. Since with the increase in the Mn-Cl distance and consequently, the decrease in the coupling strength *via* the Cl^- bridge, J_2 increases slightly, the coupling *via* the Cl^- bridge must be antiferromagnetic. On moving from compound **5.1** to **MnBrCl** and **MnICl**, the value of J_3 decreases with increasing distances and decreasing spin density on the Cl^- again confirming that the coupling between Mn centres accounted for by J_3 *via* this bridge is antiferromagnetic.

Table 5.12: Sum of spin densities on the Mn centres and the various donors attached to them in the ferromagnetic state of the different models involving substitution of the halide.

	Compound 5.1	MnBr	MnI	MnBrCl	MnICl
Mn	50.870	50.694	50.505	50.932	51.046
X (=Cl, Br, I)	1.199	1.354	1.568	1.133	1.022
O (μ_4-O)	0.049	0.052	0.033	0.065	0.064
O (phosphonate)	0.977	0.968	0.944	0.958	0.972

5.3.2.1 Overlap analysis

To further validate the conclusions obtained from the novel methodology and to understand the unusual behaviour exhibited by **MnBr** and **MnI**, overlaps between d-orbitals of Mn and the p-orbitals of the halide groups were investigated. For this purpose, the model was oriented such that the halide and Mn(II) are along the z-axis and Mn1-Mn4, that form one of the square faces of the cuboctahedra, lie in the xy-plane. As the system is highly symmetric, only the overlap between the d-orbitals of Mn1, Mn2, Mn3 and Mn4, and the p-orbitals of the halide lying closest to these Mn centres was determined. To obtain a qualitative idea about the overlaps, the overlap analysis was performed using a minimal basis set[594, 595] and the results obtained are provided in **Table 5.13**. Overlap analysis using the basis set employed for modelling these systems was also performed and the results are summarised in **Table 5.14**. In both cases, more than one d-orbital on the Mn centres overlap with the p-orbitals of the halide which is because the Mn-X-Mn (X = Cl, Br or I) angles are not equal to 90° (**Table 5.3**).

Table 5.13: Overlap matrix ($\times$ 10000) with a minimal basis set for the d-orbitals of the Mn centres and the valence p-orbitals of the halides.

	Cl			Br			I		
	p_x	p_y	p_z	p_x	p_y	p_z	p_x	p_y	p_z
Mn1									
D	0.00	0.00	0.40	0.00	0.00	0.20	0.00	0.50	0.10
D+1	0.00	0.00	0.00	0.10	0.00	0.00	0.10	0.00	0.00
D-1	0.00	5.20	1.40	0.00	6.40	2.00	0.00	6.30	3.40
D+2	0.00	2.10	1.90	0.00	2.30	2.00	0.00	1.20	2.10
D-2	0.10	0.00	0.00	0.30	0.00	0.00	0.30	0.00	0.00
Mn2									
D	0.00	0.00	0.40	0.00	0.00	0.30	0.50	0.00	0.10
D+1	5.20	0.00	1.40	6.40	0.00	2.00	6.30	0.00	3.40
D-1	0.00	0.00	0.00	0.00	0.10	0.00	0.00	0.10	0.00
D+2	2.10	0.00	1.90	2.30	0.00	2.00	1.20	0.00	2.10
D-2	0.00	0.20	0.00	0.00	0.30	0.00	0.00	0.30	0.00
Mn3									
D	0.00	0.00	0.40	0.00	0.00	0.30	0.50	0.00	0.10
D+1	5.20	0.00	1.40	6.40	0.00	2.00	6.30	0.00	3.40
D-1	0.00	0.00	0.00	0.00	0.10	0.00	0.00	0.10	0.00
D+2	2.10	0.00	1.90	2.30	0.00	2.00	1.20	0.00	2.10
D-2	0.00	0.20	0.00	0.00	0.30	0.00	0.00	0.30	0.00
Mn4									
D	0.00	0.00	0.40	0.00	0.00	0.20	0.00	0.50	0.10
D+1	0.00	0.00	0.00	0.10	0.00	0.00	0.10	0.00	0.00
D-1	0.00	5.20	1.40	0.00	6.40	2.00	0.00	6.30	3.40
D+2	0.00	2.10	1.90	0.00	2.30	2.00	0.00	1.20	2.10
D-2	0.10	0.00	0.00	0.30	0.00	0.00	0.30	0.00	0.00

The minimal basis set overlap analysis reveals that the largest overlap is between the D±1 orbitals of Mn and the p_x/p_y orbitals of the halide groups (**Table 5.13**). For Mn1 and Mn4, the largest overlap is between D+1 and p_x orbitals and since the interacting D+1 orbitals are half-filled and interact *via* a full-filled p_x orbital, the Goodenough-Kanamori-Anderson rules[334, 576, 577] suggest that this coupling should be antiferromagnetic. For Mn2 and Mn3 it is the D-1 and p_y orbitals that have the largest overlaps and based on similar arguments, these Mn centres should also be coupled antiferromagnetically. It can be seen that dominantly interacting p-orbitals for Mn1 and Mn2 are different and since these p-orbitals are orthogonal to each other, electron transfer is, in principle, forbidden and the Goodenough-Kanamori-Anderson rules suggest that this coupling should thus be ferromagnetic.[334, 576, 577] Following the same logic, the coupling between Mn1-Mn3, Mn2-Mn4 and Mn3-Mn4 pairs can be considered to be ferromagnetic. These deductions are in agreement with the conclusions reached using our novel methodology further validating its reliability.

The overlaps between d- and p- orbitals of Mn and Br/I respectively are higher, but they show the same trend as observed for Mn and Cl. The weakly overlapping orbitals, especially in case of **MnI**, have relatively larger overlaps compared to that in compound **5.1** and **MnBr** and this indicates that the coupling *via* these bridges will be stronger. This suggests that the strength of the dominant ferromagnetic/antiferromagnetic coupling between Mn centres will be diluted because of the

availability of additional coupling pathways. This may explain why J_1 does not increase for **MnI** and why J_3 decreases significantly for **MnI** compared to **MnCl** and **MnBr**. This also suggests that the electronegativity may not be a good parameter for perturbing the system.

Table 5.14: Overlap matrix ($\times 100$) for the d-orbitals of the Mn centres and the valence p-orbitals of the halides.

	Cl			Br			I		
	p_x	p_y	p_z	p_x	p_y	p_z	p_x	p_y	p_z
Mn1									
D	0.000	0.940	0.318	0.000	0.859	0.614	0.000	1.320	0.243
D+1	0.363	0.000	0.000	0.552	0.000	0.000	0.169	0.000	0.000
D-1	0.000	0.695	0.196	0.000	0.940	0.152	0.000	1.589	0.308
D+2	0.000	0.218	1.424	0.000	0.209	1.700	0.000	0.227	1.932
D-2	0.591	0.000	0.000	0.748	0.000	0.000	0.800	0.000	0.000
Mn2									
D	0.942	0.000	0.320	0.859	0.000	0.614	1.320	0.000	0.243
D+1	0.698	0.000	0.198	0.941	0.000	0.153	1.589	0.000	0.308
D-1	0.000	0.362	0.000	0.000	0.552	0.000	0.000	0.169	0.000
D+2	0.218	0.000	1.428	0.209	0.000	1.701	0.227	0.000	1.930
D-2	0.000	0.588	0.000	0.000	0.747	0.000	0.000	0.802	0.000
Mn3									
D	0.942	0.000	0.320	0.859	0.000	0.614	1.320	0.000	0.243
D+1	0.698	0.000	0.198	0.941	0.000	0.153	1.589	0.000	0.308
D-1	0.000	0.362	0.000	0.000	0.552	0.000	0.000	0.169	0.000
D+2	0.218	0.000	1.428	0.209	0.000	1.701	0.227	0.000	1.930
D-2	0.000	0.588	0.000	0.000	0.747	0.000	0.000	0.802	0.000
Mn4									
D	0.000	0.940	0.318	0.000	0.859	0.614	0.000	1.320	0.243
D+1	0.363	0.000	0.000	0.552	0.000	0.000	0.169	0.000	0.000
D-1	0.000	0.695	0.196	0.000	0.940	0.152	0.000	1.589	0.308
D+2	0.000	0.218	1.424	0.000	0.209	1.700	0.000	0.227	1.932
D-2	0.591	0.000	0.000	0.748	0.000	0.000	0.800	0.000	0.000

The overlap analysis with the full basis set used for the models shows similar behaviour as observed in the minimal basis set overlap analysis although here it is the p_z orbital of the halide interacting strongly with the d-orbitals of the Mn centres (**Table 5.14**). The increase in the overlap of the weakly overlapping orbitals with the increase in the size of the halide group is more noticeable here compared to the minimal basis set overlap analysis further confirming the role of the size of the halide in the unusual coupling behaviour displayed by **MnBr** and **MnI**.

With the full basis set, the overlap between the d-orbitals of the Mn(II) centre and the p-orbitals of halides was found to be smaller compared to the Mn(III)-Cl overlaps. Additionally, between compound **5.1**, **MnBr** and **MnI**, only minor changes are observed in the Mn(II/III)-O overlaps. This explains why the change in the halide bridge only has minor impact of the magnitude of J_2. These results are again in agreement with what was predicted by our novel methodology.

5.3.3 Oxo pathway

For investigating the oxo pathway, one can, in principle, look at the overlap between the d- and p-orbitals of Mn and oxo-groups respectively or replace the O centres with S to determine the effects of perturbing the system. The former was found to be too complicated again because of how the oxo-groups are arranged in the system with a number of d-orbitals of Mn interacting with the p-orbitals of the oxo-groups. The latter can be done but since the nature of the other pathways has been determined, the nature of the oxo-bridge can be understood by simple deduction. For J_1, the phosphonate pathway has been determined to be antiferromagnetic while the Cl^- pathway was found to be ferromagnetic. Additionally, the changes observed in J_1 on increasing the Mn-Cl distance were found to be large but even at an Mn(III)-Cl distance of 3.04 Å, the magnitude of J_1 was significant. This implies that there must be another pathway which allows for ferromagnetic coupling suggesting that the oxo-pathway is ferromagnetic. For J_2, the changes in the Mn-Cl distances had small effect on the coupling strength suggesting that the oxo-pathway dominates the coupling between the Mn(II) centres and Mn(III) centres. Since J_2 is positive, the oxo pathway must be ferromagnetic.

5.4 Conclusions

The magnetic properties of a mixed valence tridecanuclear Mn complex have been investigated using DFT. The Mn centres in this complex occupy the vertices of a cuboctahedron and the complex is stabilised by μ_4-Cl^-, μ_4-O^{2-} bridges and phosphonate groups. Three coupling constants were found to be necessary for a complete description of the exchange coupling – one (J_1) for describing the coupling between the Mn(III) centres bridged *via* μ_4-Cl^-, μ_4-O^{2-} bridges and phosphonate groups, one (J_2) for describing the coupling between the central Mn(II) and all Mn(III) centres and another (J_3) for Mn(III) centres bridged only *via* the μ_4-Cl^- bridge. The coupling in the complex was found to be dominantly ferromagnetic with the strongest coupling observed between Mn pairs that are accounted for by J_1.

The nature of coupling *via* the different pathways was analysed using the novel methodology where the system is perturbed in such a way that the symmetry is preserved and the effect of the perturbation on the coupling constants are determined. The effect of changes in both electronegativity of the bridging group, and the Mn-bridge distances on the magnitude of J-values were investigated for this purpose. It was observed however, that the use of distances in terms of perturbation serves as a more reliable method since larger (less electronegative) atoms have more diffused orbitals which may overlap with orbitals of surrounding atoms leading to abnormal changes in coupling strengths due to perturbation. The use of this methodology reveals that the phosphonate pathway is antiferromagnetic and the oxo- pathway is ferromagnetic. The Cl^- pathway is ferromagnetic for pairs of Mn centres whose coupling is accounted for by J_1, and antiferromagnetic for those whose coupling is described by J_3. These results are in agreement with the results obtained using overlap analysis which further validates the reliability of this methodology.

6 Carboxylate Based Complexes

As described in the introduction, there has been a lot of scientific effort directed towards developing an understanding of the mechanism of water oxidation by the OEC and numerous experimental and computational studies have advanced our understanding in this area.[27, 38, 46, 50, 52, 58, 61, 62, 65] Attempts to synthesise structural analogues of the OEC in the recent years have yielded some fascinating coordination complexes that bear striking structural similarities to the OEC[87-89, 131-137] but none of these complexes show OER activity.

A key aim of this work has been to develop coordination complexes that capture both the structural and catalytic characteristics of the OEC. Considering that the coordination environment of the OEC is predominantly composed of O-donors of carboxylate groups that are a part of large protein units,[27, 58] we have attempted to synthesise purely carboxylate based complexes. The strategy used for this purpose is based on comproportionation reaction and has been described in chapter **3**. Using $KMnO_4$ as the only source of Mn ions, we have succeeded in synthesising three coordination complexes. Using pivalic acid as the ligand results in the formation of a polymorph of a hexanuclear complex, $[Mn^{II}_2Mn^{III}_4(\mu_3\text{-}O)_2((CH_3)_3CCO_2)_{10}(DMF)_4]\cdot DMF\cdot H_2O$ (compound **6.1**), which is structurally similar to a previously reported class of hexanuclear Mn complexes.[596-601] Since the crystal quality of this polymorph was poor, compound **6.1** has been used for characterisation purposes. Slight modification of the synthetic procedure results in the formation of a mixed-metal octanuclear complex, $[K_2Mn^{III}_8(\mu_3\text{-}O)_4(\mu\text{-}OH)_2((CH_3)_3CCOO)_{16}(CH_3CN)_2]\cdot CHCl_3$ (compound **6.2**). This complex shows striking structural similarities to the oxygen evolving complex (OEC).[27, 55-58] When the *tert*-butyl group of the carboxylic acid is replaced with sterically less bulky biphenyl group, significant structural rearrangements occur and a dodecanuclear complex, $[Mn^{IV}_4Mn^{III}_8(\mu_3\text{-}O)_{12}(C_6H_5C_6H_4CO_2)_{16}(H_2O)_4]\cdot 3CH_3CN\cdot 13CHCl_3$ (compound **6.3**) was obtained. In this chapter we describe the structural and physicochemical properties of all three complexes.

Note: Our work on compound **6.2** has been published as a journal article (ref. 602).

6.1 $[Mn^{II}_2Mn^{III}_4(\mu_3\text{-}O)_2((CH_3)_3CCO_2)_{10}(DMF)_4]\cdot DMF\cdot H_2O$ (6.1)

Refluxing $Mn(CH_3COO)_2\cdot 4H_2O$, $KMnO_4$ and pivalic acid in a ratio of 1:4:40 in presence of phenylphosphonic acid and L(-)-proline in a mixture of CH_3CN and DMF results in the formation of compound **6.1**. The crystals were obtained within a week and were characterised by single crystal X-ray diffraction experiment. $KMnO_4$ when refluxed with excess of pivalic acid in CH_3CN results in the formation of a polymorph of compound **6.1** although the crystal quality was found to be poor.

6.1.1 Structural description

Compound **6.1** crystallises in the monoclinic crystal system and the structure solution was obtained in the space group Cc. This compound contains a hexanuclear complex $Mn_6(\mu_3\text{-}O)_2((CH_3)_3CCO_2)_{10}(DMF)_4]$ (**Figure 6.1**). The complex itself is quite symmetric but the presence of a water and a disordered DMF molecule in the asymmetric unit destroys the overall symmetry. It comprises of two edge sharing distorted Mn tetrahedra each centred around a $\mu_4\text{-}O^{2-}$ group (**Figure 6.2 (a)**). This complex is stabilised by two $\mu_4\text{-}O^{2-}$ groups, ten pivalate ligands and four DMF molecules, the latter serving as capping groups. The Mn centres on the common edge were determined to be in +III oxidation state while the other Mn centres were found to be in +II oxidation state from bond valence sum analysis (**Table 6.1**). The oxidation state of the O atoms bound only to Mn centres has also been ascertained by bond valence sum analysis (**Table 6.2**). The BVS value for O in the approximate ranges of 0.2-0.4, 1.0-1.2 and 1.8-2.0 has been suggested to indicate H_2O, OH^- and O^{2-} groups respectively.[603, 604] The values obtained for this complex do not strictly meet this proposed assignment criteria so the protonation state has been decided based on the proximity of the bond valence sum value to an integer. Complexes with similar core structure have been reported previously.[596-601]

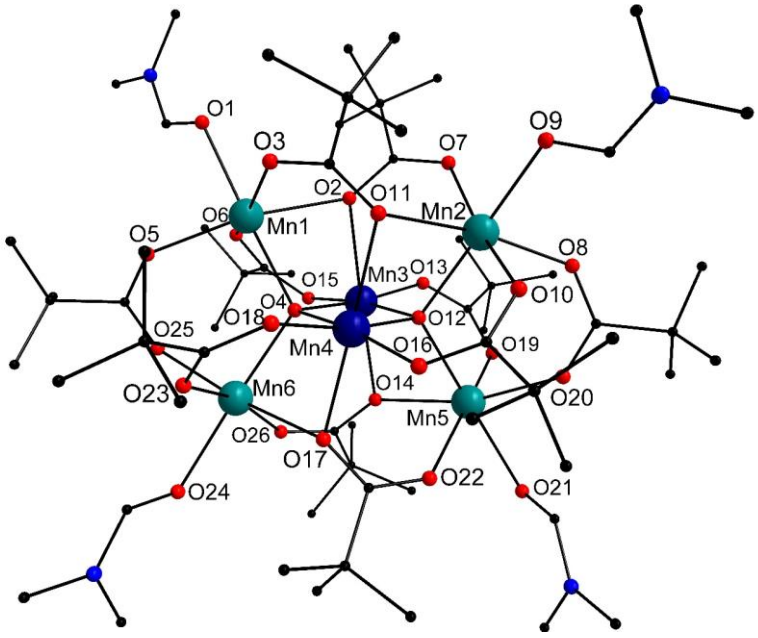

Figure 6.1: Crystal structure of the hexanuclear compound **6.1**. Colour scheme: Mn^{II} (teal), Mn^{III} (dark blue), C (black), N(blue) and O (red). All hydrogen atoms have been removed for clarity.

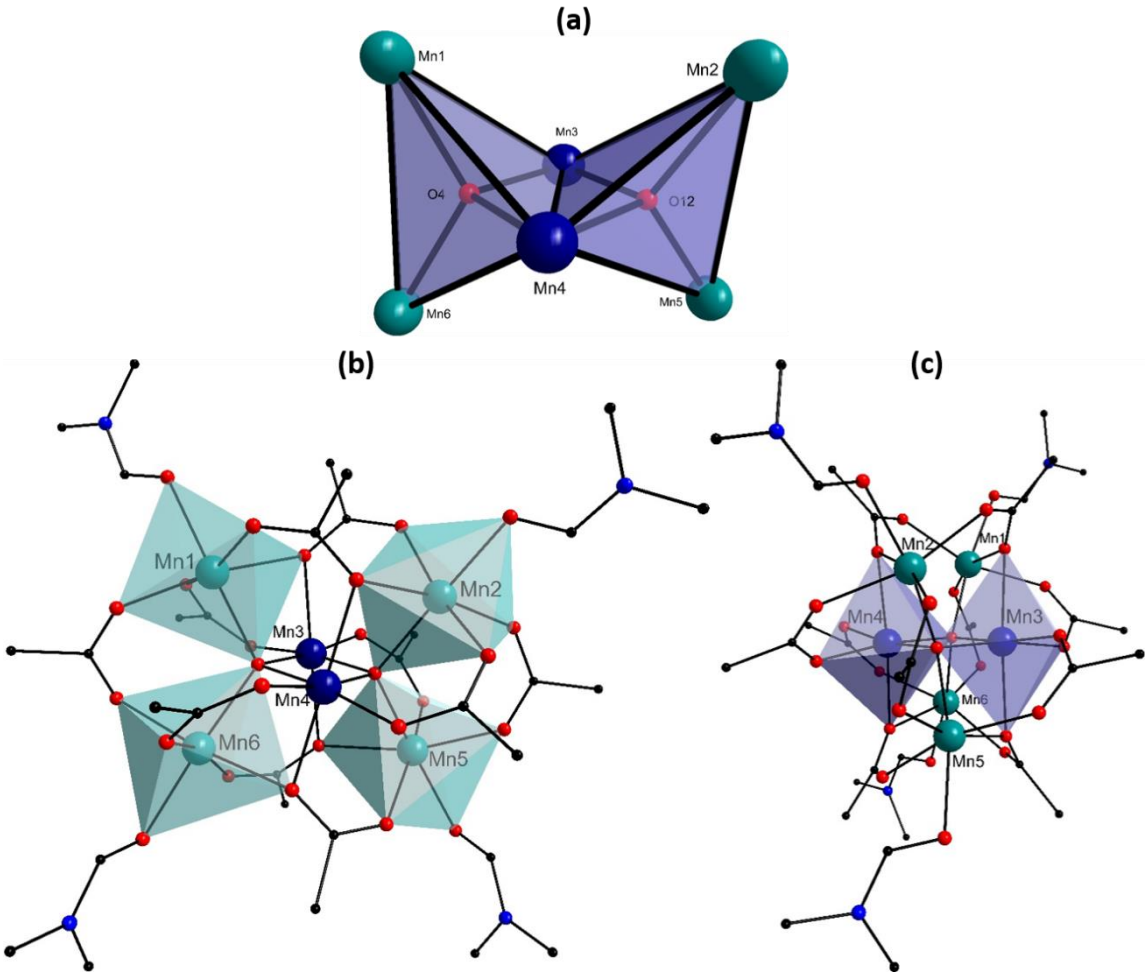

Figure 6.2: (a) Core structure of the compound **6.1**, and the octahedral environment of **(b)** the Mn^{II} centres and **(c)** Mn^{III} centres. Colour scheme: Mn^{II} (teal), Mn^{III} (dark blue), C (black), N(blue) and O (red). All hydrogen atoms have been removed for clarity.

In this complex each Mn^{II} centre resides in an octahedral environment which is fulfilled by a DMF molecule, a μ_4-O^{2-} group and O-donors of four pivalate ligands with the Mn-O distances varying between 2.1 and 2.3 Å (**Table 6.1**). Each Mn^{II} centre is linked to two Mn^{II} centres which are at different distances. The Mn^{II} centres closer to each other are linked to each other via a pivalate (which binds as a μ_2-κ*O*:κ*O'*-pivalate) and μ_4-O^{2-} and the octahedron of these centres are vertex shared at the μ_4-O^{2-} group (**Figure 6.2 (b)**). The bridging mode of the pivalate group in Harris notation[605] can be given as 2.11 mode which means that this pivalate is bound to two Mn centres with each O-donor binding to one Mn centre. From here onwards, the coordination behaviour of monodentate groups (like O^{2-}, OH^-, etc) will be described using the conventional notation while that of polydentate ligands will be given in Harris notation.

The Mn^{II} centres further away from each other are linked to each other via two pivalate groups which bind in a 3.21 mode and their octahedra are completely isolated. These centres do not lie on the same plane and the dihedral between Mn1 and Mn2, and Mn5 and Mn6 was found to be ~17°. The dihedral between Mn1 and Mn6, and Mn2 and Mn5 was found to be ~22°.

Table 6.1: Key Mn-O and Mn-Mn bond lengths and bond valence sum for each Mn centre for compound **6.1**.

Mn centre	Coordinating atom	Bond Distance (Å)	BVS	Assigned oxidation state
Mn1	O1	2.216(2)	2.085	+II
	O2	2.3390(18)		
	O3	2.1161(19)		
	O4	2.1631(18)		
	O5	2.1334(19)		
	O6	2.160(2)		
Mn2	O7	2.1345(19)	2.052	+II
	O8	2.1479(19)		
	O9	2.2220(19)		
	O10	2.1776(18)		
	O11	2.2959(18)		
	O12	2.1668(18)		
Mn3	O2	2.2358(18)	3.152	+III
	O4	1.8847(18)		
	O12	1.8862(18)		
	O13	1.9469(19)		
	O14	2.2522(18)		
	O15	1.9597(19)		
Mn4	O4	1.8887(18)	3.122	+III
	O11	2.2520(18)		
	O12	1.8940(18)		
	O16	1.9542(18)		
	O17	2.2391(18)		
	O18	1.9558(19)		
Mn5	O12	2.1893(17)	2.023	+II
	O14	2.2881(18)		
	O19	2.1445(19)		
	O20	2.1296(19)		
	O21	2.285(2)		
	O22	2.1502(19)		
Mn6	O4	2.1778(18)	2.083	+II
	O17	2.2919(19)		
	O23	2.173(2)		
	O24	2.214(2)		
	O25	2.1188(19)		
	O26	2.1375(19)		

Metals	Distance (Å)	Metals	Distance (Å)
Mn1-Mn2	4.7817(8)	Mn3-Mn4	2.8034(6)
Mn1-Mn3	3.1754(8)	Mn3-Mn5	3.1733(9)
Mn1-Mn4	3.4647(8)	Mn3-Mn6	3.4742(6)
Mn1-Mn6	3.7304(7)	Mn4-Mn5	3.5240(8)
Mn2-Mn3	3.4708(6)	Mn4-Mn6	3.1845(6)
Mn2-Mn4	3.1714(6)	Mn5-Mn6	4.8451(8)
Mn2-Mn5	3.7394(7)		

The coordination environment of the Mn^{III} centres is fulfilled by four pivalate ligands and two μ_4-O^{2-} groups (**Figure 6.2 (c)**). The octahedron of the Mn^{III} centres share an edge. The Jahn-Teller axis of these centres are along the pivalate ligands which bind in the 3.21 mode and are not parallel but at 20° to each other due to ligand constraints. The Mn-O bond with the O donors of pivalate ligands along the Jahn-Teller axis is ~2.25 Å and is ~1.95 Å otherwise. The Mn^{III}-O bonds with μ_4-O^{2-} groups are shorter (1.89 Å).

Table 6.2: BVS analysis for O atoms and their assigned protonation state in compound **6.1**.

Atom	BVS	Assignment
O4	2.136	μ_4-O^{2-}
O12	2.108	μ_4-O^{2-}

Examination of the bond lengths (**Table 6.1**) and bond angles (**Table 6.3**) for each Mn centre indicates that the coordination environment of each Mn centres deviates from ideal geometry. To quantify the extent of distortion, bond angle variance (σ^2) and distortion indices (DI) have been calculated and the values obtained are given in **Table 6.4**..[606-609] The limitation of these approaches is that they are limited to the use of bond angles but as distortion induced by changes in bond lengths are relatively smaller, they provide reasonable values. A more generalised approach for calculating the extent of distortion is provided by continuous shape measure analysis where the structure under investigation is compared with the corresponding ideal geometry for determining the extent of distortion.[610-614] The continuous shape measure analysis, in this work, has been carried out using SHAPE V2.1 code and the values obtained for the Mn centres of compound **6.1** are given in **Table 6.4**.[615] The details of all these approaches are provided in the appendix.

Table 6.3: Selected bond angles for compound **6.1**.

Bond	Bond Angle (°)	Bond	Bond Angle (°)
O4-Mn1-O2	76.83(6)	O4-Mn4-O12	83.99(7)
O6-Mn1-O2	80.44(7)	O4-Mn4-O17	84.58(7)
O6-Mn1-O1	82.27(8)	O12-Mn4-O11	84.69(7)
O3-Mn1-O1	84.35(8)	O18-Mn4-O11	86.42(7)
O5-Mn1-O6	86.21(8)	O16-Mn4-O18	86.87(8)
O5-Mn1-O1	88.16(8)	O16-Mn4-O17	87.50(7)
O3-Mn1-O2	89.14(7)	O18-Mn4-O17	89.53(7)
O6-Mn1-O4	91.37(7)	O16-Mn4-O11	89.56(7)
O5-Mn1-O4	94.71(7)	O4-Mn4-O18	94.75(8)
O1-Mn1-O2	98.77(7)	O12-Mn4-O16	95.67(8)
O3-Mn1-O4	101.10(7)	O4-Mn4-O11	98.45(7)
O3-Mn1-O5	106.03(8)	O12-Mn4-O17	99.47(7)
O3-Mn1-O6	161.55(8)	O12-Mn4-O18	170.73(8)
O5-Mn1-O2	163.94(7)	O4-Mn4-O16	171.90(8)
O4-Mn1-O1	172.84(8)	O17-Mn4-O11	175.12(7)
O12-Mn2-O11	77.83(6)	O22-Mn5-O21	76.94(7)
O10-Mn2-O9	81.16(7)	O12-Mn5-O14	77.16(7)
O10-Mn2-O11	81.75(7)	O19-Mn5-O14	81.64(7)
O7-Mn2-O9	85.75(7)	O20-Mn5-O21	82.94(8)
O8-Mn2-O10	86.66(7)	O22-Mn5-O14	88.28(7)

Bond	Bond Angle (°)	Bond	Bond Angle (°)
O8-Mn2-O9	87.47(7)	O20-Mn5-O19	89.00(8)
O12-Mn2-O10	90.24(7)	O20-Mn5-O12	91.57(7)
O7-Mn2-O11	90.47(7)	O19-Mn5-O12	94.35(7)
O9-Mn2-O11	95.14(7)	O19-Mn5-O21	94.41(7)
O8-Mn2-O12	97.83(7)	O22-Mn5-O12	95.84(7)
O7-Mn2-O12	101.74(7)	O20-Mn5-O22	103.35(8)
O7-Mn2-O8	101.86(7)	O21-Mn5-O14	109.74(7)
O7-Mn2-O10	164.08(8)	O19-Mn5-O22	163.72(8)
O8-Mn2-O11	167.56(7)	O20-Mn5-O14	164.68(7)
O12-Mn2-O9	169.65(7)	O12-Mn5-O21	169.58(7)
O4-Mn3-O12	84.31(7)	O4-Mn6-O17	77.19(6)
O12-Mn3-O14	84.41(7)	O23-Mn6-O17	81.17(7)
O4-Mn3-O2	85.19(7)	O26-Mn6-O24	84.46(8)
O13-Mn3-O15	86.53(8)	O23-Mn6-O24	84.48(8)
O13-Mn3-O2	87.72(7)	O25-Mn6-O23	86.77(8)
O15-Mn3-O14	88.13(7)	O23-Mn6-O4	89.68(7)
O13-Mn3-O14	88.48(7)	O25-Mn6-O24	89.89(8)
O15-Mn3-O2	90.09(7)	O26-Mn6-O17	90.12(7)
O12-Mn3-O13	94.61(8)	O25-Mn6-O4	95.08(7)
O4-Mn3-O15	95.51(8)	O24-Mn6-O17	96.64(7)
O12-Mn3-O2	97.44(7)	O26-Mn6-O4	100.30(7)
O4-Mn3-O14	98.67(7)	O25-Mn6-O26	103.27(8)
O12-Mn3-O15	172.42(8)	O26-Mn6-O23	165.03(8)
O4-Mn3-O13	172.62(8)	O25-Mn6-O17	165.65(7)
O2-Mn3-O14	175.90(7)	O4-Mn6-O24	172.12(7)

It can be observed from the continuous shape measure values, angle variance and distortion indices that the octahedral environment of each Mn centre is not heavily distorted (**Table 6.4**). The higher distortions for Mn1 and Mn5 compared to the other two Mn^{II} centres is because of the disordered DMF molecule which, owing to how it packs in the crystal lattice, preferentially affects Mn1 and Mn5.

Table 6.4: Continuous shape measure values, angle variance and distortion indices (using the ideal octahedral geometry as a reference) for each Mn centre for compound **6.1**.

Mn centre	Continuous shape measure value	Angle variance (σ^2)	Distortion Index
Mn1	1.378	77.83	0.0783
Mn2	0.942	63.31	0.0711
Mn3	1.102	26.54	0.0479
Mn4	1.178	30.80	0.0515
Mn5	2.246	100.18	0.0860
Mn6	0.964	60.53	0.0664

This complex crystallises along with a water and a disordered DMF molecule and the packing diagram is shown in **Figure 6.3**. The radius of the largest voids containing these solvent molecules is 2.4 Å as calculated by the 'calcvoid' routine implemented in the OLEX2 code.[616]

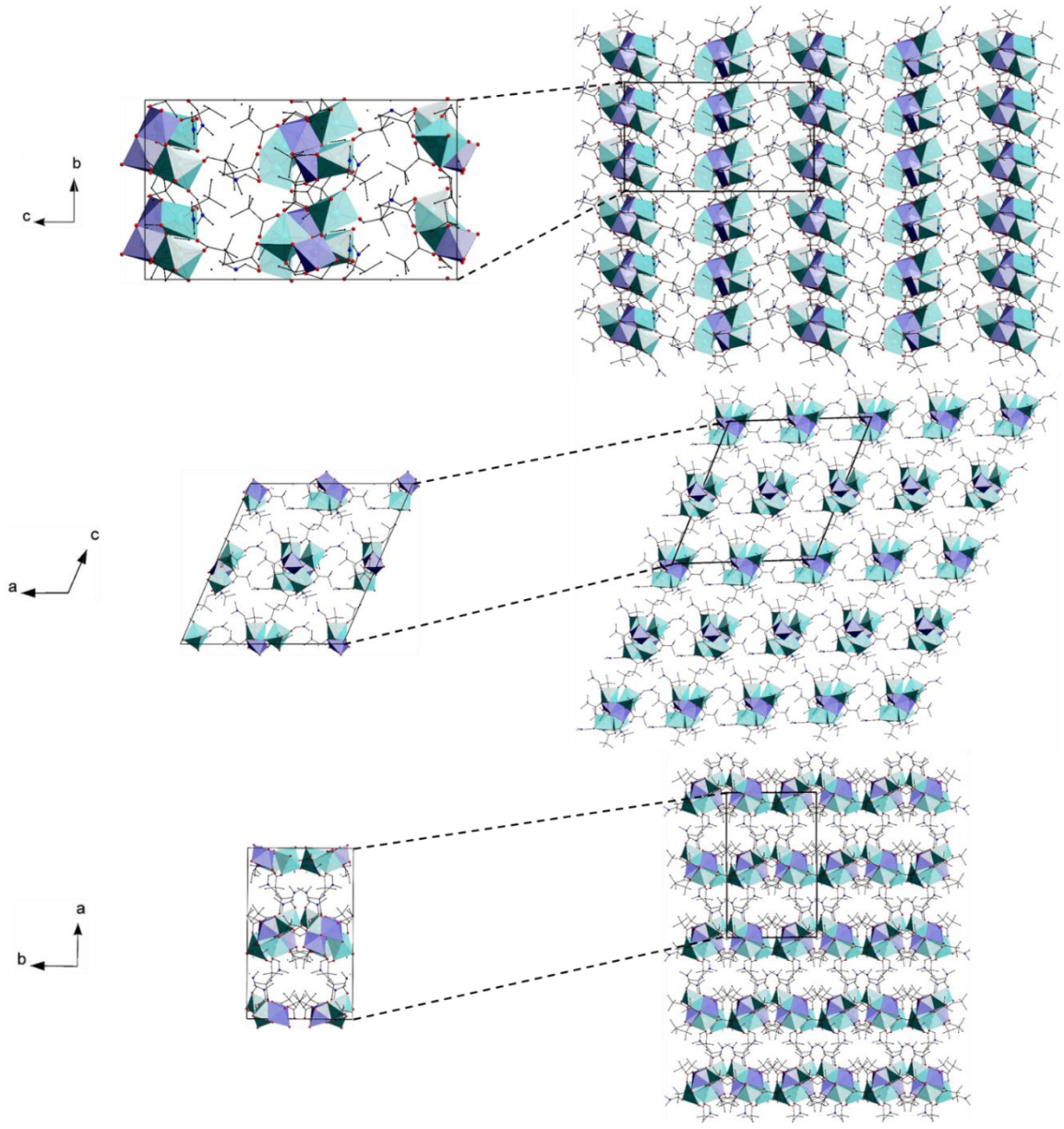

Figure 6.3: Packing diagram of compound **6.1**. Colour scheme: Mn^{II} (teal), Mn^{III} (dark blue), C (black), N(blue), O (red) and H (grey).

6.1.2 Physicochemical characterisation

Thermogravimetric analysis (TGA) analysis under N_2 atmosphere of air dried compound **6.1** shows a weight loss of ~6 % up to 120 °C due to the loss of DMF and water molecules (calcd: 5.3 %) trapped in the crystal lattice (**Figure 6.4**). This is followed by a gradual loss of the bound DMF molecules that occurs up to ~230 °C (calcd: 16.6 %, found 17.4 %). The steep drop that follows can be attributed to the partial loss of pivalate groups and it occurs up to 310 °C. Heating above 310 °C leads to cluster degradation and oxide formation.

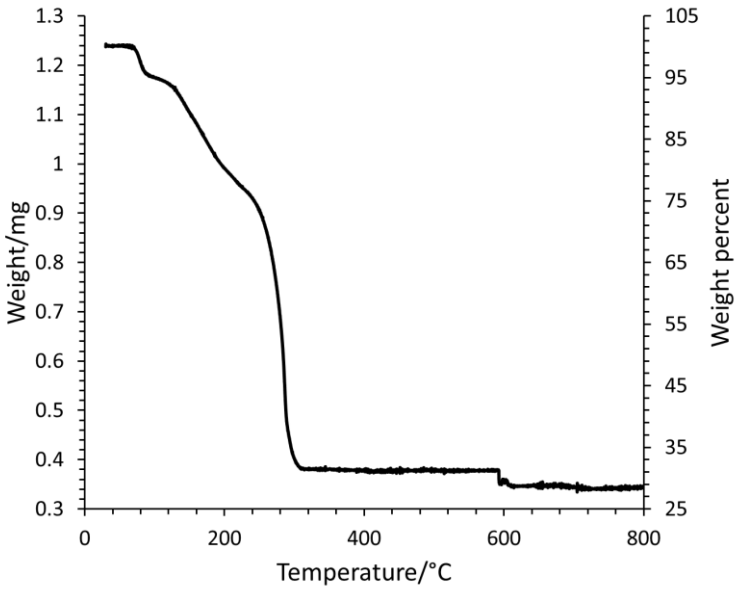

Figure 6.4: TGA analysis of compound **6.1**.

The infrared (IR) spectrum of compound **6.1** is consistent with the proposed structural model (**Figure 6.5**). The feature at ~3000 cm^{-1} corresponds to the C-H stretching vibrations. Vibration modes in the 1300-1600 cm^{-1} region are due to the organic portion of the molecule.[617] The symmetric and asymmetric stretches due to the carboxylate groups correspond to the vibration modes observed at 1408 cm^{-1} and ~1575 cm^{-1} and are in line with the expected energy variance for bridging carboxylate groups.[618] The peak at 1654 cm^{-1} can be attributed to the C-O stretch of the DMF molecules.[619, 620] The characteristic phosphonate stretches[621-623] in the region between 900-1000 cm^{-1} are missing confirming the absence of phosphonate groups.

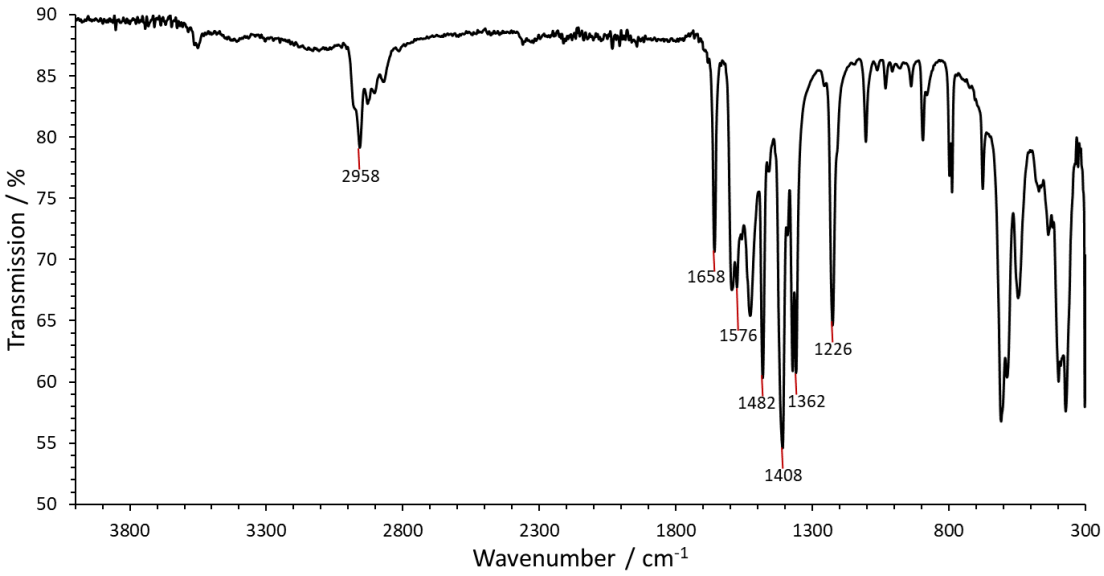

Figure 6.5: Infrared spectrum of compound **6.1**.

6.2 $[Mn^{III}_8K_2(\mu_3\text{-}O)_4(\mu\text{-}OH)_2((CH_3)_3CCOO)_{16}(CH_3CN)_2]\cdot CHCl_3$ (6.2)

Compound **6.2** can be prepared by refluxing $KMnO_4$ with excess of pivalic acid in CH_3CN followed by the addition of $CHCl_3$. Crystals were obtained in a day and were characterised by single crystal X-ray diffraction experiment.

6.2.1 Structure description

Compound **6.2** contains an octanuclear Mn complex (**Figure 6.6 (a)**) that crystallises in the monoclinic crystal system and the structure solution was obtained in the space group $P2_1/n$. The asymmetric unit contains half of the complex (**Figure 6.6 (b)**). The core structure of this complex can be described as a dimer of two distorted cubane {Mn_4K} units that are symmetry related by an inversion centre, and that are bridged by pivalate ligands and two μ_3-oxo groups, O2 and its symmetry equivalent. The oxidation state of the Mn centres and the protonation state of the O atoms bound only to Mn centres has been ascertained by bond valence sum analysis (**Table 6.5** and **Table 6.6** respectively).

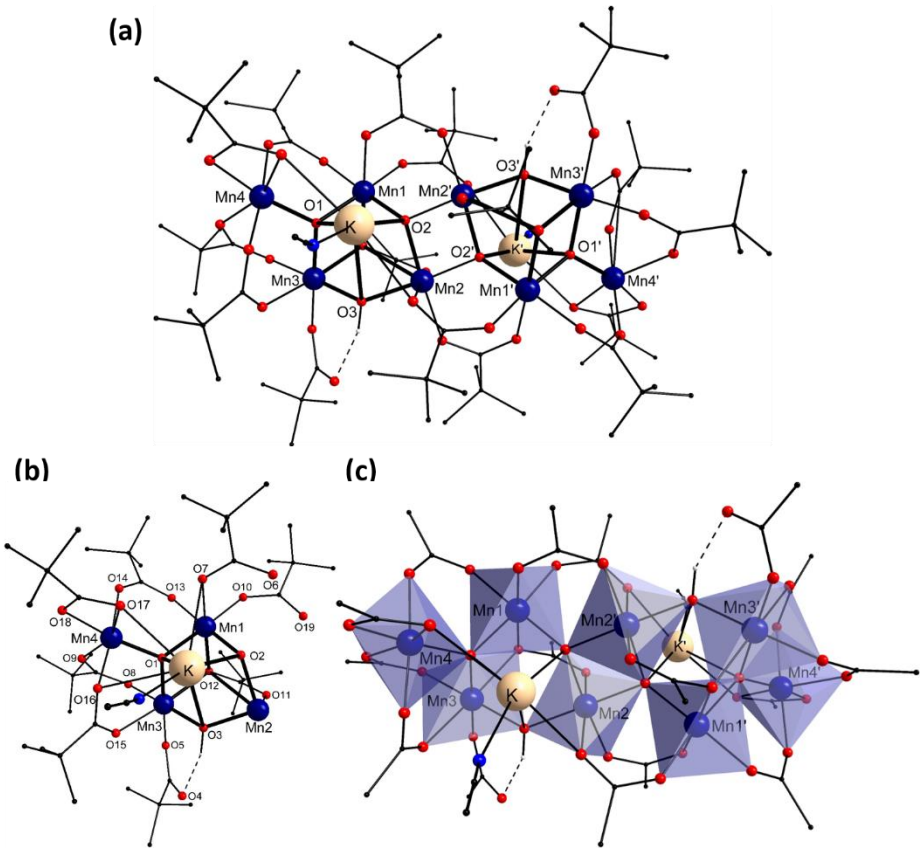

Figure 6.6: Crystal structure (**a**), the asymmetric unit (**b**) and the polyhedral representation **(c)** of the octanuclear compound **6.2**. Colour scheme: Mn^{III} (dark blue), K (tan), C (black), N(blue) and O (red). All hydrogen atoms (grey) except those attached to oxygen centres have been removed for clarity.

Each {Mn_4K} cubane unit consists of three Mn(III) ions, Mn1, Mn2 and Mn3, and a K^+ ion which is stabilised by two μ_3-O^{2-} ligands, O1 and O2, and a μ_2-OH^- O-donor, O3. The latter is further engaged

in a H-bond involving a monodentate pivalate ligand that binds to Mn3 (O-O donor–acceptor distance 2.6 Å). The {Mn_4K} unit is additionally stabilised by nine pivalate ligands out of which seven bind in 2.11 mode while one binds in a 3.21 mode and another binds in 1.10 mode.[605]

The coordination environment of Mn1 is fulfilled by two μ_3-O^{2-} groups (O1 and O2) and the O-donors from four pivalate groups (**Figure 6.7 (a)**). The Jahn-Teller axis of Mn1 is directed along the O-donors (O7 and O12) of the pivalate groups lying perpendicular to the plane containing the μ_3-O^{2-} groups. The Mn-O distances are ~2.2 Å along the Jahn-Teller axis and vary between 1.89 and 1.95 Å perpendicular to it. The octahedra of Mn1 shares a point with that of Mn2 and Mn4 at O2 and O1 respectively, and a face with that of Mn3 at O1 and O12 (**Figure 6.6 (c)**). Mn2 is coordinated to two μ_3-O^{2-} groups (O2 and its symmetry equivalent) and the O-donors of the μ_2-OH^- (O3) and three pivalate groups. The Jahn-Teller axis again lies along the pivalate groups that lie in the plane perpendicular to that containing the μ_3-O^{2-} and the μ_2-OH^- groups (**Figure 6.7 (b)**). The Mn-O bond has been found to be ~2.3 Å along the Jahn-Teller axis and ~1.9 Å perpendicular to it. The octahedra of Mn2 shares a face with that of its symmetry equivalent at O2 and its symmetry equivalent, and shares a point with the octahedra of Mn1 and Mn3 at O2 and O3 respectively. The octahedra of both Mn1 and Mn2 are slightly distorted as can be seen from continuous shape measures, angle variance and distortion indices (**Table 6.7**) and this is due to the geometrical restrictions imposed due to ligand restraints which is apparent from the bond lengths (**Table 6.5**) and bond angles (**Table 6.8**).

The O-donors of a μ_2-OH^- (O3) and four pivalate groups in addition to a μ_3-O^{2-} group (O1) fulfil the coordination environment of Mn3 (**Figure 6.7 (c)**). Out of the four pivalate groups, the one containing O5 is monodentate and is stabilised by hydrogen bonding from the μ_2-OH^- group. The Jahn-Teller axis however, is not directed along this pivalate group as may have been expected. Similar to Mn1 and Mn2, the Jahn-Teller axis lies along the pivalate groups lying perpendicular to the plane containing the monodentate pivalate group and μ_2-OH^- group. The Mn-O distances are ~2.2 Å along the Jahn-Teller axis and ~1.9 Å perpendicular to it. The coordination environment of Mn4 is fulfilled by a μ_3-O^{2-} group (O1) and the O-donors of four pivalate ligands one of which acts as a chelating group (**Figure 6.7 (d)**). The Jahn-Teller axis of Mn4 is directed along one of the O-donors of the chelating pivalate group (O17) and the pivalate ligand (O9) lying perpendicular to it with the Mn-O distances being 2.360 (2) and 2.115(2) Å respectively. The Mn-O distances in the equatorial plane range between 1.86 and 1.96 Å. The octahedron of Mn4 is the most distorted in this complex as can be seen from the continuous shape measures, angle variance and distortion indices (**Table 6.7**) and this is due to the chelating pivalate group.

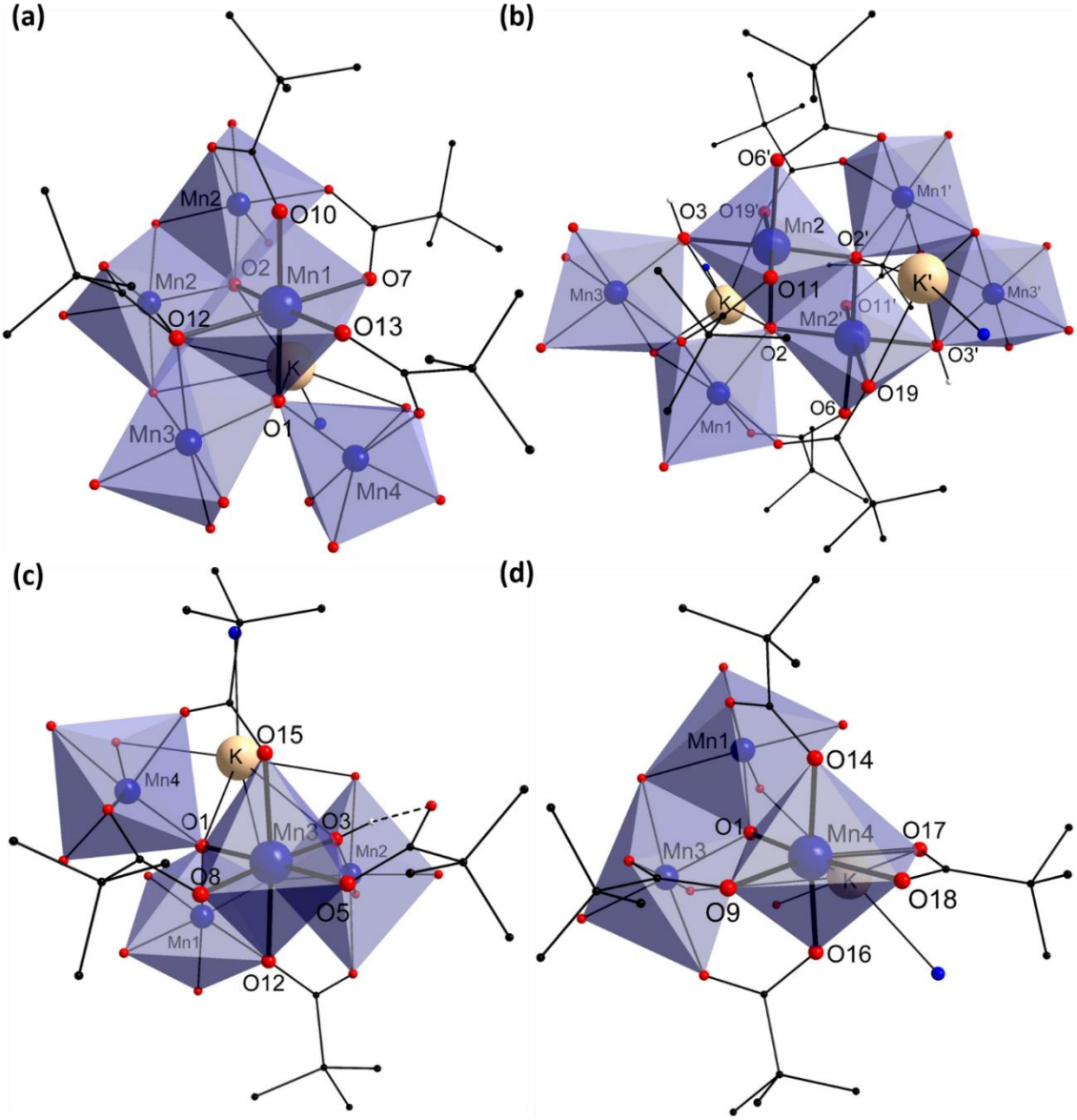

Figure 6.7: Coordination environment of Mn1 **(a)** and Mn2 **(b)**, Mn3 **(c)** and Mn4 **(d)** in compound **6.2**. Colour scheme: Mn^{III} (dark blue), K (tan), C (black), N(blue) and O (red). All hydrogen atoms (grey) except those attached to oxygen centres have been removed for clarity.

The two μ_3-O^{2-} groups, the N-donor of a CH_3CN molecule and the O-donors of four pivalate groups are bound to the K^+ ion allowing it to be well incorporated into the distorted cubane unit. The integration of a hetero-metal into a distorted cubane unit has been rarely reported for Mn coordination complexes[131-133, 135-137] even though it is highly sought after because of the presence of such a unit in the OEC – the natural water oxidation complex in photosystem-II.[27, 55-58] This complex can thus be considered as a structural mimic of the OEC.

Table 6.5: Key Mn-O, K-O, K-N and Mn-Mn bond lengths and bond valence sum for each Mn centre for compound **6.2**.

Mn centre	Coordinating atom	Bond Distance (Å)	BVS	Assigned oxidation state
Mn1	O1	1.894(2)	3.217	+III
	O2	1.9113(19)		
	O10	1.942(2)		
	O13	1.951(2)		
	O7	2.150(2)		
	O12	2.206(2)		
Mn2	O2’	1.8787(19)	3.171	+III
	O2	1.9003(19)		
	O3	1.922(2)		
	O6’	1.949(2)		
	O11	2.253(2)		
	O19	2.270(2)		
Mn3	O3	1.895(2)	3.190	+III
	O5	1.931(2)		
	O1	1.935(2)		
	O8	1.943(2)		
	O15	2.146(2)		
	O12	2.230(2)		
Mn4	O1	1.863(2)	3.148	+III
	O14	1.938(2)		
	O16	1.941(2)		
	O18	1.962(2)		
	O9	2.115(2)		
	O17	2.360(2)		
K1	O19	2.663(2)		
	O17	2.718(2)		
	O2	2.820(2)		
	N1	2.860(3)		
	O11’	2.998(2)		
	O1	2.999(2)		
	O16	3.102(2)		

Metals	Distance (Å)	Metals	Distance (Å)
K1-Mn1	3.7050(8)	Mn1-Mn4	3.3300(6)
K1-Mn2	3.6197(9)	Mn2-Mn2’	2.8509(6)
K1-Mn3	4.2087(9)	Mn2-Mn3	3.4807(7)
K1-Mn4	3.4628(9)	Mn2-Mn4	5.3419(7)
Mn1-Mn2	3.3950(7)	Mn3-Mn4	3.2828(7)
Mn1-Mn3	3.1022(6)		

’1-X,1-Y,1-Z

As all Mn centres in compound **6.2** are in +III oxidation state (**Table 6.5**), it can formally be compared to the S_{-1} state of the OEC. A thorough comparison of the crystal structure of the OEC which is in the S_1 state (with two Mn(IV) and two Mn(III)), and compound **6.2** reveals other similarities besides the presence of a distorted cubane unit containing a hetero-metal atom. Mn4, structurally relates to the dangling Mn centre of the OEC. The bond distances in the core structure of both complexes

also show noteworthy similarities (**Figure 6.8**). The minor differences arise due to ligand restraints and the reduced nature of the Mn(III) centres and their characteristic bonding features. The K-O bond distances are, on average, approximately 0.3 Å longer in comparison to the Ca-O bond distances in OEC. Most significant differences to the OEC structure are associated with the Mn3-K/Ca distance and the atom position and connectivity of the dangling Mn4 centre which, in the OEC, is additionally bound to Mn1 *via* an oxo-ligand.

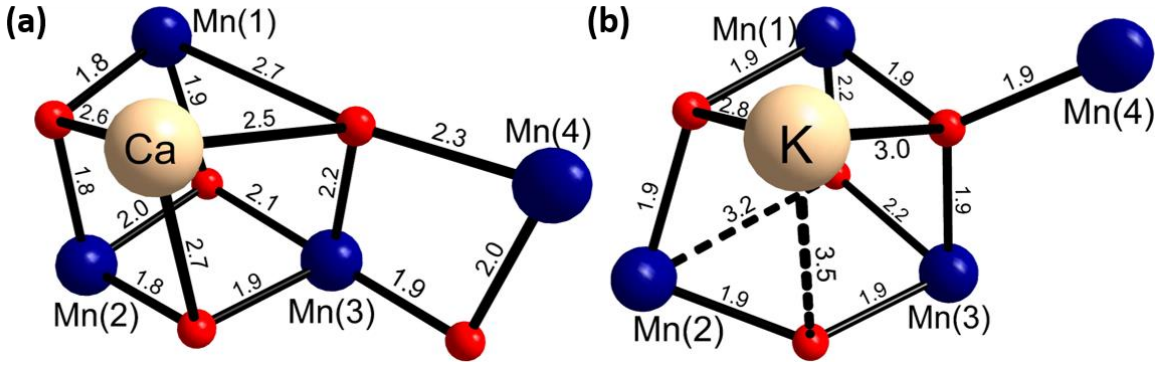

Figure 6.8: Comparison of the core of the cubane-type complex in OEC and compound **6.2**. Colour scheme: Mn^{III} (dark blue), K/Ca (tan) and O (red).

Table 6.6: BVS analysis for O atoms and their assigned protonation state in compound **6.2**.

Atom	BVS	Assignment
O1	2.135	μ_3-O^{2-}
O2	2.130	μ_3-O^{2-}
O3	1.340	μ_2-OH^-

Table 6.7: Continuous shape measure values, angle variance and distortion indices (using the ideal octahedral geometry as a reference) for each Mn centre for compound **6.2**.

Mn centre	Continuous shape measure value	Angle variance (σ^2)	Distortion Index
Mn1	0.755	28.31	0.0415
Mn2	1.144	23.60	0.0427
Mn3	0.881	20.59	0.0367
Mn4	2.491	122.79	0.0808

The system packs with a disordered $CHCl_3$ molecule which resides in voids that are 2.80 Å in radius as calculated by the 'calcvoid' routine implemented in the OLEX2 code.[616] These voids lie along the crystallographic c-axis (**Figure 6.9**). The packing is possibly stabilised by weak dispersion forces.

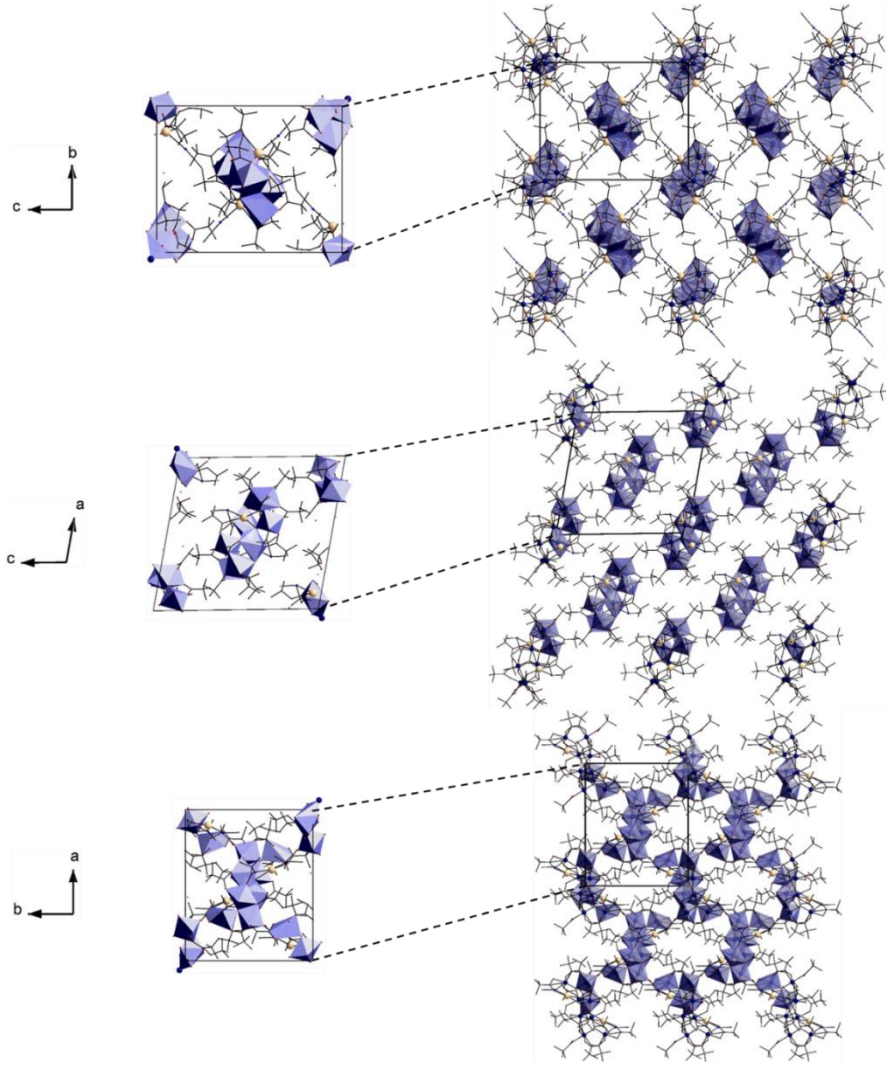

Figure 6.9: Packing diagram for compound **6.2**. The disordered $CHCl_3$ molecules have been removed for clarity. Colour scheme: Mn^{III} (dark blue), K (tan), C (black), N(blue) and O (red). All hydrogen atoms have been removed for clarity.

Table 6.8: Selected bond angles for compound **6.2**.

Bond	Bond Angle (°)	Bond	Bond Angle (°)
O10-Mn1-O13	81.55(9)	O1-Mn3-O12	80.34(8)
O1-Mn1-O12	81.84(8)	O5-Mn3-O8	85.61(9)
O2-Mn1-O7	85.58(8)	O3-Mn3-O12	86.28(8)
O10-Mn1-O7	89.36(9)	O5-Mn3-O15	88.92(9)
O1-Mn1-O2	89.59(8)	O8-Mn3-O15	89.21(9)
O13-Mn1-O7	90.22(9)	O3-Mn3-O1	90.41(9)
O1-Mn1-O13	90.30(9)	O3-Mn3-O5	90.64(9)
O10-Mn1-O12	91.37(8)	O8-Mn3-O12	92.34(8)
O2-Mn1-O12	91.94(8)	O1-Mn3-O15	92.51(8)
O13-Mn1-O12	92.26(8)	O3-Mn3-O15	92.66(9)
O1-Mn1-O7	97.77(9)	O1-Mn3-O8	93.29(9)
O2-Mn1-O10	99.06(8)	O5-Mn3-O12	98.25(8)
O1-Mn1-O10	169.21(9)	O15-Mn3-O12	172.76(8)

Bond	Bond Angle (°)	Bond	Bond Angle (°)
O2-Mn1-O13	175.74(9)	O3-Mn3-O8	175.77(9)
O7-Mn1-O12	177.49(8)	O5-Mn3-O1	178.19(9)
O3-Mn2-O19	80.91(8)	O18-Mn4-O17	60.17(9)
O2'-Mn2-O2	82.06(9)	O16-Mn4-O17	82.43(9)
O6'-Mn2-O11	85.34(8)	O14-Mn4-O18	86.68(10)
O6'-Mn2-O19	89.26(8)	O16-Mn4-O18	86.74(10)
O3-Mn2-O6'	89.85(9)	O14-Mn4-O9	89.02(9)
O2-Mn2-O11	91.35(8)	O1-Mn4-O16	91.68(9)
O21-Mn2-O19	91.86(8)	O16-Mn4-O9	92.16(9)
O2-Mn2-O3	93.19(8)	O14-Mn4-O17	93.96(9)
O21-Mn2-O11	93.78(8)	O1-Mn4-O14	94.59(9)
O3-Mn2-O11	93.89(8)	O18-Mn4-O9	97.07(10)
O2-Mn2-O19	94.28(8)	O1-Mn4-O9	97.60(9)
O21-Mn2-O6'	95.33(8)	O1-Mn4-O17	105.13(9)
O21-Mn2-O3	171.07(9)	O9-Mn4-O17	156.74(9)
O11-Mn2-O19	172.52(8)	O1-Mn4-O18	165.30(10)
O2-Mn2-O6'	175.65(9)	O14-Mn4-O16	173.41(9)

6.2.2 Physicochemical characterisation

Additional structural characterisation has been conducted using a variety of physicochemical techniques to verify the structural model. The phase purity of the bulk material has been confirmed using powder X-ray diffraction (PXRD) (**Figure 6.10 (a)**). TGA analysis was conducted in a N_2 atmosphere on a freshly dried sample (**Figure 6.10 (b)**). The initial thermogravimetric steps up to ~150 ˚C can be attributed to the loss of constitutional and coordinating solvent molecules (weight loss calcd: 8.2 %, found: 9.2 %). The next step up to ~190 ˚C results from decomposition of the two monodentate pivalate groups (weight loss calcd: 8.3 %, found: 9.5 %) followed by the loss of 14 pivalate ligands resulting in the formation of Mn oxide materials.

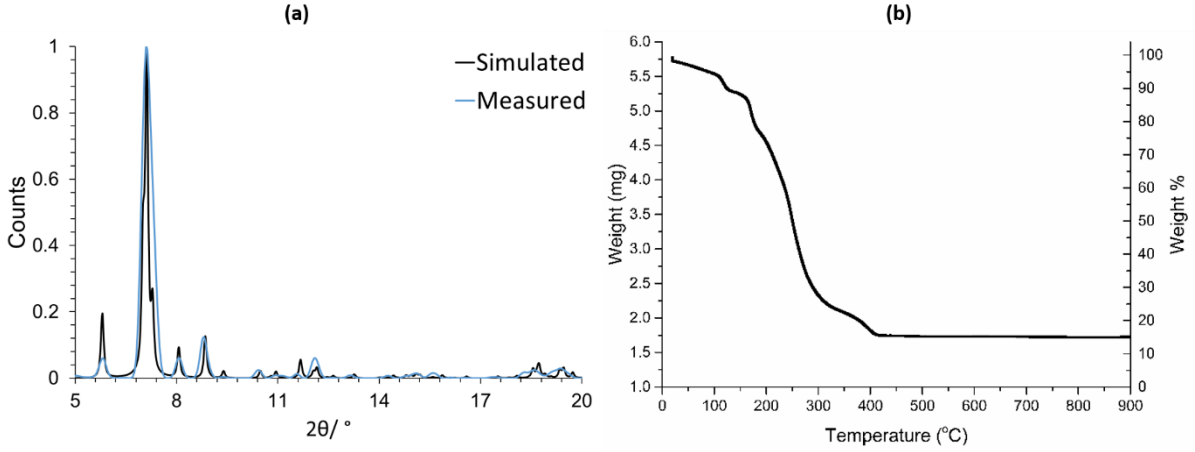

Figure 6.10: PXRD pattern **(a)** and TGA analysis **(b)** of compound **6.2**.

The IR spectrum of compound **6.2** is in agreement with the structural model obtained from single crystal XRD (**Figure 6.11**). The broad feature at 2960 cm^{-1} can be attributed to the C-H vibrations in the organic ligands.[617] The sharp feature at 1406 cm^{-1} corresponds to the symmetric stretching mode of the carboxylate groups. The vibrations due to the asymmetric stretching mode of the

carboxylate group overlaps with additional vibrations in the 1500-1600 cm^{-1} range due to the pivalate groups.[617] The bending C-H mode of $CHCl_3$ appears at 1224 cm^{-1}.[624]

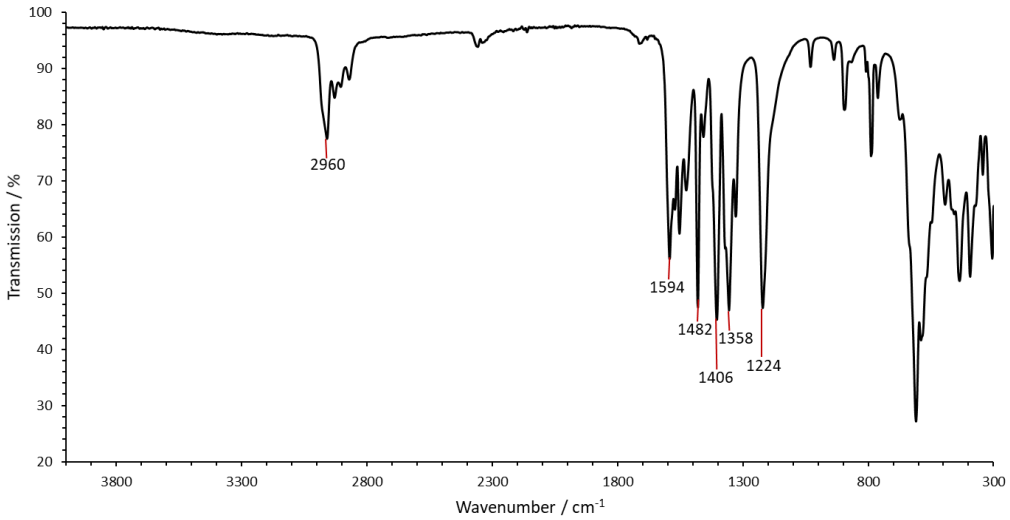

Figure 6.11: IR of compound **6.2**.

6.2.3 Magnetic properties

The temperature dependence of magnetic susceptibility was determined in the temperature range of 4-300 K (**Figure 6.12**). The room temperature value of χT was found to be 19.5 cm^3 K mol^{-1} which is lower than the expected value of 24 cm^3 K mol^{-1} for a complex with 8 Mn(III) (S = 2) centres ($C = \chi T = \frac{N\mu_B^2}{3k_B} g^2 S(S+1)$, where $\frac{N\mu_B^2}{3k_B} = 0.12505$ cm^3 K mol^{-1}, $g = 2$ is the Lande's g-factor and S is the spin). This indicates that the coupling between Mn centres is dominantly antiferromagnetic in this complex. This is further confirmed by the behaviour observed upon lowering the temperature when the χT value decreases and reaches a value of 2 cm^3 K mol^{-1} at 4 K. The presence of ferromagnetic coupling however, still cannot be completely ruled out. This behaviour also indicates that the ground state in this case will be an S = 0 state.

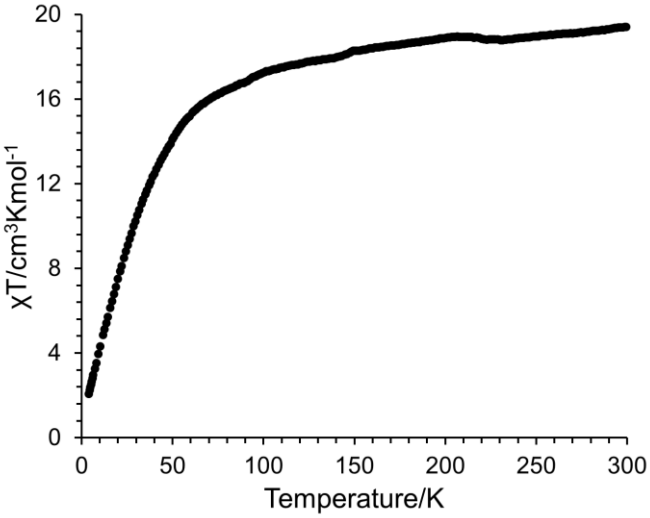

Figure 6.12: Temperature dependence of magnetic susceptibility (χT) of compound **6.2**.

6.2.4 DFT calculations

To better understand the electronic structure and quantify the strength of exchange coupling betweem the Mn centres, DFT calculations were performed. The full complex was modelled with the *tert*-butyl groups replaced with methyl groups for computational ease (**Figure 6.13**). The hybrid PBE0[433, 451] functional has been used in conjunction with the SDDALL[507] basis set having an effective core potential for the Mn and K atoms (replacing the 10 core electrons – $1s^2 2s^2 2p^6$ – of Mn and K with fully relativistic pseudopotentials), the 6-31G(d)[508] basis set for O, C and N, and 6-31G(p)[508] basis set for H. For this complex, an even tighter SCF convergence criteria ($\Delta_{energy} < 10^{-11}$ Hartrees) was employed to ensure proper convergence. The model represents the experimental structure well and the metal distances were found to be well reproduced (**Table 6.9**).

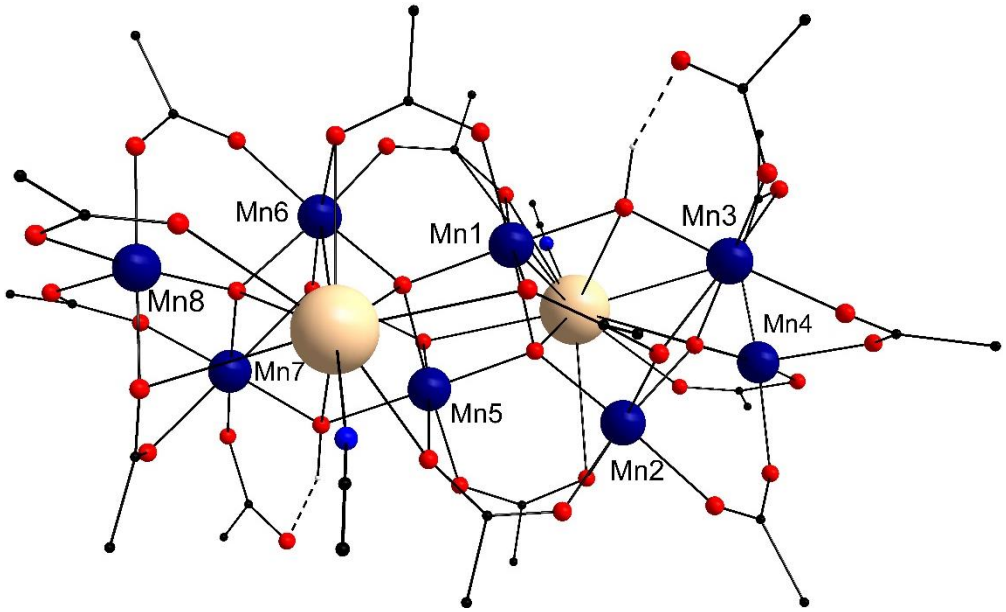

Figure 6.13: Computational model for compound **6.2**. Colour scheme: Mn^{III} (dark blue), K (tan), C (black), N(blue) and O (red). All hydrogen atoms (grey) except those attached to oxygen centres have been removed for clarity.

The methodology adopted for the calculation of the coupling constants is the one adopted in the previous chapters. 11 states were modelled for this complex and the energy of the states modelled and the spin on the Mn centres in each state are provided in **Table 6.10**. Seven coupling constants have been used to describe the coupling between the Mn centres and these take into account the coupling of Mn centres adjacent to each other (**Figure 6.14**).

The Hamiltonian for this complex can thus be given as:

$$H = -2J_1\langle s_1.s_5\rangle - 2J_2[\langle s_1.s_2\rangle + \langle s_5.s_6\rangle] - 2J_3[\langle s_1.s_3\rangle + \langle s_5.s_7\rangle] - 2J_4[\langle s_1.s_6\rangle + \langle s_2.s_5\rangle] - 2J_5[\langle s_2.s_3\rangle + \langle s_6.s_7\rangle] - 2J_6[\langle s_2.s_4\rangle + \langle s_6.s_8\rangle] - 2J_7[\langle s_3.s_4\rangle + \langle s_7.s_8\rangle]$$

Table 6.9: Comparison of some of the Mn-Mn distances in the crystal structure and the DFT model for compound **6.2**.

	Distance (Å)	
Mn centres	**XRD**	**DFT**
Mn1-Mn2	3.40	3.41
Mn1-Mn3	3.48	3.48
Mn1-Mn4	5.34	5.28
Mn1-Mn5	2.85	2.88
Mn2-Mn3	3.10	3.13
Mn2-Mn4	3.33	3.37
Mn3-Mn4	3.28	3.26
K-Mn1	3.62	3.68
K-Mn2	3.71	3.67
K-Mn3	4.21	4.44
K-Mn4	3.46	3.49

The coupling between Mn1 and Mn3, and Mn5 and Mn7 (J_3) is facilitated by μ_2-OH^- and pivalate groups while the coupling between all other Mn pairs is through μ_3-O^{2-} and pivalate groups. In line with the experimental results, the dominant coupling has been found to be antiferromagnetic and is between Mn1 and Mn2. It is apparent from **Table 6.11** that the coupling within the cubane units is dominantly ferromagnetic (J_5). The coupling constants obtained were used to determine the relative energies of the different states that were modelled using DFT and these were found to be well reproduced (< 3% error).

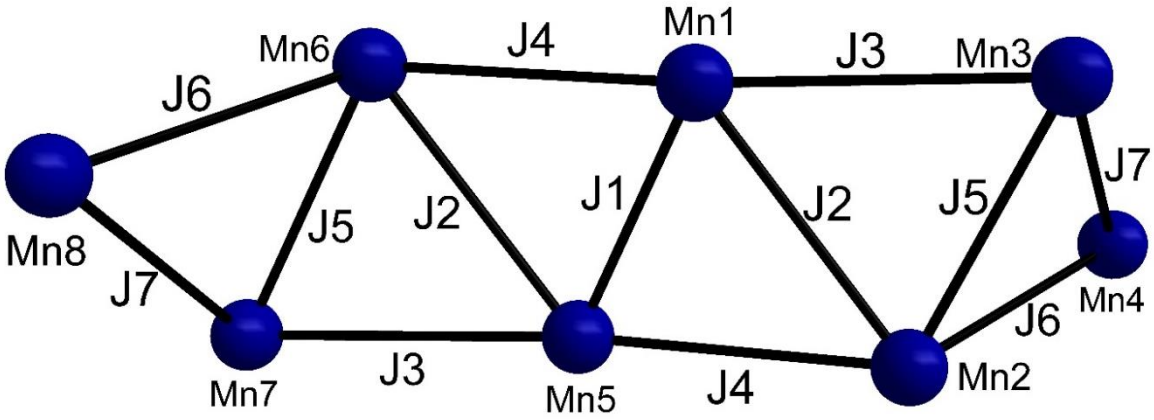

Figure 6.14: The coupling constants representing the coupling between Mn centres.

The dimension of the Hamiltonian matrix was too large ($5^8 \times 5^8$) for exact diagonalisation so the temperature dependence of magnetic susceptibility could not be determined from the coupling constants. To estimate the ground state however, the coupling constants were used in conjunction with the average spin densities and the above mentioned Hamiltonian to determine the energy of all 2^7 (=128) possible spin states. The S = 0 state was indeed found to be the ground state in agreement with the experimental observations. In this state the spin on Mn1, Mn2, Mn3 and Mn4 is opposite to that on the other Mn centres. The ferromagnetic state was calculated to be ~657 cm^{-1} higher in energy compared to the ground state (**Table 6.12**).

Table 6.10: Bader spin densities on each Mn centre (truncated to three decimal places) and the relative energies for each modelled state for compound **6.2**.

Mn1	Mn2	Mn3	Mn4	Mn5	Mn6	Mn7	Mn8	Relative Energy (cm^{-1})
3.818	3.852	-3.810	3.843	3.830	3.862	3.858	3.857	163.25
3.811	-3.794	3.849	3.835	3.818	3.862	3.858	3.858	136.47
3.830	3.862	3.858	3.858	3.830	3.862	3.858	3.858	0.00
-3.811	-3.812	3.833	3.836	3.793	-3.811	3.849	3.835	-75.79
-3.823	-3.822	-3.835	3.823	3.793	-3.811	3.849	3.835	-287.54
-3.800	-3.812	3.833	3.836	3.812	3.822	3.835	-3.822	-370.53
-3.792	3.832	-3.827	3.843	3.823	3.845	3.858	3.857	-395.62
-3.780	3.820	3.819	-3.823	3.823	3.845	3.858	3.858	-460.95
-3.811	-3.822	-3.835	3.822	3.800	3.834	-3.810	3.844	-463.21
-3.800	-3.834	3.810	-3.844	3.812	3.845	3.858	3.858	-503.95
-3.811	-3.821	-3.836	3.822	3.811	3.821	3.836	-3.822	-584.81

Table 6.11: Magnitude of J-values (cm^{-1}) and the Mn-Mn interactions that constitute each J-value for compound **6.2**.

J-value	Interacting Mn centers	Magnitude (cm^{-1})
J_1	Mn1-Mn5	-31.40 ± 0.76
J_2	Mn1-Mn2 Mn5-Mn6	1.74 ± 0.48
J_3	Mn1-Mn3 Mn5-Mn7	2.24 ± 0.48
J_4	Mn1-Mn6 Mn2-Mn5	-6.89 ± 0.43
J_5	Mn2-Mn3 Mn6-Mn7	10.24 ± 0.32
J_6	Mn2-Mn4 Mn6-Mn8	4.10 ± 0.40
J_7	Mn3-Mn4 Mn7-Mn8	-1.73 ± 0.50

Table 6.12: The relative energies (cm^{-1}) of all the unique spin states for compound **6.2**.

Configuration	Energy	Configuration	Energy	Configuration	Energy
↑↑↑↑↓↓↓↓	0	↑↓↑↓↓↑↑↑	410	↑↓↑↓↑↑↑↓	742
↑↑↑↓↓↓↓↓	35	↑↓↓↓↓↑↓↑	411	↑↑↑↓↑↓↑↓	742
↑↑↑↑↓↓↓↑	35	↑↑↓↓↓↑↑↓	437	↑↓↑↑↑↓↓↓	750
↑↑↑↓↓↓↓↑	70	↑↓↓↑↓↓↑↑	438	↑↓↓↓↑↓↑↑	751
↑↑↓↑↓↓↓↓	158	↑↓↑↓↓↑↑↓	445	↑↓↑↓↑↓↑↓	757
↑↑↑↑↓↓↑↓	159	↑↓↓↑↓↑↓↑	445	↑↑↓↑↑↓↓↓	773
↑↓↓↓↓↓↓↓	159	↑↑↓↓↓↓↑↑	488	↑↓↓↓↑↑↓↑	774
↑↑↑↑↓↑↑↑	159	↑↓↑↑↓↓↑↓	495	↑↓↑↑↑↓↓↑	785
↑↑↓↑↓↓↓↑	192	↑↑↓↓↓↑↓↑	495	↑↓↓↑↑↓↑↑	786
↑↑↑↓↓↓↑↓	193	↑↓↑↑↓↑↑↑	495	↑↓↑↑↑↑↑↑	792
↑↓↓↑↓↓↓↓	193	↑↓↑↓↓↓↑↑	495	↑↑↑↑↑↓↑↑	794
↑↓↓↓↓↓↓↑	194	↑↑↓↑↓↑↓↓	496	↑↑↓↑↑↓↓↑	807
↑↑↑↓↓↑↑↑	194	↑↓↓↓↓↑↓↓	497	↑↓↓↑↑↑↓↑	808
↑↑↑↑↓↑↑↓	194	↑↓↑↓↓↑↓↑	503	↑↑↓↑↑↑↑↑	815
↑↓↓↑↓↓↓↑	228	↑↓↑↑↓↑↑↓	530	↑↑↑↑↑↑↓↑	816
↑↑↑↓↓↑↑↓	229	↑↓↓↑↓↑↓↓	531	↑↓↑↑↑↑↑↓	827
↑↑↓↓↓↓↓↓	243	↑↓↓↓↑↓↓↓	573	↑↑↑↓↑↓↑↑	828
↑↑↑↑↓↓↑↑	245	↑↓↑↑↓↓↑↑	581	↑↓↑↑↑↓↑↓	843
↑↓↑↓↓↓↓↓	251	↑↑↓↓↓↑↓↓	581	↑↓↑↓↑↓↑↑	843
↑↑↑↑↓↑↓↑	252	↑↓↑↑↓↑↓↑	588	↑↑↓↑↑↑↑↓	850
↑↑↓↓↓↓↓↑	278	↑↓↑↓↓↑↓↓	589	↑↑↑↓↑↑↓↑	851
↑↑↑↓↓↓↑↑	279	↑↓↓↑↑↓↓↓	607	↑↑↓↓↑↓↓↓	858
↑↓↑↓↓↓↓↑	286	↑↓↓↓↑↓↓↑	608	↑↓↓↓↑↑↓↓	860
↑↑↑↓↓↑↓↑	287	↑↓↓↓↑↑↑↑	615	↑↑↓↑↑↓↑↓	865
↑↑↓↑↓↓↑↓	316	↑↑↑↑↑↓↓↓	615	↑↓↑↓↑↑↓↑	866
↑↑↓↑↓↑↑↑	317	↑↓↓↑↑↓↓↑	642	↑↑↓↓↑↓↓↑	893
↑↓↓↓↓↓↑↓	318	↑↓↓↑↑↑↑↑	650	↑↓↓↑↑↑↓↓	894
↑↓↓↓↓↑↑↑	318	↑↑↑↓↑↓↓↓	650	↑↑↓↓↑↑↑↑	900
↑↓↑↑↓↓↓↓	336	↑↓↓↓↑↑↑↓	650	↑↑↑↑↑↑↓↓	902
↑↑↑↑↓↑↓↓	338	↑↑↑↑↑↓↓↑	650	↑↓↑↑↑↓↑↑	929
↑↑↓↑↓↑↑↓	352	↑↑↑↑↑↑↑↑	657	↑↑↓↓↑↑↑↓	935
↑↓↓↑↓↓↑↓	352	↑↓↑↓↑↓↓↓	665	↑↑↑↓↑↑↓↓	937
↑↓↓↑↓↑↑↑	353	↑↓↓↓↑↓↑↓	665	↑↑↓↓↑↓↑↓	951
↑↓↓↓↓↑↑↓	353	↑↓↑↑↓↑↓↓	674	↑↓↑↑↑↑↓↑	951
↑↓↑↑↓↓↓↑	371	↑↓↓↑↑↑↑↓	684	↑↑↓↑↑↓↑↑	951
↑↑↑↓↓↑↓↓	373	↑↑↑↓↑↓↓↑	685	↑↓↑↓↑↑↓↓	952
↑↓↓↑↓↑↑↓	388	↑↑↑↓↑↑↑↑	692	↑↑↓↑↑↑↓↑	974
↑↑↓↓↓↓↑↓	402	↑↑↑↑↑↑↑↓	692	↑↑↓↓↑↓↑↑	1037
↑↑↓↓↓↑↑↑	402	↑↓↑↓↑↓↓↑	699	↑↓↑↑↑↑↓↓	1037
↑↑↓↑↓↓↑↑	402	↑↓↓↑↑↓↑↓	700	↑↑↓↓↑↑↓↑	1059
↑↓↓↓↓↓↑↑	403	↑↓↑↓↑↑↑↑	707	↑↑↓↑↑↑↓↓	1060
↑↓↑↓↓↓↑↓	409	↑↑↑↑↑↓↑↓	708	↑↑↓↓↑↑↓↓	1145
↑↑↓↑↓↑↓↑	410	↑↑↑↓↑↑↑↓	727		

6.2.5 Hydrolytic and electrochemical studies

The hydrolytic stability of compound **6.2** was investigated prior to investigation of its electrochemical behaviour. For this purpose, 20 mg of compound **6.2** was dispersed in 50 ml Millipore water and sonicated for 30 minutes. Compound **6.2** was observed to be only partially soluble and the residual material was washed, collected and dried at room temperature (**6.2***). Energy dispersive X-ray (EDX) spectroscopy measurements clearly confirm that the sample transforms upon sonication in aqueous systems giving rise to a black-brown, amorphous solid (**Figure 6.15**) with a Mn:K ratio >20:1, rather than 4:1, as observed for compound **6.2**. Additionally, the Mn:O ratio in **6.2*** was found to be ~1:3 and no residual carbon content was detected. The inherent instability of the molecular structure of compound **6.2** upon sonication in aqueous solution is further supported by changes observed in the infrared (**Figure 6.16 (a)**) and X-ray photoelectron spectroscopy (XPS) data of **6.2*** compared to compound **6.2 (Figure 6.17)**. The IR spectrum shows the absence of peaks due to the carboxylate groups in line with the EDX data. The O1s peak for **6.2*** in the XPS analysis (**Figure 6.16 (b)**) is centred at ~530.0 eV which corresponds to the O1s peaks of hydrated or defective Mn oxides[625] suggesting that compound **6.2** transforms into manganese-derived oxides. The K^+ ions, on the other hand, and oligonuclear Mn pivalate complexes are released into the aqueous solution phase upon sonication as demonstrated by IR (**Figure 6.16 (b)**) and mass spectrometry where signals corresponding to monomeric and dimeric manganese pivalate species (**Figure 6.18**) can be identified. The low solubility of compound **6.2** in water, but moreover its instability when forced to dissolve in water, renders it unsuitable for homogeneous electrochemical studies in aqueous medium. Previously conducted electrocatalytic H_2O oxidation experiments using a polymorph of compound **6.2** thus, only serve to characterise the activity of the hydrolytic decomposition products.[136]

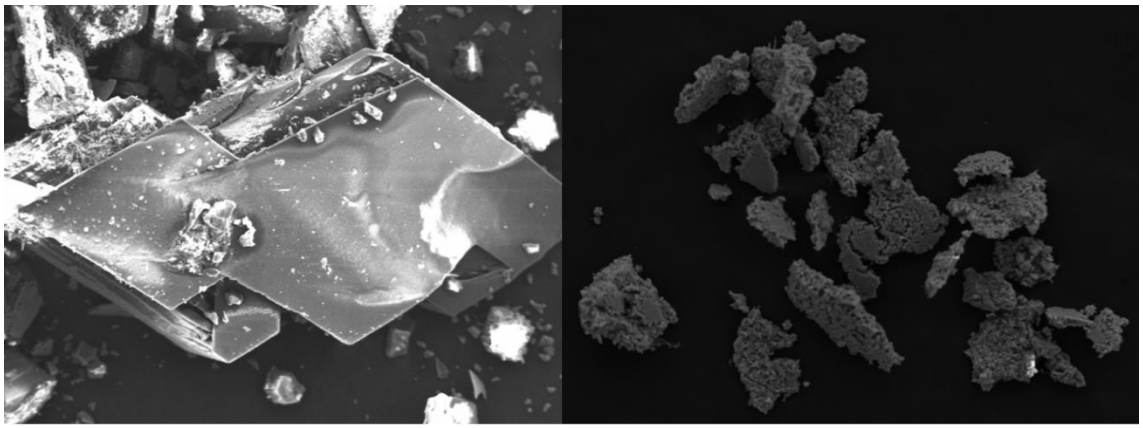

Figure 6.15: SEM images of compound **6.2** and **6.2***. These images highlight the crystalline and amorphous nature of compound **6.2** and **6.2*** respectively.

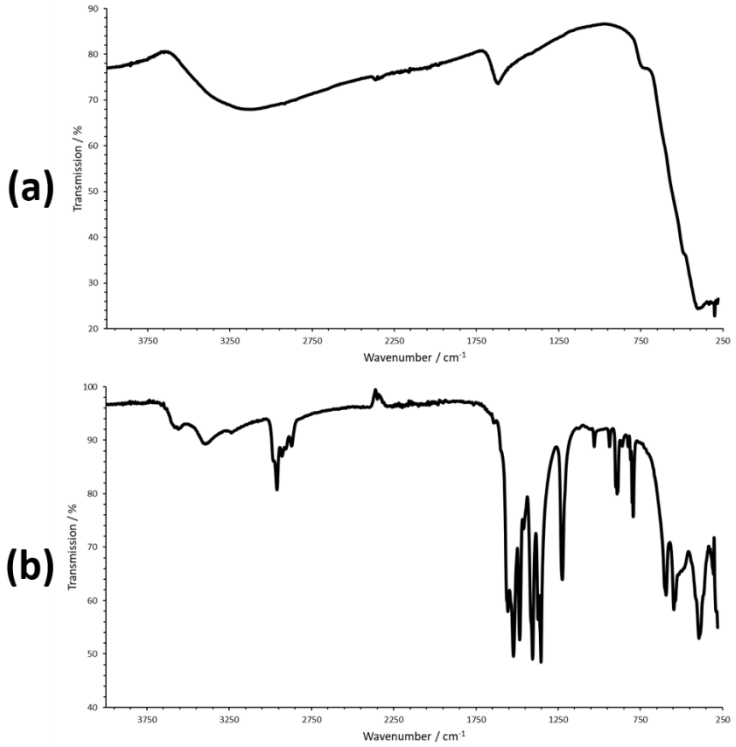

Figure 6.16: IR spectra of **6.2* (a)** and the precipitate obtained by evaporating the filtrate obtained after sonicating compound **6.2** in water.

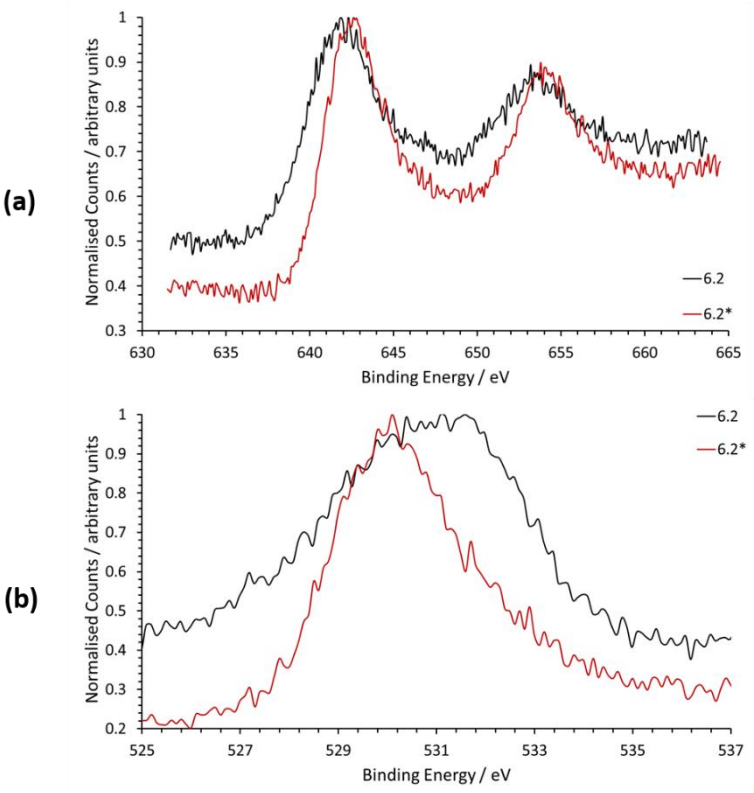

Figure 6.17: Mn 2p **(a)** and O 1s **(b)** binding energies for compound **6.2** and **6.2***.

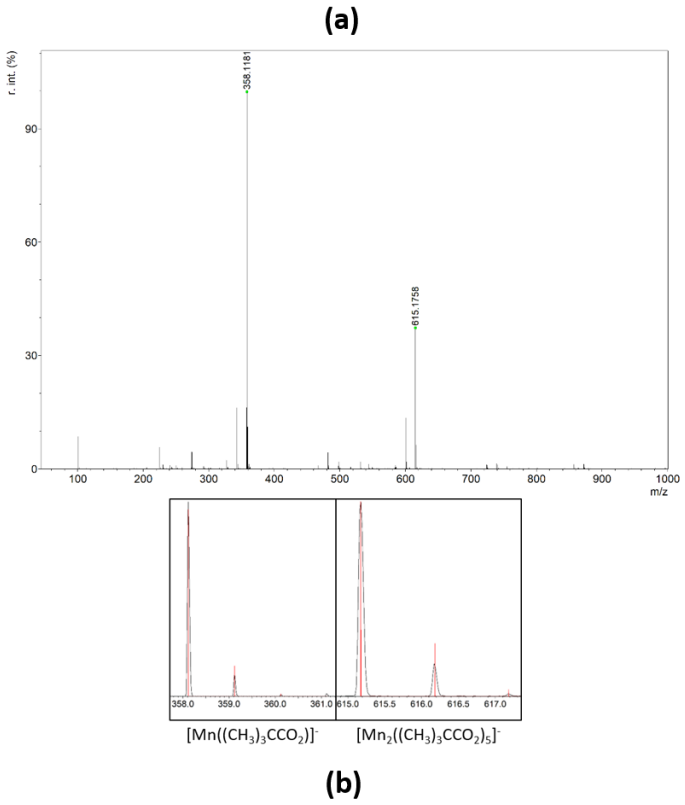

Figure 6.18: ESI-mass spectrum of the filtrate obtained after sonicating compound **6.2** in water **(a)** and the assigned fragmentation pattern **(b)**.

To investigate the electrochemical properties of compound **6.2** in neutral aqueous medium, modified carbon paste electrodes were prepared by dispersing compound **6.2** in carbon paste. Cyclic voltammetry (CV) of compound **6.2** in potassium phosphate buffer at pH 7.2 (KP*i*, 50 mM) using KNO_3 (1 M) as electrolyte, results in a strong catalytic wave due to water oxidation (**Figure 6.19**).

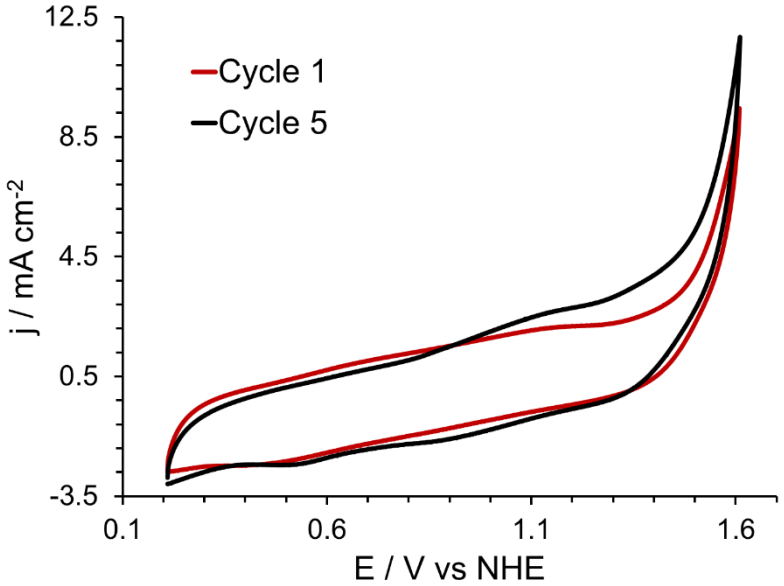

Figure 6.19: Cyclic voltammograms for compound **6.2** (40 wt-% loading) in a KP*i* buffer solution at pH 7.2.

To study the kinetic profile of this water oxidation reaction, linear sweep voltammetry (LSV) was performed using a rotating disk electrode at a low scan rate of 1 mV/s to ensure steady state conditions during the experiment. The catalyst loading of compound **6.2** was varied between 10 and 40 wt-% of the total carbon paste blend. From the electrochemical profile (**Figure 6.20**), it is evident that higher loadings significantly increase the current densities and decrease the onset potential of the water oxidation reaction. Above a catalyst loading of 40 wt-%, the electrodes become brittle and unsuitable for obtaining reproducible data and thus 40 wt-% loadings were employed in further experiments.

With 40 wt-% catalyst loading, an onset overpotential of 420 mV for the water oxidation reaction and a Tafel slope of 255 mV dec^{-1} (**Figure 6.21 (a)** and **(b)** respectively) within an overpotential range of 400-700 mV (**Table 6.13**) was observed. Similar Tafel slopes have previously been observed for other water oxidation catalysts.[626, 627] Within the 700-800 mV range, the slope was found to be slightly higher (280 mV dec^{-1}).

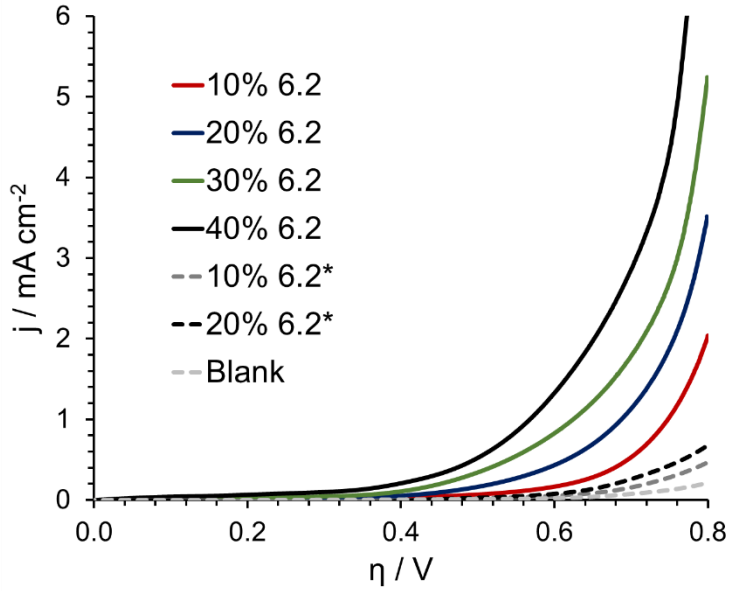

Figure 6.20: Linear sweep voltammograms for compound **6.2** and **6.2*** at different loadings.

Tafel analysis for successive linear sweep scans of compound **6.2** resulted in characteristic slope changes (**Figure 6.22**). Upon cycling, the Tafel slope above 700 mV decreases to ~230 mV dec^{-1} and a new redox peak at ca. ~1.1 V (vs NHE) is observed after 5 linear sweep cycles. The appearance of a new peak and the convolution behaviour suggests that compound **6.2** is catalytically active operating at an onset potential of 420 mV and then undergoes transformation to a new species which is catalytically active above 700 mV.

To substantiate this hypothesis, linear sweep voltammetry experiments were conducted using **6.2*** (**Figure 6.20** and **Figure 6.21**). In this case, however, the loading of **6.2*** in the blend was restricted to 20 wt-% as it became brittle at higher loadings. The electrochemical behaviour of **6.2*** bears close similarity with that observed at the later stages of the successive linear sweep experiments

using compound **6.2** thereby suggesting that compound **6.2** transforms to **6.2*** while facilitating water oxidation. The onset overpotential was found to be 695 mV for 20 wt-% **6.2*** loading in contrast to 532 mV for compound **6.2** at 20 wt-% loading. Thus, the electrochemical data of **6.2*** corresponds to that previously reported for a polymorph of compound **6.2** for which the activity has been attributed to Mn_2O_3.[136]

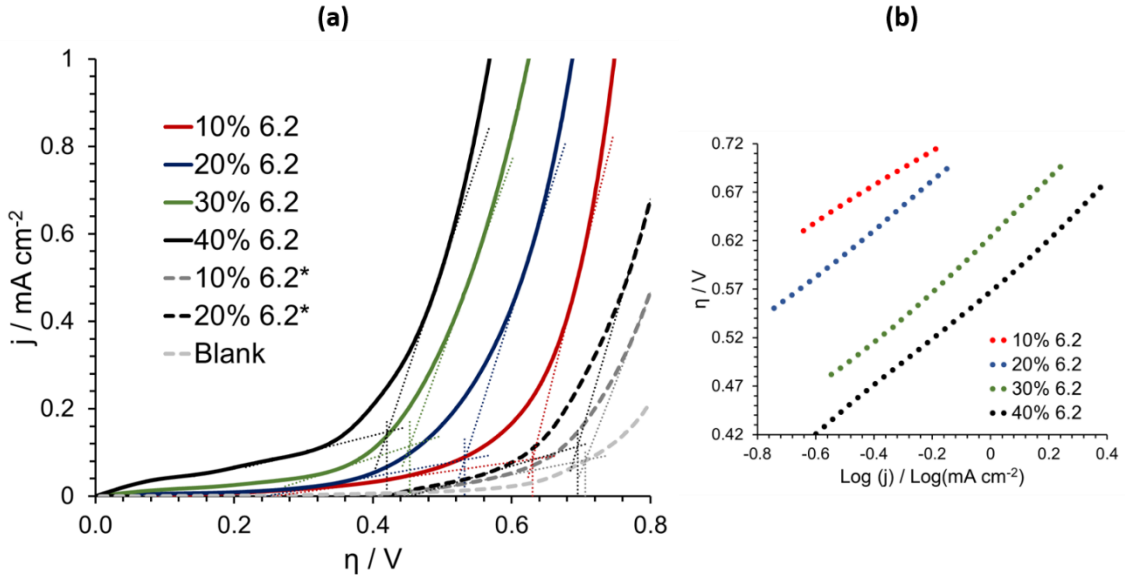

Figure 6.21: The determined onset potentials **(a)** and the Tafel slope **(b)** for compound **6.2** at different loadings.

Table 6.13: The onset overpotential for water oxidation with compound **6.2** and **6.2*** at different loadings and the Tafel slope in the overpotential range of 400-700 mV.

Loading	Onset overpotential (mV)	Tafel slope (mV dec^{-1})
10% 6.2	630	190
20% 6.2	532	245
30% 6.2	453	278
40% 6.2	420	255
10% 6.2*	706	195
20% 6.2*	695	250

To confirm the formation of oxides under these conditions, chronoamperometry (CA) at an applied potential of 1.56 V (vs NHE) was performed for 16 hours with compound **6.2**. The application of potential leads to the transformation of compound **6.2** to a less active species (**Figure 6.23**). Cyclic voltammetry (**Figure 6.24 (a)**) and linear sweep voltammetry experiments (**Figure 6.24 (b)**) were performed on this decomposed species and cyclic voltammetry after CA revealed a new oxidation peak at ~1.02 V (vs NHE). Additionally, XPS analysis of this decomposed species shows that the O1s peak is centred at ~531.5 eV (**Figure 6.25 (b)**). The appearance of this new signal[628] and the XPS analysis confirm that the decomposed material comprises of defective Mn oxides.[625]

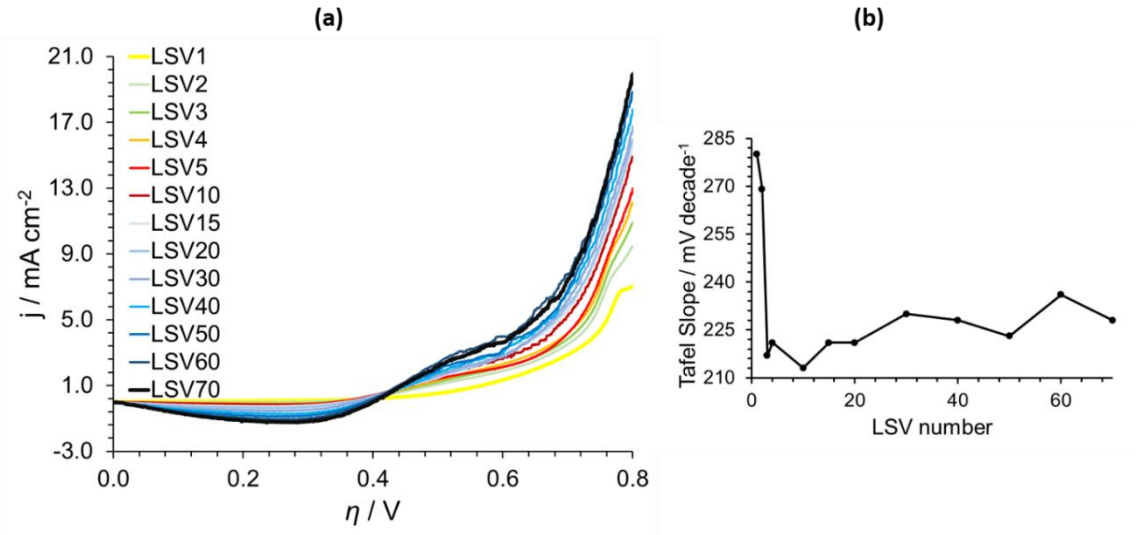

Figure 6.22: Successive linear sweep voltammograms for compound **6.2** in KP*i* buffer solution at pH 7.2 **(a)** and the Tafel slope observed for the different cycles calculated in the 700-800 mV overpotential range **(b)**.

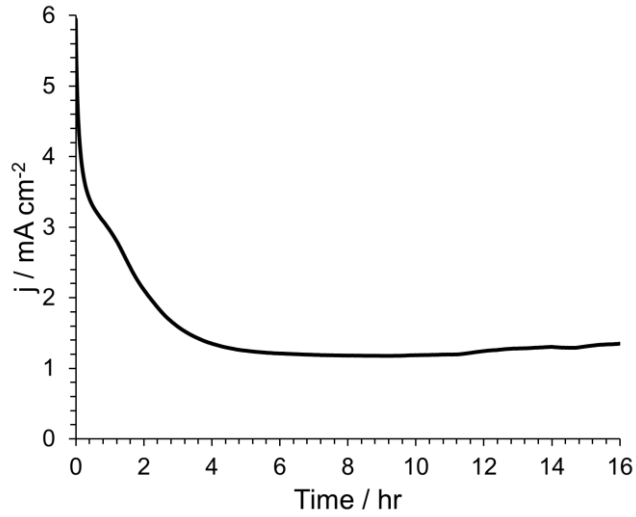

Figure 6.23: CA data for compound **6.2** at 1.56 V *vs* NHE in KP*i* buffer solution at pH 7.2.

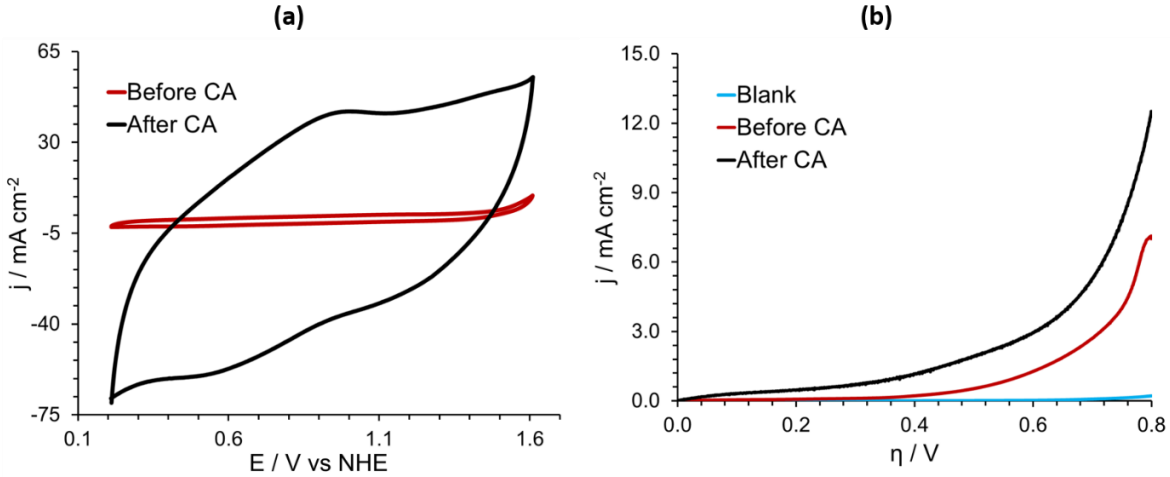

Figure 6.24: Cyclic voltammograms **(a)** and linear sweep voltammograms **(b)** for compound **6.2** in KP*i* buffer solution at pH 7.2 before and after CA.

These results demonstrate that there is an active species prior to the formation of **6.2*** and that the initial activity results from compound **6.2** and not from manganese oxide. Just like the OEC, compound **6.2** decomposes rapidly, but it appears to be highly active for water oxidation in comparison to the corresponding oxide phase. This can be inferred from a comparison of the linear sweep voltammograms of compound **6.2** and **6.2*** at 10 and 20 wt-% loading (**Figure 6.20** and **Figure 6.21**) which show that **Mn_8K_2** is highly active even though the concentration of Mn centres and hence, the number of active sites per unit weight, is much lower for compound **6.2** in comparison to **6.2***.

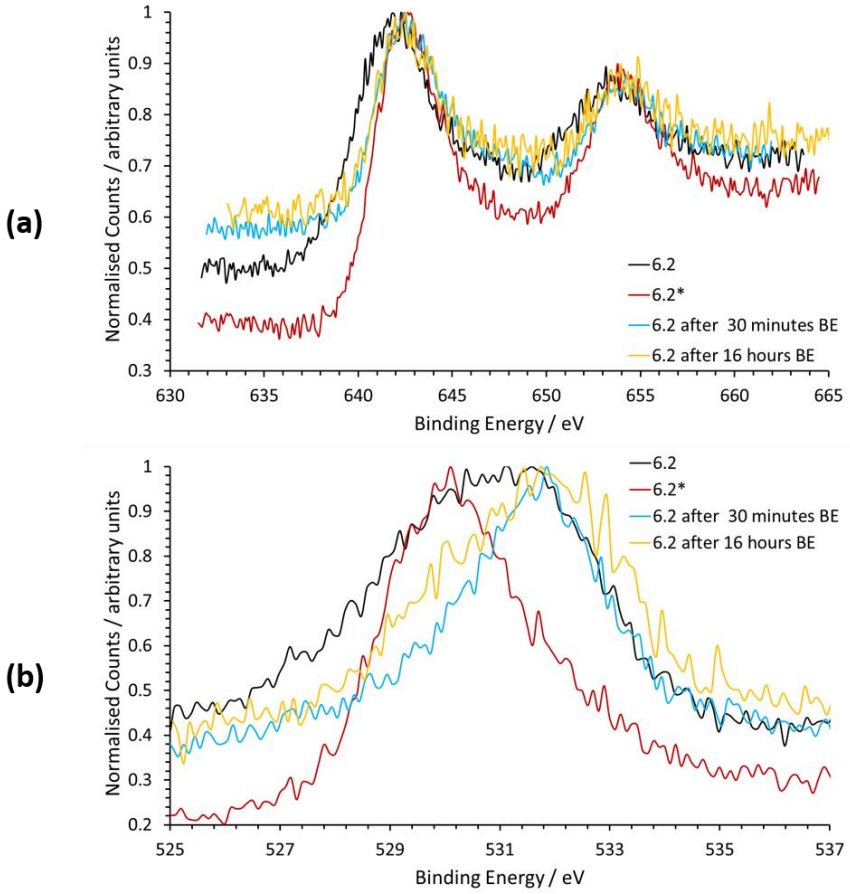

Figure 6.25: Mn 2p **(a)** and O 1s **(b)** binding energies for compound **6.2** and **6.2*** and compound **6.2** in carbon paste after CA.

Leaching during chronoamperometry was also investigated and for this purpose, linear sweep voltammetry with a rotating disk glassy carbon electrode was performed before and after chronoamperometry using the same buffer solution (**Figure 6.26**). A small increase can be observed in the current density from 0.09 mA cm^{-2} to 0.16 mA cm^{-2} at 1.6 V (vs NHE). This shows that there is a small amount of leaching. However, the activity observed cannot be associated with the leached product as this increase is negligible compared to the current densities observed for compound **6.2** and Mn_2O_3.

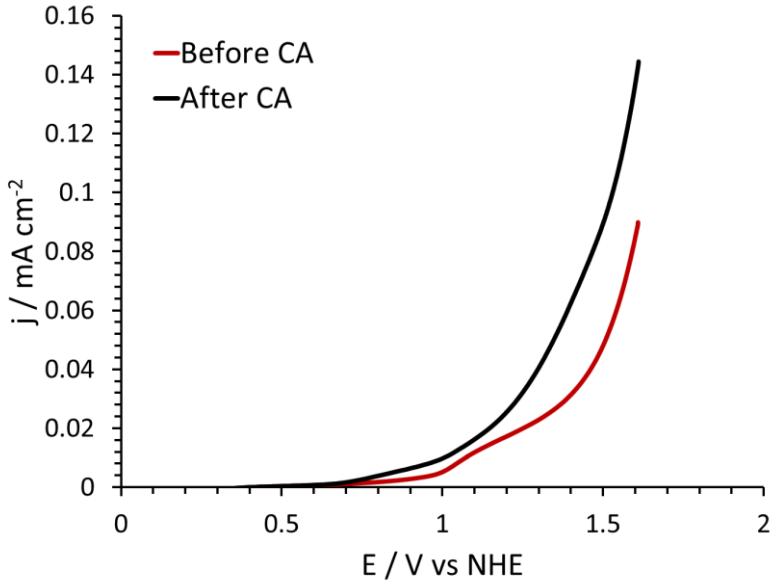

Figure 6.26: Linear sweep voltammograms using glassy carbon electrodes of the buffer solution before and after chronoamperometry.

6.3 $[Mn^{IV}_4Mn^{III}_8(\mu_3\text{-}O)_{12}(C_6H_5C_6H_4CO_2)_{16}(H_2O)_4]\cdot 3CH_3CN\cdot 13CHCl_3$ (6.3)

Refluxing $KMnO_4$ with excess of biphenyl-4-carboxylic acid in CH_3CN followed by the addition of $CHCl_3$ leads to the formation of compound **6.3**. The crystals were obtained within a week and were characterised using single crystal X-ray diffraction.

6.3.1 Structural description

Compound **6.3** crystallises in the monoclininc crystal system and the structure solution was obtained in the Cc space group. It contains a dodecanuclear complex $[Mn^{IV}_4Mn^{III}_8(\mu_3\text{-}O)_{12}(C_6H_5C_6H_4CO_2)_{16}(H_2O)_4]$ (**Figure 6.27**) with the asymmetric unit containing the whole complex. The core of this complex can be described as a $\{Mn_4O_4\}$ cubane unit encapsulated in a non-planar $\{Mn_8\}$ ring via eight additional $\mu_3\text{-}O^{2-}$ groups (**Figure 6.28 (a)**). The complex is further stabilised by 16 biphenyl-4-carboxylate groups, and four additional water molecules complete the coordination environment. Bond valence sum analysis shows that the Mn centres belonging to the cubane unit are in +IV oxidation state while those belonging to the ring are in +III oxidation state (**Table 6.14**). This suggests that the oxidation state that gets stabilised does not solely depend upon the ratio of Mn(II) and Mn(VII) salts but also varies with the other reaction conditions employed. We believe that the +III/IV oxidation states are achieved by oxidising biphenyl-4-carboxylic acid. The protonation state of the O atoms bound only to Mn centres has also been confirmed by bond valence sum analysis (**Table 6.15**).

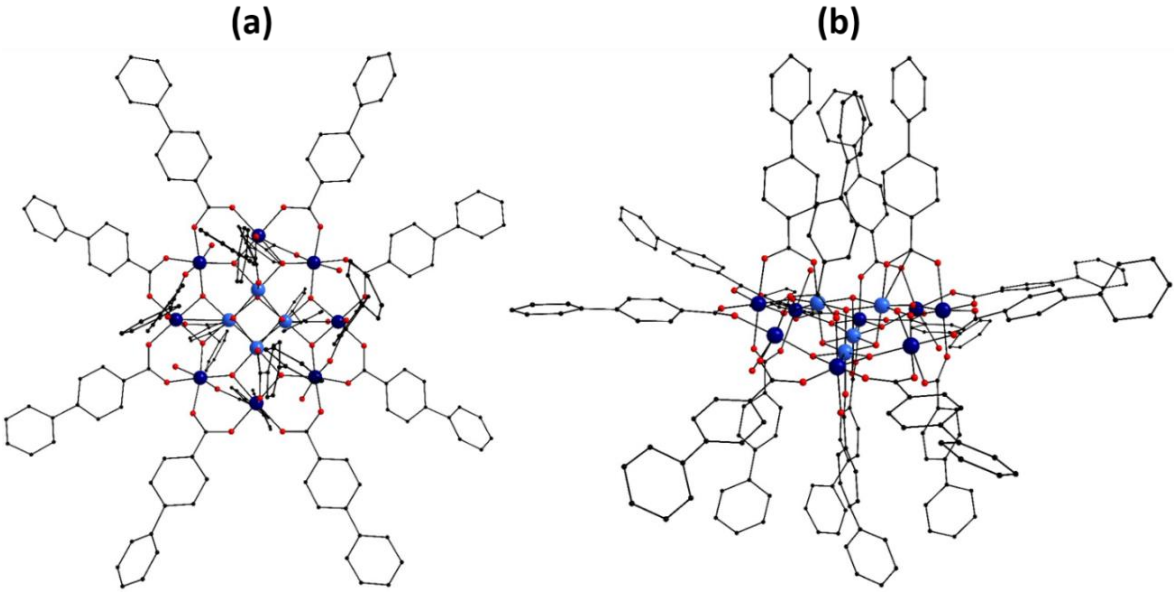

Figure 6.27: (a) and **(b)** The structure of the dodecadecanuclear compound **6.3** in two different orientations. Colour scheme: Mn^{IV} (light blue), Mn^{III} (dark blue), C (black) and O (red). All hydrogen atoms have been removed for clarity.

The coordination environment of the Mn(IV) centres (Mn1-Mn4) comprises of five $\mu_3\text{-}O^{2-}$ groups and an O-donor of a biphenyl-4-carboxylate group. The Mn-O distances for these centres vary between 1.85 and 1.95 Å. The angle variance, distortion indices and continuous shape measure

values reveal minimal distortion of the octahedral coordination environment of the Mn(IV) centres (**Table 6.16**). The octahedron for each Mn(IV) centre shares an edge with that of the other Mn(IV) centres and one Mn(III) centre, and a vertex with two additional Mn(III) centres (**Figure 6.28 (b)**).

Table 6.14: Key Mn-O and Mn-Mn bond lengths and bond valence sum for each Mn centre for compound **6.3**.

Mn centre	Coordinating atom	Bond Distance (Å)	BVS	Assigned oxidation state
Mn1	O6	1.847(12)	4.026	+IV
	O7	1.872(10)		
	O1	1.907(13)		
	O45	1.924(14)		
	O3	1.929(12)		
	O2	1.933(11)		
Mn2	O8	1.856(11)	4.075	+IV
	O9	1.859(12)		
	O2	1.903(12)		
	O36	1.911(15)		
	O1	1.925(12)		
	O4	1.930(10)		
Mn3	O10	1.820(12)	3.955	+IV
	O11	1.881(12)		
	O4	1.920(12)		
	O27	1.941(14)		
	O2	1.949(11)		
	O3	1.951(11)		
Mn4	O5	1.856(12)	4.035	+IV
	O12	1.863(12)		
	O3	1.895(13)		
	O14	1.918(15)		
	O1	1.929(12)		
	O4	1.947(11)		
Mn5	O6	1.896(13)	3.072	+III
	O5	1.916(13)		
	O18	1.957(13)		
	O47	2.018(14)		
	O16	2.165(15)		
	O48	2.201(13)		
Mn6	O7	1.878(11)	3.343	+III
	O6	1.879(12)		
	O40	1.918(13)		
	O46	1.942(13)		
	O44	2.184(14)		
	O42	2.194(15)		
Mn7	O8	1.888(12)	3.282	+III
	O7	1.896(11)		
	O39	1.932(14)		
	O38	1.947(12)		
	O41	2.135(15)		
	O43	2.221(14)		

Mn centre	Coordinating atom	Bond Distance (Å)	BVS	Assigned oxidation state
Mn8	O9	1.879(12)	3.228	+III
	O8	1.888(12)		
	O31	1.936(13)		
	O37	1.977(12)		
	O35	2.192(14)		
	O33	2.197(15)		
Mn9	O10	1.899(12)	3.215	+III
	O9	1.915(12)		
	O30	1.922(13)		
	O29	1.967(14)		
	O32	2.135(15)		
	O34	2.217(13)		
Mn10	O11	1.844(12)	3.401	+III
	O10	1.901(12)		
	O24	1.905(13)		
	O28	1.969(12)		
	O22	2.153(14)		
	O26	2.169(14)		
Mn11	O12	1.877(12)	3.317	+III
	O11	1.912(13)		
	O23	1.914(13)		
	O20	1.951(13)		
	O21	2.139(15)		
	O25	2.194(13)		
Mn12	O5	1.874(12)	3.279	+III
	O12	1.904(12)		
	O17	1.928(13)		
	O19	1.954(12)		
	O13	2.175(14)		
	O15	2.189(14)		

Metals	Distance (Å)	Metals	Distance (Å)
Mn1-Mn2	2.818(4)	Mn3-Mn9	3.450(4)
Mn1-Mn3	2.976(4)	Mn3-Mn10	2.783(4)
Mn1-Mn4	2.813(5)	Mn3-Mn11	3.448(5)
Mn1-Mn5	3.452(5)	Mn3-Mn12	4.841(5)
Mn1-Mn6	2.788(4)	Mn4-Mn5	3.448(4)
Mn1-Mn7	3.451(4)	Mn4-Mn6	4.829(4)
Mn1-Mn8	4.831(4)	Mn4-Mn10	4.858(4)
Mn1-Mn12	4.866(5)	Mn4-Mn11	3.458(4)
Mn2-Mn3	2.818(4)	Mn4-Mn12	2.795(5)
Mn2-Mn4	2.970(5)	Mn5-Mn6	3.380(5)
Mn2-Mn6	4.859(4)	Mn5-Mn12	3.308(5)
Mn2-Mn7	3.456(4)	Mn6-Mn7	3.303(4)
Mn2-Mn8	2.784(5)	Mn7-Mn8	3.388(4)
Mn2-Mn9	3.454(4)	Mn8-Mn9	3.304(4)
Mn2-Mn10	4.835(4)	Mn9-Mn10	3.383(4)
Mn3-Mn4	2.818(5)	Mn10-Mn11	3.298(5)
Mn3-Mn8	4.855(4)	Mn11-Mn12	3.386(5)

Table 6.15: BVS analysis for O atoms and their assigned protonation state in compound **6.3**.

Atom	BVS	Assignment
O1	1.909	μ_3-O^{2-}
O2	1.870	μ_3-O^{2-}
O3	1.888	μ_3-O^{2-}
O4	1.849	μ_3-O^{2-}
O5	2.162	μ_3-O^{2-}
O6	2.208	μ_3-O^{2-}
O7	2.158	μ_3-O^{2-}
O8	2.187	μ_3-O^{2-}
O9	2.148	μ_3-O^{2-}
O10	2.220	μ_3-O^{2-}
O11	2.181	μ_3-O^{2-}
O12	2.164	μ_3-O^{2-}
O25	0.309	H_2O
O34	0.291	H_2O
O43	0.288	H_2O
O48	0.304	H_2O

Based on the coordination environment of Mn(III) centres, they can be divided into two groups:

1. Type 1: Mn centres bound to a water molecule (Mn5, Mn7, Mn9 and Mn11)
2. Type 2: Mn centres not bound to a water molecule (Mn6, Mn8, Mn10 and Mn12).

Type 1 Mn centres reside in an octahedral environment which is fulfilled by two μ_3-O^{2-} groups and the O-donors of three biphenyl-4-carboxylate groups in addition to a water molecule. The Jahn-Teller axis is directed towards the water molecule and the carboxylate O-donor opposite to it. The Mn-O distances are ~2.2 Å along the Jahn-Teller axis and range from 1.8-2.0 Å perpendicular to it. The octahedron of these Mn centres shares a vertex with the octahedron of two Mn(IV) centres and type 2 Mn (III) centres (**Figure 6.28 (b)**).

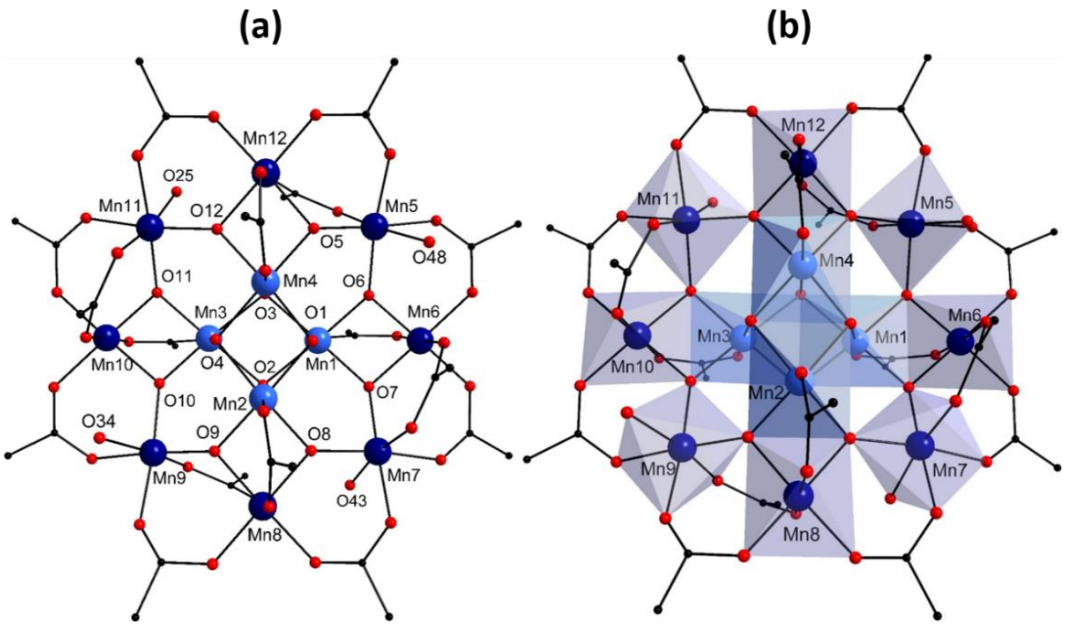

Figure 6.28: (a) Core structure and **(b)** polyhedral representation of compound **6.3**. Colour scheme: Mn^{IV} (light blue), Mn^{III} (dark blue), C (black) and O (red). All hydrogen atoms have been removed for clarity.

Table 6.16: Continuous shape measure values, angle variance and distortion indices (using the ideal octahedral geometry as a reference) for each Mn centre for compound **6.3**.

Mn centre	Continuous shape measure value	Angle variance (σ^2)	Distortion Index
Mn1	0.463	32.71	0.0525
Mn2	0.449	32.35	0.0519
Mn3	0.556	37.35	0.0557
Mn4	0.473	33.87	0.0513
Mn5	0.554	22.35	0.0451
Mn6	0.856	27.06	0.0507
Mn7	0.649	21.16	0.0427
Mn8	0.791	24.94	0.0489
Mn9	0.603	20.14	0.0419
Mn10	0.778	27.02	0.0499
Mn11	0.626	21.61	0.0444
Mn12	0.754	24.53	0.0472

The coordination environment of type 2 Mn centres is fulfilled by two μ_3-O^{2-} groups and the O-donors of four biphenyl-4-carboxylate groups. The Jahn-Teller axis for these Mn centres is directed along the carboxylate O-donors that lie perpendicular to the plane containing the μ_3-O^{2-} groups. The Mn-O bond is ~2.2 Å along the Jahn-Teller axis and ~1.9 Å perpendicular to it. The octahedron of these Mn centres is the most distorted in comparison to the other Mn centres. The octahedron of these Mn centres shares a vertex with the octahedron of two type 1 Mn(III) centres and an edge with the octahedron of a Mn(IV) centre (**Figure 6.28 (b)**).

Table 6.17: Selected bond angles for compound **6.3**.

Bond	Bond Angle (°)	Bond	Bond Angle (°)
O3-Mn1-O2	80.4(4)	O39-Mn7-O43	82.8(6)
O6-Mn1-O7	83.6(5)	O38-Mn7-O41	84.2(6)
O1-Mn1-O2	84.3(5)	O39-Mn7-O38	84.2(6)
O1-Mn1-O3	84.4(5)	O38-Mn7-O43	86.4(6)
O6-Mn1-O1	88.7(6)	O8-Mn7-O41	89.0(6)
O7-Mn1-O1	91.0(5)	O8-Mn7-O38	91.1(5)
O7-Mn1-O45	91.8(6)	O8-Mn7-O43	92.0(6)
O6-Mn1-O45	92.1(6)	O7-Mn7-O39	92.3(5)
O45-Mn1-O3	92.8(6)	O7-Mn7-O43	92.3(6)
O45-Mn1-O2	94.8(5)	O8-Mn7-O7	92.4(5)
O6-Mn1-O3	96.9(5)	O39-Mn7-O41	95.4(6)
O7-Mn1-O2	98.6(5)	O7-Mn7-O41	97.0(5)
O6-Mn1-O2	172.7(6)	O41-Mn7-O43	170.6(6)
O7-Mn1-O3	175.4(6)	O8-Mn7-O39	173.1(6)
O1-Mn1-O45	177.1(6)	O7-Mn7-O38	176.4(5)
O1-Mn2-O4	79.8(5)	O9-Mn8-O8	82.7(5)
O8-Mn2-O9	84.1(5)	O8-Mn8-O35	83.9(6)
O2-Mn2-O1	84.6(5)	O31-Mn8-O37	85.0(5)
O2-Mn2-O4	85.5(5)	O9-Mn8-O35	85.6(6)
O8-Mn2-O2	88.1(5)	O37-Mn8-O33	86.6(5)
O9-Mn2-O36	89.6(6)	O31-Mn8-O35	89.7(6)
O9-Mn2-O2	91.5(6)	O8-Mn8-O33	92.3(6)
O8-Mn2-O36	93.0(6)	O37-Mn8-O35	93.1(6)
O36-Mn2-O4	93.3(6)	O31-Mn8-O33	94.1(6)

Bond	Bond Angle (°)	Bond	Bond Angle (°)
O36-Mn2-O1	94.2(6)	O9-Mn8-O33	94.7(6)
O8-Mn2-O1	97.2(5)	O8-Mn8-O37	95.4(5)
O9-Mn2-O4	98.5(5)	O9-Mn8-O31	96.7(6)
O8-Mn2-O4	173.1(5)	O8-Mn8-O31	173.6(6)
O9-Mn2-O1	175.9(6)	O35-Mn8-O33	176.2(6)
O2-Mn2-O36	178.5(6)	O9-Mn8-O37	177.8(6)
O2-Mn3-O3	79.4(5)	O30-Mn9-O29	82.9(6)
O10-Mn3-O11	83.4(5)	O30-Mn9-O34	84.3(6)
O4-Mn3-O2	84.5(5)	O29-Mn9-O32	85.2(6)
O4-Mn3-O3	84.7(5)	O29-Mn9-O34	85.2(6)
O10-Mn3-O4	87.7(5)	O10-Mn9-O32	89.4(6)
O11-Mn3-O27	90.8(6)	O10-Mn9-O9	91.2(5)
O11-Mn3-O4	91.7(5)	O10-Mn9-O34	91.6(6)
O10-Mn3-O27	92.0(6)	O9-Mn9-O34	92.5(6)
O27-Mn3-O2	93.0(6)	O9-Mn9-O30	92.7(6)
O27-Mn3-O3	95.4(6)	O10-Mn9-O29	93.1(5)
O10-Mn3-O2	96.9(5)	O30-Mn9-O32	94.0(6)
O11-Mn3-O3	99.9(5)	O9-Mn9-O32	97.0(6)
O10-Mn3-O3	171.8(6)	O32-Mn9-O34	170.4(6)
O11-Mn3-O2	176.2(6)	O10-Mn9-O30	174.5(5)
O4-Mn3-O27	177.4(6)	O9-Mn9-O29	175.3(6)
O1-Mn4-O4	79.3(5)	O11-Mn10-O10	82.2(5)
O5-Mn4-O12	83.9(5)	O10-Mn10-O26	83.7(6)
O3-Mn4-O1	84.7(5)	O24-Mn10-O28	84.4(5)
O3-Mn4-O4	85.6(5)	O11-Mn10-O26	85.2(6)
O12-Mn4-O3	88.6(6)	O28-Mn10-O22	87.8(5)
O5-Mn4-O3	91.0(5)	O24-Mn10-O26	89.6(6)
O5-Mn4-O14	91.0(6)	O10-Mn10-O22	92.0(5)
O12-Mn4-O14	92.0(6)	O28-Mn10-O26	93.1(5)
O14-Mn4-O4	92.5(6)	O11-Mn10-O22	93.8(5)
O14-Mn4-O1	94.5(6)	O24-Mn10-O22	94.7(6)
O12-Mn4-O4	96.7(5)	O11-Mn10-O24	96.5(6)
O5-Mn4-O1	99.7(5)	O10-Mn10-O28	96.7(5)
O12-Mn4-O1	172.4(6)	O10-Mn10-O24	173.2(6)
O5-Mn4-O4	176.5(6)	O22-Mn10-O26	175.7(5)
O3-Mn4-O14	178.0(6)	O11-Mn10-O28	178.1(6)
O18-Mn5-O48	82.8(6)	O23-Mn11-O20	83.1(6)
O18-Mn5-O47	82.9(6)	O23-Mn11-O25	83.6(6)
O47-Mn5-O48	85.2(6)	O20-Mn11-O25	84.3(6)
O47-Mn5-O16	85.5(6)	O20-Mn11-O21	85.7(6)
O6-Mn5-O16	88.8(6)	O12-Mn11-O21	88.9(6)
O6-Mn5-O47	91.5(5)	O12-Mn11-O20	91.5(6)
O6-Mn5-O48	92.0(6)	O11-Mn11-O23	91.9(6)
O6-Mn5-O5	92.4(5)	O12-Mn11-O25	91.9(6)
O5-Mn5-O48	92.9(6)	O12-Mn11-O11	93.3(5)
O5-Mn5-O18	93.1(6)	O11-Mn11-O25	93.5(5)
O18-Mn5-O16	95.4(6)	O23-Mn11-O21	94.7(6)
O5-Mn5-O16	96.3(5)	O11-Mn11-O21	96.5(6)
O16-Mn5-O48	170.7(5)	O21-Mn11-O25	170.0(6)
O6-Mn5-O18	172.7(6)	O12-Mn11-O23	173.3(6)
O5-Mn5-O47	175.8(6)	O11-Mn11-O20	174.8(6)
O7-Mn6-O6	82.5(5)	O5-Mn12-O12	82.3(5)
O6-Mn6-O44	83.9(6)	O12-Mn12-O13	84.1(6)
O40-Mn6-O46	84.1(6)	O17-Mn12-O19	84.6(6)

Bond	Bond Angle (°)	Bond	Bond Angle (°)
O7-Mn6-O44	86.0(5)	O5-Mn12-O13	87.1(6)
O46-Mn6-O42	86.1(6)	O19-Mn12-O15	87.1(5)
O40-Mn6-O44	89.9(6)	O17-Mn12-O13	89.2(6)
O6-Mn6-O42	92.7(5)	O19-Mn12-O13	91.6(6)
O40-Mn6-O42	93.4(6)	O12-Mn12-O15	92.7(5)
O7-Mn6-O42	93.9(5)	O17-Mn12-O15	94.0(6)
O46-Mn6-O44	93.9(6)	O5-Mn12-O15	94.1(5)
O6-Mn6-O46	96.2(5)	O12-Mn12-O19	95.5(5)
O7-Mn6-O40	97.1(5)	O5-Mn12-O17	97.5(5)
O6-Mn6-O40	173.9(6)	O12-Mn12-O17	173.4(6)
O44-Mn6-O42	176.6(6)	O13-Mn12-O15	176.4(5)
O7-Mn6-O46	178.8(5)	O5-Mn12-O19	177.6(6)

The packing of this complex allows for a significant porosity. The diffracting component of the solvent molecules trapped in the crystal lattice however, was removed using the squeeze subroutine in PLATON[629] due to the diffuse nature of this electron density. The electron density in the voids (3714 electrons per unit cell) may correspond to 13 $CHCl_3$ and 3 CH_3CN molecules per formula unit. The use of the calcvoid routine implemented in OLEX[616] reveals that each direction is penetrable by a sphere of radius 3.40 Å and the radius of the largest void was found to be 4.60 Å. The packing arrangement along the crystallographic c-axis resembles the argyle pattern (**Figure 6.29**).

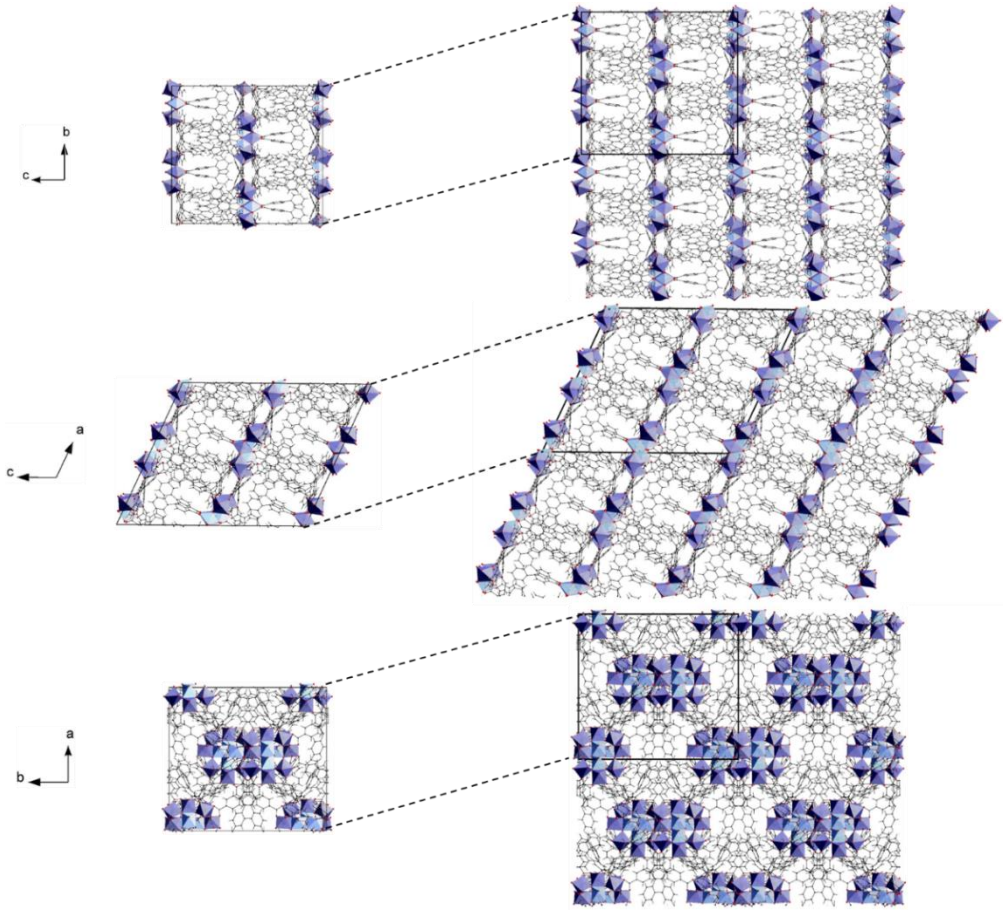

Figure 6.29: Packing diagram of compound **6.3**. Colour scheme: Mn^{IV} (light blue), Mn^{III} (dark blue), C (black) and O (red).

6.3.2 Physicochemical characterisation

The IR spectrum of compound **6.3** (**Figure 6.30**) is consistent with the structure determined by XRD. The small feature centred at 3030 cm^{-1} is due to the C-H stretching vibrations of the phenyl groups.[617] The vibrational mode due to the asymmetric stretching of the carboxylate group overlaps with the other peaks in the 1500-1600 cm^{-1} range due to C-C stretches of the aromatic rings.[630] The symmetric stretching vibration of the carboxylate group also overlaps with the peak vibration modes at 1386 cm^{-1} due to the vibrations of the organic molecules.[617] The energy variance between the two peaks fulfils the criteria for bridging carboxylate groups.[618]

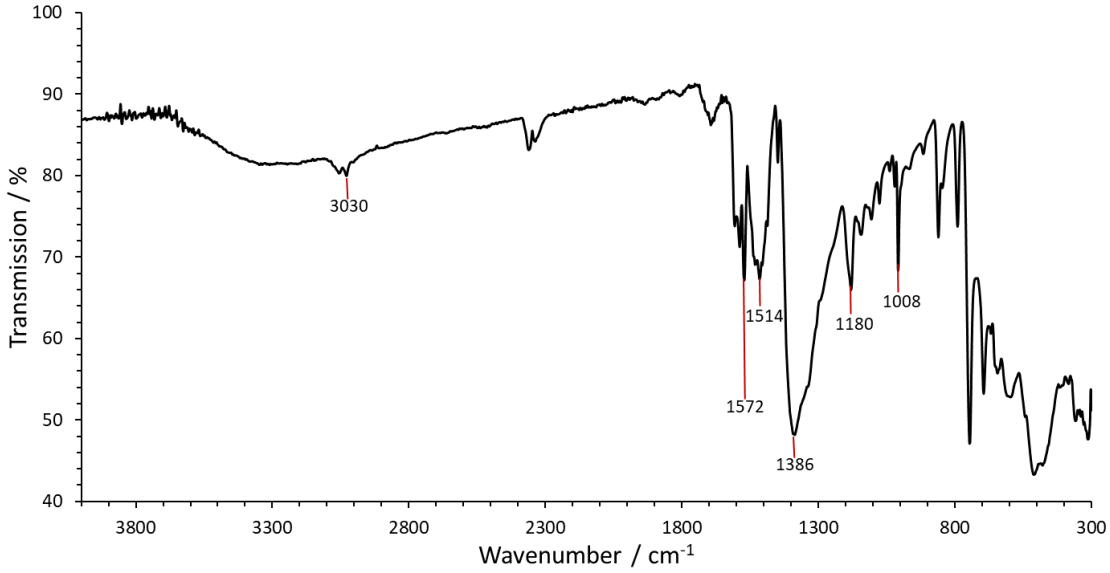

Figure 6.30: IR spectrum of compound **6.3**.

Further characterisation has not been performed as this complex is quite similar to some other $\{Mn_{12}\}$ coordination complexes which have been previously reported. This reported analogues of this complex have been found to possess SMM properties besides being active for water oxidation.[104, 105, 112, 113, 533]

6.4 Conclusions

Using the synthetic strategy described in chapter **3**, we have synthesised three coordination complexes (compounds **6.1**-**6.3**). All the three compounds have been characterised using various analytical techniques. Using pivalic acid, compounds **6.1** and **6.2** were obtained. Compound **6.1** contains a mixed-valence hexanuclear complex in which the Mn centres reside at the vertices of two edge sharing tetrahedra. The Mn centres on the common edge were determined to be in +III oxidation state while the other Mn centres were found to be in +II oxidation state.

Compound **6.2** contains a mixed-metal octanuclear complex where all Mn centres were found to be in +III oxidation state. It is a dimer of two $\{Mn_4K\}$ distorted cubane units that have a dangling Mn centre attached and that are symmetry related to each other by an inversion centre. The structural features of this complex have been found to bear striking similarities with those of the natural water oxidation catalyst. The structure can formally be compared with the S_{-1} state of the OEC. The electronic structure of this complex reveals strong antiferromagnetic interactions between the two cubane units and ferromagnetic interactions within them. The complex was found to be unstable under hydrolytic conditions and thus, to stabilise the molecular species and to investigate its electrocatalytic behaviour, it was dispersed in a protective carbon paste matrix. The investigation of its electrochemical behaviour revealed that similar to the OEC, it shows high catalytic activity and also undergoes rapid decomposition under oxidative, hydrolytic conditions. Electrodes with a 40 wt-% loading of compound **6.2**, give rise to an onset overpotential of 420 mV and a Tafel slope of 255 mV dec^{-1} at pH = 7.2.

Varying the carboxylic acid used in the synthesis results in structural rearrangements and with biphenyl-4-carboxylic acid, compound **6.3** was obtained. This compound contains a mixed-valence dodecanuclear complex whose core contains a $\{Mn_4\}$ cubane unit surrounded by a $\{Mn_8\}$ ring. The Mn centres in the cubane unit were found to be in +IV oxidation state while those forming the ring were found to be in +III oxidation state. This complex is structurally similar to the first characterised SMM.

The difference in the structural characteristics of these compounds illustrates the diversity that can be achieved by introducing subtle changes to the synthetic protocol. The structural and electronic characteristics of compound **6.2** and their similarity to the OEC suggests that this complex can potentially serve as a reference system for understanding the mechanism of natural water oxidation by the OEC. It also indicates that further variation of the synthetic conditions may lead to better OEC mimics which will be the aim of future endeavours.

7 Mixed Carboxylate-Phosphonate Complexes

The previous chapter illustrated how the synthetic approach described in chapter **3** can lead to complexes exhibiting a wide spectrum of structural and electronic characteristics. It was also observed how this strategy resulted in a compound (**6.2**) that structurally resembles the OEC and can promote the OER. Similar to the OEC, this compound has been found to decompose quickly and due to absence of any self-healing pathway, is unable to perform the OER for extended periods. It was observed that decomposition of this complex results in the formation of oxide species which indicates the lack of structural stability.

To address the problem of structural stability, one approach is to enhance the metal-ligand bond strength that should, in principle, result in a more robust system. Phosphonate groups can potentially serve as promising ligand groups for this purpose due to their strong affinity towards metal ions. Furthermore, their versatile binding capabilities make them highly suitable for stabilising high nuclearity molecular species.[536, 561-563] We have thus investigated the combined use of carboxylate and phosphonate groups.

Using the synthetic strategy described in chapter **3**, we have isolated a series of structurally related compounds. We have synthesised a dodecanuclear complex, $[Mn^{II}_{12}(\mu_3\text{-}OH)_4((C_6H_5)PO_3)_4((CH_3)_3CCO_2)_{12}((CH_3)_2CSO)_6]\cdot DMSO\cdot 34CH_3CN$ (compound **7.1**). By varying the reaction conditions, we have also synthesised a pentadecanuclear complex, $[Mn^{II}_6Mn^{III}_9(\mu_3\text{-}O)_4((CH_3)_3CCO_2)_{11}((CH_3)_3CCO_2H)(C_6H_5PO_3)_6(\mu\text{-}CH_3O)_6(\mu_3\text{-}CH_3O)_2(CH_3OH)_5]$ (compound **7.2**). We have also synthesised a less symmetric version of this pentadecanuclear complex, $[Mn^{II}_5Mn^{III}_{10}(\mu_3\text{-}O)_4((CH_3)_3CCO_2)_{7.15}(CH_3CO_2)_{4.85}(C_6H_5PO_3)_6(\mu\text{-}CH_3O)_6(\mu_3\text{-}CH_3O)_2(CH_3OH)_5]\cdot 2CH_3CN\cdot CH_3OH$ (compound **7.3**). Furthermore, we have synthesised a tetradecanuclear complex, $[Mn^{II}_4Mn^{III}_{10}(\mu_3\text{-}O)_4(\mu_3\text{-}OH)_2(\mu\text{-}CH_3O)_9(CH_3OH)_2(H_2O)_2((C_6H_5)PO_3)_3((CH_3)_3CCO_2)_{10}(CH_3CO_2)_3]$ (compound **7.4**) by modifying the reaction conditions. We have also synthesised a tridecanuclear complex, $[(Mn^{II}_{0.5}Mn^{III}_{0.5})_2Mn^{III}_{11}(\mu_3\text{-}O)_8((C_6H_5)PO_3)_4((CH_3)_3CCO_2)_{10}(\mu\text{-}CH_3O)_4(\mu\text{-}CH_3OH)_4]\cdot CH_3OH\cdot CH_3CN$ (compound **7.5**). These complexes serve as examples of geometries that are rarely observed in Mn coordination chemistry and some of them reveal interesting electrochemical behaviour. In this chapter, the synthesis, structural features, and magnetic and electrochemical properties of these complexes are discussed.

7.1 $[Mn^{II}_{12}(\mu_3\text{-}OH)_4((C_6H_5)PO_3)_4((CH_3)_3CCO_2)_{12}(DMSO)_6]\cdot DMSO\cdot 34CH_3CN$ (7.1)

Comproportionation reaction between $Mn(CH_3COO)_2\cdot 4H_2O$ and $KMnO_4$ in presence of phenylphosphonic acid, pivalic acid and L(-)-proline in the ratio 1:4:2:40:2 in a mixture of CH_3CN and DMSO leads to the formation of $[Mn^{II}_{12}(\mu_3\text{-}OH)_4((C_6H_5)PO_3)_4((CH_3)_3CCO_2)_{12}(DMSO)_6]\cdot$solvent, compound **7.1**. The crystals were obtained within a week and were characterised by single crystal X-ray diffraction.

7.1.1 Structure description

Compound **7.1** crystallises in a rhombohedral crystal system and the structure solution was obtained in the space group $R\bar{3}c$. It contains a dodecanuclear Mn complex, $[Mn^{II}_{12}(\mu_3\text{-}OH)_4((C_6H_5)PO_3)_4((CH_3)_3CCO_2)_{12}(DMSO)_6]$ (**Figure 7.1**), and the asymmetric unit contains half of the complex (**Figure 7.2**). The Mn centres adopt an octahedral coordination environment and reside at the vertices of a truncated tetrahedron (**Figure 7.3**). A truncated tetrahedron is a solid obtained by truncating all the vertices of a regular tetrahedron. It contains four triangular faces and four hexagonal faces. The truncated tetrahedral geometry is quite rare in Mn chemistry and there is only

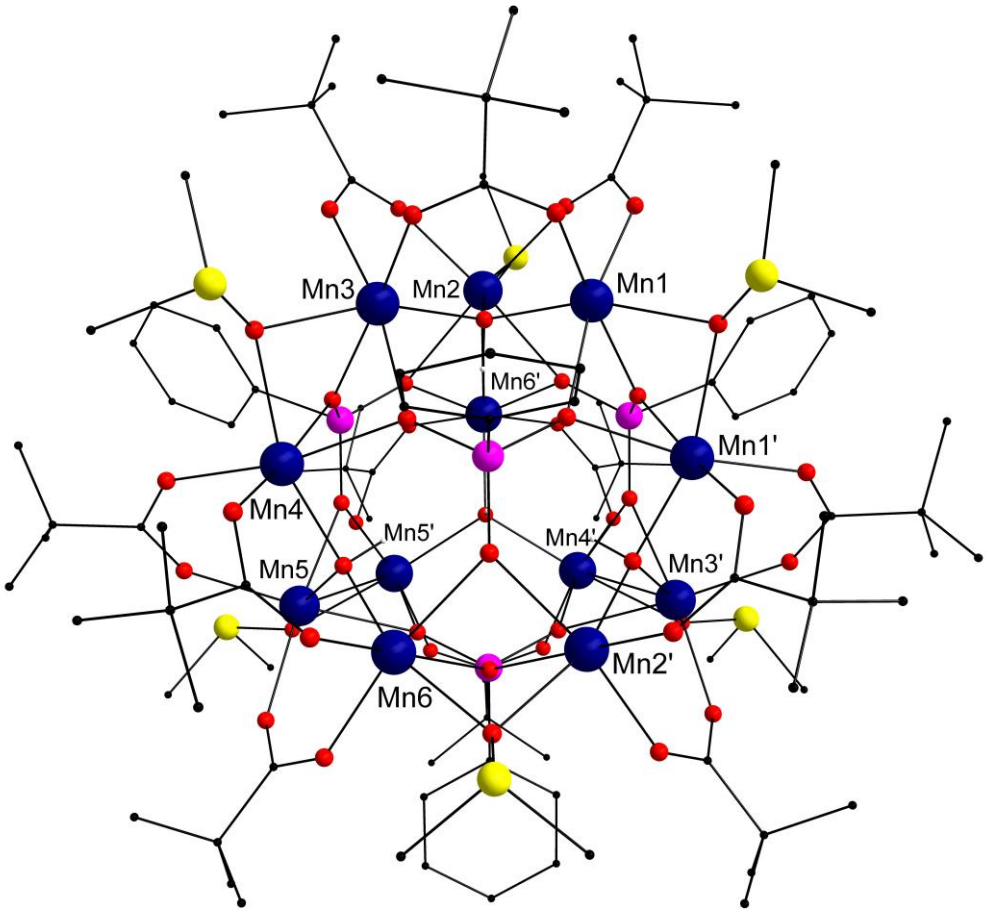

Figure 7.1: Crystal structure of the dodecanuclear compound **7.1**. Colour scheme: Mn^{II} (deep blue), C (black), S (yellow), P (pink) and O (red). All hydrogen atoms (grey) except those of the μ_3-OH^- group have been removed for clarity.

one reported structure which exhibits a distorted truncated tetrahedron geometry.[546] Continuous shape measure analysis[610-614] was performed on compound **7.1** to determine the deviation from an ideal truncated tetrahedron and a value of 0.138 was obtained suggesting minimal distortion and this can also be seen from **Figure 7.3 (a)**. Overall, the system is stabilised by four phenylphosphonate groups, four μ_3-OH^- groups, twelve pivalates and six DMSO molecules. The hexagonal faces of this truncated tetrahedron are capped by phenylphosphonate groups which bind in the 6.222 mode (Harris notation)[605] while the triangular faces are capped by μ_3-OH^- groups (**Figure 7.3 (b)**). The P atoms of the phosphonate groups lie ~1.13 Å above the hexagonal faces while the μ_3-OH^- groups lie ~0.37 Å below the plane of the Mn(II) centres directed towards the centre of the cage. The oxidation state of the Mn centres has been calculated to be +II and the isolated O atoms have been ascertained to be singly protonated using bond valence sum analysis (**Table 7.1** and **Table 7.2** respectively).

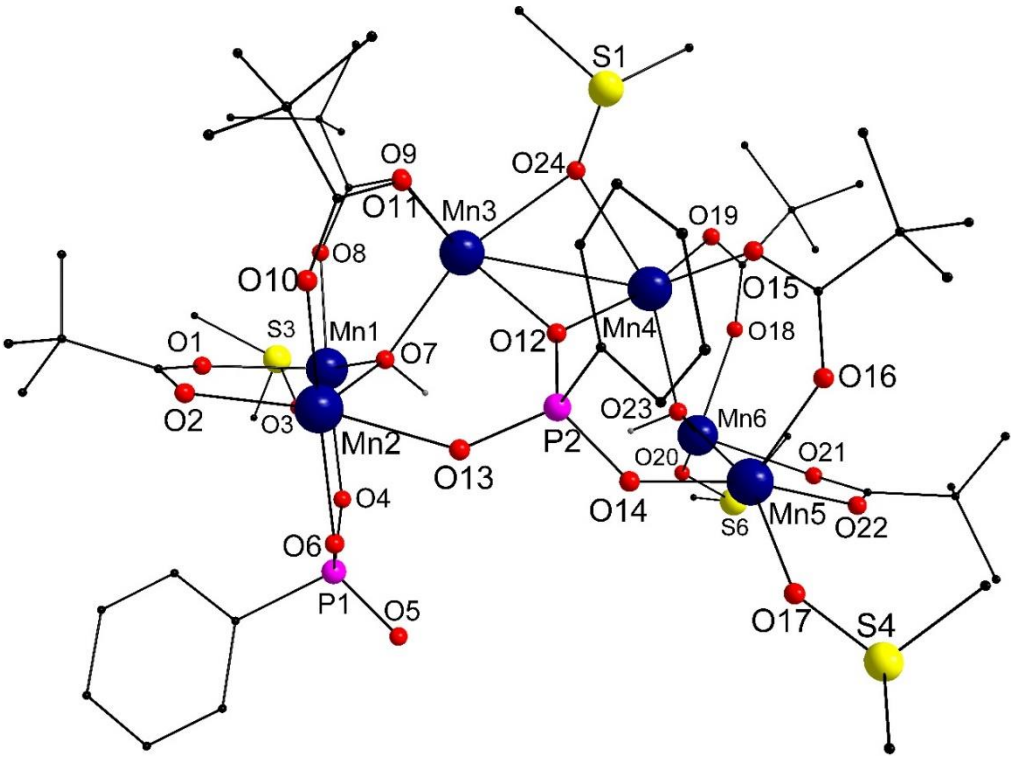

Figure 7.2: Asymmetric unit of the dodecanuclear compound **7.1**. Colour scheme: Mn^{II} (deep blue), C (black), S (yellow), P (pink) and O (red). All hydrogen atoms (grey) except those of the μ_3-OH^- group have been removed for clarity.

The structure can be divided into 4 triangular $\{Mn_3\}$ units out of which two are present in the asymmetric unit and the Mn centres in both units display similar structural features. The Mn-Mn distances between Mn centres residing on the triangular faces vary between 3.52 and 3.56 Å (**Table 7.1**). The four $\{Mn_3\}$ triangles are stabilised by the phenylphosphonate and DMSO groups which allow the octahedron of the Mn centres in different $\{Mn_3\}$ units to share a face (**Figure 7.4**). The Mn-Mn distance between Mn centres bound to μ_2-DMSO is 3.072(2) Å.

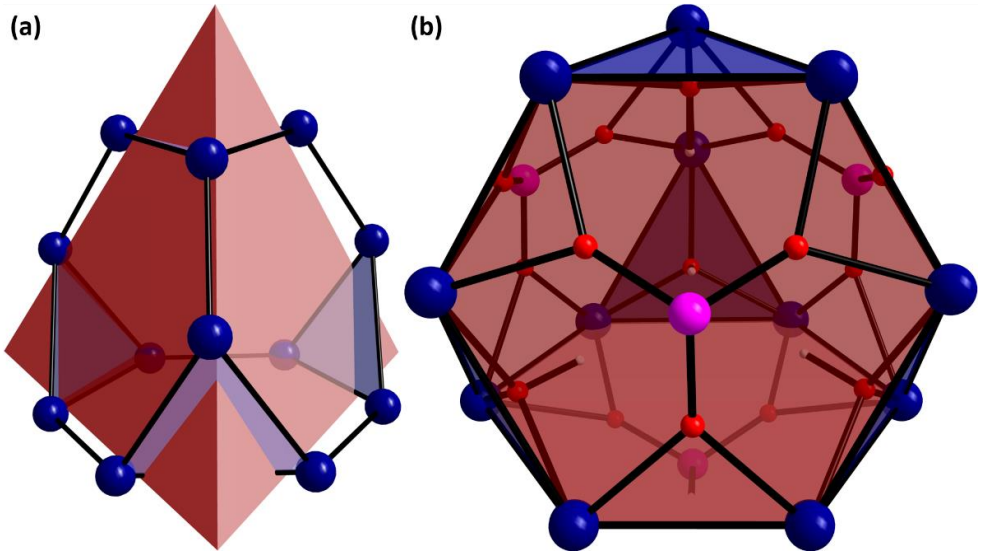

Figure 7.3: (a) Core structure of the dodecanuclear compound **7.1** superimposed on a perfect tetrahedron. **(b)** Polyhedron representation of the core structure of compound **7.1**. Colour scheme: Mn^{II} (deep blue), C (black), S (yellow), P (pink) and O (red). The triangular and the hexagonal faces have been highlighted in blue and red respectively.

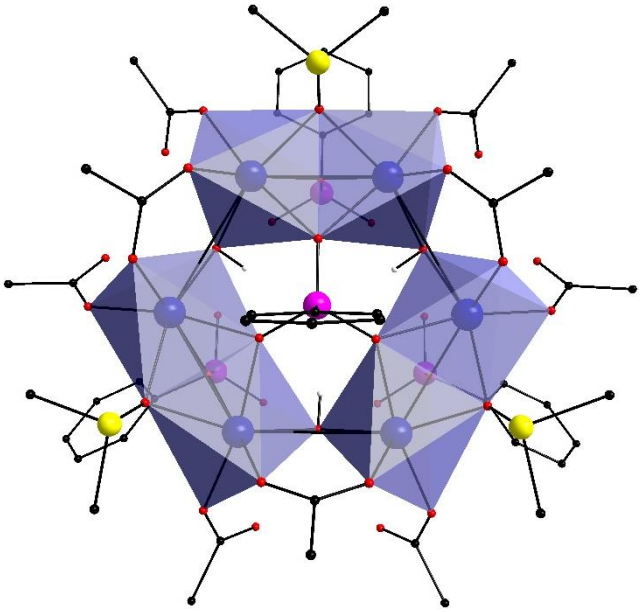

Figure 7.4: Polyhedral representation of one of the hexagonal faces of compound **7.1**. Colour scheme: Mn^{II} (deep blue), C (black), S (yellow), P (pink) and O (red). All hydrogen atoms (grey) except those of the μ_3-OH^- group have been removed for clarity.

Table 7.1: Key Mn-O and Mn-Mn bond lengths and bond valence sum for each Mn centre for compound **7.1**.

Mn centre	Coordinating atom	Bond Distance (Å)	BVS	Assigned oxidation state
Mn1	O1	2.126(4)	2.194	+II
	O3	2.234(4)		
	O4'	2.223(3)		
	O4	2.235(3)		
	O7	2.081(3)		
	O8	2.108(4)		

Mn centre	Coordinating atom	Bond Distance (Å)	BVS	Assigned oxidation state
Mn2	O2	2.130(5)	2.136	+II
	O6	2.255(4)		
	O7	2.076(3)		
	O10	2.126(4)		
	O13	2.254(4)		
	O20'	2.233(4)		
Mn3	O5'	2.218(3)	2.203	+II
	O7	2.087(3)		
	O9	2.103(4)		
	O11	2.131(4)		
	O12	2.233(4)		
	O24	2.222(4)		
Mn4	O5'	2.242(3)	2.190	+II
	O12	2.218(3)		
	O15	2.107(4)		
	O19	2.119(4)		
	O23	2.088(3)		
	O24	2.237(4)		
Mn5	O14	2.214(3)	2.200	+II
	O14'	2.244(3)		
	O16	2.106(4)		
	O17	2.223(4)		
	O22	2.121(4)		
	O23	2.090(4)		
Mn6	O6'	2.258(4)	2.148	+II
	O13'	2.256(4)		
	O18	2.125(5)		
	O20	2.236(4)		
	O21	2.127(5)		
	O23	2.065(3)		

Metals	Distance (Å)	Metals	Distance (Å)
Mn1-Mn2	3.561(2)	Mn2-Mn6	3.072(2)
Mn1-Mn3	3.520(2)	Mn3-Mn4	3.072(2)
Mn1-Mn4	6.652(2)	Mn3-Mn5'	6.654(2)
Mn1-Mn6	5.755(1)	Mn3-Mn6'	5.723(2)
Mn2-Mn3	3.564(2)	Mn4-Mn5	3.523(2)
Mn2-Mn4'	5.753(2)	Mn4-Mn6	3.558(2)
Mn2-Mn5'	5.755(2)	Mn5-Mn6	3.562(2)

'+Y,+X,3/2-Z

Within each triangular unit, the octahedral coordination environment of each Mn^{II} centre is fulfilled by O donors from a μ_3-OH^- group, a DMSO molecule, two phosphonate groups, and two pivalate groups (**Figure 7.5 (a)**) with the octahedron of the Mn centres sharing a vertex at the μ_3-OH^- group (**Figure 7.5 (b)**) and the Mn-O distance is 2.08 ± 0.01 Å for the O donor of the μ_3-OH^- group. Mn centres bind to the O donors of the phosphonate groups with the Mn-O bond varying between 2.22 – 2.26 Å which is similar to the distance between Mn and the O donors of the DMSO molecules. The pivalate groups bind relatively strongly with the Mn-O bond being ~2.12 Å (**Table 7.1**). The

continuous shape measure values for each Mn centre varies between 0.6 - 0.8 suggesting minor deviations from the ideal octahedral geometry and is in agreement with the angle variance and distortion indices for the Mn centres (**Table 7.3**). The minor distortions can be attributed to the ligand restraints imposed because of the geometry which can be seen from the bond lengths (**Table 7.1**) and bond angles (**Table 7.4**).

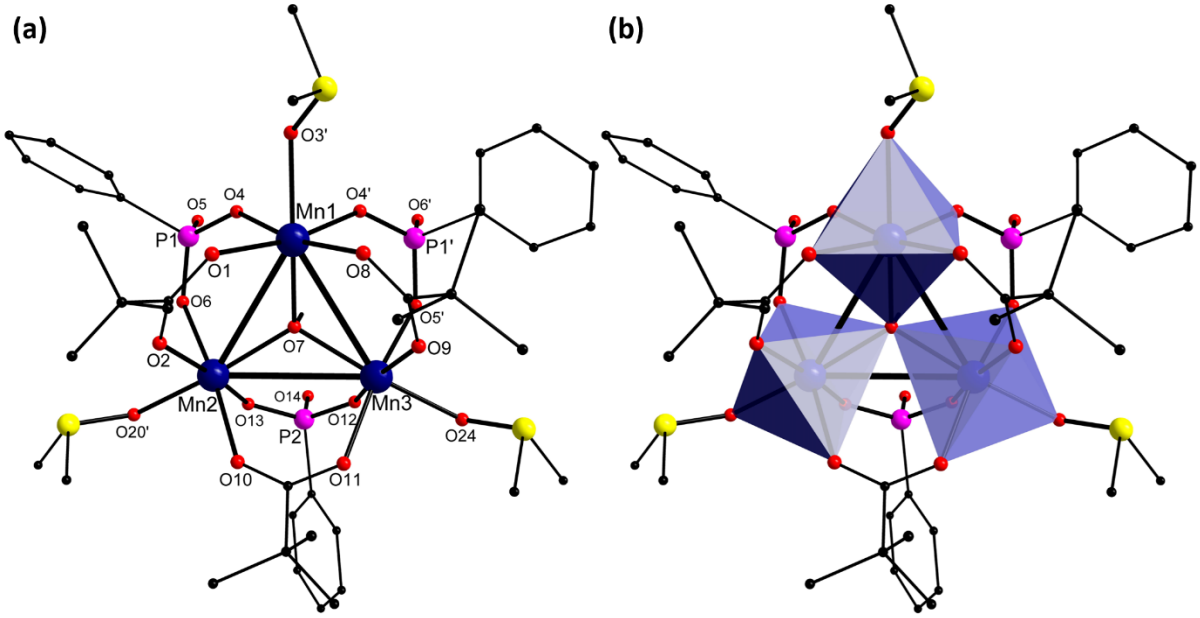

Figure 7.5: (a) The $\{Mn_3\}$ unit of compound **7.1** and **(b)** its polyhedral representation. Colour scheme: Mn^{II} (deep blue), C (black), S (yellow), P (pink) and O (red). All hydrogen atoms (grey) except those of the μ_3-OH^- group have been removed for clarity.

Table 7.2: BVS analysis for O atoms and their assigned protonation state in compound **7.1**.

Atom	BVS	Assignment
O7	1.365	μ_3-OH^-
O23	1.367	μ_3-OH^-

Table 7.3: Continuous shape measure values, angle variance and distortion indices (using the ideal octahedral geometry as a reference) for each Mn centre for compound **7.1**.

Mn centre	Continuous shape measure value	Angle variance (σ^2)	Distortion Index
Mn1	0.711	69.21	0.0750
Mn2	0.625	56.53	0.0667
Mn3	0.729	68.66	0.0746
Mn4	0.776	72.16	0.0761
Mn5	0.738	70.02	0.0754
Mn6	0.606	58.09	0.0673

The packing in this complex allows for potential porosity (**Figure 7.6**). The 'calcvoid' routine in OLEX2[616] reveals that the structure can be permeated by a sphere of radius 2.6 Å along each crystallographic direction. The radius of the largest spherical void was found to be 8.6 Å. The electron density found within these pores (14357 electrons per unit cell) may correspond to 1 DMSO and 34 CH_3CN molecules per formula unit but due to its diffused nature, it could not be resolved. The packing is stabilised by weak dispersion forces. Along the crystallographic c-axis, the complex packs in a honeycomb fashion with a screw axis coinciding with the centre of the hexagons (**Figure 7.6**).

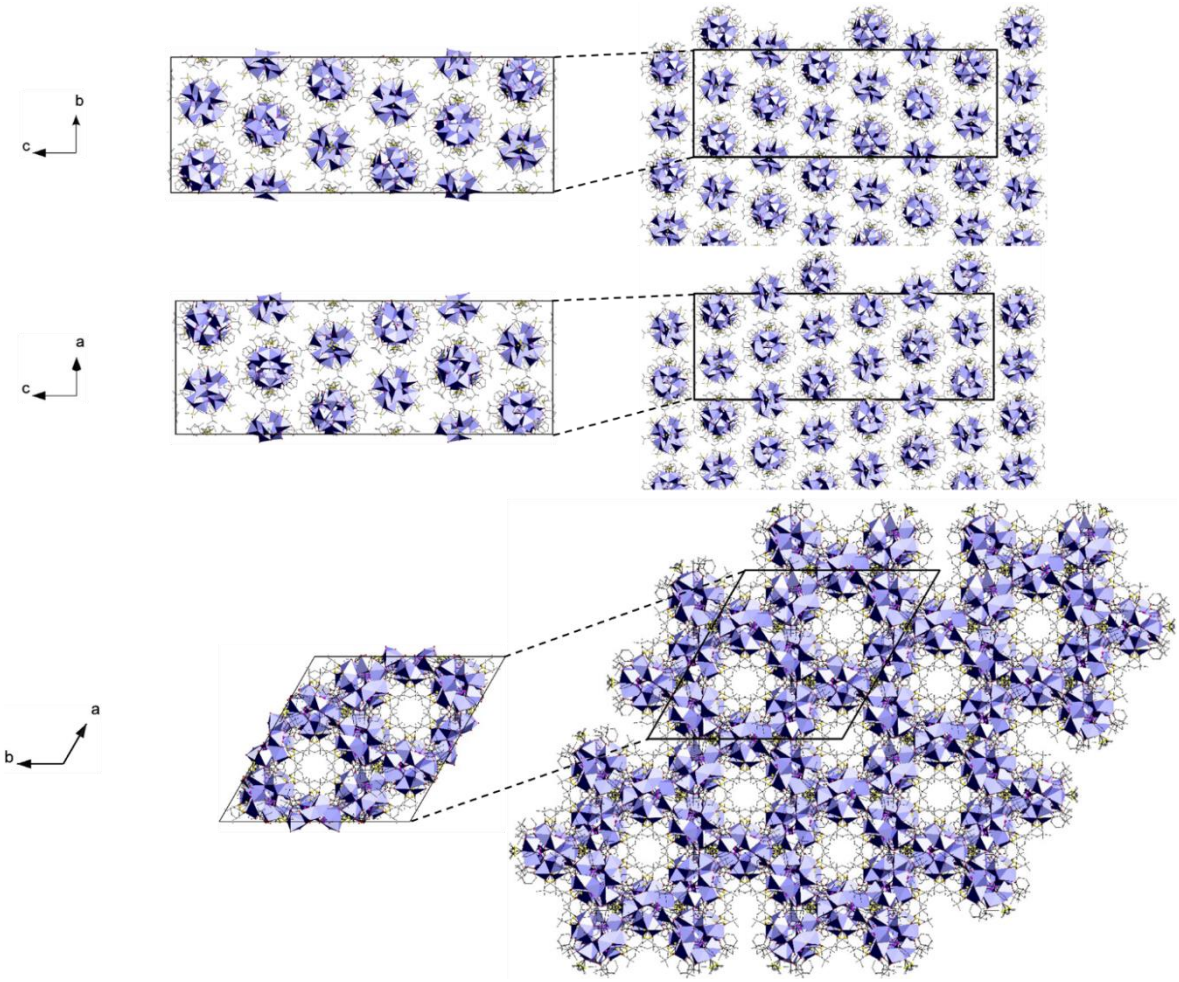

Figure 7.6: Packing diagram of compound **7.1**. Colour scheme: Mn^{II} (deep blue), C (black), S (yellow), P (pink) and O (red). All hydrogen atoms (grey) except those of the μ_3-OH^- group have been removed for clarity.

Table 7.4: Selected bond angles for compound **7.1**.

Bond	Bond Angle (°)	Bond	Bond Angle (°)
O4'-Mn1-O4	76.72(14)	O12-Mn4-O5'	76.53(12)
O3-Mn1-O4	78.19(11)	O24-Mn4-O5'	77.83(13)
O4'-Mn1-O3	78.45(11)	O12-Mn4-O24	78.26(13)
O7-Mn1-O4	86.56(13)	O23-Mn4-O5'	86.49(13)
O7-Mn1-O4'	88.07(13)	O23-Mn4-O12	88.23(13)
O8-Mn1-O1	90.13(16)	O15-Mn4-O19	89.86(16)
O1-Mn1-O3	92.71(15)	O19-Mn4-O24	92.42(17)
O8-Mn1-O3	92.77(13)	O15-Mn4-O24	93.00(15)
O8-Mn1-O4'	95.70(14)	O15-Mn4-O12	95.83(15)
O1-Mn1-O4	96.26(14)	O19-Mn4-O5'	96.50(15)
O7-Mn1-O1	99.27(16)	O23-Mn4-O19	99.56(16)
O7-Mn1-O8	101.13(15)	O23-Mn4-O15	101.33(15)
O7-Mn1-O3	161.56(14)	O23-Mn4-O24	161.26(14)
O8-Mn1-O4	169.13(15)	O15-Mn4-O5'	169.01(14)
O1-Mn1-O4'	169.61(15)	O19-Mn4-O12	169.29(16)
O20'-Mn2-O6	77.50(13)	O14-Mn5-O14'	76.78(13)
O20'-Mn2-O13	77.63(14)	O17-Mn5-O14'	77.87(12)
O13-Mn2-O6	80.38(13)	O14-Mn5-O17	78.50(12)
O7-Mn2-O6	88.53(13)	O23-Mn5-O14'	86.61(13)
O7-Mn2-O13	88.67(13)	O23-Mn5-O14	87.97(13)
O10-Mn2-O2	90.96(17)	O16-Mn5-O22	90.21(16)
O2-Mn2-O20'	93.70(17)	O22-Mn5-O17	92.74(15)
O2-Mn2-O6	93.73(16)	O16-Mn5-O17	92.76(14)
O10-Mn2-O13	93.83(16)	O16-Mn5-O14	95.38(15)
O10-Mn2-O20'	94.08(16)	O22-Mn5-O14'	96.41(14)
O7-Mn2-O10	98.81(16)	O23-Mn5-O22	99.31(16)
O7-Mn2-O2	98.87(16)	O23-Mn5-O16	101.34(15)
O7-Mn2-O20'	161.79(14)	O23-Mn5-O17	161.34(14)
O2-Mn2-O13	170.35(16)	O16-Mn5-O14'	168.74(15)
O10-Mn2-O6	170.59(15)	O22-Mn5-O14	169.80(16)
O5'-Mn3-O12	76.72(12)	O20-Mn6-O6'	77.39(14)
O24-Mn3-O12	78.24(13)	O20-Mn6-O13'	77.54(14)
O5'-Mn3-O24	78.64(13)	O13'-Mn6-O6'	80.31(13)
O7-Mn3-O12	86.69(13)	O23-Mn6-O13'	88.56(13)
O7-Mn3-O5'	87.89(12)	O23-Mn6-O6'	88.58(13)
O9-Mn3-O11	90.25(16)	O18-Mn6-O21	90.65(18)
O11-Mn3-O24	92.39(16)	O18-Mn6-O20	93.46(16)
O9-Mn3-O24	92.65(15)	O18-Mn6-O6'	93.87(16)
O9-Mn3-O5'	95.84(14)	O21-Mn6-O20	93.98(17)
O11-Mn3-O12	95.97(14)	O21-Mn6-O13'	94.00(16)
O7-Mn3-O11	99.53(16)	O23-Mn6-O21	98.97(16)
O7-Mn3-O9	101.08(15)	O23-Mn6-O18	99.33(16)
O7-Mn3-O24	161.70(14)	O23-Mn6-O20	161.63(14)
O9-Mn3-O12	169.14(15)	O18-Mn6-O13'	170.13(16)
O11-Mn3-O5'	169.35(16)	O21-Mn6-O6'	170.47(15)

7.1.2 Physicochemical characterisation

To verify the structural model, a number of physicochemical techniques were employed. PXRD pattern of compound **7.1** is consistent with the one simulated using the structural model confirming the phase purity of the material (**Figure 7.7 (a)**). The PXRD pattern obtained on the same sample stored for a week exhibited broader peaks indicating partial loss of crystallinity. TGA analysis (**Figure 7.7 (b)**) under a N_2 atmosphere on a sample of compound **7.1** dried in air reveals that most of the solvent molecules trapped in the crystal lattice are lost when it is dried in air which explains the partial loss in crystallinity. The shallow drop till 80 °C corresponds to the loss of remaining CH_3CN molecules trapped in the crystal lattice (weight loss calcd: 1.3 %, found: 1.7 %) and it is followed by the loss of the trapped and bound DMSO molecules up to 200 °C (weight loss calcd: 14.9 %, found: 15 %). The sharp drop observed between 200 and 315 °C corresponds to the partial loss of pivalate groups. Further heating leads to partial decomposition of the phenyl phosphonate groups and probable phosphate formation.

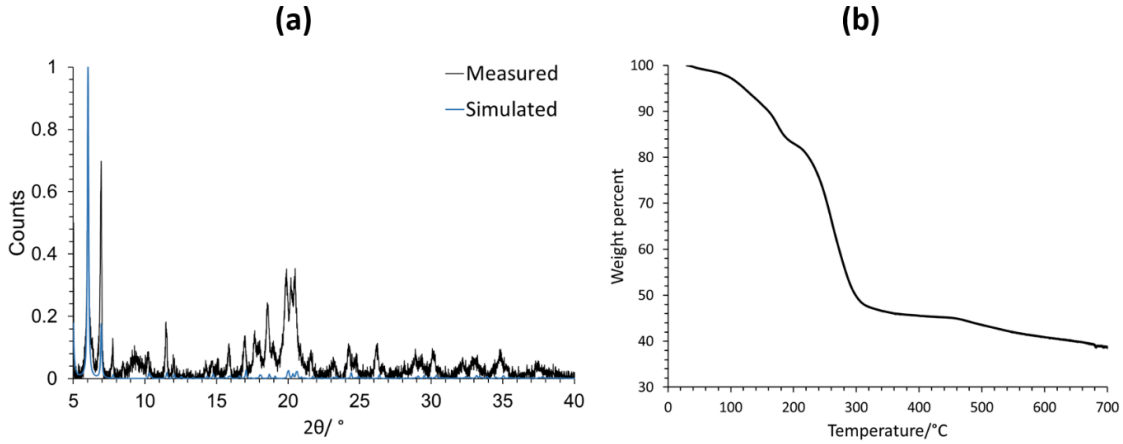

Figure 7.7: (a) The PXRD pattern and **(b)** TGA analysis of compound **7.1**.

The infrared spectrum of compound **7.1** (**Figure 7.8**) is consistent with the structure determined by XRD. The broad distinctive feature at 2960 cm^{-1} is due to the C-H vibrations in the organic ligands.[617] The vibration modes at 1418 and 1588 cm^{-1} correspond to the symmetric and asymmetric stretching modes of the carboxylate groups and the energy variance between the two is in line with that observed for bidentate bridging carboxylate groups.[618] Additional modes in the same range can be attributed to the vibrations of the organic moieties – both aliphatic and aromatic.[617] The feature in the 970-1000 cm^{-1} range correspond to the stretching of the phosphonate groups.[621-623]

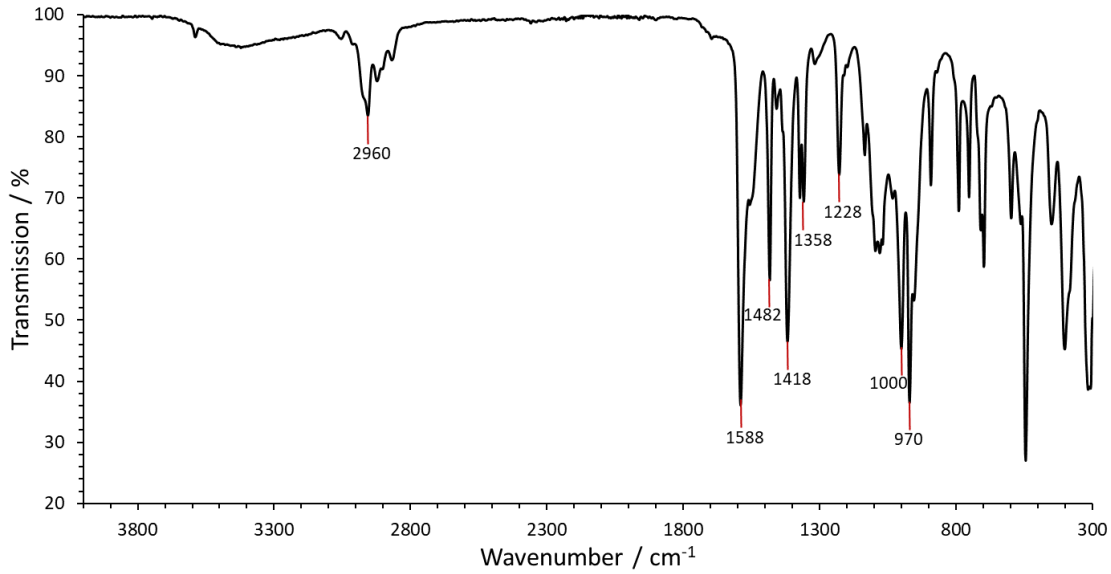

Figure 7.8: Infrared spectrum of compound **7.1**.

7.1.3 Magnetic properties

The temperature dependence of magnetic susceptibility was determined in the 4-300 K temperature range (**Figure 7.9**). The room temperature χT value was found to be 31.5 cm^3 K mol^{-1} which is significantly lower than the expected value of 52.5 cm^3 K mol^{-1} for a system with 12 Mn^{II} (S = 5/2) centres. This suggests that the coupling between the Mn centres is dominantly antiferromagnetic. This is further confirmed by the behaviour observed upon lowering the temperature when the χT value decreases and reaches 4 cm^3 K mol^{-1} at 4 K. This behaviour also indicates that the ground state in this case will be an S = 0 state.

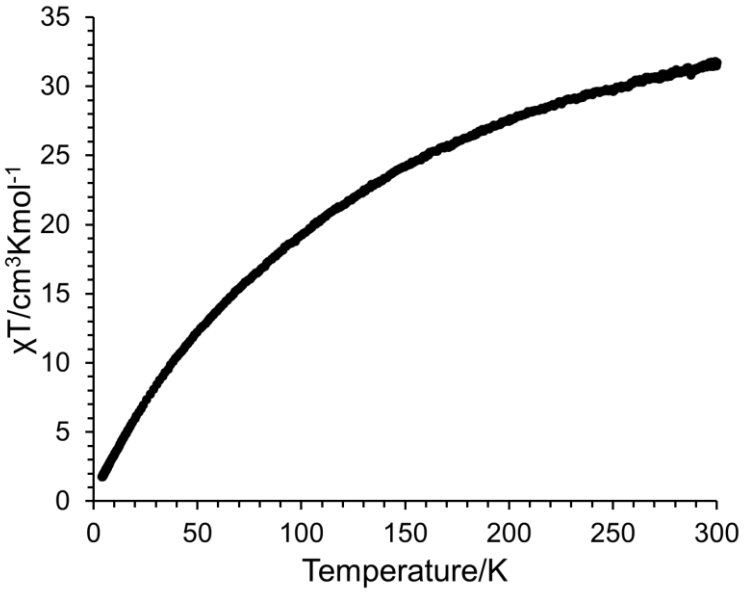

Figure 7.9: Temperature dependence of magnetic susceptibility (χT) of compound **7.1**.

7.1.4 DFT calculations

To quantify the strength of coupling between the Mn centres, DFT calculations were performed. The *tert*-butyl groups were replaced with methyl groups in the model for computational ease (**Figure 7.10**). The hybrid PBE0[433, 451] functional has been used in conjunction with the SDDALL[507] basis set having an effective core potential for the Mn atoms (replacing the 10 core electrons – $1s^2 2s^2 2p^6$ – of Mn with fully relativistic pseudopotentials), the 6-31G(d)[508] basis set for O, C and N, 6-31G(2d)[631] basis set for phosphorus and chlorine and 6-31G(p)[508] basis set for H The model represents the experimental structure well and the metal distances were found to be reproduced with errors <0.1 Å (**Table 7.5**).

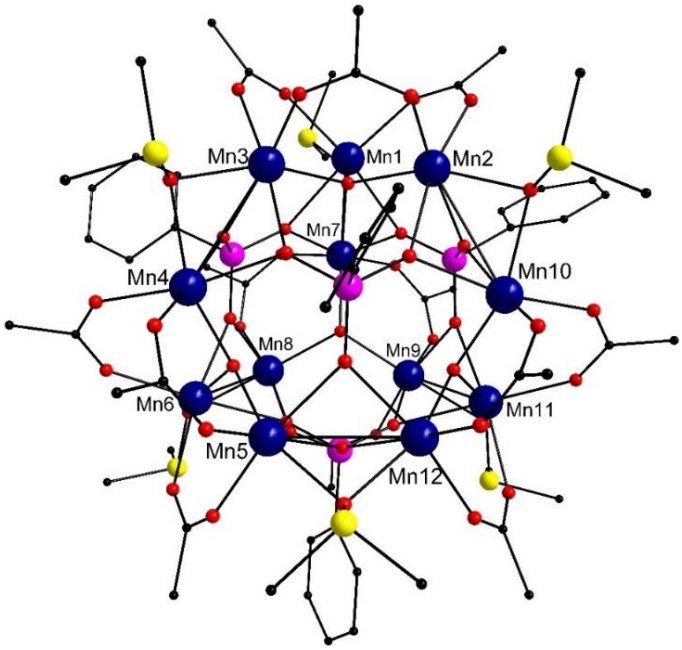

Figure 7.10: DFT model used for calculation of the magnetic properties of compound **7.1**. Colour scheme: Mn^{II} (deep blue), C (black), S (yellow), P (pink) and O (red). All hydrogen atoms have been removed for clarity. The number scheme here represents the one followed in the computational model.

The methodology adopted for the calculation of coupling constants is the same as that described in previous chapters. A total of 19 spin states were modelled for this complex and three coupling constants have been used to describe the coupling behaviour. The energy of the modelled states and the Bader spin density on the Mn centres in each state are given in **Table 7.6**. The spin densities indicate a small but equal amount of delocalisation of the unpaired electrons from each Mn centre. The coupling constants represent the coupling between Mn centres with nearest neighbours belonging to different triangular units (J_1), the Mn centres forming the triangular unit (J_2) (**Figure 7.11 (a)**) and the Mn centres forming the hexagonal faces (J_3) (**Figure 7.11 (b)**). The coupling between Mn centres that are not connected to each other *via* any ligand has not been considered since such pairs are quite far apart which implies that the through space coupling will be negligible and hence can be ignored.

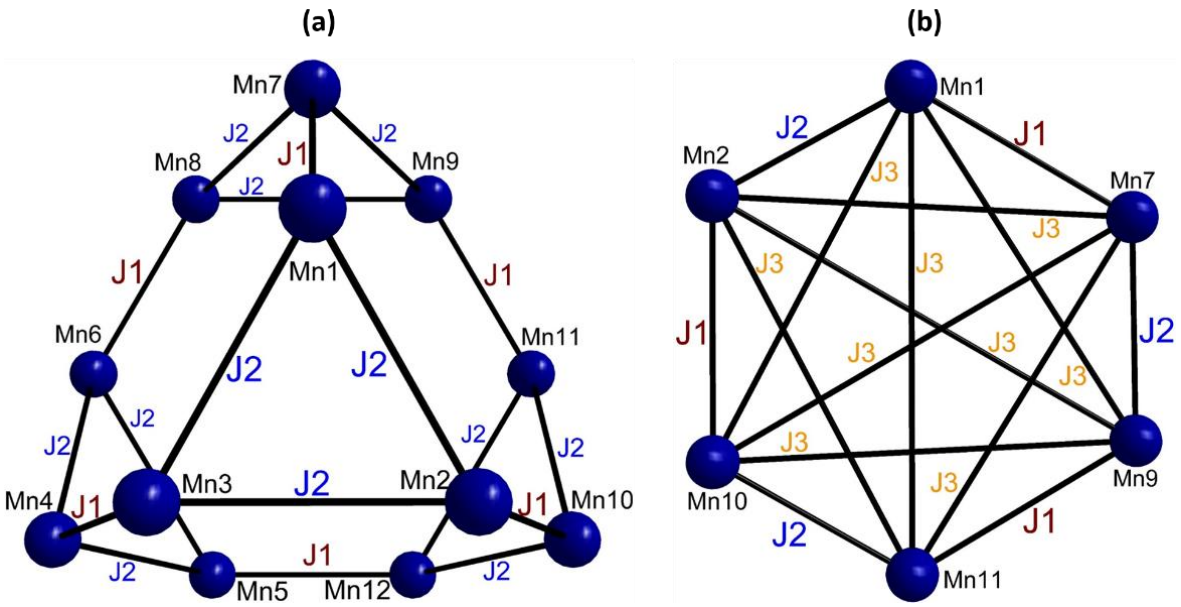

Figure 7.11: The coupling constants representing the coupling between **(a)** Mn centres between and within the triangular units and **(b)** on one of the hexagonal faces.

Table 7.5: Comparison of some of the Mn-Mn distances in the crystal structure and the DFT model.

	Distance (Å)			Distance (Å)	
Mn centres	**DFT**	**XRD**	**Mn centres**	**DFT**	**XRD**
Mn1-Mn2	3.50	3.52	Mn2-Mn7	5.77	5.73
Mn1-Mn3	3.55	3.56	Mn2-Mn8	7.52	7.50
Mn1-Mn4	5.83	5.76	Mn2-Mn9	6.64	6.60
Mn1-Mn5	7.61	7.53	Mn2-Mn10	3.15	3.07
Mn1-Mn6	6.76	6.65	Mn2-Mn11	5.75	5.73
Mn1-Mn7	3.15	3.07	Mn2-Mn12	5.78	5.73
Mn1-Mn8	5.77	5.73	Mn3-Mn4	3.14	3.07
Mn1-Mn9	5.77	3.56	Mn3-Mn5	5.83	5.76
Mn1-Mn10	5.80	5.74	Mn3-Mn6	5.79	5.76
Mn1-Mn11	6.66	6.61	Mn3-Mn7	5.76	5.73
Mn1-Mn12	7.56	7.50	Mn3-Mn8	6.60	6.60
Mn2-Mn3	3.57	3.56	Mn3-Mn9	7.51	7.50
Mn2-Mn4	5.82	5.75	Mn3-Mn10	5.80	5.72
Mn2-Mn5	6.74	6.65	Mn3-Mn11	7.54	7.50
Mn2-Mn6	7.60	7.53	Mn3-Mn12	6.66	6.60

Table 7.6: Bader spin densities on each Mn centre (truncated to three decimal places) and the relative energies for each modelled state for compound **7.1**.

Mn1	Mn2	Mn3	Mn4	Mn5	Mn6	Mn7	Mn8	Mn9	Mn10	Mn11	Mn12	Relative energy (cm^{-1})
4.693	4.693	4.696	4.695	4.693	4.693	4.695	4.693	4.695	4.694	4.695	4.692	0.00
-4.692	-4.691	-4.693	4.694	4.692	4.693	4.693	4.693	4.695	4.692	4.695	4.692	-221.04
-4.692	-4.691	-4.695	-4.695	-4.691	-4.691	4.693	4.691	4.694	4.691	4.694	4.691	-286.88
-4.681	4.688	4.691	4.695	4.693	4.693	4.694	4.693	4.695	4.694	4.695	4.693	-356.37
4.689	-4.680	4.691	4.695	4.692	4.693	4.695	4.693	4.695	4.693	4.695	4.693	-359.23
4.688	4.688	-4.684	4.695	4.693	4.693	4.695	4.693	4.695	4.694	4.695	4.692	-360.98
-4.686	-4.686	4.686	4.695	4.692	4.693	4.693	4.693	4.695	4.691	4.694	4.693	-430.9
-4.687	4.682	-4.688	4.694	4.693	4.693	4.694	4.693	4.695	4.693	4.695	4.692	-436.61
-4.687	4.682	-4.688	4.694	4.693	4.693	4.693	4.693	4.695	4.693	4.695	4.692	-436.82
-4.691	-4.691	-4.694	-4.684	4.687	4.688	4.692	4.693	4.695	4.691	4.695	4.692	-456.48
-4.691	-4.691	-4.695	-4.690	-4.687	4.683	4.691	4.692	4.694	4.691	4.695	4.691	-511.73
-4.691	-4.692	-4.693	4.689	-4.681	4.688	4.692	4.693	4.694	4.692	4.695	4.691	-566.14
-4.687	4.682	-4.690	-4.684	4.688	4.688	4.693	4.693	4.695	4.693	4.695	4.692	-672.44
-4.691	-4.692	-4.694	-4.685	4.687	4.688	4.692	4.693	4.694	-4.682	4.690	4.687	-688.11
-4.681	4.688	4.691	4.690	-4.679	4.688	4.694	4.693	4.695	4.694	4.695	4.691	-713.77
-4.687	-4.686	4.684	-4.683	4.687	4.688	4.691	4.693	4.695	4.692	4.694	4.693	-788.55
-4.692	-4.691	-4.695	-4.690	-4.687	4.682	4.688	-4.681	4.690	4.692	4.695	4.690	-850.6
-4.692	-4.692	-4.694	-4.685	4.687	4.688	-4.683	4.689	4.690	-4.683	4.689	4.687	-895.42
-4.692	-4.691	-4.693	4.689	4.686	-4.681	4.688	4.686	-4.683	4.688	4.688	-4.680	-1253.22

The Hamiltonian for this complex can be given as:

$$
\begin{aligned}
H = -2J_1[\langle s_1.s_7\rangle + \langle s_2.s_{10}\rangle + \langle s_3.s_4\rangle + \langle s_5.s_{12}\rangle + \langle s_6.s_8\rangle + \langle s_9.s_{11}\rangle] \\
- 2J_2[\langle s_1.s_2\rangle + \langle s_1.s_3\rangle + \langle s_2.s_3\rangle + \langle s_4.s_5\rangle + \langle s_4.s_6\rangle + \langle s_5.s_6\rangle + \langle s_7.s_8\rangle \\
+ \langle s_7.s_9\rangle + \langle s_8.s_9\rangle + \langle s_{10}.s_{11}\rangle + \langle s_{10}.s_{12}\rangle + \langle s_{11}.s_{12}\rangle] \\
- 2J_3[\langle s_1.s_4\rangle + \langle s_1.s_6\rangle + \langle s_1.s_8\rangle + \langle s_1.s_9\rangle + \langle s_1.s_{10}\rangle + \langle s_1.s_{11}\rangle + \langle s_2.s_4\rangle \\
+ \langle s_2.s_5\rangle + \langle s_2.s_7\rangle + \langle s_2.s_9\rangle + \langle s_2.s_{11}\rangle + \langle s_2.s_{12}\rangle + \langle s_3.s_5\rangle + \langle s_3.s_6\rangle + \langle s_3.s_7\rangle \\
+ \langle s_3.s_8\rangle + \langle s_3.s_{10}\rangle + \langle s_3.s_{12}\rangle + \langle s_4.s_7\rangle + \langle s_4.s_8\rangle + \langle s_4.s_{10}\rangle + \langle s_4.s_{12}\rangle \\
+ \langle s_5.s_8\rangle + \langle s_5.s_9\rangle + \langle s_5.s_{10}\rangle + \langle s_5.s_{11}\rangle + \langle s_6.s_7\rangle + \langle s_6.s_9\rangle + \langle s_6.s_{10}\rangle \\
+ \langle s_6.s_{11}\rangle + \langle s_7.s_{10}\rangle + \langle s_7.s_{11}\rangle + \langle s_8.s_{11}\rangle + \langle s_8.s_{12}\rangle + \langle s_9.s_{10}\rangle + \langle s_9.s_{12}\rangle]
\end{aligned}
$$

Two phenyl phosphonate groups and a DMSO molecule facilitates the coupling between Mn pairs represented by J_1. The pair of Mn centres represented by J_2 are coupled *via* the pivalate groups (replaced with acetate groups in the model) and μ_3-OH$^-$ groups. J_3 describes the coupling between Mn centres solely bridged by the phenyl phosphonate groups. It is worth noting that the J_3 includes terms representing two types of pairs of Mn centres – ones with one Mn centre between them (e.g. Mn1 and Mn9 in **Figure 7.11 (b)**) and ones with two Mn centres between them (e.g. Mn1 and Mn11). The Mn-Mn distances for both sets are different but since the same group bridges both pairs, the coupling should be the same.

All the three coupling constants (J-values) calculated were found to be antiferromagnetic which is in line with the experimental observations (**Figure 7.9**). The coupling constants obtained were used to determine the relative energies of the different states that were modelled using DFT and these were found to be well reproduced (< 2% error). The coupling between Mn centres within the triangular units was found to be the strongest whereas the coupling (J_3) between Mn centre residing on the hexagonal faces was found to be quite weak (**Table 7.7**).

Table 7.7: Magnitude of J-values, the Mn-Mn distances between Mn centres associated with each J-value and the ligands bridging the Mn centres associated with each J-value.

J-value	Mn-Mn distance (Å)	Ligand Bridges	Coupling Strength (cm^{-1})
J_1	3.14 ± 0.01	Phenyl phosphonate, DMSO	-2.59 ± 0.23
J_2	3.54 ± 0.04	Pivalate, μ_3-OH$^-$	-6.48 ± 0.16
J_3	5.78 ± 0.05 / 6.68 ± 0.08	Phenyl phosphonate	-0.12 ± 0.05

The dependence of magnetic susceptibility on temperature could not be calculated using these coupling constants because the Hamiltonian matrix for this system is too big ($5^{12} \times 5^{12}$) for exact diagonalisation. To determine the ground state however, the coupling constants were used in conjunction with the average spin densities and the above mentioned Hamiltonian to determine the energy of all 2^{11} (=2048) possible spin states. The S = 0 state was indeed found to be the ground state in agreement with the experimental observations. The ferromagnetic state was calculated to

be ~1523 cm^{-1} higher in energy compared to the ground state and was determined to be the highest in energy (**Table 7.8**).

Table 7.8: The relative energy of the some of the key states out of the 2048 possible unique states for compound **7.1**. The energy of all the other states was found to be close (within 1 cm^{-1}) to one of the levels given in this table.

Configuration	Energy (cm^{-1})	Configuration	Energy (cm^{-1})
↑↓↑↓↑↓↓↑↓↑↑↓	0	↑↑↑↓↓↓↓↑↓↓↑	616
↑↓↑↓↑↓↓↑↑↑↑↓	57	↑↓↑↑↓↑↓↓↓↑↑↑	617
↑↓↑↓↑↓↓↓↑↑↑↓	109	↑↓↓↓↑↑↑↑↓↑↑	622
↑↓↑↑↑↓↓↑↑↑↑↓	114	↑↑↑↓↓↓↑↑↓↓↓↑	668
↑↓↑↓↑↑↑↓↑↑↑↓	119	↑↓↑↓↑↓↓↓↓↑↑↑	669
↑↓↑↑↑↓↓↓↑↑↑↓	161	↑↑↑↑↑↑↓↓↑↓↑↓	673
↑↓↑↓↑↓↑↓↑↑↑↓	166	↑↑↓↓↑↑↓↓↓↓↓↓	674
↑↓↑↓↓↑↑↓↑↑↑↓	171	↑↓↑↓↑↑↓↓↓↓↓↓	679
↑↓↑↓↑↓↑↓↑↓↓↑	208	↑↑↑↓↓↓↑↑↓↑↓↑	725
↑↓↑↓↑↓↑↑↓↓↓↑	213	↑↓↑↑↑↓↑↑↑↓↓↓	726
↑↓↑↑↑↓↑↓↑↑↑↓	223	↑↑↑↓↓↓↑↑↓↑↑↓	730
↑↓↑↑↓↑↑↓↑↑↑↓	228	↑↓↑↓↑↑↑↑↑↓↓↓	731
↑↓↑↓↑↑↓↑↑↓↑↑	233	↑↓↑↓↑↓↑↑↑↑↑↑	741
↑↓↑↓↑↓↑↓↓↓↓↑	265	↑↓↑↓↓↑↓↓↓↓↓↓	746
↑↓↑↑↓↓↑↓↑↑↑↓	275	↑↓↑↓↓↑↑↑↑↑↑↑	747
↑↓↑↓↑↑↓↓↓↑↑↓	280	↑↑↑↓↓↓↓↓↑↑↑↓	782
↑↓↑↑↓↑↑↑↓↓↓↑	285	↑↓↑↑↓↓↑↑↑↓↓↓	783
↑↓↑↑↑↓↑↓↓↓↓↑	322	↑↓↑↑↑↓↓↓↓↓↓↓	788
↑↓↑↓↑↑↓↓↓↑↓↓	337	↑↓↑↑↓↑↓↓↓↓↓↓	793
↑↓↑↑↑↓↓↓↓↑↑↓	389	↑↓↓↓↓↓↓↓↓↓↓↑	808
↑↓↓↓↑↑↓↓↓↑↓↓	394	↑↓↑↑↑↓↑↑↑↑↑↑	809
↑↓↑↓↑↓↑↑↑↑↑↓	399	↑↓↑↑↑↑↑↑↑↑↑↓	813
↑↓↑↓↑↓↑↑↑↓↓↑	441	↑↓↑↑↓↑↑↑↑↑↑↑	814
↑↓↑↓↑↑↓↓↓↓↓↑	446	↑↓↑↑↓↑↑↑↑↓↓↓	845
↑↓↑↑↓↑↓↓↓↓↓↑	451	↑↓↑↑↓↓↓↓↓↓↓↓	855
↑↓↓↓↑↓↓↓↓↑↓↓	461	↑↑↑↓↓↓↑↓↑↑↑	896
↑↓↑↑↑↓↑↑↑↑↑↓	462	↑↑↑↓↑↑↓↓↓↓↓	897
↑↑↓↑↓↑↑↑↑↓↑↑	466	↑↑↓↓↑↑↑↑↑↑↑	922
↑↓↑↓↑↑↑↑↑↑↑↓	467	↑↓↑↓↓↓↑↑↑↑↑	959
↑↑↑↑↓↓↓↓↑↓↑↓	492	↑↑↑↓↓↓↑↓↑↓↓↓	1010
↑↓↓↓↑↓↑↑↑↓↓↑	493	↑↓↑↑↑↑↓↓↓↓↓↓	1011
↑↓↑↓↑↓↓↓↓↓↓↑	503	↑↑↑↑↓↓↓↓↓↓↓	1073
↑↓↑↑↓↓↑↑↑↑↑↓	508	↑↓↑↓↓↓↓↓↓↓↓	1093
↑↓↑↓↓↑↑↑↑↑↑↓	513	↑↑↑↑↑↑↑↑↑↑↓	1165
↑↓↑↑↑↓↓↓↓↓↓↑	555	↑↓↑↑↑↑↑↑↑↑↑	1166
↑↓↑↓↓↑↓↓↓↑↑↑	560	↑↑↑↑↑↑↓↓↓↓↓	1234
↑↓↓↓↑↓↓↓↓↓↓↑	565	↑↑↑↓↓↑↑↑↑↑↑	1306
↑↓↑↓↑↑↑↑↓↑↑	575	↑↑↑↑↑↑↑↑↑↑↑	1523
↑↓↑↑↓↑↑↑↑↑↓	576		

7.1.5 Electrochemical studies

To be consistent with the methodology employed and described in chapter 6, the electrochemical behaviour of compound **7.1** was investigated using modified carbon paste electrodes. The preparation of these electrodes requires dispersing compound **7.1** in commercially available carbon paste. All experiments were carried out in potassium phosphate buffer at pH 7.2 (KPi, 50 mM) using KNO_3 (1 M) as electrolyte. Cyclic voltammetry of compound **7.1** was performed at a scan rate of 50 mV/s which led to a strong catalytic oxidation wave (**Figure 7.12**).

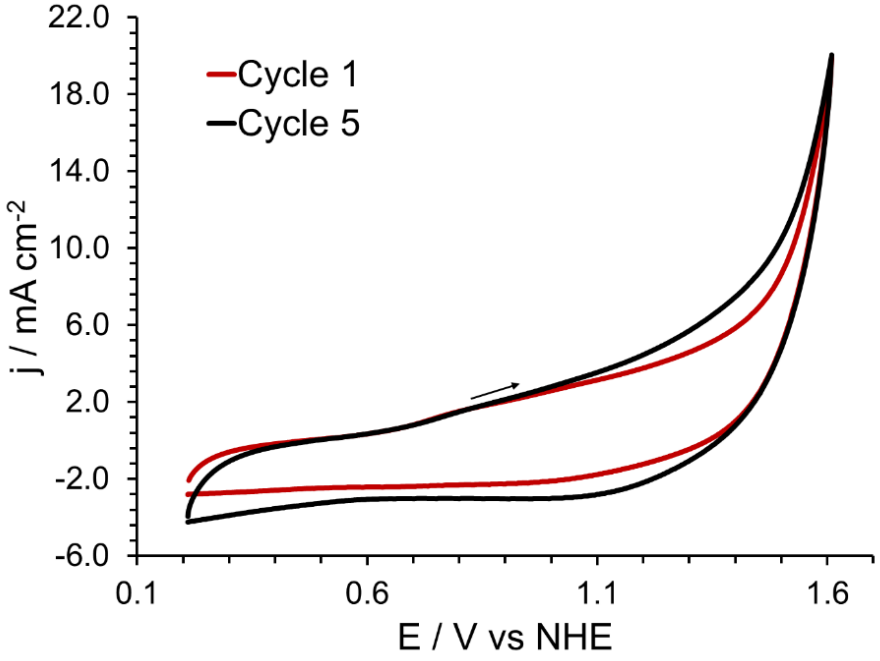

Figure 7.12: Cyclic voltammograms for compound **7.1** (40 wt-% loading) in a KP*i* buffer solution at pH 7.2.

To study the kinetic profile, linear sweep experiments with the catalyst loading varying between 10-40 wt-% were performed using a rotating disk electrode (**Figure 7.13**). To ensure steady state conditions, these experiments were conducted at a scan rate of 1 mV/s. Loadings higher than 40 wt-% make the blends brittle and unsuitable for obtaining reproducible results and thus, all further experiments were carried out with 40 wt-% loading. It can be seen that higher loadings lead to higher current densities and lower overpotentials (**Figure 7.14**). The onset potential was found to be 251 mV with 40 wt% catalyst loading (**Table 7.9**). The Tafel slope was found to remain constant with loadings (~320-340 mV dec^{-1}) indicating similar kinetics (**Figure 7.14 (b)** and **Table 7.9**). The lower Tafel slope for 30 wt-% loading maybe a potential outlier but further work will be required to establish that. The Tafel slope above 600 mV for 40 wt-% loading was found to be 630 mV dec^{-1} and not been shown in **Figure 7.14 (b)**.

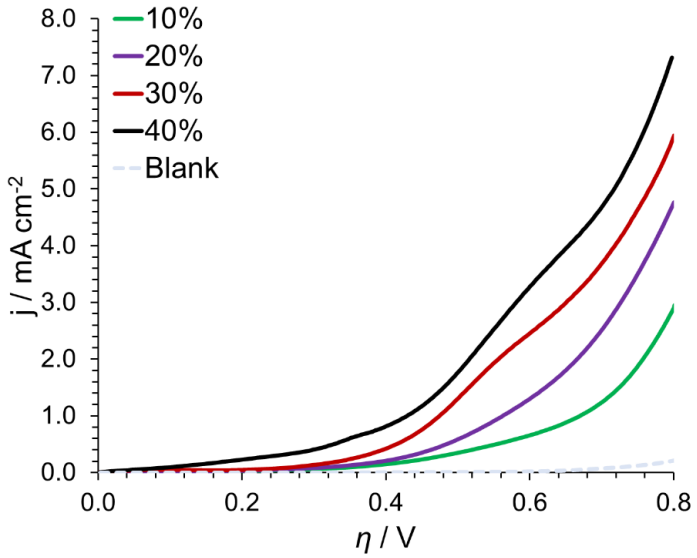

Figure 7.13: Linear sweep voltammograms for compound **7.1** at different loadings.

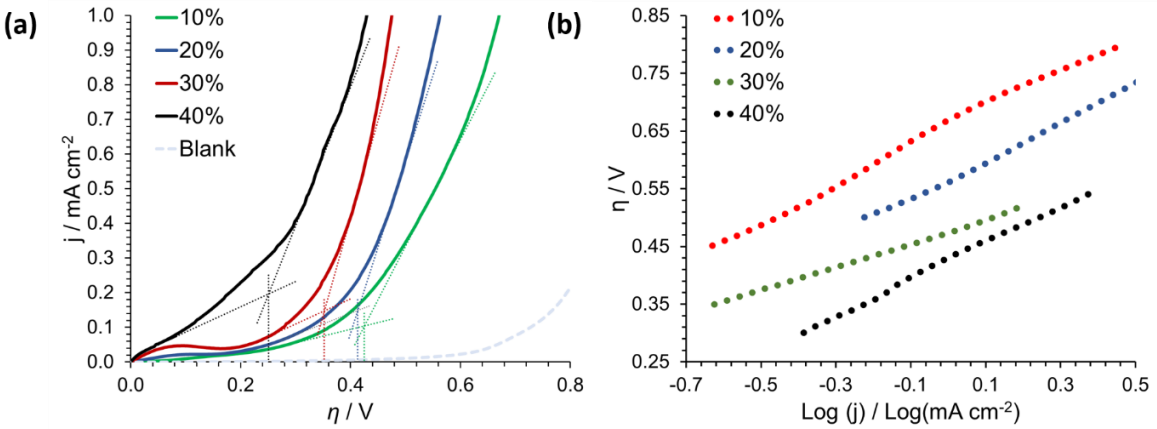

Figure 7.14: (a) The determined onset potentials and **(b)** the Tafel slope for compound **7.1** at different loadings.

Table 7.9: The onset overpotential and Tafel slope for water oxidation with compound **7.1** at different loadings

Loading	Onset overpotential (mV)	Tafel slope (mV dec^{-1})
10%	425	335
20%	413	338
30%	352	203
40%	251	317

To determine the electrochemical behaviour of compound **7.1** over extended periods, successive linear sweep experiments were performed (**Figure 7.15 (a)**). The first few cycles show large variations and cycles after the 10^{th} one are almost coincident. It was observed that initially the Tafel slope (**Figure 7.15 (b)**) increases up to 637 mV dec^{-1} for the 9^{th} cycle after which it decreases and goes down to 305 mV dec^{-1} (cycle 40) in the overpotential range of 300-550 mV. After cycle 40, the

electrochemical behaviour around 300 mV of overpotential changes again and in the 300-550 mV overpotential range a non-linear behaviour was observed due to which after the 40th cycle, the reported Tafel slope has been calculated in the 400-600 mV overpotential range.

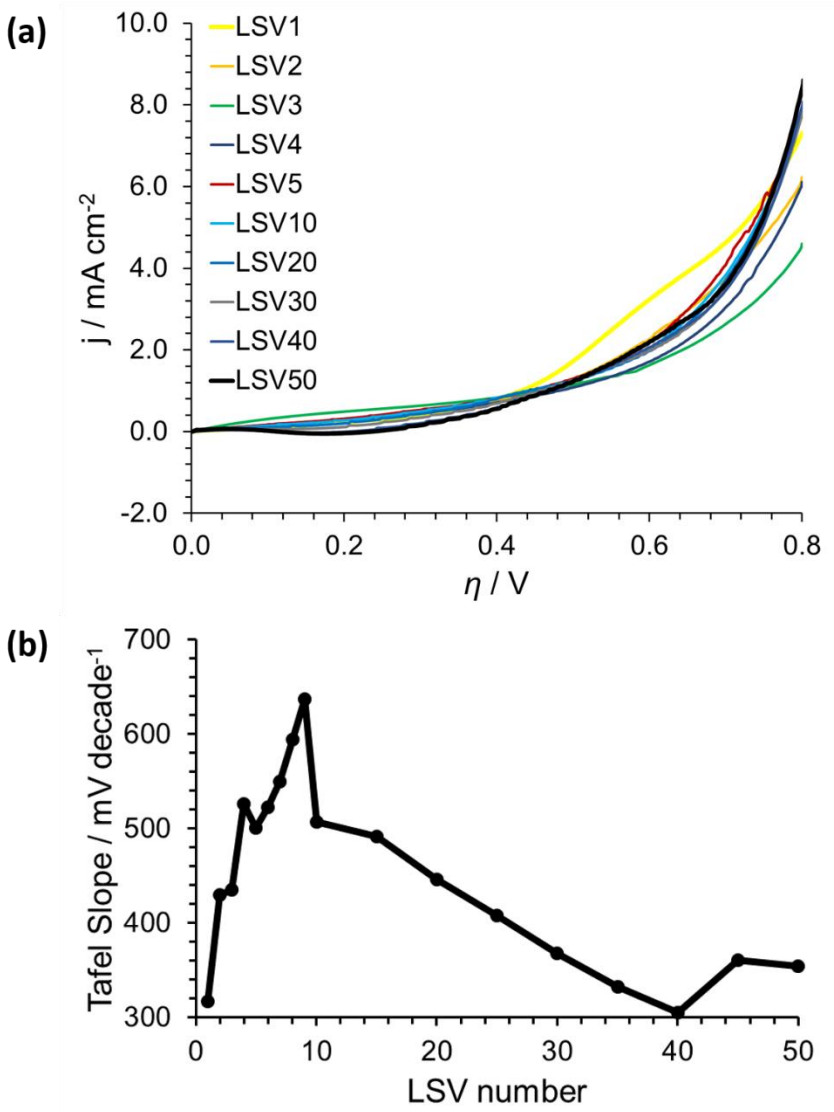

Figure 7.15: (a) Successive linear sweep voltammograms for compound **7.1** in KP*i* buffer solution at pH 7.2 and **(b)** the Tafel slope observed for the different cycles calculated in the 300-500 mV overpotential range. Note that the Tafel slopes for cycles 45 and 50 have been calculated in the 400-600 mV overpotential range.

To obtain insight into the stability of compound **7.1**, chronoamperometry (CA) experiment was conducted for 16 hours at an applied potential of 1.56 V (vs NHE). It was observed that the current density initially decreases and then starts increasing. A maximum in the current density is achieved in ~3.5 hours after which it starts decreasing again (**Figure 7.16**). The CA was followed up with cyclic voltammetry and linear sweep voltammetry and a broad new peak can be observed at ~1.04 V (vs NHE) (**Figure 7.17 (a)**) along with some additional redox activity that still occurs at higher potential (**Figure 7.17 (b)**).

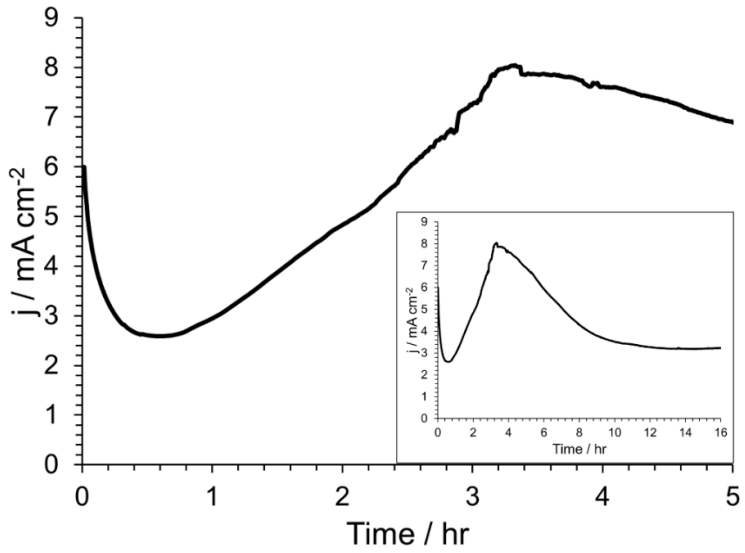

Figure 7.16: CA data for compound **7.1** at 1.56 V *vs* NHE in KP*i* buffer solution at pH 7.2 for the first 5 hours and the entire 16 hour duration (inset).

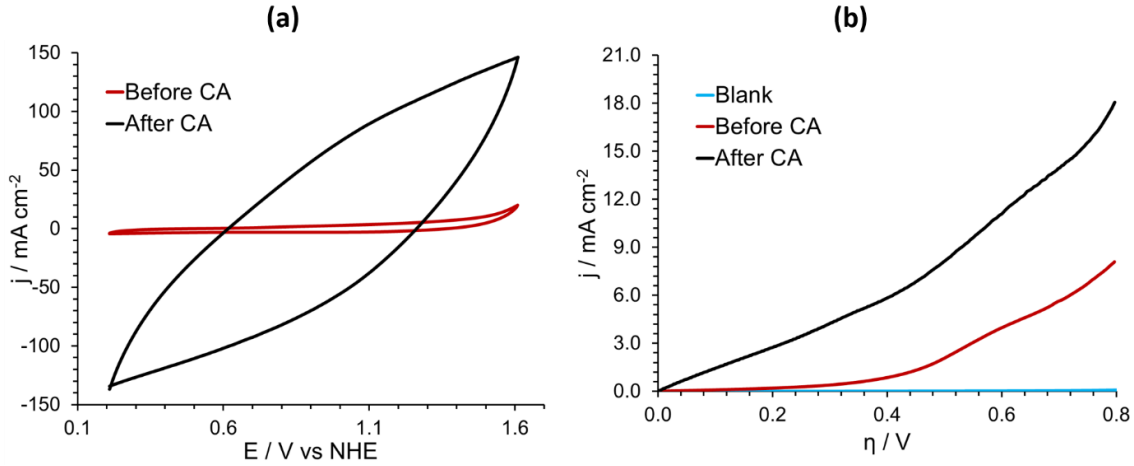

Figure 7.17: (a) Cyclic voltammograms and **(b)** linear sweep voltammograms for compound **7.1** in KP*i* buffer solution at pH 7.2 before and after CA.

The possibility of leaching during CA was also investigated. For this purpose, linear sweep voltammetry using a rotating disk glassy carbon electrode was performed before and after chronoamperometry using the same buffer solution. It was observed that the current density increases from 0.09 mA cm^{-2} to 0.41 mA cm^{-2} which suggests that leaching does occur (**Figure 7.18**). The current density however, is still significantly low compared to that observed for compound **7.1**. The structure of this dodecanuclear complex suggests that this complex needs to be activated before it can catalyse water oxidation since there are no water molecules bound to the Mn centres. Among DMSO molecules, the pivalate groups and the phosphonate groups, it is more likely that the DMSO molecules get replaced with water during water oxidation because pivalate and phosphonate groups are chelating and hence, strongly bound. Such substitution may explain the electrochemical behaviour observed above 500 mV of overpotential with 40 wt-% catalyst loading

(**Figure 7.13**). This structural transformation may also be the cause of the large variations observed between the first and the 10th cycle of the successive linear sweep experiment (**Figure 7.15 (a)**). This is further indicated by the initial increase in the Tafel slope up to the 9th cycle. Cycles after the 10th one are almost coincident indicating that the transformation is complete. The Tafel slope during these cycles decreases suggesting higher activity which is to be expected for a system with water molecules attached to it. Since the Tafel slopes have been calculated in the same overpotential range, it confirms that compound **7.1** transforms to a different species which is more active in the same overpotential range. After the 40th cycle, the Tafel slope increases again indicating the decomposition of the transformed species.

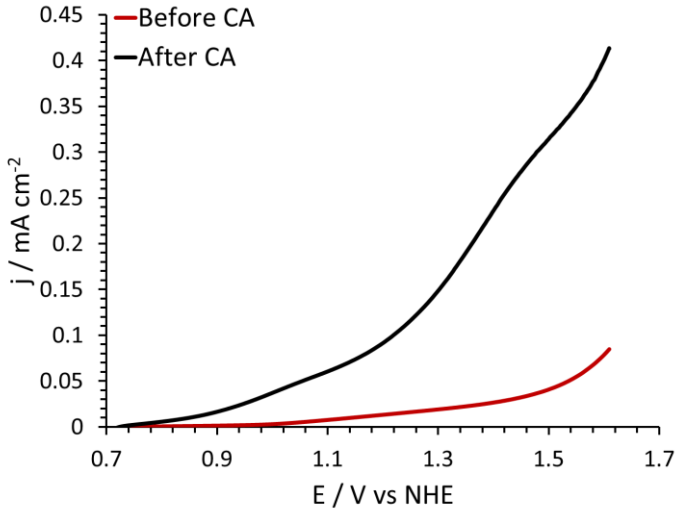

Figure 7.18: Linear sweep voltammograms using glassy carbon electrodes of the buffer solution before and after chronoamperometry.

The data obtained from the CA experiment is in agreement with our observations in the successive linear sweep voltammetry experiments. An initial decrease is observed due to capacitance effects (**Figure 7.16**).[632] The applied potential results in the transformation of compound **7.1** to an active species, the concentration of which reaches a maximum in ~3.5 hours corresponding to the peak observed in **Figure 7.16**. The transformed species then decomposes to a less active species with time as indicated by the decrease in the current density during CA. Cyclic voltammetry after CA reveals a broad new peak at ~1.04 V (vs NHE) (**Figure 7.17 (a)**) which indicates that the decomposed species may be Mn_2O_3.[628] The Tafel slope after CA was found to be 790 mv dec^{-1} above 400 mV of overpotential implying poor kinetics of the decomposed species.

These results demonstrate that the initial OER activity is derived from an active species structurally related to compound **7.1** that has water molecules bound to the Mn sites. We propose that this species is essentially compound **7.1** with the DMSO molecules replaced with water molecules. This species has been found to be active at overpotentials as low as 251 mV which is much lower compared to compound **6.3**.

7.2 $[Mn^{II}_6Mn^{III}_9(\mu_3\text{-}O)_4((CH_3)_3CCO_2)_{11}((CH_3)_3CCO_2H)(C_6H_5PO_3)_6(\mu\text{-}CH_3O)_6(\mu_3\text{-}CH_3O)_2(CH_3OH)_5]$ (7.2)

To investigate whether the counterion of the Mn(II) salt can play a role in stabilising different end products, the ratio of Mn^{II}:Mn^{VII} was varied. In low concentrations and absence of a Mn^{II} salt, all crystallisation attempts failed although a red solution was obtained each time indicating the possible reduction of Mn(VII) *via* the excess pivalic acid. By refluxing $KMnO_4$, $Mn(CH_3COO)_2{\cdot}4H_2O$, phenylphosphonic acid, pivalic acid and L(-)-proline in the ratio 1:4:2.5:20:1, in a mixture of CH_3CN and CH_3OH, compound **7.2** was obtained. The crystals of this compound were obtained within a week and were characterised by single crystal X-ray diffraction experiment.

7.2.1 Structural description

Compound **7.2** crystallises in a trigonal crystal system and the structure was solved in the space group $R\bar{3}$. This complex contains a pentadecanuclear complex $[Mn_{15}(\mu_3\text{-}O)_4((CH_3)_3CCO_2)_{11}((CH_3)_3CCO_2H)(C_6H_5PO_3)_6(\mu\text{-}CH_3O)_6(\mu_3\text{-}CH_3O)_2(CH_3OH)_5]$ (**Figure 7.19 (a)**) and the asymmetric unit of this complex contains a third of the complex (**Figure 7.19 (b)**). The core of this complex can essentially be described as an augmented truncated tetrahedron. An augmented truncated tetrahedron is a solid in which a triangular cupola unit is attached to one of the hexagonal faces of a truncated tetrahedron (**Figure 7.20**). The overall structure is stabilised by four $\mu_3\text{-}O^{2-}$, two $\mu_3\text{-}CH_3O^-$ groups and six phenylphosphonate ligands, six methoxy and eleven pivalate groups. The three hexagonal and pentagonal faces are each capped by phenylphosphonate groups. The phosphonates on the hexagonal faces bind in 6.222 mode while those on the pentagonal faces bind in 5.221 mode. The phosphorus centre on the hexagonal faces is ~0.68 Å above the Mn plane while that on the

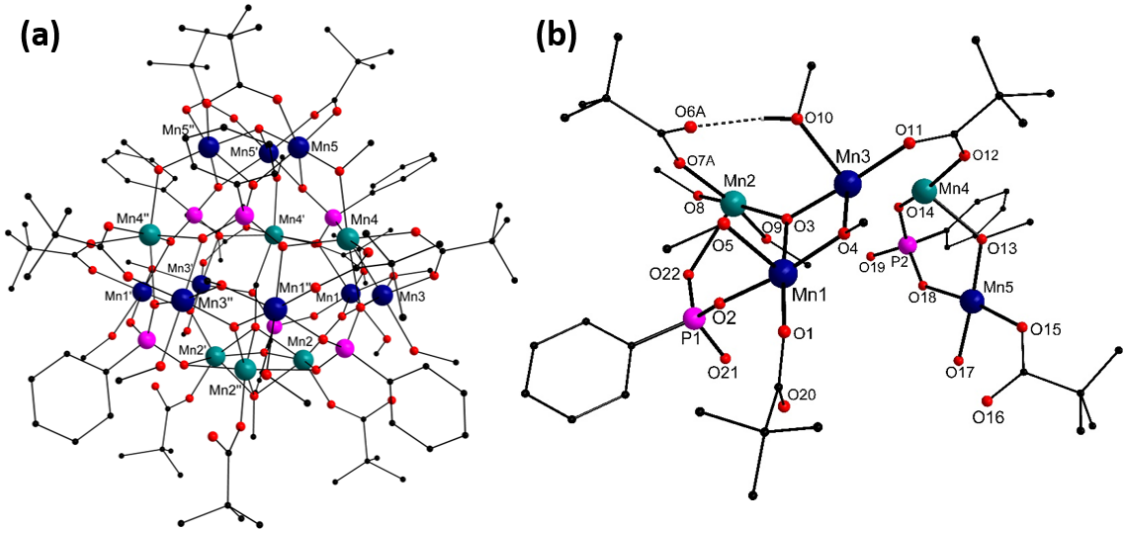

Figure 7.19: (a) Crystal structure and **(b)** the asymmetric unit of the pentadecanuclear compound **7.2**. The hydrogen bonds are shown with dashed lines. Colour scheme: Mn^{II} (teal), Mn^{III} (dark blue), P (pink), C (black) and O (red). All hydrogen atoms (grey) except those of the $\mu_3\text{-}OH^-$ group have been removed for clarity.

pentagonal faces is ~1.64 Å above the Mn plane. The vertices of the hexagonal faces comprise of Mn1, Mn3, Mn4 and Mn5 (and their symmetry equivalents) and all hexagonal faces are joined at the $\{Mn_3\}$ triangular face formed by Mn5 and its symmetry equivalents. The vertices of the pentagonal faces comprise of Mn1, Mn2, Mn3 and Mn4 along with their symmetry equivalents and are joined at the $\{Mn_3\}$ triangular face formed by Mn2 and its symmetry equivalents.

The triangular face formed by Mn5 is centred around a μ_3-O^{2-} (O17) group while that formed by Mn2 is centred around two μ_3-CH_3O^- (containing O8 and O9) groups. O17 lies ~0.68 Å above the $\{Mn_3\}$ plane and O8 and O9 are ~1.18 Å below and above the $\{Mn_3\}$ plane respectively. The other triangular faces formed by Mn1, Mn2 and Mn3 are centred around μ_3-O^{2-} groups (O3 and its symmetry equivalents) and these faces lie between the pentagonal faces. O3 on the other hand, lies in the plane of the Mn centres. Bond valence sum analysis reveals that Mn2 and Mn4 are in +II oxidation state while the others are in +III oxidation state (**Table 7.10**) and confirms that all the O atoms bound only to Mn centres are μ_3-O^{2-} groups (**Table 7.11**).

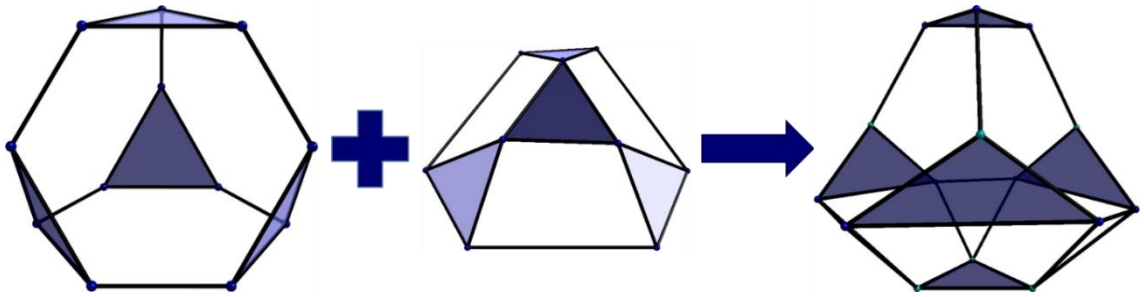

Figure 7.20: The core structure of compound **7.2** consists of a triangular cupola fused to an truncated tetrahedron resulting in the augmented truncated tetrahedron geometry. Mn^{II} and Mn^{III} for compound **7.2** are shown in teal and dark blue respectively.

The octahedral coordination environment of Mn1 comprises of a μ_3-O^{2-} group (O3) and O-donors from two phosphonates (O2 and O14'), a μ-CH_3O^- group (O4), a partially (67 %) occupied methanol (O5), a partially occupied (33 %) pivalic acid group and a pivalate group (O1) with the Jahn-Teller axis oriented along the O-donor of one of the phosphonates (O14) and the disordered site occupied partially by the O-donors of the methanol and pivalic acid groups. The octahedron of Mn1 shares a vertex with that of the Mn(II) centres (via O3 and O14) and an edge (involving O3 and O4) with that of Mn3 (**Figure 7.21 (a)**). The Mn-O distances along the Jahn-Teller axis are ~2.3 Å while those perpendicular to it are ~1.9 Å (**Table 7.11**). The octahedral geometry is slightly distorted as can been seen from the continuous shape measure value, the angle variance and the distortion index (**Table 7.12**). The distortion is because of the ligand constraints imposed by the geometry of the complex as indicated by the bond angles (**Table 7.13**).

Mn2 also lies in an octahedral coordination environment which is fulfilled by a μ_3-O^{2-} group (O3), and O-donors from two phosphonates (O22 and O22''), two μ_3-CH_3O^- groups (O8 and O9) and a pivalate group (O7A) (**Figure 7.21 (b)**) with the Mn-O bond lengths varying between 2.0 and 2.3 Å

(**Table 7.10**). The octahedron of Mn2 shares a face (containing O8, O9 and O22) with the octahedron of its symmetry equivalents and a vertex (O3) with that of Mn1 and Mn3.

Table 7.10: Key Mn-O and Mn-Mn bond lengths and bond valence sum for each Mn centre for compound **7.2**.

Mn centre	Coordinating atom	Bond Distance (Å)	BVS	Assigned oxidation state
Mn1	O1	1.929(9)	3.263	+III
	O2	1.878(8)		
	O3	1.869(8)		
	O4	1.891(8)		
	O5	2.326(10)		
	O14’	2.289(6)		
Mn2	O3	2.051(9)	2.109	+II
	O8	2.157(6)		
	O9	2.161(6)		
	O22’’	2.205(8)		
	O7A	2.061(8)		
	O7B	2.009(6)		
	O22	2.305(9)		
Mn3	O3	1.866(8)	3.137	+III
	O4	1.932(8)		
	O10	2.184(8)		
	O11	1.956(9)		
	O19’	2.215(7)		
	O21’’	1.975(8)		
Mn4	O12	2.147(8)	1.854	+II
	O13	2.152(6)		
	O14	2.163(7)		
	O19’	2.218(7)		
	O20’’	2.188(8)		
	O21’’	2.329(7)		
Mn5	O13	1.871(6)	3.212	+III
	O15	1.956(7)		
	O16’’	2.115(7)		
	O17	1.874(4)		
	O18’	2.273(6)		
	O18	2.006(6)		

Metals	Distance (Å)	Metals	Distance (Å)
Mn1-Mn2	3.496(3)	Mn2-Mn3	3.585(3)
Mn1-Mn3	2.874(5)	Mn3-Mn4	3.330(3)
Mn1-Mn4'	3.663(3)	Mn4-Mn5	3.545(2)
Mn2-Mn2'	3.129(4)	Mn5-Mn5'	3.024(4)

’1+Y-X,1-X,+Z; ”1-Y,+X-Y,+Z

Mn3 is bound to a μ_3-O^{2-} group (O3) and O-donors of a μ-CH_3O^- group (O4), a methanol (O10), a pivalate group (O11) and two phosphonate groups (O19’ and O21’’) and its octahedron shares a vertex with that of Mn2 and Mn4 (via O3 and O21 respectively) besides sharing an edge with Mn1 (**Figure 7.21 (c)**). The Jahn-Teller axis of Mn3 is oriented along the O-donors of one of the

phosphonate (O19') and the methanol group (O10) and is parallel to that of Mn1. The Mn-O bond along the Jahn-Teller axis is ~2.2 Å but varies between 1.9 and 2.0 Å otherwise (**Table 7.10**).

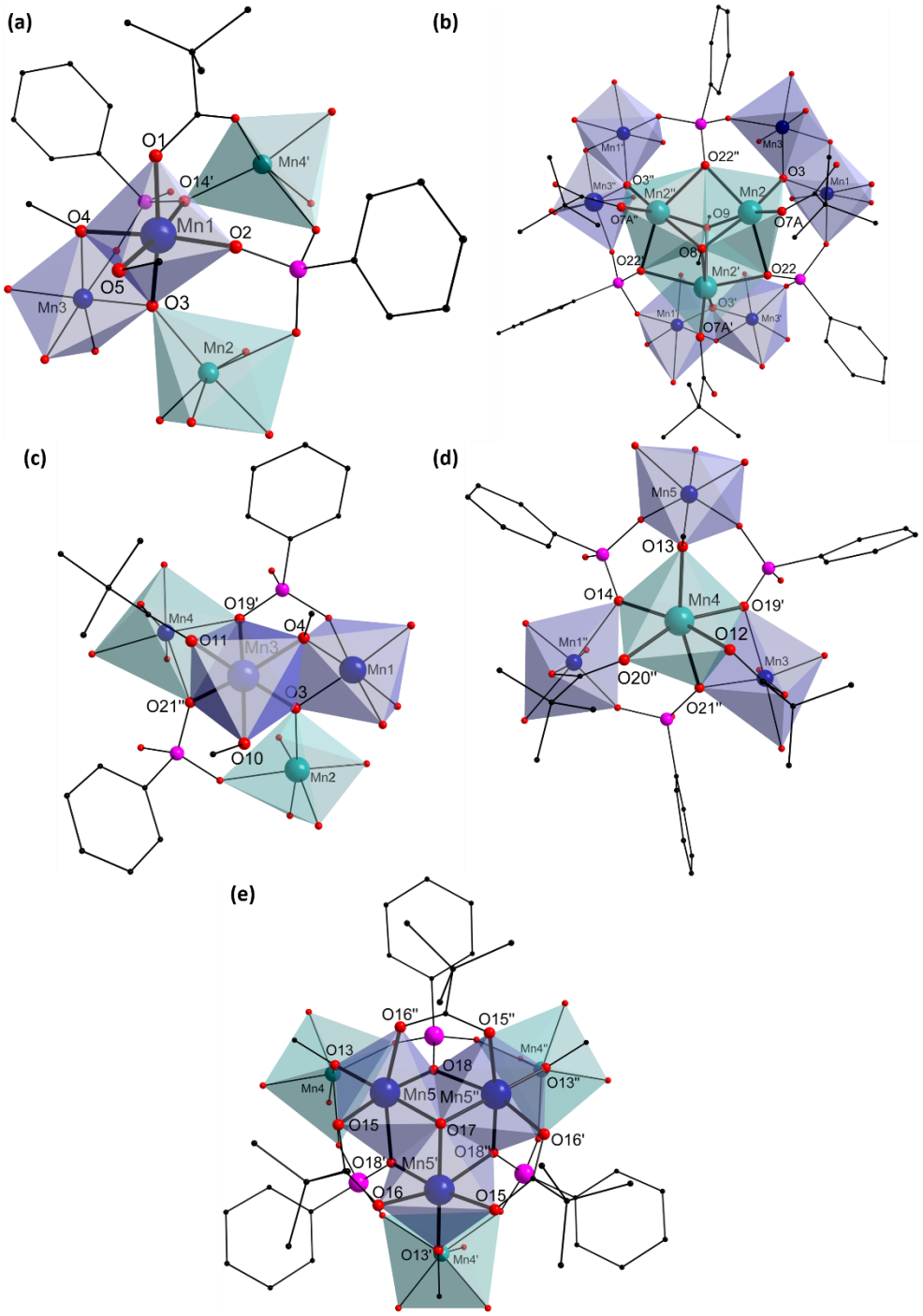

Figure 7.21: Coordination environment of **(a)** Mn1, **(b)** Mn2, **(c)** Mn3, **(d)** Mn4 and **(e)** Mn5 in compound **7.2**. Colour scheme: Mn^{II} (teal), Mn^{III} (dark blue), P (pink), C (black) and O (red).

The coordination behaviour of Mn4 is similar to that of Mn2 and it is bound to the O-donors of three phosphonates (O14, O19' and O21''), two pivalates (O12 and O20'') and a μ-CH_3O^- group (O13) (**Figure 7.21 (d)**). The octahedral environment of Mn4 however, is more distorted compared to that of Mn2 and is the most distorted coordination environment in this complex based on the

continuous shape measure values (**Table 7.12**).The octahedron of Mn4 shares a vertex with those of Mn1 and Mn5 (O20 and O13 respectively), and an edge with Mn3 (O12 and O19).

The octahedral coordination environment of Mn5, of all the Mn centres in this complex, is the least distorted (**Table 7.12**) and is fulfilled by a μ_3-O^{2-} group (O17) and O-donors of two phosphonates (O18 and O18'), two pivalates (O15 and O16) and a μ-CH_3O^- group (O13) (**Figure 7.21 (e)**). The octahedron of Mn5 shares an edge (containing O17 and O18) with that of its symmetry equivalents besides sharing a vertex with the octahedron of Mn4 (O13). The Jahn-Teller axis in this case is along the O-donors of a phosphonate group (O18) and a pivalate group ($O16^1$) with the Mn-O distance lying between 2.1 and 2.3 Å. The Mn-O distances in the plane perpendicular to the Jahn-Teller axis vary between 1.9 and 2.0 Å (**Table 7.10**).

Table 7.11: BVS analysis for O atoms and their assigned protonation state in compound **7.2**.

Atom	BVS	Assignment
O3	1.990	μ_3-O^{2-}
O17	2.205	μ_3-O^{2-}

Table 7.12: Continuous shape measure values, angle variance and distortion indices (using the ideal octahedral geometry as a reference) for each Mn centre for compound **7.2**.

Mn centre	Continuous shape measure value	Angle variance (σ^2)	Distortion Index
Mn1	1.370	30.74	0.0498
Mn2	1.797	155.86	0.1219
Mn3	1.228	36.84	0.0555
Mn4	2.442	116.8	0.0881
Mn5	1.021	41.10	0.0542

Table 7.13: Selected bond angles for compound **7.2**.

Bond	Bond Angle (°)	Bond	Bond Angle (°)
O3-Mn1-O4	81.1(4)	O21''-Mn3-O19'	79.5(3)
O1-Mn1-O5	82.0(4)	O3-Mn3-O4	80.1(4)
O2-Mn1-O5	86.0(4)	O11-Mn3-O10	85.7(4)
O4-Mn1-O5	86.4(4)	O3-Mn3-O10	87.0(4)
O3-Mn1-O14'	88.5(3)	O4-Mn3-O19'	88.4(3)
O2-Mn1-O1	89.0(3)	O3-Mn3-O19'	92.1(3)
O4-Mn1-O14'	90.2(3)	O4-Mn3-O11	92.2(3)
O1-Mn1-O14'	92.7(3)	O11-Mn3-O21''	92.3(3)
O4-Mn1-O1	93.0(4)	O4-Mn3-O10	94.8(3)
O3-Mn1-O5	96.5(4)	O11-Mn3-O19'	95.6(3)
O3-Mn1-O2	96.7(4)	O3-Mn3-O21''	96.9(3)
O2-Mn1-O14'	97.7(3)	O21''-Mn3-O10	97.1(3)
O2-Mn1-O4	171.8(3)	O4-Mn3-O21''	167.5(3)
O14'-Mn1-O5	173.5(4)	O3-Mn3-O11	168.9(4)
O3-Mn1-O1	174.0(4)	O10-Mn3-O19'	176.4(3)
O8-Mn2-O9	66.4(3)	O19'-Mn4-O21''	72.4(2)
O8-Mn2-O22	77.1(2)	O12-Mn4-O20''	80.1(3)
O9-Mn2-O22	77.43(19)	O14-Mn4-O20''	83.0(3)
O8-Mn2-O22''	79.3(2)	O12-Mn4-O21''	84.6(3)

Bond	Bond Angle (°)	Bond	Bond Angle (°)
O9-Mn2-O22''	79.6(2)	O12-Mn4-O19'	85.1(3)
O7A-Mn2-O8	91.2(4)	O13-Mn4-O14	89.6(2)
O3-Mn2-O22''	95.0(5)	O13-Mn4-O19'	89.8(2)
O7A-Mn2-O22	95.3(3)	O12-Mn4-O13	91.0(3)
O3-Mn2-O9	98.9(3)	O20''-Mn4-O21''	93.1(3)
O7A-Mn2-O22''	100.2(5)	O14-Mn4-O21''	99.8(2)
O3-Mn2-O7A	103.6(4)	O13-Mn4-O20''	103.4(3)
O3-Mn2-O22	103.7(3)	O14-Mn4-O19'	112.1(2)
O22''-Mn2-O22	152.2(3)	O20''-Mn4-O19'	160.2(3)
O7A-Mn2-O9	157.3(4)	O13-Mn4-O21''	161.9(2)
O3-Mn2-O8	165.0(3)	O12-Mn4-O14	162.8(3)
O17-Mn5-O18'	76.4(3)	O13-Mn5-O18	93.6(3)
O17-Mn5-O18	83.4(3)	O13-Mn5-O15	93.8(3)
O17-Mn5-O16''	86.2(3)	O13-Mn5-O16''	96.9(3)
O18-Mn5-O18'	86.5(3)	O13-Mn5-O18'	100.3(2)
O18-Mn5-O16''	88.7(3)	O16''-Mn5-O18'	162.4(3)
O17-Mn5-O15	89.0(3)	O15-Mn5-O18	172.0(3)
O15-Mn5-O18'	89.1(2)	O13-Mn5-O17	175.7(4)
O15-Mn5-O16''	93.5(3)		

The system packs tightly without any voids for solvents. The packing arrangement is stabilised by π-π stacking of the phenyl rings belonging to the phenylphosphonate groups which is evident from the packing diagram along the b-axis (**Figure 7.22**). Along the crystallographic c-axis the complex packs in an interpenetrated honeycomb type arrangement with a screw axis running along it.

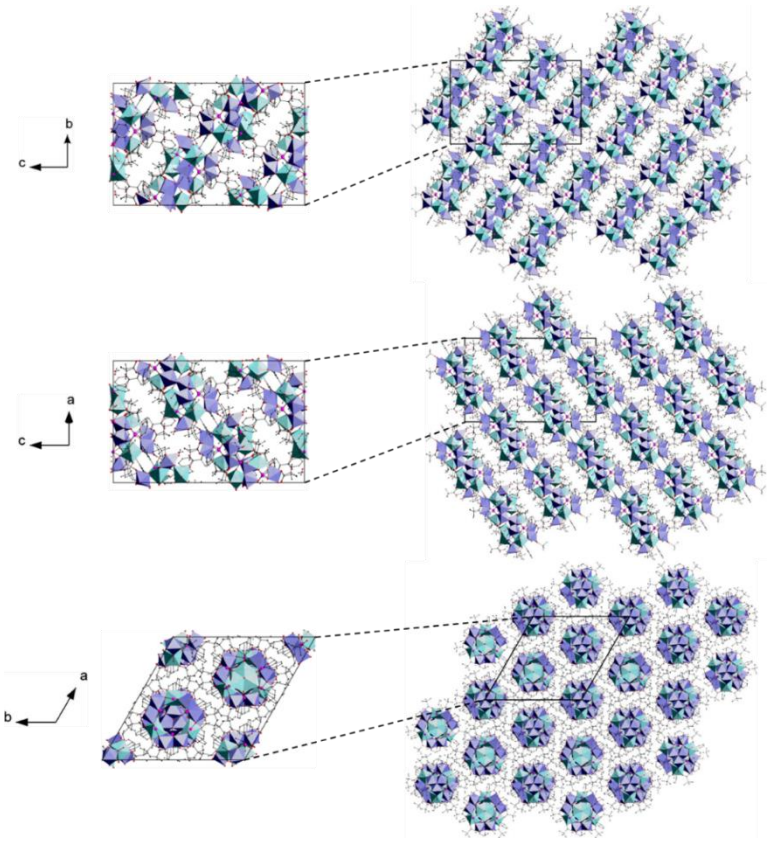

Figure 7.22: Packing diagram for compound **7.2**. Colour scheme: Mn^{II} (teal), Mn^{III} (dark blue), P (pink), C (black) and O (red). All hydrogen atoms have been removed for clarity.

7.2.2 Physicochemical Characterisation

The infrared spectrum of compound **7.2** (**Figure 7.23**) is consistent with the structure determined by XRD. The vibrational mode at 3440 cm^{-1} corresponds to the –OH stretching vibrations of the hydrogen bonded methanol molecules.[633, 634] The signal centred at 2930 cm^{-1} can be attributed to the C-H vibrations in the organic ligands.[617] The vibrational modes at 1416 and 1540 cm^{-1} correspond to the symmetric and asymmetric stretching modes of the carboxylate groups and the gap between the two peaks is in agreement with that observed for bidentate bridging carboxylate groups.[618] Additional peaks in the same range are due to the vibrations of the organic moieties – both aliphatic and aromatic.[617] The strong peak at 980 cm^{-1} range corresponds to the stretching of the phosphonate group.[621-623]

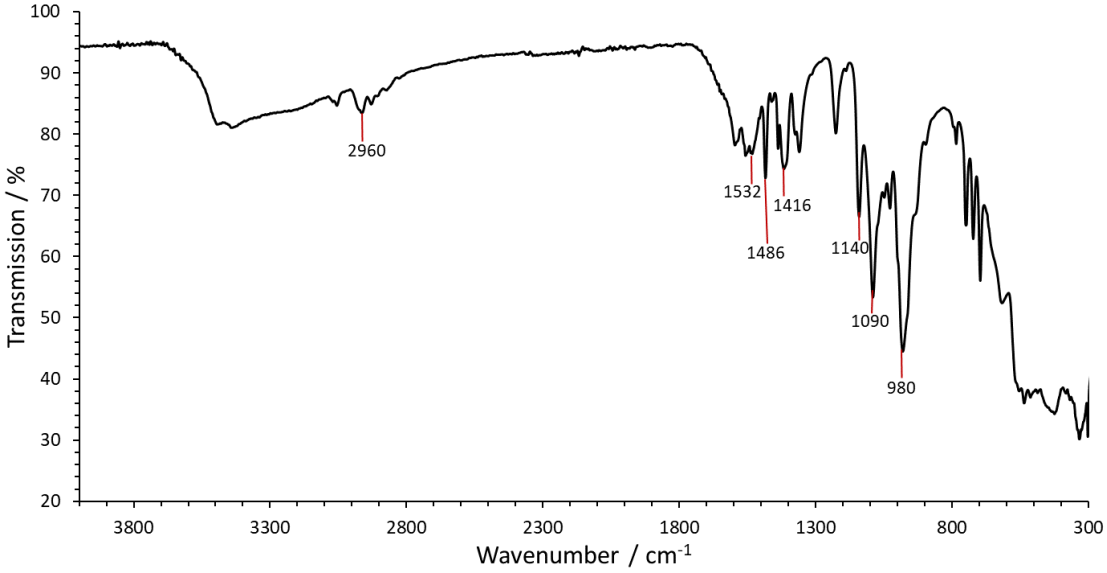

Figure 7.23: Infrared spectrum of compound **7.2**.

Further characterisation of this compound was not carried out due to poor yields. A more detailed characterisation of an asymmetric analogue of this complex however, has been described in the following discussion.

7.3 $[Mn^{II}_5Mn^{III}_{10}(\mu_3\text{-}O)_4((CH_3)_3CCO_2)_{7.15}(CH_3CO_2)_{4.85}(C_6H_5PO_3)_6(\mu\text{-}CH_3O)_6(\mu_3\text{-}CH_3O)_2(CH_3OH)_5]\cdot 2CH_3CN\cdot CH_3OH$ (7.3)

Refluxing $KMnO_4$, $Mn(CH_3COO)_2\cdot 4H_2O$, pivalic acid and acetic acid in a ratio of 1:5:10:20 in presence of phenylphosphonic acid and 2,6-pyridinedimethanol in a mixture of CH_3CN and CH_3OH leads to the formation of compound **7.3**. Crystals of compound **7.3** were obtained within a day and they were characterised by single crystal X-ray diffraction.

7.3.1 Structure description

Compound **7.3** crystallises in a trigonal crystal system and the structure solution was obtained in the space group $R\bar{3}$. This compound contains a pentadecanuclear complex, $[Mn^{II}_5Mn^{III}_{10}(\mu_3\text{-}O)_4((CH_3)_3CCO_2)_{7.15}(CH_3CO_2)_{4.85}(C_6H_5PO_3)_6(\mu\text{-}CH_3O)_6(\mu_3\text{-}CH_3O)_2(CH_3OH)_5]$ (**Figure 7.24**) and the asymmetric unit of this complex contains the whole molecule. The core of this complex can be described as an augmented truncated tetrahedron and is very similar to that of compound **7.2**. Mn1-Mn3 here can be compared with Mn2 and its symmetry equivalents of compound **7.2** while Mn4-Mn9 resemble Mn1 and Mn3, and their symmetry equivalents of compound **7.2**. In the same way, Mn10-Mn12 and Mn13-Mn15 can be considered equivalent to Mn4 and Mn5 of compound **7.2** respectively. The P centres of the phosphonate groups are ~0.69 and 1.67 Å above the hexagonal and pentagonal faces respectively, similar to compound **7.2** and the μ_3-O^{2-} and μ_3-CH_3O^- groups also reside in positions similar to those observed in compound **7.2**. Some of the sites occupied by pivalate ligands in compound **7.2** have been replaced with acetate ligands – partially in some cases and completely in others.

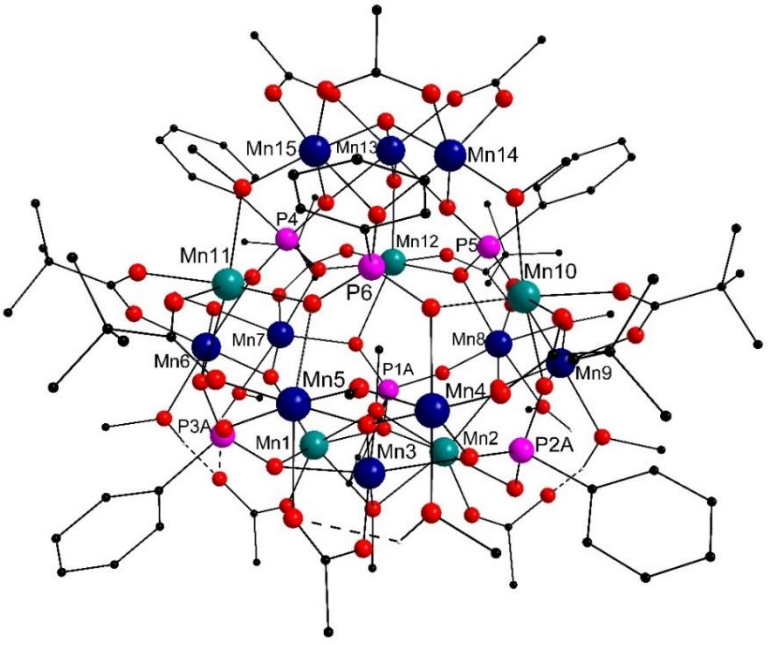

Figure 7.24: Crystal structure of the dodecanuclear compound **7.3**. For clarity, only the parts with the highest occupancies are shown. Colour scheme: Mn^{II} (teal), Mn^{III} (dark blue), P (pink), C (black) and O (red). All hydrogen atoms (grey) except those of the μ_3-OH^- group have been removed for clarity.

Unlike compound **7.2** however, the structure was found to be heavily disordered. The phosphonate groups binding to the pentagonal faces in 5.221 mode are disordered in two and three positions with roughly equal occupancies. There is additional disorder on the *tert*-butyl and methanol groups. Due to the disorder, the sharing of octahedra cannot be uniquely defined and thus has not been attempted. Considering the structural similarities however, the sharing should be similar to that observed in compound **7.2**.

Although there are only minor structural differences between compound **7.3** and **7.2** in terms of the coordination environment of Mn centres, bond-distances (**Table 7.14**) and bond angles (**Table 7.15**), the electronic structure shows some notable differences as indicated by bond valence sum analysis (**Table 7.14** and **Table 7.16**). Unlike compound **7.2** where nine Mn centres are in oxidation state +III, compound **7.3** contains ten Mn centres that reside in +III oxidation state. Here Mn1, Mn2 and Mn10-Mn12 are in +II oxidation state while the rest are in the +III oxidation state. Mn3 serves as the additional Mn centre exhibiting the higher oxidation state which lowers the overall symmetry of the molecule.

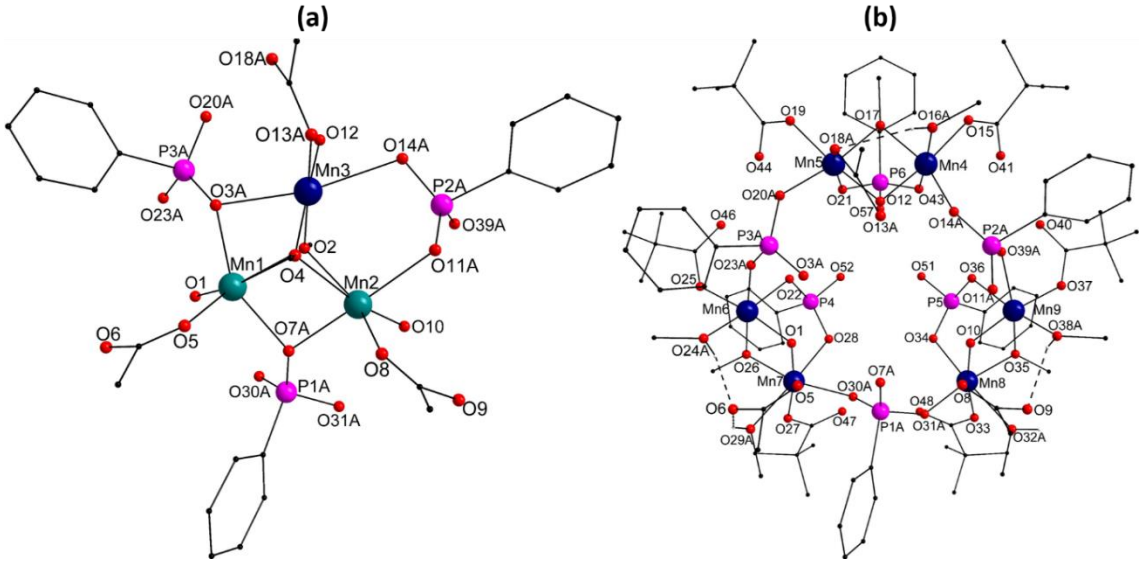

Figure 7.25: The coordination environment of **(a)** Mn1-Mn3 and **(b)** Mn4-Mn9. Only the parts with the largest occupancy are shown here. Colour scheme: Mn^{II} (teal), Mn^{III} (dark blue), P (pink), C (black) and O (red).

Mn1, Mn2 and Mn3 are stabilised by two μ_3-CH_3O^- groups (O2 and O4). The coordination environment of Mn1 and Mn2 is further fulfilled by a μ_3-O^{2-} group and O-donors from two phenyl phosphonate groups and a partially occupied pivalate and acetate groups with the Mn-O distances ranging between 2.1 and 2.4 Å. The coordination environment of Mn3 is fulfilled by a μ_3-O^{2-} group and O-donors from two phenyl phosphonate groups and a disordered acetate group that binds to Mn4 and Mn5 (**Figure 7.25 (a)**). Although the structure is heavily disordered, the Mn-O distances for Mn3 clearly confirm the presence of Jahn-Teller distortion thereby indicating Mn3 to be in +III oxidation state which is in agreement with the result obtained from the bond valence sum analysis.

The Jahn-Teller axis is directed along the two phosphonate groups and the Mn-O bond is ~2.3 Å long. The Mn-O distances perpendicular to the Jahn-Teller axis are ~1.9 Å. The octahedra of Mn1-Mn3 are distorted as indicated by angle variance, distortion index and continuous shape measure values (**Table 7.17**) and this is partly due to the disorder which makes it difficult to determine the true extent of distortion. For this compound, all distortion parameters have been determined using centres with highest occupancies.

Table 7.14: Key Mn-O and Mn-Mn bond lengths and bond valence sum for each Mn centre for compound **7.3**.

Mn centre	Coordinating atom	Bond Distance (Å)	BVS	Assigned oxidation state
Mn1	O5	2.057(10)	2.191	+II
	O1	2.080(8)		
	O7A	2.100(18)		
	O2	2.243(8)		
	O3A	2.256(15)		
	O4	2.321(10)		
Mn2	O8	2.049(10)	1.974	+II
	O10	2.096(8)		
	O7A	2.203(18)		
	O2	2.247(8)		
	O4	2.327(10)		
	O11A	2.409(10)		
Mn3	O12	1.856(8)	3.203	+III
	O13A	1.904(19)		
	O4	1.912(9)		
	O2	1.920(8)		
	O3A	2.209(14)		
	O14A	2.476(12)		
Mn4	O12	1.845(9)	3.139	+III
	O17	1.887(8)		
	O15	1.926(10)		
	O14A	2.002(13)		
	O43	2.282(9)		
	O16A	2.30(3)		
Mn5	O12	1.859(9)	3.290	+III
	O17	1.884(8)		
	O20A	1.907(12)		
	O19	1.928(11)		
	O21	2.262(8)		
	O18A	2.28(3)		
Mn6	O1	1.856(7)	3.275	+III
	O26	1.920(8)		
	O25	1.929(7)		
	O23A	1.948(12)		
	O24A	2.142(17)		
	O22	2.254(7)		

Mn centre	Coordinating atom	Bond Distance (Å)	BVS	Assigned oxidation state
Mn7	O1	1.858(7)	2.967	+III
	O26	1.915(8)		
	O27	1.929(8)		
	O30A	2.046(13)		
	O28	2.254(7)		
	O29A	2.386(18)		
Mn8	O31A	1.845(13)	3.291	+III
	O10	1.848(7)		
	O35	1.921(8)		
	O33	1.931(8)		
	O34	2.260(7)		
	O32A	2.412(17)		
Mn9	O10	1.846(7)	3.095	+III
	O35	1.918(8)		
	O37	1.939(7)		
	O39A	2.085(14)		
	O38A	2.135(16)		
	O36	2.266(7)		
Mn10	O42	2.140(8)	2.095	+II
	O40	2.148(8)		
	O36	2.168(7)		
	O41	2.169(10)		
	O43	2.191(7)		
	O39A	2.276(13)		
Mn11	O45	2.142(8)	2.097	+II
	O46	2.142(8)		
	O44	2.161(9)		
	O22	2.168(7)		
	O21	2.201(7)		
	O23B	2.277(13)		
Mn12	O48	2.158(8)	1.991	+II
	O47	2.159(8)		
	O49	2.166(8)		
	O28	2.172(7)		
	O34	2.182(7)		
	O30A	2.409(16)		
Mn13	O49	1.883(7)	3.134	+III
	O54	1.889(7)		
	O53	2.044(10)		
	O50	2.049(10)		
	O52	2.102(8)		
	O51	2.106(8)		
Mn14	O54	1.872(8)	3.154	+III
	O42	1.873(8)		
	O55	2.006(9)		
	O56	2.054(9)		
	O51	2.135(7)		
	O57	2.149(8)		

Mn centre	Coordinating atom	Bond Distance (Å)	BVS	Assigned oxidation state
Mn15	O54	1.868(8)	3.160	+III
	O45	1.875(8)		
	O59	2.002(9)		
	O58	2.055(9)		
	O57	2.138(8)		
	O52	2.149(8)		

Metals	Distance (Å)	Metals	Distance (Å)
Mn1-Mn2	3.203(3)	Mn6-Mn7	2.845(3)
Mn1-Mn3	3.089(2)	Mn6-Mn11	3.454(2)
Mn1-Mn6	3.571(2)	Mn7-Mn12	3.509(4)
Mn1-Mn7	3.565(2)	Mn8-Mn9	2.844(2)
Mn2-Mn3	3.087(3)	Mn8-Mn12	3.504(2)
Mn2-Mn8	3.565(3)	Mn9-Mn10	3.454(2)
Mn2-Mn9	3.574(4)	Mn10-Mn14	3.541(2)
Mn3-Mn4	3.333(3)	Mn11-Mn15	3.540(3)
Mn3-Mn5	3.331(3)	Mn12-Mn13	3.565(2)
Mn4-Mn5	2.826(4)	Mn13-Mn14	3.009(2)
Mn4-Mn10	3.533(4)	Mn13-Mn15	3.010(3)
Mn5-Mn11	3.534(2)	Mn14-Mn15	3.007(3)

The coordination environment of Mn4 and Mn5 is fulfilled by a μ_3-O^{2-} group and O-donors from a μ-CH_3O^- group, a pivalate group, two phenyl phosphonate groups with the final coordination site being partially occupied by the acetate group that binds to Mn3 in addition to a partially occupied CH_3OH O-donor (**Figure 7.25 (b)**). The Jahn-Teller axis of both is directed towards this disordered site and the O-donor of the phosphonate located opposite to it with the Mn-O distance being ~2.3 Å. The Mn-O distances perpendicular to the Jahn-Teller axis are ~1.9 Å. The coordination environment of Mn6-Mn9 is similar to that of Mn4 and Mn5 with the exception of the disordered site which in this case, is fully occupied by the O-donor of a disordered CH_3OH molecule. The Mn-O distances are similar to those observed for Mn4 and Mn5.

Table 7.15: Selected bond angles for compound **7.3**.

Bond	Bond Angle (°)	Bond	Bond Angle (°)
O2-Mn1-O4	62.0(3)	O10-Mn8-O35	81.4(3)
O3A-Mn1-O4	69.9(5)	O31A-Mn8-O32A	83.4(6)
O2-Mn1-O3A	74.4(4)	O33-Mn8-O32A	83.7(6)
O7A-Mn1-O2	74.4(6)	O35-Mn8-O32A	85.4(5)
O7A-Mn1-O4	84.7(5)	O35-Mn8-O34	88.4(3)
O5-Mn1-O4	89.2(4)	O31A-Mn8-O33	90.4(5)
O1-Mn1-O7A	96.6(5)	O35-Mn8-O33	90.4(3)
O5-Mn1-O7A	97.8(6)	O10-Mn8-O32A	90.6(6)
O1-Mn1-O2	101.1(3)	O10-Mn8-O34	91.8(3)
O1-Mn1-O3A	101.3(5)	O33-Mn8-O34	93.0(3)
O5-Mn1-O3A	103.2(5)	O31A-Mn8-O10	96.7(5)
O5-Mn1-O1	108.2(4)	O31A-Mn8-O34	102.8(5)
O7A-Mn1-O3A	146.5(6)	O31A-Mn8-O35	168.7(5)
O5-Mn1-O2	150.5(4)	O10-Mn8-O33	170.4(3)
O1-Mn1-O4	162.1(3)	O34-Mn8-O32A	173.0(5)

Bond	Bond Angle (°)	Bond	Bond Angle (°)
O2-Mn2-O4	61.8(3)	O39A-Mn9-O36	73.8(4)
O7A-Mn2-O2	72.4(5)	O10-Mn9-O35	81.6(3)
O8-Mn2-O11A	79.4(4)	O37-Mn9-O38A	87.2(5)
O7A-Mn2-O4	82.4(5)	O35-Mn9-O36	88.2(3)
O10-Mn2-O11A	85.7(4)	O37-Mn9-O39A	89.4(4)
O8-Mn2-O4	88.9(4)	O10-Mn9-O38A	90.7(5)
O4-Mn2-O11A	93.7(5)	O35-Mn9-O37	91.0(3)
O10-Mn2-O7A	98.5(5)	O10-Mn9-O36	91.7(3)
O8-Mn2-O7A	99.0(6)	O37-Mn9-O36	91.9(3)
O10-Mn2-O2	101.5(3)	O39A-Mn9-O38A	95.5(5)
O2-Mn2-O11A	107.0(3)	O10-Mn9-O39A	98.8(4)
O8-Mn2-O10	108.2(4)	O35-Mn9-O38A	102.5(5)
O8-Mn2-O2	150.1(4)	O35-Mn9-O39A	162.0(4)
O10-Mn2-O4	162.4(3)	O38A-Mn9-O36	169.3(5)
O7A-Mn2-O11A	175.8(6)	O10-Mn9-O37	171.6(3)
O12-Mn3-O14A	62.2(4)	O36-Mn10-O39A	72.1(4)
O4-Mn3-O2	75.7(4)	O40-Mn10-O39A	78.2(4)
O4-Mn3-O3A	78.6(5)	O40-Mn10-O41	80.1(3)
O2-Mn3-O3A	82.1(5)	O41-Mn10-O43	83.1(3)
O13A-Mn3-O14A	86.2(16)	O40-Mn10-O36	84.9(3)
O12-Mn3-O13A	91.0(14)	O42-Mn10-O43	88.7(3)
O13A-Mn3-O3A	92.5(16)	O42-Mn10-O36	89.7(3)
O13A-Mn3-O4	95.7(14)	O42-Mn10-O40	93.4(3)
O12-Mn3-O2	97.6(4)	O42-Mn10-O41	97.7(4)
O12-Mn3-O3A	100.8(5)	O41-Mn10-O39A	98.2(4)
O2-Mn3-O14A	101.2(4)	O43-Mn10-O39A	104.4(4)
O4-Mn3-O14A	118.4(4)	O36-Mn10-O43	111.7(3)
O3A-Mn3-O14A	163.0(5)	O42-Mn10-O39A	160.4(4)
O13A-Mn3-O2	170.6(15)	O40-Mn10-O43	163.2(3)
O12-Mn3-O4	173.3(4)	O36-Mn10-O41	163.6(3)
O12-Mn4-O14A	73.3(4)	O22-Mn11-O23B	71.0(4)
O15-Mn4-O16A	79.0(9)	O46-Mn11-O23B	78.8(4)
O12-Mn4-O17	81.8(3)	O46-Mn11-O44	80.2(4)
O14A-Mn4-O16A	83.6(10)	O44-Mn11-O21	83.0(3)
O17-Mn4-O16A	84.4(9)	O46-Mn11-O22	85.0(3)
O12-Mn4-O43	86.5(3)	O45-Mn11-O21	89.4(3)
O17-Mn4-O43	88.9(3)	O45-Mn11-O22	90.4(3)
O17-Mn4-O15	91.4(4)	O46-Mn11-O45	93.1(3)
O15-Mn4-O43	93.9(4)	O45-Mn11-O44	97.7(4)
O12-Mn4-O16A	99.8(9)	O44-Mn11-O23B	98.7(5)
O14A-Mn4-O43	105.7(4)	O21-Mn11-O23B	103.5(4)
O15-Mn4-O14A	112.9(5)	O22-Mn11-O21	111.6(3)
O17-Mn4-O14A	150.1(5)	O45-Mn11-O23B	160.2(4)
O43-Mn4-O16A	170.1(9)	O46-Mn11-O21	163.2(3)
O12-Mn4-O15	173.3(4)	O44-Mn11-O22	163.5(4)
O20A-Mn5-O18A	75.8(10)	O28-Mn12-O30A	68.7(4)
O20A-Mn5-O19	77.6(6)	O47-Mn12-O30A	77.9(4)
O12-Mn5-O18A	80.2(8)	O48-Mn12-O47	80.3(3)
O12-Mn5-O17	81.6(3)	O47-Mn12-O28	83.5(3)
O12-Mn5-O21	86.0(3)	O48-Mn12-O34	84.0(3)
O17-Mn5-O21	88.9(3)	O49-Mn12-O34	88.9(3)
O17-Mn5-O19	91.7(4)	O49-Mn12-O28	89.2(3)
O17-Mn5-O18A	93.8(8)	O48-Mn12-O49	93.9(4)
O19-Mn5-O21	94.6(4)	O47-Mn12-O49	94.3(4)
O19-Mn5-O18A	99.6(8)	O34-Mn12-O30A	104.5(4)

Bond	Bond Angle (°)	Bond	Bond Angle (°)
O20A-Mn5-O21	104.5(5)	O48-Mn12-O30A	105.8(4)
O12-Mn5-O20A	108.7(5)	O28-Mn12-O34	112.1(3)
O17-Mn5-O20A	163.4(5)	O49-Mn12-O30A	157.1(4)
O21-Mn5-O18A	165.4(7)	O48-Mn12-O28	163.7(3)
O12-Mn5-O19	173.3(5)	O47-Mn12-O34	164.2(3)
O1-Mn6-O26	81.8(3)	O54-Mn13-O51	80.6(3)
O23A-Mn6-O24A	84.5(6)	O54-Mn13-O52	80.8(3)
O23A-Mn6-O22	84.9(4)	O52-Mn13-O51	86.2(3)
O25-Mn6-O24A	87.7(5)	O54-Mn13-O53	86.9(4)
O26-Mn6-O22	88.4(3)	O54-Mn13-O50	87.2(4)
O25-Mn6-O23A	89.2(6)	O53-Mn13-O52	87.9(3)
O1-Mn6-O24A	90.3(5)	O50-Mn13-O51	88.0(3)
O26-Mn6-O25	91.1(3)	O49-Mn13-O50	95.0(4)
O1-Mn6-O22	91.2(3)	O49-Mn13-O53	95.3(4)
O25-Mn6-O22	92.2(3)	O53-Mn13-O50	95.4(4)
O1-Mn6-O23A	98.3(6)	O49-Mn13-O52	96.8(3)
O26-Mn6-O24A	102.2(5)	O49-Mn13-O51	97.1(3)
O24A-Mn6-O22	169.4(5)	O53-Mn13-O51	166.9(4)
O1-Mn6-O25	172.0(3)	O50-Mn13-O52	167.4(4)
O26-Mn6-O23A	173.3(5)	O49-Mn13-O54	176.7(3)
O30A-Mn7-O28	74.0(5)	O54-Mn14-O51	80.2(3)
O1-Mn7-O26	81.8(3)	O54-Mn14-O57	80.2(3)
O27-Mn7-O29A	83.6(6)	O51-Mn14-O57	84.6(3)
O26-Mn7-O29A	85.3(5)	O54-Mn14-O56	87.1(4)
O26-Mn7-O28	89.1(3)	O55-Mn14-O51	88.5(3)
O26-Mn7-O27	90.6(3)	O54-Mn14-O55	88.7(4)
O1-Mn7-O29A	90.9(6)	O56-Mn14-O57	89.1(3)
O27-Mn7-O30A	91.5(5)	O42-Mn14-O56	94.6(3)
O1-Mn7-O28	91.8(3)	O42-Mn14-O55	94.8(4)
O27-Mn7-O28	92.9(3)	O55-Mn14-O56	95.5(4)
O1-Mn7-O30A	97.1(4)	O42-Mn14-O57	96.1(3)
O30A-Mn7-O29A	111.7(6)	O42-Mn14-O51	97.8(3)
O26-Mn7-O30A	163.0(5)	O56-Mn14-O51	166.6(3)
O1-Mn7-O27	171.1(3)	O55-Mn14-O57	167.8(4)
O28-Mn7-O29A	173.4(5)	O54-Mn14-O42	176.0(3)
O54-Mn15-O52	80.0(3)	O45-Mn15-O59	94.7(4)
O54-Mn15-O57	80.6(3)	O59-Mn15-O58	95.5(4)
O57-Mn15-O52	84.5(3)	O45-Mn15-O57	96.0(3)
O54-Mn15-O58	87.2(3)	O45-Mn15-O52	98.0(3)
O59-Mn15-O52	88.3(3)	O58-Mn15-O52	166.6(3)
O54-Mn15-O59	88.5(4)	O59-Mn15-O57	167.9(4)
O58-Mn15-O57	89.4(3)	O54-Mn15-O45	176.2(3)
O45-Mn15-O58	94.5(3)		

Table 7.16: BVS analysis for O atoms and their assigned protonation state in compound **7.3**.

Atom	BVS	Assignment
O1	1.995	μ_3-O^{2-}
O10	2.018	μ_3-O^{2-}
O12	2.331	μ_3-O^{2-}
O54	2.191	μ_3-O^{2-}

Mn10-Mn12 are bound to the O-donors of a μ-CH_3O^- group, two pivalate groups and three phenyl phosphonate groups with the Mn-O distance varying between 2.1 and 2.4 Å (**Figure 7.26 (a)**). The triangular {Mn_3} unit comprising of Mn13-Mn15 is centred around a μ_3-O^{2-} group (**Figure 7.26 (b)**). The coordination environment of Mn13 is fulfilled by the O-donors of a μ-CH_3O^- group, two acetate groups and two phenyl phosphonate groups. Mn14 and Mn15 have a similar coordination environment with the exception of one of the acetate groups which is replaced with a partially occupied acetate and pivalate group with the acetate having the major occupancy (75%). The coordination environment of these three Mn centres is the least disordered but based on the Mn-O distances, it is not very clear whether the Jahn-Teller distortion leads to elongation or compression. Knowledge of how the d-orbitals are filled can provide a definite answer and DFT calculations on this complex will be carried out in the future to better understand the electronic picture of this complex. If one assumes that these Mn centres are axially compressed, the Jahn-Teller axis is directed along the μ_3-O^{2-} group and the μ-CH_3O^- group located opposite to it with Mn-O bond being ~1.9 Å. The Mn-O distance for these Mn centres lies between 2.0 and 2.1 Å in the direction perpendicular to the Jahn-Teller axis.

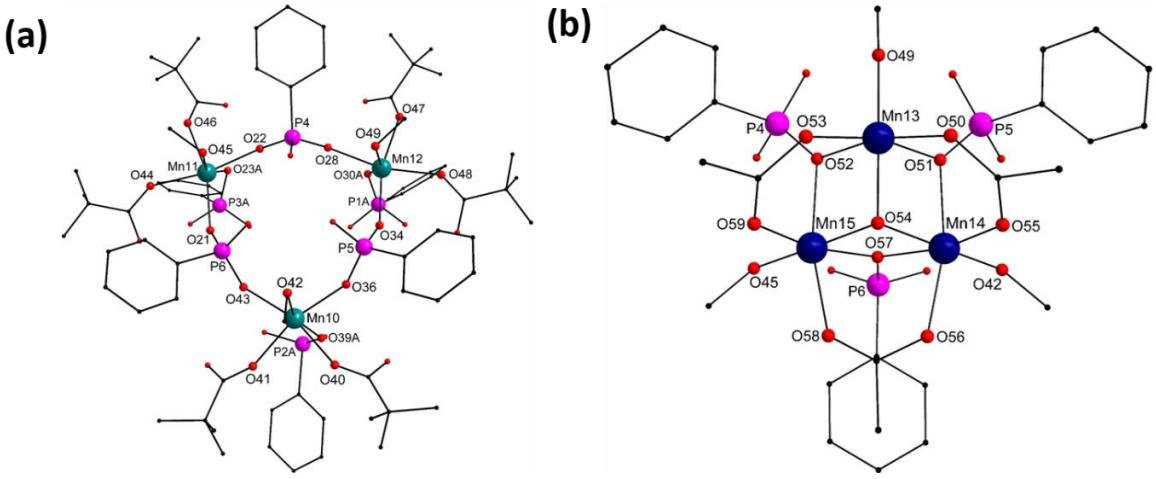

Figure 7.26: The coordination environment of **(a)** Mn10-Mn12 and **(b)** Mn13-Mn15. Only the parts with the largest occupancy are shown here. Colour scheme: Mn^{II} (teal), Mn^{III} (dark blue), P (pink), C (black) and O (red).

The packing of this complex, unlike compound **7.2**, allows for solvent molecules to be trapped in the triangular voids that are directed along the crystallographic c-axis (**Figure 7.27**). Due to the crystal quality, these molecules could not be structurally resolved and the electron density due to these molecules (corresponding to 1583 electrons) was subjected to the 'squeeze' routine as implemented in the PLATON code.[629, 635] The treated electron density may correspond to one CH_3OH and two CH_3CN molecules per formula unit. The largest spherical voids holding these molecules are 4.6 Å in radius and these voids are connected to each other *via* channels that can be penetrated by a sphere of radius 2.4 Å as calculated using the 'calcvoid' routine of OLEX2 code.[616]

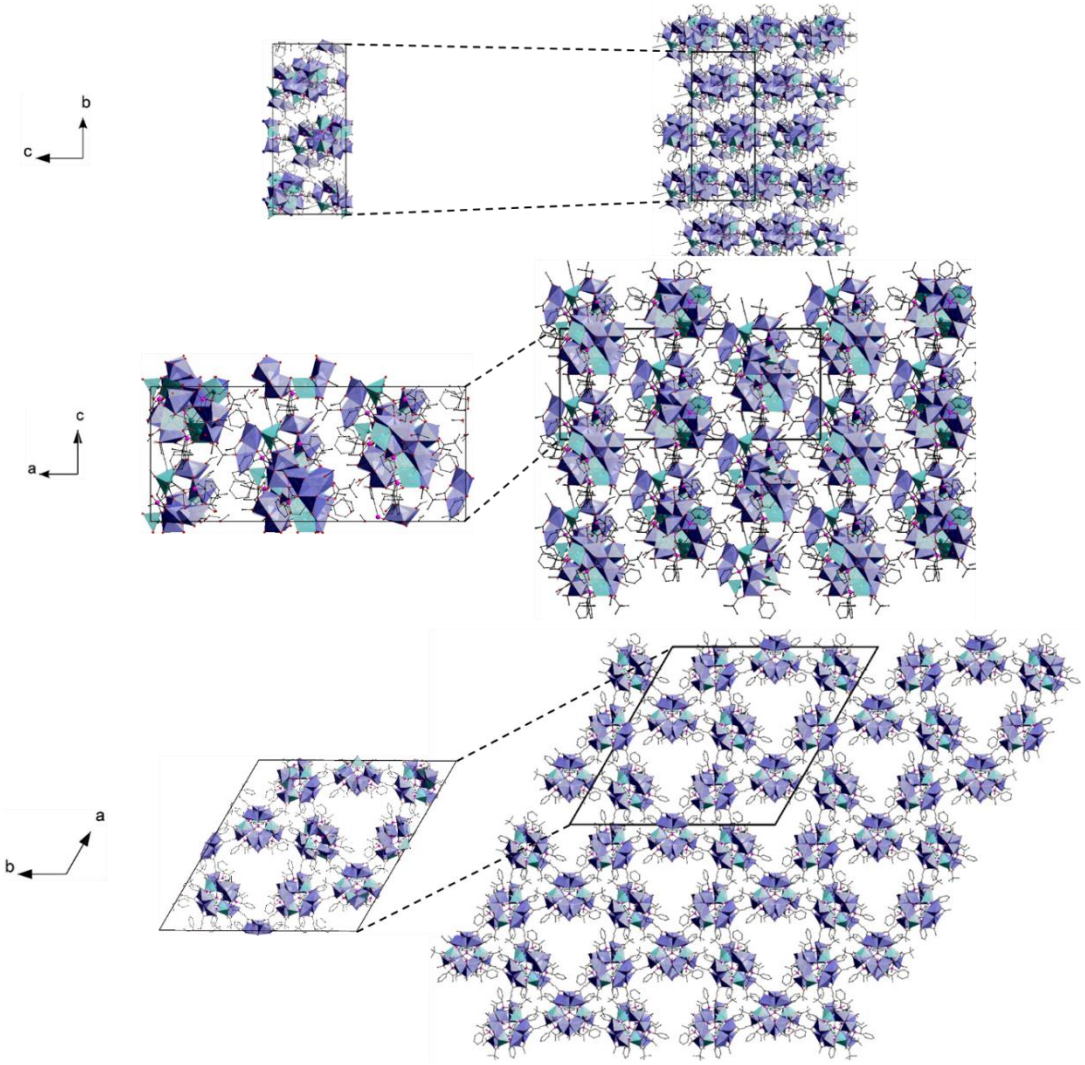

Figure 7.27: Packing diagram of compound **7.3**. Only the parts with the largest occupancy are shown here. Colour scheme: Mn^{II} (teal), Mn^{III} (dark blue), P (pink), C (black) and O (red). All hydrogen atoms (grey) except those of the μ_3-OH^- group have been removed for clarity.

Table 7.17: Continuous shape measure values, angle variance and distortion indices (using the ideal octahedral geometry as a reference) for each Mn centre for compound **7.2**.

Mn centre	Continuous shape measure value	Angle variance (σ^2)	Distortion Index
Mn1	3.170	233.11	0.1457
Mn2	3.216	201.30	0.1273
Mn3	1.889	211.84	0.1221
Mn4	3.121	130.64	0.0984
Mn5	2.964	111.80	0.0949
Mn6	1.352	32.48	0.0451
Mn7	2.349	83.95	0.0672
Mn8	2.136	36.60	0.0498
Mn9	1.694	56.03	0.0568
Mn10	2.499	131.76	0.1007
Mn11	3.182	131.85	0.0994
Mn12	3.105	159.66	0.1095
Mn13	0.625	35.65	0.0571
Mn14	0.686	36.99	0.0556
Mn15	0.697	36.78	0.0555

7.3.2 Physicochemical characterisation

Physicochemical characterisation was carried out to further support the structural model obtained using single crystal X-ray crystallography. Unlike compound **7.2** which forms block like crystals, compound **7.3** crystallises as micro-sized hollow rods which has been confirmed by SEM analysis (**Figure 7.28 (a)**). The phase purity of the sample was confirmed using PXRD (**Figure 7.28 (b)**). The peak broadening observed in the PXRD pattern indicates partial loss of crystallinity.

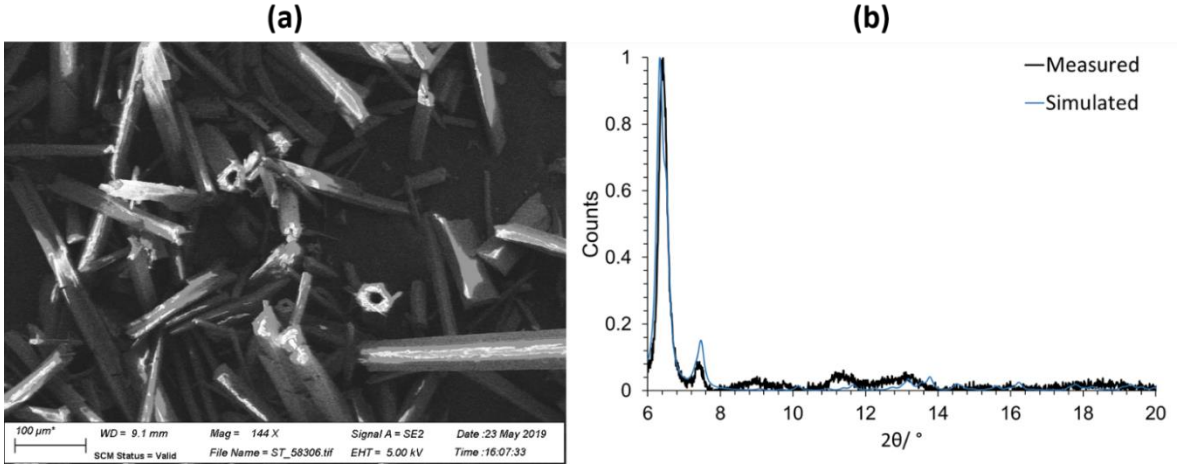

Figure 7.28: (a) Scanning electron micrograph and **(b)** PXRD pattern for compound **7.3**.

TGA analysis (**Figure 7.29**) of air dried compound **7.3** under an atmosphere of N_2 reveals a drop up to ~80 °C which represents the loss of the solvent molecules (one CH_3OH and two CH_3CN molecules per formula unit) trapped in the lattice (weight loss calcd: 3.4 %, found: 3.7 %). The next drop up to ~170 °C is due to the loss of water and methanol molecules bound to the complex (weight loss calcd: 5.2 %, found: 5.1 %). This is followed by the loss of acetate groups and pivalate groups up to ~500 °C (weight loss calcd: 29.3 %, found: ~31 %) which is succeeded by, based on the weight loss, the partial decomposition of the phosphonate groups up to ~600 °C. The gradual weight loss at higher temperatures most likely corresponds to the formation of phosphate and oxide species.

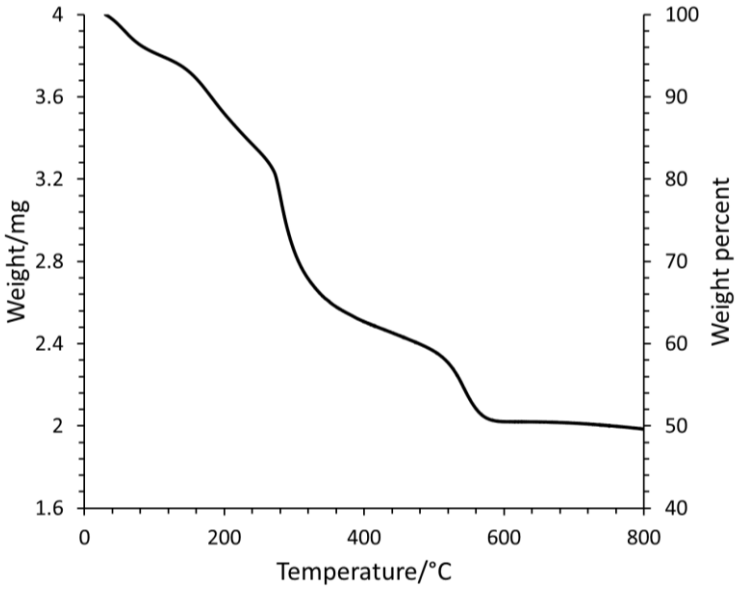

Figure 7.29: TGA analysis of compound **7.3**.

The infrared spectrum of compound **7.3** (**Figure 7.30**) is consistent with the structure determined by XRD. The broad distinctive feature around 2960 cm^{-1} is due to the C-H vibrations in the organic ligands.[617] The strong vibration mode at 1402 cm^{-1} corresponds to the symmetric carboxylate stretching while that at 1558 cm^{-1} corresponds to the asymmetric stretching which is in line with the behaviour observed for bidentate bridging carboxylate groups.[618] Other vibrations observed in the same region are due to *tert*-butyl groups.[617] The intense peak at 976 cm^{-1} and the shoulder attached to it corresponds to the stretching of the phosphonate group.[621-623]

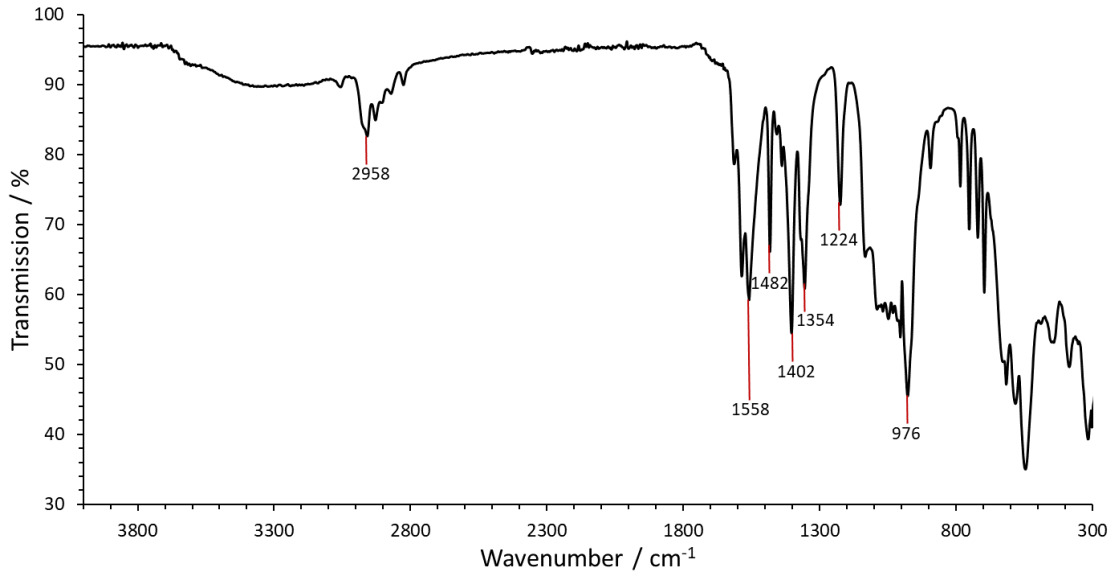

Figure 7.30: Infrared spectrum of compound **7.3**.

7.3.3 Magnetic properties

The temperature dependence of magnetic susceptibility was determined in the temperature range of 4-300 K (**Figure 7.31**). The room temperature χT value of 44 cm^3 K mol^{-1} is significantly lower than the expected value of 51.875 cm^3 K mol^{-1} for a system with 5 Mn^{II} (S = 5/2) centres and 10 Mn^{III} (S = 2) centres. This suggests that the coupling between the Mn centres is dominantly antiferromagnetic. This is further confirmed by the behaviour observed upon lowering the temperature when the χT value decreases and reaches 13 cm^3 K mol^{-1} at 4 K. Considering that even at 4 K, the χT value is quite high, the presence of ferromagnetic coupling cannot be ruled out. Additionally, the presence of multiple $\{Mn_3\}$ triangular units and odd number of unpaired spins can result in spin frustration leading to ground states with larger overall spin.[528, 578]

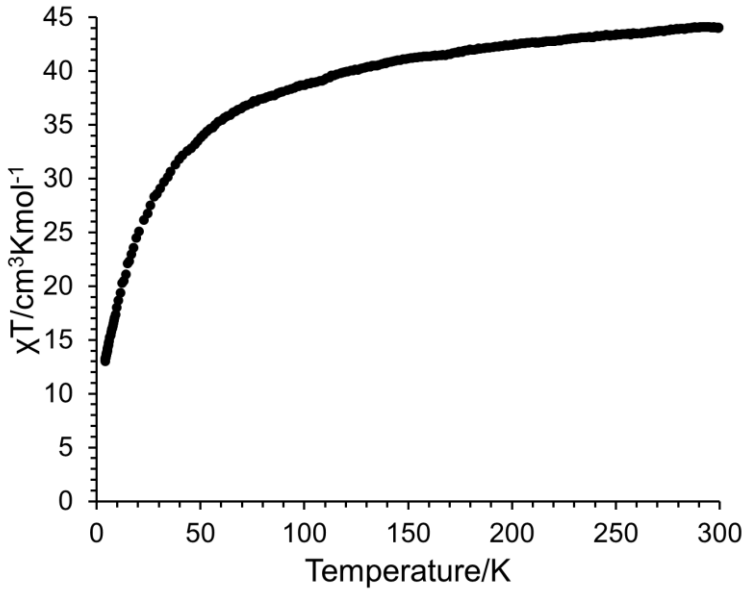

Figure 7.31: Temperature dependence of magnetic susceptibility (χT) of compound **7.3**.

7.3.4 Electrochemical studies

For consistency, the electrochemical properties of compound **7.3** were investigated using modified carbon paste electrodes which were prepared by dispersing compound **7.3** in commercially available carbon paste. Cyclic voltammetry of compound **7.3** at a scan rate of 50 mV/s in potassium phosphate buffer at pH 7.2 (KP*i*, 50 mM) using KNO_3 (1 M) as electrolyte, results in a strong catalytic wave (**Figure 7.32**).

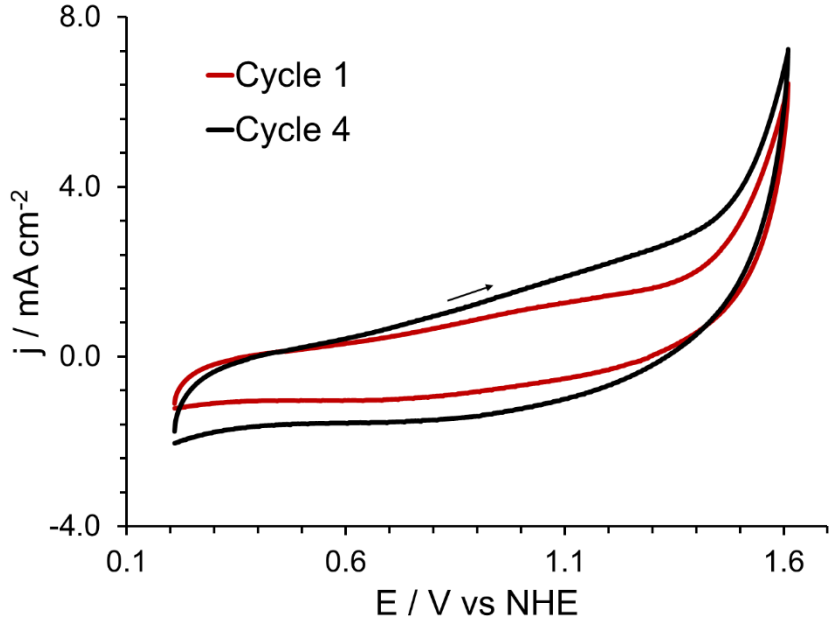

Figure 7.32: Cyclic voltammograms for compound **7.3** (40 wt-% loading) in a KP*i* buffer solution at pH 7.2.

To investigate the kinetic profile of this reaction, linear sweep voltammetry experiments with varying catalytic loadings were performed using a rotating disk electrode packed with carbon paste mixture. These experiments were performed at a low scan rate of 1 mV/s to ensure steady state conditions with the catalytic loading varied between 10 and 40 wt-%. Loadings higher than 40 wt-% made the blend brittle and hence were not used. Within 10-40 wt-% catalyst loading range, higher loadings lead to higher current densities (**Figure 7.33**). Unlike compound **7.1** however, the onset overpotential and Tafel slopes beyond 20 wt-% loading does not vary with catalyst loading (**Table 7.18** and **Figure 7.34**). With 40 wt-% loading, the onset potential was determined to be 521 mV dec^{-1} and the Tafel slope was determined to be 220 mV dec^{-1} in the overpotential range of 500-650 mV. For 30 and 40 wt-% loading, the Tafel slope decreases to 107 and 100 mV dec^{-1} respectively in the 650-700 mV overpotential range. The Tafel slope above 700 mV of overpotential for 30 and 40 wt-% catalyst loading was found to be 750 mV dec^{-1}.

Table 7.18: The onset overpotential and Tafel slope for water oxidation with compound **7.3** at different loadings.

Loading	Onset overpotential (mV)	Tafel slope (mV dec^{-1})
10%	605	218
20%	516	225
30%	512	230
40%	521	220

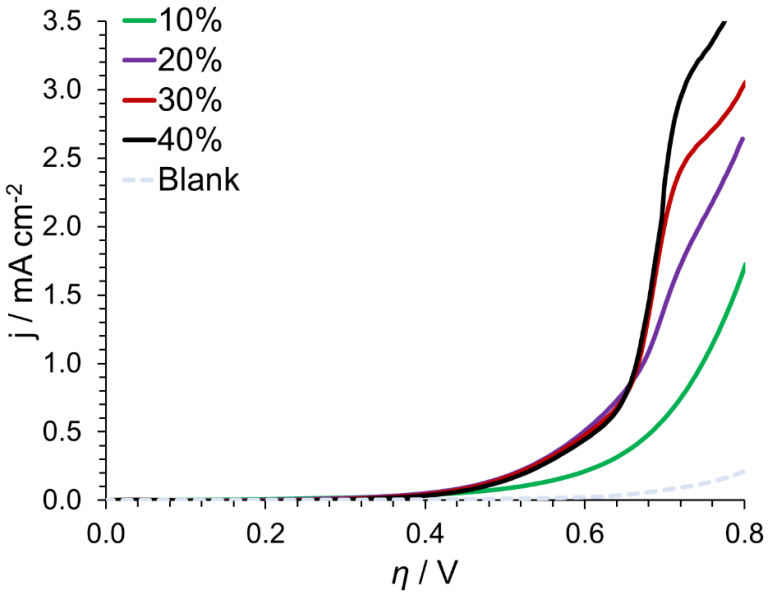

Figure 7.33: Linear sweep voltammograms for compound **7.3** at different loadings.

Successive linear sweep experiments were conducted to determine the stability of the complex under repeated application of varying potential over an extended period and to obtain further insight into the electrochemical behaviour of this complex. It was observed that during the 50 linear sweep cycles performed, the current density increases with each cycle (**Figure 7.35 (a)**). From the 15th cycle, an additional redox peak can be observed at ~50 mV of overpotential (or ~0.85 V vs NHE).

The Tafel slope in the overpotential range of 500-650 mV increases from 220 to 409 mV dec^{-1} up to the 10th cycle (**Figure 7.35 (b)**) and then decreases to 397 mV dec^{-1} by the 15th cycle and achieves a constant value of ~380 mV dec^{-1} from the 25th cycle. The Tafel slope in the overpotential range of 700-800 mV decreases from 750 mV dec^{-1} and reaches a fairly constant value of 250 mV dec^{-1} (**Figure 7.35 (c)**).

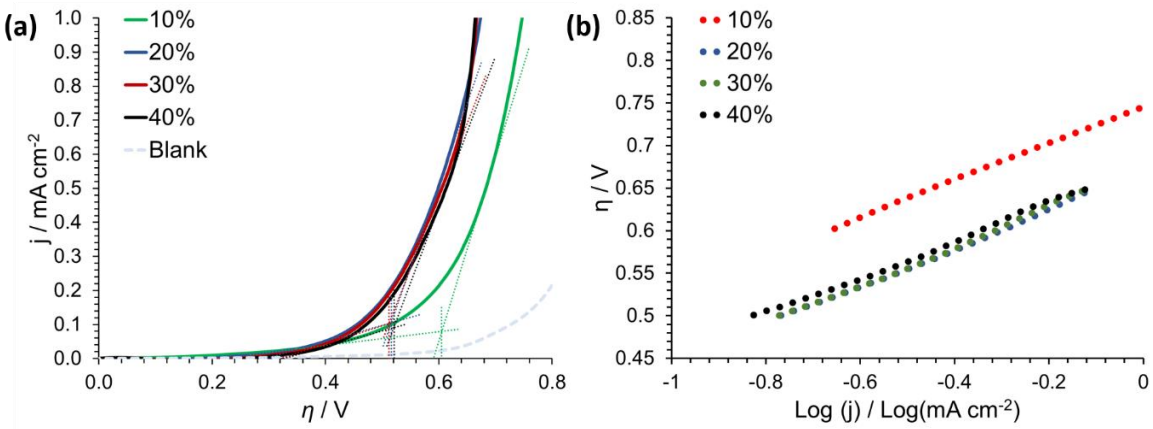

Figure 7.34: (a) The determined onset potentials and **(b)** the Tafel slope for compound **7.3** at different loadings.

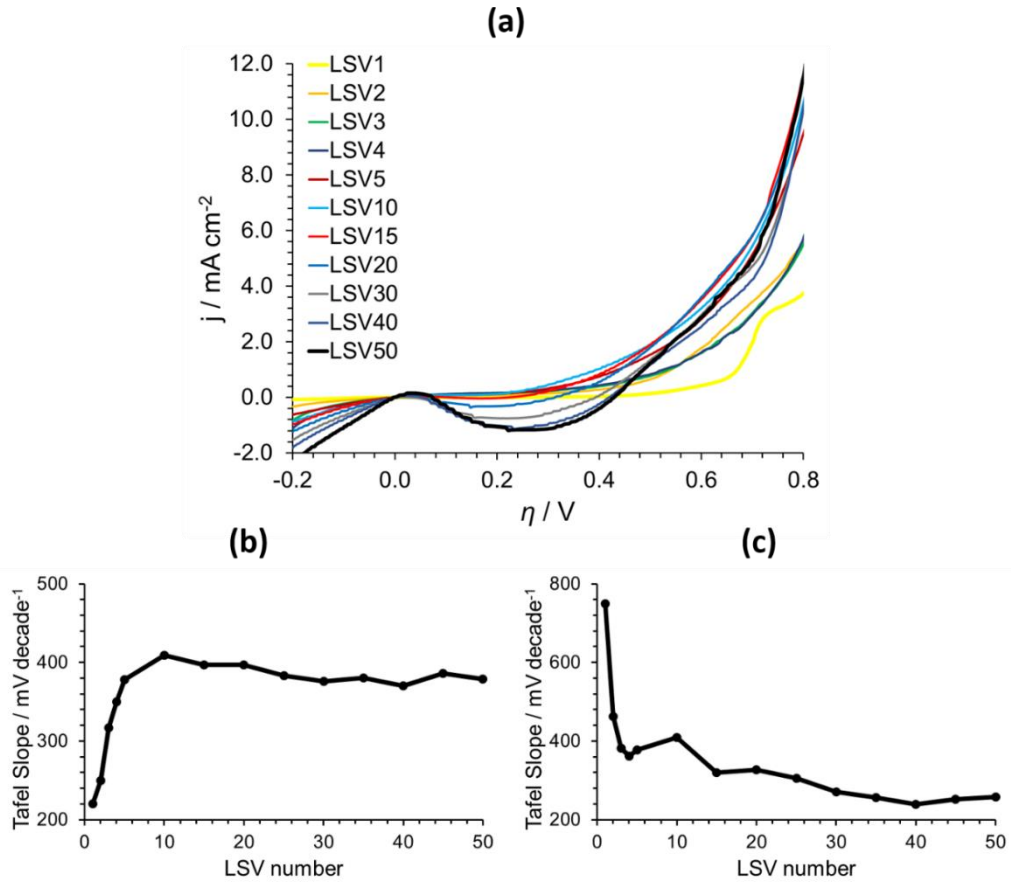

Figure 7.35: (a) Successive linear sweep voltammograms for compound **7.3** in KP*i* buffer solution at pH 7.2 and the Tafel slope observed for the different cycles calculated in the **(b)** 500-650 and **(c)** 700-800 mV overpotential range**.**

To investigate the stability of the complex, CA was also performed for 16 hours at an applied potential of 1.56 V (vs NHE). The current density, after decreasing for some time due to capacitance effects,[632] increases (**Figure 7.36 (a)**). Further investigation on the time required for the current density to stabilise was not studied but cyclic voltammetry and linear sweep voltammetry experiments were performed after CA. A broad new peak can be observed around ~1.06 V (vs NHE) (**Figure 7.37 (a)**) with some additional redox activity occurring at higher potential (**Figure 7.37 (b)**).

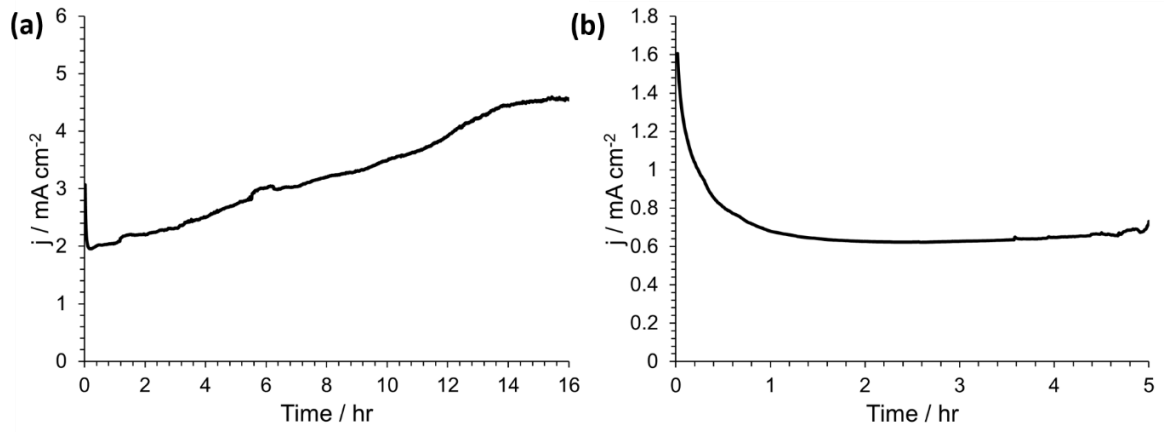

Figure 7.36: CA data for compound **7.3** at **(a)** 1.56 V and **(b)** 1.41 V *vs* NHE in KP*i* buffer solution at pH 7.2.

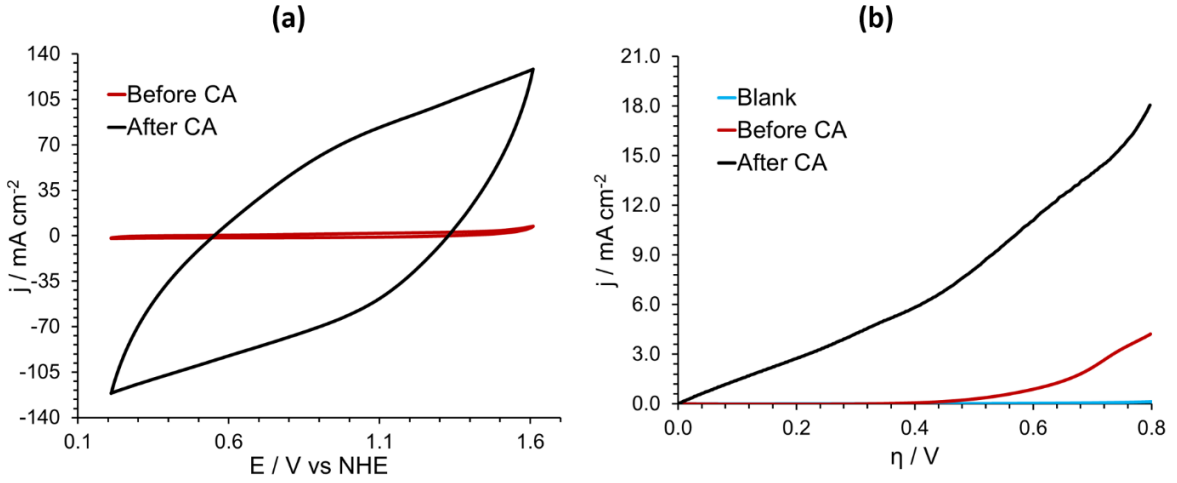

Figure 7.37: (a) Cyclic voltammograms and **(b)** linear sweep voltammograms for compound **7.3** in KP*i* buffer solution at pH 7.2 before and after CA.

CA experiment was also carried out at 1.41.V vs NHE for 5 hours (**Figure 7.36 (b)**) to determine the electrochemical behaviour at η < 700 mV. The observed activity was found to remain constant at this potential.

Leaching during chronoamperometry was also investigated and for this purpose, linear sweep voltammetry was conducted with a rotating disk glassy carbon electrode was performed before and after chronoamperometry using the same buffer solution. The current density increases from 0.13 mA cm^{-2} to 0.37 mA cm^{-2} after the CA at 1.56 V vs NHE indicating that there is some leaching (**Figure**

7.38). The overall current density however, is negligible compared to that observed for compound **7.3** (**Figure 7.35**) suggesting that the observed activity cannot be attributed to the leached product but has to be due to species derived from compound **7.3**.

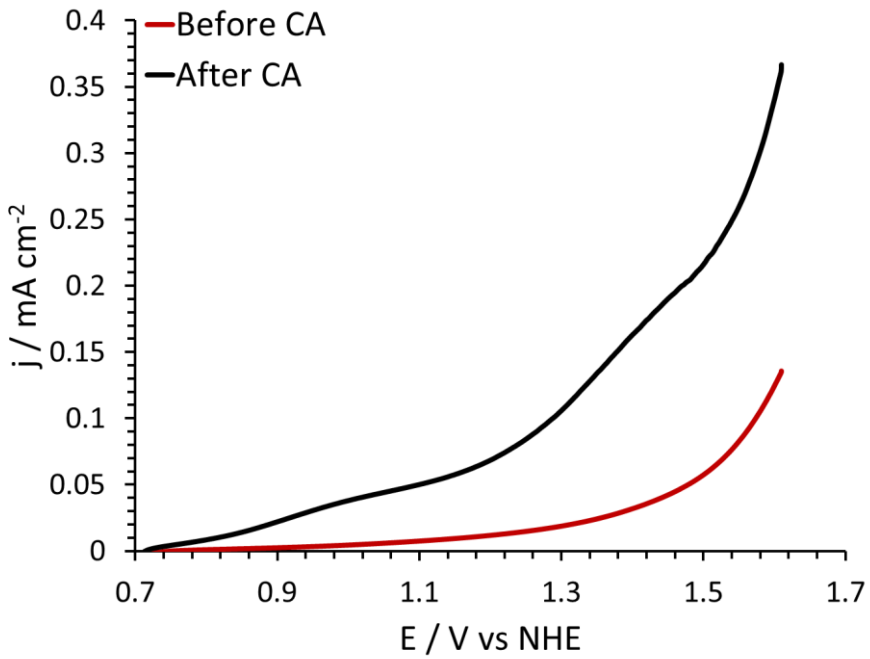

Figure 7.38: Linear sweep voltammograms using glassy carbon electrodes of the buffer solution before and after chronoamperometry.

From a structural perspective, this complex contains numerous sites for potential OER activity. The Mn(III) centres Mn4-Mn9 are coordinated to CH_3OH molecules which can easily be replaced with water molecules to initiate the OER. Cyclic voltammetry indeed reveals a catalytic wave corresponding to water oxidation. The similarity in the behaviour of the 1st and the 4th cycle indicates that there is no observable decomposition during this period which implies that the initial activity must be derived from compound **7.3**. It is quite interesting to see that the catalyst loading does not affect the initial activity as highlighted by the similar Tafel slopes. The activity at higher overpotentials however, does change and the Tafel slope goes down from 220 to 100 mV dec^{-1} for 40 wt-% loading. Such an increase in activity suggests a change in the mechanism pointing to the presence of multiple active sites per molecule. The increase in the Tafel slope above 700 mV of overpotential is possibly due to mass transfer effects.

During the successive linear sweep experiments, there is a significant increase in the current density on advancing from the first to the second cycle indicating that the complex undergoes some initial transformations which may be associated with the substitution of the CH_3OH groups with water molecules. The additional peak that appears in the 15th cycle and the cycles that follow at ~50 mV of overpotential (or ~0.85 V vs NHE) indicates further transformation of the complex. During this experiment the Tafel slope in the overpotential range of 500-650 mV increases from 220 to 409 mV dec^{-1} up to the 10th cycle (**Figure 7.35 (b)**) indicating a decrease in the activity suggesting that that

the complex is decomposing. The Tafel slope then decreases to 397 mV dec^{-1} by the 15th cycle and achieves a constant value of ~380 mV dec^{-1} from the 25th cycle indicating that the complex has transformed to a species that is less active compared to the active species derived from compound **7.3**. The Tafel slope in the overpotential range of 700-800 mV shows a contrasting behaviour (**Figure 7.35 (c)**). The Tafel slope in this range decreases from 750 mV dec^{-1} and reaches a fairly constant value of 250 mV dec^{-1} suggesting that this transformed species is quite active at higher overpotentials. Since this decrease in the Tafel slope is observed only at higher overpotentials, it can be concluded that the activity observed at lower overpotentials is due to a species derived from the compound **7.3**.

CA performed at an applied potential of 1.56 V (vs NHE) shows a constant increase in the current density (**Figure 7.36 (a)**) which is consistent with the successive LSV experiment where the transformation of compound **7.3** to a species active above an overpotential of 700 mV was observed. Cyclic voltammetry performed after the CA experiment at 1.56 V vs. NHE reveals a broad new peak around ~1.06 V (vs NHE) (**Figure 7.37 (a)**). The additional peak at ~1.06 V suggests that the transformed species is Mn_2O_3.[628]

The CA experiment at 1.41.V vs NHE shows a constant current density for 5 hours. This suggests that compound **7.3** is quite stable at this potential. This suggests that compound **7.3** can promote water oxidation for extended periods without rapid degradation. In light of this experiments it can be proposed that the decomposition behaviour observed in the other experiments could be due to application of higher potential. However, further work is required to substantiate this proposition.

7.4 $[Mn^{II}_4Mn^{III}_{10}(\mu_3\text{-}O)_4(\mu_3\text{-}OH)_2(\mu\text{-}CH_3O)_9(CH_3OH)_2(H_2O)_2((C_6H_5)PO_3)_3((CH_3)_3CCO_2)_{10}(CH_3CO_2)_3]$ (7.4)

Refluxing $KMnO_4$, $Mn(CH_3COO)_2{\cdot}4H_2O$, phenylphosphonic acid and pivalic acid in a ratio of 1:5:2.5:20 in presence of 2,6-pyridinedimethanol in a mixture of CH_3CN and CH_3OH results in the formation of compound **7.4**. Dark block crystals of compound **7.4** were obtained within a week which were characterised by single crystal X-ray diffraction experiment.

7.4.1 Structure description

Compound **7.4** crystallises in the triclinic crystal system and the structure was solved in the space group $P\bar{1}$. It contains a tetradecanuclear complex $[Mn_{14}(\mu_3\text{-}O)_4(\mu_3\text{-}OH)_2(\mu\text{-}CH_3O)_9(CH_3OH)_2(H_2O)_2((C_6H_5)PO_3)_3((CH_3)_3CCO_2)_{10}(CH_3CO_2)_3]$ (**Figure 7.39**), and the asymmetric unit again contains the whole complex. The core structure of this complex can be considered equivalent to a truncated tetrahedron where two additional Mn centres (Mn1 and Mn2) are attached to one of the hexagonal faces (**Figure 7.40**). The result of such an addition is the distortion of the two hexagonal faces that are in direct contact with the additional Mn centres. The structure is stabilised by two $\mu_3\text{-}OH^-$, four $\mu_3\text{-}O^{2-}$, nine $\mu\text{-}CH_3O^-$, three phenylphosphonate and ten pivalate groups in addition to acetate, methanol and water molecules. What is fascinating here is the presence of acetate groups in this structure because the only source of acetate groups in the reaction mixture is $Mn(CH_3COO)_2$ which highlights the non-innocent nature of the counterion of the Mn^{II} salt.

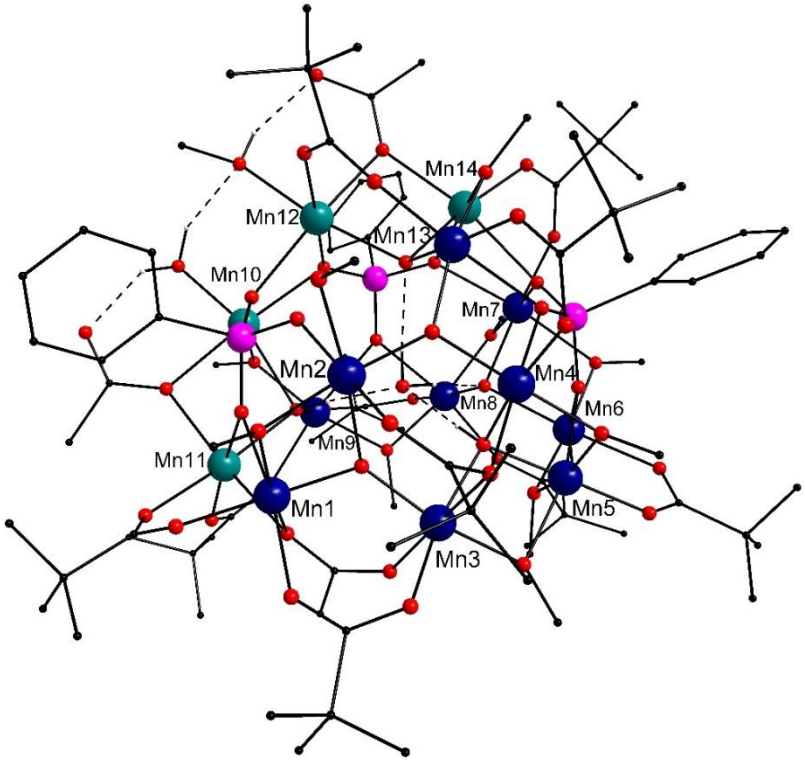

Figure 7.39: Asymmetric unit of the tetradecanuclear compound **7.4**. The hydrogen bonds are shown with dashed lines. Colour scheme: Mn^{II} (teal), Mn^{III} (dark blue), P (pink), C (black) and O (red). All hydrogen atoms (grey) except those of the oxygen centres have been removed for clarity.

The core structure is stabilised by three phenylphosphonate groups, four μ_3-O^{2-} groups and two μ_3-OH^- groups (**Figure 7.41**). The phenylphosphonate groups bind to the hexagonal faces with two of the phenylphosphonate groups (containing P1 and P2) bound to the less distorted hexagonal faces away from Mn1 and Mn2 in 6.222 binding mode. The third phosphonate group (containing P3) joins Mn1 and Mn2 to the main body and is bound to the Mn centres in 5.221 mode. The μ_3-OH^- groups (O1 and O9) and two of the μ_3-O^{2-} groups (O13 and O20) are bound to the triangular $\{Mn_3\}$ faces as depicted in **Figure 7.41**. The remaining two μ_3-O^{2-} groups (O4 and O14) bind Mn1 and Mn2 to the $\{Mn_{12}\}$ unit. The triangular faces do not correspond to equilateral triangles which is mainly due to the distortion induced by the additional Mn centres. A water molecule (O54) resides at the centre of this complex and is hydrogen bonded to both μ_3-OH^- groups and the μ_3-O^{2-} groups (O13 and O20) bound to the triangular faces. These μ_3-OH^- groups and the μ_3-O^{2-} groups (O13 and O20) are ~0.76 Å below the plane of the corresponding $\{Mn_3\}$ unit. O4 also lies 0.309(10) Å below the $\{Mn_3\}$ plane while O14 lies in the plane.

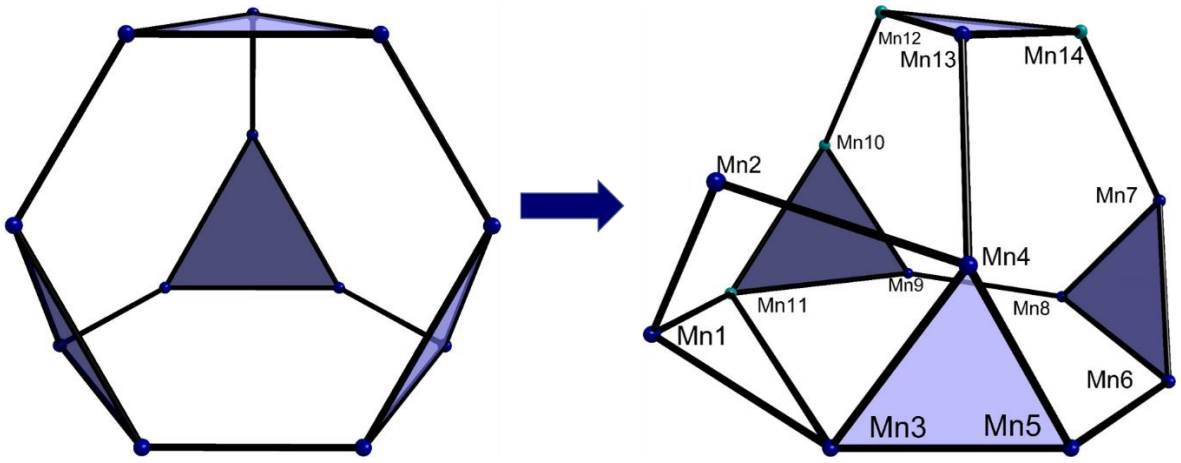

Figure 7.40: Comparison of the core structure of compound **7.4** with an ideal truncated tetrahedron. Mn^{II} and Mn^{III} for compound **7.4** are shown in teal and dark blue respectively.

All Mn centres reside in an octahedral coordination environment and 12 of the 14 Mn centres adopt different coordination environments in terms of the ligands coordinated to the Mn centres (**Table 7.19**). A list of key bond distances is provided in **Table 7.20**.

The oxidation state of the Mn centres was determined using bond valence sum analysis (**Table 7.20**) and the Mn centres Mn10, Mn11, Mn12 and Mn14 were found to be in +II oxidation state while all other were determined to be in +III oxidation state. Bond valence sum analysis was also used to determine the protonation state of the O atoms bound only to Mn centres (**Table 7.21**). The values obtained in some cases do not strictly meet the proposed criteria for assignment[603, 604] so the protonation state has been decided based on the proximity of the bond valence sum value to an integer.

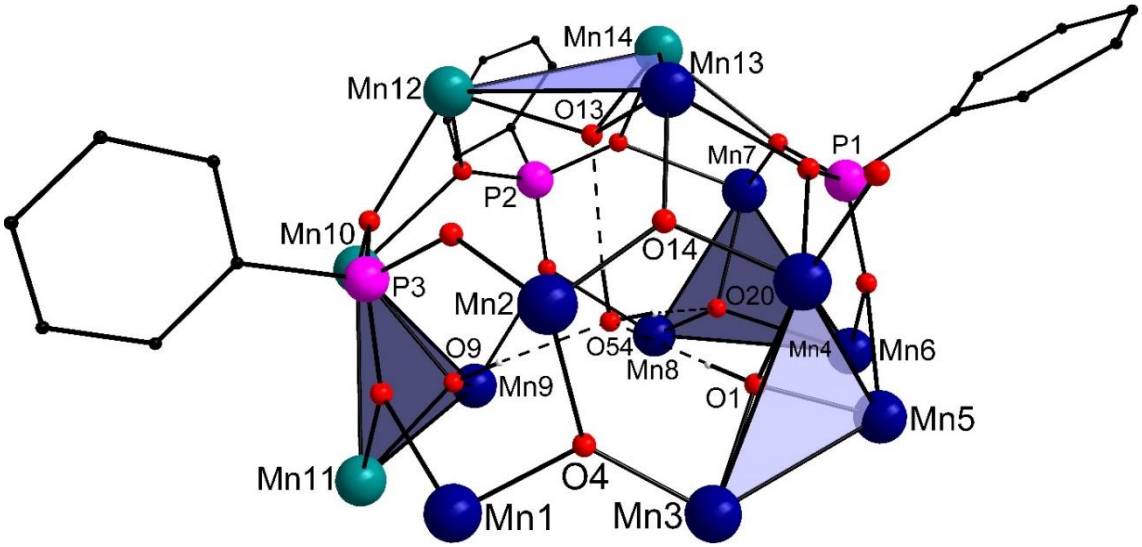

Figure 7.41: Core structure of compound **7.4**. Colour scheme: Mn^{II} (teal), Mn^{III} (dark blue), P (pink), C (black) and O (red). All hydrogen atoms (grey) except those of the oxygen centres have been removed for clarity.

Using the oxidation state of the Mn centres as a criterion, one can divide the structure into three parts:

1. The additional Mn centres – Mn1 and Mn2 (unit 1).
2. Two triangular Mn^{III} units – Mn3, Mn4 and Mn5 (unit 2), and Mn6, Mn7 and Mn8 (unit 3).
3. Two triangular mixed-valence units – Mn9, Mn10 and Mn11 (unit 4), and Mn12, Mn3 and Mn14 (unit 5).

Table 7.19: Coordinating ligands for each Mn centre in compound **7.4**. The number in bracket adjacent to each ligand specifies the number of the corresponding ligand molecules attached to a given Mn centre. The Mn centres in bold have the same set of ligands in their coordination environment.

Mn centre	Coordinating Ligands
Mn1	CH_3COO^- (1), CH_3O^- (1), μ_3-O^{2-} (1), pivalate (2), phosphonate (1)
Mn2	CH_3OH (1), CH_3O^- (1), μ_3-O^{2-} (2), pivalate (1), phosphonate (1)
Mn3	CH_3COO^- (1), μ_3-OH^- (1), CH_3O^- (1), μ_3-O^{2-} (1), pivalate (2)
Mn4	μ_3-OH^- (1), CH_3O^- (1), μ_3-O^{2-} (1), pivalate (2), phosphonate (1)
Mn5	μ_3-OH^- (1), CH_3O^- (3), pivalate (1), phosphonate (1)
Mn6	CH_3O^- (2), μ_3-O^{2-} (1), pivalate (2), phosphonate (1)
Mn7	CH_3O^- (2), μ_3-O^{2-} (1), pivalate (1), phosphonate (2)
Mn8	CH_3O^- (2), μ_3-O^{2-} (1), pivalate (2), phosphonate (1)
Mn9	μ_3-OH^- (1), CH_3O^- (2), pivalate (2), phosphonate (1)
Mn10	CH_3COO^- (1), μ_3-OH^- (1), CH_3O^- (1), phosphonate (2), H_2O (1)
Mn11	CH_3COO^- (2), μ_3-OH^- (1), pivalate (2), phosphonate (1)
Mn12	CH_3COO^- (1), μ_3-OH^- (1), CH_3OH (1), μ_3-O^{2-} (1), pivalate (1), phosphonate (2)
Mn13	CH_3O^- (1), μ_3-O^{2-} (2), pivalate (2), phosphonate (1)
Mn14	CH_3O^- (1), μ_3-O^{2-} (1), pivalate (1), phosphonate (2)

All Mn centres reside in an octahedral coordination environment and within each trinuclear unit, the octahedron of the Mn centres share an edge with each other besides sharing edges with the octahedron of the Mn centres residing in the adjacent trinuclear units. Within unit 1, the

octahedron of Mn1 and Mn2 are edge shared besides sharing a vertex with that of Mn3. Additionally, the octahedron of Mn1 shares an edge with that of Mn11 while the octahedron of Mn2 shares a vertex with that of Mn4 and Mn13.

Mn1 and Mn2 of unit 1 are bound to each other by μ_3-O^{2-} (O4), μ-CH_3O^- (05), and a phenylphosphonate (P3) group (**Figure 7.42**). The Jahn-Teller axis for both is along the Mn-O4 bond but Mn1 exhibits an axial compression while Mn2 is axially elongated with the Mn1-O4 and Mn2-O4 bond lengths being 1.818(6) and 2.216(6) Å respectively (**Table 7.20**). The O-donor (O50) of a pivalate group also binds along the Jahn-Teller axis of Mn1 to form a Mn-O bond of 1.920(6) Å while for Mn2, the O-donor (O53) of a CH_3OH group binds along the Jahn-Teller axis and forms a Mn-O bond of 2.252(7) Å. The coordination environment of Mn1 is further fulfilled by the O donors of an acetate and another pivalate group while that of Mn2 is fulfilled by a pivalate and another μ_3-O^{2-} (O14) group. The pivalates bind in a 2.11 mode while the acetate group binds in a 3.21 mode. The distance between Mn1 and Mn2 is 2.994(2) Å which corresponds to the shortest Mn-Mn distance within this complex (**Table 7.20**). Mn1 is linked to Mn3 of unit 2 by a μ_3-O^{2-} (O4), a pivalate and an acetate group. Mn2 is linked to both Mn3 and Mn4 of unit 2 via μ_3-O^{2-} (O4 and O14) groups and a pivalate group. O14 also links Mn2 to Mn13 of unit 5 while both Mn1 and Mn2 are linked to Mn12 of the same unit via a phosphonate group (P3). Unit 1 is also linked to unit 4 with Mn1 being linked to Mn11 by a phosphonate, a pivalate and an acetate and Mn2 being linked to Mn10 by only the phosphonate group.

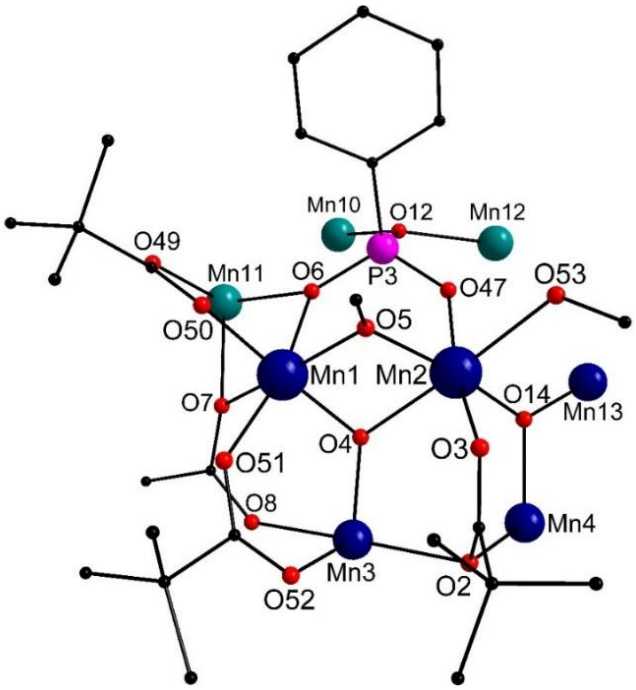

Figure 7.42: Coordination environment of unit 1 of compound **7.4**. Colour scheme: Mn^{II} (teal), Mn^{III} (dark blue), P (pink), C (black) and O (red). All hydrogen atoms have been removed for clarity.

Table 7.20: Key Mn-O and Mn-Mn bond lengths and bond valence sum for each Mn centre for compound **7.4**.

Mn centre	Coordinating atom	Bond Distance (Å)	BVS	Assigned oxidation state
Mn1	O4	1.818(6)	3.200	+III
	O5	2.002(7)		
	O6	2.183(6)		
	O7	2.053(6)		
	O50	1.920(6)		
	O51	2.095(7)		
Mn2	O3	1.998(7)	3.125	+III
	O4	2.126(6)		
	O5	1.933(6)		
	O14	1.893(6)		
	O47	1.926(6)		
	O53	2.252(7)		
Mn3	O1	1.910(6)	3.162	+III
	O2	2.446(6)		
	O4	1.854(6)		
	O8	2.167(6)		
	O17	1.913(6)		
	O52	1.969(6)		
Mn4	O1	1.926(6)	3.233	+III
	O2	2.195(6)		
	O14	1.887(6)		
	O15	2.142(6)		
	O18	1.923(6)		
	O43	1.964(7)		
Mn5	O1	1.888(6)	3.236	+III
	O16	2.220(6)		
	O17	2.106(6)		
	O18	1.939(7)		
	O19	1.978(6)		
	O41	1.905(6)		
Mn6	O16	2.018(6)	3.123	+III
	O19	1.926(6)		
	O20	2.166(6)		
	O21	1.874(7)		
	O37	1.949(7)		
	O40	2.184(7)		
Mn7	O20	1.992(7)	2.771	+III
	O21	2.176(6)		
	O22	2.037(6)		
	O26	2.213(6)		
	O29	1.974(7)		
	O39	1.959(9)		
Mn8	O20	1.902(6)	3.214	+III
	O28	2.175(6)		
	O29	1.923(7)		
	O30	1.953(7)		
	O35	1.954(7)		
	O36	2.120(8)		

Mn centre	Coordinating atom	Bond Distance (Å)	BVS	Assigned oxidation state
Mn9	O9	1.934(6)	3.255	+III
	O28	2.231(7)		
	O30	1.928(6)		
	O31	1.872(6)		
	O32	2.112(8)		
	O34	1.955(7)		
Mn10	O9	2.224(6)	2.184	+II
	O10	2.250(6)		
	O12	2.118(6)		
	O27	2.196(6)		
	O31	2.115(7)		
	O48	2.107(7)		
Mn11	O6	2.160(6)	2.115	+II
	O7	2.307(6)		
	O9	2.186(6)		
	O10	2.206(6)		
	O33	2.073(8)		
	O49	2.161(7)		
Mn12	O12	2.162(6)	2.074	+II
	O13	2.172(6)		
	O24	2.244(6)		
	O27	2.249(6)		
	O45	2.101(7)		
	O46	2.191(7)		
Mn13	O13	1.929(6)	3.106	+III
	O14	1.923(6)		
	O15	2.276(6)		
	O23	1.912(7)		
	O42	1.972(7)		
	O44	2.144(7)		
Mn14	O13	2.182(6)	2.277	+II
	O22	2.244(6)		
	O23	2.099(7)		
	O24	2.177(7)		
	O26	2.128(6)		
	O38	2.085(8)		

Metals	Distance (Å)	Metals	Distance (Å)
Mn1-Mn2	2.994(2)	Mn6-Mn8	3.593(2)
Mn1-Mn3	3.256(2)	Mn7-Mn8	2.948(2)
Mn1-Mn11	3.326(3)	Mn7-Mn14	3.249(3)
Mn2-Mn3	3.589(2)	Mn8-Mn9	3.139(2)
Mn2-Mn4	3.275(2)	Mn9-Mn10	3.086(3)
Mn2-Mn13	3.512(2)	Mn9-Mn11	3.670(3)
Mn3-Mn4	3.129(2)	Mn10-Mn11	3.305(2)
Mn3-Mn5	3.005(2)	Mn10-Mn12	3.316(2)
Mn4-Mn5	2.915(3)	Mn12-Mn13	3.636(2)
Mn4-Mn13	3.038(2)	Mn12-Mn14	3.230(2)
Mn5-Mn6	3.104(3)	Mn13-Mn14	3.136(3)
Mn6-Mn7	3.102(2)		

All Mn centres of unit 2 are connected to each other via the μ_3-OH^- group (O1) with the Mn-O1 bond varying from 1.89-1.93 Å (**Figure 7.43**). The Mn centres in this unit reside in an elongated octahedral environment. The Jahn-Teller axes of Mn3 and Mn4 are perpendicular to each other directed towards the μ_3-O^{2-} (O2) group such that the Mn-O bond is 2.446(6) and 2.195(6) Å respectively. The O donor from an acetate (O8) and a phosphonate group (O15) also lie on the Jahn-Teller axes of Mn3 and Mn4 respectively. The coordination environment of both Mn3 and Mn4 is further fulfilled by O donors from a μ_3-O^{2-}, and O-donors of a μ-CH_3O^- and a pivalate group with the Mn-O bonds varying between 1.85-1.97 Å. For Mn5, the O donor of the phosphonate group (O16) and a μ-CH_3O^- group (O17) lies along the Jahn-Teller axis forming an Mn-O bond of 2.220(6) and 2.106(6) Å respectively. Mn5 is further bound to O donors of two μ-CH_3O^- groups and a pivalate group with the Mn-O bond varying between 1.91-1.98 Å. Mn4 and Mn5 are bridged to Mn centres of unit 3 and unit 5 via phenylphosphonate, pivalate and methoxy groups.

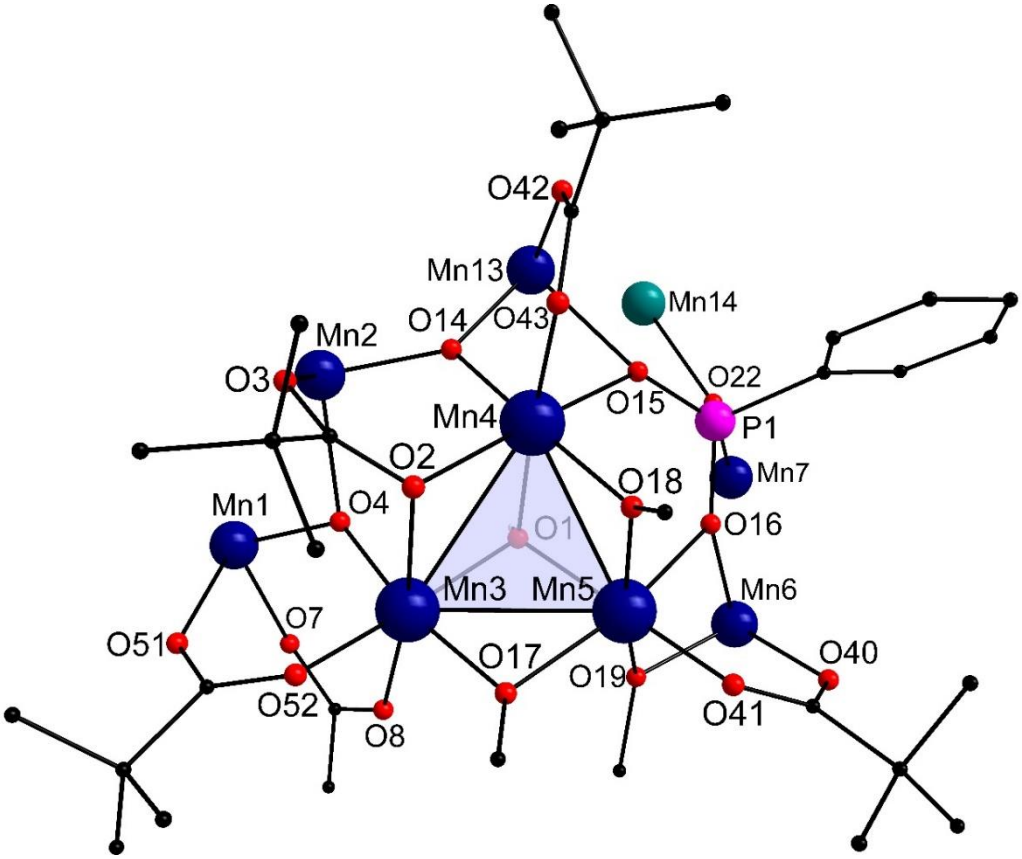

Figure 7.43: Coordination environment of unit 2 of compound **7.4**. Colour scheme: Mn^{II} (teal), Mn^{III} (dark blue), P (pink), C (black) and O (red). All hydrogen atoms (grey) except those of the oxygen centres have been removed for clarity.

The coordination environment of Mn6 consists of O donors from a μ_3-O^{2-} group (O20) and the O-donors of a phosphonate group (O16), two μ-CH_3O^- groups (O19 and O21) and two pivalate groups (O37 and O40) with the Jahn-Teller axis lying along O40 and O20 (**Figure 7.44**). The Mn-O distance varies between 1.87 and 2.01 Å perpendicular to the Jahn-Teller axis and is ~2.2 Å along it. For both Mn7 and Mn8, the Jahn-Teller axis is directed towards the same phosphonate group (containing

P2). Mn7 is coordinated to a μ_3-O^{2-} group (O20) in addition to the O-donors of two phosphonate groups (O22 and O26), a pivalate group (O39) and two μ-CH_3O^- groups (O21 and O29). The coordination environment of Mn8 is fulfilled by the O-donors of two μ-CH_3O^- (O29 and O30), two pivalate groups (O35 and O36) and a phosphonate group (O28) besides O20. The Mn-O distances for both Mn7 and Mn8 along the Jahn-Teller axis are ~2.2 Å while perpendicular to it, the distances vary between 1.96 and 2.04 Å for Mn7 and 1.90 and 1.95 Å for Mn8. Mn6 and Mn8 are the only two Mn centres in this complex that have the same ligands fulfilling their coordination spheres. Mn7 is linked to each Mn centre of unit 5 via the two phosphonate groups containing P1 and P2, and a pivalate group besides being linked to Mn9 and Mn10 of unit 4 via a phosphonate group (P2). The same phosphonate group also links Mn8 to Mn9 and Mn10 of unit 4 and Mn12 of unit 5.

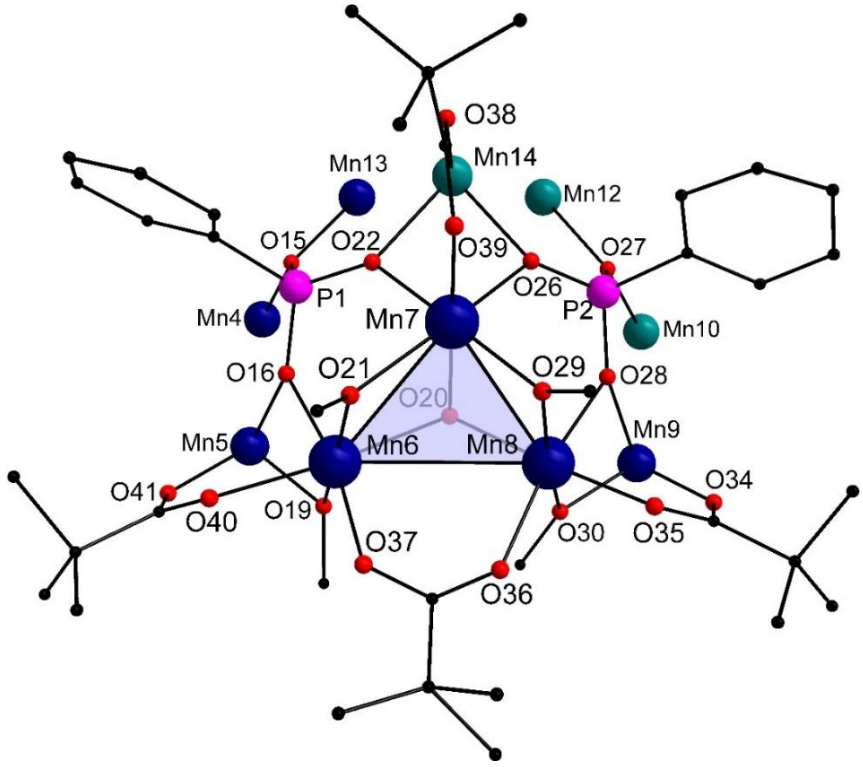

Figure 7.44: Coordination environment of unit 3 of compound **7.4**. Colour scheme: Mn^{II} (teal), Mn^{III} (dark blue), P (pink), C (black) and O (red). All hydrogen atoms (grey) except those of the oxygen centres have been removed for clarity.

All Mn centres of unit 4 bind to the μ_3-OH^- O-donor (O9) and in this unit, only Mn9 is in oxidation state +III. Its Jahn-Teller axis is along the O donors of the phosphonate (O28) and a pivalate (O32) group with the Mn-O bonds being 2.231(7) and 2.112(8) Å respectively (**Figure 7.45**). O donors from a μ_3-OH^-, a pivalate and two μ-CH_3O^- groups fulfil the remaining coordination sites of Mn9 with the Mn-O distance ranging from 1.87-1.96 Å. For Mn10, in addition to O9, the O-donors of a μ-CH_3O^- (O31), a H_2O molecule (O48), an acetate (O10) and two phenylphosphonate groups (O27 and O47) fulfil the coordination environment and the Mn-O distance varies between 2.11 and 2.25 Å. Mn11 binds to the O-donors of a phenylphosphonate (O6), two acetates (O7 and O10) and two pivalate groups (O33 and O49) with the Mn-O distance lying in the 2.16-2.31 Å range. Between the two

acetate groups, one is bidentate joining Mn11 to Mn1 and Mn3 while the other is monodentate and is stabilised by hydrogen bonding from the water molecule attached to Mn10.

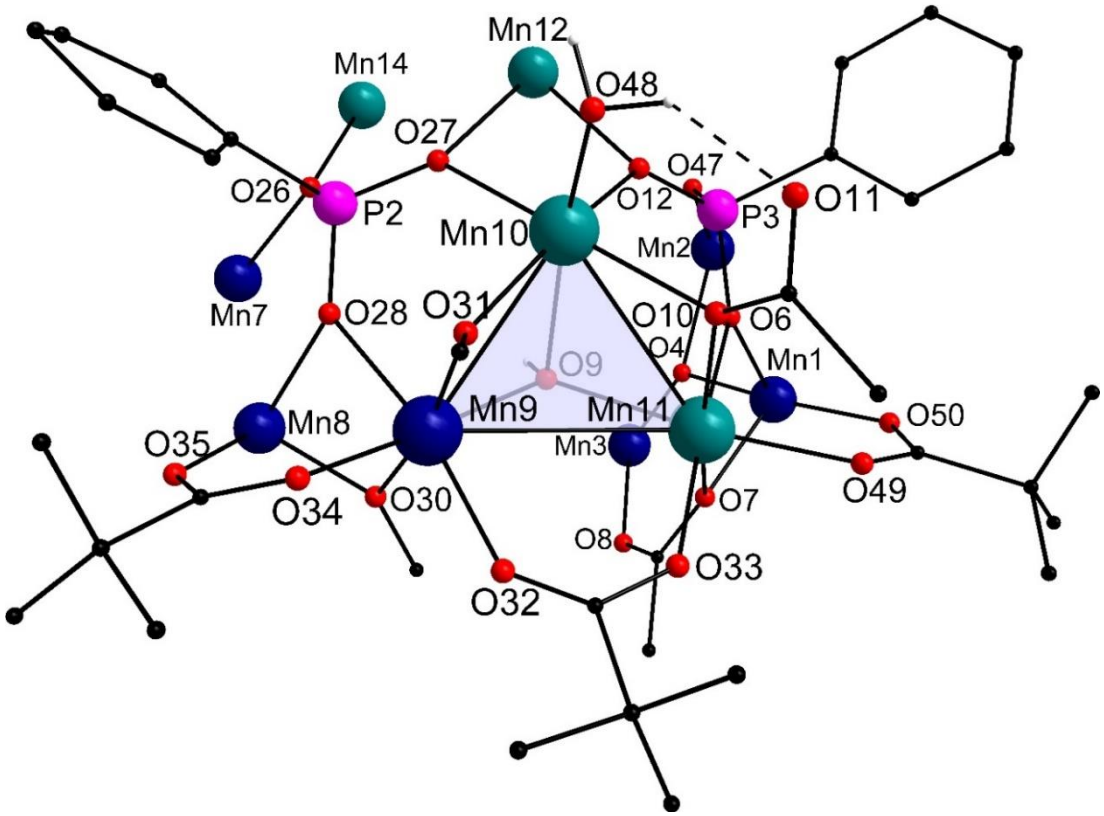

Figure 7.45: Coordination environment of unit 4 of compound **7.4**. Colour scheme: Mn^{II} (teal), Mn^{III} (dark blue), P (pink), C (black) and O (red). All hydrogen atoms (grey) except those of the oxygen centres have been removed for clarity.

Mn centres in unit 5 bind to O donors of all the three phosphonates with Mn12 and Mn14 linked to two phosphonate groups each while Mn13 binds to only one (**Figure 7.46**). The Jahn-Teller axis of Mn13 is along the O donor of the phosphonate group (O15) and a pivalate group (O44) with Mn-O bonds of 2.276(6) and 2.144(7) Å respectively. Two μ_3-O^{2-} groups (O13 and O14) and O-donors of another pivalate group (O42) and a μ-CH_3O^- (O13) complete the coordination environment of Mn13 with the Mn-O distances varying between 1.92-1.98 Å. Mn12 is bonded to a μ_3-O^{2-} (O13) and the O donors of a CH_3OH (O46), a pivalate (O45) and a monodentate acetate group (O24) in addition to the two phenylphosphonate groups (O12 and O27) and the Mn-O distances vary from 2.10 to 2.25 Å. The monodentate acetate is hydrogen bonded to the CH_3OH molecule. The octahedral geometry of Mn14 is completed by a μ_3-O^{2-} (O13) and the O-donors of a μ-CH_3O^- (O23), a pivalate (O38), a monodentate acetate (O24) and two phosphonate groups (O22 and O26) with the Mn-O bond ranging from 2.10 to 2.44 Å.

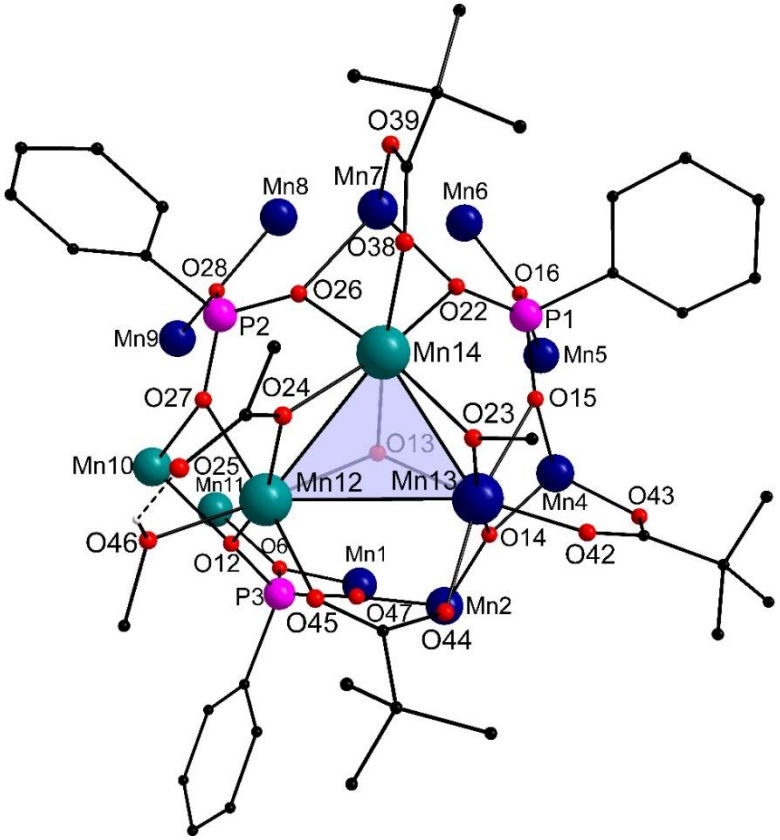

Figure 7.46: Coordination environment of unit 5 of compound **7.4**. Colour scheme: Mn^{II} (teal), Mn^{III} (dark blue), P (pink), C (black) and O (red). All hydrogen atoms (grey) except those of the oxygen centres have been removed for clarity.

Table 7.21: BVS analysis for O atoms and their assigned protonation state in compound **7.4**.

Atom	BVS	Assignment	Atom	BVS	Assignment
O1	2.013	μ_3-O^{2-}	O14	2.051	μ_3-O^{2-}
O4	2.002	μ_3-O^{2-}	O20	1.549	μ_3-O^{2-}
O9	1.277	μ_3-OH^-	O48	0.425	H_2O
O13	1.336	μ_3-OH^-			

Table 7.22: Continuous shape measure values, angle variance and distortion indices (using the ideal octahedral geometry as a reference) for each Mn centre for compound **7.4**.

Mn centre	Continuous shape measure value	Angle variance (σ^2)	Distortion Index
Mn1	1.314	42.42	0.0554
Mn2	1.361	48.08	0.0601
Mn3	2.018	65.28	0.0616
Mn4	0.736	26.02	0.0438
Mn5	1.728	70.63	0.0726
Mn6	1.024	42.30	0.0595
Mn7	1.083	51.77	0.0632
Mn8	0.953	35.79	0.0513
Mn9	1.023	36.05	0.0517
Mn10	1.545	80.63	0.0770
Mn11	0.961	61.35	0.0699
Mn12	0.834	58.06	0.0616
Mn13	1.173	46.93	0.0621
Mn14	1.522	100.26	0.0831

Table 7.23: Selected bond angles for compound **7.4**.

Bond	Bond Angle (°)	Bond	Bond Angle (°)
O7-Mn1-O6	79.5(2)	O30-Mn8-O28	77.9(3)
O4-Mn1-O5	81.6(3)	O20-Mn8-O29	81.5(3)
O50-Mn1-O51	82.8(3)	O35-Mn8-O36	84.4(3)
O5-Mn1-O6	88.2(2)	O35-Mn8-O28	88.8(3)
O50-Mn1-O6	89.1(3)	O30-Mn8-O35	90.2(3)
O7-Mn1-O51	90.7(3)	O29-Mn8-O35	91.4(3)
O50-Mn1-O5	91.3(3)	O20-Mn8-O28	91.9(3)
O50-Mn1-O7	93.8(3)	O29-Mn8-O28	92.4(3)
O4-Mn1-O51	93.9(3)	O30-Mn8-O36	94.0(3)
O4-Mn1-O7	94.2(3)	O20-Mn8-O36	95.8(3)
O4-Mn1-O6	95.4(2)	O29-Mn8-O36	95.8(3)
O5-Mn1-O51	102.3(3)	O20-Mn8-O30	96.9(3)
O5-Mn1-O7	166.6(3)	O36-Mn8-O28	169.5(3)
O51-Mn1-O6	166.8(3)	O29-Mn8-O30	170.2(3)
O4-Mn1-O50	171.5(3)	O20-Mn8-O35	172.9(3)
O5-Mn2-O4	75.9(3)	O30-Mn9-O28	77.0(2)
O47-Mn2-O53	82.9(3)	O31-Mn9-O9	84.6(3)
O3-Mn2-O53	83.0(3)	O34-Mn9-O32	84.6(3)
O5-Mn2-O3	88.2(3)	O34-Mn9-O28	87.5(3)
O14-Mn2-O47	89.1(3)	O31-Mn9-O34	88.9(3)
O47-Mn2-O5	89.4(3)	O30-Mn9-O34	89.6(3)
O14-Mn2-O53	92.4(3)	O31-Mn9-O28	90.9(3)
O3-Mn2-O4	93.3(3)	O9-Mn9-O28	92.5(2)
O14-Mn2-O4	94.7(2)	O30-Mn9-O32	95.0(3)
O14-Mn2-O3	95.8(3)	O9-Mn9-O32	96.2(3)
O5-Mn2-O53	97.2(3)	O30-Mn9-O9	96.7(3)
O47-Mn2-O4	100.1(2)	O31-Mn9-O32	96.8(3)
O47-Mn2-O3	165.3(3)	O31-Mn9-O30	167.9(3)
O14-Mn2-O5	170.0(3)	O32-Mn9-O28	168.8(3)
O4-Mn2-O53	172.4(3)	O9-Mn9-O34	173.5(3)
O1-Mn3-O2	79.1(2)	O31-Mn10-O9	72.4(2)
O1-Mn3-O17	81.5(3)	O12-Mn10-O27	80.1(2)
O52-Mn3-O2	84.5(3)	O9-Mn10-O10	80.3(2)
O52-Mn3-O8	87.2(3)	O48-Mn10-O10	85.9(3)
O4-Mn3-O1	87.3(2)	O31-Mn10-O10	90.1(3)
O4-Mn3-O2	88.0(2)	O12-Mn10-O10	91.6(2)
O17-Mn3-O2	90.8(2)	O48-Mn10-O31	92.1(3)
O4-Mn3-O8	91.3(2)	O12-Mn10-O9	93.7(2)
O17-Mn3-O52	91.5(3)	O27-Mn10-O9	94.4(2)
O17-Mn3-O8	91.6(3)	O31-Mn10-O27	96.5(2)
O4-Mn3-O52	99.5(3)	O48-Mn10-O27	101.5(3)
O1-Mn3-O8	109.5(3)	O48-Mn10-O12	102.4(3)
O1-Mn3-O52	162.0(3)	O48-Mn10-O9	159.0(3)
O4-Mn3-O17	168.8(3)	O31-Mn10-O12	165.5(2)
O8-Mn3-O2	171.3(2)	O27-Mn10-O10	169.9(2)
O18-Mn4-O1	80.0(3)	O6-Mn11-O7	74.6(2)
O14-Mn4-O15	84.1(2)	O49-Mn11-O7	81.7(2)
O1-Mn4-O2	85.5(2)	O9-Mn11-O10	82.1(2)
O18-Mn4-O2	87.6(3)	O6-Mn11-O49	86.8(2)
O43-Mn4-O15	89.1(3)	O6-Mn11-O9	87.2(2)
O18-Mn4-O15	90.7(2)	O6-Mn11-O10	89.1(2)
O14-Mn4-O43	91.1(3)	O33-Mn11-O49	89.8(3)
O43-Mn4-O2	91.7(3)	O49-Mn11-O10	95.0(2)
O18-Mn4-O43	92.3(3)	O33-Mn11-O9	96.5(3)

Bond	Bond Angle (°)	Bond	Bond Angle (°)
O1-Mn4-O15	93.5(2)	O33-Mn11-O10	97.0(3)
O14-Mn4-O1	96.8(2)	O33-Mn11-O7	99.1(3)
O14-Mn4-O2	97.5(3)	O9-Mn11-O7	99.4(2)
O1-Mn4-O43	171.9(3)	O10-Mn11-O7	163.5(2)
O14-Mn4-O18	173.8(3)	O33-Mn11-O6	173.2(3)
O15-Mn4-O2	178.2(2)	O49-Mn11-O9	173.4(3)
O19-Mn5-O16	74.5(2)	O12-Mn12-O27	78.0(2)
O1-Mn5-O17	77.1(2)	O13-Mn12-O24	83.0(2)
O1-Mn5-O18	80.6(2)	O45-Mn12-O46	84.5(3)
O18-Mn5-O16	89.0(2)	O24-Mn12-O27	85.4(2)
O1-Mn5-O16	90.1(2)	O46-Mn12-O27	88.0(2)
O41-Mn5-O19	91.2(3)	O46-Mn12-O24	88.4(2)
O41-Mn5-O18	92.5(3)	O12-Mn12-O46	88.8(2)
O41-Mn5-O16	94.9(3)	O45-Mn12-O24	89.7(3)
O1-Mn5-O19	97.0(3)	O13-Mn12-O27	92.2(2)
O18-Mn5-O17	97.1(3)	O45-Mn12-O13	94.5(2)
O19-Mn5-O17	98.4(3)	O12-Mn12-O13	99.6(2)
O41-Mn5-O17	98.9(3)	O45-Mn12-O12	106.4(3)
O18-Mn5-O19	163.4(3)	O12-Mn12-O24	163.3(3)
O17-Mn5-O16	164.6(2)	O45-Mn12-O27	171.2(3)
O1-Mn5-O41	171.4(3)	O13-Mn12-O46	171.4(3)
O19-Mn6-O16	80.5(3)	O14-Mn13-O15	79.8(2)
O21-Mn6-O20	81.2(2)	O23-Mn13-O13	80.9(3)
O37-Mn6-O40	84.0(3)	O42-Mn13-O15	83.3(3)
O16-Mn6-O40	84.3(2)	O42-Mn13-O44	84.3(3)
O19-Mn6-O40	87.9(3)	O23-Mn13-O15	88.9(3)
O21-Mn6-O16	90.5(3)	O14-Mn13-O42	89.0(3)
O16-Mn6-O20	90.9(2)	O23-Mn13-O42	90.6(3)
O19-Mn6-O20	93.6(2)	O13-Mn13-O15	92.5(2)
O21-Mn6-O37	94.0(3)	O14-Mn13-O44	95.6(3)
O19-Mn6-O37	95.8(3)	O23-Mn13-O44	95.6(3)
O21-Mn6-O40	96.5(3)	O14-Mn13-O13	98.5(3)
O37-Mn6-O20	100.9(3)	O13-Mn13-O44	100.4(3)
O37-Mn6-O16	167.9(3)	O44-Mn13-O15	166.8(2)
O21-Mn6-O19	169.6(3)	O23-Mn13-O14	168.6(3)
O20-Mn6-O40	174.7(3)	O13-Mn13-O42	170.6(3)
O29-Mn7-O20	78.1(3)	O23-Mn14-O13	71.2(2)
O20-Mn7-O21	78.4(2)	O26-Mn14-O22	77.7(2)
O22-Mn7-O26	80.3(2)	O38-Mn14-O22	81.4(3)
O39-Mn7-O22	89.2(3)	O24-Mn14-O13	84.4(2)
O22-Mn7-O21	89.7(2)	O26-Mn14-O24	89.7(2)
O20-Mn7-O26	92.0(2)	O26-Mn14-O13	90.7(2)
O39-Mn7-O26	92.5(3)	O38-Mn14-O26	91.2(3)
O29-Mn7-O21	94.0(3)	O13-Mn14-O22	92.2(2)
O29-Mn7-O26	94.5(3)	O23-Mn14-O24	93.6(3)
O20-Mn7-O22	94.7(2)	O23-Mn14-O22	97.2(2)
O39-Mn7-O21	97.7(3)	O38-Mn14-O24	102.6(3)
O39-Mn7-O29	98.4(3)	O38-Mn14-O23	106.2(3)
O21-Mn7-O26	165.6(2)	O23-Mn14-O26	161.1(3)
O29-Mn7-O22	171.0(3)	O24-Mn14-O22	166.9(2)
O39-Mn7-O20	174.4(3)	O38-Mn14-O13	172.8(3)

This system packs quite compactly without any solvent molecule and accessible voids (**Figure 7.47**). The phenyl rings attached to P1 and P2, the *tert*-butyl groups attached to C15, C30, C66, C92 and C101) of two pivalate ligands and the methyl group attached to O30 were disordered and were modelled as two parts but only the major part has been shown here for clarity. The stabilisation of the packing is probably achieved by weak dispersion forces and not due to π-π stacking because the closest phenyl rings are those attached to P3 and the distance between their centroids is ~4.8 Å.

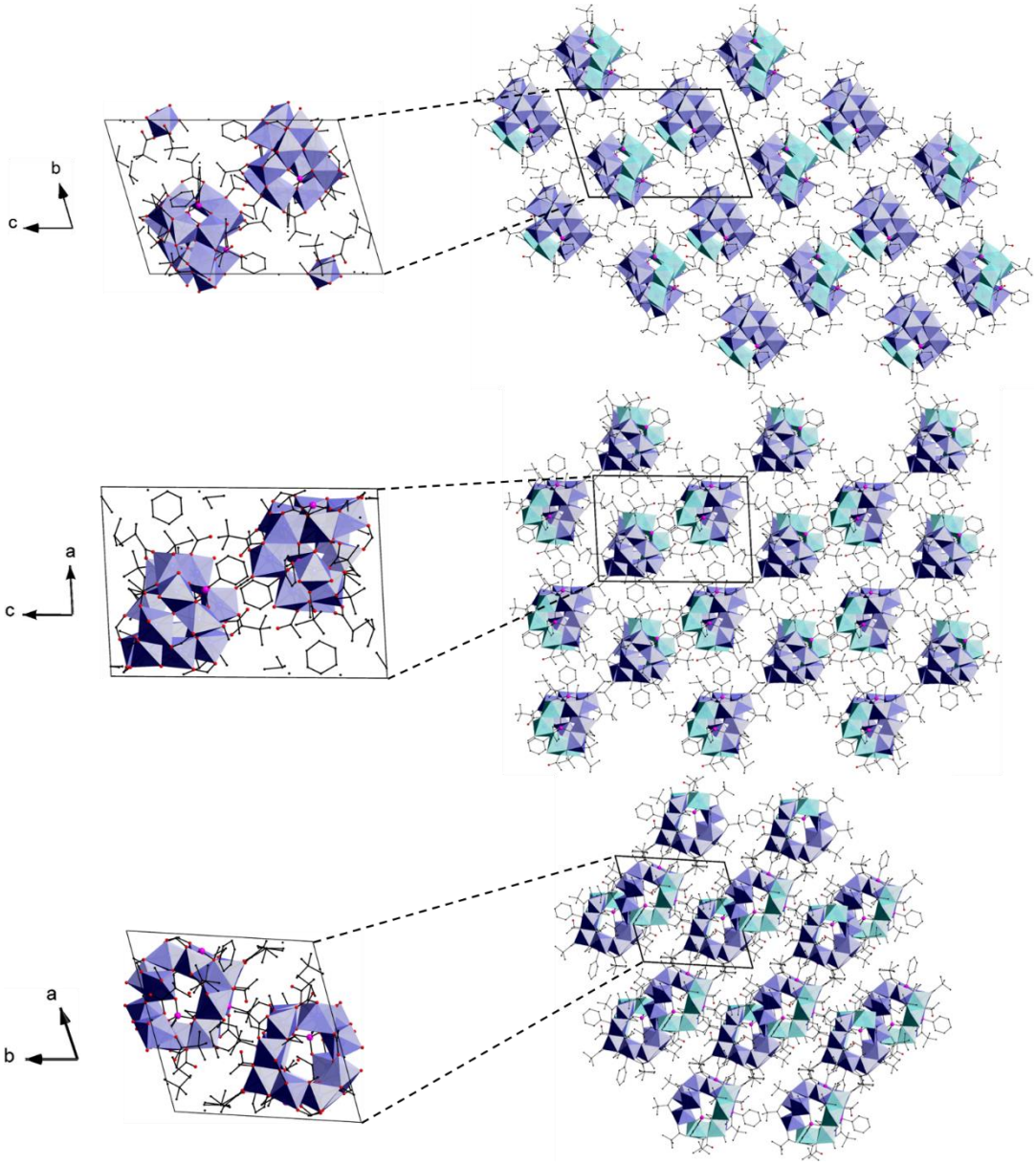

Figure 7.47: Packing diagram of compound **7.4**. Colour scheme: Mn^{II} (teal), Mn^{III} (dark blue), P (pink), C (black) and O (red).

7.4.2 Physicochemical characterisation

The phase purity of the bulk material was determined using powder X-Ray diffraction (PXRD) and it was found to be in agreement with the simulated pattern (**Figure 7.48**). Infrared spectrum of compound **7.4** is also in line with the proposed structure determined by XRD (**Figure 7.49**). The signal between 2962-2870 cm^{-1} corresponds to the C-H vibrations of the organic ligands.[617] The symmetric and asymmetric stretches of the carboxylate groups were observed at 1406 and 1538 cm^{-1} respectively and are in line with the expected energy variance for bridging carboxylate groups.[618] The additional features in the 1300-1600 cm^{-1} range are due to vibrations of the organic moieties of the molecule.[617] The band between 940 and 1050 cm^{-1} correspond to the stretching of the phosphonate group.[621-623]

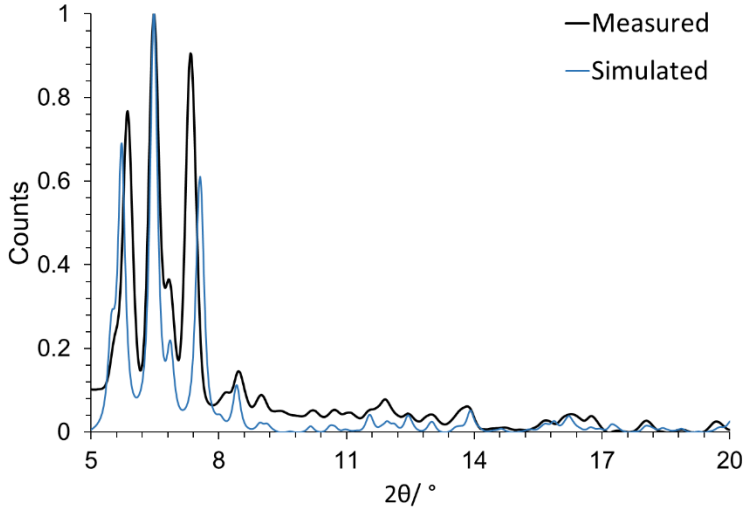

Figure 7.48: Measured and simulated PXRD pattern for compound **7.4**.

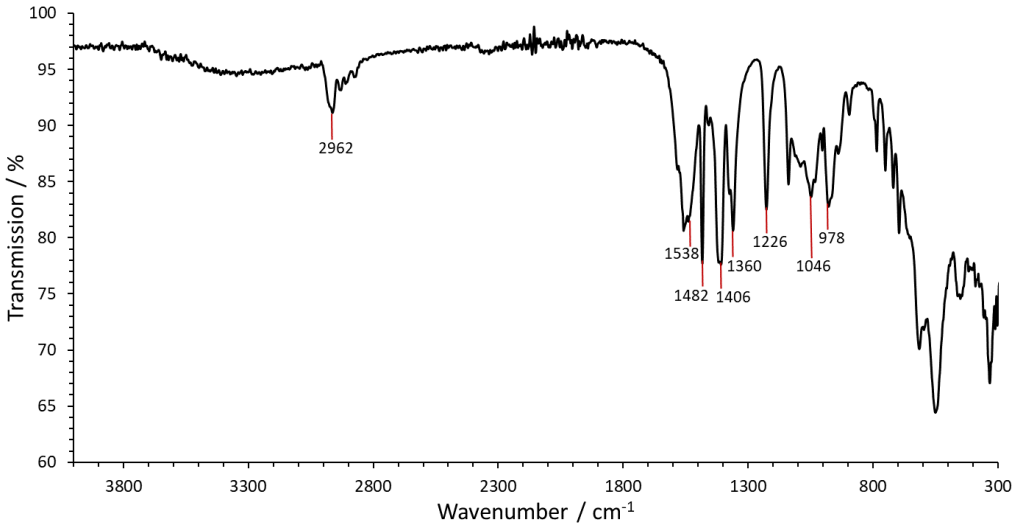

Figure 7.49: Infrared spectrum of compound **7.4**.

7.4.3 Magnetic properties

The magnetic properties of compound **7.4** were studied on a microcrystalline sample and the temperature dependence of magnetic susceptibility was determined in the temperature range of 4-300 K (**Figure 7.50**). The room temperature χT value was found to be 38.5 cm^3 K mol^{-1} which is significantly lower than the expected value of 47.5 cm^3 K mol^{-1} for a system with 4 Mn^{II} (S = 2.5) and 10 Mn^{III} (S = 2) centres. This suggests that the exchange coupling between the Mn centres is dominantly antiferromagnetic. Upon lowering the temperature, this value decreases and reaches 11.7 cm^3 K mol^{-1} at 4 K. For a system with an even number of electrons with solely antiferromagnetic coupling between the paramagnetic centres, S = 0 states form the ground state. Since χT is significantly higher at 4 K, ferromagnetic coupling in this system cannot be ruled out. The presence of ferromagnetic coupling is also supported by the feature observed at ~17 K. Additionally, the presence of triangular units and the asymmetry in the structure can potentially lead to higher spin ground states.

Electrochemical studies for this complex have not been performed due to poor yields of this compound.

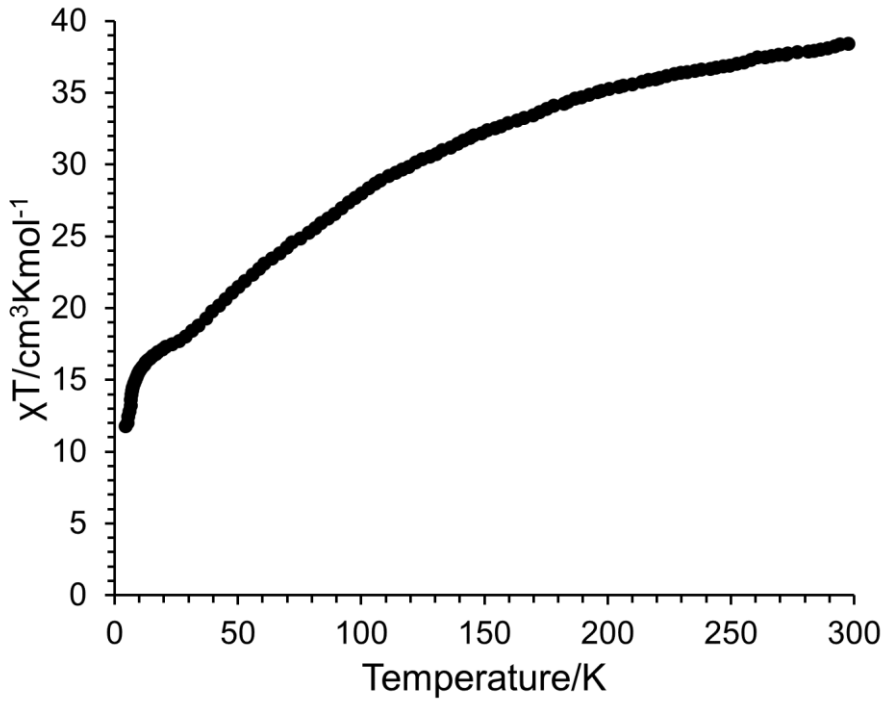

Figure 7.50: Temperature dependence of magnetic susceptibility (χT) of compound **7.4**.

7.5 $[(Mn^{II}_{0.5}Mn^{III}_{0.5})_2Mn^{III}_{11}(\mu_3\text{-}O)_8((C_6H_5)PO_3)_4((CH_3)_3CCO_2)_{10}(\mu\text{-}CH_3O)_4(\mu\text{-}CH_3OH)_4]\cdot CH_3OH\cdot CH_3CN$ (7.5)

Compound **7.5** can be prepared by refluxing $KMnO_4$, $Mn(CH_3COO)_2{\cdot}4H_2O$, phenylphosphonic acid and pivalic acid in a ratio of 1:5:2.5:40 in presence of 2,6-pyridinedimethanol in a mixture of CH_3CN and CH_3OH. Dark block crystals of compound **7.5** were obtained within a week which were characterised by single crystal X-ray diffraction.

7.5.1 Structural description

Compound **7.5**, like compound **7.4**, crystallises in the triclinic crystal system and the structure was solved in the space group $P\bar{1}$. This compound contains a tridecanuclear complex $[Mn_{13}(\mu_3\text{-}O)_8((C_6H_5)PO_3)_4((CH_3)_3CCO_2)_{10}(\mu\text{-}CH_3O)_4(\mu\text{-}CH_3OH)_4]$, with the asymmetric unit containing the whole complex (**Figure 7.51 (a)**). The core structure of this system can be considered as a truncated tetrahedron that has been distorted to an extent that it transforms to a distorted elongated gyrobifastigium with twelve Mn centres at the vertices and one in the centre (**Figure 7.51 (b)**). An elongated gyrobifastigium contains two prismatic units augmented to a cube such that the dihedral angle between the two prismatic units is 90°. Although the gyrobifastigium geometry (in which two prismatic units are fused together at 90° to each other) has been observed in a number of complexes,[593] this is the first complex that exhibits the elongated gyrobifastigium geometry as far as we know. The synthetic protocol for both compounds **7.4** and **7.5** is quite similar as both use an excess of pivalic acid but the influence of subtle differences is immense.

The triangular prismatic $\{Mn_6\}$ units are stabilised by two $\mu_3\text{-}O^{2-}$, two $\mu\text{-}CH_3O^-$, two phenylphosphonate and five pivalate groups (**Figure 7.51 (c)**). The pivalate and phosphonate groups bind in 2.11 and 4.211 mode (Harris notation[605]) respectively. The $\mu_3\text{-}O^{2-}$ groups form the centre of triangular $\{Mn_3\}$ units and lie ~0.19 Å below the $\{Mn_3\}$ plane. The $\{Mn_6\}$ units are linked to each other via $\mu\text{-}CH_3OH$ and $\mu\text{-}CH_3O^-$ in addition to four $\mu_3\text{-}O^{2-}$ groups bound to the central Mn (Mn11). The dihedral between the two triangular prisms is 87° which is close to the expected value of 90° for the elongated gyrobifastigium geometry.

Within each $\{Mn_6\}$ unit, the Mn centres can be divided into two different types based on their proximity to Mn11: type-1 – that are closer to Mn11 (Mn1 – Mn8) and type-2 – that are further away (Mn9, Mn10, Mn12 and Mn13). The type-1 Mn centres are ~3.3 Å away from Mn11 and are coordinated to a $\mu\text{-}CH_3O^-$, $\mu\text{-}CH_3OH$, a pivalate, a phosphonate and two $\mu_3\text{-}O^{2-}$ groups. The type-2 Mn centres, on the other hand are coordinated to a $\mu_3\text{-}O^{2-}$, two phosphonates and three pivalates and are ~4.4 Å away from Mn11. Bond valence sum analysis was used to identify the oxidation state of each Mn centre (**Table 7.24**). A +III oxidation state can be assigned to all Mn centres except Mn10 and Mn13. The bond valence sum for Mn10 and Mn13 is close to 2.5 which suggests that these may possess an intermediate oxidation state. Such an assignment is required for the charge neutrality

of the complex. Bond valence sum analysis has also been used to determine the protonation states of the O atoms bound only to Mn centres (**Table 7.25**). The values obtained in some cases do not strictly meet the proposed criteria for assignment[603, 604] so the protonation state has been decided based on the proximity of the bond valence sum value to an integer.

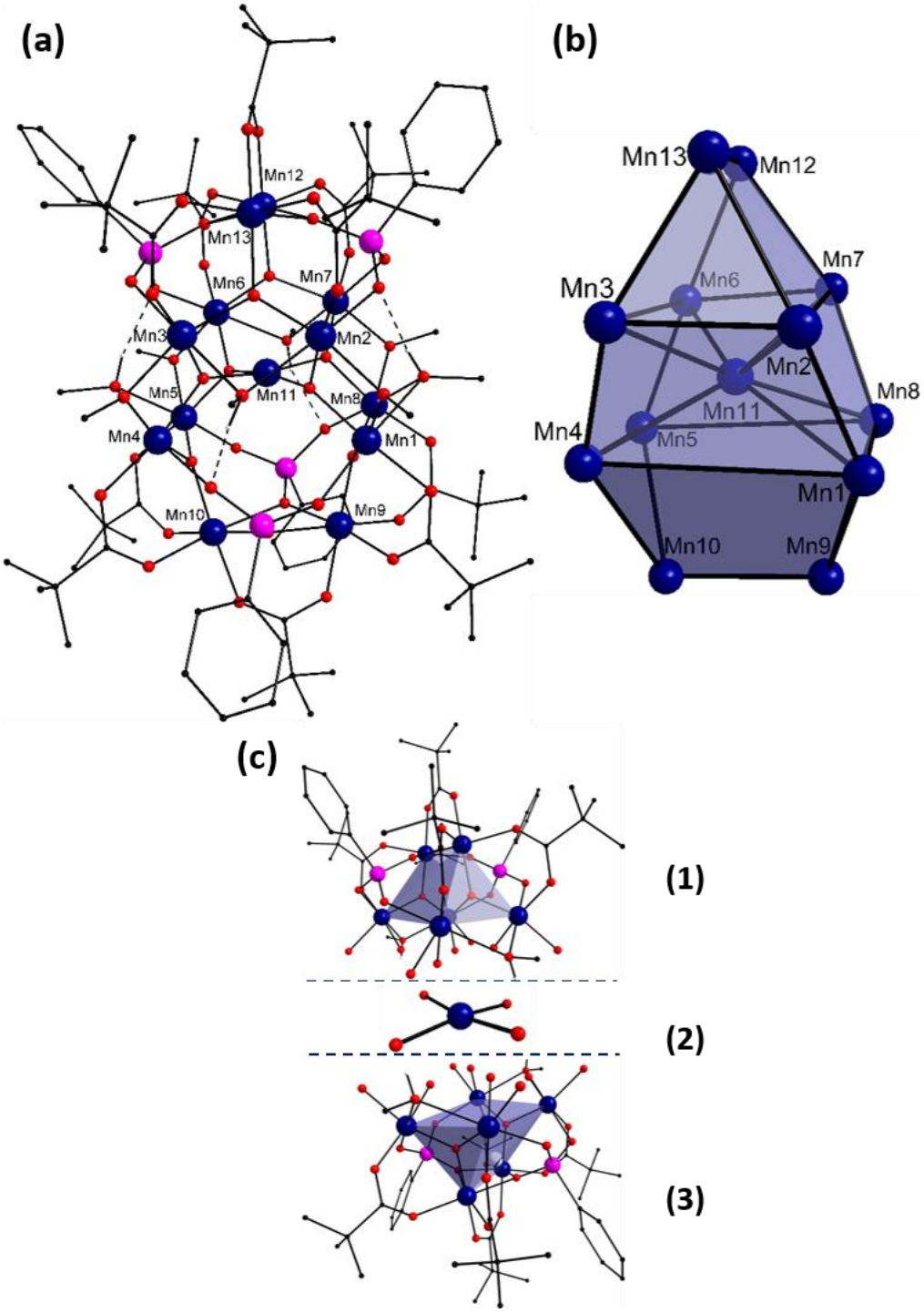

Figure 7.51: (a) Crystal structure of the tridecanuclear compound **7.5**, **(b)** polyhedron representation of the core of the complex and **(c)** with the constituent trigonal prismatic units of the complex. The hydrogen bonds are shown with dashed lines. Colour scheme: Mn^{III} (dark blue), P (pink), C (black) and O (red). All hydrogen atoms (grey) except those belonging to methanol molecules have been removed for clarity.

Within one {Mn_6} unit comprising of Mn1, Mn4, Mn5, Mn8, Mn9 and Mn10 (**Figure 7.52**), for the type-1 Mn centres, the O-donors of the phosphonate and the μ-CH_3OH lie along the Jahn-Teller axis. The Mn-$O_{methanol}$ distance for each Mn centre is 2.4 Å while the Mn-$O_{phosphonate}$ bond length is ~2.12 Å for Mn1 and Mn5, and ~2.16 Å for Mn4 and Mn8. The slight difference in the bond lengths is because of hydrogen bonding with the μ-CH_3OH from the other {Mn_6} unit with the phosphonate O-donors ($O_{phosphonate}$-H distance and $O_{phosphonate}$-$O_{methanol}$ distances being ~1.93 Å and ~2.74 Å respectively)[636] bound to Mn4 and Mn8. The Mn1-O8 (μ_3-O^{2-} group) and Mn8-O8 distance is 1.924(5) Å while the Mn4-O4 and Mn5-O5 distances are 1.906(6) and 1.916(5) Å respectively. The Mn-O bond distances between the type-1 Mn centres and the μ_3-O^{2-} groups shared with the central Mn are quite short and lie between 1.84-1.86 Å. The distance between Mn and O of μ-CH_3O^- has been found to be between 1.95-1.98 Å while that between Mn, and O-donors of pivalate groups has been found to vary between 1.91-1.94 Å. The octahedral environment of the type-1 Mn centres is only slightly distorted as illustrated by the small continuous shape measure values[611-614] and the distortion indices (**Table 7.26**). The distortion is in part due to the Jahn-Teller axis of the Mn^{III} centres and partially because of the geometrical restrictions imposed by the coordinating ligands and this can be observed from the bond distances (**Table 7.24**) and bond angles (**Table 7.27**). The octahedron of these Mn centres shares an edge with the octahedra of each other and a vertex with the octahedra of type-2 Mn centres (**Figure 7.53**).

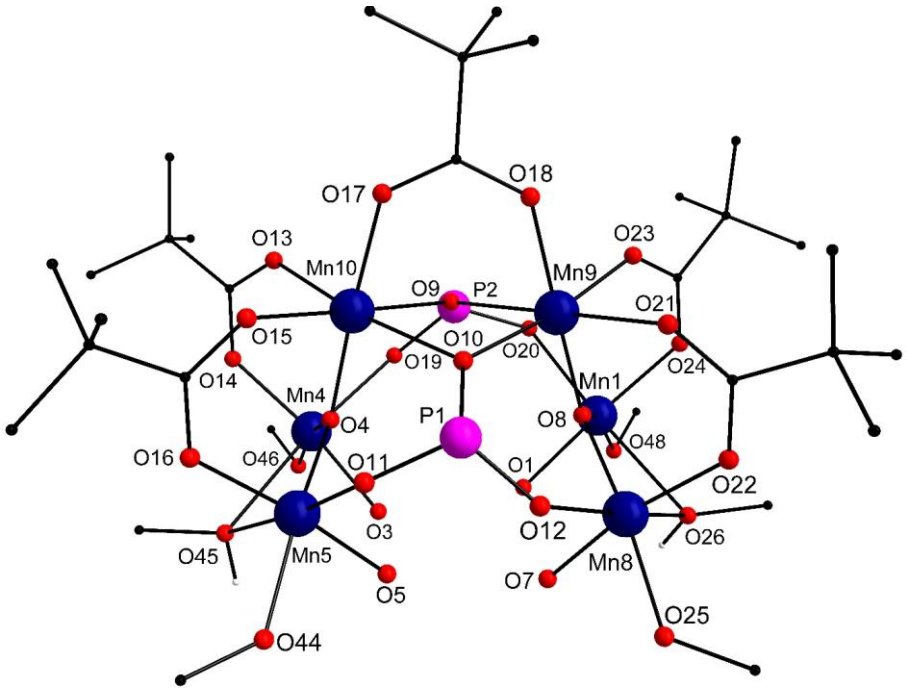

Figure 7.52: {Mn_6} unit of compound **7.5**. Colour scheme: Mn^{III} (dark blue), P (pink), C (black) and O (red). All hydrogens (grey) except the methanolic hydrogens have been removed for clarity.

Table 7.24: Key Mn-O and Mn-Mn bond lengths and bond valence sum for each Mn centre for compound **7.5**.

Mn centre	Coordinating atom	Bond Distance (Å)	BVS	Assigned oxidation state
Mn1	O1	1.850(5)	3.192	+III
	O8	1.924(5)		
	O20	2.117(5)		
	O24	1.938(5)		
	O26	2.391(5)		
	O48	1.959(5)		
Mn2	O1	1.859(5)	3.139	+III
	O2	1.898(5)		
	O29	2.181(5)		
	O33	1.919(6)		
	O47	2.450(5)		
	O48	1.977(5)		
Mn3	O2	1.913(5)	3.182	+III
	O3	1.846(5)		
	O35	1.916(6)		
	O38	2.156(5)		
	O46	1.971(6)		
	O47	2.428(6)		
Mn4	O3	1.862(5)	3.189	+III
	O4	1.906(6)		
	O14	1.911(6)		
	O19	2.177(5)		
	O45	2.433(6)		
	O46	1.948(6)		
Mn5	O4	1.916(5)	3.241	+III
	O5	1.835(6)		
	O11	2.112(6)		
	O16	1.915(6)		
	O44	1.978(6)		
	O45	2.417(6)		
Mn6	O5	1.875(5)	3.211	+III
	O6	1.903(6)		
	O27	2.421(6)		
	O39	2.153(6)		
	O43	1.909(6)		
	O44	1.942(6)		
Mn7	O6	1.918(5)	3.213	+III
	O7	1.854(5)		
	O25	1.965(5)		
	O27	2.402(6)		
	O28	2.117(6)		
	O41	1.918(5)		
Mn8	O7	1.859(5)	3.161	+III
	O8	1.924(5)		
	O12	2.162(6)		
	O22	1.910(5)		
	O25	1.961(5)		
	O26	2.409(6)		

Mn centre	Coordinating atom	Bond Distance (Å)	BVS	Assigned oxidation state
Mn9	O8	1.863(5)	3.094	+III
	O9	2.199(5)		
	O10	1.976(5)		
	O18	1.930(6)		
	O21	2.180(6)		
	O23	2.002(6)		
Mn10	O4	1.921(6)	2.697 (assuming valence III)/ 2.925 (assuming valence II)	+II/III
	O9	2.051(5)		
	O10	2.241(5)		
	O13	2.147(6)		
	O15	2.054(7)		
	O17	2.003(7)		
Mn11	O1	1.852(5)	3.139	+III
	O3	1.846(5)		
	O5	1.849(6)		
	O7	1.851(5)		
Mn12	O6	1.895(6)	2.924	+III
	O30	2.181(5)		
	O31	2.041(5)		
	O37	1.942(7)		
	O40	2.043(6)		
	O42	2.134(6)		
Mn13	O2	1.944(5)	2.669 (assuming valence III)/ 2.895 (assuming valence II)	+ II/III
	O30	2.066(5)		
	O31	2.212(6)		
	O32	2.129(6)		
	O34	2.060(7)		
	O36	2.005(8)		

Metals	Distance (Å)	Metals	Distance (Å)
Mn1-Mn2	2.967(1)	Mn4-Mn11	3.285(2)
Mn1-Mn4	5.074(2)	Mn5-Mn6	2.961(2)
Mn1-Mn8	3.269(2)	Mn5-Mn8	5.073(2)
Mn1-Mn9	3.254(1)	Mn5-Mn10	3.294(2)
Mn1-Mn11	3.328(2)	Mn5-Mn11	3.306(2)
Mn2-Mn3	3.237(2)	Mn6-Mn7	3.237(2)
Mn2-Mn7	5.067(2)	Mn6-Mn11	3.281(2)
Mn2-Mn11	3.260(2)	Mn6-Mn12	3.342(2)
Mn2-Mn13	3.369(2)	Mn7-Mn8	2.954(2)
Mn3-Mn4	2.968(2)	Mn7-Mn11	3.325(2)
Mn3-Mn6	5.090(2)	Mn7-Mn12	3.267(2)
Mn3-Mn11	3.290(2)	Mn8-Mn9	3.326(2)
Mn3-Mn13	3.303(2)	Mn8-Mn11	3.283(2)
Mn4-Mn5	3.266(2)	Mn9-Mn10	3.243(2)

The type-2 Mn centres (Mn9 and Mn10) within the same {Mn_6} unit reside in a less distorted octahedral environment compared to type-1 Mn centres (**Table 7.26**). The octahedron of these Mn centres shares an edge with that of each other (**Figure 7.53**). The Jahn-Teller axis for each Mn centre is directed along the O-donors of different phosphonate groups (O9 and O10) in such a way that the Jahn-Teller axis for Mn9 is parallel to that of Mn10. This leads to Mn9-O9 and Mn10-O10

distances being 2.199(5) and 2.241(5) Å respectively while the Mn9-O10 and Mn10-O9 distances are 1.976(5) and 2.051(5) Å respectively. The Mn-O distance between Mn and the O of the pivalate ligand coordinated along the Jahn-Teller axis for Mn9 and Mn10 has been found to be 2.180(6) and 2.147(6) Å respectively. The Mn-O distance between Mn and O of other pivalate groups has been found to between ~1.9 and 2.1 Å. The distance between the μ_3-O^{2-} groups (O8 and O4) and Mn9 and Mn10 has been found to be 1.863(5) and 1.921(6) Å respectively. For both type-1 and type-2 Mn centres of the other {Mn_6} unit which comprises of Mn2, Mn3, Mn6, Mn7, Mn12 and Mn13 the Mn-O distances have been found to be similar (**Table 7.24**).

Table 7.25: BVS analysis for O atoms and their assigned protonation state in compound **7.5**.

Atom	BVS	Assignment	Atom	BVS	Assignment
O1	2.329	μ_3-O^{2-}	O5	2.336	μ_3-O^{2-}
O2	1.958	μ_3-O^{2-}	O6	2.026	μ_3-O^{2-}
O3	2.344	μ_3-O^{2-}	O7	2.323	μ_3-O^{2-}
O4	1.977	μ_3-O^{2-}	O8	2.041	μ_3-O^{2-}

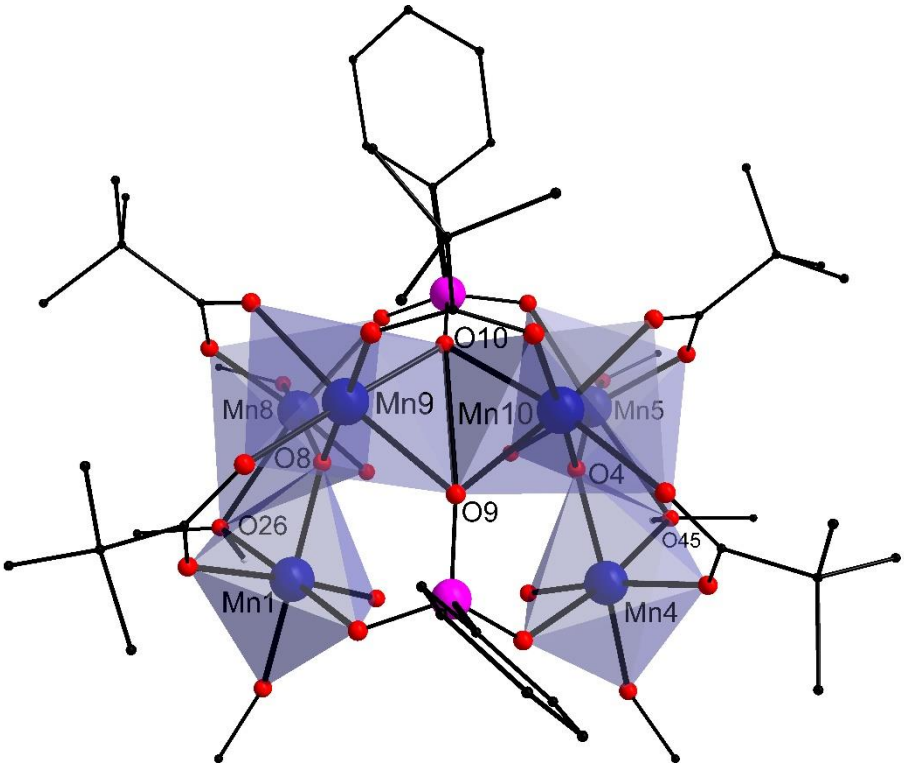

Figure 7.53: Polyhedral representation of one of the {Mn_6} units of compound **7.5**. The oxygen atoms labelled here are the ones shared between the octahedrons of the Mn centres. Colour scheme: Mn^{III} (dark blue), P (pink), C (black) and O (red). All hydrogen atoms have been removed for clarity.

The central Mn is in oxidation state +III and resides in a slightly distorted square planar environment that is exclusively fulfilled by μ_3-O^{2-} groups. The possibility of the coordination environment of this Mn centre being tetrahedral was also examined using continuous shape measure analysis.[611-614] Such a description, however, leads to a higher continuous shape measure values (**Table 7.26**)

indicating that the coordination environment is square planar. All Mn-O bond lengths are ~1.85 Å which is quite short and there are only 187 structures out of 1620 structures in the CCDC database[637] that contain μ_3-O^{2-} groups with Mn-O bond lengths shorter than 1.86 Å.

This system crystallises along with a CH_3CN and CH_3OH molecule and other partially occupied solvent molecules which could not be resolved due to the crystal quality and were removed using the squeeze routine as implemented in the PLATON code.[629, 635] The crystal packing is shown in **Figure 7.54**. The *tert*-butyl groups (attached to C17 and C51) of two pivalate ligands and phenyl rings of two phenylphosphonate groups (P3 and P4) were disordered and were modelled as two parts but the figure shows only one part for clarity. The packing is stabilised by π-π interaction between the phenylphosphonate groups and the interaction of the complex with the solvent molecules trapped in the lattice.

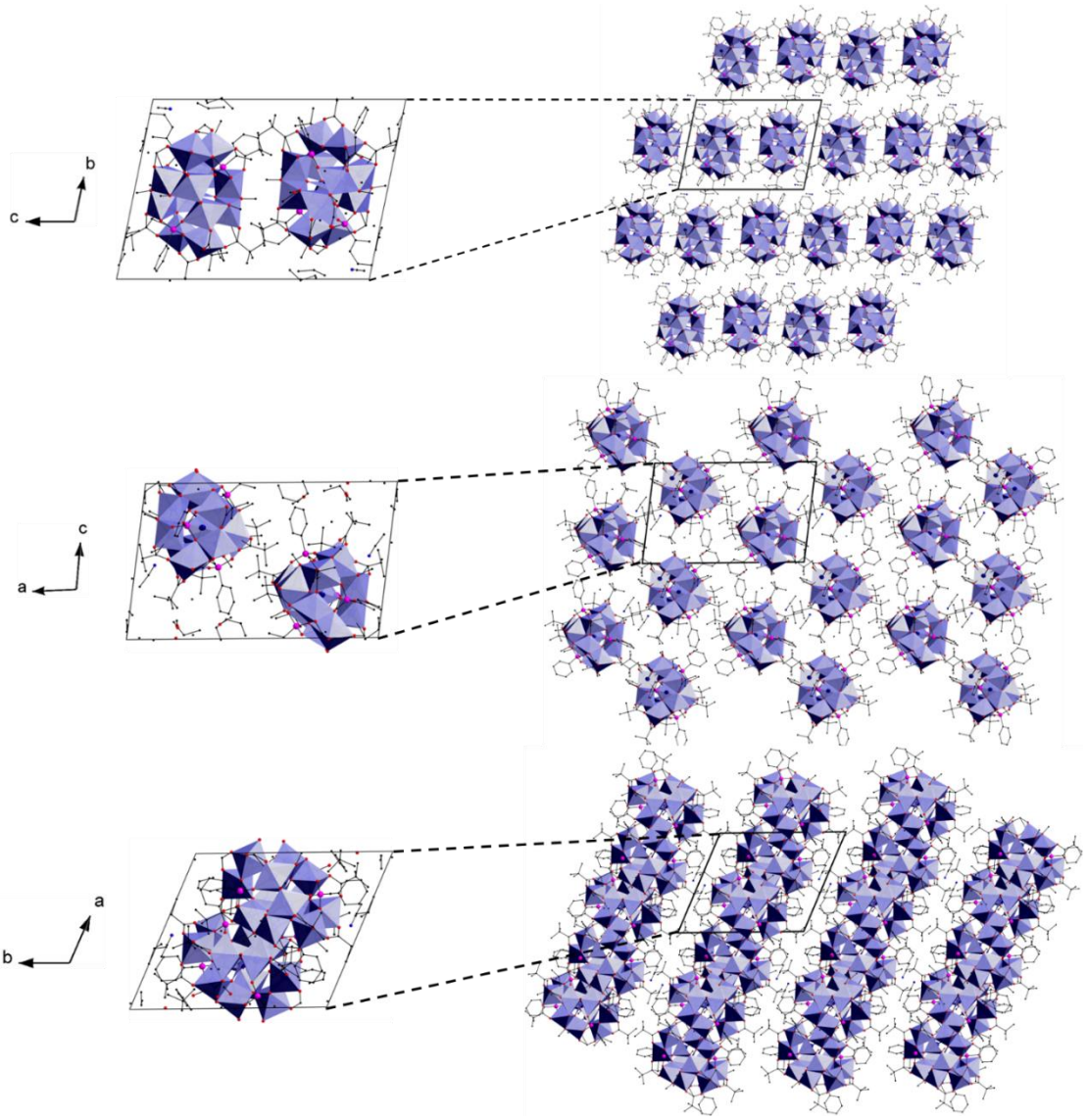

Figure 7.54: Packing diagram of compound **7.5**. Colour scheme: Mn^{III} (dark blue), P (pink), C (black), O (red), N (blue) and H (grey).

Table 7.26: Continuous shape measure values, angle variance and distortion indices for each Mn centre for compound **7.5**. All values are obtained using octahedral geometry as reference unless otherwise stated.

Mn centre	Continuous shape measure value	Angle variance (σ^2)	Distortion Index
Mn1	1.537	53.03	0.0611
Mn2	1.637	45.76	0.0588
Mn3	1.639	46.42	0.0556
Mn4	1.694	52.36	0.0623
Mn5	1.583	48.78	0.0570
Mn6	1.499	46.32	0.0593
Mn7	1.468	47.91	0.0570
Mn8	1.580	47.77	0.0611
Mn9	0.733	23.84	0.0402
Mn10	0.675	30.41	0.0410
Mn11	0.651 (square planar) /25.985 (tetrahedral)		
Mn12	0.524	19.87	0.0360
Mn13	0.511	23.99	0.0373

Table 7.27: Selected bond angles for compound **7.5.**

Bond	Bond Angle (°)	Bond	Bond Angle (°)
O8-Mn1-O26	77.5(2)	O1-Mn2-O48	77.5(2)
O1-Mn1-O48	78.2(2)	O2-Mn2-O47	78.6(2)
O48-Mn1-O26	86.2(2)	O1-Mn2-O47	82.0(2)
O24-Mn1-O20	86.8(2)	O48-Mn2-O29	89.8(2)
O24-Mn1-O26	89.1(2)	O1-Mn2-O2	90.9(2)
O1-Mn1-O26	89.35(19)	O1-Mn2-O29	91.8(2)
O1-Mn1-O8	90.1(2)	O33-Mn2-O47	92.1(2)
O48-Mn1-O20	94.6(2)	O33-Mn2-O48	93.7(2)
O1-Mn1-O20	94.8(2)	O48-Mn2-O47	94.2(2)
O8-Mn1-O24	94.8(2)	O33-Mn2-O29	94.8(2)
O24-Mn1-O48	96.4(2)	O2-Mn2-O29	96.2(2)
O8-Mn1-O20	102.4(2)	O2-Mn2-O33	97.2(2)
O8-Mn1-O48	160.1(2)	O2-Mn2-O48	167.1(2)
O1-Mn1-O24	174.5(2)	O1-Mn2-O33	169.0(2)
O20-Mn1-O26	175.87(19)	O29-Mn2-O47	171.79(19)
O3-Mn3-O46	77.2(2)	O4-Mn4-O45	77.0(2)
O2-Mn3-O47	78.85(19)	O3-Mn4-O46	77.4(2)
O35-Mn3-O47	86.4(2)	O3-Mn4-O45	81.7(2)
O46-Mn3-O47	88.7(2)	O46-Mn4-O19	90.1(2)
O35-Mn3-O38	89.0(2)	O3-Mn4-O4	90.9(2)
O3-Mn3-O2	90.3(2)	O3-Mn4-O19	92.0(2)
O3-Mn3-O47	91.2(2)	O14-Mn4-O19	92.8(2)
O46-Mn3-O38	92.7(2)	O14-Mn4-O46	93.4(2)
O3-Mn3-O38	93.5(2)	O46-Mn4-O45	93.4(2)
O2-Mn3-O35	95.5(2)	O14-Mn4-O45	94.3(2)
O35-Mn3-O46	96.4(2)	O4-Mn4-O14	97.6(2)
O2-Mn3-O38	100.7(2)	O4-Mn4-O19	98.2(2)
O2-Mn3-O46	162.2(2)	O4-Mn4-O46	165.9(2)
O3-Mn3-O35	173.2(2)	O3-Mn4-O14	169.6(2)
O38-Mn3-O47	175.3(2)	O19-Mn4-O45	171.9(2)
O4-Mn5-O45	77.2(2)	O5-Mn6-O44	77.8(2)
O5-Mn5-O44	77.8(2)	O6-Mn6-O27	78.2(2)

Bond	Bond Angle (°)	Bond	Bond Angle (°)
O16-Mn5-O45	86.9(2)	O5-Mn6-O27	82.0(2)
O16-Mn5-O11	88.4(3)	O44-Mn6-O39	89.5(2)
O44-Mn5-O45	89.1(2)	O5-Mn6-O39	91.5(2)
O5-Mn5-O4	90.9(2)	O43-Mn6-O27	91.5(2)
O5-Mn5-O45	91.0(2)	O5-Mn6-O6	91.6(2)
O44-Mn5-O11	93.6(2)	O43-Mn6-O44	93.5(3)
O5-Mn5-O11	93.9(2)	O44-Mn6-O27	93.7(2)
O16-Mn5-O4	94.2(2)	O43-Mn6-O39	95.7(2)
O16-Mn5-O44	96.5(2)	O6-Mn6-O43	96.2(3)
O4-Mn5-O11	101.0(2)	O6-Mn6-O39	97.3(2)
O4-Mn5-O44	162.2(3)	O6-Mn6-O44	167.6(2)
O5-Mn5-O16	173.9(3)	O5-Mn6-O43	168.6(3)
O11-Mn5-O45	174.9(2)	O39-Mn6-O27	171.9(2)
O6-Mn7-O27	78.4(2)	O8-Mn8-O26	77.07(19)
O7-Mn7-O25	78.4(2)	O7-Mn8-O25	78.4(2)
O41-Mn7-O27	87.1(2)	O7-Mn8-O26	82.2(2)
O25-Mn7-O27	87.2(2)	O25-Mn8-O12	89.1(2)
O41-Mn7-O28	88.1(2)	O7-Mn8-O8	91.5(2)
O7-Mn7-O27	90.0(2)	O22-Mn8-O26	92.1(2)
O7-Mn7-O6	90.2(2)	O7-Mn8-O12	92.2(2)
O25-Mn7-O28	92.9(2)	O22-Mn8-O25	93.1(2)
O7-Mn7-O28	94.7(2)	O22-Mn8-O12	94.4(2)
O6-Mn7-O41	95.2(2)	O22-Mn8-O8	96.3(2)
O41-Mn7-O25	95.4(2)	O25-Mn8-O26	96.3(2)
O6-Mn7-O28	102.3(2)	O8-Mn8-O12	96.5(2)
O6-Mn7-O25	161.7(2)	O8-Mn8-O25	168.6(2)
O7-Mn7-O41	173.3(2)	O7-Mn8-O22	169.1(2)
O28-Mn7-O27	175.24(19)	O12-Mn8-O26	171.30(19)
O10-Mn9-O9	78.9(2)	O9-Mn10-O10	76.40(19)
O18-Mn9-O23	84.6(2)	O17-Mn10-O10	84.7(2)
O18-Mn9-O9	87.1(2)	O17-Mn10-O9	87.9(2)
O23-Mn9-O21	88.7(2)	O17-Mn10-O15	88.7(3)
O18-Mn9-O10	88.9(2)	O15-Mn10-O13	90.2(2)
O18-Mn9-O21	90.3(2)	O4-Mn10-O10	91.3(2)
O8-Mn9-O21	90.6(2)	O4-Mn10-O9	91.5(2)
O8-Mn9-O9	92.2(2)	O4-Mn10-O15	91.6(2)
O8-Mn9-O23	93.1(2)	O4-Mn10-O13	91.7(2)
O8-Mn9-O10	93.3(2)	O17-Mn10-O13	92.3(2)
O10-Mn9-O21	95.4(2)	O9-Mn10-O13	94.0(2)
O23-Mn9-O9	96.6(2)	O15-Mn10-O10	99.2(2)
O10-Mn9-O23	172.3(2)	O13-Mn10-O10	170.0(2)
O21-Mn9-O9	173.8(2)	O9-Mn10-O15	174.7(2)
O8-Mn9-O18	177.5(2)	O4-Mn10-O17	176.0(2)
O5-Mn11-O7	89.7(2)	O3-Mn11-O5	90.7(2)
O7-Mn11-O1	90.5(2)	O5-Mn11-O1	169.9(2)
O3-Mn11-O1	90.6(2)	O3-Mn11-O7	171.6(2)
O31-Mn12-O30	79.7(2)	O30-Mn13-O31	78.4(2)
O37-Mn12-O40	86.2(3)	O36-Mn13-O31	85.4(3)
O37-Mn12-O30	87.2(3)	O36-Mn13-O30	87.5(2)
O40-Mn12-O42	88.6(2)	O36-Mn13-O34	88.7(2)
O37-Mn12-O31	88.9(2)	O34-Mn13-O32	89.7(2)
O6-Mn12-O42	90.4(2)	O2-Mn13-O32	90.4(2)
O37-Mn12-O42	90.9(3)	O2-Mn13-O30	91.8(2)
O6-Mn12-O30	91.6(2)	O2-Mn13-O31	91.9(2)

Bond	Bond Angle (°)	Bond	Bond Angle (°)
O6-Mn12-O31	91.8(2)	O2-Mn13-O34	91.9(2)
O6-Mn12-O40	93.1(2)	O36-Mn13-O32	92.2(3)
O31-Mn12-O42	94.8(2)	O30-Mn13-O32	93.0(2)
O40-Mn12-O30	96.9(2)	O34-Mn13-O31	98.7(2)
O31-Mn12-O40	174.1(3)	O32-Mn13-O31	171.1(2)
O42-Mn12-O30	174.1(2)	O34-Mn13-O30	175.4(2)
O6-Mn12-O37	178.5(3)	O2-Mn13-O36	177.3(3)

7.5.2 Physicochemical characterisation

The structural model has been verified using a number of physicochemical techniques. The infrared spectrum of compound fits the proposed structural model (**Figure 7.55**). The feature at ~2950 cm^{-1} can be attributed to the C-H stretching vibrations.[617] The vibrational modes at 1404 and 1556 cm^{-1} correspond to the symmetric and asymmetric stretching modes of the carboxylate groups and the difference between the two peaks is in line with the behaviour observed for bidentate bridging carboxylate groups.[618] The additional features in the 1300-1600 cm^{-1} range are due to vibrations of the organic moieties of the molecule.[617] The stretching vibrations of the phosphonate ligands can be found between 930-982 cm^{-1}. The strong signal at 970 cm^{-1} and the shoulder attached to it corresponds to the stretching mode of the phosphonate group.[621-623]

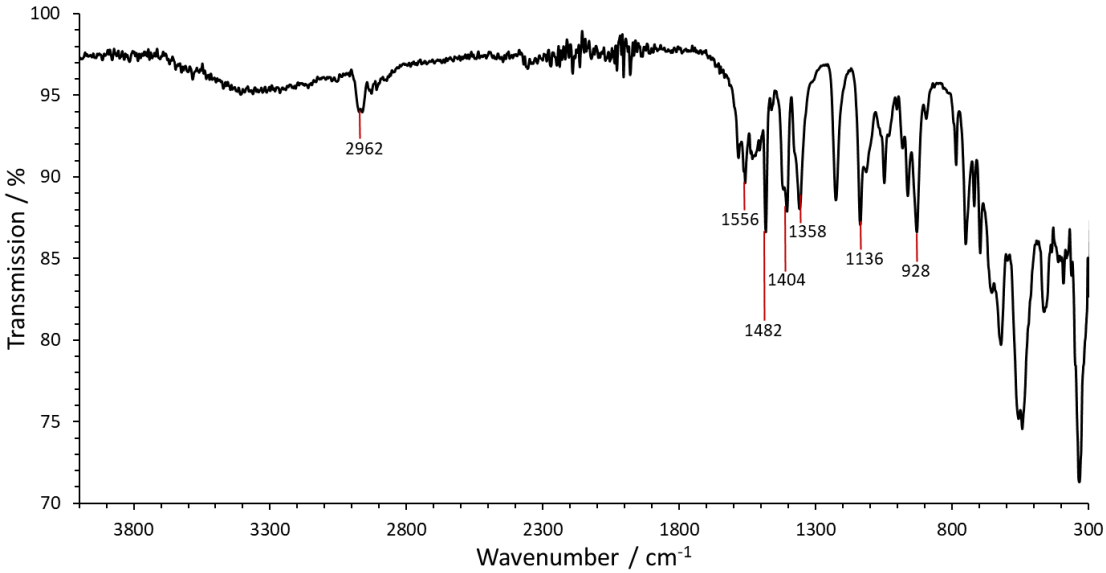

Figure 7.55: Infrared spectrum of compound **7.5**.

7.5.3 Magnetic properties

The temperature dependence of magnetic susceptibility was determined in the 4 – 300 K temperature range on hand picked crystals (**Figure 7.56**). The room temperature χT value was found to be 30.5 cm^3 K mol^{-1} which is lower than the expected value of 39 cm^3 K mol^{-1} for a system with 13 Mn^{III} (S = 2) centres. This observation is characteristic of predominantly strong antiferromagnetic interaction between Mn centres. On lowering the temperature, the χT value decreases to 12.8 cm^3 K mol^{-1} at 4 K. Such a behaviour confirms the presence of dominant antiferromagnetic interactions within the complex. The presence of ferromagnetic interactions, however, cannot be ruled out because the χT value is still higher than the expected value of 3 cm^3 K mol^{-1} corresponding to purely antiferromagnetic interactions. Additionally, the slight variations observed at ~8 and 75 K indicate the potential presence of ferromagnetic coupling. The presence of multiple {Mn_3} triangular units and odd number of unpaired spins can result in spin frustration which can also lead to ground states with larger overall spin.[528, 578]

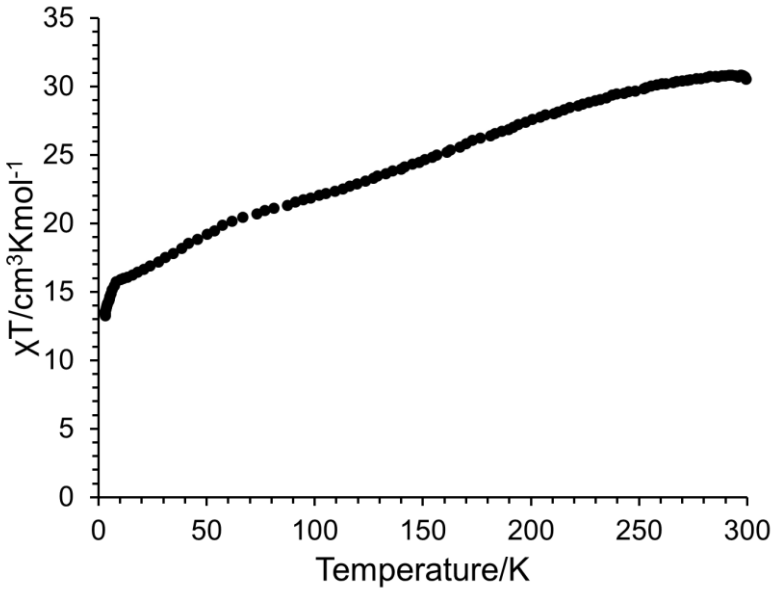

Figure 7.56: Temperature dependence of magnetic susceptibility (χT) of compound **7.5**.

Electrochemical studies for this complex have not been performed due to poor yields of this compound.

7.6 Conclusions

Five high nuclearity Mn complexes containing both phosphonate and carboxylate ligands were synthesised using the synthetic strategy described in chapter **3**. All complexes were characterised using a variety of analytical techniques and the observations were found to be consistent with the structural model. All complexes are structurally related to the truncated tetrahedron geometry which is quite rare for Mn complexes. Mn centres in the dodecanuclear compound **7.1** reside at the vertices of a truncated tetrahedron. In the pentadecanuclear compounds **7.2** and **7.3** the Mn centres reside at the vertices of an augmented truncated tetrahedron while in the tetradecanuclear compound **7.4**, twelve of the Mn centres reside at the vertices of a highly distorted truncated tetrahedron and the remaining two cap one of the hexagonal faces. Compound **7.5** can be described as a truncated tetrahedron that has been distorted to an extent that it transforms to a distorted elongated gyrobifastigium with twelve Mn centres at the vertices and one in the centre. The increase in the distortion of the regular truncated tetrahedron geometry as one goes from compound **7.1** to **7.5** is marked by a decrease in the number of regular hexagonal faces.

Compound **7.1** was found to contain all Mn centres in +II oxidation state while the compounds **7.2** and **7.3** are mixed valence compounds with Mn centres in +II and +III oxidation states. Compound **7.4** was also found to be mixed valence with Mn centres in +II and +III oxidation states. Compound **7.5** was to contain Mn centres in +III and intermediate (+2.5) oxidation states.

The magnetic properties of compound **7.1** reveal that the exchange coupling between the Mn centres is dominantly antiferromagnetic. This was further confirmed using DFT calculations by which an S = 0 state was found to be the ground state. In case of compounds **7.3**-**7.5** too, the experimental data suggested the presence of dominant antiferromagnetic interactions between Mn centres at high temperatures. However, it also indicates a ground state with larger number of unpaired electrons for all three complexes.

The electrochemical behaviour of compounds **7.1** and **7.3** in aqueous media was determined using carbon paste electrodes which were prepared by mixing the compounds with carbon paste. Both compounds were determined to be active for water oxidation and the current density was found to increase with the catalytic loading. For compound **7.1**, an initial structural transformation was observed during the application of external potential. This transformation has been attributed to the oxidation of the Mn(II) centres and the substitution of labile DMSO molecules with water. In case of compound **7.3**, the activity has been found to be due to species derived from this complex but transformation of the complex is observed during the water oxidation reaction. The current density in case of compound **7.1** was found to be higher than that in compound **7.3** and the mechanism in both cases was found to be different as indicated by different Tafel slopes. The former has also been found to be active at relatively lower overpotentials (251 mV at 40 wt-%

catalytic loading) compared to the latter for which the onset overpotential was found to be 521 mV at 40 wt-% catalytic loading.

Like the OEC, both complexes decompose during the water oxidation reaction and the decomposed species in both complexes is most likely a Mn based oxide moiety but further characterisation is required to confirm this. The initial activity however, can unarguably be attributed to species derived from the parent complexes and not the decomposed species as the latter has been found to be active only at very high overpotentials.

We have thus shown how the interplay between carboxylate and phosphonate based ligands leads to the formation of a series of high nuclearity coordination complexes that are structurally related to the truncated tetrahedron geometry. The decrease in the symmetry gives rise to complex magnetic behaviour. Additionally, some of these complexes have been found to be active for the OER. Further investigation of the electrochemical properties of these complexes may provide some information about tuning the ligand environment for enhanced OER activity.

8 Phosphonate Based Complexes

In the previous chapter it was observed that the use of carboxylate and phosphonate based ligands can also lead to high nuclearity complexes. It was also observed that these complexes can perform water oxidation half-reaction under electrochemical conditions. The versatile nature of the phosphonate ligands and their high binding affinity towards metal ions is well established.[536, 561-563] As the Schmitt group has already been developing the chemistry of phosphonate groups for the past few years,[384, 542-545] we decided to further pursue the use of phosphonate based ligands for synthesising high nuclearity complexes and to test their electrochemical behaviour.

Considering the similarity in the synthetic protocol of the $\{Mn_6\}$ and the asymmetric $\{Mn_{13}\}$ complexes previously reported by us,[542, 543, 545] we believed that these complexes must be structurally related. In this chapter, we describe the structural and physicochemical properties of a dodecanuclear complex $[Mn^{II}_4Mn^{III}_8Br_2(\mu_3\text{-}O)_4((CH_3)_3CPO_3)_{10}((CH_3)_3CPO_3H)_2(4\text{-picoline})_6(H_2O)_{10}]\cdot 2CH_3CN$ (compound **8.1**) (4-picoline = $(CH_3)C_5H_4N$) which may serve as an intermediate between the two structures. Using the synthetic strategy described in chapter **3**, we have also synthesised a series of high nuclearity complexes that are structurally related to the $\{Mn_{13}\}$ complex.[542] We have synthesised a tridecanuclear complex, $Na[Na_{0.4}(Mn^{II}_{0.5}Mn^{III}_{0.5})Mn^{III}_{12}(\mu_4\text{-}O)_2(\mu_3\text{-}O)_4(\mu\text{-}O)_{0.4}(\mu\text{-}OH)_{1.6}((CH_3)_3CPO_3)_{10}(4\text{-picoline})_4(\mu\text{-}CH_3O)_4(CH_3OH)_2][(Mn^{II}_{0.5}Mn^{III}_{0.5})Mn^{III}_{12}(\mu_4\text{-}O)_2(\mu_3\text{-}O)_4(\mu\text{-}OH)_2((CH_3)_3CPO_3)_{10}((CH_3)_3CPO_3H)_2(4\text{-picoline})_4(\mu\text{-}CH_3O)_4]$ (compound **8.2**) that is structurally similar to the previously reported $\{Mn_{13}\}$ complex.[542] We have also synthesised $K[K_2(Mn^{II}_{0.5}Mn^{III}_{0.5})Mn^{III}_{12}(\mu_4\text{-}O)_2(\mu_3\text{-}O)_4(\mu\text{-}OH)_2((CH_3)_3CPO_3)_{10}((CH_3)_3CO_2)_2(\mu\text{-}CH_3O)_4(CH_3OH)_6][(Mn^{II}_{0.5}Mn^{III}_{0.5})Mn^{III}_{12}(\mu_4\text{-}O)_2(\mu_3\text{-}O)_4(\mu\text{-}OH)_2((CH_3)_3CPO_3)_{10}((CH_3)_3CPO_3H)_2(\mu\text{-}CH_3O)_4(CH_3OH)_4]$ (compound **8.3**) where the $\{Mn_{13}\}$ units are linked together by K^+ ions. Furthermore, we have synthesised $[Mn^{II}Mn^{III}_{12}Ca_2(\mu_4\text{-}O)_2(\mu_3\text{-}O)_6((CH_3)_3CPO_3)_{10}((C_6H_5)_2PO_2)_2((CH_3)_3CCO_2H)_2(\mu\text{-}CH_3O)_4(CH_3OH)_{5.15}(CH_3CN)_{0.85}]$ (compound **8.4**) and $[Mn^{II}_3Mn^{III}_{12}Ca_2(\mu_4\text{-}O)_4(\mu_3\text{-}O)_2(\mu_3\text{-}OH)_2((CH_3)_3CPO_3)_8((C_6H_5)_2PO_2)_2((CH_3)_3CCO_2)_4(CH_3CO_2)_2(\mu\text{-}CH_3O)_8(CH_3OH)_2]$ (compound **8.5**). The structural and physicochemical properties of these complexes are described in this chapter.

8.1 $[Mn^{II}_4Mn^{III}_8Br_2(\mu_3\text{-}O)_4((CH_3)_3CPO_3)_{10}((CH_3)_3CPO_3H)_2((CH_3)C_5H_4N)_6(H_2O)_{10}]\cdot 2CH_3CN$ (8.1)

Compound **8.1** was prepared by comproportionation reaction between $MnBr_2$ and $KMnO_4$ in presence of *tert*-butyl phosphonic acid and 4-picoline in CH_3CN. The reaction mixture was stirred for five hours, filtered and left undisturbed at room temperature and tiny red crystals of compound **8.1** formed within one day. The crystal structure of compound **8.1** was determined using single crystal X-ray diffraction measurements.

8.1.1 Structure description

Compound **8.1** crystallises in the triclinic crystal system and the structure solution was solved in the space group $P\bar{1}$. It comprises of a dodecanuclear Mn complex $[Mn^{II}_4Mn^{III}_8Br_2(\mu_3\text{-}O)_4((CH_3)_3CPO_3)_{10}((CH_3)_3CPO_3H)_2((CH_3)C_5H_4N)_6(H_2O)_{10}]$ (**Figure 8.1**), and the asymmetric unit of this complex contains half of the molecule (**Figure 8.2**). This overall structure is stabilised by four $\mu_3\text{-}O^{2-}$ groups and twelve *tert*-butyl phosphonate groups two of which are partially protonated. Furthermore, 4-picoline and water molecules serve as capping ligands. The core structure of this compound is quite an open one and is in the shape of an "S" (**Figure 8.1**). It contains two

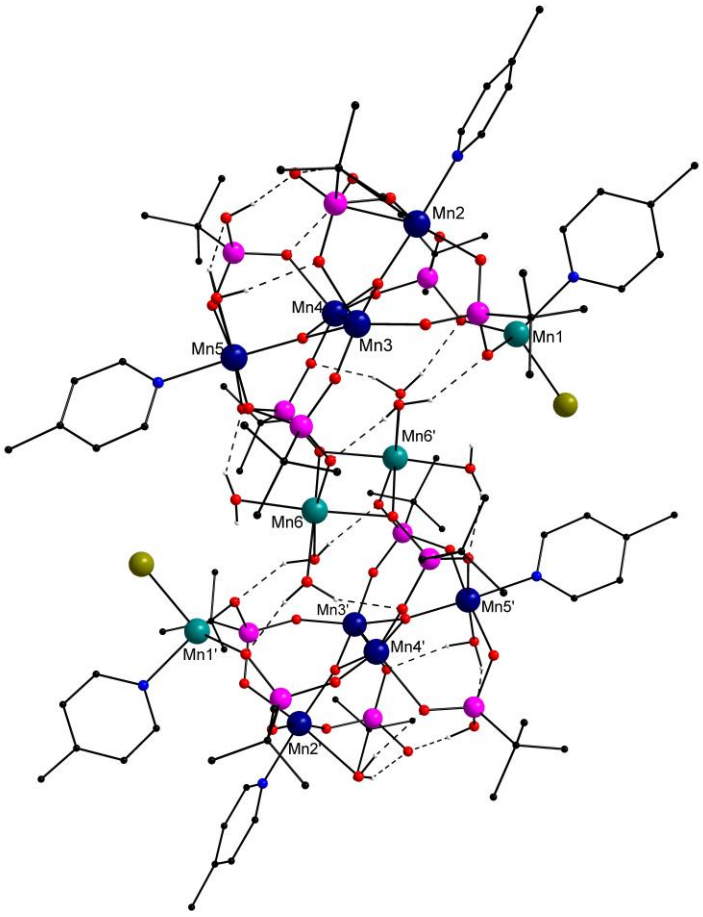

Figure 8.1: Crystal structure of the dodecanuclear compound **8.1**. The hydrogen bonds are shown with dashed lines. Colour scheme: Mn^{II} (teal), Mn^{III} (dark blue), Br (dark yellow), P (pink), C (black) and O (red). All hydrogen atoms (grey) except those attached to oxygen centres have been removed for clarity.

characteristic tetranuclear {Mn_4} see-saw subunits[638] (**Figure 8.3**) that are linked *via* the Mn6 centres. There are two additional dangling Mn1 centres that are linked to the tetranuclear units. The tetranuclear units are stabilised by two μ_3-O^{2-} groups and six *tert*-butyl phosphonate groups. The phosphonates containing P3 and P4 are partially protonated and bind to the Mn centres in a 2.110 mode (Harris notation)[605] while all the others bind in a 3.111 mode. The Mn centres forming the see-saw component (Mn2-Mn5) are in +III oxidation state while the others (Mn1 and Mn6) are in +II oxidation state as determined by bond valence sum analysis (**Table 8.1**).[639] The protonation state of the O atoms bound only to Mn centres has also been determined using bond valence sum analysis (**Table 8.2**). The BVS values for O in the approximate ranges of 0.2-0.4, 1.0-1.2 and 1.8-2.0 indicate H_2O, OH^- and O^{2-} groups respectively.[603, 604] The two asymmetric units are joined together via two phosphonate groups bound to Mn6.

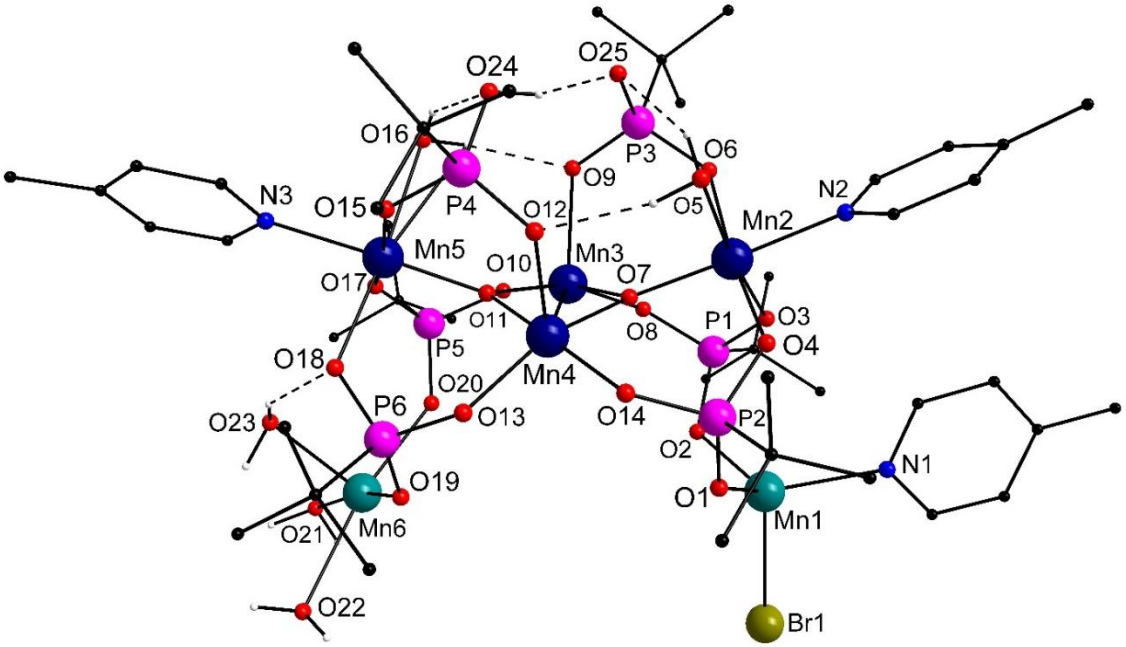

Figure 8.2: Asymmetric unit of the dodecanuclear compound **8.1**. The hydrogen bonds are shown with dashed lines. Colour scheme: Mn^{II} (teal), Mn^{III} (dark blue), Br (dark yellow), P (pink), C (black) and O (red). All hydrogen atoms (grey) except those attached to oxygen centres have been removed for clarity.

The coordination water molecules and the partially protonated *tert*-butyl phosphonate groups form an extensive hydrogen bond network (**Figure 8.2**). These partially protonated phosphonate groups are hydrogen bonded to each other via the hydrogen atom lying between O24 and O25. Additionally, the water molecules containing O5 and O16 are hydrogen bonded to these phosphonate groups. There are three water molecules bound to Mn6 out of which one (containing O23) is hydrogen bonded to the O-donor (O18) of the phosphonate group containing P6. The hydrogen atoms of the water molecule containing O21 are hydrogen bonded to the O-donors (O1 and O13) of the phosphonate groups that contain P2 and P6 and belong to the symmetry equivalent of the asymmetric unit. In a similar manner, the hydrogen atoms of the water molecule that

contains O22 are hydrogen bonded to the O-donors (O2 and O20) of the phosphonate groups containing P1 and P5 of the other half of the complex.

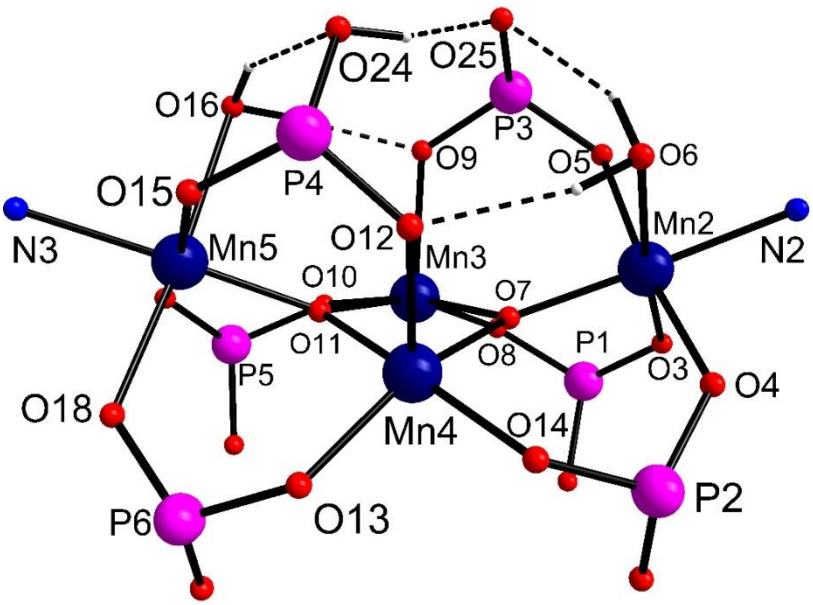

Figure 8.3: The core structure of the compound **8.1** highlighting the tetranuclear see-saw unit. Colour scheme: Mn^{III} (dark blue), P (pink) and O (red). All hydrogen atoms (grey) except those attached to oxygen centres have been removed for clarity.

This dodecanuclear complex contains Mn in tetrahedral (Mn1), square pyramidal (Mn3 and Mn4) and octahedral (Mn2, Mn5 and Mn6) coordination environments. The tetrahedral coordination environment of Mn1(II) is comprised of a bromide, the N-donor (N1) of a 4-picoline group and the O-donors (O1 and O2) of two *tert*-butyl phosphonate groups (**Figure 8.4 (a)**). The O-donors of the phosphonate groups are hydrogen bonded to the water molecules bound to Mn6. The Mn-O distances are ~2.0 Å while the Mn-N and Mn-Br distances are 2.170(6) and 2.5289(13) Å respectively. The tetrahedron of Mn1 is isolated from the other Mn centres but Mn1 is linked to Mn2-Mn4 via the phosphonate groups.

Mn2(III) resides in a slightly distorted octahedral coordination environment which is fulfilled by a μ_3-O^{2-} group (O7), the N-donor (N2) of a 4-picoline group, and the O-donors of a water molecule (O5) and three *tert*-butyl phosphonate groups (O3, O4 and O6) (**Figure 8.4 (b)**). The deviation from ideal geometry are due to Jahn-Teller distortion and ligand restraints which are highlighted by the bond distances (**Table 8.1**) and bond angles (**Table 8.3**). The octahedron of Mn2 is vertex shared with the polyhedra of Mn3 and Mn4 at O7. The Jahn-Teller axis is directed towards the water molecule and the O-donor of the phosphonate (O3) lying opposite to it with the Mn-O distance being 2.363(5) and 2.100(5) Å respectively. The Mn-ligand distances perpendicular to the Jahn-Teller axis vary between 1.9 and 2.1 Å.

Table 8.1: Key Mn-O and Mn-Mn bond lengths and bond valence sum for each Mn centre for compound **8.1**.

Mn centre	Coordinating atom	Bond Distance (Å)	BVS	Assigned oxidation state
Mn1	Br1	2.5290(13)	2.054	+II
	O1	2.033(4)		
	O2	2.027(4)		
	N1	2.171(6)		
Mn2	O3	2.100(5)	3.166	+III
	O4	1.913(4)		
	O5	2.363(5)		
	O6	1.906(4)		
	O7	1.883(4)		
	N2	2.063(5)		
Mn3	O7	1.886(4)	3.153	+III
	O8	1.899(4)		
	O9	2.102(4)		
	O10	1.888(4)		
	O11	1.919(4)		
Mn4	O7	1.898(4)	3.162	+III
	O11	1.871(4)		
	O12	2.087(4)		
	O13	1.918(4)		
	O14	1.910(4)		
Mn5	O11	1.889(4)	3.123	+III
	O15	1.916(4)		
	O16	2.332(5)		
	O17	1.882(4)		
	O18	2.134(4)		
	N3	2.103(6)		
Mn6	O19	2.225(4)	1.998	+II
	O19’	2.155(4)		
	O20	2.143(4)		
	O21	2.180(4)		
	O22	2.379(4)		
	O23	2.149(5)		

Metals	Distance (Å)	Metals	Distance (Å)
Mn1-Mn2	4.216(2)	Mn3-Mn6’	5.296(1)
Mn2-Mn3	3.375(1)	Mn4-Mn5	3.373(1)
Mn2-Mn4	3.487(1)	Mn4-Mn6’	4.445(1)
Mn3-Mn4	2.826(1)	Mn5-Mn6	4.673(1)
Mn3-Mn5	3.518(1)	Mn6-Mn6’	3.252(1)

’1-X,1-Y,1-Z

Table 8.2: BVS analysis for O atoms and their assigned protonation state in compound **8.1**.

Atom	BVS	Assignment	Atom	BVS	Assignment
O5	0.196	H_2O	O21	0.349	H_2O
O7	2.117	μ_3-O^{2-}	O22	0.204	H_2O
O11	2.097	μ_3-O^{2-}	O23	0.379	H_2O
O16	0.213	H_2O			

Mn3(III) and Mn4(III) reside in a square pyramidal environment with an edge shared between the two at the two μ_3-O^{2-} groups, O7 and O11 (**Figure 8.5 (a)** and **(b)**). The coordination environment of both is further fulfilled by the O-donors of three *tert*-butyl phosphonate groups. To minimise interelectronic repulsion, the Jahn-Teller axes for Mn3 and Mn4 are directed towards the apical position and is fulfilled by the O-donors (O9 and O12 respectively) of the phosphonate groups. The Mn-O distance along the Jahn-Teller axis is ~2.1 Å while that perpendicular to it is ~1.9 Å.

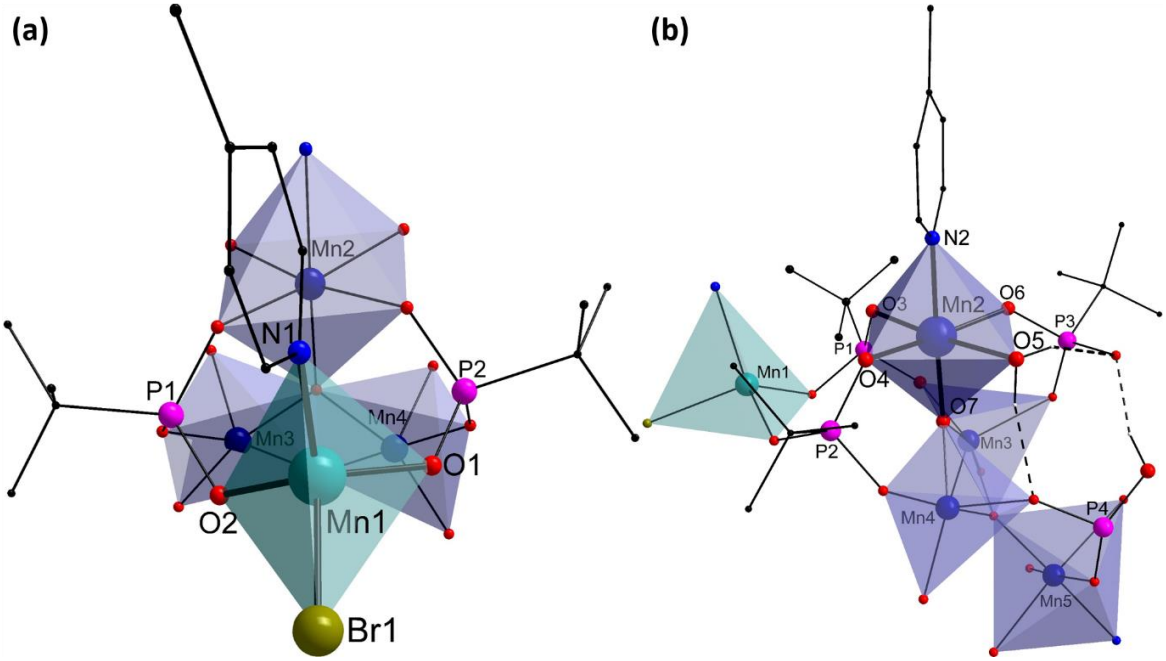

Figure 8.4: Coordination environment of **(a)** Mn1 and **(b)** Mn2 in compound **8.1**. Colour scheme: Mn^{II} (teal), Mn^{III} (dark blue), Br (dark yellow), P (pink), C (black) and O (red). All hydrogen atoms (grey) except those attached to oxygen centres have been removed for clarity.

The continuous shape measure values for Mn3 and Mn4 are the largest amongst all Mn centres (**Table 8.4**). Instead of using a square pyramid geometry as a reference geometry, if one uses a spherical square pyramid reference geometry, the distortions are found to be less, indicating that the environment resembles more closely to that of the spherical square pyramid. A spherical square pyramid is essentially a square pyramid where the vertices are distributed spherically around the centre of mass. For an ideal spherical square pyramid, the apical-basal bond angles are ~104.45° while the basal-basal bond angles are ~86.5° unlike a square pyramid where all angles are 90°. Ligand restraints lead to Mn3 and Mn4 exhibiting such a behaviour. A comparison of the coordination environments of Mn3 and Mn4 with the trigonal bipyramidal geometry was also made but it resulted in higher continuous shape measure values – 4.558 and 3.511 respectively – indicating that the environment is best represented as a spherical square pyramid.

The octahedral coordination environment of Mn5(III) is similar to that of Mn2 and fulfilled by a μ_3-O^{2-} group (O11), the N-donor (N3) of a 4-picoline group and the O-donors of a water molecule (O16) and three *tert*-butyl phosphonate groups (O15, O17 and O18) (**Figure 8.5 (c)**). The octahedron

shares a vertex with the polyhedra of Mn3 and Mn4 at O11. The Jahn-Teller axis is again along the O-donors of the water molecule (O16) and the phosphonate group (O18) lying opposite to the water molecule and is almost perpendicular (~85°) to that of Mn2. The Mn-O16 and Mn-O18 distances are 2.332(5) and 2.134(4) Å respectively. The Mn-ligand distances perpendicular to the Jahn-Teller axis lie in the range of 1.9-2.1 Å.

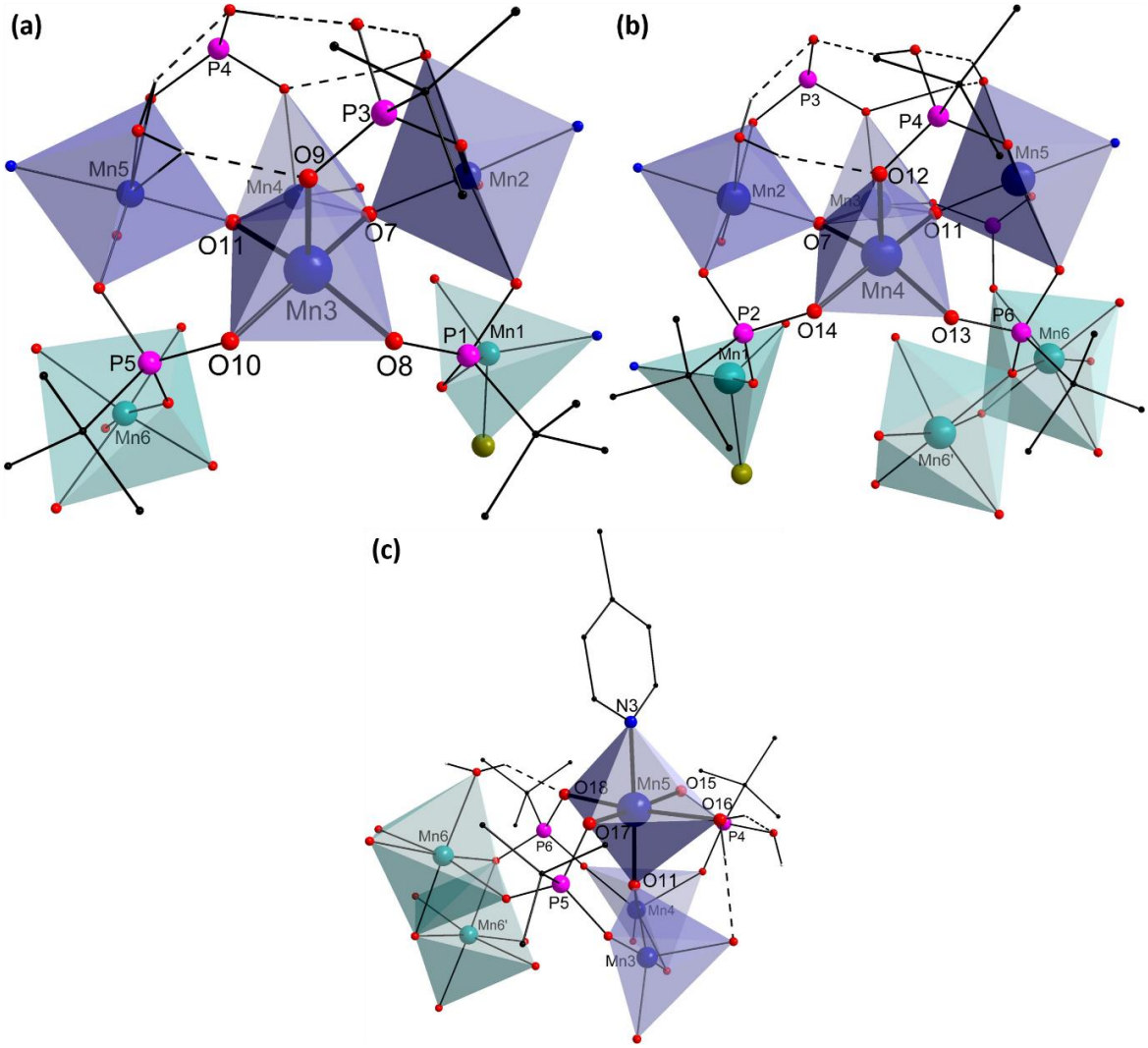

Figure 8.5: Coordination environment of **(a)** Mn3**, (b)** Mn4 and **(c)** Mn5 in compound **8.1**. Colour scheme: Mn^{II} (teal), Mn^{III} (dark blue), Br (dark yellow), P (pink), C (black) and O (red). All hydrogen atoms (grey) except those attached to oxygen centres have been removed for clarity.

Mn6(II) also lies in an octahedral environment which is fulfilled by the O-donors of three phosphonate groups and three water molecules with the Mn-O distances varying between 2.1 and 2.4 Å (**Figure 8.6**). The octahedron of Mn6 shares an edge with that of its symmetry equivalent at O19 and O19'. Based on the continuous shape measure values, the environment of Mn6 is less distorted than that of Mn5. The bond angle variance and distortion index for Mn6 and Mn5, however, say otherwise. This is due to the fact that the Jahn-Teller distortion of Mn5 is not taken into account in the calculation of bond angle variance and distortion index but is implicitly included

in the calculation of continuous shape measures. Hence, instances where angular distortions are similar, continuous shape measures provide a more realistic picture of the structural environment.

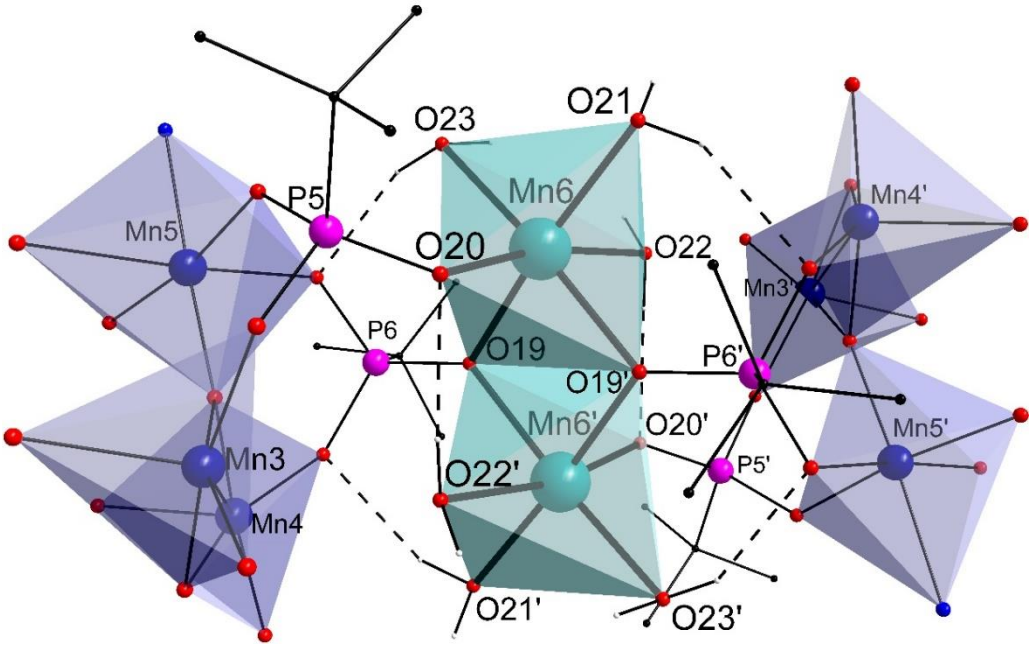

Figure 8.6: Coordination environment of Mn6 in compound **8.1**. Colour scheme: Mn^{II} (teal), Mn^{III} (dark blue), Br (dark yellow), P (pink), C (black) and O (red). All hydrogen atoms (grey) except those attached to oxygen centres have been removed for clarity.

Table 8.3: Selected bond angles for compound **8.1**.

Bond	Bond Angle (°)	Bond	Bond Angle (°)
N1-Mn1-Br1	99.52(16)	O1-Mn1-Br1	111.54(13)
O2-Mn1-Br1	106.20(13)	O1-Mn1-N1	112.78(19)
O2-Mn1-O1	107.73(18)	O2-Mn1-N1	118.62(19)
N2-Mn2-O5	85.47(19)	O7-Mn2-O4	93.08(18)
O4-Mn2-O5	85.83(18)	O4-Mn2-O3	93.19(18)
O6-Mn2-N2	86.2(2)	O7-Mn2-O6	93.29(18)
O6-Mn2-O5	86.88(19)	O6-Mn2-O3	93.53(19)
O4-Mn2-N2	87.2(2)	O6-Mn2-O4	170.5(2)
N2-Mn2-O3	89.48(19)	O3-Mn2-O5	174.90(17)
O7-Mn2-O5	92.13(17)	O7-Mn2-N2	177.6(2)
O7-Mn2-O3	92.92(18)		
O7-Mn3-O11	81.05(18)	O7-Mn3-O9	95.96(18)
O10-Mn3-O8	90.45(19)	O11-Mn3-O9	96.60(18)
O10-Mn3-O11	91.80(18)	O8-Mn3-O9	102.55(19)
O7-Mn3-O8	92.93(18)	O8-Mn3-O11	160.44(19)
O10-Mn3-O9	95.11(18)	O7-Mn3-O10	167.44(19)
O11-Mn4-O7	82.00(18)	O11-Mn4-O12	94.60(18)
O14-Mn4-O13	88.74(17)	O7-Mn4-O12	98.56(18)
O7-Mn4-O14	91.73(18)	O13-Mn4-O12	105.19(18)
O14-Mn4-O12	93.83(17)	O7-Mn4-O13	156.17(19)
O11-Mn4-O13	93.94(18)	O11-Mn4-O14	170.15(19)

Bond	Bond Angle (°)	Bond	Bond Angle (°)
O15-Mn5-O16	85.82(18)	O19[1]-Mn6-O22	80.70(16)
N3-Mn5-O18	85.94(19)	O19-Mn6-O22	83.18(15)
O17-Mn5-N3	86.2(2)	O19[1]-Mn6-O19	84.10(17)
O17-Mn5-O16	87.79(18)	O21-Mn6-O22	84.85(15)
O15-Mn5-N3	88.5(2)	O20-Mn6-O19'	88.61(16)
N3-Mn5-O16	89.64(19)	O23-Mn6-O21	89.55(17)
O11-Mn5-O16	91.33(18)	O23-Mn6-O19	90.16(17)
O17-Mn5-O11	91.46(19)	O20-Mn6-O23	92.93(17)
O17-Mn5-O18	92.86(18)	O20-Mn6-O19	93.15(16)
O15-Mn5-O18	93.11(18)	O19[1]-Mn6-O21	95.81(16)
O11-Mn5-O18	93.12(17)	O23-Mn6-O22	97.45(17)
O11-Mn5-O15	94.00(18)	O20-Mn6-O21	98.97(16)
O17-Mn5-O15	171.68(19)	O21-Mn6-O19	167.88(16)
O18-Mn5-O16	175.48(17)	O20-Mn6-O22	168.98(16)
O11-Mn5-N3	177.4(2)	O23-Mn6-O19'	174.13(17)

Table 8.4: Continuous shape measure values, angle variance and distortion indices for each Mn centre for compound **8.1** ([1]tetrahedral, [2]octahedral, [3]spherical square pyramidal and [4]square pyramidal geometry).

Mn centre	Continuous shape measure value	Angle variance (σ^2)	Distortion Index
Mn1[1]	0.742	42.34	0.0449
Mn2[2]	0.585	11.47	0.0344
Mn3	0.485[3] /1.201[4]	50.69[4]	0.0607[4]
Mn4	0.706[3] /1.483[4]	60.56[4]	0.065[4]
Mn5[2]	0.620	9.38	0.0296
Mn6[2]	0.589	34.97	0.0532

This system packs with numerous disordered acetonitrile molecules some of which are partially occupied and due to their highly disordered nature, most of them could not be refined. The packing diagram is shown in **Figure 8.7**. These solvent molecules reside in voids which mainly lie along the crystallographic a-axis which can be penetrated by a sphere of 1.2 Å as determined using the calcvoid routine as implemented in OLEX2.[616] The radius of the largest sphere holding these solvent molecules was found to be 2.8 Å. The 4-picoline groups are not π-π stacked and the stabilisation of the packing is probably due to weak interaction between the clusters and with the acetonitrile molecules packed in the lattice.

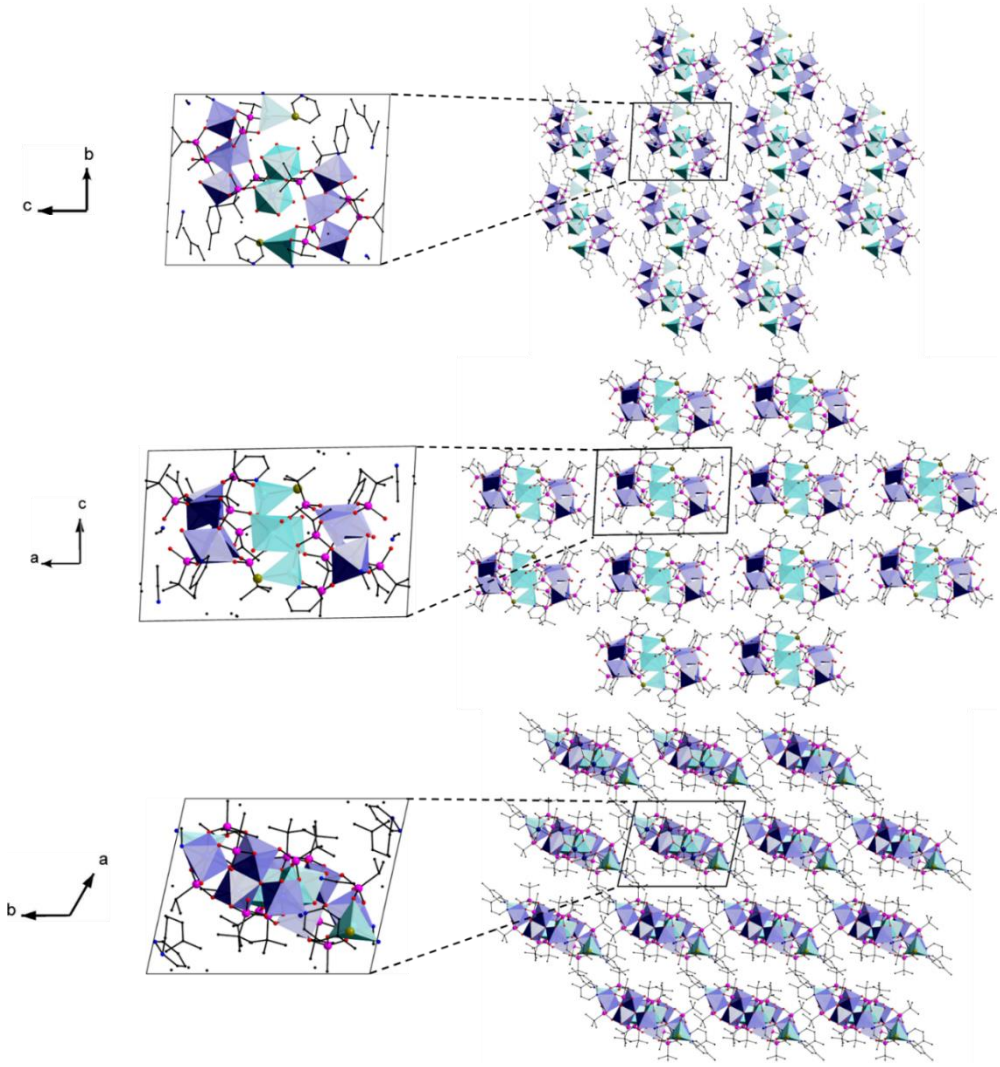

Figure 8.7: Packing diagram of compound **8.1**. Colour scheme: Mn^{II} (teal), Mn^{III} (dark blue), Br (dark yellow), P (pink), C (black) and O (red). All hydrogen atoms have been removed for clarity.

8.1.2 Physicochemical characterisation

Physicochemical characterisation was carried out to further support the structural model obtained using single crystal X-ray crystallography. The compound was dried in air and the constitutional solvent molecules were removed. Thermogravimetric analysis (TGA) under an atmosphere of N_2 of compound **8.1** (**Figure 8.8**) dried in air reveals an initial drop between 100 and 125 °C due to the loss of water molecules (weight loss calcd: 5.5 %, found: 6.0 %). This is followed by the loss of 4-picoline groups and the partial decomposition of the *tert*-butyl phosphonate groups occurs which is followed by the formation of phosphate and oxide species.

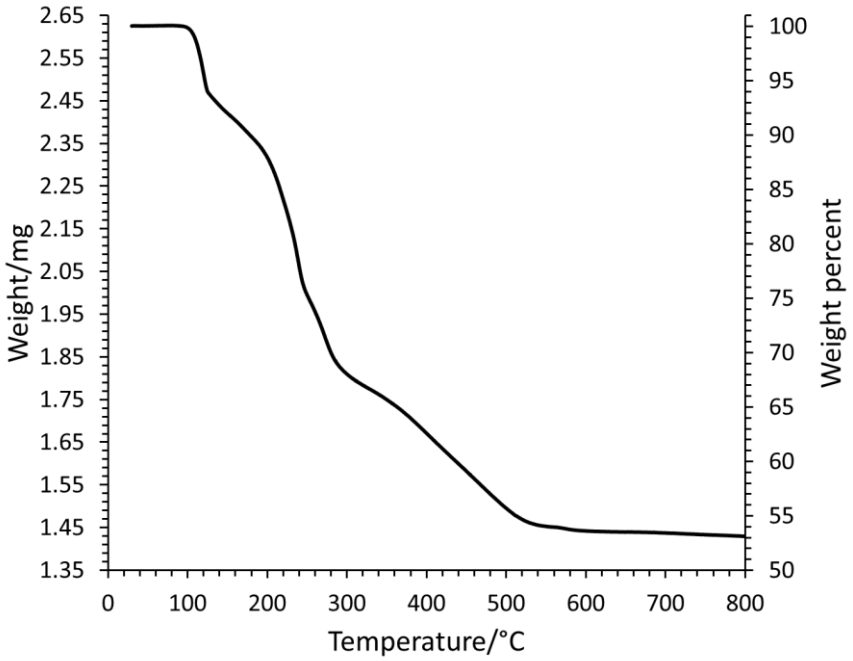

Figure 8.8: TGA analysis of compound **8.1**.

Infrared spectrum of dried compound **8.1** is in agreement with the proposed structural model (**Figure 8.9**). The feature at ~2900 cm^{-1} corresponds to the C-H vibrations.[617] The signals in the 1300-1600 cm^{-1} range are due to vibrations of the organic moieties of the molecule.[617] The stretching vibrations of the hydrogen bonded water molecules appear at 3400 cm^{-1}.[633, 634] The strong vibrational modes around 970 cm^{-1} can be attributed to the stretching vibrations of the CPO_3 groups of the phosphonate ligands.[621-623]

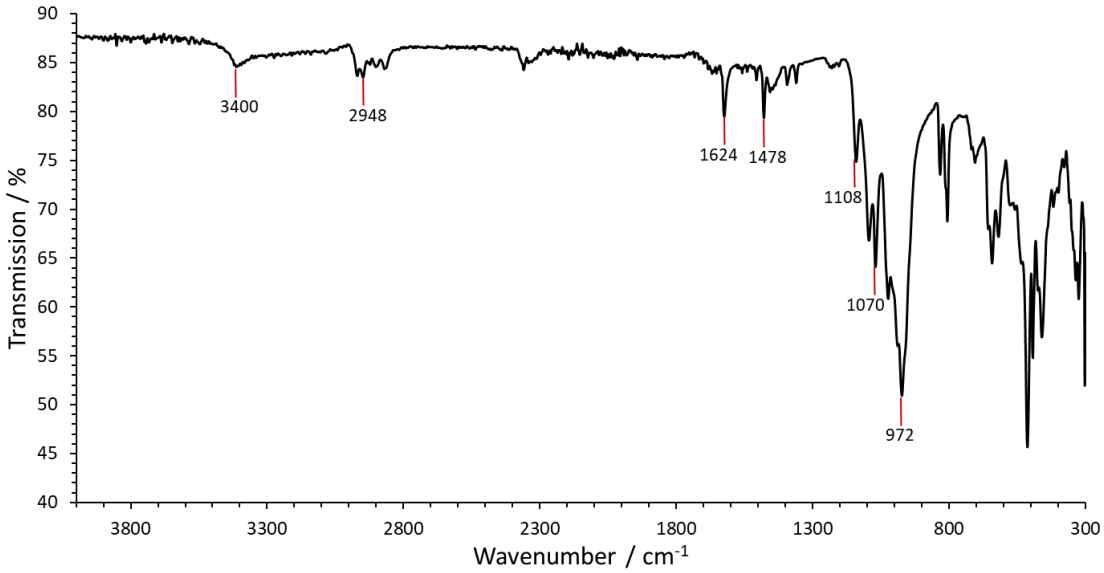

Figure 8.9: Infrared spectrum of compound **8.1**.

8.2 $Na[Na_{0.4}(Mn^{II}_{0.5}Mn^{III}_{0.5})Mn^{III}_{12}(\mu_4\text{-}O)_2(\mu_3\text{-}O)_4(\mu\text{-}O)_{0.4}(\mu\text{-}OH)_{1.6}((CH_3)_3CPO_3)_{10}(4\text{-picoline})_4(\mu\text{-}CH_3O)_4(CH_3OH)_2][(Mn^{II}_{0.5}Mn^{III}_{0.5})Mn^{III}_{12}(\mu_4\text{-}O)_2(\mu_3\text{-}O)_4(\mu\text{-}OH)_2((CH_3)_3CPO_3)_{10}((CH_3)_3CPO_3H)_2(4\text{-picoline})_4(\mu\text{-}CH_3O)_4]\cdot 5CH_3OH$ (8.2)

Compound **8.2** was prepared by comproportionation reaction between $Mn(CH_3COO)_2{\cdot}4H_2O$ and $KMnO_4$ in presence of NaI, *tert*-butyl phosphonic acid and 4-picoline in CH_3CN/CH_3OH mixture. The reaction mixture was stirred for five hours, filtered and left undisturbed at room temperature and crystals of compound **8.2** were obtained in one day. The crystal structure of compound **8.2** was determined using single crystal X-ray diffraction measurements.

8.2.1 Structural description

Compound **8.2** contains a tridecanuclear complex (**Figure 8.10**) that crystallises in the triclinic crystal system and the structure was solved in the space group $P\bar{1}$. The asymmetric unit contains half of this complex (**Figure 8.11**). The tridecanuclear complex in this compound exists in two forms that are slightly different – one contains partially protonated *tert*-butyl phosphonate groups while the other contains methanol molecules instead. Both forms are stabilised by two OH^- groups, four CH_3O^-, six O^{2-} and ten phosphonate groups. The two forms lie adjacent to each other and the methanol molecules are hydrogen bonded to the partially protonated *tert*-butyl phosphonate groups.

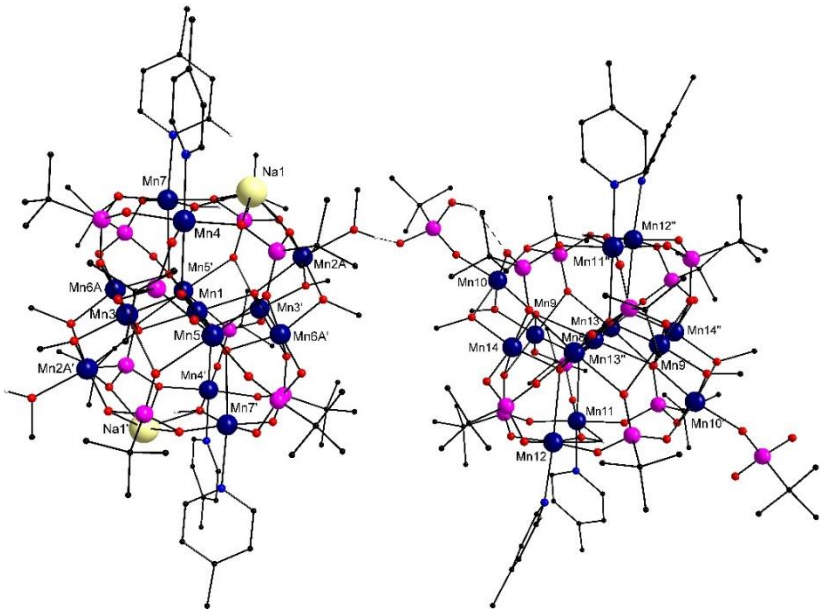

Figure 8.10: Crystal structure of the tridecanuclear compound **8.2**. Colour scheme: Mn (deep blue), Na (light yellow), C (black), P (pink) and O (red). All hydrogen atoms (grey) except those bound to O centres have been removed for clarity. Hydrogen bonds are shown with dashed lines.

The core structure in both forms comprises of a three layered metal-centered distorted cuboctahedron with a brucite[640-642] like $\{Mn_7\}$ disc sandwiched between two $\{Mn_3\}$ triangular units. The triangular units are staggered in a trigonal antiprismatic fashion and are bound to the central $\{Mn_7\}$ disc by $\mu_4\text{-}O^{2-}$ groups and the O-donors of $\mu\text{-}CH_3O^-$ and *tert*-butyl phosphonate groups which

bind in 4.211 and 3.111 modes. The oxidation state of each Mn centre has been determined using bond valence sum analysis (**Table 8.5**) which has also been used for the proper assignment of the protonation states of the O centres bound only to Mn (**Table 8.6**).

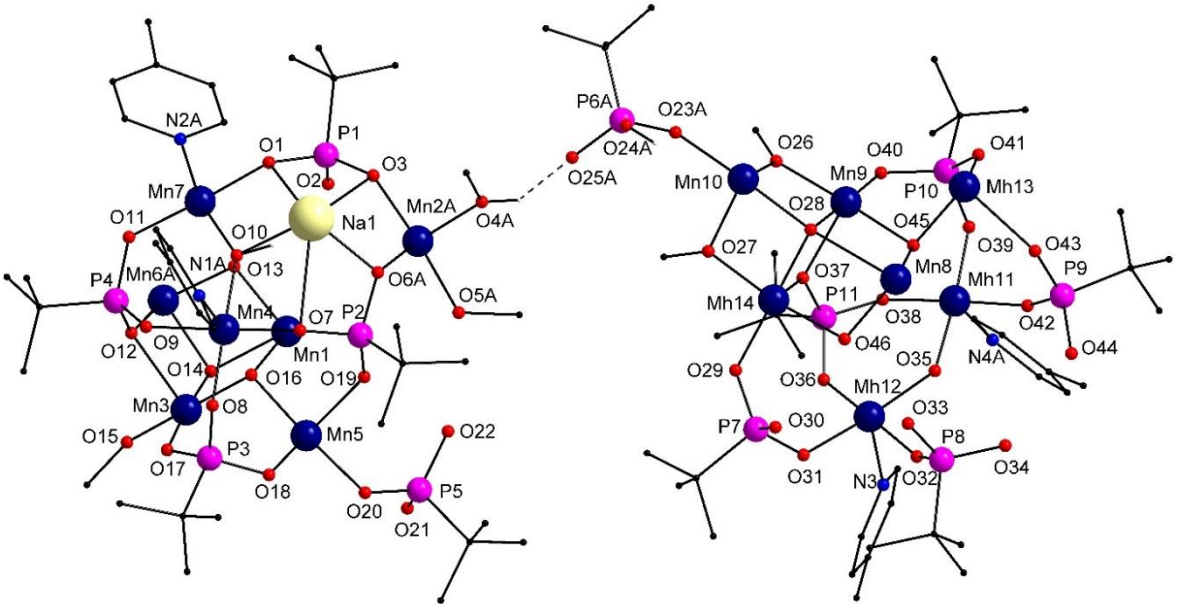

Figure 8.11: Asymmetric unit of compound **8.2**. Colour scheme: Mn (deep blue), Na (light yellow), C (black), P (pink) and O (red). All hydrogen atoms (grey) except those bound to O centres have been removed for clarity. Hydrogen bonds are shown with dashed lines.

Mn1, Mn3, Mn5, Mn6A/B and their symmetry equivalents form the $\{Mn_7\}$ disc (**Figure 8.12**). Mn1 resides in a distorted octahedral environment (**Table 8.7**) which is fufilled by four μ_3-O^{2-} (O13 and O16 and their symmetry equivalents) and two μ_4-O^{2-} groups (O14 and its symmetry equivalent) (**Figure 8.12 (a)**). The bond valence sum for this centre is quite close to 2.5 indicating that this Mn centre may display variable valency. The coordination environment is axially compressed along O13 and its symmetry equivalent. The Mn-O distances are ~1.96 Å for O13 and O13', and ~2.14 Å otherwise. The octahedron of Mn1 shares a vertex with the octahedron of Mn2 and an edge with that of Mn3, Mn5 and Mn6 (**Figure 8.12 (b)**).

Mn3(III) is bound to a μ_4-O^{2-} (O14) and a μ_3-O^{2-} (O16) group along with the O-donors of a μ-CH_3O^- (O15) and three phosphonate groups (O2, O12 and O17) (**Figure 8.12 (a)**). The phosphonate O-donors O2 and O12 reside at the Jahn-Teller elongated sites with the Mn-O bond being ~2.2 Å. The Mn-O distances for the O-donors perpendicular to the Jahn-Teller axis is ~1.9 Å. The octahedral coordination environment of Mn5 is satisfied by two μ_3-O^{2-} (O13 and O16) groups and the O-donors of four phosphonate groups (O2, O18, O19 and O20) with the Jahn-Teller axis directed towards two of the phosphonate O-donors (O2 and O19). The Mn-O distances are in the 2.2-2.3 Å range along the Jahn-Teller axis and vary between 1.9 and 2.0 Å perpendicular to it.

Mn6 was also found to be disordered and was modelled as two parts – Mn6A and Mn6B. The coordination environment for both parts is similar to that of Mn3 with a μ_3-O^{2-} (O13) and a μ_4-O^{2-}

(O14) group along with the O-donors of a μ-CH_3O^- (O5A/B) and three phosphonate groups (O12, O19 and O22) fulfilling it (**Figure 8.12 (a)**). The O-donors O12 and O19 of the phosphonate groups reside along the Jahn-Teller elongated sites.

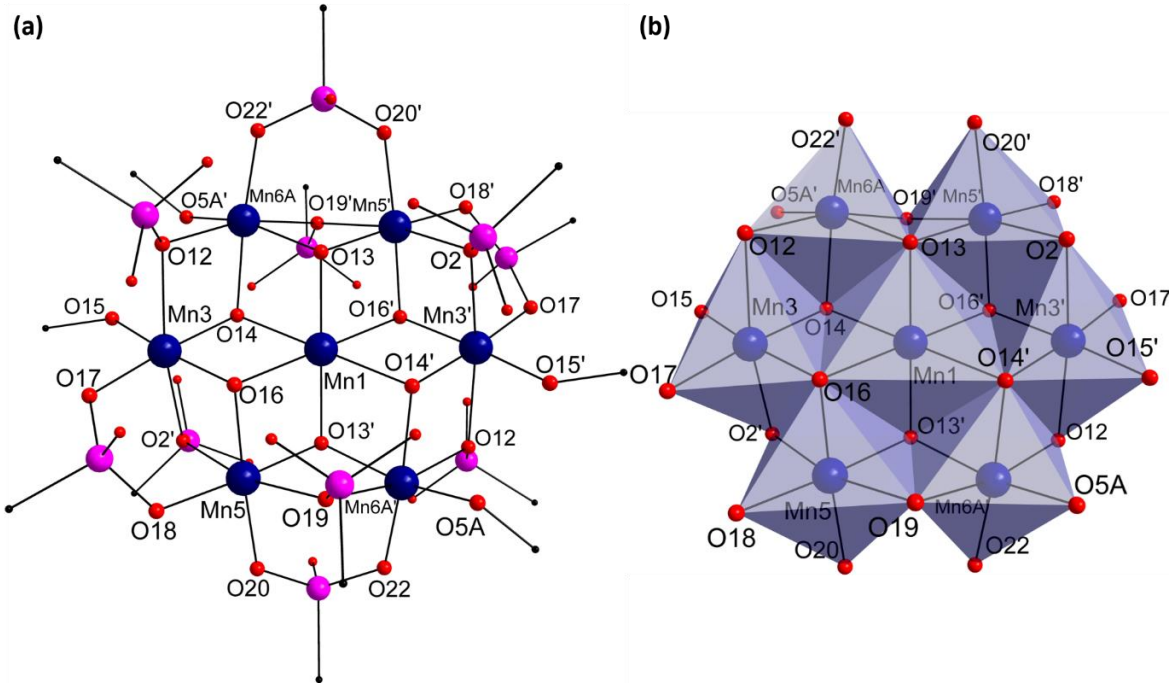

Figure 8.12: (a) Coordination environment of Mn centres constituting the {Mn_7} disc and **(b)** polyhedral representation of the {Mn_7} disc in compound **8.2**. Colour scheme: Mn (deep blue), C (black), P (pink) and O (red). *tert*-Butyl groups have been removed for clarity.

The Jahn-Teller axis of the Mn centres forming the vertices of the {Mn_7} disc are arranged in such a way that they are joined to each other at an angle that ranges between 77-85°. The deviation from 90° may be due to the presence of Mn2A/B which is bound to the {Mn_7} disc via a μ_4-O^{2-} group (O14). This is supported by the observation that the Jahn-Teller axes of Mn6A/B and Mn3 (which are closest to Mn2) are at ~77° to each other and this angle increases as one moves further along the disc. Such a deviation may affect the magnetic properties of this complex.

The trinuclear units capping the hexagonal {Mn_7} disc is comprised of Mn2A/B, Mn4 and Mn7 (**Figure 8.13**). The Mn2 centre was found to be disordered crystallographically and was modelled as two parts – Mn2A and Mn2B – and the disorder is due to the partially occupied Na^+ ion present in the vicinity. For both parts, the oxidation state has been determined to be +III and both are coordinated to a μ_4-O^{2-} (O14) and the O-donors of a methanol (O4A/B), two μ-CH_3O^- (O5A/B and O15) and two phosphonate groups (O3 and O6A/B) (**Figure 8.13**). The Jahn-Teller axis is directed along the μ_4-O^{2-} and the methanol O-donor with the Mn-O distances being ~2.2 Å along the Jahn-Teller axis and varying between 1.8-2.0 Å perpendicular to it. The octahedron of both parts share an edge with the octahedron of Mn3 and Mn6A/B at O5A/B and O14 respectively.

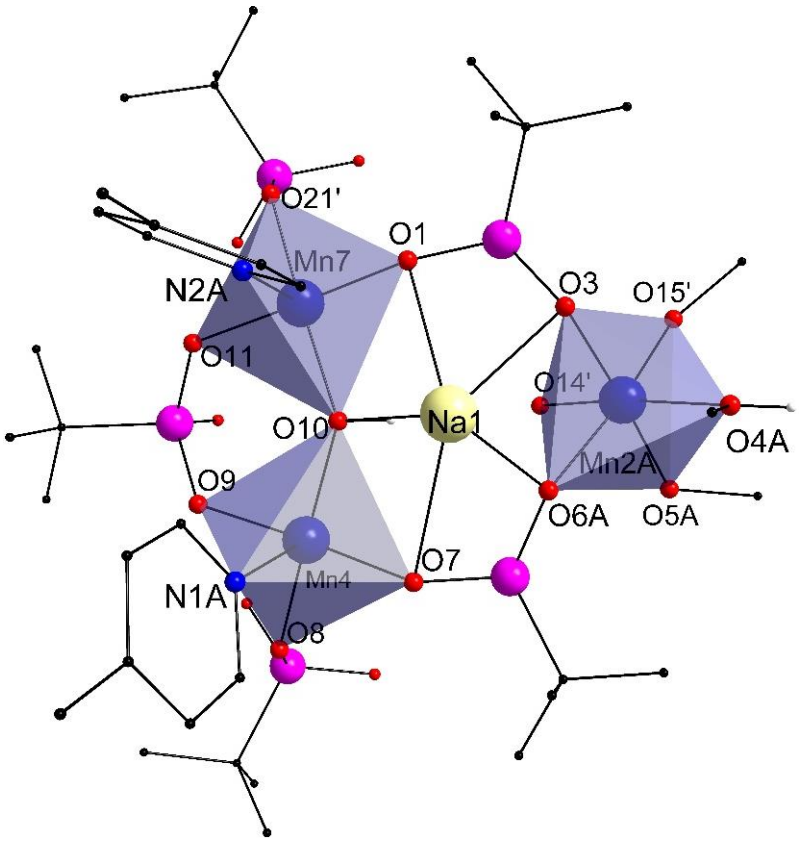

Figure 8.13: Coordination environment of Mn2A, Mn4, Mn7 and Na in compound **8.2**. Colour scheme: Mn (deep blue), Na (light yellow), C (black), P (pink), O (red) and H (grey).

Table 8.5: Key Mn-O and Mn-Mn bond lengths and bond valence sum for each Mn centre for compound **8.2**.

Mn centre	Coordinating atom	Bond Distance (Å)	BVS	Assigned oxidation state
Mn1	O13’	1.958(4)	2.609	+II/III
	O13	1.958(4)		
	O14	2.138(5)		
	O14’	2.138(5)		
	O16’	2.139(5)		
	O16	2.139(5)		
Mn2A	O3	1.842(7)	3.259	+III
	O5A	1.928(8)		
	O6A	1.971(7)		
	O4A	2.100(8)		
	O15’	1.992(5)		
	O14’	2.177(6)		
Mn2B	O5B	1.900(3)	2.963	+III
	O6B	1.960(3)		
	O4B	2.000(3)		
	O3	2.383(12)		
	O15'	1.913(11)		
	O14’	2.175(11)		

Mn centre	Coordinating atom	Bond Distance (Å)	BVS	Assigned oxidation state
Mn3	O16	1.908(4)	3.178	+III
	O17	1.911(4)		
	O15	1.926(4)		
	O14	1.937(4)		
	O12	2.211(5)		
	O2’	2.220(5)		
Mn4	O7	1.870(5)	3.088	+III
	O9	1.873(5)		
	O8	1.899(5)		
	O10	1.931(5)		
	N1A	2.276(8)		
Mn5	O16	1.914(4)	3.080	+III
	O20	1.914(4)		
	O18	1.921(4)		
	O13’	1.972(4)		
	O19	2.223(4)		
	O2’	2.253(4)		
Mn6A	O5A’	1.960(12)	3.138	+III
	O13	1.975(14)		
	O14	2.030(3)		
	O12	2.114(18)		
	O22’	1.800(2)		
	O19’	2.300(2)		
Mn6B	O14	1.811(12)	3.368	+III
	O13	1.872(11)		
	O5B’	1.941(3)		
	O12	2.272(13)		
	O22’	2.013(13)		
	O19’	2.110(13)		
Mn7	O1	1.849(5)	3.089	+III
	O11	1.874(5)		
	O21’	1.908(5)		
	O10	1.935(5)		
	N2A	2.299(8)		
Mn8	O46	1.948(4)	2.696	+II/III
	O46’’	1.948(4)		
	O45’’	1.968(4)		
	O45	1.968(4)		
	O28’’	2.402(4)		
	O28	2.402(4)		
Mn9	O26	1.901(5)	3.172	+III
	O40	1.909(4)		
	O28	1.923(4)		
	O45	1.950(4)		
	O37	2.214(4)		
	O33’’	2.224(4)		

Mn centre	Coordinating atom	Bond Distance (Å)	BVS	Assigned oxidation state
Mn10	O23A	1.948(6)	3.129	+III
	O34''	1.973(5)		
	O28	1.974(4)		
	O27	1.987(5)		
	O26	2.068(5)		
	O44''	2.074(5)		
Mn11	O42	1.863(4)	3.110	+III
	O38	1.874(4)		
	O39	1.897(4)		
	O35	1.932(4)		
	N4A	2.266(4)		
Mn12	O32	1.853(5)	3.174	+III
	O36	1.868(4)		
	O31	1.891(4)		
	O35	1.932(4)		
	N3	2.242(6)		
Mn13	O30''	1.910(4)	3.130	+III
	O41	1.911(4)		
	O45	1.928(4)		
	O46''	1.944(4)		
	O43	2.230(4)		
	O33''	2.239(5)		
Mn14	O28	1.906(4)	3.159	+III
	O29	1.911(4)		
	O27	1.917(5)		
	O46	1.954(4)		
	O43''	2.211(4)		
	O37	2.233(4)		

Metals	Distance (Å)	Metals	Distance (Å)
Mn1-Mn3	3.105(4)	Mn6A-Mn7	3.661(5)
Mn1-Mn5	2.993(4)	Mn8-Mn13	2.908(3)
Mn1-Mn6A	3.118(4)	Mn8-Mn14	3.108(3)
Mn2A-Mn3'	3.014(3)	Mn9-Mn10	2.968(1)
Mn2A-Mn4	5.320(3)	Mn9-Mn11	3.817(1)
Mn2A-Mn5	5.251(3)	Mn9-Mn13	3.042(1)
Mn2A-Mn6A'	3.127(4)	Mn9-Mn14	3.081(1)
Mn2A-Mn7	5.165(3)	Mn10-Mn11''	5.445(1)
Mn2B-Na1	3.539(5)	Mn10-Mn12''	5.347(1)
Mn3-Mn4	3.693(1)	Mn10-Mn13''	5.213(2)
Mn3-Mn5	2.981(1)	Mn10-Mn14	2.948(1)
Mn3-Mn6A	3.124(4)	Mn11-Mn12	3.647(1)
Mn4-Mn5	3.857(4)	Mn11-Mn13	3.927(1)
Mn4-Mn7	3.643(5)	Mn12-Mn13''	3.936(1)
Mn5-Mn6A'	3.115(4)	Mn12-Mn14	3.805(1)
Mn5-Mn7'	3.982(2)	Mn13-Mn14''	3.057(1)

'2-X,2-Y,1-Z; ''1-X,1-Y,-Z

Table 8.6: BVS analysis for O atoms and their assigned protonation state in compound **8.2**.

Atom	BVS	Assignment
O10	1.253	μ_3-OH^-
O13	1.709	μ_3-O^{2-}
O14	1.786	μ_4-O^{2-}
O16	1.689	μ_3-O^{2-}
O28	2.055	μ_4-O^{2-}
O35	1.256	μ_3-OH^-
O45	1.803	μ_3-O^{2-}
O46	1.802	μ_3-O^{2-}

Mn4 and Mn7 reside in a square pyramidal environment and not a spherical square pyramidal environment which was confirmed by continuous shape measure analysis (**Table 8.7**) which gives a slightly higher value (~1.2) when spherical square pyramidal geometry is used as reference. The coordination environment of both Mn centres is fulfilled by the O-donors of a μ-OH^-, three phosphonate groups and the N-donor of a 4-picoline group (**Figure 8.13**). The Jahn-Teller axis for both is directed along the 4-picoline N-donor with the Mn-N bond being close to 2.3 Å. The Mn-O distances on the other hand vary between 1.85 and 1.95 Å. These Mn centres are relatively isolated from the other Mn centres and their polyhedra only share a vertex with each other at the μ-OH^- group (O10).

Table 8.7: Continuous shape measure values, angle variance and distortion indices for each Mn centre for compound **8.2** ([1]octahedral and [2]square pyramid geometry).

Mn centre	Continuous shape measure value	Angle variance (σ^2)	Distortion Index
Mn1[1]	2.820	167.86	0.1360
Mn2A[1]	0.883	45.23	0.0527
Mn3[1]	0.897	34.23	0.0522
Mn4[2]	0.832	9.37	0.0239
Mn5[1]	0.988	30.03	0.0460
Mn6A[1]	1.178	86.42	0.9344
Mn7[2]	0.669	9.60	0.0258
Mn8[1]	4.073	197.41	0.1427
Mn9[1]	0.884	31.75	0.0559
Mn10[1]	0.560	32.49	0.0487
Mn11[2]	0.929	13.06	0.0270
Mn12[2]	0.753	8.00	0.0313
Mn13[1]	0.988	32.20	0.0491
Mn14[1]	0.919	30.44	0.0235

The Mn centres in the other form that contains the partially protonated *tert*-butyl phosphonate group reside in coordination environments similar to those described for the form above (**Figure 8.14**). This form was found to be less disordered with only the partially protonated phosphonate group being disordered and it was modelled as two parts. The central Mn centre in this case (Mn8) has a bond valence sum value of 2.696 suugesting that this centre may exist in both +II and +III oxidation state. The partially protonated phosphonate group is coordinated to Mn10 (**Figure 8.14 (c)**) which, like Mn2, is further coordinated to a μ_4-O^{2-} (O28) and the O-donors of two μ-CH_3O^- (O26

and O27) and two fully deprotonated phosphonate groups (O34 and O44). The Jahn-Teller axis for this Mn centre is directed along the μ_4-O^{2-} and the partially protonated phosphonate O-donor (O23A/B). The bond distances for Mn10 are slightly shorter than those observed for both Mn2A and Mn2B.

This complex bears some structural similarities with some of the previously reported Mn complexes. These complexes contain a {Mn_7} disc stabilised by carboxylate and phosphonate ligands.[368, 384, 542, 544, 643-647] A number of these complexes also show similar trinuclear units as found in compound **8.2**.[384, 542, 544, 645-647] The capping of the trinuclear units has been observed only in two cases where an additional Mn^{II} centre was found to cap the trinuclear units.[645, 647]

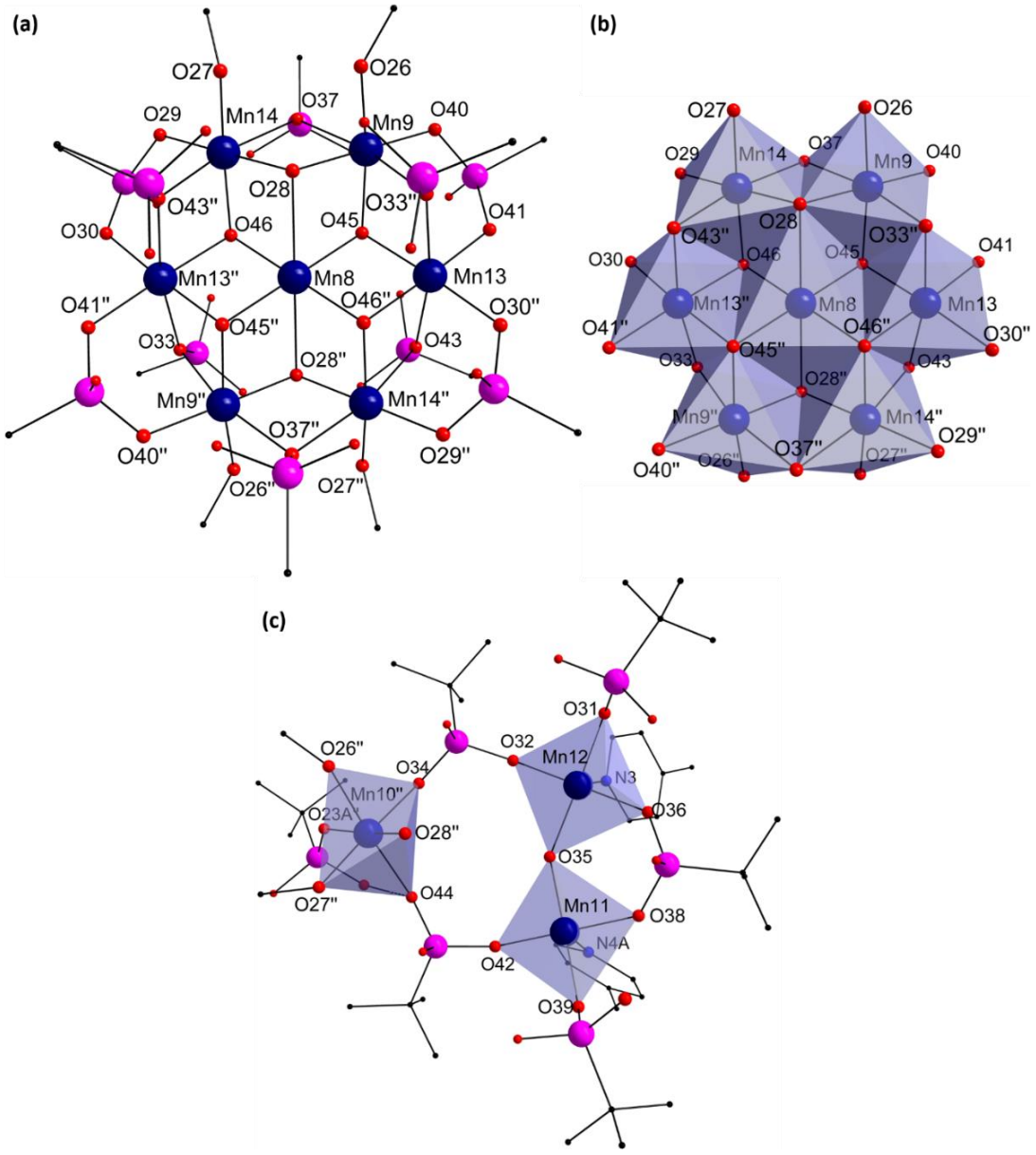

Figure 8.14: (a) Coordination environment of Mn centres constituting the {Mn_7} disc, **(b)** polyhedral representation of the {Mn_7} disc and **(c)** coordination environment of Mn centres the trinuclear unit in the other form of the tridecanuclear complex in compound **8.2**. Colour scheme: Mn (deep blue), C (black), P (pink), O (red) and H (grey).

Table 8.8: Selected bond angles for compound **8.2**.

Bond	Bond Angle (°)	Bond	Bond Angle (°)
O14-Mn1-O16	75.21(15)	O5A-Mn2A-O14’	76.9(3)
O14’-Mn1-O16’	75.21(15)	O15’-Mn2A-O14’	77.60(19)
O13’-Mn1-O14’	77.94(17)	O5A-Mn2A-O6A	88.3(3)
O13-Mn1-O14	77.94(17)	O5A-Mn2A-O15’	88.4(3)
O13-Mn1-O16’	80.13(17)	O6A-Mn2A-O14’	89.8(3)
O13’-Mn1-O16	80.13(17)	O3-Mn2A-O15’	90.4(2)
O13’-Mn1-O16’	99.87(17)	O3-Mn2A-O6A	91.8(3)
O13-Mn1-O16	99.87(17)	O3-Mn2A-O4A	92.1(3)
O13-Mn1-O14’	102.06(17)	O6A-Mn2A-O4A	93.3(3)
O13’-Mn1-O14	102.06(17)	O5A-Mn2A-O4A	93.7(3)
O14’-Mn1-O16	104.79(15)	O3-Mn2A-O14’	97.3(2)
O14-Mn1-O16’	104.79(15)	O15’-Mn2A-O4A	99.0(3)
O13’-Mn1-O13	180.00(6)	O6A-Mn2A-O15’	167.4(3)
O14-Mn1-O14’	180.0(2)	O4A-Mn2A-O14’	170.1(3)
O16’-Mn1-O16	180.0(2)	O3-Mn2A-O5A	174.2(3)
O15’-Mn2B-O3	77.8(4)	O14-Mn3-O12	81.52(18)
O15’-Mn2B-O14’	79.3(4)	O15-Mn3-O14	85.3(2)
O14’-Mn2B-O3	83.0(4)	O16-Mn3-O14	85.5(2)
O5B-Mn2B-O14’	87.358(9)	O14-Mn3-O2’	85.52(18)
O5B-Mn2B-O6B	90.0(12)	O16-Mn3-O2’	86.09(17)
O4B-Mn2B-O3	92.2(11)	O15-Mn3-O12	86.8(2)
O6B-Mn2B-O14’	92.840(6)	O15-Mn3-O2’	90.11(19)
O15’-Mn2B-O4B	93.2(11)	O17-Mn3-O2’	91.24(19)
O6B-Mn2B-O3	93.3(8)	O16-Mn3-O17	92.09(19)
O6B-Mn2B-O4B	94.1(13)	O16-Mn3-O12	94.85(18)
O5B-Mn2B-O4B	97.1(14)	O17-Mn3-O15	96.96(19)
O5B-Mn2B-O15’	97.713(9)	O17-Mn3-O12	101.78(19)
O15’-Mn2B-O6B	168.7(10)	O12-Mn3-O2’	166.89(16)
O5B-Mn2B-O3	169.9(10)	O16-Mn3-O15	170.3(2)
O4B-Mn2B-O14’	171.7661(13)	O17-Mn3-O14	176.1(2)
O9-Mn4-N1A	86.5(3)	O7-Mn4-O8	91.2(2)
O9-Mn4-O8	87.8(2)	O9-Mn4-O10	91.4(2)
O7-Mn4-N1A	88.0(3)	O10-Mn4-N1A	96.4(3)
O8-Mn4-N1A	89.6(3)	O8-Mn4-O10	173.8(2)
O7-Mn4-O10	90.1(2)	O7-Mn4-O9	174.4(2)
O13’-Mn5-O19	82.44(16)	O5A’-Mn6A-O14	79.9(8)
O16-Mn5-O2’	85.03(17)	O13-Mn6A-O14	80.3(9)
O16-Mn5-O13’	85.62(19)	O13-Mn6A-O19’	80.3(8)
O16-Mn5-O19	87.21(17)	O14-Mn6A-O12	81.9(5)
O13’-Mn5-O2’	87.33(16)	O5A’-Mn6A-O19’	82.0(7)
O18-Mn5-O2’	88.83(17)	O14-Mn6A-O19’	82.3(11)
O20-Mn5-O18	89.11(19)	O22’-Mn6A-O19’	92.1(5)
O20-Mn5-O19	89.12(19)	O5A’-Mn6A-O12	94.4(6)
O16-Mn5-O18	92.7(2)	O22’-Mn6A-O13	95.0(6)
O20-Mn5-O13’	92.81(18)	O13-Mn6A-O12	97.8(5)
O20-Mn5-O2’	98.40(19)	O22’-Mn6A-O5A’	103.2(9)
O18-Mn5-O19	101.21(17)	O22’-Mn6A-O12	103.7(14)
O19-Mn5-O2’	167.60(15)	O5A’-Mn6A-O13	155.0(17)
O18-Mn5-O13’	175.92(18)	O12-Mn6A-O19’	164.2(13)
O16-Mn5-O20	176.18(19)	O22’-Mn6A-O14	173.2(12)
O5B’-Mn6B-O12	78.3(9)	O45’’-Mn8-O28’’	73.68(15)
O5B’-Mn6B-O22’	81.466(8)	O45-Mn8-O28	73.68(15)

Bond	Bond Angle (°)	Bond	Bond Angle (°)
O14-Mn6B-O12	82.5(4)	O46-Mn8-O28	75.02(16)
O13-Mn6B-O19’	88.0(5)	O46’’-Mn8-O28’’	75.02(16)
O14-Mn6B-O13	88.9(6)	O46-Mn8-O45’’	82.78(15)
O13-Mn6B-O22’	91.5(4)	O46’’-Mn8-O45	82.78(15)
O22’-Mn6B-O12	91.8(5)	O46’’-Mn8-O45’’	97.22(15)
O22’-Mn6B-O19’	92.4(5)	O46-Mn8-O45	97.22(15)
O14-Mn6B-O19’	93.2(6)	O46’’-Mn8-O28	104.98(16)
O13-Mn6B-O12	95.7(4)	O46-Mn8-O28’’	104.98(16)
O14-Mn6B-O5B’	97.4(10)	O45-Mn8-O28’’	106.32(15)
O19’-Mn6B-O5B’	98.559(8)	O45’’-Mn8-O28	106.32(15)
O13-Mn6B-O5B’	170.6(11)	O28-Mn8-O28’’	180
O19’-Mn6B-O12	174.3(5)	O45’’-Mn8-O45	180.00(10)
O14-Mn6B-O22’	174.4(7)	O46’’-Mn8-O46	180
O1-Mn7-N2A	84.7(4)	O1-Mn7-O21’	91.9(2)
O11-Mn7-O21’	88.5(2)	O10-Mn7-N2A	92.4(3)
O1-Mn7-O10	88.7(2)	O211-Mn7-N2A	94.8(4)
O11-Mn7-N2A	90.9(4)	O211-Mn7-O10	172.8(2)
O11-Mn7-O10	91.4(2)	O1-Mn7-O11	175.5(2)
O28-Mn9-O37	82.52(16)	O28-Mn10-O26	78.60(18)
O45-Mn9-O33’’	82.82(16)	O28-Mn10-O27	79.36(18)
O26-Mn9-O28	84.1(2)	O27-Mn10-O44’’	87.62(19)
O28-Mn9-O33’’	85.08(16)	O34’’-Mn10-O26	87.8(2)
O28-Mn9-O45	86.05(17)	O27-Mn10-O26	91.2(2)
O26-Mn9-O37	88.18(19)	O23A-Mn10-O26	91.8(3)
O26-Mn9-O33’’	93.0(2)	O23A-Mn10-O34’’	92.0(4)
O40-Mn9-O33’’	93.46(16)	O34’’-Mn10-O44’’	92.4(2)
O45-Mn9-O37	93.88(16)	O28-Mn10-O44’’	93.04(17)
O40-Mn9-O45	94.31(17)	O34’’-Mn10-O28	93.71(19)
O26-Mn9-O40	95.4(2)	O23A-Mn10-O27	94.9(4)
O40-Mn9-O37	98.95(16)	O23A-Mn10-O44’’	96.5(3)
O37-Mn9-O33’’	167.37(15)	O23A-Mn10-O28	168.6(3)
O26-Mn9-O45	169.6(2)	O26-Mn10-O44’’	171.63(19)
O40-Mn9-O28	178.45(19)	O34’’-Mn10-O27	173.1(2)
O42-Mn11-N4A	87.4(2)	O36-Mn12-N3	86.4(2)
O38-Mn11-O39	88.68(19)	O32-Mn12-O35	88.2(2)
O42-Mn11-O35	88.7(2)	O36-Mn12-O31	88.69(19)
O39-Mn11-N4A	89.22(19)	O32-Mn12-N3	89.5(2)
O38-Mn11-N4A	89.64(19)	O31-Mn12-N3	90.7(3)
O38-Mn11-O35	90.51(18)	O36-Mn12-O35	91.16(18)
O42-Mn11-O39	92.5(2)	O32-Mn12-O31	92.4(2)
O35-Mn11-N4A	98.6(2)	O35-Mn12-N3	95.5(3)
O39-Mn11-O35	172.17(19)	O31-Mn12-O35	173.7(2)
O42-Mn11-O38	176.8(2)	O32-Mn12-O36	175.8(2)
O46’’-Mn13-O43	82.27(16)	O28-Mn14-O37	82.37(16)
O45-Mn13-O33’’	82.91(16)	O46-Mn14-O43’’	82.52(16)
O45-Mn13-O46’’	83.96(16)	O28-Mn14-O27	82.85(19)
$O30^2$-Mn13-O41	87.76(17)	O28-Mn14-O43’’	85.98(16)
O41-Mn13-O33’’	88.43(18)	O28-Mn14-O46	87.64(17)
$O30^2$-Mn13-O43	88.55(17)	O27-Mn14-O43’’	90.42(18)
O45-Mn13-O43	89.43(16)	O27-Mn14-O37	90.56(18)
O46’’-Mn13-O33’’	89.93(16)	O29-Mn14-O46	92.87(18)
$O30^2$-Mn13-O46’’	93.78(17)	O29-Mn14-O43’’	93.96(17)
O41-Mn13-O45	94.55(16)	O46-Mn14-O37	94.50(16)
$O30^2$-Mn13-O33’’	98.84(18)	O29-Mn14-O27	96.6(2)

Bond	Bond Angle (°)	Bond	Bond Angle (°)
O41-Mn13-O43	99.20(17)	O29-Mn14-O37	97.72(16)
O43-Mn13-O33''	169.61(15)	O43''-Mn14-O37	168.09(15)
$O30^2$-Mn13-O45	177.15(18)	O27-Mn14-O46	168.54(19)
O41-Mn13-O46''	177.91(18)	O28-Mn14-O29	179.5(2)

The packing arragement in this complex allows for some solvent molecules to be trapped in the crystal lattice (**Figure 8.15**). The 'calcvoid' routine in OLEX2 reveals that the structure contains voids that can be permeated by a sphere of radius 2.2 Å. The electron density found within these voids (100 electrons per unit cell) may correspond to some Na^+ ions and five CH_3OH molecules per formula unit but due to its diffused nature, they could not be resolved.

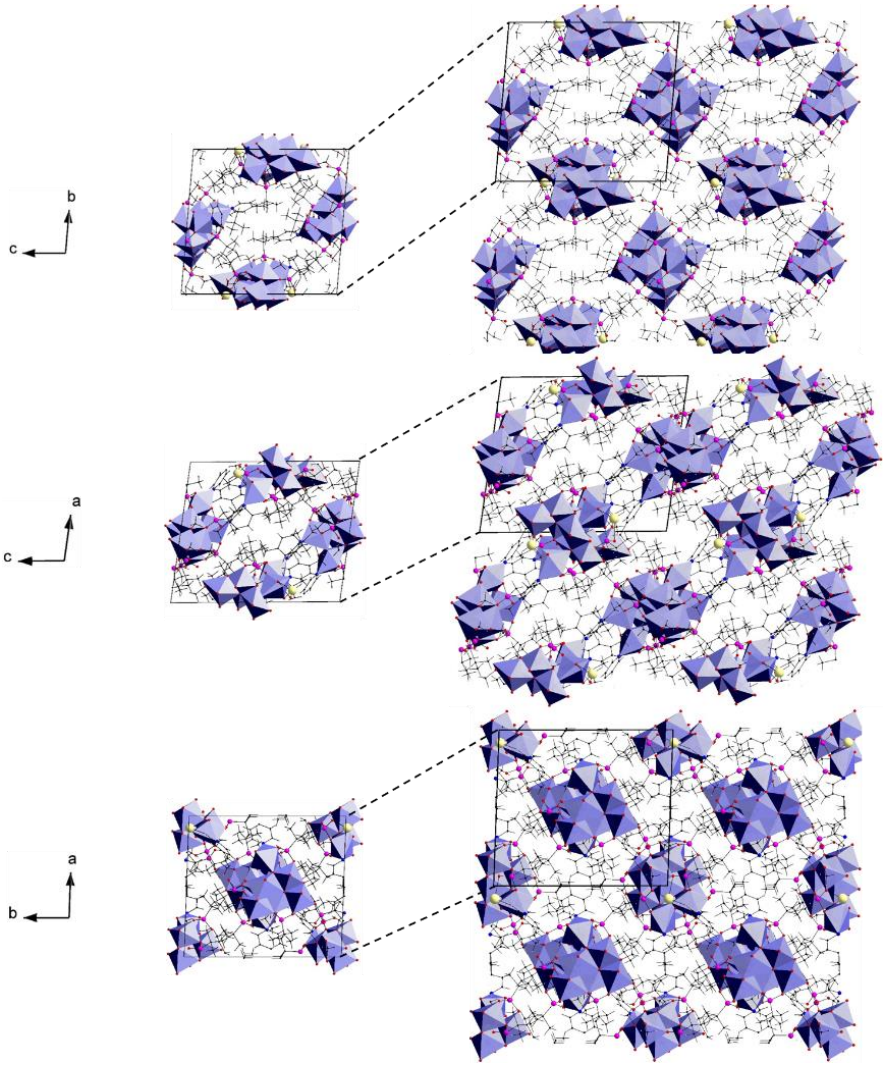

Figure 8.15: Packing diagram of compound **8.2**. Colour scheme: Mn (blue), Na (tan), P(pink), C (black) and O (red).

8.2.2 Physicochemical characterisation

A number of physicochemical techniques were employed to verify the structural model. The Mn:Na ratio in this complex was determined to be 26:1.1 using EDX analysis which is close to the expected ratio of 26:1.4 confirming the presence of an extra Na^+ ion in the crystal lattice.

TGA analysis reveals (**Figure 8.16**) an intial drop up to 70 °C due to the loss of the five CH_3OH molecules trapped in the crystal lattice (weight loss calcd: 2.7 %, found: 2.7 %). This is followed by the loss of the bound CH_3OH, 4-picoline and methoxy groups up to 320 °C (weight loss calcd: 17.9 %, found: 17.8 %). Above 320 °C, the partial decomposition of the *tert*-butyl phosphonate groups and the subsequent formation of the oxide and phosphate species occurs.

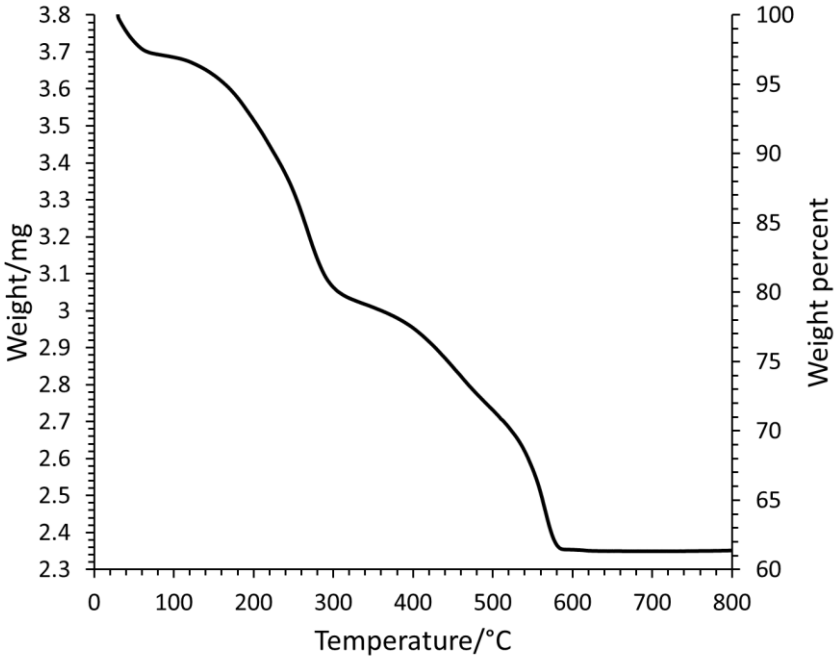

Figure 8.16: TGA analysis of compound **8.2**.

The IR spectrum of compound **8.2** is in agreement with the proposed structural model (**Figure 8.17**). The feature centred at ~2900 cm^{-1} corresponds to the C-H vibrations.[617] The signals in the 1300-1600 cm^{-1} range are due to vibrations of the organic moieties of the molecule.[617] The strong vibrational mode at 972 cm^{-1} corresponds to the stretching vibration of the phosphonate groups.[621-623]

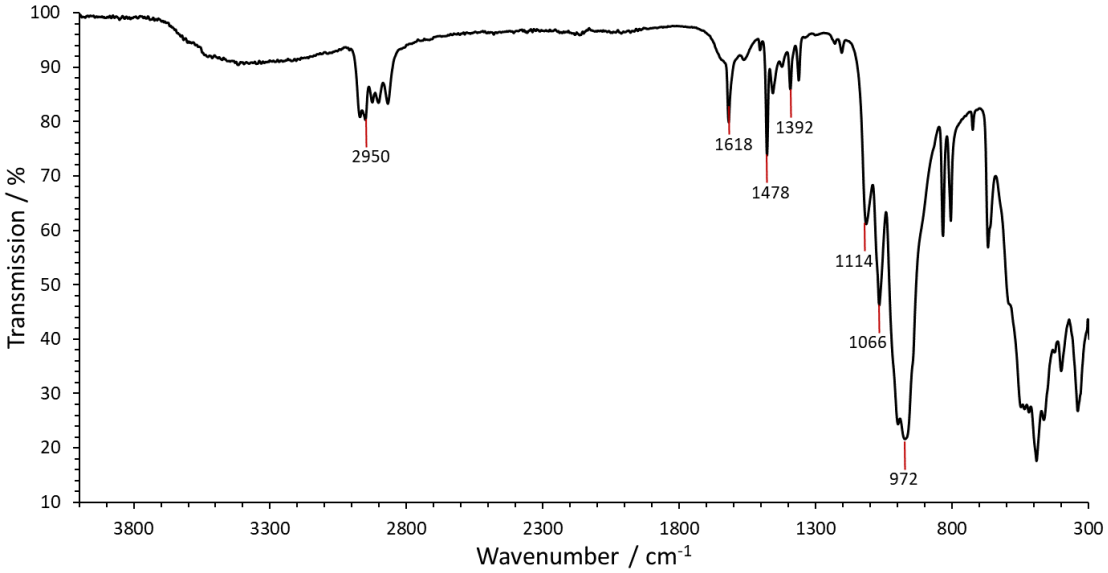

Figure 8.17: Infrared spectrum of compound **8.2**.

8.3 $K[K_2(Mn^{II}_{0.5}Mn^{III}_{0.5})Mn^{III}_{12}(\mu_4\text{-}O)_2(\mu_3\text{-}O)_4(\mu\text{-}OH)_2((CH_3)_3CPO_3)_{10}((CH_3)_3CO_2)_2(\mu\text{-}CH_3O)_4(CH_3OH)_6][(Mn^{II}_{0.5}Mn^{III}_{0.5})Mn^{III}_{12}(\mu_4\text{-}O)_2(\mu_3\text{-}O)_4(\mu\text{-}OH)_2((CH_3)_3CPO_3)_{10}((CH_3)_3CPO_3H)_2(\mu\text{-}CH_3O)_4(CH_3OH)_4]\cdot 2CH_3OH$ (8.3)

Having dangling partially protonated phosphonate groups in compound **8.2** provides the potential opportunity to link such units together by cationic species and hence this possibility was investigated. It was observed that refluxing $KMnO_4$ with $Mn(CH_3COO)_2\cdot 4H_2O$ with *tert*-butyl phosphonic acid and pivalic acid in the ratio 1:4:5:10 resulted in the formation of compound **8.3**, $K[K_2Mn_{13}(\mu_4\text{-}O)_2(\mu_3\text{-}O)_4(\mu\text{-}OH)_2((CH_3)_3CPO_3)_{10}((CH_3)_3CO_2)_2(\mu\text{-}CH_3O)_4(CH_3OH)_6][Mn_{13}(\mu_4\text{-}O)_2(\mu_3\text{-}O)_4(\mu\text{-}OH)_2((CH_3)_3CPO_3)_{10}((CH_3)_3CPO_3H)_2(\mu\text{-}CH_3O)_4(CH_3OH)_4]\cdot 2CH_3OH$. The crystals were obtained within a week and were characterised using single crystal X-ray diffraction.

8.3.1 Structure description

Compound **8.3** crystallises in the triclinic crystal system and the structure was solved in the space group $P\bar{1}$. Compound **8.3** is a one-dimensional polymer of the tridecanuclear complex similar to that of compound **8.2**, that are bound to each other by K^+ ions (**Figure 8.18**). The asymmetric unit contains half of this complex (**Figure 8.19**). The tridecanuclear complex in this case too exists in two different forms one contains partially protonated phosphonate group while the other contains a pivalate group. These ligands lie at the periphery and bind to the K^+ ion. Both forms are stabilised by two OH^- groups, four CH_3O^-, six O^{2-} and ten phosphonate groups.

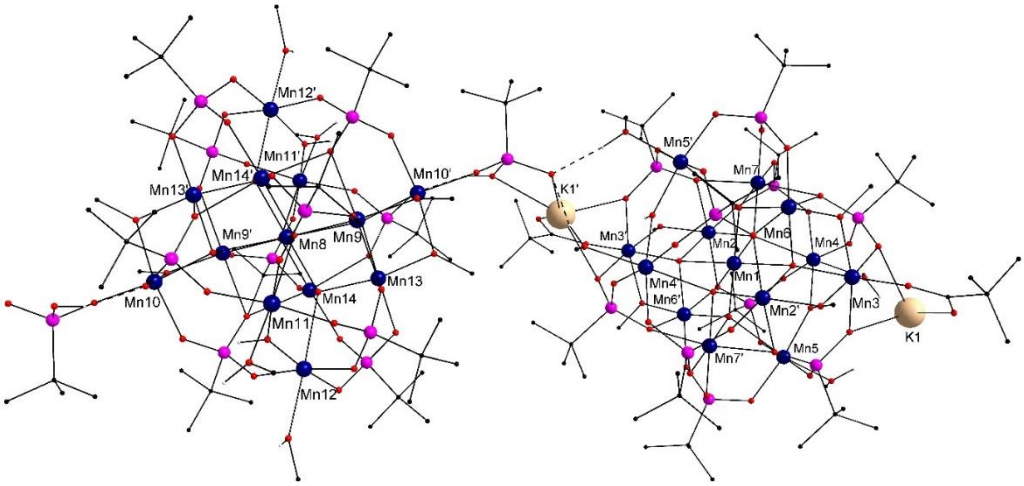

Figure 8.18: Crystal structure of the tridecanuclear compound **8.3**. Colour scheme: Mn (deep blue), K (tan), C (black), P (pink) and O (red). All hydrogen atoms (grey) except those bound to O centres have been removed for clarity. Hydrogen bonds are shown with dashed lines.

Similar to compound **8.2**, the core structure of this complex comprises of a three layered metal-centred distorted cuboctahedron with the top and bottom $\{Mn_3\}$ layers sandwiching the central $\{Mn_7\}$ layer. The overall structure is stabilised by $\mu_4\text{-}O^{2-}$ groups and the O-donors of $\mu\text{-}CH_3O^-$ and *tert*-butyl phosphonate groups which bind in 4.211 and 3.111 modes. The oxidation state of each Mn centre has been determined using bond valence sum analysis (**Table 8.9**) which has also been

used for the proper assignment of the protonation states of the O centres bound only to Mn (**Table 8.10**). The oxidation state of all Mn centres except Mn1 and Mn8 has been found to be +III. For Mn1 and Mn8, the bond valence sum has been determined to close to 2.5 suggesting that these Mn centres display intermediate oxidation state.

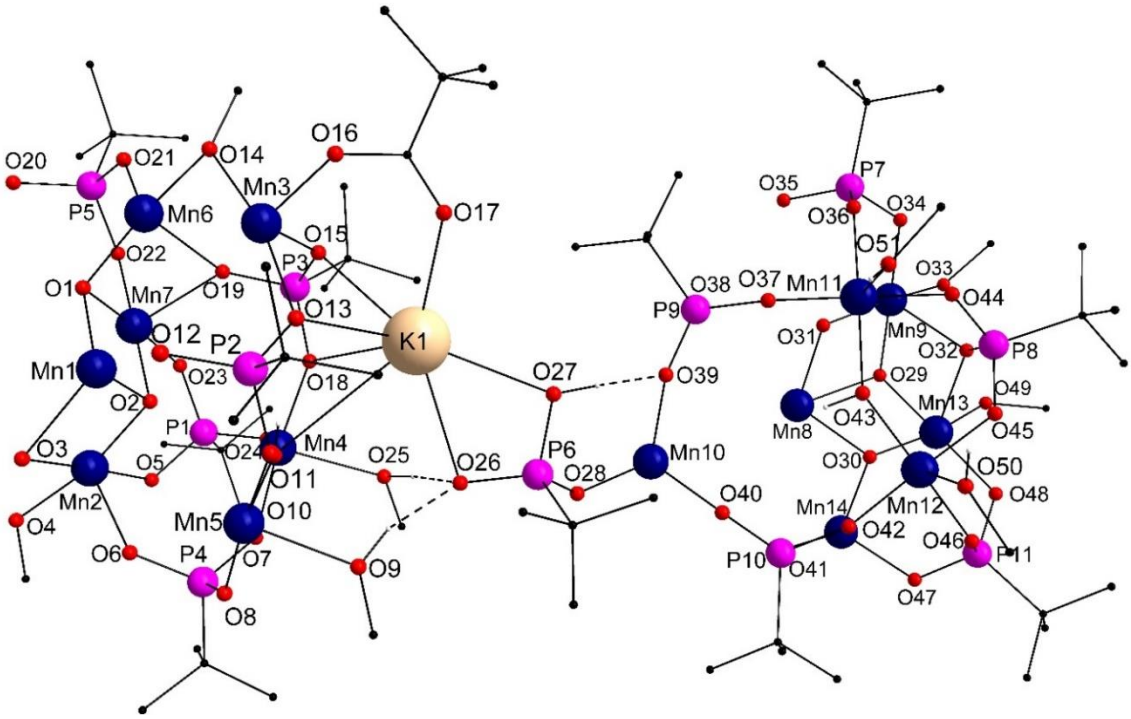

Figure 8.19: Asymmetric unit of compound **8.3**. Colour scheme: Mn (deep blue), K (tan), C (black), P (pink) and O (red). All hydrogen atoms (grey) except those bound to O centres have been removed for clarity. Hydrogen bonds are shown with dashed lines.

The {Mn_7} disc is comprised of Mn1, Mn2, Mn6, Mn7 and their symmetry equivalents (**Figure 8.20**). Mn1 resides in an octahedral environment which is fufilled by four μ_3-O^{2-} (O1 and O2 and their symmetry equivalents) and two μ_4-O^{2-} groups (O3 and its symmetry equivalent) (**Figure 8.20 (a)**). The coordination environment of Mn1 is axially elongated with the Jahn-Teller axis directed along O3 and its symmetry equivalent. The bond distances are ~2.4 Å along the Jahn-Teller axis and vary between 1.95-2.00 Å perpendicular to it. The octahedron of Mn1 shares a vertex with the octahedron of Mn3 and an edge with that of Mn2, Mn6 and Mn7 (**Figure 8.20 (b)**).

The coordination environment of Mn2 is fulfilled by a μ_3-O^{2-} (O2) and a μ_4-O^{2-} (O3) groups in addition to the O-donors of a methoxy group (O4), and three phosphonate groups (O5, O6 and O12') (**Figure 8.20 (a)**). The Jahn-Teller axis is directed along two of the phosphonate O-donors (O6 and O12') with the Mn-O distance being ~2.2 Å. The Mn-O distances perpendicular to the Jahn-Teller axis range between ~1.91 and 1.95 Å. The octahedron of Mn2 shares an edge with the octahedron of Mn3, Mn6 and Mn7.

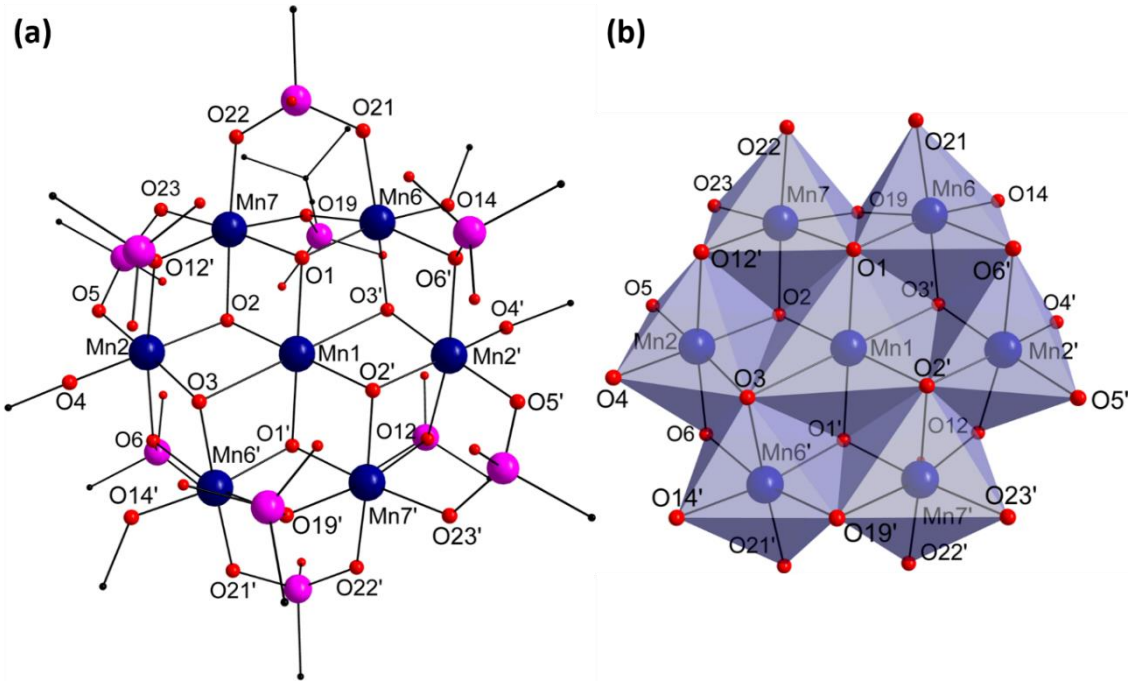

Figure 8.20: (a) Coordination environment of Mn centres constituting the {Mn_7} disc and **(b)** polyhedral representation of the {Mn_7} disc in compound **8.3**. Colour scheme: Mn (deep blue), P (pink), O (red) and C (black). *tert*-Butyl groups have been removed for clarity.

Mn6 and Mn7 also reside in an octahedral coordination environment (**Figure 8.20 (a)**). Two μ_3-O^{2-} groups (O1 and O3') along with the O-donors of a methoxy (O14) and three phosphonate groups (O6', O19 and O21) fulfil the coordination envrionemnt of Mn6. Mn7 resides in a similar coordination environment with the methoxy O-donor replaced by another phosphonate O-donor. For both Mn centres, the Jahn-Teller axis is directed along the phosphonate O-donors such that they are mutally perpendicular to each other. The Mn-O distances along the Jahn-Teller axis are ~2.2 Å and vary between 1.88-1.96 Å perpendicular to it. The octahedron of both Mn centres share an edge with each other at O1 and O19 (**Figure 8.20 (b)**). Similar to compound **8.2**, the Jahn-Teller axis of the Mn centres forming the vertices of the {Mn_7} disc are arranged in such a way that they are joined to each other at an angle that ranges between 77-85°.

Mn3-Mn5 constitute the trinuclear units capping the central layer (**Figure 8.21**). Mn3 is coordinated to a μ_4-O^{2-} (O3') group in addition to the O-donors of a pivalate group (O16), two methoxy groups (O4' and O14) and two phosphonate groups (O13 and O15) (**Figure 8.21**). One of the phosphonate O-donors (O13) and the methoxy O-donor (O14) lying opposite to it occupy the Jahn-Teller axis elongated site with the Mn-O bond being ~2.1 Å. The Mn-O distance perpendicular to the Jahn-Teller axis vary between 1.9 and 2.0 Å. The octahedron of Mn3 shares an edge with Mn6 in addition to sharing an edge with that of Mn2 and a vertex with that of Mn1.

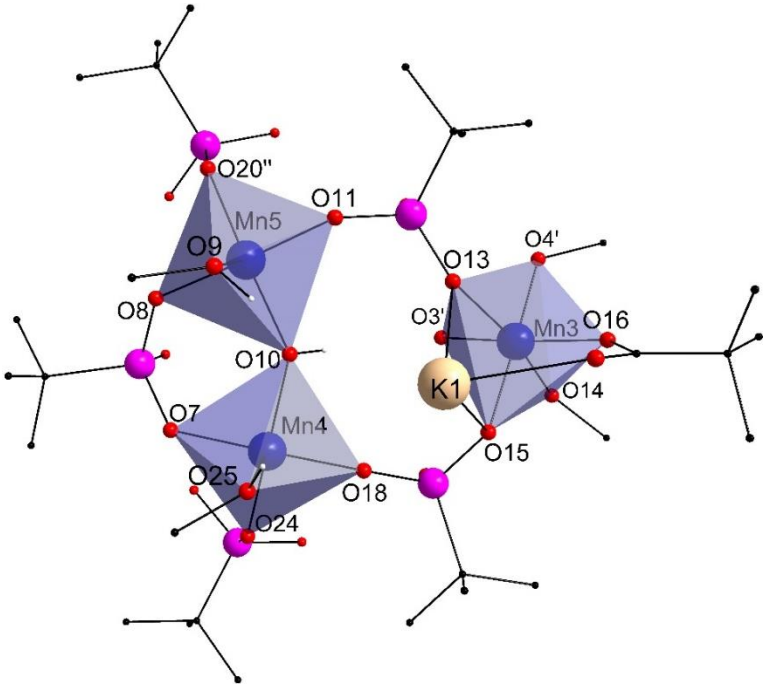

Figure 8.21: Coordination environment of Mn3-Mn5 in compound **8.3**. Colour scheme: Mn (deep blue), K (tan), C (black), P (pink), O (red) and H (grey).

Mn4 and Mn5 similar to compound **8.2** reside in a square pyramidal coordination environment (**Figure 8.21**) which was confirmed by continuous shape measure analysis (**Table 8.11**). A higher continuous shape measure value (~1.2) was obtained when spherical square pyramidal geometry was used as reference. The coordination environment of both Mn4 and Mn5 is fulfiiled by a μ-OH^- group (O10) in addition to a methanol and three phosphonate O-donors with the Jahn-Teller axis directed along the methanol O-donor with the Mn-O distance being ~2.2 Å. Perpendicular to the Jahn-Teller axis, the Mn-O distances are ~1.9 Å. The polyhedron of these Mn centres share a vertex with each other at O10.

Table 8.9: Key metal-ligand and metal-metal bond lengths and bond valence sum for each Mn centre and Ca centre for compound **8.3**.

Metal centre	Coordinating atom	Bond Distance (Å)	BVS	Assigned oxidation state
Mn1	O2	1.946(3)	2.659	+II/III
	O2’	1.946(3)		
	O1’	1.998(3)		
	O1	1.998(3)		
	O3’	2.357(3)		
	O3	2.358(3)		
Mn2	O5	1.908(3)	3.188	+III
	O4	1.922(3)		
	O3	1.925(3)		
	O2	1.944(3)		
	O6	2.178(3)		
	O12’	2.204(3)		

Metal centre	Coordinating atom	Bond Distance (Å)	BVS	Assigned oxidation state
Mn3	O16	1.913(3)	3.158	+III
	O4’	1.960(3)		
	O3’	1.965(3)		
	O15	1.968(3)		
	O13	2.109(3)		
	O14	2.118(3)		
Mn4	O18	1.871(3)	3.090	+III
	O7	1.876(3)		
	O24	1.888(3)		
	O10	1.934(4)		
	O25	2.223(3)		
Mn5	O11	1.866(3)	3.084	+III
	O8	1.884(3)		
	O20’	1.891(3)		
	O10	1.938(3)		
	O9	2.208(4)		
Mn6	O14	1.884(3)	3.171	+III
	O21	1.905(3)		
	O1	1.937(3)		
	O3’	1.942(3)		
	O6’	2.237(3)		
	O19	2.240(3)		
Mn7	O22	1.920(3)	3.078	+III
	O23	1.922(3)		
	O1	1.934(3)		
	O2	1.956(3)		
	O12’	2.205(3)		
	O19	2.245(3)		
Mn8	O31	1.970(3)	2.556	+II/III
	O31’’	1.970(3)		
	O30’’	2.004(3)		
	O30	2.004(3)		
	O29’’	2.367(3)		
	O29	2.367(3)		
Mn9	O33	1.902(3)	3.192	+III
	O34	1.903(3)		
	O29	1.930(3)		
	O31	1.945(3)		
	O41’’	2.207(3)		
	O32	2.213(3)		
Mn10	O28	1.947(3)	3.148	+III
	O40	1.977(4)		
	O29’’	1.983(3)		
	O49’’	1.987(3)		
	O33’’	2.026(4)		
	O39	2.088(3)		
Mn11	O37	1.867(3)	3.110	+III
	O44	1.871(3)		
	O36	1.889(3)		
	O43	1.927(3)		
	O51	2.234(4)		

Metal centre	Coordinating atom	Bond Distance (Å)	BVS	Assigned oxidation state
Mn12	O42	1.863(3)	3.100	+III
	O45	1.876(3)		
	O46	1.881(4)		
	O43	1.932(4)		
	O50	2.254(5)		
Mn13	O48	1.918(3)	3.150	+III
	O49	1.919(3)		
	O29	1.921(3)		
	O30	1.937(3)		
	O38''	2.214(3)		
	O32	2.222(3)		
Mn14	O47	1.913(3)	3.088	+III
	O35''	1.919(3)		
	O30	1.940(3)		
	O31''	1.953(3)		
	O41	2.211(3)		
	O38''	2.241(3)		
K1	O17	2.595(5)		
	O13	2.665(3)		
	O15	2.770(3)		
	O27	2.781(5)		
	O26	2.862(4)		
	O18	3.163(4)		

Metals	Distance (Å)	Metals	Distance (Å)
Mn1-Mn2	3.0637	Mn9-Mn10	2.9569(9)
Mn1-Mn7	2.948	Mn9-Mn11	3.733(1)
Mn2-Mn3	2.9380(9)	Mn9-Mn13	3.094(1)
Mn2-Mn4	3.791(1)	Mn9-Mn14	3.056(1)
Mn2-Mn6	3.096(1)	Mn10-Mn11	5.363(1)
Mn2-Mn7	3.041(1)	Mn10-Mn12	5.396(1)
Mn3-Mn5	5.481(1)	Mn10-Mn13	2.960(1)
Mn3-Mn6	2.970(1)	Mn11-Mn12	3.644(1)
Mn4-Mn5	3.653(1)	Mn11-Mn14	3.898(1)
Mn4-Mn7	3.956(1)	Mn12-Mn13	3.723(1)
Mn5-Mn6	3.726(1)	Mn12-Mn14	3.874(1)
Mn5-Mn7	3.9013(9)	Mn13-Mn14	3.044(1)
Mn6-Mn7	3.045(1)	K1-Mn4	4.270(2)
Mn8-Mn9	3.116	K1-Mn10	5.791(1)
Mn8-Mn13	3.1272	K1-Mn3	3.600(1)
Mn8-Mn14	2.9443	K1-Mn5	4.656(2)

'1-X,2-Y,2-Z; "-X,1-Y,1-Z

Table 8.10: BVS analysis for O atoms and their assigned protonation state in compound **8.3**.

Atom	BVS	Assignment			
O1	1.815	μ_3-O^{2-}	O29	2.036	μ_4-O^{2-}
O2	1.853	μ_3-O^{2-}	O30	1.795	μ_3-O^{2-}
O3	2.042	μ_4-O^{2-}	O31	1.815	μ_3-O^{2-}
O10	1.243	μ_3-OH^-	O43	1.265	μ_3-OH^-

The coordination envrionment of K1 is fulfilled by the O-donors of a pivalate group (O17) and three phosphonate groups with two of the phosphonates acting as chelating groups (**Figure 8.22**). These O-donors reside at the vertices of a distorted pentagonal pyramid and the K-O distances vary between 2.6-3.2 Å (**Table 8.9**).

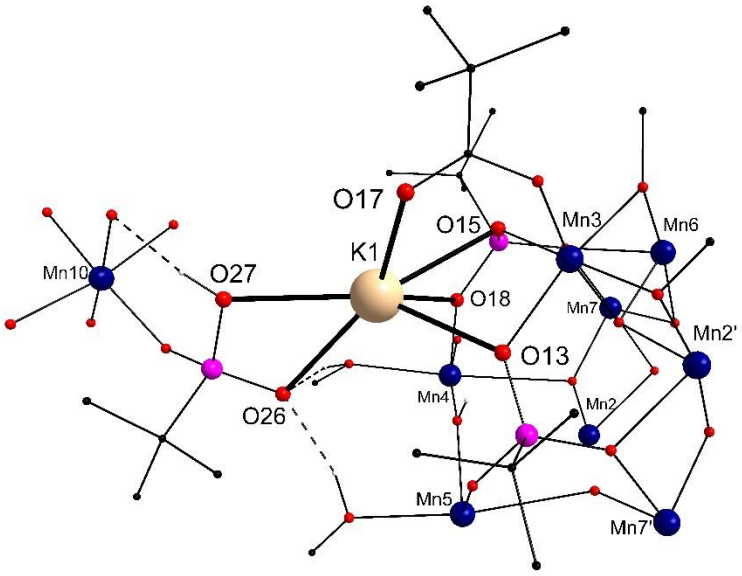

Figure 8.22: Coordination environment of K^+ ion in compound **8.3**. Colour scheme: K (tan), Mn (deep blue), C (black), P (pink), O (red) and H (grey).

Table 8.11: Continuous shape measure values, angle variance and distortion indices for each Mn centre for compound **8.3** ([1]octahedral and [2]square pyramid geometry).

Mn centre	Continuous shape measure value	Angle variance (σ^2)	Distortion Index
Mn1[1]	3.662	185.13	0.14
Mn2[1]	0.778	26.66	0.0499
Mn3[1]	0.720	35.49	0.0471
Mn4[2]	0.920	17.19	0.0383
Mn5[2]	0.792	43.62	0.0621
Mn6[1]	1.106	11.4	0.0239
Mn7[1]	0.829	27.49	0.044
Mn8[1]	3.706	189.8	0.1416
Mn9[1]	0.866	31.45	0.0528
Mn10[1]	0.561	31.9	0.0487
Mn11[2]	0.834	12.48	0.0316
Mn12[2]	0.797	8.99	0.0285
Mn13[1]	0.901	33.55	0.0551
Mn14[1]	0.974	34.65	0.0503

The Mn centres in the other form that contains the partially protonated *tert*-butyl phosphonate group reside in coordination environments similar to those described for the form above (**Figure 8.23**). The central Mn in this form (Mn8) also has a bond valence sum of 2.556 suggesting that, like Mn1, this Mn centre may exhibit variable valency. The partially protonated phosphonate group is coordinated to K1 and Mn10. The former is further bound to the O-donors of a pivalate and two phosphonate groups (**Figure 8.23 (c)**). Mn10 is further coordinated to a μ_4-O^{2-} group (O29'') and the

O-donors of two methoxy (O33'' and O49'') and two phosphonate groups (O39 and O40). O39 is further engaged in hydrogen bonding with the partially protonated phosphonate group (donor-acceptor distance: ~1.82 Å).[636] The coordination environment of all other Mn centres in this form is similar to that observed for the corresponding Mn centres in the other form.

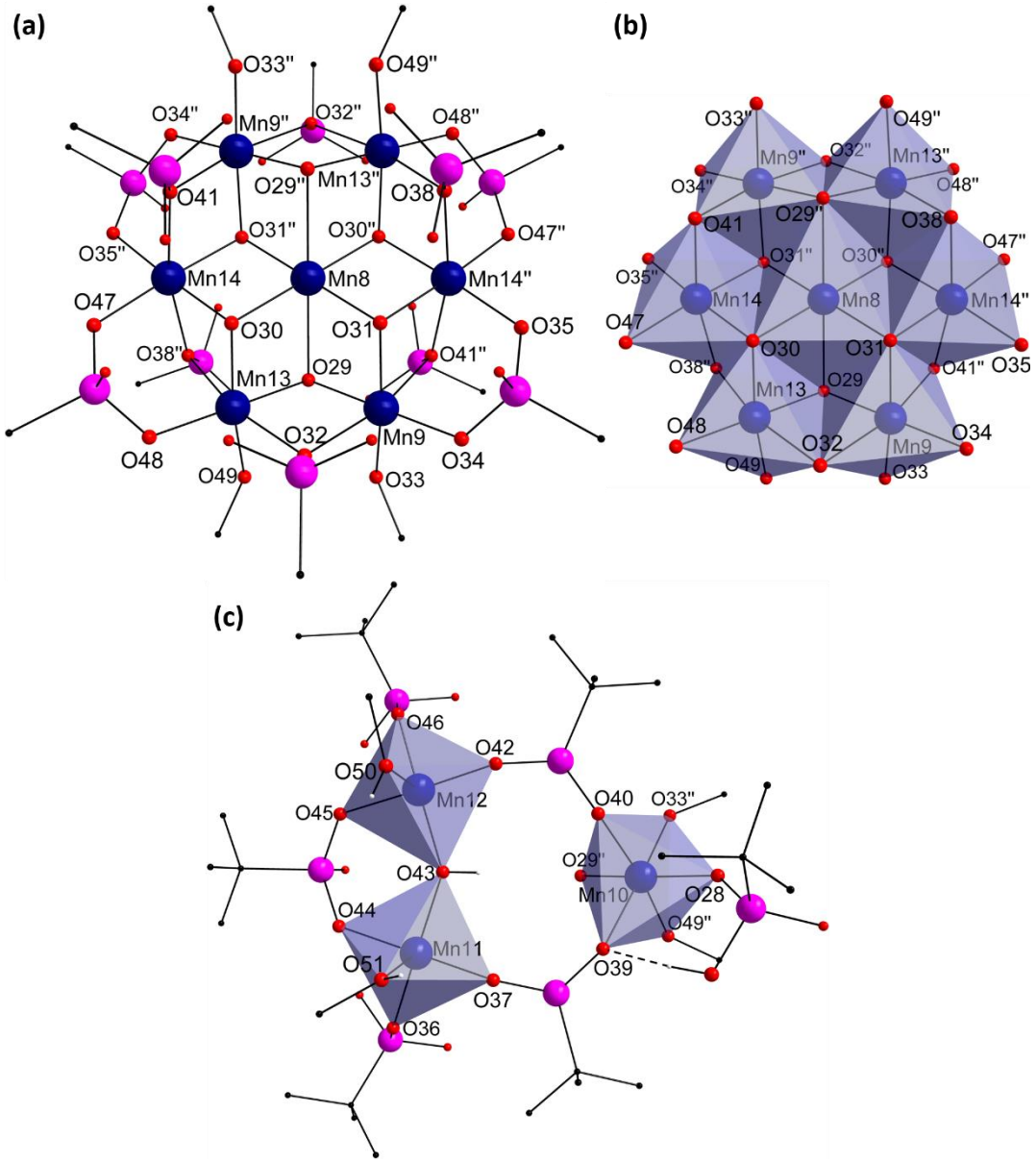

Figure 8.23: (a) Coordination environment of Mn centres constituting the {Mn_7} disc, **(b)** polyhedral representation of the {Mn_7} disc and **(c)** coordination environment of Mn centres the trinuclear unit in the other form of the tridecanuclear complex in compound **8.3**. Colour scheme: Mn (deep blue), C (black), P (pink), O (red) and H (grey).

The packing in this complex is such that the linear chains formed by the tetradecanuclear complex run parallel to each other as is evident from the packing diagram along the crystallographic a-axis (**Figure 8.24**). The packing arragement allows for some solvent molecules to be trapped in the crystal lattice. These molecules could not be structurally resolved and the electron density due to these molecules (corresponding to 50 electrons) was subjected to the 'squeeze' routine as implemented in the PLATON code. The treated electron density may correspond to an additional K^+ ion and two CH_3OH molecules per unit cell. The largest spherical voids holding these molecules are 2.4 Å in radius as calculated by the calcvoid routine implemented in OLEX2.

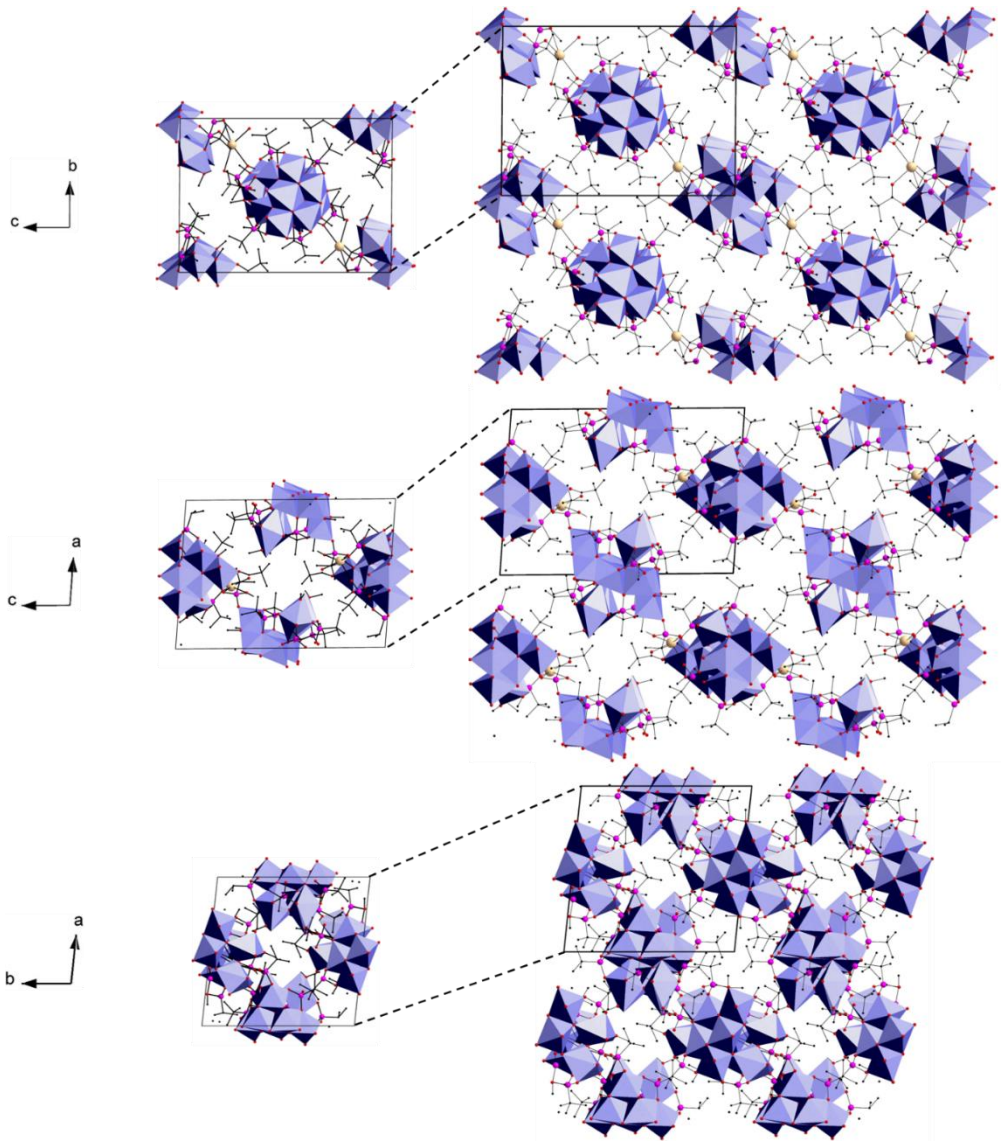

Figure 8.24: Packing diagram of compound **8.3**. Colour scheme: Mn (blue), K (tan), P(pink), C (black) and O (red).

Table 8.12: Selected bond angles for compound **8.3**.

Bond	Bond Angle (°)	Bond	Bond Angle (°)
O1'-Mn1-O3	73.64(10)	O4-Mn2-O3	82.54(12)
O1-Mn1-O3'	73.64(10)	O2-Mn2-O12'	82.95(11)
O21-Mn1-O3'	76.87(10)	O3-Mn2-O6	83.22(11)
O2-Mn1-O3	76.87(10)	O3-Mn2-O12'	87.36(11)
O2'-Mn1-O'	81.69(11)	O4-Mn2-O12'	88.13(12)
O2-Mn1-O1	81.69(11)	O3-Mn2-O2	88.28(11)
O2'-Mn1-O1	98.31(11)	O5-Mn2-O2	92.33(12)
O2-Mn1-O1'	98.31(11)	O2-Mn2-O6	93.67(11)
O2'-Mn1-O3	103.13(10)	O4-Mn2-O6	93.68(12)
O2-Mn1-O3'	103.13(10)	O5-Mn2-O6	94.48(12)
O1-Mn1-O3	106.36(10)	O5-Mn2-O12'	94.95(12)
O1'-Mn1-O3'	106.36(10)	O5-Mn2-O4	97.18(13)
O1'-Mn1-O1	180	O4-Mn2-O2	167.49(13)
O2-Mn1-O2'	180	O6-Mn2-O12'	170.10(11)
O3'-Mn1-O3	180.00(19)	O5-Mn2-O3	177.66(12)
O3'-Mn3-O14	78.19(11)	O16-Mn3-O15	92.61(14)
O4'-Mn3-O3'	80.57(12)	O16-Mn3-O14	93.73(14)
O15-Mn3-O14	87.46(13)	O3'-Mn3-O15	95.80(12)
O3'-Mn3-O13	88.55(12)	O16-Mn3-O13	99.61(15)
O4'-Mn3-O14	89.52(13)	O13-Mn3-O14	166.65(12)
O4'-Mn3-O13	89.77(13)	O16-Mn3-O3'	168.04(14)
O16-Mn3-O4'	90.65(14)	O4'-Mn3-O15	175.70(14)
O15-Mn3-O13	92.45(13)		
O18-Mn4-O10	85.97(15)	O8-Mn5-O9	87.44(14)
O18-Mn4-O25	86.41(13)	O8-Mn5-O20'	88.43(13)
O7-Mn4-O25	87.83(13)	O11-Mn5-O9	88.73(14)
O7-Mn4-O24	88.30(13)	O11-Mn5-O20'	90.14(15)
O7-Mn4-O10	91.20(14)	O11-Mn5-O10	90.21(15)
O10-Mn4-O25	93.08(14)	O10-Mn5-O9	90.95(14)
O18-Mn4-O24	95.48(14)	O8-Mn5-O10	91.84(14)
O24-Mn4-O25	96.53(13)	O20'-Mn5-O9	98.05(14)
O24-Mn4-O10	170.35(14)	O20'-Mn5-O10	170.99(14)
O18-Mn4-O7	173.43(14)	O11-Mn5-O8	175.68(14)
O3'-Mn6-O6'	81.29(11)	O2-Mn7-O12'	82.65(11)
O1-Mn6-O19	83.29(11)	O1-Mn7-O2	83.07(11)
O14-Mn6-O3'	84.72(12)	O1-Mn7-O19	83.19(11)
O3'-Mn6-O19	85.23(11)	O22-Mn7-O19	88.43(11)
O1-Mn6-O3'	85.24(11)	O1-Mn7-O12'	88.76(11)
O14-Mn6-O6'	85.62(13)	O23-Mn7-O12'	89.74(11)
O21-Mn6-O19	90.39(12)	O22-Mn7-O23	90.20(12)
O1-Mn6-O61	92.65(11)	O2-Mn7-O19	90.48(10)
O14-Mn6-O21	94.98(13)	O23-Mn7-O2	93.07(12)
O21-Mn6-O1	95.04(12)	O22-Mn7-O1	93.67(12)
O14-Mn6-O19	96.08(12)	O23-Mn7-O19	97.90(11)
O21-Mn6-O6'	103.12(12)	O22-Mn7-O12'	98.02(11)
O6'-Mn6-O19	166.21(10)	O121-Mn7-O19	170.01(10)
O14-Mn6-O1	169.96(13)	O23-Mn7-O1	176.01(12)
O21-Mn6-O3'	175.55(12)	O22-Mn7-O2	176.67(12)
O30''-Mn8-O29''	74.55(11)	O31-Mn9-O41''	82.21(12)
O30-Mn8-O29	74.55(11)	O29-Mn9-O32	82.25(12)
O31-Mn8-O29	75.17(11)	O33-Mn9-O29	83.93(14)
O31''-Mn8-O29''	75.18(11)	O29-Mn9-O41''	85.34(12)

Bond	Bond Angle (°)	Bond	Bond Angle (°)
O31''-Mn8-O30	82.03(12)	O29-Mn9-O31	86.89(13)
O31-Mn8-O30''	82.04(12)	O33-Mn9-O32	90.30(14)
O31-Mn8-O30	97.96(12)	O33-Mn9-O41''	90.95(14)
O31''-Mn8-O30''	97.96(12)	O34-Mn9-O41''	93.34(12)
O31''-Mn8-O29	104.83(11)	O34-Mn9-O31	93.79(13)
O31-Mn8-O29''	104.83(11)	O31-Mn9-O32	94.51(12)
O30-Mn8-O29''	105.45(11)	O33-Mn9-O34	95.23(14)
O30''-Mn8-O29	105.45(11)	O34-Mn9-O32	99.10(13)
O29-Mn8-O29''	180	O41''-Mn9-O32	167.32(11)
O30''-Mn8-O30	180.00(8)	O33-Mn9-O31	168.98(15)
O31-Mn8-O31''	180	O34-Mn9-O29	178.42(14)
O29''-Mn10-O49''	79.17(13)	O28-Mn10-O39	93.44(14)
O29''-Mn10-O33''	79.43(12)	O28-Mn10-O49''	94.24(15)
O49''-Mn10-O39	85.76(15)	O29''-Mn10-O39	95.19(12)
O40-Mn10-O33''	89.05(16)	O28-Mn10-O40	95.48(16)
O49''-Mn10-O33''	91.01(16)	O28-Mn10-O29''	168.70(15)
O40-Mn10-O29''	91.29(14)	O40-Mn10-O49''	170.28(15)
O28-Mn10-O33''	91.62(14)	O33''-Mn10-O39	174.18(13)
O40-Mn10-O39	93.31(16)		
O37-Mn11-O51	85.93(16)	O42-Mn12-O50	85.26(18)
O44-Mn11-O51	87.00(16)	O45-Mn12-O50	87.09(18)
O37-Mn11-O43	87.40(15)	O42-Mn12-O43	88.52(16)
O44-Mn11-O36	88.61(13)	O45-Mn12-O46	88.52(15)
O36-Mn11-O51	90.82(16)	O45-Mn12-O43	91.23(14)
O44-Mn11-O43	90.92(14)	O46-Mn12-O50	92.3(2)
O37-Mn11-O36	93.93(14)	O42-Mn12-O46	92.53(17)
O43-Mn11-O51	96.01(17)	O43-Mn12-O50	93.8(2)
O37-Mn11-O44	172.51(15)	O42-Mn12-O45	172.31(16)
O36-Mn11-O43	173.12(16)	O46-Mn12-O43	173.94(17)
O29-Mn13-O32	82.20(12)	O31''-Mn14-O41	81.92(12)
O49-Mn13-O29	82.42(14)	O30-Mn14-O38''	82.53(12)
O30-Mn13-O38''	83.32(12)	O30-Mn14-O31''	84.15(12)
O29-Mn13-O38''	85.58(12)	O47-Mn14-O35''	88.49(13)
O29-Mn13-O30	87.30(13)	O35''-Mn14-O41	88.79(13)
O49-Mn13-O32	88.34(14)	O30-Mn14-O41	88.89(12)
O49-Mn13-O38''	92.14(14)	O31''-Mn14-O38''	88.89(12)
O48-Mn13-O38''	92.56(13)	O47-Mn14-O38''	88.89(13)
O48-Mn13-O30	93.60(14)	O47-Mn14-O30	93.48(13)
O30-Mn13-O32	93.98(12)	O35''-Mn14-O31''	93.96(12)
O48-Mn13-O49	96.54(14)	O35''-Mn14-O38''	99.53(13)
O48-Mn13-O32	99.69(13)	O47-Mn14-O41	99.99(13)
O38''-Mn13-O32	167.60(12)	O41-Mn14-O38''	168.03(11)
O49-Mn13-O30	169.07(15)	O47-Mn14-O31''	176.94(12)
O48-Mn13-O29	177.83(15)	O35''-Mn14-O30	177.19(13)

8.3.2 Physicochemical characterisation

Physicochemical characterisation was carried out to further support the structural model obtained using single crystal X-ray crystallography. Powder X-ray diffraction analysis confirms the phase purity of the compound (**Figure 8.25 (a)**). EDX measurements reveal a Mn:K ratio of 8.57:1 which is close to the expected ratio of 8.67:1 confirming the presence of the additional K^+ ion in the voids. TGA analysis reveals (**Figure 8.25 (b)**) an intial drop up to 70 °C due to the loss of solvent molecules trapped in the crystal lattice. This is followed by the loss of coordinating methanol molecules upto 225 °C. Beyond 225 °C, the decomposition of organic ligands and the formation of phosphate and oxide species occurs.

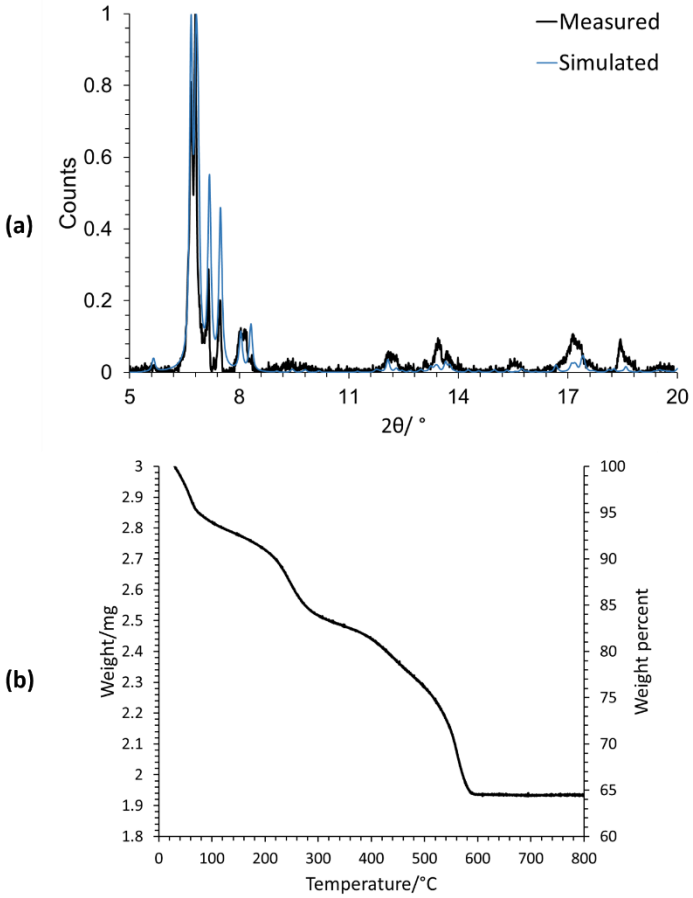

Figure 8.25: (a) PXRD pattern and **(b)** TGA analysis of compound **8.3**.

The infrared spectrum (**Figure 8.26**) of compound **8.3** reveals a broad distinctive feature centred around 2900 cm^{-1} which is due to the C-H vibrations in the organic ligands.[617] The other vibrational modes in the 1300-1500 cm^{-1} range are due to the tert-butyl groups.[617] The vibrational mode at 3400 cm^{-1} is due to the hydrogen bonding network.[633, 634] The strong signal at 962 cm^{-1} corresponds to the stretching vibrations of the phosphonate groups.[621-623]

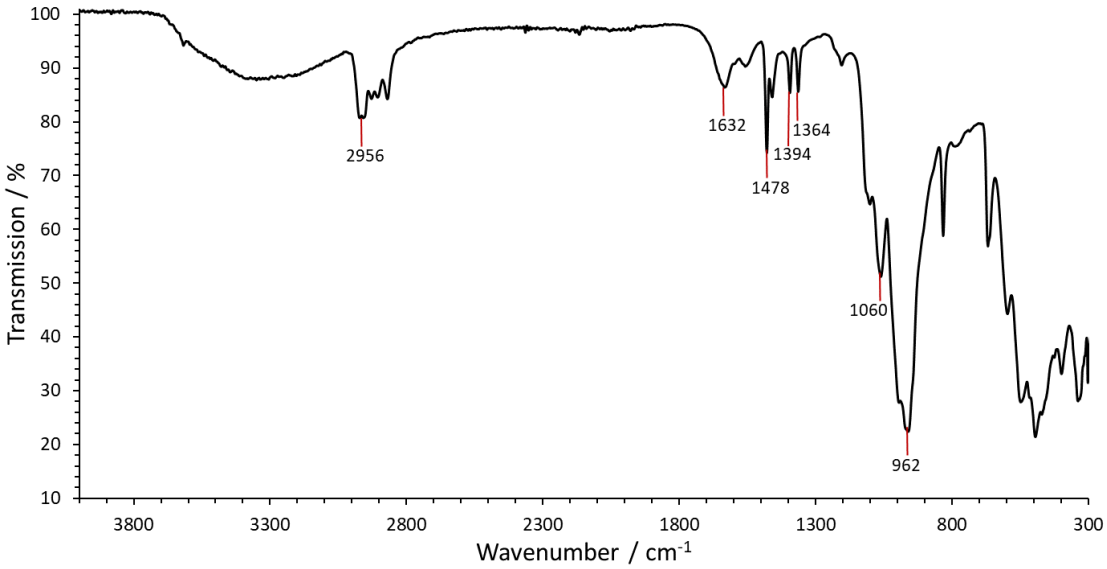

Figure 8.26: Infrared spectrum of compound **8.3**.

8.4 $[Mn^{II}Mn^{III}_{12}Ca_2(\mu_4\text{-}O)_2(\mu_3\text{-}O)_6((CH_3)_3CPO_3)_{10}((C_6H_5)_2PO_2)_2((CH_3)_3CCO_2H)_2(\mu\text{-}CH_3O)_4(CH_3OH)_{5.15}(CH_3CN)_{0.85}]\cdot CH_3OH\cdot CH_3CN$ (8.4)

Compound **8.2** reveals that the triangular units of the $\{Mn_{13}\}$ complex can potentially be capped by cations as partial occupancy by Na^+ was observed in one of its forms. This possibility was investigated using alkali and alkaline earth metals and it was observed that refluxing $KMnO_4$ with $Mn(CH_3COO)_2\cdot 4H_2O$ and $Ca(CH_3COO)_2$ with diphenylphosphinic acid and *tert*-butyl phosphonic acid in the ratio 1:4:5:5:5 in presence of excess of pivalic acid lead to the formation of compound **8.4**. The crystals were obtained within a week and were characterised using single crystal X-ray diffraction.

8.4.1 Structure description

Compound **8.4** crystallises in the triclinic crystal system and the structure was solved in the space group $P\bar{1}$. It comprises of a heterometallic tridecanuclear $\{Mn_{13}Ca_2\}$ complex (**Figure 8.27**) with the asymmetric unit containing half of it (**Figure 8.28**). The core of this complex, similar to that of compounds **8.2** and **8.3**, consists of a three layered metal-centred distorted cuboctahedron with the top and bottom layers capped by Ca(II). The $\{Mn_{13}\}$ unit here is stabilised by ten *tert*-butyl phosphonate groups which bind in 4.211 and 3.111 modes, four $\mu\text{-}CH_3O^-$ and eight oxo-groups while the Ca centres are joined to the main unit via phosphonate groups that bind in 5.221 mode and a diphenylphosphinate group binding in 2.11 mode. The Ca^{2+} ion lies ~2.03 Å above the $\{Mn_3\}$ plane and the incorporation of Ca^{2+} ion here does not lead to disorder in the core structure.

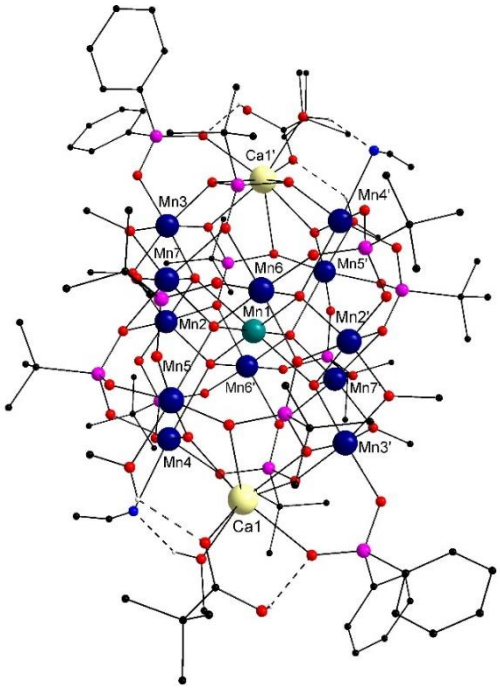

Figure 8.27: Crystal structure of the tridecanuclear compound **8.4**. Colour scheme: Mn(II) (teal), Mn(III) (deep blue), Ca (light yellow), C (black), P (pink) and O (red). All hydrogen atoms (grey) except those bound to O centres have been removed for clarity. Hydrogen bonds are shown with dashed lines.

The oxidation states of Mn centres has been determined using bond valence sum analysis (**Table 8.13**). Similar to compounds **8.2** and **8.3** the oxidation states of all Mn centres except Mn1 has been found to be +III, and a +II oxidation state has been assigned to the Ca centre as was expected. For Mn1, bond valence parameters for a valence of +II leads to a value of 2.626 while that for +III results in a value of 2.422. The oxidation state of Mn1 is thus not very well defined and this may be due to the poor quality of the data set obtained from the single crystal X-ray diffraction. For charge balance reasons, the oxidation state of this centre has been assumed to be +II but the possibility that the pivalate and/or CH_3OH groups may be partially deprotonated to accommodate the extra half charge on the cluster cannot be ruled out. The protonation states of the O centres bound only to the Mn centres was also determined using bond valence sum analysis (**Table 8.14**) and they were all determined to be O^{2-} groups.

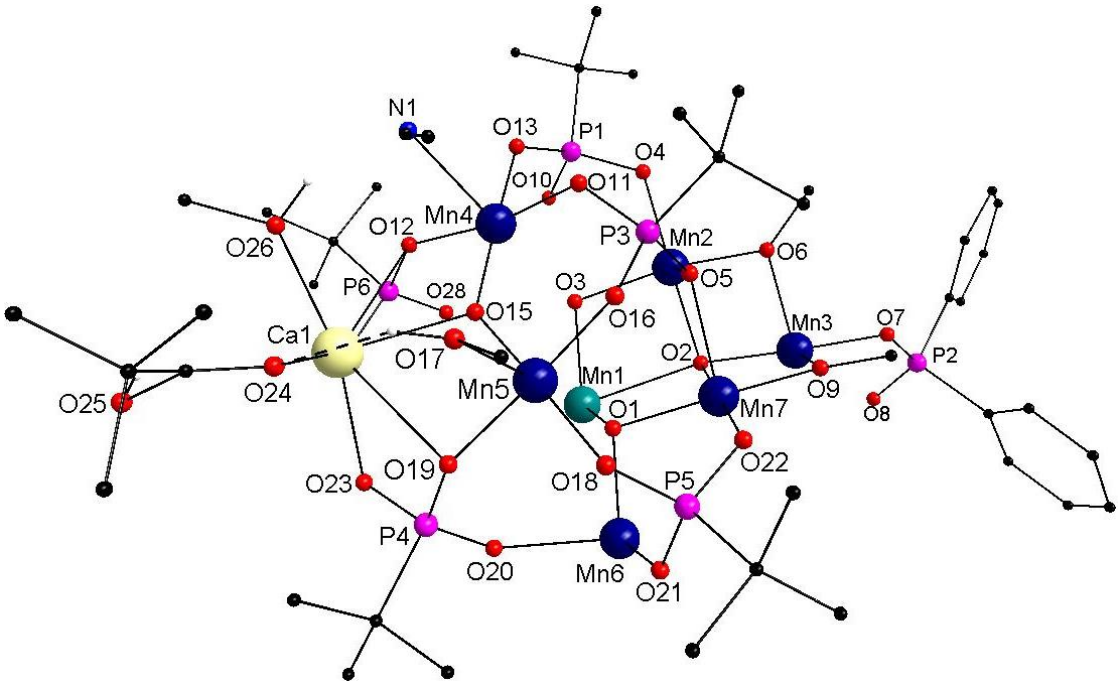

Figure 8.28: Asymmetric unit of compound **8.4**. Colour scheme: Mn(II) (teal), Mn(III) (deep blue), Ca (light yellow), C (black), P (pink) and O (red). All hydrogen atoms (grey) except those bound to O centres have been removed for clarity. Hydrogen bonds are shown with dashed lines.

Mn1, Mn2, Mn6 and Mn7 form the central $\{Mn_7\}$ layer (**Figure 8.29**). Mn1 is coordinated to two μ_4-O^{2-} and four μ_3-O^{2-} groups (**Figure 8.29 (a)**) with the Mn-O distances varying between 2.0 and 2.4 Å (**Table 8.13**). It resides in a highly distorted octahedral environment (**Table 8.15**) and its octahedron shares a vertex with that of Mn3 and an edge with the octahedra of Mn2, Mn6 and Mn7 (**Figure 8.29 (b)**). The octahedron of Mn2 is fulfilled by a μ_4-O^{2-} (O2), a μ_3-O^{2-} (O3) and the O-donors of a μ-CH_3O^- (O6) and three phosphonate groups (**Figure 8.29 (a)**). The Jahn-Teller axis for this Mn centre is directed along the O-donors of two phosphonate groups (O5 and O20) with the Mn-O distance being 2.203(6) and 2.272(6) Å respectively. The octahedron of Mn2 shares a vertex with that of Mn7 and a face with the octahedra of Mn3 and Mn6 (**Figure 8.29 (b)**).

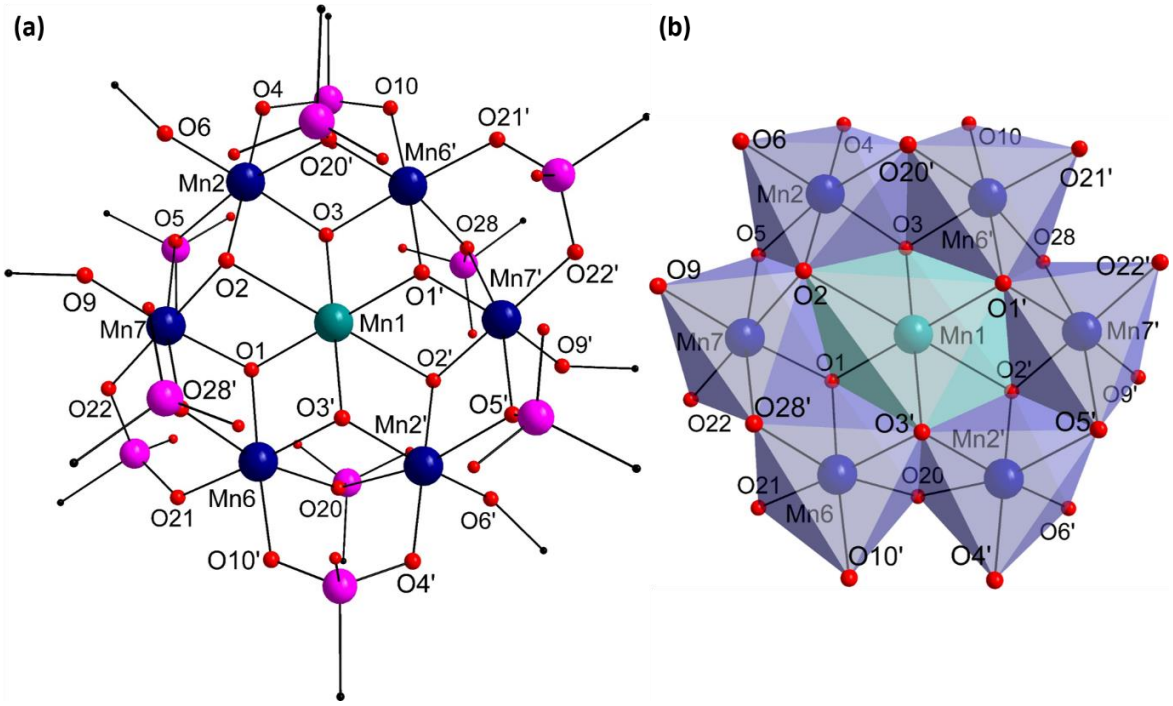

Figure 8.29: (a) Coordination environment of Mn centres constituting the {Mn_7} disc and **(b)** polyhedral representation of the {Mn_7} disc in compound **8.4**. Colour scheme: Mn(II) (teal), Mn(III) (deep blue), C (black), P (pink) and O (red).

The octahedral coordination environment of Mn6 is satisfied by two μ_3-O^{2-} (O1 and O3) and four *tert*-butyl phosphonate O-donors (**Figure 8.29 (a)**) with the Jahn-Teller axis directed towards two of the phosphonate O-donors (O20 and O28). The Mn-O distances for Mn6 are ~2.3 Å along the Jahn-Teller axis and ~1.95 Å perpendicular to it. Mn7 resides in a coordination environment similar to that of Mn2 with a μ_4-O^{2-} (O2), a μ_3-O^{2-} (O1) and the O-donors of a μ-CH_3O^- (O9) and three phosphonate groups fulfilling it (**Figure 8.29 (a)**). The octahedron of these Mn centres share a face with each other at the two oxo-groups. For this complex, the Jahn-Teller axis of the Mn centres forming the vertices of the {Mn_7} disc are joined to each other at an angle that ranges between 75-85°.

Mn3, Mn4 and Mn5 constitute the trinuclear unit capping the {Mn_7} disc. Mn3 binds to the O-donors of two μ-CH_3O^- (O6 and O9), two phosphonate (O23 and O27) and a diphenylphosphinate group (O7) in addition to a μ_4-O^{2-} group (O2) (**Figure 8.30**). The Jahn-Teller distortion does not influence Mn3 as much and this is apparent from the bond lengths (**Table 8.13**) which vary between 1.9-2.1 Å. This may be due to constraints imposed by the ligand environment. The octahedron of Mn3 is edge shared with that of Mn7.

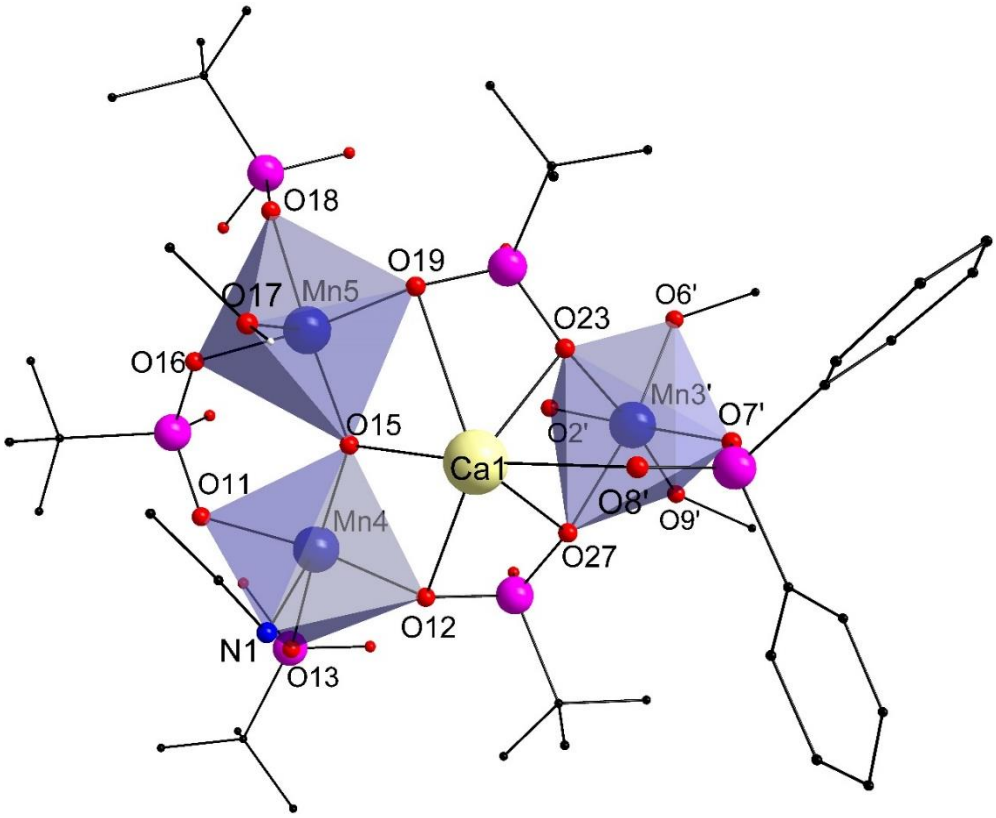

Figure 8.30: Coordination environment of Mn3-Mn5 in compound **8.4**. Colour scheme: Mn(III) (deep blue), Ca (light yellow), C (black), P (pink) and O (red). All hydrogen atoms (grey) except those bound to O centres have been removed for clarity.

Table 8.13: Key metal-ligand and metal-metal bond lengths and bond valence sum for each Mn centre and Ca centre for compound **8.4**.

Metal centre	Coordinating atom	Bond Distance (Å)	BVS	Assigned oxidation state
Mn1	O3 O3’ O1’ O1 O2’ O2	1.994(6) 1.994(6) 2.009(6) 2.009(6) 2.417(6) 2.417(6)	2.422(assumed valence: III) /2.626(assumed valence: II)	+II
Mn2	O6 O4 O2 O3 O5 O20’	1.918(7) 1.921(7) 1.926(6) 1.955(6) 2.203(6) 2.272(6)	3.081	+III
Mn3	O2 O7 O9 O23’ O6 O27’	1.937(6) 1.959(7) 2.030(7) 2.036(7) 2.042(7) 2.079(7)	3.049	+III

Metal centre	Coordinating atom	Bond Distance (Å)	BVS	Assigned oxidation state
Mn4	O15	1.876(8)	2.860	+III
	O11	1.899(8)		
	O12	1.905(8)		
	O13	1.958(7)		
	N1	2.392(14)		
Mn5	O16	1.870(7)	2.975	+III
	O15	1.873(8)		
	O19	1.915(7)		
	O18	1.936(8)		
	O17	2.327(9)		
Mn6	O21	1.926(6)	2.992	+III
	O10’	1.929(6)		
	O3’	1.953(6)		
	O1	1.970(6)		
	O20	2.230(6)		
	O28’	2.233(6)		
Mn7	O9	1.916(7)	3.088	+III
	O22	1.921(6)		
	O2	1.923(6)		
	O1	1.944(6)		
	O5	2.229(6)		
	O28’	2.271(7)		
Ca1	O26	2.320(10)	2.112	+II
	O23	2.378(8)		
	O15	2.389(8)		
	O27	2.396(7)		
	O24	2.399(10)		
	O8’	2.461(7)		
	O19	2.826(9)		
	O12	2.850(9)		

Metals	Distance (Å)	Metals	Distance (Å)
Mn1-Mn2	3.147(2)	Mn3-Mn7	2.946(2)
Mn1-Mn6	2.948(2)	Mn4-Mn5	3.471(3)
Mn1-Mn7	3.144(2)	Mn4-Mn6’	3.913(3)
Mn2-Mn3	2.955(2)	Mn5-Mn6	3.889(3)
Mn2-Mn4	3.727(2)	Mn5-Mn7	3.711(2)
Mn2-Mn6’	3.068(3)	Mn6-Mn7	3.076(2)
Mn2-Mn7	3.103(2)	Ca1-Mn3’	3.397(3)
Mn3-Mn4’	5.355(3)	Ca1-Mn4	3.557(3)
Mn3-Mn5’	5.331(3)	Ca1-Mn5	3.537(3)

’1-X,1-Y,1-Z

Table 8.14: BVS analysis for O atoms and their assigned protonation state in compound **8.4**.

Atom	BVS	Assignment
O1	1.728	μ_3-O^{2-}
O2	2.086	μ_4-O^{2-}
O3	1.760	μ_3-O^{2-}
O15	1.787	μ_3-O^{2-}

Mn4 and Mn5 reside in a square pyramidal coordination environment fulfilled with similar coordinating ligands. The square pyramidal geometry is confirmed by continuous shape measure analysis (**Table 8.15**) which gives a higher value (~1.7) when a spherical square pyramid geometry is used as a reference. Mn4 is coordinated to the O-donors of three phosphonates (O11, O12 and O13) and the N-donor of a partially occupied CH_3CN group (N1) in addition to a μ_3-O^{2-} group (O15) (**Figure 8.30**). The site partially occupied by CH_3CN is further occupied by the O-donor of a partially occupied CH_3OH molecule. The coordination environment of Mn5 is similar but the partially occupied site of Mn4 is fully occupied by a CH_3OH O-donor here (**Figure 8.30**). The Jahn-Teller axis in both cases is along the CH_3CN/CH_3OH groups. The Mn-ligand distances in the equatorial plane lie in 1.9-2.0 Å while those along the Jahn-Teller axis are in the 2.3-2.4 Å range. The polyhedron of both share a vertex with each other at O15.

The Ca^{2+} ion in this complex is eight coordinated and is well incorporated into the {Mn_{13}} unit via a μ_3-O^{2-} (O15) and the O-donors of two chelating phosphonate groups and a diphenylphosphinate ligand which satisfy six of the coordination sites (**Figure 8.31**). It is further coordinated to a methanol molecule and a pivalic acid that is hydrogen bonded to a diphenylphosphinate O-donor (O8) and the Ca-O distances vary between 2.3 and 2.9 Å. There is an extensive hydrogen bonding network associated with the ligands coordinated to the Ca^{2+} ions which allow for better integration of Ca^{2+} ion into the core structure. The Ca^{2+} ion in this complex does not simply act as a mere counterion but potentially affects the electronic behaviour of the {Mn_{13}} core. This is further supported by previous reports where a Mn^{II} centre was found to cap the trinuclear units.[645, 647]

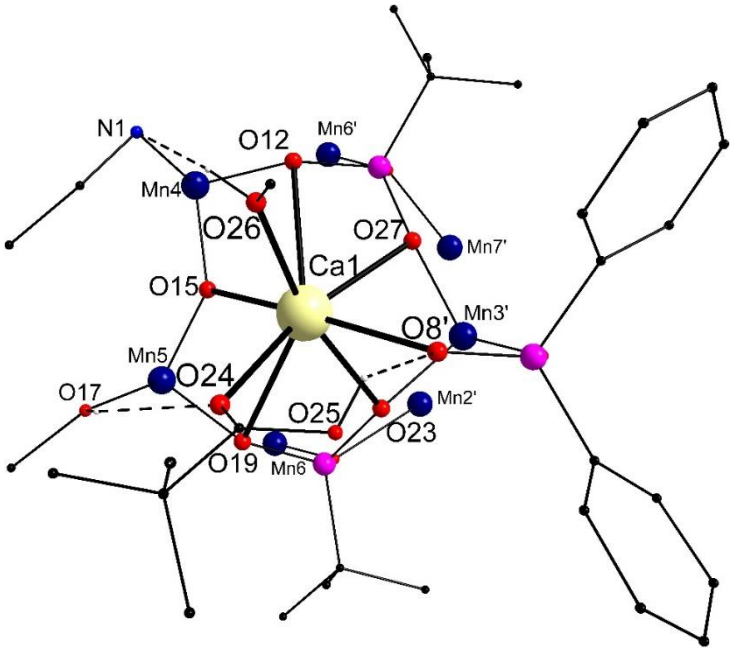

Figure 8.31: Coordination environment of Ca^{2+} ion and the associated hydrogen bonding network in compound **8.4**. Colour scheme: Mn(III) (deep blue), Ca (light yellow), C (black), P (pink) and O (red). All hydrogen atoms (grey) except those bound to O centres have been removed for clarity. Hydrogen bonds are shown with dashed lines.

The packing arragement in this complex (**Figure 8.32**) allows for some solvent molecules to be trapped in the crystal lattice. These molecules could not be structurally resolved and the electron density due to these molecules (corresponding to 41 electrons) was subjected to the 'squeeze' routine as implemented in the PLATON code. The treated electron density may correspond to a CH_3OH and a CH_3CN molecule per formula unit. The largest spherical voids holding these molecules are 2.6 Å in radius as calculated by the calcvoid routine implemented in OLEX2.

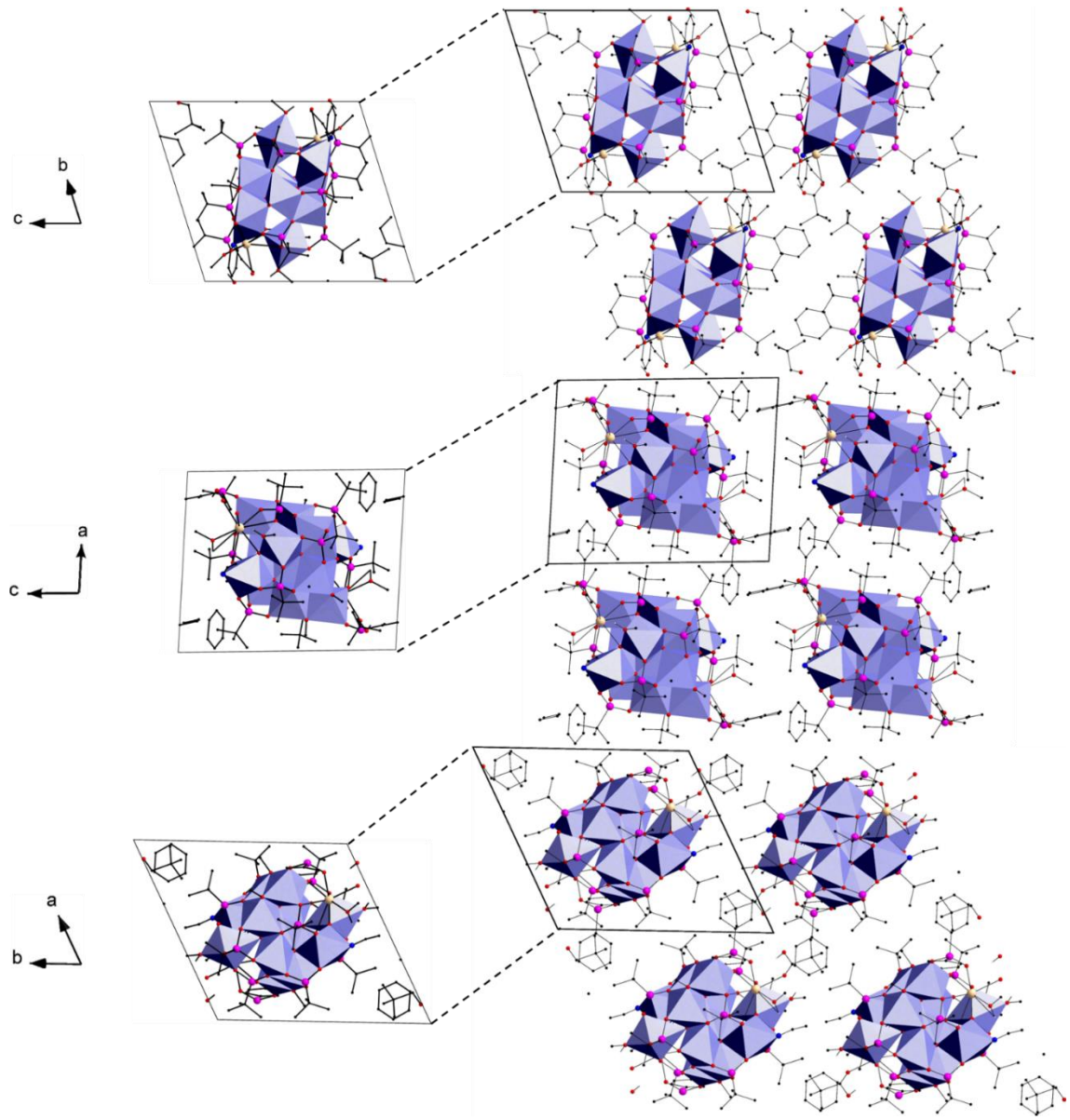

Figure 8.32: Packing diagram of compound **8.4**. Colour scheme: Mn (blue), Ca (tan), P(pink), C (black) and O (red).

Table 8.15: Continuous shape measure values, angle variance and distortion indices for each Mn centre for compound **8.4** ([1]octahedral and [2]square pyramid geometry).

Mn centre	Continuous shape measure value	Angle variance (σ^2)	Distortion Index
Mn1[1]	3.928	198.12	0.1430
Mn2[1]	0.938	32.40	0.0535
Mn3[1]	0.563	34.57	0.0448
Mn4[2]	1.154	17.52	0.0322
Mn5[2]	0.938	18.03	0.0338
Mn6[1]	0.858	28.92	0.0450
Mn7[1]	1.052	36.98	0.0554

Table 8.16: Selected bond angles for compound **8.4**.

Bond	Bond Angle (°)	Bond	Bond Angle (°)
O1'-Mn1-O2'	74.2(2)	O3-Mn1-O2'	105.6(2)
O1-Mn1-O2	74.2(2)	O31-Mn1-O2	105.6(2)
O31-Mn1-O2'	74.4(2)	O1'-Mn1-O2	105.8(2)
O3-Mn1-O2	74.4(2)	O1-Mn1-O2'	105.8(2)
O31-Mn1-O1	82.8(2)	O1'-Mn1-O1	180.0(4)
O3-Mn1-O1'	82.8(2)	O2-Mn1-O2'	180
O31-Mn1-O1'	97.2(2)	O3-Mn1-O3[1]	180
O3-Mn1-O1	97.2(2)		
O2-Mn2-O5	82.1(2)	O2-Mn3-O6	79.7(3)
O3-Mn2-O20'	82.1(2)	O2-Mn3-O9	79.7(3)
O6-Mn2-O2	83.1(3)	O23'-Mn3-O27'	87.7(3)
O2-Mn2-O20'	85.2(2)	O23'-Mn3-O6	88.6(3)
O2-Mn2-O3	87.7(3)	O7-Mn3-O27'	89.8(3)
O6-Mn2-O20'	90.8(3)	O7-Mn3-O23'	90.0(3)
O6-Mn2-O5	91.4(3)	O9-Mn3-O27'	90.1(3)
O4-Mn2-O20'	93.5(3)	O2-Mn3-O23'	91.5(3)
O3-Mn2-O5	93.6(3)	O2-Mn3-O27'	92.4(3)
O4-Mn2-O3	93.6(3)	O9-Mn3-O6	92.4(3)
O6-Mn2-O4	95.4(3)	O7-Mn3-O6	98.2(3)
O4-Mn2-O5	99.3(3)	O7-Mn3-O9	98.8(3)
O5-Mn2-O20'	166.8(2)	O9-Mn3-O23'	170.9(3)
O6-Mn2-O3	168.8(3)	O6-Mn3-O27'	171.2(3)
O4-Mn2-O2	178.1(3)	O2-Mn3-O7	177.3(3)
O12-Mn4-N1	82.2(4)	O19-Mn5-O17	83.7(3)
O11-Mn4-N1	86.7(4)	O16-Mn5-O17	84.5(3)
O13-Mn4-N1	87.6(5)	O16-Mn5-O18	86.9(3)
O11-Mn4-O13	88.4(3)	O19-Mn5-O18	88.9(3)
O15-Mn4-O12	88.6(4)	O15-Mn5-O19	89.4(4)
O12-Mn4-O13	89.4(4)	O18-Mn5-O17	89.5(4)
O15-Mn4-O11	94.4(3)	O15-Mn5-O17	93.8(4)
O15-Mn4-N1	96.6(5)	O16-Mn5-O15	95.5(3)
O11-Mn4-O12	168.7(3)	O16-Mn5-O19	167.5(3)
O15-Mn4-O13	175.1(4)	O15-Mn5-O18	176.0(4)
O1-Mn6-O28'	82.7(2)	O2-Mn7-O5	81.5(2)
O3'-Mn6-O20	83.3(2)	O1-Mn7-O28'	82.3(2)
O3'-Mn6-O1	84.9(3)	O9-Mn7-O2	83.0(3)
O3'-Mn6-O28'	87.8(3)	O2-Mn7-O28'	84.4(2)
O1-Mn6-O20	88.5(3)	O2-Mn7-O1	88.1(3)
O10'-Mn6-O20	89.1(3)	O9-Mn7-O5	90.2(3)

Bond	Bond Angle (°)	Bond	Bond Angle (°)
O21-Mn6-O10[1]	89.5(3)	O9-Mn7-O28'	91.9(3)
O21-Mn6-O28'	89.5(3)	O22-Mn7-O1	92.6(3)
O21-Mn6-O1	92.8(3)	O1-Mn7-O5	93.3(3)
O10'-Mn6-O3'	92.9(3)	O22-Mn7-O28'	93.4(3)
O21-Mn6-O20	99.1(3)	O9-Mn7-O22	96.1(3)
O10'-Mn6-O28'	99.3(3)	O22-Mn7-O5	100.8(3)
O20-Mn6-O28'	168.0(2)	O5-Mn7-O28'	165.4(2)
O21-Mn6-O3'	176.6(3)	O9-Mn7-O1	169.9(3)
O10'-Mn6-O1	176.9(3)	O22-Mn7-O2	177.6(3)

8.4.2 Physicochemical characterisation

A number of physicochemical techniques were employed to verify the structural model. The Mn:Ca ratio in this complex was determined to be 6.25:1 using EDX analysis which is close to the expected ratio of 6.50:1.

TGA analysis (**Figure 8.33**) under an atmosphere of N_2 of compound **8.4** dried in air reveals a drop up to 100 °C which represents the loss of the CH_3OH and CH_3CN molecules trapped in the crystal lattice (weight loss calcd: 2.2 %, found: 2.2 %). This is followed by the loss of the bound CH_3OH and CH_3CN molecules up to 250 °C (weight loss calcd: 6.0 %, found: 6.0 %). Further heating results in ligand decomposition.

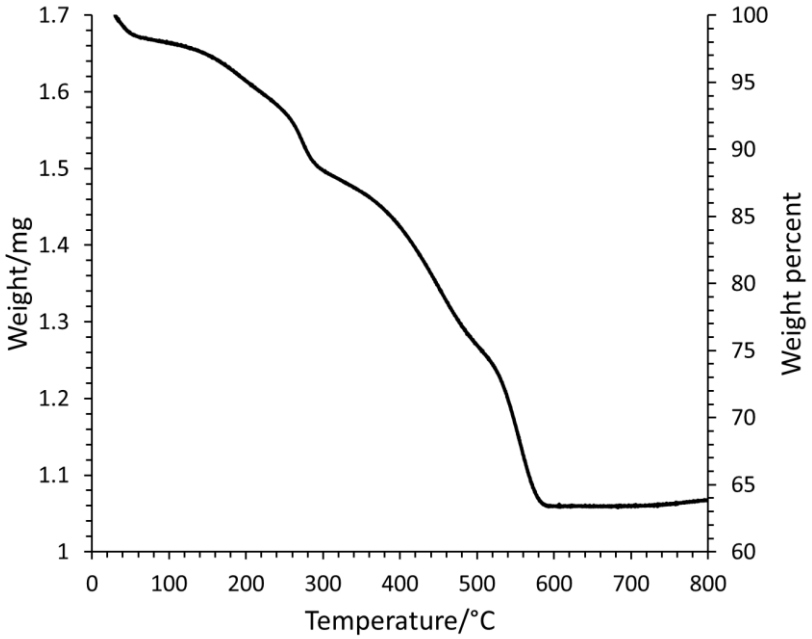

Figure 8.33: TGA analysis of compound **8.4**.

The IR spectrum of compound **8.4** is in agreement with the proposed structural model (**Figure 8.34**). The feature centred at ~2900 cm^{-1} corresponds to the C-H vibrations.[617] The signals in the 1300-1600 cm^{-1} range are due to vibrations of the organic moieties of the molecule and these overshadow the signals doe to the stretching vibrations of the carboxylate groups.[617] The strong vibrational mode at 970 cm^{-1} corresponds to the stretching vibration of the phosphonate groups.[621-623]

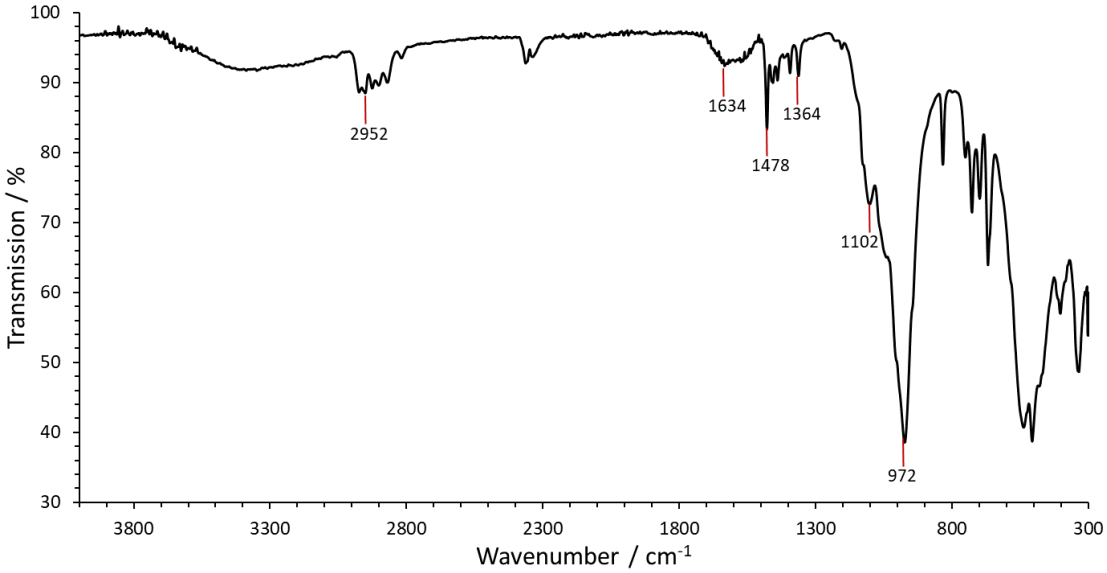

Figure 8.34: Infrared spectrum of compound **8.4**.

8.5 $[Mn^{II}_3Mn^{III}_{12}Ca_2(\mu_4\text{-}O)_4(\mu_3\text{-}O)_2(\mu_3\text{-}OH)_2((CH_3)_3CPO_3)_8((C_6H_5)_2PO_2)_2((CH_3)_3CCO_2)_4(CH_3CO_2)_2(\mu\text{-}CH_3O)_8(CH_3OH)_2]\cdot 2CH_3OH\cdot 2CH_3CN$ (8.5)

Based on the synthetic strategy described in chapter 3, the ratios of Mn^{II} and Mn^{VII} were varied. On refluxing $Mn(CH_3COO)_2\cdot 4H_2O$, $KMnO_4$ and $Ca(CH_3COO)_2$ with diphenylphosphinic acid and *tert*-butyl phosphonic acid in the ratio 5:1:5:5:5 in presence of excess of pivalic acid, compound **8.5** was formed. Tiny crystals were formed within a day and were characterised using single crystal X-ray diffraction.

8.5.1 Structure description

Compound **8.5** crystallises in the monoclinic crystal system and the structure was solved in the space group $P2_1/c$. It comprises of a heterometallic pentadecanuclear $\{Mn_{15}Ca_2\}$ complex (**Figure 8.35**) with the asymmetric unit containing half of the structure (**Figure 8.36**). The core of this complex consists of a three layered metal-centred distorted cuboctahedron with the top and bottom layers capped by Ca and an additional Mn centre. This complex is essentially an extension of compound **8.4** with an additional Mn centre bridged to the core structure. The core structure is stabilised by two OH^-, six O^{2-}, eight $\mu\text{-}CH_3O^-$ moieties, eight *tert*-butyl phosphonate ligands binding in 6.222, 5.221 and 3.111 modes and four pivalate groups which bind in 2.11 mode. Additionally, two diphenylphosphinate ligands, two acetate groups and two methanol molecules also coordinate to the complex. The presence of an acetate again highlights the importance of the counterion used in the reaction mixture.

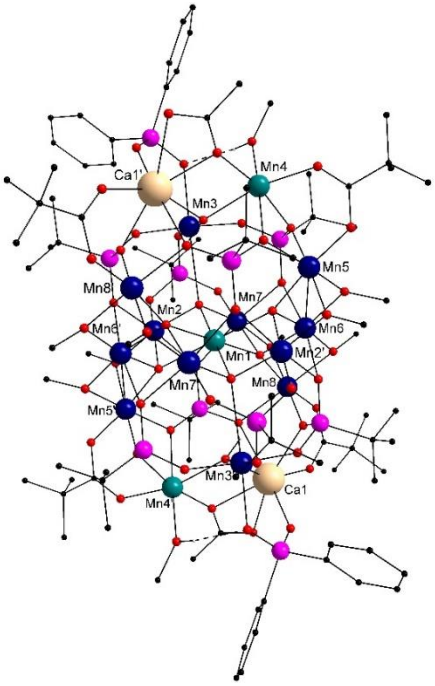

Figure 8.35: Crystal structure of the pentadecanuclear compound **8.5**. Colour scheme: Mn(II) (teal), Mn(III) (deep blue), Ca (light yellow), C (black), P (pink) and O (red). All hydrogen atoms (grey) except those bound to O centres have been removed for clarity. Hydrogen bonds are shown with dashed lines.

The addition of a Mn centre to the triangular {Mn_3} units pushes these layers closer to the {Mn_7} disc and this is characterised by an increase in the number of μ_4-O^{2-} groups in comparison to compounds **8.2**-**8.4**. Consequently, two of the Mn centres in the trinuclear layer are octahedrally coordinated unlike the previous complexes where only one of those Mn centres was found to the octahedrally coordinated.

The oxidation state for the Mn centres has been determined using bond valence sum analysis (**Table 8.17**). Unlike the other complexes discussed in this chapter, for this complex, a +II oxidation state can be confidently assigned to the central Mn (Mn1). The additional Mn centre (Mn4) has also been found to be in +II oxidation state while all the others have been found to be in +III oxidation state. The protonation state of the O centres bound only to Mn has also been ascertained using bond valence sum analysis (**Table 8.18**).

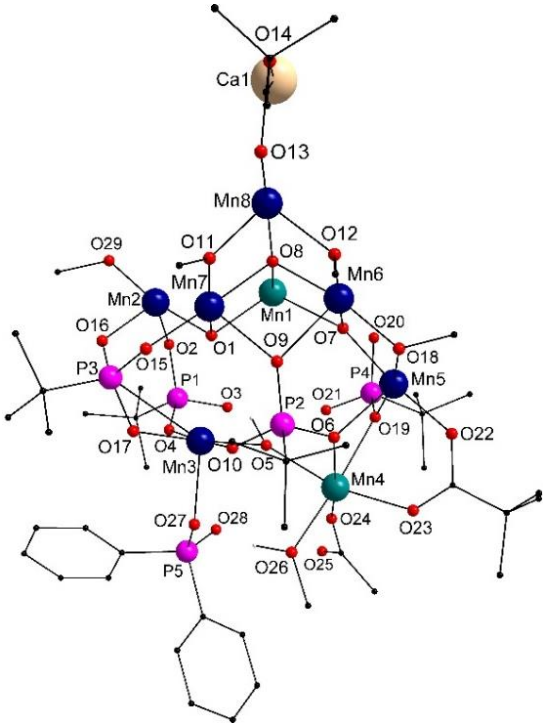

Figure 8.36: Asymmetric unit of the pentadecanuclear compound **8.5**. Colour scheme: Mn(II) (teal), Mn(III) (deep blue), Ca (light yellow), C (black), P (pink) and O (red). All hydrogen atoms (grey) except those bound to O centres have been removed for clarity.

The central {Mn_7} layer in this complex is comprised of Mn1, Mn2, Mn6 and Mn7 (**Figure 8.37**). Mn1 resides in a distorted octahedral environment (**Table 8.19**) which is fulfilled by four μ_4-O^{2-} and two μ_3-O^{2-} groups (**Figure 8.37 (a)**). The distortion is due to the ligand restraints as is evident particularly from the bond angles (**Table 8.20**). The Mn-O distances range between 2.1 and 2.3 Å which is a smaller range in comparison to those observed in the other {Mn_{13}} complexes discussed in this chapter. The octahedron of Mn1 shares a vertex with the octahedron of Mn5 and an edge with the octahedra of Mn2 and Mn5-Mn8 (**Figure 8.37 (b)**).

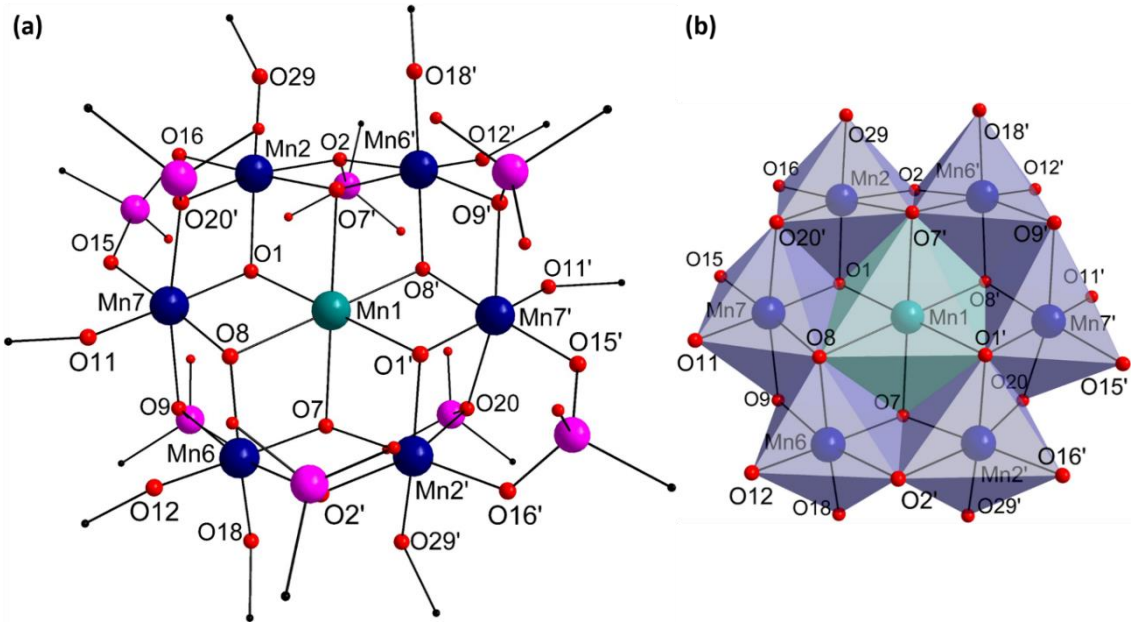

Figure 8.37: (a) Coordination environment of Mn centres constituting the $\{Mn_7\}$ disc and **(b)** polyhedral representation of the $\{Mn_7\}$ disc in compound **8.5**. Colour scheme: Mn(II) (teal), Mn(III) (deep blue), C (black), P (pink) and O (red).

Table 8.17: Key metal-ligand and metal-metal bond lengths and bond valence sum for each Mn centre and Ca centre for compound **8.5**.

Metal centre	Coordinating atom	Bond Distance (Å)	BVS	Assigned oxidation state
Mn1	O1	2.096(5)	2.032	+II
	O1’	2.096(5)		
	O8’	2.242(4)		
	O8	2.242(4)		
	O7	2.256(5)		
	O7’	2.256(5)		
Mn2	O29	1.884(5)	3.119	+III
	O16	1.902(5)		
	O1	1.923(5)		
	O7’	2.005(5)		
	O2	2.227(4)		
	O20’	2.231(4)		
Mn3	O4	1.905(5)	2.963	+III
	O10	1.909(5)		
	O17	1.919(5)		
	O5	1.925(5)		
	O27	2.173(5)		
Mn4	O24	2.076(6)	2.182	+II
	O6	2.133(5)		
	O23	2.136(6)		
	O26	2.145(6)		
	O5	2.242(5)		
	O19	2.297(5)		

Mn centre	Coordinating atom	Bond Distance (Å)	BVS	Assigned oxidation state
Mn5	O22	1.930(5)	3.058	+III
	O7	1.950(4)		
	O18	1.963(5)		
	O19	1.991(5)		
	O29’	2.101(5)		
	O6	2.185(5)		
Mn6	O12	1.862(5)	3.237	+III
	O18	1.921(5)		
	O7	1.923(5)		
	O8	1.961(5)		
	O9	2.196(5)		
	O2’	2.207(5)		
Mn7	O15	1.903(5)	3.156	+III
	O1	1.906(5)		
	O11	1.923(5)		
	O8	1.954(5)		
	O9	2.217(5)		
	O20’	2.236(5)		
Mn8	O13	1.914(5)	3.059	+III
	O8	1.939(4)		
	O11	1.965(5)		
	O3’	1.998(5)		
	O12	2.132(5)		
	O21’	2.185(5)		
Ca1	O28’	2.190(6)	2.503	+II
	O14	2.244(6)		
	O24’	2.310(6)		
	O3’	2.345(5)		
	O21’	2.411(5)		
	O5’	2.420(5)		
	O25’	2.717(7)		

Metals	Distance (Å)	Metals	Distance (Å)
Mn1-Mn2	3.086(2)	Mn3-Mn7	3.886(1)
Mn1-Mn7	3.041(1)	Mn4-Ca1’	3.461(2)
Mn2-Mn3	3.873(2)	Mn4-Mn5	3.143(2)
Mn2-Mn5’	2.990(1)	Mn5-Mn6	2.870(2)
Mn2-Mn6’	3.157(2)	Mn6-Mn7	3.154(2)
Mn2-Mn7	3.021(2)	Mn6-Mn8	2.929(2)
Mn3-Ca1’	3.785(2)	Mn7-Mn8	2.953(1)
Mn3-Mn4	3.695(2)	Mn8-Ca1	3.358(2)

’1-X,1-Y,1-Z

Table 8.18: BVS analysis for O atoms and their assigned protonation state in compound **8.5**.

Atom	BVS	Assignment
O1	1.755	μ_3-O^{2-}
O5	1.206	μ_3-OH^{-}
O7	2.042	μ_3-O^{2-}
O8	2.084	μ_3-O^{2-}

Mn2 is also octahedrally coordinated and binds to two oxo-groups (O1 and O7) and the O-donors of a μ-CH_3O^- (O29) and three phosphonate groups (O2, O16 and O20) (**Figure 8.37 (a)**). The sites directed towards the Jahn-Teller axis for Mn2 are fulfilled by two of the phosphonate O-donors O2 and O20 with the Mn-O distance being 2.227(4) and 2.231(4) respectively. The other Mn-O bonds perpendicular to the Jahn-Teller axis are 1.9-2.0 Å long. The octahedron of Mn2 shares an edge with the octahedra of Mn5-Mn7 (**Figure 8.37 (b)**).

Mn6 and Mn7 also form part of the {Mn_7} disc with the former being coordinated to two oxo-groups and the O-donors of two μ_2-CH_3O^- and two phosphonate groups. The latter resides in a similar coordination environment with one of the μ_2-CH_3O^- O-donor replaced by that of one of the phosphonate group (**Figure 8.37 (a)**). Their octahedra share an edge with each other and with the octahedron of Mn8 (**Figure 8.37 (b)**).

It is interesting to note that the octahedra of each Mn centre forming the periphery of the {Mn_7} disc (i.e. Mn2, Mn6, Mn7 and their symmetry equivalents) are distorted to similar extents as depicted by the continuous shape measure values, angle variances and distortion indices (**Table 8.19**). Additionally, for this complex, the Jahn-Teller axis of the Mn centres forming the vertices of the {Mn_7} disc are joined to each other at an angle ranging between 80-85° which is smaller range compared to that observed in compounds **8.2**-**8.4**.

Mn3, Mn5 and Mn8 form the trinuclear unit capping the central {Mn_7} disc. Mn3 resides in a square pyramidal environment and not a spherical square pyramidal environment as confirmed by continuous shape measure analysis (**Table 8.19**) which gives a higher value (0.901) when a spherical square pyramid is used as reference. Unlike compounds **8.2**-**8.4**, where two Mn centres in the trinuclear units reside in a square pyramidal environment, only Mn3 here resides in a square pyramidal environment and it is coordinated to a μ_3-OH^- (O5) and the O donors of the phosphinate and three phosphonate groups (**Figure 8.38**). The phosphinate O-donor occupies the axial position and the Mn-bond is 2.173(5) Å. The Mn-O bonds in the equatorial plane are ~1.9 Å. The polyhedron of Mn3 shares a vertex with the octahedron of Mn4 at O5.

Mn5 is coordinated to a μ_4-O^{2-} (O7) and the O-donors of a pivalate (O22), two μ_2-CH_3O^- (O18 and O29) and two phosphonate groups (O6 and O19) (**Figure 8.38**). The Jahn-Teller axis is directed along one of the μ_2-CH_3O^- O-donor (O29) and the phosphonate O-donor (O6) residing opposite to it with the Mn-O distances being 2.101(5) and 2.185(5) respectively. The Mn-O distance perpendicular to the Jahn-Teller axis vary between 1.9-2.0 Å. The octahedron of Mn5 shares an edge with Mn6 at O7 and O18 (**Figure 8.38 (d)**).

Mn8 resides in a coordination environment similar to that of Mn5 with a μ_4-O^{2-} (O8) and the O-donors of a pivalate (O13), two μ_2-CH_3O^- (O11 and O12) and two phosphonate groups (O3 and O21) fulfil it (**Figure 8.38**). The Jahn-Teller axis is again along the O-donors of one of the μ_2-CH_3O^- O-donor

(O12) and the phosphonate O-donor (O21) residing opposite to it. The Mn-O distances along the Jahn-Teller axis range between 2.1-2.2 Å, and 1.9-2.0 Å perpendicular to it.

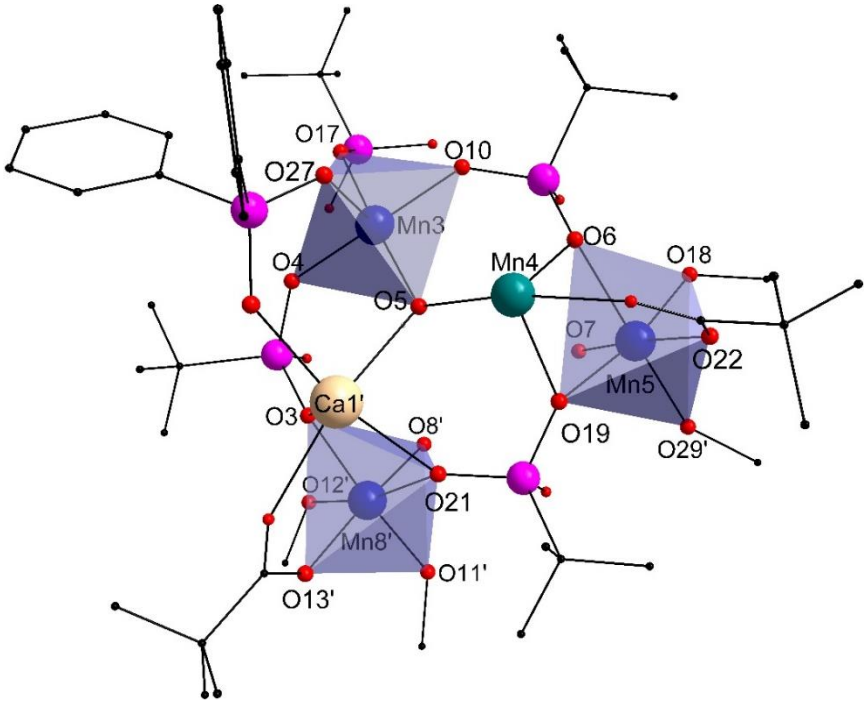

Figure 8.38: Coordination environment Mn3, Mn5 and Mn8 in compound **8.5**. Colour scheme: Mn(II) (teal), Mn(III) (deep blue), Ca (light yellow), C (black), P (pink) and O (red).

Mn4(II) resides over the trinuclear unit and is coordinated to a μ_3-OH^- along with the O-donors of a methanol, an acetate, a pivalate and two phosphonate groups (**Figure 8.39**). The Mn-O distances vary between 2.1-2.3 Å. The octahedron of Mn4 shares an edge with that of Mn5 at two of the phosphonate O-donors.

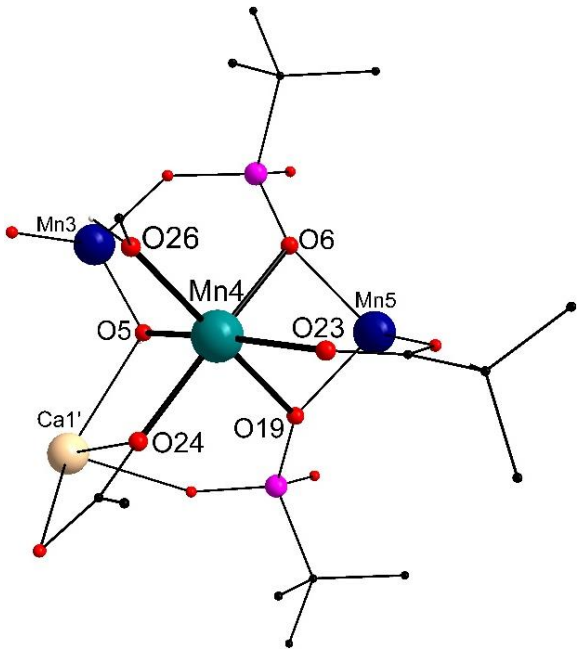

Figure 8.39: Coordination environment Mn4 in compound **8.5**. Colour scheme: Mn(II) (teal), Mn(III) (deep blue), Ca (light yellow), C (black), P (pink) and O (red).

The coordination environment of Ca^{2+} ion is similar to that observed in compound **8.4** except that here, it resides in 7-coordinate environment instead of an 8-coordinate environment. The coordination environment is fulfilled by a μ_3-OH^- and the O-donors of a pivalate, a chelating acetate and two phosphonate groups with the Ca-O distances lying in the 2.2-2.7 Å range (**Figure 8.40**). Ca^{2+} is thus well incorporated into the core structure but unlike compound **8.4**, a hydrogen bonding network does not exist here.

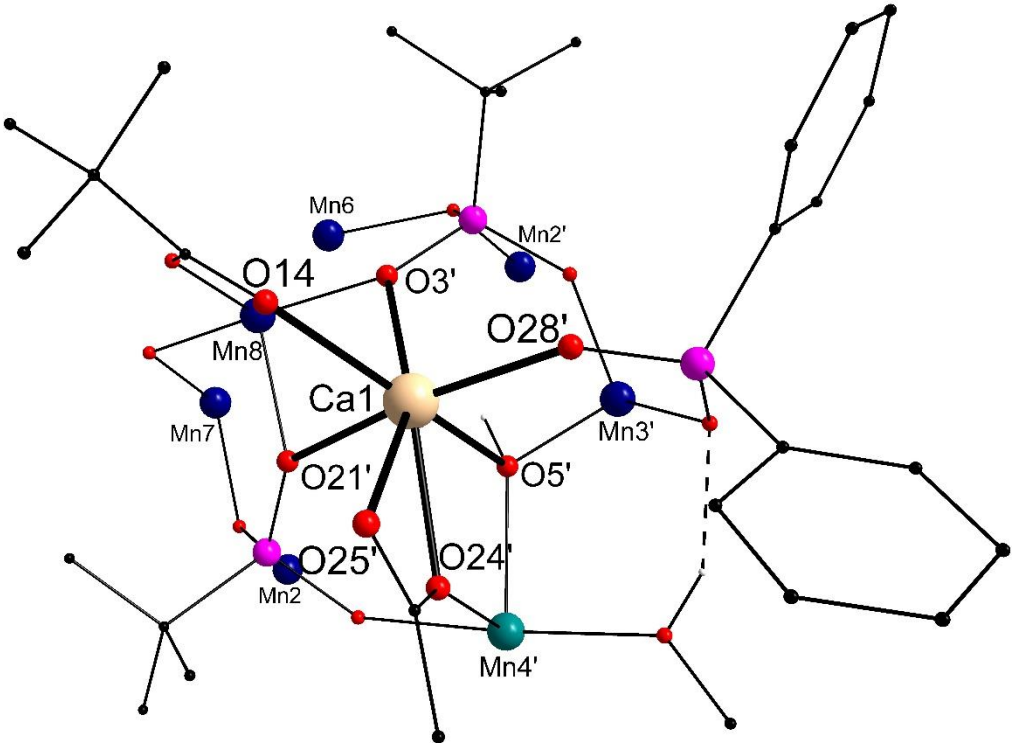

Figure 8.40: Coordination environment of Ca in compound **8.5**. Colour scheme: Mn(II) (teal), Mn(III) (deep blue), Ca (light yellow), C (black), P (pink) and O (red). All hydrogen atoms (grey) except those bound to O centres have been removed. Hydrogen bonds are shown with dashed lines.

Table 8.19: Continuous shape measure values, angle variance and distortion indices for each Mn centre for compound **8.5** ([1]octahedral and [2]square pyramid geometry).

Mn centre	Continuous shape measure value	Angle variance (σ^2)	Distortion Index
Mn1[1]	3.300	198.4	0.1479
Mn2[1]	1.051	43.78	0.0565
Mn3[2]	0.466	7.80	0.0223
Mn4[1]	0.525	46.31	0.0631
Mn5[1]	0.734	30.50	0.0495
Mn6[1]	1.017	36.22	0.0500
Mn7[1]	1.048	39.46	0.0586
Mn8[1]	0.830	31.92	0.0499

The molecules in this compound pack to give a layered structure along the crystallographic b-axis (**Figure 8.41**). The system packs with solvent molecules whose electron density was too diffuse to be resolved. The diffracting component of this electron density (equivalent to 160 electrons) was removed using the squeeze subroutine in PLATON and it may correspond to two CH_3CN and two CH_3OH molecules per formula unit. The calcvoid routine in OLEX2 reveals that the largest voids in this structure have a radius of 2.6 Å where these solvent molecules are likely to reside. It also shows that the structure can be penetrated by a sphere of radius 1.8 Å along the crystallographic c-axis which indicates that this system may be porous along this direction.

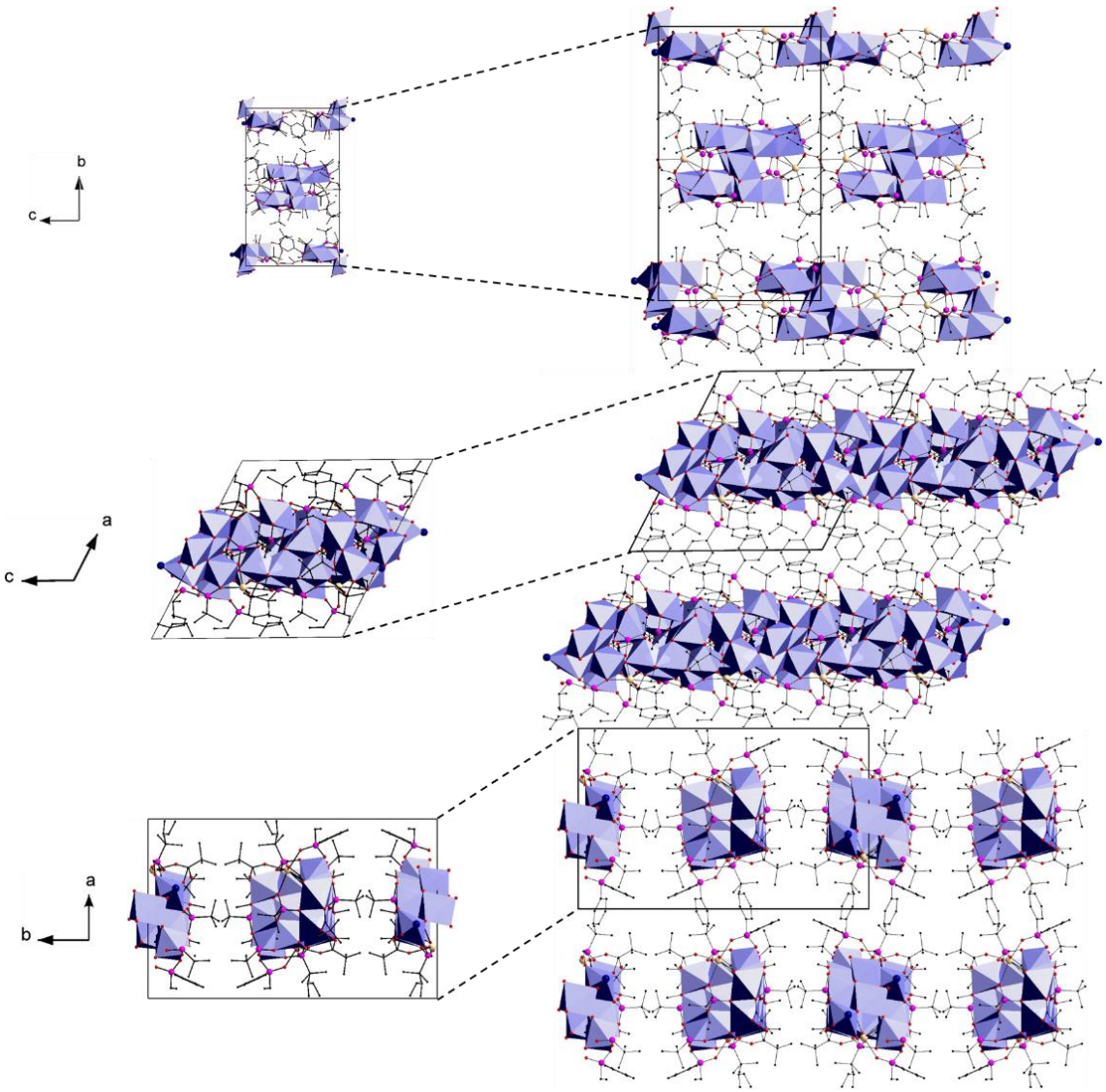

Figure 8.41: Packing diagram of compound **8.5**. Colour scheme: Mn (blue), Ca (tan), P(pink), C (black) and O (red).

Table 8.20: Selected bond angles for compound **8.5**.

Bond	Bond Angle (°)	Bond	Bond Angle (°)
O1'-Mn1-O7	78.25(18)	O7'-Mn2-O2	79.83(18)
O8-Mn1-O7	73.62(17)	O1-Mn2-O20'	82.48(18)
O8'-Mn1-O7'	73.62(17)	O29-Mn2-O7'	83.40(20)
O1'-Mn1-O8'	78.20(18)	O7'-Mn2-O20'	83.94(18)
O1-Mn1-O8	78.20(18)	O1-Mn2-O7'	88.80(20)
O1-Mn1-O7'	78.25(18)	O29-Mn2-O20'	90.09(19)
O1'-Mn1-O7'	101.75(18)	O29-Mn2-O2	91.09(19)
O1-Mn1-O7	101.75(18)	O16-Mn2-O20'	92.70(20)
O1-Mn1-O8'	101.80(18)	O29-Mn2-O16	93.10(20)
O1'-Mn1-O8	101.80(18)	O1-Mn2-O2	94.05(19)
O8'-Mn1-O7	106.38(17)	O16-Mn2-O1	94.20(20)
O8-Mn1-O7'	106.38(17)	O16-Mn2-O2	103.70(20)
O1-Mn1-O1'	180.00	O2-Mn2-O20'	163.48(19)
O7'-Mn1-O7	180.00(18)	O29-Mn2-O1	169.80(20)
O8'-Mn1-O8	180.00	O16-Mn2-O7'	175.10(20)
O10-Mn3-O17	87.50(20)	O4-Mn3-O5	92.00(20)
O5-Mn3-O27	88.80(20)	O4-Mn3-O27	93.60(20)
O4-Mn3-O17	89.50(20)	O17-Mn3-O27	95.40(20)
O10-Mn3-O27	90.20(20)	O4-Mn3-O10	175.30(20)
O10-Mn3-O5	90.70(20)	O17-Mn3-O5	175.40(20)
O6-Mn4-O19	80.68(18)	O7-Mn5-O29'	79.30(20)
O5-Mn4-O19	82.36(18)	O7-Mn5-O18	83.10(20)
O24-Mn4-O5	84.00(20)	O18-Mn5-O6	84.80(20)
O23-Mn4-O19	84.30(20)	O19-Mn5-O6	86.73(19)
O6-Mn4-O5	86.38(19)	O18-Mn5-O29'	89.30(20)
O6-Mn4-O23	87.00(20)	O7-Mn5-O19	90.80(20)
O24-Mn4-O26	90.10(20)	O22-Mn5-O6	92.40(20)
O24-Mn4-O19	91.40(20)	O22-Mn5-O19	92.60(20)
O26-Mn4-O5	93.80(20)	O7-Mn5-O6	93.80(20)
O6-Mn4-O26	97.20(20)	O22-Mn5-O29'	94.20(20)
O23-Mn4-O26	99.30(20)	O22-Mn5-O18	94.40(20)
O24-Mn4-O23	100.90(20)	O19-Mn5-O29'	98.40(20)
O23-Mn4-O5	165.90(20)	O18-Mn5-O19	169.30(20)
O24-Mn4-O6	168.30(20)	O29'-Mn5-O6	171.46(18)
O26-Mn4-O19	175.70(20)	O22-Mn5-O7	173.00(20)
O8-Mn6-O9	80.82(19)	O8-Mn7-O9	80.41(19)
O7-Mn6-O2'	82.10(18)	O11-Mn7-O8	80.80(20)
O18-Mn6-O7	85.00(20)	O1-Mn7-O20'	82.71(18)
O12-Mn6-O8	86.90(20)	O8-Mn7-O20'	86.01(19)
O7-Mn6-O8	87.89(19)	O11-Mn7-O20'	87.65(19)
O12-Mn6-O2'	89.99(19)	O1-Mn7-O8	90.40(20)
O8-Mn6-O2'	90.23(19)	O11-Mn7-O9	93.20(20)
O18-Mn6-O9	90.80(20)	O15-Mn7-O1	93.40(20)
O7-Mn6-O9	91.48(19)	O15-Mn7-O20'	93.70(20)
O12-Mn6-O9	95.50(20)	O1-Mn7-O9	94.25(19)
O18-Mn6-O2'	97.20(20)	O15-Mn7-O11	95.40(20)
O12-Mn6-O18	101.30(20)	O15-Mn7-O9	100.00(20)
O18-Mn6-O8	168.90(20)	O9-Mn7-O20'	166.08(19)
O9-Mn6-O2'	169.20(19)	O1-Mn7-O11	167.40(20)
O12-Mn6-O7	170.50(20)	O15-Mn7-O8	176.20(20)
O8-Mn8-O11	80.20(20)	O8-Mn8-O3'	93.10(20)
O8-Mn8-O12	80.35(19)	O13-Mn8-O3'	94.40(20)

Bond	Bond Angle (°)	Bond	Bond Angle (°)
O31-Mn8-O21'	84.56(19)	O11-Mn8-O21'	96.60(20)
O31-Mn8-O12	88.10(20)	O13-Mn8-O21'	96.60(20)
O11-Mn8-O12	89.70(20)	O12-Mn8-O21'	168.64(18)
O8-Mn8-O21'	91.40(19)	O13-Mn8-O8	169.50(20)
O13-Mn8-O11	92.10(20)	O11-Mn8-O3'	173.17(19)
O13-Mn8-O12	92.50(20)		

8.5.2 Physicochemical characterisation

Physicochemical characterisation was carried out to further support the structural model obtained using single crystal X-ray crystallography. The Mn:Ca ratio in this complex was determined to be 7.23:1 using EDX analysis which is close to the expected ratio of 7.5:1.

TGA analysis (**Figure 8.42**) under an atmosphere of N_2 of compound **8.5** dried in air reveals a drop up to ~70 °C which represents the loss of the CH_3OH molecules trapped in the crystal lattice (weight loss calcd: 1.8 %, found: 2.4 %). This is followed by the loss of lattice CH_3CN molecules and the CH_3OH molecules bound to the complex up to 230 °C (weight loss calcd: 4.1 %, found: 3.4 %). Between 230 and 300 °C, the bound methoxy groups are lost (weight loss calcd: 7.0 %, found: 5.7 %). Above 300 °C the acetate and pivalate groups are lost. This is followed by the partial decomposition of phosphinate and phosphonate groups, and the formation of oxide and phosphate species.

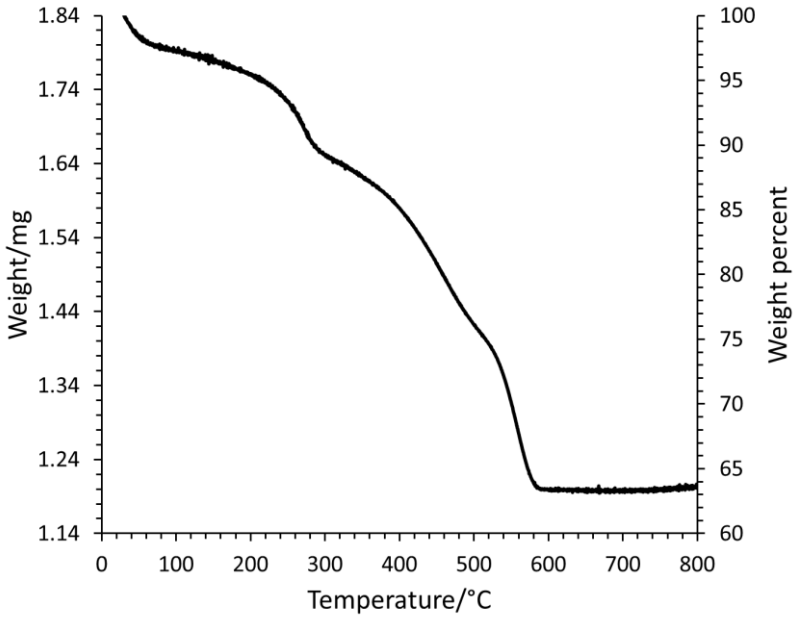

Figure 8.42: TGA analysis of compound **8.5**.

The infrared spectrum of compound **8.5** (**Figure 8.43**) is consistent with the structure determined by XRD. The broad distinctive feature centred at 2900 cm^{-1} is due to the C-H vibrations in the organic ligands.[617] The vibration mode at 1404 cm^{-1} corresponds to the symmetric carboxylate stretching while that centred at 1560 cm^{-1} corresponds to the asymmetric stretching. The energy variance between the two peaks in consistent with that exhibited by bridging carboxylate groups.[618] The additional features in the 1300-1600 cm^{-1} range are due to vibrations of the organic moieties of the molecule.[617] The strong signal at 970 cm^{-1} and the shoulder attached to it corresponds to the stretching mode of the phosphonate group.[621-623]

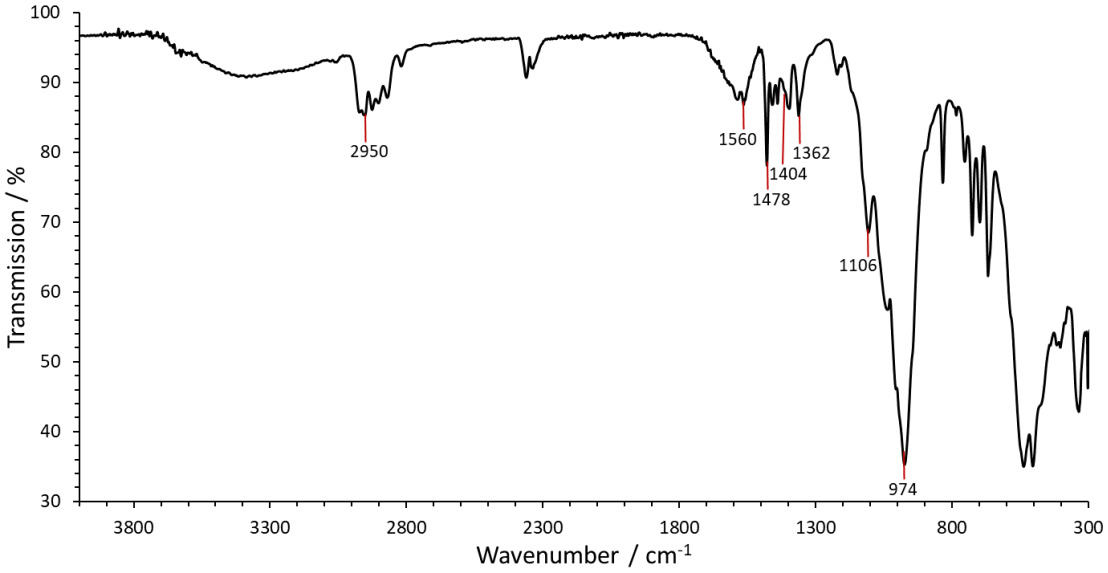

Figure 8.43: Infrared spectrum of compound **8.5**.

8.6 Electrochemical studies of compounds 8.2 and 8.3 – preliminary results

Due to time constraints, a preliminary investigation of the electrochemical behaviour of only compounds **8.2** and **8.3** was conducted. For this purpose, modified carbon paste electrodes were prepared by dispersing compounds **8.1** and **8.3** in carbon paste. Cyclic voltammetry (CV) of compound **8.2** in potassium phosphate buffer at pH 7.2 (KP*i*, 50 mM) using KNO_3 (1 M) as electrolyte, results in a strong catalytic wave due to water oxidation (**Figure 8.44**). Compound **8.3** shows similar behaviour as can be expected.

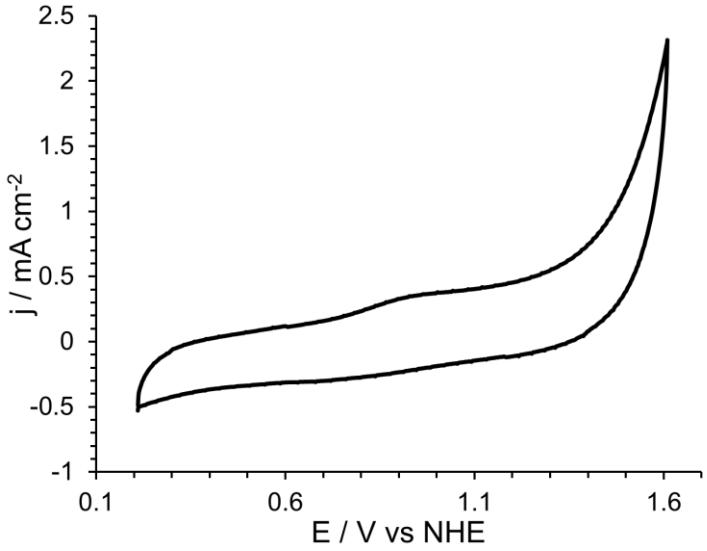

Figure 8.44: Cyclic voltammogram for compound **8.2** (10 wt-% loading) in a KP*i* buffer solution at pH 7.2.

To study the kinetic profile of this water oxidation reaction, linear sweep voltammetry (LSV) was performed using a rotating disk electrode at a low scan rate of 1 mV/s to ensure steady state conditions during the experiment. The catalyst loading of both compounds was varied between 10 and 20 wt-% of the total carbon paste blend. Higher loadings were not tested due to time constraints. From the electrochemical profile, it is evident that higher loadings increase the current densities (**Figure 8.45**) and decrease the onset potential of the water oxidation reaction for both compounds (**Figure 8.46 (a)** and **Table 8.21**). The Tafel slope also tends to decrease with increased catalytic loading (**Figure 8.46 (b)** and **Table 8.21**). Further increment in the catalytic loading may result in improved catalytic performance.

It can be observed that the onset potential for compound **8.3** is 50-60 mV lower than that of compound **8.2** and the Tafel slopes are similar. The similarity in Tafel slopes indicates that the reaction may occur via a similar mechanism which suggests that the lowering of the onset potential must be due to the presence of K^+ ions in compound **8.3**. This hypothesis is consistent with previous reports[87-89] but further investigation is required to confirm this.

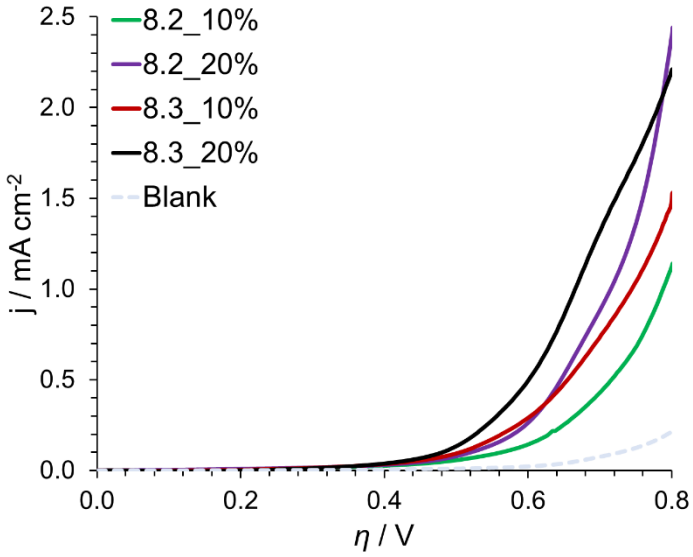

Figure 8.45: Linear sweep voltammograms for compound **8.2** and **8.3** at different loadings.

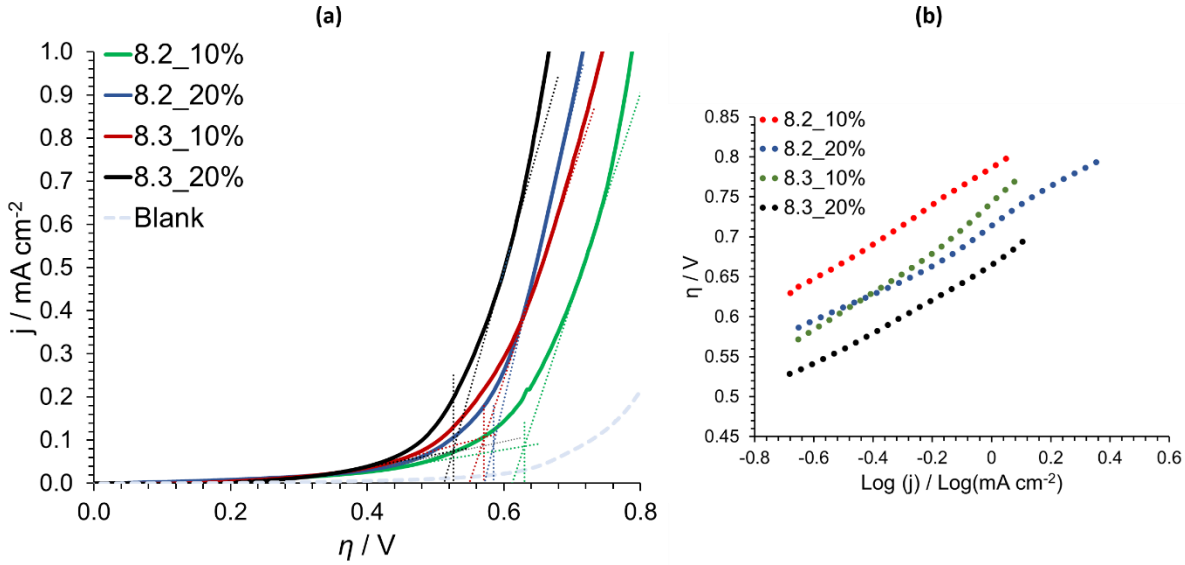

Figure 8.46: The determined **(a)** onset potentials and the **(b)** Tafel slope for compounds **8.2** and **8.3** at different loadings.

Table 8.21: The onset overpotential for water oxidation with compound **8.2** and **8.3** and the Tafel slope at different loadings above the onset potential.

Loading	Onset overpotential (mV)	Tafel slope (mV dec^{-1})
10% 8.2	630	233
20% 8.2	585	216
10% 8.3	571	267
20% 8.3	526	211

8.7 Conclusions

Five novel phosphonate based complexes have been synthesised using *tert*-butyl phosphonic acid and characterised using various analytical techniques. In presence of *tert*-butyl phosphonic acid and 4-picoline groups, compound **8.1** was formed. This compound contains a dodecanuclear complex whose core structure resembles the 'S' shape and it contains Mn in octahedral, spherical square pyramidal and tetrahedral coordination environments. The coordinating water molecules in this complex give rise to a complex intramolecular hydrogen bonding network.

A series of complexes structurally related to the previously reported tridecanuclear $\{Mn_{13}\}$ complex have also been synthesised. Each of these complexes consists of a three layered metal-centered distorted cuboctahedron with a $\{Mn_7\}$ disc sandwiched between two $\{Mn_3\}$ triangular units. Compound **8.2**, besides containing the $\{Mn_7\}$ disc and the $\{Mn_3\}$ triangular units, contains dangling partially protonated *tert*-butyl phosphonate groups which is quite fascinating as it provides the potential oppurtunity to link the $\{Mn_{13}\}$ units together. Attempts to link the dangling phosphonate groups observed in compound **8.2** resulted in the formation of compound **8.3** where the $\{Mn_{13}\}$ units are linked together by K^+ ions forming 1-D chains.

Compound **8.2** also revealed that the triangular units of the $\{Mn_{13}\}$ complex can potentially be capped by cations as partial occupancy by Na^+ ion was observed. This possibility was investigated using alkali and alkaline earth metals and was realised in compound **8.4** where Ca^{2+} ions were found to cap the triangular units. Introducing slight modifications to the synthesis of compound **8.4** yields compound **8.5**, where it was observed that an additional Mn centre can be added to further cap the triangular units.

The preliminary electrochemistry results for compounds **8.2** and **8.3** reveal that these compounds can catalyse water oxidation. Additionally, it was observed that the onset potential for compound **8.3** is lower than that for **8.2** and this may be attributed to the presence of K^+ ions in the former. However, further investigation is required for cofirming this.

By means of the series of $\{Mn_{13}\}$ complex discussed in this chapter, we have shown how the structural attributes of compound **8.2** were modified by controlling the reaction conditions. The modifications introduced to the structure may affect the magnetic properties which may be investigated in the future. Additionally, OER activity is observed in these complexes and the addition of a heterometal has been observed to affect the onset potential. Further investigation of the electrochemical behaviour of these complexes may allow us to obtain more insight into the role of Ca^{2+} in the OEC.

9 Conclusions and Future Work

In this work, we have reported the development of a computational methodology for investigating the magnetic properties of high nuclearity complexes, and a synthetic approach for the synthesis of high nuclearity Mn coordination complexes. The synthesised complexes have been characterised using various analytical techniques. The magnetic properties of some of the synthesised complexes have been studied experimentally and using the developed computational approach. Furthermore, we have investigated the OER activity of some of the synthesised complexes under electrochemical conditions in aqueous media using carbon paste electrodes.

For the development of the computational approach, we have used the previously reported phosphonate based $\{Mn_6\}$ and $\{Mn_{13}\}$ complexes as models. DFT calculations, primarily performed using the PBE0 functional and atom centred basis sets, were used to probe the electronic structure. FORTRAN codes were written for the calculation of coupling constants and determination of the temperature dependence of magnetic susceptibility. To understand the mechanism of coupling between metals centres *via* different bridges, we have developed a novel methodology that involves perturbing the system in such a way that the symmetry is retained and then analysing the effect of the perturbation on the coupling strength.

The investigation of the magnetic properties of the $\{Mn_6\}$ complex in its ground state revealed that the coupling is dominantly antiferromagnetic and two coupling constants were required for the accurate description of its electronic properties. The Cl^- ion residing at the centre of this complex was found to play a key role in coupling the Mn centres. The problem of experimentally fitting coupling constants to the magnetic susceptibility was highlighted. Investigation of the mechanism of coupling between Mn centres using our methodology reveals that the coupling *via* the phosphonate bridge is antiferromagnetic while the central Cl^- ion can couple the Mn centres ferromagnetically or antiferromagnetically depending upon where they are located with respect to each other. These results were found to be in line with those obtained by overlap analysis thus supporting the reliability of our methodology.

The oxidation of this cage was also computationally investigated and it was observed that the $\{Mn_6\}$ cage can potentially accommodate the loss of at least four electrons which is accompanied by expansion of the cage. The oxidation changes the coupling behaviour between Mn centres and for understanding these changes, one needs to take into account the oxidation state of the interacting Mn centres, the spin density on the O-donors of phosphonate groups and the Mn-Cl overlaps. It was also observed that the oxidation of the cage results in switching of the nature of coupling between some Mn centres and stabilisation of intermediate spin states.

The reliability of our computational approach was further tested by modelling the magnetic properties of a highly symmetric $\{Mn_{13}\}$ complex where the Mn centres are bridged by Cl^-, O^{2-} and *tert*-butyl phosphonate groups. It was observed that for this complex, the coupling is dominantly

ferromagnetic and three coupling constants were required for the accurate description of its magnetic properties. The nature of coupling *via* the different pathways was analysed using our methodology and the coupling *via* the oxo- bridge was found to be ferromagnetic. The phosphonate bridge was again found to be antiferromagnetic while Cl^- ion was found to couple Mn centres either ferromagnetically or antiferromagnetically depending upon their relative positions. These results were found to be in agreement with the results obtained using overlap analysis further validating the reliability of our methodology.

The synthetic approach for synthesising high nuclearity Mn coordination complexes developed in this work is a facile self-assembly approach based on the comproportionation reaction between Mn^{II} and Mn^{VII} salts in presence of carboxylate and/or phosphonate based ligands. In an attempt to structurally mimic the OEC, we synthesised carboxylate based high nuclearity complexes. Using $KMnO_4$ as the only source of Mn ions, we synthesised three complexes (compounds **6.1**-**6.3**). The use of pivalic acid resulted in the formation of compounds **6.1** and **6.2** while the use of biphenyl-4-carboxylic acid resulted in the formation of compound **6.3**. The synthesis of these complexes indicated that the oxidation state that is stabilised does not solely depend upon the ratio of Mn(II) and Mn(VII) salts but also varies with the other reaction conditions employed. The impact that the steric nature of the ligands participating in the reaction has on directing the reaction towards the formation of different end products was also highlighted in the synthesis of these complexes.

Compound **6.1** was found to contain a hexanuclear complex in which the Mn centres reside at the vertices of two edge sharing tetrahedra. Compound **6.2** was found to contain a mixed-metal octanuclear Mn complex. This complex is essentially a dimer of two $\{Mn_4K\}$ distorted cubane units that have a dangling Mn centre attached and that are symmetry related to each other by an inversion centre. This complex is structurally similar to the OEC and can formally be compared with the S_{-1} state of the OEC. Compound **6.3** was found to contain a dodecanuclear complex whose core structure contains a $\{Mn_4\}$ cubane unit surrounded by a $\{Mn_8\}$ ring.

Due to the structural similarities between compound **6.2** and the OEC, further studies were conducted. The electronic structure of this complex reveals strong antiferromagnetic interactions between the two cubane units and ferromagnetic interactions within them which results in the stabilisation of the S = 0 spin state. The investigation of its electrochemical behaviour revealed that similar to the OEC, it shows high catalytic activity and also undergoes rapid decomposition under oxidative, hydrolytic conditions. Electrodes with a 40 wt-% loading of compound **6.2**, gave rise to an onset overpotential of 420 mV and a Tafel slope of 255 mV dec^{-1} at pH = 7.2.

To understand the interplay between phosphonate and carboxylate groups, and to investigate the possibility of forming high nuclearity complexes containing both carboxylate and phosphonate ligands, we made use of pivalic acid and phenylphosphonic acid as the primary ligands. Using a sterically less hindered but strongly binding phenylphosphonic acid and a sterically demanding

pivalic acid, we succeeded in isolating five structurally related complexes (compounds **7.1**-**7.5**) and the importance of having both ligands in the reaction mixture for obtaining these complexes is highlighted by these complexes. The synthesis of these complexes also revealed the effect of the counterion of the Mn^{II} salt on the end product and the importance of the choice of solvent used for the reaction. Additionally, it was observed that varying the ratio of the Mn^{II} and Mn^{VII} salts can also lead to stabilisation of different end products. It was also observed that an excess of carboxylic acid is required to suppress the formation of complexes that exclusively contain phosphonate ligands

Compound **7.1** was found to contain a dodecanuclear complex in which the Mn centres reside at the vertices of a regular truncated tetrahedron. Compounds **7.2** and **7.3** were found to contain a pentadecanuclear complex in which Mn centres reside at the vertices of an augmented truncated tetrahedron. Significant distortion of the truncated tetrahedral geometry is observed in compounds **7.4** and **7.5** with the former containing a tetradecanuclear complex which has two additional Mn centres attached to one of the hexagonal faces. In the latter case, the distortion leads to transformation of the core structure of the tridecanuclear complex to a distorted elongated gyrobifastigium with twelve Mn centres at the vertices and one in the centre. A clear decrease in the number of regular hexagonal faces is observed as one moves from compound **7.1** to **7.5** further indicating the increase in the distortion. The increase in distortion gives rise to complex magnetic properties with compound **7.1** displaying dominant antiferromagnetic interactions and an S = 0 ground state at low temperatures while compound **7.5** showed the presence of ferromagnetic interactions and intermediate spin ground state.

The electrochemical studies of compounds **7.1** and **7.3** in aqueous media revealed OER activity. The former was found to be active at relatively lower overpotentials (251 mV at 40 wt-% catalytic loading) compared to the latter (521 mV at 40 wt-% catalytic loading). Both complexes were found to decompose during the water oxidation reaction but the initial activity was unarguably attributed to species derived from the parent complexes and not the decomposed species as the latter was observed to be active only at very high overpotentials.

For synthesising high nuclearity complexes where the Mn centres are primarily coordinated by phosphonate groups, we modified the synthesis of the previously reported *tert*-butyl phosphonate based $\{Mn_6\}$ and $\{Mn_{13}\}$ complexes. This resulted in the isolation of five novel complexes (compounds **8.1**-**8.5**). Compound **8.1** was found to contain a dodecanuclear complex whose core structure resembles the 'S' shape and contains Mn in octahedral, spherical square pyramidal and tetrahedral coordination environments. Compounds **8.2**-**8.5** were found to contain complexes that are structurally related to the previously reported $\{Mn_{13}\}$ complex in that they contain a three layered metal-centered distorted cuboctahedron with a brucite-like $\{Mn_7\}$ core capped by two $\{Mn_3\}$ units. Compound **8.2** was found to contain partially protonated terminal phosphonate groups that were exploited to form 1-D chains (compound **8.3**) using K^+ ions as the linker. Compound **8.2**

was also observed to contain a partially occupied Na^+ ion capping the trinuclear units which was exploited to form the Mn-Ca mixed metal compounds **8.4** and **8.5**.

The preliminary electrochemistry results for compounds **8.2** and **8.3** in aqueous media reveal that these compounds can catalyse the oxidiation of water. Additionally, it was observed that the onset potential for compound **8.3** is lower than that for **8.2** and this may be attributed to the presence of K^+ ions in the former.

To conclude, we have developed a computational methodology for the calculation of exchange coupling constants and devised a novel methodology for determining the mechanism of coupling *via* each ligand bridge in instances where multiple ligand groups bridge a given pair of metal centres. We have also developed a synthetic approach which involves the modification of the comproportionation reaction and have illustrated the versatility of this approach. We have demonstrated the application of this approach for modifying previously known structures, for accessing rare geometrical arrangements and for synthesising OEC mimics. Keeping in mind the versatility of the computational and synthetic approaches discussed and based on the results obtained using these approaches, a number of directions for future work emerge and some of the possible avenues that can be explored are discussed below.

We believe that the complexes reported in this thesis represent only a small subset of the possible complexes that can be generated using our synthetic approach. Varying the reaction conditions further and expanding the set of ligands used can potentially give rise to complexes of varying nuclearities and geometries. One can not only modulate the steric and electronic properties of carboxylate and phosphonate based ligands but also make use of other family of ligands like boronic acids, amino acids and nitrogen based ligands.

Considering that the carboxylate based octanuclear complex (compound **6.2**) bears structural similarity with the OEC, this complex can be used as a starting point for understanding the mechanism of OER by the OEC. The synthetic strategy can be modified to replace the K^+ ions with Ca^{2+} ions and to include pyridine type ligands. These modifications would allow structurally mimicking the OEC even more closely. Furthermore, the computational approach developed in this work can be used to understand the mechanism of water oxidation *via* this complex and determine the effect of the magnetic properties on the OER activity. Additionally, the effect of the ligand environment on the magnetic properties can be investigated computationally. This would allow the determination of the optimal ligand environment for efficient OER catalysis. This information can then be used to direct the synthetic approach to synthesise such a complex thereby allowing us to move forward in generating efficient OER catalysts.

The series of mixed carboxylate-phosphonate based complexes provides a set of structurally related complexes with varying levels of distortion. Further investigation of the magnetic properties of these complexes may help obtain some correlation between the magnetic behaviour of these

complexes and their structural symmetry. Additionally, since two members of this series have observed to be OER active, it will be interesting to investigate the electrochemical properties of the other complexes.

The magnetic properties and OER activity of the phosphonate based complexes can be explored in greater detail. Computational and experimental investigation of the magnetic properties of these complexes will shed some light on the effect of the structural modifications introduced in compounds **8.2**-**8.5** on their magnetic properties. Additionally, the OER activity detected for compounds **8.2** and **8.3** and the trends observed demand a rigorous investigation of the electrochemical properties of compounds **8.2**-**8.5**. Determining the OER activity of the Ca^{2+} containing compounds **8.4** and **8.5** may also provide some insight on the role of Ca^{2+} in the OEC.

Considering how all materials reported for OER activity in this thesis tend to decompose, increasing their stability or developing self-healing pathways can prove helpful in making these materials perform the OER for extended periods. Considering the case of Ru dimeric complexes, where the increase in stability came at the cost of reduced activity, the latter appears to be more appealing. For developing self-healing pathways, we need to build our understanding of how Nature repairs the OEC during the OER and this will require a combined computational and experimental approach to realise. Advancement in this respect will allow us to focus on the enhancing the activity of the OER catalysts instead of their stability.

10 Experimental

10.1 Materials and Methods

Reagents

All chemicals used were of reagent grade and were purchased from Sigma-Aldrich, Alfa Aesar or Acros Organics and were used without further purification. Solvents were supplied by in-house suppliers, and were of technical grade or higher. These were also used without further purification.

Single crystal X-ray diffraction analysis

Single crystal X-ray Diffraction datasets were collected by Dr. Brendan Twamley, Dr. Nianyong Zhu, Dr. Amal Cherian Kathalikkattil, Friedrich Steuber or Paul Wix. The solution and refinement of the dataset was also performed by them besides myself.

A suitable crystal was selected and immersed in oil, mounted in a mitiGen loop on a Bruker APEX-II CCD diffractometer equipped with a Mo-Kα source (λ = 0.71073 Å) and a Cu-Kα source (λ = 1.5418 Å). The crystal was kept at 100 K during data collection using a Cobra cryostream low- temperature apparatus. The diffraction frames were integrated and processed using the Bruker SAINT software package. The data were corrected for absorption effects using the multi-scan method (SADABS).[648] Using Olex2,[616] the structure was solved with the XT[649] structure solution program using Intrinsic Phasing and refined with the XL[650] refinement package using Least Squares minimisation.

Some structures contain large solvent accessible void volume and the electron density due to the solvent molecules residing in these voids was too diffuse. To account for the diffracting component of the diffuse electron density, the squeeze subroutine in PLATON[629] was used. This routine generates a reflection file by that excludes the diffraction contributions of the diffuse electron density. The final results are based on the new reflection data.

Powder X-ray diffraction analysis

For structurally robust samples, powder X-ray diffraction data was collected on a Bruker D2 Phaser diffractometer using Cu-Kα radiation at 30 kV and 10 mA, with a step size of 0.02° (2θ) between 5 and 55° (2θ), and data were collected at 25°C. The samples were grounded and loaded on a low-background silicon sample holder.

For samples that were observed to be sensitive to solvation, powder XRD patterns were measured by Dr. Brendan Twamley, Dr. Nianyong Zhu, Dr. Amal Cherian Kathalikkattil or Paul Wix, by sealing crystalline samples under solvent in a glass capillary or by incorporating the sample in grease. The capillaries/grease samples were mounted and centred on a goniometer head on a Bruker APEX II diffractometer for data collection. The data were collected upon 360° ϕ rotational frames at 2θ values of 10° and 20°, with exposure times of 10 minutes per frame at a detector distance of 120

mm. Overlapping sections of data were combined and the data was processed using the Bruker APEX II routine XRD2-Eval subprogram.

Analysis of the data and background subtraction was performed using DIFFRAC.EVA program.[651]

Thermogravimetric analysis

Thermogravimetric analysis (TGA) was carried out using a Perkin Elmer Pyris-1 Thermogravimetric analyser that had been previously calibrated using nickel and iron standards. The analysis was performed under a N_2 stream at a flow rate of 20 mL min^{-1}. Measurements were carried out between 25°C and 700-900°C at a heating rate of 2, 3 or 5°C per minute.

Fourier-Transform Infrared (FTIR) spectroscopy

Infrared data in the 4000-300 cm^{-1} region were obtained using a PerkinElmer Spectrum One FT-IR spectrometer with a universal Attenuated Total Reflectance (ATR) sampling accessory.

The following symbols have been used to describe the spectra: w weak, m medium, s strong, b broad, sh shoulder.

Scanning electron microscopy (SEM)

SEM experiments were performed by Dr. Guanghua Jin or Éadaoin Whelan using a Zeiss ULTRA plus scanning electron microscope using both InLens and SE2 detectors at a 5 kV acceleration voltage.

Energy-dispersive X-ray (EDX) spectroscopy

EDX spectroscopy was carried by Dr. Guanghua Jin or Éadaoin Whelan on samples with the Zeiss ULTRA plus scanning electron microscope using a 20 mm^2 Oxford Inca EDX detector and a 20 kV acceleration voltage.

X-ray photoelectron spectroscopy (XPS)

XPS experiments were carried out by Dr. Ross Lundy and these were performed under ultra-high vacuum condition (<5x10-10 mbar) using a VG Scientific ESCAlab Mk II system equipped with a hemispherical analyser using Al Kα X-rays (1486.6 eV). The emitted photoelectrons were collected at a take-off angle of 90 ° from the samples surface. The analyser pass energy was set to 100 eV for survey scans and 40 eV for high-resolution core scans, yielding an overall resolution of 1.5 eV. Photoemission peak positions were corrected to C 1s at a binding energy of 284.8 eV.

Elemental analysis

Quantitative elemental analysis was performed by Dr. Ann Connolly and Dr. Rónán Crowley using an Exeter Analytical CE 440 at the Analytical Laboratory, UCD Belfield, Dublin.

Magnetic measurements

All magnetic susceptibility measurements were carried out by Dr. Munuswamy Venkatesan on a 5 T MPMS SQUID from Quantum Design. Temperature dependence of magnetic susceptibility was measured in the temperature range of 2-300 K in an applied magnetic field of 0.1 T.

Electrochemical experiments

Electrochemical measurements were performed on Biologic VSP potentiostat. The Ohmic drop was measured prior to each experiment and compensated using the positive feedback compensation as implemented in the instrument. The typical three-electrode set-up used for all the experiments was composed of Ag/AgCl (KCl 3M) reference electrode, carbon paste (CP) working electrodes (surface area = 0.07 cm^2), and a Pt mesh. All the measurements were carried out in a 50 mM potassium phosphate (KP_i) buffer solution with KNO_3 (1 M) as electrolyte at pH 7.2. The CP blends were prepared by mixing CP and the desired amount of catalyst in an agate mortar, then the mixtures were inserted inside the CP electrode pocket. The linear sweep voltammetry (LSV) measurements were conducted using an ALS RRDE-3A set-up with a CP rotating disc electrode (surface area = 0.07 cm^2) at 1,600 r.p.m., and at a scan rate of 1 mV s^{-1}. Tafel data were extracted from the LSV measurements. Bulk water electrolysis was performed using the same conditions as stated for the LSV measurements.

All the applied potentials ($\mathrm{E_{app}}$) were converted to the normal hydrogen electrode (NHE) reference scale using $\mathrm{E_{NHE}} = \mathrm{E_{Ag/AgCl}} + 0.210\ (\mathrm{V})$. The overpotentials were calculated by subtracting the thermodynamic water oxidation potential ($\mathrm{E^0_{H_2O/O_2}}$) to $\mathrm{E_{app}}$ as:

$$\eta = \mathrm{E_{app}} - \mathrm{E^0_{H_2O/O_2}}$$

Where $\mathrm{E^0_{H_2O/O_2}}$ was corrected by the pH value employing the Nerst equation:

$$\mathrm{E^0_{H_2O/O_2}} = 1.229 - (0.059 \times \mathrm{pH})\ (\mathrm{V})\ \text{vs NHE at } 25℃$$

The geometrical area of the CP electrode was used to calculate all the current densities. The onset potentials were estimated from the intersection point between the tangent lines of the Faradaic current at 0.5 mA cm^{-2} and the non-Faradic current.

For measurements in non-aqueous media, a saturated calomel electrode was used as a reference electrode along with a Pt counter electrode. For the working electrode, a glassy carbon electrode was used and the sample was mechanically deposited on the electrode surface. The measurements were conducted in an electrolyte solution of 0.1 M $Bu^n_4NPF_6$ in acetonitrile. Before the measurement, the solution was purged with N_2 to remove oxygen and during the measurements, the solution was kept under an atmosphere of N_2. The cyclic voltammograms were recorded at a scan rate of 100 mV/s. The reported potentials were converted to the normal hydrogen electrode (NHE) reference scale using $\mathrm{E_{NHE}} = \mathrm{E_{Calomel}} + 0.244\ (V)$.

10.2 Syntheses

[Cl⊂Mn$^{III}_6$(tert-butyl-PO$_3$)$_8$(4-picoline)$_6$]Cl (4.1)

The procedure published in the literature was followed for the synthesis of this compound.[545] $MnCl_2 \cdot 2H_2O$ (0.162 g, 1.00 mmol), $KMnO_4$ (0.032 g, 0.20 mmol), *tert*-butyl phosphonic acid (0.136 g, 1.00 mmol) and 1,4-phenylenediacetic acid (0.193 g, 1.00 mmol) were combined in CH_3CN (25 mL) and sonicated for 2 minutes followed by the addition of 4-picoline (0.24 mL, 2.47 mmol). The solution was then stirred at room temperature for 5 hours. The dark brown/red solution was then filtered and the filtrate was then allowed to evaporate slowly. Dark red crystals were formed within a week which were isolated by filtration, washed with CH_3CN and air dried.

Yield: 40% (based on Mn). Elemental analysis ($C_{68}H_{114}Cl_2Mn_6N_6O_{24}P_8$): Calculated (%) – C 39.88, H 5.61, N 4.10; found (%) – C 39.22, H 5.63, N 3.91.

IR ($\bar{\vartheta}$/cm^{-1}): 2920 (b), 1622 (w), 1478 (w), 1146 (s), 1074 (w), 1022 (s), 812 (w), 804 (m), 724 (w), 662 (m).

[Mn$_6$(μ_3-O)$_2$((CH$_3$)$_3$CCO$_2$)$_{10}$((CH$_3$)$_2$NCHO)$_4$]·((CH$_3$)$_2$NCHO)·H$_2$O (6.1)

$Mn(CH_3COO)_2 \cdot 4H_2O$ (0.025 g, 0.10 mmol), $KMnO_4$ (0.063 g, 0.40 mmol) and pivalic acid (0.408 g, 4.00 mmol) were combined in CH_3CN (20 mL). After refluxing this solution for 30 minutes, phenylphosphonic acid (0.032 g, 0.20 mmol) was added. The solution was then refluxed again for 10 minutes and L(-)-proline (0.022 g, 0.20 mmol) was added. The resultant solution was refluxed again for 15 minutes. The light red coloured solution was then filtered and DMF (10 mL) was added to it. This solution was then boiled till it was reduced to 1/3rd of its original volume. This solution was then filtered and the filtrate was then allowed to evaporate slowly. Red crystals were obtained within one week which were isolated by filtration, washed with DMF and air dried.

Yield: ~10% (based on Mn).

IR ($\bar{\vartheta}$/cm^{-1}): 2930 (b), 1658 (m), 1594 (m), 1576 (m), 1528 (s), 1482 (s), 1408 (s), 1390 (m), 1372 (s), 1360 (s), 1226 (s), 1210 (wsh), 1104 (w), 1032 (w), 894 (w), 798 (w), 788 (w), 676 (w), 608 (s).

[Mn$_8$K$_2$(μ_3-O)$_4$(μ-OH)$_2$((CH$_3$)$_3$CCOO)$_{16}$(CH$_3$CN)$_2$]·CHCl$_3$ (6.2)

$KMnO_4$ (0.079 g, 0.50 mmol) and pivalic acid (0.408 g, 4.00 mmol) were added to 20 mL of CH_3CN. The solution was refluxed for 2.5 hours. To the hot solution, 8 mL of $CHCl_3$ was added and the resultant was stirred for 5 minutes. The brown/red solution was then filtered and the filtrate was then allowed to evaporate slowly. Dark red crystals were obtained within a day. The crystallization was found to be dependent on the humidity and temperature and small variation in the $CH_3CN/CHCl_3$ ratio can lead to good quality crystals. The crystals were washed with $CH_3CN/CHCl_3$ (20/10 mL) mixture and dried.

Yield: 32% (based on Mn). Elemental analysis ($C_{85}H_{153}Cl_3K_2Mn_8N_2O_{38}$): Calculated (%) – C 41.92, H 6.33, N 1.15; found (%) – C 41.29, H 6.23, N 0.65.

IR ($\bar{\vartheta}$/cm^{-1}): 2958 (mb), 1594 (m), 1572 (m), 1554 (m), 1526 (m), 1480 (m), 1458 (w), 1404 (m), 1368 (msh), 1356 (m), 1328 (m), 1220 (m), 1030 (w), 938 (w), 896 (w), 790 (w), 694 (s), 762 (w), 672 (w), 610 (s).

[$Mn_{12}(\mu_3\text{-}O)_{12}(C_6H_5C_6H_4CO_2)_{16}(H_2O)_4$]·solvent (6.3)

$KMnO_4$ (0.020 g, 0.25 mmol) and 4-biphenylcarboxylic acid (0.198 g, 1.00 mmol) were combined in CH_3CN (20 mL). The solution was refluxed for 2.5 hours. To the hot solution, 8 mL of $CHCl_3$ was added and the resultant was stirred for 5 minutes. The brown/red solution was then filtered and the filtrate was then allowed to evaporate slowly. Red crystals were obtained within one week which were isolated by manual separation, washed with $CH_3CN/CHCl_3$ (20/10 mL) mixture and air dried.

Yield: (few crystals) ~2% (based on Mn).

IR ($\bar{\vartheta}$/cm^{-1}): 3028 (wb), 1694 (w), 1606 (m), 1588 (m), 1572 (m), 1514 (mb), 1448 (w), 1386 (sb), 1180 (m), 1142 (w), 1106 (w), 1076 (w), 1020 (w), 1008 (m), 916 (w), 858 (m), 846 (msh), 790 (m), 744 (s), 694 (s), 644 (sb).

[$Mn^{II}_{12}(\mu_3\text{-}OH)_4((C_6H_5)PO_3)_4((CH_3)_3CCO_2)_{12}(DMSO)_6$]·solvent (7.1)

$Mn(CH_3COO)_2{\cdot}4H_2O$ (0.025 g, 0.10 mmol), $KMnO_4$ (0.063 g, 0.40 mmol) and pivalic acid (0.408 g, 4.00 mmol) were combined in CH_3CN (20 mL). After refluxing this solution for 30 minutes, phenylphosphonic acid (0.032 g, 0.20 mmol) was added. The solution was then refluxed again for 10 minutes and L(-)-proline (0.022 g, 0.20 mmol) was added. The resultant solution was refluxed again for 15 minutes. The light coloured solution was then filtered and DMSO (10 mL) was added to it. This solution was then boiled till it was reduced to 1/3rd of its original volume. This solution was then filtered and the filtrate was then allowed to evaporate slowly. Pale coloured crystals were obtained within one week which were isolated by filtration, washed with DMSO and air dried.

Yield: 20% (based on Mn). Elemental analysis ($C_{96}H_{164}Mn_{12}O_{46}P_4S_6$): Calculated (%) – C 38.06, H 5.46, N 0.00, S 6.35; found (%) – C 37.49, H 5.43, N 0.00, S 6.54.

IR ($\bar{\vartheta}$/cm^{-1}): 2954 (mb), 1590 (s), 1556 (msh), 1482 (m), 1418 (s), 1372 (m), 1358 (m), 1404 (m), 1318 (wb), 1228 (w), 1134 (w), 1096 (w), 1078 (m), 1068 (m), 1032 (m), 1000 (s), 970 (s), 954 (msh), 892 (w), 790 (w), 752 (w), 708 (m), 698 (m).

[$Mn_{15}(\mu_3\text{-}O)_4((CH_3)_3CCO_2)_{11}((CH_3)_3CCO_2H)(C_6H_5PO_3)_6(\mu\text{-}CH_3O)_6(\mu_3\text{-}CH_3O)_2(CH_3OH)_5$] (7.2)

$Mn(CH_3COO)_2{\cdot}4H_2O$ (0.025 g, 0.10 mmol), $KMnO_4$ (0.063 g, 0.40 mmol) and pivalic acid (0.204 g, 2.00 mmol) were combined in CH_3CN (15 mL). After refluxing this solution for 2 minutes,

phenylphosphonic acid (0.040 g, 0.25 mmol) was added. The solution was then refluxed again for 2 minutes and L(-)-proline (0.011 g, 0.10 mmol) was added. The resultant solution was refluxed again for 2 minutes after which CH_3OH (20 mL) was added to the solution and the solution was then refluxed for 2.5 hours. The dark brown/red solution was then filtered and the filtrate was then allowed to evaporate slowly. Small red crystals were obtained within one week which were isolated by manual separation, washed with CH_3CN/CH_3OH (15/20 mL) mixture and air dried.

Yield: (few crystals) < 1% (based on Mn).

IR ($\bar{\vartheta}/cm^{-1}$): 3446 (wb), 2964 (wb), 1594 (wb), 1556 (w), 1532 (wb), 1484 (m), 1460 (w), 1438 (w), 1416 (mb), 1366 (wsh), 1358 (w), 1226 (w), 1136 (m), 1140 (m), 1090 (s), 1072, (ssh), 1048 (m), 1026 (m), 980 (s), 934 (msh), 894 (w), 784 (w), 748 (m), 722 (m), 696 (s), 616 (sb).

$[Mn_{15}(\mu_3\text{-}O)_4((CH_3)_3CCO_2)_{7.15}(CH_3CO_2)_{4.85}(C_6H_5PO_3)_6(\mu\text{-}CH_3O)_6(\mu_3\text{-}CH_3O)_2(CH_3OH)_5]\cdot 2CH_3CN\cdot\ CH_3OH$ (7.3)

$Mn(CH_3COO)_2\cdot 4H_2O$ (0.125 g, 0.50 mmol), $KMnO_4$ (0.016 g, 0.10 mmol), pivalic acid (0.204 g, 2.00 mmol) and CH_3COOH (0.060 g, 1 mmol) were combined in CH_3CN (15 mL). After refluxing this solution for 2 minutes, phenylphosphonic acid (0.040 g, 0.25 mmol) was added. The solution was then refluxed again for 2 minutes and 2,6-pyridinemethanol (0.014 g, 0.10 mmol) was added. The resultant solution was refluxed again for 2 minutes after which CH_3OH (20 mL) was added to the solution and the solution was then refluxed for 2.5 hours. The dark brown/red solution was then filtered and the filtrate was then allowed to evaporate slowly. Dark needle-like crystals were obtained during the time period of one week which were isolated by manual separation, washed with CH_3CN/CH_3OH (15/20 mL) mixture and air dried.

Yield: 40% (based on Mn). Elemental analysis ($C_{88}H_{143}Mn_{15}O_{58}P_6$): Calculated (%) – C 33.67, H 4.59, N 0.00; found (%) – C 33.08, H 4.23, N 0.00.

IR ($\bar{\vartheta}/cm^{-1}$): 2958 (wb), 1612 (w), 1584 (s), 1554 (m), 1482 (s), 1456 (w), 1438 (w), 1402 (s), 1364 (ssh), 1354 (s), 1404 (m), 1224 (m), 1132 (m), 1068 (sb), 1078 (m), 1046 (sb), 1004 (s), 976 (s), 894 (w), 784 (w), 750 (m), 720 (m), 696 (m), 620 (ssh), 616 (s).

$[Mn_{14}(\mu_3\text{-}O)_4(\mu_3\text{-}OH)_2(\mu\text{-}CH_3O)_9(CH_3OH)_2(H_2O)_2((C_6H_5)PO_3)_3((CH_3)_3CCO_2)_{10}(CH_3CO_2)_3]$ (7.4)

$Mn(CH_3COO)_2\cdot 4H_2O$ (0.125 g, 0.50 mmol), $KMnO_4$ (0.016 g, 0.10 mmol) and pivalic acid (0.204 g, 2.00 mmol) were combined in CH_3CN (15 mL). After refluxing this solution for 2 minutes, phenylphosphonic acid (0.040 g, 0.25 mmol) was added. The solution was then refluxed again for 2 minutes and 2,6-pyridinemethanol (0.014 g, 0.10 mmol) was added. The resultant solution was refluxed again for 2 minutes after which CH_3OH (20 mL) was added to the solution and the solution was then refluxed for 2.5 hours. The dark brown/red solution was then filtered and the filtrate was

then allowed to evaporate slowly. Dark block-like red crystals were obtained within one week which were isolated by manual separation, washed with CH_3CN/CH_3OH (15/20 mL) mixture and air dried. Yield: (few crystals) < 2% (based on Mn).

IR ($\bar{\vartheta}/cm^{-1}$): 2962 (wb), 1582 (m), 1558 (s), 1538 (sb), 1482 (s), 1456 (m), 1408 (sb), 1374 (msh), 1360 (s), 1226 (m), 1138 (m), 1088 (m), 1048 (m), 1002 (w), 976 (mb), 938 (m), 894 (w), 784 (w), 750 (w), 718 (m), 696 (m), 652 (ssh), 614 (s).

$[Mn_{13}(\mu_3\text{-}O)_8((C_6H_5)PO_3)_4((CH_3)_3CCO_2)_{10}(\mu\text{-}CH_3O)_4(\mu\text{-}CH_3OH)_4]\cdot CH_3OH\cdot CH_3CN$ (7.5)

$Mn(CH_3COO)_2\cdot 4H_2O$ (0.125 g, 0.50 mmol), $KMnO_4$ (0.016 g, 0.10 mmol) and pivalic acid (0.408 g, 4.00 mmol) were combined in CH_3CN (15 mL). After refluxing this solution for 2 minutes, phenylphosphonic acid (0.040 g, 0.25 mmol) was added. The solution was then refluxed again for 2 minutes and 2,6-pyridinemethanol (0.014 g, 0.10 mmol) was added. The resultant solution was refluxed again for 2 minutes after which CH_3OH (20 mL) was added to the solution and the solution was then refluxed for 2.5 hours. The dark brown/red solution was then filtered and the filtrate was then allowed to evaporate slowly. Dark block-like red crystals were obtained during the time period of one week which were isolated by manual separation, washed with CH_3CN/CH_3OH (15/20 mL) mixture and air dried.

Yield: (few crystals) < 1% (based on Mn).

IR ($\bar{\vartheta}/cm^{-1}$): 2964 (wb), 1582 (w), 1558 (w), 1526 (wb), 1482 (m), 1462 (w), 1410 (msh), 1404 (m), 1372 (msh), 1358 (m), 1224 (m), 1136 (m), 1114 (w), 1048 (m), 1002 (w), 980 (w), 962 (m), 928 (m), 894 (w), 784 (w), 750 (m), 718 (m), 696 (m), 654 (ssh), 620 (s).

$[Mn_{12}Br_2(\mu_3\text{-}O)_4((CH_3)_3CPO_3)_{10}((CH_3)_3CPO_3H)_2((CH_3)C_5H_4N)_6(H_2O)_{10}]\cdot 2CH_3CN$ (8.1)

$MnBr_2\cdot 4H_2O$ (0.287 g, 1.00 mmol), $KMnO_4$ (0.032 g, 0.20 mmol) and *tert*-butyl phosphonic acid (0.136 g, 1.00 mmol) were combined in CH_3CN (25 mL) and sonicated for 2 minutes followed by the addition of 4-picoline (0.24 mL, 2.47 mmol). The solution was then stirred at room temperature for 5 hours. The dark brown/red solution was then filtered and the filtrate was then allowed to evaporate slowly. Small red crystals were formed in a day which were isolated by filtration, washed with CH_3CN and air dried.

Yield: 12% (based on Mn). Elemental analysis ($C_{84}H_{172}Br_2Mn_{12}O_{50}P_{12}$): Calculated (%) – C 30.98, H 5.32, N 2.58; found (%) – C 31.37, H 5.24, N 2.57.

IR ($\bar{\vartheta}/cm^{-1}$): 3412 (wb), 2948 (wb), 1624 (w), 1506 (w), 1478 (w), 1458 (w), 1392 (w), 1360 (w), 1220 (wb), 1140 (m), 1094 (m), 1068 (s), 1022 (s), 988 (ssh), 972 (s), 832 (m), 806 (m), 704 (m), 648 (msh), 642 (m), 618 (m).

Na[$Na_{0.4}Mn_{13}(\mu_4\text{-}O)_2(\mu_3\text{-}O)_4(\mu\text{-}O)_{0.4}(\mu\text{-}OH)_{1.6}((CH_3)_3CPO_3)_{10}$(4-picoline)$_4(\mu\text{-}CH_3O)_4(CH_3OH)_2$]

[$Mn_{13}(\mu_4\text{-}O)_2(\mu_3\text{-}O)_4(\mu\text{-}OH)_2((CH_3)_3CPO_3)_{10}((CH_3)_3CPO_3H)_2$(4-picoline)$_4(\mu\text{-}CH_3O)_4$]·5$CH_3OH$ (8.2)

$Mn(CH_3COO)_2{\cdot}4H_2O$ (0.125 g, 0.50 mmol), $KMnO_4$ (0.016 g, 0.10 mmol), *tert*-butyl phosphonic acid (0.069 g, 0.50 mmol) and NaI (0.075 g, 0.5 mmol) were combined in CH_3CN/CH_3OH (15/10 mL) mixture and sonicated for 2 minutes followed by the addition of 4-picoline (0.12 mL, 1.25 mmol). The solution was then stirred at room temperature for 5 hours. The dark brown/red solution was then filtered and the filtrate was then allowed to evaporate slowly. Small red crystals were formed in a day and were isolated by filtration, washed with CH_3CN/CH_3OH (15/10 mL) and air dried.

Yield: 18% (based on Mn).

IR ($\bar{\vartheta}/cm^{-1}$): 2948 (mb), 1618 (m), 1558 (w), 1502 (w), 1478 (m), 1456 (m), 1422 (w), 1392 (m), 1362 (m), 1204 (w), 1114 (s), 1066 (s), 1070 (m), 996 (s), 972 (s), 832 (s), 804 (s), 724 (m), 668 (s), 660 (ssh).

K[$K_2Mn_{13}(\mu_4\text{-}O)_2(\mu_3\text{-}O)_4(\mu\text{-}OH)_2((CH_3)_3CPO_3)_{10}((CH_3)_3CO_2)_2(\mu\text{-}CH_3O)_4(CH_3OH)_6$][$Mn_{13}(\mu_4\text{-}O)_2(\mu_3\text{-}O)_4(\mu\text{-}OH)_2((CH_3)_3CPO_3)_{10}((CH_3)_3CPO_3H)_2(\mu\text{-}CH_3O)_4(CH_3OH)_4$]·2$CH_3OH$ (8.3)

$Mn(CH_3COO)_2{\cdot}4H_2O$ (0.025 g, 0.10 mmol), $KMnO_4$ (0.063 g, 0.40 mmol), pivalic acid (0.102 g, 1.00 mmol) and *tert*-butyl phosphonic acid (0.069 g, 0.50 mmol) were combined in CH_3CN (25 mL) and refluxed. After refluxing this solution for 30 minutes, 2,6-pyridinemethanol (0.014 g, 0.10 mmol) was added. The resultant solution was then refluxed overnight. To the hot solution, CH_3OH (20 mL) was added and the resultant was stirred for 5 minutes. The red solution was then filtered and the filtrate was then allowed to evaporate slowly. Small red crystals were obtained within one week which were isolated by filtration, washed with CH_3CN/CH_3OH (15/20 mL) mixture and air dried.

Yield: 16% (based on Mn). Elemental analysis ($C_{114}H_{286}K_3Mn_{26}O_{104}P_{22}$): Calculated (%) – C 24.68, H 5.20, N 0.0; found (%) – C 24.51, H 4.54, N 0.00.

IR ($\bar{\vartheta}/cm^{-1}$): 2960 (mb), 1632 (wb), 1558 (w), 1478 (m), 1458 (m), 1394 (w), 1364 (w), 1202 (w), 1110 (s), 1060 (s), 994 (s), 960 (sb), 832 (s), 668 (s).

[$Mn_{13}Ca_2(\mu_4\text{-}O)_2(\mu_3\text{-}O)_6((CH_3)_3CPO_3)_{10}((C_6H_5)_2PO_2)_2((CH_3)_3CCO_2H)_2(\mu\text{-}CH_3O)_4(CH_3OH)_{5.15}$

($CH_3CN)_{0.85}$]·CH_3OH·CH_3CN (8.4)

$Mn(CH_3COO)_2{\cdot}4H_2O$ (0.025 g, 0.10 mmol), $KMnO_4$ (0.063 g, 0.40 mmol), pivalic acid (0.408 g, 4.00 mmol) and $Ca(CH_3COO)_2$ (0.069 g, 0.5 mmol) were combined in CH_3CN (20 mL) and refluxed for 5 minutes. Diphenylphosphinic acid (0.109 g, 0.5 mmol) was added to the solution which was then refluxed again for 5 minutes. *tert*-Butyl phosphonic acid (0.069 g, 0.50 mmol) was then added to the solution which was again refluxed for 5 minutes. To this solution, CH_3OH (20 mL) was added and the resultant was refluxed for 2.5 hours. The red solution was then filtered and the filtrate was

then allowed to evaporate slowly. Small red crystals were obtained within one week which were isolated by manual separation, washed with CH_3CN/CH_3OH (10/10 mL) mixture and air dried.
Yield: (few crystals) < 2% (based on Mn).
IR ($\bar{\vartheta}$/cm^{-1}): 2950 (mb), 1478 (m), 1456 (w), 1440 (w), 1414 (w), 1394 (w), 1362 (w), 1204 (w), 1120 (msh), 1102 (m), 1042 (sh), 1004 (ssh), 972 (s), 832 (m), 750 (m), 726 (m), 698 (m), 668 (s).

[$Mn_{15}Ca_2(\mu_4\text{-}O)_4(\mu_3\text{-}O)_2(\mu_3\text{-}OH)_2((CH_3)_3CPO_3)_8((C_6H_5)_2PO_2)_2((CH_3)_3CCO_2)_4(CH_3CO_2)_2(\mu\text{-}CH_3O)_8(CH_3OH)_2$]·$2CH_3OH$·$2CH_3CN$ (8.5)

$Mn(CH_3COO)_2{\cdot}4H_2O$ (0.125 g, 0.50 mmol), $KMnO_4$ (0.016 g, 0.10 mmol), pivalic acid (0.408 g, 4.00 mmol) and $Ca(CH_3COO)_2$ (0.069 g, 0.5 mmol) were combined in CH_3CN (20 mL) and refluxed for 5 minutes. Diphenylphosphinic acid (0.109 g, 0.5 mmol) was added to the solution which was then refluxed again for 5 minutes. *tert*-Butyl phosphonic acid (0.069 g, 0.50 mmol) was then added to the solution which was again refluxed for 5 minutes. To this solution, CH_3OH (20 mL) was added and the resultant was refluxed for 2.5 hours. The red solution was then filtered and the filtrate was then allowed to evaporate slowly. Small red crystals were obtained within one week which were isolated by filtration, washed with CH_3CN/CH_3OH (10/10 mL) mixture and air dried.
Yield: 12% (based on Mn).
IR ($\bar{\vartheta}$/cm^{-1}): 2952 (mb), 1586 (w), 1564 (w), 1478 (m), 1458 (w), 1438 (w), 1410 (w), 1396 (w), 1362 (w), 1220 (w), 1204 (w), 1126 (msh), 1106 (m), 1036 (s), 998 (ssh), 972 (s), 832 (m), 784 (w), 752 (m), 726 (m), 698 (m), 668 (s).

11 Bibliography

1. Global Energy Statistical Yearbook, https://www.enerdata.net/publications/world-energy-statistics-supply-and-demand.html, (accessed 22 October, 2019).
2. N. S. Lewis and D. G. Nocera, *Proc. Natl. Acad. Sci. U.S.A.*, 2006, **103**, 15729-15735.
3. Q. Zhang, E. Uchaker, S. L. Candelaria and G. Cao, *Chem. Soc. Rev.*, 2013, **42**, 3127-3171.
4. M. S. Dresselhaus and I. L. Thomas, *Nature*, 2001, **414**, 332-337.
5. M. M. Abu-Khader, *Prog. Nucl. Energy*, 2009, **51**, 225-235.
6. D. S. Sholl and R. P. Lively, *Nature*, 2016, **532**, 435-437.
7. D. MacKay, *Sustainable Energy - without the hot air*, UIT Cambridge, Cambridge, 2008.
8. M. J. Goodfellow, H. R. Williams and A. Azapagic, *Energy Policy*, 2011, **39**, 6199-6210.
9. C. McCombie and M. Jefferson, *Energy Policy*, 2016, **96**, 758-769.
10. N. T. Rempe, *Prog. Nucl. Energy*, 2007, **49**, 365-374.
11. L. Rodriguez-Penalonga and B. Y. M. Soria, *Energies*, 2017, **10**, 1235.
12. J. Schröder, N. Rossignol and M. Van Oudheusden, *Saf. Sci.*, 2016, **85**, 258-265.
13. I. Dincer and C. Acar, *Int. J. Energy Res.*, 2015, **39**, 585-606.
14. C. D. Hanning and A. Evans, *BMJ*, 2012, **344**, e1527.
15. A. Ansar, B. Flyvbjerg, A. Budzier and D. Lunn, *Energy Policy*, 2014, **69**, 43-56.
16. O. Ellabban, H. Abu-Rub and F. Blaabjerg, *Renew. Sust. Energ. Rev.*, 2014, **39**, 748-764.
17. M. Thirugnanasambandam, S. Iniyan and R. Goic, *Renew. Sust. Energ. Rev.*, 2010, **14**, 312-322.
18. N. L. Panwar, S. C. Kaushik and S. Kothari, *Renew. Sust. Energ. Rev.*, 2011, **15**, 1513-1524.
19. D. Parra, M. Swierczynski, D. I. Stroe, S. A. Norman, A. Abdon, J. Worlitschek, T. O'Doherty, L. Rodrigues, M. Gillott, X. Zhang, C. Bauer and M. K. Patel, *Renew. Sust. Energ. Rev.*, 2017, **79**, 730-749.
20. H. Chen, T. N. Cong, W. Yang, C. Tan, Y. Li and Y. Ding, *Prog. Nat. Sci.*, 2009, **19**, 291-312.
21. G. L. Soloveichik, *Annu. Rev. Chem. Biomol. Eng*, 2011, **2**, 503-527.
22. S. Vazquez, S. M. Lukic, E. Galvan, L. G. Franquelo and J. M. Carrasco, *IEEE Trans. Ind. Electro*, 2010, **57**, 3881-3895.
23. B. B. McKeon, J. Furukawa and S. Fenstermacher, *Proc. IEEE*, 2014, **102**, 951-963.
24. B. Scrosati and J. Garche, *J. Power Sources*, 2010, **195**, 2419-2430.
25. T. Xu, W. Wang, M. L. Gordin, D. Wang and D. Choi, *JOM*, 2010, **62**, 24-30.
26. J. B. Goodenough and K.-S. Park, *J. Am. Chem. Soc.*, 2013, **135**, 1167-1176.
27. Y. Umena, K. Kawakami, J. R. Shen and N. Kamiya, *Nature*, 2011, **473**, 55-60.
28. N. N. Greenwood and A. Earnshaw, in *Chemistry of the Elements (Second Edition)*, Butterworth-Heinemann, Oxford, 1997, ch. 4, pp. 68-106.

29. C. Fabjan, J. Garche, B. Harrer, L. Jörissen, C. Kolbeck, F. Philippi, G. Tomazic and F. Wagner, *Electrochim. Acta*, 2001, **47**, 825-831.
30. A. Z. Weber, M. M. Mench, J. P. Meyers, P. N. Ross, J. T. Gostick and Q. Liu, *J. Appl. Electrochem.*, 2011, **41**, 1137.
31. J. O. Abe, A. P. I. Popoola, E. Ajenifuja and O. M. Popoola, *Int. J. Hydrogen Energy*, 2019, **44**, 15072-15086.
32. U. Bossel, *Proc. IEEE*, 2006, **94**, 1826-1837.
33. O. V. Marchenko and S. V. Solomin, *Int. J. Hydrogen Energy*, 2015, **40**, 3801-3805.
34. R. Shinnar, *Technol. Soc.*, 2003, **25**, 455-476.
35. N. A. A. Rusman and M. Dahari, *Int. J. Hydrogen Energy*, 2016, **41**, 12108-12126.
36. U. B. Demirci, *Int. J. Hydrogen Energy*, 2017, **42**, 9978-10013.
37. A. Grahame and K.-F. Aguey-Zinsou, *Inorganics*, 2018, **6**, 106-143.
38. A. J. Bard and M. A. Fox, *Acc. Chem. Res.*, 1995, **28**, 141-145.
39. S. Uemiya, *Top. Catal.*, 2004, **29**, 79-84.
40. A. Haryanto, S. Fernando, N. Murali and S. Adhikari, *Energ. Fuel*, 2005, **19**, 2098-2106.
41. T. L. LeValley, A. R. Richard and M. Fan, *Int. J. Hydrogen Energy*, 2014, **39**, 16983-17000.
42. M. Mohamedali, A. Henni and H. Ibrahim, in *Hydrogen Production Technologies*, Scrivener Publishing LLC, 2017, DOI: 10.1002/9781119283676.ch1, pp. 1-76.
43. B. M. Hunter, H. B. Gray and A. M. Muller, *Chem. Rev.*, 2016, **116**, 14120-14136.
44. M. D. Kärkäs, O. Verho, E. V. Johnston and B. Åkermark, *Chem. Rev.*, 2014, **114**, 11863-12001.
45. J. R. Galán-Mascarós, *ChemElectroChem*, 2015, **2**, 37-50.
46. V. Krewald, M. Retegan and D. A. Pantazis, *Solar Energy for Fuels*, 2016, **371**, 23-48.
47. M. Perez-Navarro, F. Neese, W. Lubitz, D. A. Pantazis and N. Cox, *Curr. Opin. Chem. Biol.*, 2016, **31**, 113-119.
48. J. P. McEvoy and G. W. Brudvig, *Chem. Rev.*, 2006, **106**, 4455-4483.
49. H. Dau and M. Haumann, *Coord. Chem. Rev.*, 2008, **252**, 273-295.
50. H. Dau and I. Zaharieva, *Acc. Chem. Res.*, 2009, **42**, 1861-1870.
51. J. Barber, *Chem. Soc. Rev.*, 2009, **38**, 185-196.
52. J. Yano and V. Yachandra, *Chem. Rev.*, 2014, **114**, 4175-4205.
53. C. Tommos and G. T. Babcock, *Biochim. Biophys. Acta, Bioenerg.*, 2000, **1458**, 199-219.
54. G. C. Dismukes, R. Brimblecombe, G. A. N. Felton, R. S. Pryadun, J. E. Sheats, L. Spiccia and G. F. Swiegers, *Acc. Chem. Res.*, 2009, **42**, 1935-1943.
55. K. H. Rhee, E. P. Morriss, J. Barber and W. Kuhlbrandt, *Nature*, 1998, **396**, 283-286.
56. A. Zouni, H. T. Witt, J. Kern, P. Fromme, N. Krauss, W. Saenger and P. Orth, *Nature*, 2001, **409**, 739-743.

57. K. N. Ferreira, T. M. Iverson, K. Maghlaoui, J. Barber and S. Iwata, *Science*, 2004, **303**, 1831-1838.
58. M. Suga, F. Akita, K. Hirata, G. Ueno, H. Murakami, Y. Nakajima, T. Shimizu, K. Yamashita, M. Yamamoto, H. Ago and J. R. Shen, *Nature*, 2015, **517**, 99-103.
59. B. Kok, B. Forbush and M. Mcgloin, *Photochem. Photobiol.*, 1970, **11**, 457-475.
60. H. Isobe, M. Shoji, S. Yamanaka, H. Mino, Y. Umena, K. Kawakami, N. Kamiya, J. R. Shen and K. Yamaguchi, *Phys. Chem. Chem. Phys.*, 2014, **16**, 11911-11923.
61. P. E. M. Siegbahn, *Phys. Chem. Chem. Phys.*, 2014, **16**, 11893-11900.
62. V. Krewald, M. Retegan, N. Cox, J. Messinger, W. Lubitz, S. DeBeer, F. Neese and D. A. Pantazis, *Chem. Sci.*, 2015, **6**, 1676-1695.
63. W. Ames, D. A. Pantazis, V. Krewald, N. Cox, J. Messinger, W. Lubitz and F. Neese, *J. Am. Chem. Soc.*, 2011, **133**, 19743-19757.
64. A. Klauss, M. Haumann and H. Dau, *Proc. Natl. Acad. Sci. U.S.A.*, 2012, **109**, 16035-16040.
65. H. Dau and M. Haumann, *Biochim. Biophys. Acta, Bioenerg.*, 2007, **1767**, 472-483.
66. A. Klauss, M. Haumann and H. Dau, *J. Phys. Chem. B*, 2015, **119**, 2677-2689.
67. J. Barber, P. E. M. Siegbahn, D. Nocera, H. Dau, F. Armstrong and P. Rich, *Philos. Trans. R. Soc. London, Ser. B*, 2008, **363**, 1228-1228.
68. P. E. M. Siegbahn, *Chem.: Eur. J*, 2006, **12**, 9217-9227.
69. H. Nilsson, F. Rappaport, A. Boussac and J. Messinger, *Nat. Commun.*, 2014, **5**, 4305.
70. Y. Guo, H. Li, L.-L. He, D.-X. Zhao, L.-D. Gong and Z.-Z. Yang, *Phys. Chem. Chem. Phys.*, 2017, **19**, 13909-13923.
71. J. G. Metz, P. J. Nixon, M. Rogner, G. W. Brudvig and B. A. Diner, *Biochemistry*, 1989, **28**, 6960-6969.
72. I. Vass and S. Styring, *Biochemistry*, 1991, **30**, 830-839.
73. K. G. V. Havelius and S. Styring, *Biochemistry*, 2007, **46**, 7865-7874.
74. A. Zavafer, M. H. Cheah, W. Hillier, W. S. Chow and S. Takahashi, *Sci. Rep.*, 2015, **5**, 16363.
75. S. V. Baranov, G. M. Ananyev, V. V. Klimov and G. C. Dismukes, *Biochemistry*, 2000, **39**, 6060-6065.
76. C.-I. Lee, K. V. Lakshmi and G. W. Brudvig, *Biochemistry*, 2007, **46**, 3211-3223.
77. J. P. McEvoy and G. W. Brudvig, *Phys. Chem. Chem. Phys.*, 2004, **6**, 4754-4763.
78. D. Bovi, D. Narzi and L. Guidoni, *Angew. Chem. Int. Ed.*, 2013, **52**, 11744-11749.
79. M. Retegan, N. Cox, W. Lubitz, F. Neese and D. A. Pantazis, *Phys. Chem. Chem. Phys.*, 2014, **16**, 11901-11910.
80. T. Lohmiller, N. Cox, J. H. Su, J. Messinger and W. Lubitz, *J. Biol. Chem.*, 2012, **287**, 24721-24733.
81. D. F. Ghanotakis, G. T. Babcock and C. F. Yocum, *FEBS Lett.*, 1984, **167**, 127-130.

82. G. W. Brudvig, *Philos. Trans. R. Soc. London, Ser. B*, 2008, **363**, 1211-1218.

83. J. S. Vrettos, D. A. Stone and G. W. Brudvig, *Biochemistry*, 2001, **40**, 7937-7945.

84. A. Boussac and A. W. Rutherford, *Biochemistry*, 1988, **27**, 3476-3483.

85. A. Boussac, F. Rappaport, P. Carrier, J. M. Verbavatz, R. Gobin, D. Kirilovsky, A. W. Rutherford and M. Sugiura, *J. Biol. Chem.*, 2004, **279**, 22809-22819.

86. N. Ishida, M. Sugiura, F. Rappaport, T. L. Lai, A. W. Rutherford and A. Boussac, *J. Biol. Chem.*, 2008, **283**, 13330-13340.

87. E. Y. Tsui and T. Agapie, *Proc. Natl. Acad. Sci. U.S.A.*, 2013, **110**, 10084-10088.

88. E. Y. Tsui, J. S. Kanady and T. Agapie, *Inorg. Chem.*, 2013, **52**, 13833-13848.

89. E. Y. Tsui, R. Tran, J. Yano and T. Agapie, *Nat. Chem.*, 2013, **5**, 293.

90. M. Stebler, A. Ludi and H. B. Buergi, *Inorg. Chem.*, 1986, **25**, 4743-4750.

91. J. E. Sarneski, M. Didiuk, H. H. Thorp, R. H. Crabtree, G. W. Brudvig, J. W. Faller and G. K. Schulte, *Inorg. Chem.*, 1991, **30**, 2833-2835.

92. M.-N. Collomb, A. Deronzier, A. l. Richardot and J. Pe'caut, *New J. Chem.*, 1999, **23**, 351-354.

93. J. Limburg, J. S. Vrettos, L. M. Liable-Sands, A. L. Rheingold, R. H. Crabtree and G. W. Brudvig, *Science*, 1999, **283**, 1524-1527.

94. J. D. Blakemore, R. H. Crabtree and G. W. Brudvig, *Chem. Rev.*, 2015, **115**, 12974-13005.

95. D. N. Hendrickson, G. Christou, E. A. Schmitt, E. Libby, J. S. Bashkin, S. Y. Wang, H. L. Tsai, J. B. Vincent, P. D. W. Boyd, J. C. Huffman, K. Folting, Q. Y. Li and W. E. Streib, *J. Am. Chem. Soc.*, 1992, **114**, 2455-2471.

96. S. Y. Wang, H. L. Tsai, E. Libby, K. Folting, W. E. Streib, D. N. Hendrickson and G. Christou, *Inorg. Chem.*, 1996, **35**, 7578-7589.

97. W. F. Ruettinger, C. Campana and G. C. Dismukes, *J. Am. Chem. Soc.*, 1997, **119**, 6670-6671.

98. M. Yagi, K. V. Wolf, P. J. Baesjou, S. L. Bernasek and G. C. Dismukes, *Angew. Chem. Int. Ed.*, 2001, **40**, 2925-2928.

99. R. Brimblecombe, G. F. Swiegers, G. C. Dismukes and L. Spiccia, *Angew. Chem. Int. Ed.*, 2008, **47**, 7335-7338.

100. P. L. Feng, C. C. Beedle, C. Koo, W. Wernsdorfer, M. Nakano, S. Hill and D. N. Hendrickson, *Inorg. Chem.*, 2008, **47**, 3188-3204.

101. R. Brimblecombe, A. Koo, G. C. Dismukes, G. F. Swiegers and L. Spiccia, *J. Am. Chem. Soc.*, 2010, **132**, 2892-2894.

102. R. Al-Oweini, A. Sartorel, B. S. Bassil, M. Natali, S. Berardi, F. Scandola, U. Kortz and M. Bonchio, *Angew. Chem. Int. Ed.*, 2014, **53**, 11182-11185.

103. B. Schwarz, J. Forster, M. K. Goetz, D. Yucel, C. Berger, T. Jacob and C. Streb, *Angew. Chem. Int. Ed.*, 2016, **55**, 6329-6333.

104. G. Maayan, N. Gluz and G. Christou, *Nat. Catal.*, 2018, **1**, 48-54.

105. T. Ghosh and G. Maayan, *Angew. Chem. Int. Ed.*, 2019, **58**, 2785-2790.

106. R. K. Hocking, R. Brimblecombe, L.-Y. Chang, A. Singh, M. H. Cheah, C. Glover, W. H. Casey and L. Spiccia, *Nat. Chem.*, 2011, **3**, 461-466.

107. K. J. Young, Y. Gao and G. W. Brudvig, *Aust. J. Chem.*, 2011, **64**, 1221-1228.

108. G. Berggren, A. Thapper, P. Huang, P. Kurz, L. Eriksson, S. Styring and M. F. Anderlund, *Dalton Trans.*, 2009, DOI: 10.1039/B906175D, 10044-10054.

109. H. Chen, J. W. Faller, R. H. Crabtree and G. W. Brudvig, *J. Am. Chem. Soc.*, 2004, **126**, 7345-7349.

110. Y. L. Gao, R. H. Crabtree and G. W. Brudvig, *Inorg. Chem.*, 2012, **51**, 4043-4050.

111. T. Lis, *Acta Crystallogr. B*, 1980, **36**, 2042-2046.

112. P. D. W. Boyd, Q. Li, J. B. Vincent, K. Folting, H. R. Chang, W. E. Streib, J. C. Huffman, G. Christou and D. N. Hendrickson, *J. Am. Chem. Soc.*, 1988, **110**, 8537-8539.

113. R. Sessoli, H. L. Tsai, A. R. Schake, S. Wang, J. B. Vincent, K. Folting, D. Gatteschi, G. Christou and D. N. Hendrickson, *J. Am. Chem. Soc.*, 1993, **115**, 1804-1816.

114. Y. Yan, J. S. Lee and D. A. Ruddy, *Inorg. Chem.*, 2015, **54**, 4550-4555.

115. W. A. A. Arafa, M. D. Kärkäs, B.-L. Lee, T. Åkermark, R.-Z. Liao, H.-M. Berends, J. Messinger, P. E. M. Siegbahn and B. Åkermark, *Phys. Chem. Chem. Phys.*, 2014, **16**, 11950-11964.

116. C.-Y. Yeh, C. J. Chang and D. G. Nocera, *J. Am. Chem. Soc.*, 2001, **123**, 1513-1514.

117. W. Lai, R. Cao, G. Dong, S. Shaik, J. Yao and H. Chen, *J. Phys. Chem. Lett.*, 2012, **3**, 2315-2319.

118. M. Z. Ertem and C. J. Cramer, *Dalton Trans.*, 2012, **41**, 12213-12219.

119. R. McGuire Jr, D. K. Dogutan, T. S. Teets, J. Suntivich, Y. Shao-Horn and D. G. Nocera, *Chem. Sci.*, 2010, **1**, 411-414.

120. Y. Lin, K.-H. Wu, Q. Lu, Q. Gu, L. Zhang, B. Zhang, D. Su, M. Plodinec, R. Schlögl and S. Heumann, *J. Am. Chem. Soc.*, 2018, **140**, 14717-14724.

121. T. Wada, K. Tsuge and K. Tanaka, *Inorg. Chem.*, 2001, **40**, 329-337.

122. S. M. Gorun, R. T. Stibrany and A. Lillo, *Inorg. Chem.*, 1998, **37**, 836-837.

123. I. G. de Muro, M. Insausti, L. Lezama, M. K. Urtiaga, M. I. Arriortua and T. Rojo, *J. Chem. Soc., Dalton Trans.*, 2000, DOI: 10.1039/B005661H, 3360-3364.

124. A. Mishra, W. Wernsdorfer, K. A. Abboud and G. Christou, *Chem. Commun.*, 2005, DOI: 10.1039/B413680B, 54-56.

125. I. J. Hewitt, J.-K. Tang, N. T. Madhu, R. Clérac, G. Buth, C. E. Anson and A. K. Powell, *Chem. Commun.*, 2006, DOI: 10.1039/B518026K, 2650-2652.

126. A. Mishra, J. Yano, Y. Pushkar, V. K. Yachandra, K. A. Abboud and G. Christou, *Chem. Commun.*, 2007, DOI: 10.1039/B701355H, 1538-1540.

127. L. B. Jerzykiewicz, J. Utko, M. Duczmal and P. Sobota, *Dalton Trans.*, 2007, DOI: 10.1039/B613320G, 825-826.

128. E. S. Koumousi, S. Mukherjee, C. M. Beavers, S. J. Teat, G. Christou and T. C. Stamatatos, *Chem. Commun.*, 2011, **47**, 11128-11130.

129. S. Nayak, H. P. Nayek, S. Dehnen, A. K. Powell and J. Reedijk, *Dalton Trans.*, 2011, **40**, 2699-2702.

130. Y. J. Park, J. W. Ziller and A. S. Borovik, *J. Am. Chem. Soc.*, 2011, **133**, 9258-9261.

131. J. S. Kanady, E. Y. Tsui, M. W. Day and T. Agapie, *Science*, 2011, **333**, 733-736.

132. S. Mukherjee, J. A. Stull, J. Yano, T. C. Stamatatos, K. Pringouri, T. A. Stich, K. A. Abboud, R. D. Britt, V. K. Yachandra and G. Christou, *Proc. Natl. Acad. Sci. U.S.A.*, 2012, **109**, 2257-2262.

133. J. S. Kanady, P. H. Lin, K. M. Carsch, R. J. Nielsen, M. K. Takase, W. A. Goddard and T. Agapie, *J. Am. Chem. Soc.*, 2014, **136**, 14373-14376.

134. C. Chen, C. Zhang, H. Dong and J. Zhao, *Dalton Trans.*, 2015, **44**, 4431-4435.

135. C. X. Zhang, C. H. Chen, H. X. Dong, J. R. Shen, H. Dau and J. Q. Zhao, *Science*, 2015, **348**, 690-693.

136. Y. Mousazade, M. R. Mohammadi, P. Chernev, R. Bikas, R. Bagheri, Z. L. Song, T. Lis, H. Dau and M. M. Najafpour, *Catal. Sci. Technol.*, 2018, **8**, 4390-4398.

137. C. Chen, Y. Chen, R. Yao, Y. Li and C. Zhang, *Angew. Chem. Int. Ed.*, 2019, **58**, 3939-3942.

138. S. Mauthe, I. Fleischer, T. M. Bernhardt, S. M. Lang, R. N. Barnett and U. Landman, *Angew. Chem.*, 2019, **131**, 8592-8597.

139. M. Shoji, H. Isobe, T. Nakajima and K. Yamaguchi, *Chem. Phys. Lett.*, 2015, **640**, 23-30.

140. Y. Yu, C. Hu, X. H. Liu and J. Y. Wang, *Chembiochem*, 2015, **16**, 1981-1983.

141. L. C. Sun, *Science*, 2015, **348**, 635-636.

142. E. H. Yu, X. Wang, U. Krewer, L. Li and K. Scott, *Energy Environ. Sci.*, 2012, **5**, 5668-5680.

143. A. Harriman, *Philos. Trans. R. Soc. A*, 2013, **371**, 20110415.

144. Y. Lee, J. Suntivich, K. J. May, E. E. Perry and Y. Shao-Horn, *J. Phys. Chem. Lett.*, 2012, **3**, 399-404.

145. L. C. Seitz, C. F. Dickens, K. Nishio, Y. Hikita, J. Montoya, A. Doyle, C. Kirk, A. Vojvodic, H. Y. Hwang, J. K. Norskov and T. F. Jaramillo, *Science*, 2016, **353**, 1011-1014.

146. E. A. Paoli, F. Masini, R. Frydendal, D. Deiana, C. Schlaup, M. Malizia, T. W. Hansen, S. Horch, I. E. L. Stephens and I. Chorkendorff, *Chem. Sci.*, 2015, **6**, 190-196.

147. A. Harriman, I. J. Pickering, J. M. Thomas and P. A. Christensen, *J. Chem. Soc., Faraday Trans.1*, 1988, **84**, 2795-2806.

148. C. C. L. McCrory, S. Jung, I. M. Ferrer, S. M. Chatman, J. C. Peters and T. F. Jaramillo, *J. Am. Chem. Soc.*, 2015, **137**, 4347-4357.

149. B. Zhang, X. L. Zheng, O. Voznyy, R. Comin, M. Bajdich, M. Garcia-Melchor, L. L. Han, J. X. Xu, M. Liu, L. R. Zheng, F. P. G. de Arquer, C. T. Dinh, F. J. Fan, M. J. Yuan, E. Yassitepe, N. Chen, T. Regier, P. F. Liu, Y. H. Li, P. De Luna, A. Janmohamed, H. L. L. Xin, H. G. Yang, A. Vojvodic and E. H. Sargent, *Science*, 2016, **352**, 333-337.

150. J. Suntivich, K. J. May, H. A. Gasteiger, J. B. Goodenough and Y. Shao-Horn, *Science*, 2011, **334**, 1383-1385.

151. A. Grimaud, K. J. May, C. E. Carlton, Y.-L. Lee, M. Risch, W. T. Hong, J. Zhou and Y. Shao-Horn, *Nat. Commun.*, 2013, **4**, 2439.

152. E. Gülzow, *J. Power Sources*, 1996, **61**, 99-104.

153. I. Roger, M. A. Shipman and M. D. Symes, *Nat. Rev. Chem.*, 2017, **1**, 0003.

154. D. M. Robinson, Y. B. Go, M. Mui, G. Gardner, Z. Zhang, D. Mastrogiovanni, E. Garfunkel, J. Li, M. Greenblatt and G. C. Dismukes, *J. Am. Chem. Soc.*, 2013, **135**, 3494-3501.

155. R. Pokhrel, M. K. Goetz, S. E. Shaner, X. Wu and S. S. Stahl, *J. Am. Chem. Soc.*, 2015, **137**, 8384-8387.

156. M. Huynh, D. K. Bediako and D. G. Nocera, *J. Am. Chem. Soc.*, 2014, **136**, 6002-6010.

157. T. Takashima, K. Hashimoto and R. Nakamura, *J. Am. Chem. Soc.*, 2012, **134**, 1519-1527.

158. M. Mahdi Najafpour, D. Jafarian Sedigh, S. Maedeh Hosseini and I. Zaharieva, *Inorg. Chem.*, 2016, **55**, 8827-8832.

159. Z. Morgan Chan, D. A. Kitchaev, J. Nelson Weker, C. Schnedermann, K. Lim, G. Ceder, W. Tumas, M. F. Toney and D. G. Nocera, *Proc. Natl. Acad. Sci. U.S.A.*, 2018, **115**, E5261-E5268.

160. I. Zaharieva, P. Chernev, M. Risch, K. Klingan, M. Kohlhoff, A. Fischer and H. Dau, *Energy Environ. Sci.*, 2012, **5**, 7081-7089.

161. Y. Gorlin, B. Lassalle-Kaiser, J. D. Benck, S. Gul, S. M. Webb, V. K. Yachandra, J. Yano and T. F. Jaramillo, *J. Am. Chem. Soc.*, 2013, **135**, 8525-8534.

162. M. M. Najafpour, B. Haghighi, D. J. Sedigh and M. Z. Ghobadi, *Dalton Trans.*, 2013, **42**, 16683-16686.

163. H. Seo, K. H. Cho, H. Ha, S. Park, J. S. Hong, K. Jin and K. T. Nam, *J. Korean Ceram. Soc*, 2017, **54**, 1-8.

164. B. Zhang, H. Chen, Q. Daniel, B. Philippe, F. Yu, M. Valvo, Y. Li, R. B. Ambre, P. Zhang, F. Li, H. Rensmo and L. Sun, *ACS Catal.*, 2017, **7**, 6311-6322.

165. J. Wei, Y. Liu, Y. Ding, C. Luo, X. Du and J. Lin, *Chem. Commun.*, 2014, **50**, 11938-11941.

166. W. T. Osowiecki, S. W. Sheehan, K. J. Young, A. C. Durrell, B. Q. Mercado and G. W. Brudvig, *Dalton Trans.*, 2015, **44**, 16873-16881.

167. M. Huynh, C. Shi, S. J. L. Billinge and D. G. Nocera, *J. Am. Chem. Soc.*, 2015, **137**, 14887-14904.

168. C.-H. Kuo, I. M. Mosa, A. S. Poyraz, S. Biswas, A. M. El-Sawy, W. Song, Z. Luo, S.-Y. Chen, J. F. Rusling, J. He and S. L. Suib, *ACS Catal.*, 2015, **5**, 1693-1699.

169. C. E. Frey, F. Kwok, D. Gonzáles-Flores, J. Ohms, K. A. Cooley, H. Dau, I. Zaharieva, T. N. Walter, H. Simchi, S. E. Mohney and P. Kurz, *Sustain. Energy Fuels*, 2017, **1**, 1162-1170.

170. K. Izumiya, E. Akiyama, H. Habazaki, N. Kumagai, A. Kawashima and K. Hashimoto, *Electrochim. Acta*, 1998, **43**, 3303-3312.

171. K. Fujimura, T. Matsui, K. Izumiya, N. Kumagai, E. Akiyama, H. Habazaki, A. Kawashima, K. Asami and K. Hashimoto, *Mater. Sci. Eng. A*, 1999, **267**, 254-259.

172. M. Kölbach, S. Fiechter, R. van de Krol and P. Bogdanoff, *Catal. Today*, 2017, **290**, 2-9.

173. F. Zhou, C. McDonnell-Worth, H. Li, J. Li, L. Spiccia and D. R. Macfarlane, *J. Mater. Chem. A*, 2015, **3**, 16642-16652.

174. J. S. Mondschein, J. F. Callejas, C. G. Read, J. Y. C. Chen, C. F. Holder, C. K. Badding and R. E. Schaak, *Chem. Mater.*, 2017, **29**, 950-957.

175. J. B. Gerken, J. G. McAlpin, J. Y. C. Chen, M. L. Rigsby, W. H. Casey, R. D. Britt and S. S. Stahl, *J. Am. Chem. Soc.*, 2011, **133**, 14431-14442.

176. M. W. Kanan and D. G. Nocera, *Science*, 2008, **321**, 1072-1075.

177. D. A. Lutterman, Y. Surendranath and D. G. Nocera, *J. Am. Chem. Soc.*, 2009, **131**, 3838-3839.

178. M. W. Kanan, J. Yano, Y. Surendranath, M. Dincă, V. K. Yachandra and D. G. Nocera, *J. Am. Chem. Soc.*, 2010, **132**, 13692-13701.

179. Y. Surendranath, M. Dincă and D. G. Nocera, *J. Am. Chem. Soc.*, 2009, **131**, 2615-2620.

180. J. He, Y. Peng, Z. Sun, W. Cheng, Q. Liu, Y. Feng, Y. Jiang, F. Hu, Z. Pan, Q. Bian and S. Wei, *Electrochim. Acta*, 2014, **119**, 64-71.

181. Y. Surendranath, M. W. Kanan and D. G. Nocera, *J. Am. Chem. Soc.*, 2010, **132**, 16501-16509.

182. A. J. Esswein, Y. Surendranath, S. Y. Reece and D. G. Nocera, *Energy Environ. Sci.*, 2011, **4**, 499-504.

183. R. Zhang, Y.-C. Zhang, L. Pan, G.-Q. Shen, N. Mahmood, Y.-H. Ma, Y. Shi, W. Jia, L. Wang, X. Zhang, W. Xu and J.-J. Zou, *ACS Catal.*, 2018, **8**, 3803-3811.

184. M. S. Burke, L. J. Enman, A. S. Batchellor, S. Zou and S. W. Boettcher, *Chem. Mater.*, 2015, **27**, 7549-7558.

185. J. B. Gerken, S. E. Shaner, R. C. Massé, N. J. Porubsky and S. S. Stahl, *Energy Environ. Sci.*, 2014, **7**, 2376-2382.

186. T. W. Hamann, *Dalton Trans.*, 2012, **41**, 7830-7834.

187. W. L. Kwong, C. C. Lee, A. Shchukarev, E. Björn and J. Messinger, *J. Catal.*, 2018, **365**, 29-35.

188. Y. Wu, M. Chen, Y. Han, H. Luo, X. Su, M.-T. Zhang, X. Lin, J. Sun, L. Wang, L. Deng, W. Zhang and R. Cao, *Angew. Chem. Int. Ed.*, 2015, **54**, 4870-4875.

189. D. R. Chowdhury, L. Spiccia, S. S. Amritphale, A. Paul and A. Singh, *J. Mater. Chem. A*, 2016, **4**, 3655-3660.

190. M. E. G. Lyons and M. P. Brandon, *Int. J. Electrochem. Sci.*, 2008, **3**, 1463-1503.

191. M. E. G. Lyons and R. L. Doyle, *Int. J. Electrochem. Sci.*, 2012, **7**, 9488-9501.

192. R. L. Doyle and M. E. G. Lyons, *J. Electrochem. Soc.*, 2013, **160**, H142-H154.

193. S. Shen, *J. Mater. Res.*, 2013, **29**, 29-46.

194. K. Sivula, F. Le Formal and M. Grätzel, *ChemSusChem*, 2011, **4**, 432-449.

195. B. Klahr, S. Gimenez, F. Fabregat-Santiago, J. Bisquert and T. W. Hamann, *Energy Environ. Sci.*, 2012, **5**, 7626-7636.

196. L. M. Peter, *J. Solid State Electrochem.*, 2013, **17**, 315-326.

197. M. J. Katz, S. C. Riha, N. C. Jeong, A. B. F. Martinson, O. K. Farha and J. T. Hupp, *Coord. Chem. Rev.*, 2012, **256**, 2521-2529.

198. N. T. Hahn, H. Ye, D. W. Flaherty, A. J. Bard and C. B. Mullins, *ACS Nano*, 2010, **4**, 1977-1986.

199. X. Zong, S. Thaweesak, H. Xu, Z. Xing, J. Zou, G. Lu and L. Wang, *Phys. Chem. Chem. Phys.*, 2013, **15**, 12314-12321.

200. F. E. Osterloh, *Chem. Soc. Rev.*, 2013, **42**, 2294-2320.

201. C. He, X. Wu and Z. He, *J. Phys. Chem. C*, 2014, **118**, 4578-4584.

202. I. Roger and M. D. Symes, *J. Am. Chem. Soc.*, 2015, **137**, 13980-13988.

203. X. Ji, L. Cui, D. Liu, S. Hao, J. Liu, F. Qu, Y. Ma, G. Du, A. M. Asiri and X. Sun, *Chem. Commun.*, 2017, **53**, 3070-3073.

204. M. Dincă, Y. Surendranath and D. G. Nocera, *Proc. Natl. Acad. Sci. U.S.A.*, 2010, **107**, 10337-10341.

205. D. K. Bediako, Y. Surendranath and D. G. Nocera, *J. Am. Chem. Soc.*, 2013, **135**, 3662-3674.

206. B. S. Yeo and A. T. Bell, *J. Phys. Chem. C*, 2012, **116**, 8394-8400.

207. A. Singh, S. L. Y. Chang, R. K. Hocking, U. Bach and L. Spiccia, *Energy Environ. Sci.*, 2013, **6**, 579-586.

208. L.-K. Wu, J.-M. Hu, J.-Q. Zhang and C.-N. Cao, *J. Mater. Chem. A*, 2013, **1**, 12885-12892.

209. D. A. Corrigan, *J. Electrochem. Soc.*, 1987, **134**, 377-384.

210. L. Trotochaud, J. K. Ranney, K. N. Williams and S. W. Boettcher, *J. Am. Chem. Soc.*, 2012, **134**, 17253-17261.

211. M. Görlin, J. Ferreira de Araújo, H. Schmies, D. Bernsmeier, S. Dresp, M. Gliech, Z. Jusys, P. Chernev, R. Kraehnert, H. Dau and P. Strasser, *J. Am. Chem. Soc.*, 2017, **139**, 2070-2082.

212. M. Wiechen, I. Zaharieva, H. Dau and P. Kurz, *Chem. Sci.*, 2012, **3**, 2330-2339.

213. M. M. Najafpour, T. Ehrenberg, M. Wiechen and P. Kurz, *Angew. Chem. Int. Ed.*, 2010, **49**, 2233-2237.

214. M. M. Najafpour, K. C. Leonard, F.-R. F. Fan, M. A. Tabrizi, A. J. Bard, C. K. King'ondu, S. L. Suib, B. Haghighi and S. I. Allakhverdiev, *Dalton Trans.*, 2013, **42**, 5085-5091.

215. D. González-Flores, I. Zaharieva, J. Heidkamp, P. Chernev, E. Martínez-Moreno, C. Pasquini, M. R. Mohammadi, K. Klingan, U. Gernet, A. Fischer and H. Dau, *ChemSusChem*, 2016, **9**, 379-387.

216. H. Simchi, K. A. Cooley, J. Ohms, L. Huang, P. Kurz and S. E. Mohney, *Inorg. Chem.*, 2018, **57**, 785-792.

217. M. M. Najafpour, M. Z. Ghobadi, D. J. Sedigh and B. Haghighi, *RSC Adv.*, 2014, **4**, 39077-39081.

218. M. M. Najafpour, M. Zarei Ghobadi, B. Sarvi, S. Madadkhani, D. Jafarian Sedigh, P. Rafighi, M. Tavahodi, J.-R. Shen and S. I. Allakhverdiev, *Int. J. Hydrogen Energy*, 2016, **41**, 5504-5512.

219. M. M. Najafpour, M. Z. Ghobadi, B. Sarvi and B. Haghighi, *Dalton Trans.*, 2015, **44**, 15271-15278.

220. M. Huynh, T. Ozel, C. Liu, E. C. Lau and D. G. Nocera, *Chem. Sci.*, 2017, **8**, 4779-4794.

221. I. A. Moreno-Hernandez, C. A. MacFarland, C. G. Read, K. M. Papadantonakis, B. S. Brunschwig and N. S. Lewis, *Energy Environ. Sci.*, 2017, **10**, 2103-2108.

222. H.-C. Chiu, W.-H. Huang, L.-C. Hsu, Y.-G. Lin, Y.-H. Lai and C.-Y. Lin, *Sustain. Energy Fuels*, 2018, **2**, 271-279.

223. Q. Wang, T. Hisatomi, Q. Jia, H. Tokudome, M. Zhong, C. Wang, Z. Pan, T. Takata, M. Nakabayashi, N. Shibata, Y. Li, I. D. Sharp, A. Kudo, T. Yamada and K. Domen, *Nat. Mater.*, 2016, **15**, 611.

224. H. Lyu, T. Hisatomi, Y. Goto, M. Yoshida, T. Higashi, M. Katayama, T. Takata, T. Minegishi, H. Nishiyama, T. Yamada, Y. Sakata, K. Asakura and K. Domen, *Chem. Sci.*, 2019, **10**, 3196-3201.

225. B. Zhang and L. Sun, *Chem. Soc. Rev.*, 2019, **48**, 2216-2264.

226. Z. N. Zahran, Y. Tsubonouchi, E. A. Mohamed and M. Yagi, *ChemSusChem*, 2019, **12**, 1775-1793.

227. S. W. Gersten, G. J. Samuels and T. J. Meyer, *J. Am. Chem. Soc.*, 1982, **104**, 4029-4030.

228. J. A. Gilbert, D. S. Eggleston, W. R. Murphy, D. A. Geselowitz, S. W. Gersten, D. J. Hodgson and T. J. Meyer, *J. Am. Chem. Soc.*, 1985, **107**, 3855-3864.

229. D. Geselowitz and T. J. Meyer, *Inorg. Chem.*, 1990, **29**, 3894-3896.

230. C. W. Chronister, R. A. Binstead, J. Ni and T. J. Meyer, *Inorg. Chem.*, 1997, **36**, 3814-3815.

231. R. A. Binstead, C. W. Chronister, J. Ni, C. M. Hartshorn and T. J. Meyer, *J. Am. Chem. Soc.*, 2000, **122**, 8464-8473.

232. F. Liu, J. J. Concepcion, J. W. Jurss, T. Cardolaccia, J. L. Templeton and T. J. Meyer, *Inorg. Chem.*, 2008, **47**, 1727-1752.

233. D. Moonshiram, I. Alperovich, J. J. Concepcion, T. J. Meyer and Y. Pushkar, *Proc. Natl. Acad. Sci. U.S.A.*, 2013, **110**, 3765-3770.

234. D. Moonshiram, J. W. Jurss, J. J. Concepcion, T. Zakharova, I. Alperovich, T. J. Meyer and Y. Pushkar, *J. Am. Chem. Soc.*, 2012, **134**, 4625-4636.

235. J. K. Hurst, J. Zhou and Y. Lei, *Inorg. Chem.*, 1992, **31**, 1010-1017.

236. H. Yamada, T. Koike and J. K. Hurst, *J. Am. Chem. Soc.*, 2001, **123**, 12775-12780.

237. H. Yamada, W. F. Siems, T. Koike and J. K. Hurst, *J. Am. Chem. Soc.*, 2004, **126**, 9786-9795.

238. J. K. Hurst, J. L. Cape, A. E. Clark, S. Das and C. Qin, *Inorg. Chem.*, 2008, **47**, 1753-1764.

239. X. Yang and M.-H. Baik, *J. Am. Chem. Soc.*, 2004, **126**, 13222-13223.

240. X. Yang and M.-H. Baik, *J. Am. Chem. Soc.*, 2006, **128**, 7476-7485.

241. R. Bianco, P. J. Hay and J. T. Hynes, *J. Phys. Chem. A*, 2011, **115**, 8003-8016.

242. J. W. Jurss, J. J. Concepcion, J. M. Butler, K. M. Omberg, L. M. Baraldo, D. G. Thompson, E. L. Lebeau, B. Hornstein, J. R. Schoonover, H. Jude, J. D. Thompson, D. M. Dattelbaum, R. C. Rocha, J. L. Templeton and T. J. Meyer, *Inorg. Chem.*, 2012, **51**, 1345-1358.

243. E. L. Lebeau, S. A. Adeyemi and T. J. Meyer, *Inorg. Chem.*, 1998, **37**, 6476-6484.

244. L. A. Gallagher and T. J. Meyer, *J. Am. Chem. Soc.*, 2001, **123**, 5308-5312.

245. F. Liu, T. Cardolaccia, B. J. Hornstein, J. R. Schoonover and T. J. Meyer, *J. Am. Chem. Soc.*, 2007, **129**, 2446-2447.

246. X. Yang and M.-H. Baik, *J. Am. Chem. Soc.*, 2008, **130**, 16231-16240.

247. J. W. Jurss, J. C. Concepcion, M. R. Norris, J. L. Templeton and T. J. Meyer, *Inorg. Chem.*, 2010, **49**, 3980-3982.

248. C. Sens, I. Romero, M. Rodríguez, A. Llobet, T. Parella and J. Benet-Buchholz, *J. Am. Chem. Soc.*, 2004, **126**, 7798-7799.

249. R. Zong and R. P. Thummel, *J. Am. Chem. Soc.*, 2005, **127**, 12802-12803.

250. Z. Deng, H.-W. Tseng, R. Zong, D. Wang and R. Thummel, *Inorg. Chem.*, 2008, **47**, 1835-1848.

251. L. Francàs, X. Sala, E. Escudero-Adán, J. Benet-Buchholz, L. Escriche and A. Llobet, *Inorg. Chem.*, 2011, **50**, 2771-2781.

252. Y. Xu, T. Åkermark, V. Gyollai, D. Zou, L. Eriksson, L. Duan, R. Zhang, B. Åkermark and L. Sun, *Inorg. Chem.*, 2009, **48**, 2717-2719.

253. Y. Xu, A. Fischer, L. Duan, L. Tong, E. Gabrielsson, B. Åkermark and L. Sun, *Angew. Chem. Int. Ed.*, 2010, **49**, 8934-8937.

254. H.-W. Tseng, R. Zong, J. T. Muckerman and R. Thummel, *Inorg. Chem.*, 2008, **47**, 11763-11773.

255. J. J. Concepcion, J. W. Jurss, J. L. Templeton and T. J. Meyer, *J. Am. Chem. Soc.*, 2008, **130**, 16462-16463.

256. D. J. Wasylenko, C. Ganesamoorthy, B. D. Koivisto, M. A. Henderson and C. P. Berlinguette, *Inorg. Chem.*, 2010, **49**, 2202-2209.

257. Y. V. Geletii, B. Botar, P. Kögerler, D. A. Hillesheim, D. G. Musaev and C. L. Hill, *Angew. Chem. Int. Ed.*, 2008, **47**, 3896-3899.

258. A. Sartorel, M. Carraro, G. Scorrano, R. D. Zorzi, S. Geremia, N. D. McDaniel, S. Bernhard and M. Bonchio, *J. Am. Chem. Soc.*, 2008, **130**, 5006-5007.

259. Y. V. Geletii, Z. Huang, Y. Hou, D. G. Musaev, T. Lian and C. L. Hill, *J. Am. Chem. Soc.*, 2009, **131**, 7522-7523.

260. C. Besson, Z. Huang, Y. V. Geletii, S. Lense, K. I. Hardcastle, D. G. Musaev, T. Lian, A. Proust and C. L. Hill, *Chem. Commun.*, 2010, **46**, 2784-2786.

261. M. Murakami, D. Hong, T. Suenobu, S. Yamaguchi, T. Ogura and S. Fukuzumi, *J. Am. Chem. Soc.*, 2011, **133**, 11605-11613.

262. S. Ogo, M. Miyamoto, Y. Ide, T. Sano and M. Sadakane, *Dalton Trans.*, 2012, **41**, 9901-9907.

263. S. Ogo, S. Moroi, T. Ueda, K. Komaguchi, S. Hayakawa, Y. Ide, T. Sano and M. Sadakane, *Dalton Trans.*, 2013, **42**, 7190-7195.

264. F. M. Toma, A. Sartorel, M. Iurlo, M. Carraro, P. Parisse, C. Maccato, S. Rapino, B. R. Gonzalez, H. Amenitsch, T. Da Ros, L. Casalis, A. Goldoni, M. Marcaccio, G. Scorrano, G. Scoles, F. Paolucci, M. Prato and M. Bonchio, *Nat. Chem.*, 2010, **2**, 826-831.

265. M. Quintana, A. M. López, S. Rapino, F. M. Toma, M. Iurlo, M. Carraro, A. Sartorel, C. Maccato, X. Ke, C. Bittencourt, T. Da Ros, G. Van Tendeloo, M. Marcaccio, F. Paolucci, M. Prato and M. Bonchio, *ACS Nano*, 2013, **7**, 811-817.

266. S.-X. Guo, Y. Liu, C.-Y. Lee, A. M. Bond, J. Zhang, Y. V. Geletii and C. L. Hill, *Energy Environ. Sci.*, 2013, **6**, 2654-2663.

267. N. D. McDaniel, F. J. Coughlin, L. L. Tinker and S. Bernhard, *J. Am. Chem. Soc.*, 2008, **130**, 210-217.

268. J. F. Hull, D. Balcells, J. D. Blakemore, C. D. Incarvito, O. Eisenstein, G. W. Brudvig and R. H. Crabtree, *J. Am. Chem. Soc.*, 2009, **131**, 8730-8731.

269. J. D. Blakemore, N. D. Schley, D. Balcells, J. F. Hull, G. W. Olack, C. D. Incarvito, O. Eisenstein, G. W. Brudvig and R. H. Crabtree, *J. Am. Chem. Soc.*, 2010, **132**, 16017-16029.

270. G. F. Moore, J. D. Blakemore, R. L. Milot, J. F. Hull, H.-e. Song, L. Cai, C. A. Schmuttenmaer, R. H. Crabtree and G. W. Brudvig, *Energy Environ. Sci.*, 2011, **4**, 2389-2392.

271. T. P. Brewster, J. D. Blakemore, N. D. Schley, C. D. Incarvito, N. Hazari, G. W. Brudvig and R. H. Crabtree, *Organometallics*, 2011, **30**, 965-973.

272. J. D. Blakemore, N. D. Schley, G. W. Olack, C. D. Incarvito, G. W. Brudvig and R. H. Crabtree, *Chem. Sci.*, 2011, **2**, 94-98.

273. D. Hong, M. Murakami, Y. Yamada and S. Fukuzumi, *Energy Environ. Sci.*, 2012, **5**, 5708-5716.

274. A. Lewandowska-Andralojc, D. E. Polyansky, C.-H. Wang, W.-H. Wang, Y. Himeda and E. Fujita, *Phys. Chem. Chem. Phys.*, 2014, **16**, 11976-11987.

275. T. Abe, K. Nagai, S. Kabutomori, M. Kaneko, A. Tajiri and T. Norimatsu, *Angew. Chem. Int. Ed.*, 2006, **45**, 2778-2781.

276. D. K. Dogutan, R. McGuire and D. G. Nocera, *J. Am. Chem. Soc.*, 2011, **133**, 9178-9180.

277. H. Lei, A. Han, F. Li, M. Zhang, Y. Han, P. Du, W. Lai and R. Cao, *Phys. Chem. Chem. Phys.*, 2014, **16**, 1883-1893.

278. D. Wang and J. T. Groves, *Proc. Natl. Acad. Sci. U.S.A.*, 2013, **110**, 15579-15584.

279. T. Nakazono, A. R. Parent and K. Sakai, *Chem. Commun.*, 2013, **49**, 6325-6327.

280. H.-Y. Du, S.-C. Chen, X.-J. Su, L. Jiao and M.-T. Zhang, *J. Am. Chem. Soc.*, 2018, **140**, 1557-1565.

281. Q. Daniel, R. B. Ambre, B. Zhang, B. Philippe, H. Chen, F. Li, K. Fan, S. Ahmadi, H. Rensmo and L. Sun, *ACS Catal.*, 2017, **7**, 1143-1149.

282. M. L. Rigsby, S. Mandal, W. Nam, L. C. Spencer, A. Llobet and S. S. Stahl, *Chem. Sci.*, 2012, **3**, 3058-3062.

283. M. M. Najafpour and H. Feizi, *Catal. Sci. Technol.*, 2018, **8**, 1840-1848.

284. Z. Huang, Z. Luo, Y. V. Geletii, J. W. Vickers, Q. Yin, D. Wu, Y. Hou, Y. Ding, J. Song, D. G. Musaev, C. L. Hill and T. Lian, *J. Am. Chem. Soc.*, 2011, **133**, 2068-2071.

285. S. Goberna-Ferrón, L. Vigara, J. Soriano-López and J. R. Galán-Mascarós, *Inorg. Chem.*, 2012, **51**, 11707-11715.

286. J. Soriano-López, S. Goberna-Ferrón, L. Vigara, J. J. Carbó, J. M. Poblet and J. R. Galán-Mascarós, *Inorg. Chem.*, 2013, **52**, 4753-4755.

287. X.-B. Han, Z.-M. Zhang, T. Zhang, Y.-G. Li, W. Lin, W. You, Z.-M. Su and E.-B. Wang, *J. Am. Chem. Soc.*, 2014, **136**, 5359-5366.

288. S. Goberna-Ferrón, J. Soriano-López, J. R. Galán-Mascarós and M. Nyman, *Eur. J. Inorg. Chem.*, 2015, **2015**, 2833-2840.

289. M. Blasco-Ahicart, J. Soriano-López and J. R. Galán-Mascarós, *ChemElectroChem*, 2017, **4**, 3296-3301.

290. M. Blasco-Ahicart, J. Soriano-López, J. J. Carbó, J. M. Poblet and J. R. Galan-Mascaros, *Nat. Chem.*, 2017, **10**, 24.

291. J. Soriano-López, S. Goberna-Ferrón, J. J. Carbó, J. M. Poblet and J. R. Galán-Mascarós, in *Adv. Inorg. Chem.*, eds. R. van Eldik and L. Cronin, Academic Press, 2017, vol. 69, pp. 155-179.

292. S. J. Folkman, J. Soriano-Lopez, J. R. Galán-Mascarós and R. G. Finke, *J. Am. Chem. Soc.*, 2018, **140**, 12040-12055.

293. M. Martin-Sabi, J. Soriano-López, R. S. Winter, J.-J. Chen, L. Vilà-Nadal, D.-L. Long, J. R. Galán-Mascarós and L. Cronin, *Nat. Catal.*, 2018, **1**, 208-213.

294. A. Ghosh, A. D. Ryabov, S. M. Mayer, D. C. Horner, D. E. Prasuhn, S. Sen Gupta, L. Vuocolo, C. Culver, M. P. Hendrich, C. E. F. Rickard, R. E. Norman, C. P. Horwitz and T. J. Collins, *J. Am. Chem. Soc.*, 2003, **125**, 12378-12379.

295. W. C. Ellis, N. D. McDaniel, S. Bernhard and T. J. Collins, *J. Am. Chem. Soc.*, 2010, **132**, 10990-10991.

296. J. L. Fillol, Z. Codolà, I. Garcia-Bosch, L. Gómez, J. J. Pla and M. Costas, *Nat. Chem.*, 2011, **3**, 807-813.

297. M. K. Coggins, M.-T. Zhang, A. K. Vannucci, C. J. Dares and T. J. Meyer, *J. Am. Chem. Soc.*, 2014, **136**, 5531-5534.

298. W. A. Hoffert, M. T. Mock, A. M. Appel and J. Y. Yang, *Eur. J. Inorg. Chem.*, 2013, **2013**, 3846-3857.

299. Z. Codolà, I. Gamba, F. Acuña-Parés, C. Casadevall, M. Clémancey, J.-M. Latour, J. M. Luis, J. Lloret-Fillol and M. Costas, *J. Am. Chem. Soc.*, 2019, **141**, 323-333.

300. D. Hong, S. Mandal, Y. Yamada, Y.-M. Lee, W. Nam, A. Llobet and S. Fukuzumi, *Inorg. Chem.*, 2013, **52**, 9522-9531.

301. K. G. Kottrup, S. D'Agostini, P. H. van Langevelde, M. A. Siegler and D. G. H. Hetterscheid, *ACS Catal.*, 2018, **8**, 1052-1061.

302. M. Okamura, M. Kondo, R. Kuga, Y. Kurashige, T. Yanai, S. Hayami, V. K. K. Praneeth, M. Yoshida, K. Yoneda, S. Kawata and S. Masaoka, *Nature*, 2016, **530**, 465.

303. V. K. K. Praneeth, M. Kondo, M. Okamura, T. Akai, H. Izu and S. Masaoka, *Chem. Sci.*, 2019, **10**, 4628-4639.

304. M. Zhang, M.-T. Zhang, C. Hou, Z.-F. Ke and T.-B. Lu, *Angew. Chem. Int. Ed.*, 2014, **53**, 13042-13048.

305. Y. Han, Y. Wu, W. Lai and R. Cao, *Inorg. Chem.*, 2015, **54**, 5604-5613.

306. G.-Y. Luo, H.-H. Huang, J.-W. Wang and T.-B. Lu, *ChemSusChem*, 2016, **9**, 485-491.

307. L. Wang, L. Duan, R. B. Ambre, Q. Daniel, H. Chen, J. Sun, B. Das, A. Thapper, J. Uhlig, P. Dinér and L. Sun, *J. Catal.*, 2016, **335**, 72-78.

308. J.-W. Wang, C. Hou, H.-H. Huang, W.-J. Liu, Z.-F. Ke and T.-B. Lu, *Catal. Sci. Technol.*, 2017, **7**, 5585-5593.

309. J. Shen, M. Wang, T. He, J. Jiang and M. Hu, *Chem. Commun.*, 2018, **54**, 9019-9022.

310. C. Singh, S. Mukhopadhyay and S. K. Das, *Inorg. Chem.*, 2018, **57**, 6479-6490.

311. L.-H. Zhang, F. Yu, Y. Shi, F. Li and H. Li, *Chem. Commun.*, 2019, **55**, 6122-6125.

312. H. M. Shahadat, H. A. Younus, N. Ahmad, M. A. Rahaman, Z. A. K. Khattak, S. Zhuiykov and F. Verpoort, *Catal. Sci. Technol.*, 2019, **9**, 5651-5659.

313. J.-W. Wang, W.-J. Liu, D.-C. Zhong and T.-B. Lu, *Coord. Chem. Rev.*, 2019, **378**, 237-261.

314. Q. Zhang and J. Guan, *ChemSusChem*, 2019, **12**, 3209-3235.

315. S. M. Barnett, K. I. Goldberg and J. M. Mayer, *Nat. Chem.*, 2012, **4**, 498-502.

316. T. Ghosh, P. Ghosh and G. Maayan, *ACS Catal.*, 2018, **8**, 10631-10640.

317. M. K. Coggins, M.-T. Zhang, Z. Chen, N. Song and T. J. Meyer, *Angew. Chem. Int. Ed.*, 2014, **53**, 12226-12230.

318. S. Cui, M. Qian, X. Liu, Z. Sun and P. Du, *ChemSusChem*, 2016, **9**, 2365-2373.

319. Y. Liu, Y. Han, Z. Zhang, W. Zhang, W. Lai, Y. Wang and R. Cao, *Chem. Sci.*, 2019, **10**, 2613-2622.

320. K. J. Fisher, K. L. Materna, B. Q. Mercado, R. H. Crabtree and G. W. Brudvig, *ACS Catal.*, 2017, **7**, 3384-3387.

321. F. Chen, N. Wang, H. Lei, D. Guo, H. Liu, Z. Zhang, W. Zhang, W. Lai and R. Cao, *Inorg. Chem.*, 2017, **56**, 13368-13375.

322. W.-S. Gao, J.-M. Wang, N.-N. Shi, C.-N. Chen, Y.-H. Fan and M. Wang, *New J. Chem.*, 2019, **43**, 4640-4647.

323. P. Atkins, T. Overton, J. P. Rourke, M. T. Weller, F. Armstrong and 2009, in *Shriver and Atkins' Inorganic Chemistry (5th edition)*, Oxford University Press, Oxford 2009, ch. 20, pp. 473-506.

324. C. E. Housecroft and A. G. Sharpe, in *Inorganic Chemistry. 4th Edition*, Pearson, Harlow, 2012, ch. 20, pp. 665-715.

325. O. Kahn, in *Molecular magnetism*, VCH Publishers, Inc., USA 1993, ch. 1, pp. 1-8.

326. J. H. Van Vleck, in *The theory of electric and magnetic susceptibilities*, Oxford : Oxford university press, 1932, ch. 9, pp. 226-261.

327. J.-P. Launay and M. Verdaguer, in *Electrons in Molecules: From Basic Principles to Molecular Electronics*, Oxford University Press, Oxford, 2013, ch. 2, pp. 78-204.

328. K. Takeda and K. Awaga, in *Chemistry of Nanomolecular Systems: Towards the Realization of Molecular Devices*, eds. T. Nakamura, T. Matsumoto, H. Tada and K.-i. Sugiura, Springer Berlin Heidelberg, Berlin, Heidelberg, 2003, ch. Single-Molecule Magnets, pp. 41-57.

329. D. Gatteschi and R. Sessoli, *Angew. Chem. Int. Ed.*, 2003, **42**, 268-297.

330. D. Gatteschi, R. Sessoli and J. Villain, *Molecular nanomagnets*, Oxford University Press 2006.

331. M. Feng and M.-L. Tong, *Chem.: Eur. J*, 2018, **24**, 7574-7594.

332. E. Coronado, *Nat. Rev. Mater*, 2020, **5**, 87-104.

333. E. Ruiz, in *Comprehensive Inorganic Chemistry II (Second Edition)*, eds. J. Reedijk and K. Poeppelmeier, Elsevier, Amsterdam, 2013, ch. 9.20, pp. 501-549.

334. J. B. Goodenough, in *Magnetism and the chemical bond*, Interscience Publishers, 1963, ch. 3, pp. 157-354.

335. K. A. Gschneidner, V. K. Pecharsky and A. O. Tsokol, *Rep. Prog. Phys.*, 2005, **68**, 1479-1539.

336. B. G. Shen, J. R. Sun, F. X. Hu, H. W. Zhang and Z. H. Cheng, *Adv. Mater.*, 2009, **21**, 4545-4564.

337. X. Moya, S. Kar-Narayan and N. D. Mathur, *Nat. Mater.*, 2014, **13**, 439-450.

338. R. Bagai and G. Christou, *Chem. Soc. Rev.*, 2009, **38**, 1011-1026.

339. Y. D. Xiao, R. Paudel, J. Liu, C. Ma, Z. S. Zhang and S. K. Zhou, *Int. J. Mol. Med.*, 2016, **38**, 1319-1326.

340. A. P. Ramirez, *J. Phys. Condens. Matter*, 1997, **9**, 8171-8199.

341. M. Fiebig, *J. Phys. D*, 2005, **38**, R123-R152.

342. L. Bogani and W. Wernsdorfer, *Nat. Mater.*, 2008, **7**, 179-186.

343. G. A. Timco, T. B. Faust, F. Tuna and R. E. P. Winpenny, *Chem. Soc. Rev.*, 2011, **40**, 3067-3075.

344. P. Santini, S. Carretta, F. Troiani and G. Amoretti, *Phys. Rev. Lett.*, 2011, **107**, 230502.

345. A. Furrer and O. Waldmann, *Rev. Mod. Phys.*, 2013, **85**, 367-420.

346. J. M. Frost, K. L. M. Harriman and M. Murugesu, *Chem. Sci.*, 2016, **7**, 2470-2491.

347. L. Spree and A. A. Popov, *Dalton Trans.*, 2019, **48**, 2861-2871.

348. C. A. P. Goodwin, F. Ortu, D. Reta, N. F. Chilton and D. P. Mills, *Nature*, 2017, **548**, 439-442.

349. F.-S. Guo, B. M. Day, Y.-C. Chen, M.-L. Tong, A. Mansikkamäki and R. A. Layfield, *Angew. Chem. Int. Ed.*, 2017, **56**, 11445-11449.

350. F.-S. Guo, B. M. Day, Y.-C. Chen, M.-L. Tong, A. Mansikkamäki and R. A. Layfield, *Science*, 2018, **362**, 1400-1403.

351. O. Waldmann, *Inorg. Chem.*, 2007, **46**, 10035-10037.

352. E. Ruiz, J. Cirera, J. Cano, S. Alvarez, C. Loose and J. Kortus, *Chem. Commun.*, 2008, DOI: 10.1039/B714715E, 52-54.

353. F. Neese and D. A. Pantazis, *Faraday Discuss.*, 2011, **148**, 229-238.

354. J. R. Long, in *The Chemistry Of Nanostructured Materials*, World Scientific, 2003, pp. 291-315.

355. C. J. Milios and R. E. P. Winpenny, in *Molecular Nanomagnets and Related Phenomena*, ed. S. Gao, Springer Berlin Heidelberg, Berlin, Heidelberg, 2015, pp. 1-109.

356. S.-S. Bao and L.-M. Zheng, *Coord. Chem. Rev.*, 2016, **319**, 63-85.

357. R. Sessoli, D. Gatteschi, A. Caneschi and M. A. Novak, *Nature*, 1993, **365**, 141-143.

358. H. J. Eppley, H.-L. Tsai, N. de Vries, K. Folting, G. Christou and D. N. Hendrickson, *J. Am. Chem. Soc.*, 1995, **117**, 301-317.

359. C. Boskovic, M. Pink, J. C. Huffman, D. N. Hendrickson and G. Christou, *J. Am. Chem. Soc.*, 2001, **123**, 9914-9915.

360. M. Soler, W. Wernsdorfer, K. A. Abboud, J. C. Huffman, E. R. Davidson, D. N. Hendrickson and G. Christou, *J. Am. Chem. Soc.*, 2003, **125**, 3576-3588.

361. R. Bagai and G. Christou, *Inorg. Chem.*, 2007, **46**, 10810-10818.

362. A. J. Tasiopoulos, A. Vinslava, W. Wernsdorfer, K. A. Abboud and G. Christou, *Angew. Chem. Int. Ed.*, 2004, **43**, 2117-2121.

363. A. M. Ako, I. J. Hewitt, V. Mereacre, R. Clerac, W. Wernsdorfer, C. E. Anson and A. K. Powell, *Angew. Chem. Int. Ed.*, 2006, **45**, 4926-4929.

364. G. Aromí and E. K. Brechin, in *Single-Molecule Magnets and Related Phenomena*, ed. R. Winpenny, Springer Berlin Heidelberg, Berlin, Heidelberg, 2006, pp. 1-67.

365. J. Larionova, M. Gross, M. Pilkington, H. Andres, H. Stoeckli-Evans, H. U. Gudel and S. Decurtins, *Angew. Chem. Int. Ed.*, 2000, **39**, 1605-1609.

366. Z. J. Zhong, H. Seino, Y. Mizobe, M. Hidai, A. Fujishima, S. Ohkoshi and K. Hashimoto, *J. Am. Chem. Soc.*, 2000, **122**, 2952-2953.

367. M. Murugesu, M. Habrych, W. Wernsdorfer, K. A. Abboud and G. Christou, *J. Am. Chem. Soc.*, 2004, **126**, 4766-4767.

368. T. C. Stamatatos, K. A. Abboud, W. Wernsdorfer and G. Christou, *Angew. Chem. Int. Ed.*, 2007, **46**, 884-888.

369. S. Kang, H. Zheng, T. Liu, K. Hamachi, S. Kanegawa, K. Sugimoto, Y. Shiota, S. Hayami, M. Mito, T. Nakamura, M. Nakano, M. L. Baker, H. Nojiri, K. Yoshizawa, C. Duan and O. Sato, *Nat. Commun.*, 2015, **6**, 5955.

370. G. Novitchi, G. Pilet and D. Luneau, *C. R. Chim.*, 2012, **15**, 937-942.

371. M.-H. Liu, C.-I. Yang, G.-H. Lee and H.-L. Tsai, *Inorg. Chem. Commun.*, 2011, **14**, 1136-1139.

372. A.-R. Tomsa, J. Martínez-Lillo, Y. Li, L.-M. Chamoreau, K. Boubekeur, F. Farias, M. A. Novak, E. Cremades, E. Ruiz, A. Proust, M. Verdaguer and P. Gouzerh, *Chem. Commun.*, 2010, **46**, 5106-5108.

373. Y. Zhang, J.-J. Zhang, A.-Q. Jia, Z.-F. Xin and Q.-F. Zhang, *J. Cluster Sci.*, 2018, **29**, 1345-1352.

374. M. Soler, W. Wernsdorfer, K. Folting, M. Pink and G. Christou, *J. Am. Chem. Soc.*, 2004, **126**, 2156-2165.

375. E.-C. Yang, S.-Y. Huang, W. Wernsdorfer, L.-X. Hong, M. Damjanovic, L. Niekamp and G.-H. Lee, *RSC Adv.*, 2019, **9**, 37740-37746.

376. Y. Cui, H. Zhu, L. Wang, B. Li, Z. Han and J. Luo, *J. Magn. Magn. Mater.*, 2018, **458**, 90-94.

377. R. Inglis, L. F. Jones, G. Karotsis, A. Collins, S. Parsons, S. P. Perlepes, W. Wernsdorfer and E. K. Brechin, *Chem. Commun.*, 2008, DOI: 10.1039/B811796A, 5924-5926.

378. T. Taguchi, W. Wernsdorfer, K. A. Abboud and G. Christou, *Inorg. Chem.*, 2010, **49**, 199-208.

379. E. K. Brechin, M. Soler, G. Christou, M. Helliwell, S. J. Teat and W. Wernsdorfer, *Chem. Commun.*, 2003, DOI: 10.1039/B302057F, 1276-1277.

380. C. Boskovic, E. K. Brechin, W. E. Streib, K. Folting, J. C. Bollinger, D. N. Hendrickson and G. Christou, *J. Am. Chem. Soc.*, 2002, **124**, 3725-3736.

381. T. Taguchi, W. Wernsdorfer, K. A. Abboud and G. Christou, *Inorg. Chem.*, 2010, **49**, 10579-10589.

382. B. Cordero, O. Roubeau, S. J. Teat and A. Escuer, *Dalton Trans.*, 2011, **40**, 7127-7129.

383. E. C. Sañudo, W. Wernsdorfer, K. A. Abboud and G. Christou, *Inorg. Chem.*, 2004, **43**, 4137-4144.

384. L. Zhang, T. Chimamkpam, C. I. Onet, N. Zhu, R. Clérac and W. Schmitt, *Dalton Trans.*, 2016, **45**, 17705-17713.

385. T. C. Stamatatos, D. Foguet-Albiol, W. Wernsdorfer, K. A. Abboud and G. Christou, *Chem. Commun.*, 2011, **47**, 274-276.

386. E. K. Brechin, M. Soler, J. Davidson, D. N. Hendrickson, S. Parsons and G. Christou, *Chem. Commun.*, 2002, DOI: 10.1039/B206386G, 2252-2253.

387. S. Piligkos, G. Rajaraman, M. Soler, N. Kirchner, J. van Slageren, R. Bircher, S. Parsons, H.-U. Güdel, J. Kortus, W. Wernsdorfer, G. Christou and E. K. Brechin, *J. Am. Chem. Soc.*, 2005, **127**, 5572-5580.

388. J. Yoo, A. Yamaguchi, M. Nakano, J. Krzystek, W. E. Streib, L.-C. Brunel, H. Ishimoto, G. Christou and D. N. Hendrickson, *Inorg. Chem.*, 2001, **40**, 4604-4616.

389. J. Yoo, E. K. Brechin, A. Yamaguchi, M. Nakano, J. C. Huffman, A. L. Maniero, L.-C. Brunel, K. Awaga, H. Ishimoto, G. Christou and D. N. Hendrickson, *Inorg. Chem.*, 2000, **39**, 3615-3623.

390. M. Murugesu, J. Raftery, W. Wernsdorfer, G. Christou and E. K. Brechin, *Inorg. Chem.*, 2004, **43**, 4203-4209.

391. C. J. Milios, R. Inglis, R. Bagai, W. Wernsdorfer, A. Collins, S. Moggach, S. Parsons, S. P. Perlepes, G. Christou and E. K. Brechin, *Chem. Commun.*, 2007, DOI: 10.1039/B705170K, 3476-3478.

392. J. E. McGrady and R. Stranger, *Inorg. Chem.*, 1999, **38**, 550-558.

393. V. Krewald, M. Retegan, F. Neese, W. Lubitz, D. A. Pantazis and N. Cox, *Inorg. Chem.*, 2016, **55**, 488-501.

394. F. Rappaport and B. A. Diner, *Coord. Chem. Rev.*, 2008, **252**, 259-272.

395. L. V. Kulik, B. Epel, W. Lubitz and J. Messinger, *J. Am. Chem. Soc.*, 2005, **127**, 2392-2393.

396. T. Lohmiller, W. Ames, W. Lubitz, N. Cox and S. K. Misra, *Appl. Magn. Reson.*, 2013, **44**, 691-720.

397. J. M. Peloquin and R. D. Britt, *Biochim. Biophys. Acta, Bioenerg.*, 2001, **1503**, 96-111.

398. A. Haddy, *Photosynth. Res.*, 2007, **92**, 357-368.

399. L. V. Kulik, B. Epel, W. Lubitz and J. Messinger, *J. Am. Chem. Soc.*, 2007, **129**, 13421-13435.

400. Y. Jiao, R. Sharpe, T. Lim, J. W. H. Niemantsverdriet and J. Gracia, *J. Am. Chem. Soc.*, 2017, **139**, 16604-16608.

401. W. Mtangi, V. Kiran, C. Fontanesi and R. Naaman, *J. Phys. Chem. Lett.*, 2015, **6**, 4916-4922.

402. W. Zhang, K. Banerjee-Ghosh, F. Tassinari and R. Naaman, *ACS Energy Lett.*, 2018, **3**, 2308-2313.

403. W. Mtangi, F. Tassinari, K. Vankayala, A. Vargas Jentzsch, B. Adelizzi, A. R. A. Palmans, C. Fontanesi, E. W. Meijer and R. Naaman, *J. Am. Chem. Soc.*, 2017, **139**, 2794-2798.

404. S. Chrétien and H. Metiu, *J. Chem. Phys.*, 2008, **129**, 074705.

405. E. Torun, C. M. Fang, G. A. de Wijs and R. A. de Groot, *J. Phys. Chem. C*, 2013, **117**, 6353-6357.

406. J. Gracia, *Phys. Chem. Chem. Phys.*, 2017, **19**, 20451-20456.

407. J. Gracia, R. Sharpe and J. Munarriz, *J. Catal.*, 2018, **361**, 331-338.

408. X. Miao, S. Zhou, L. Wu, J. Zhao and L. Shi, *ACS Sustain. Chem. Eng.*, 2018, **6**, 12337-12342.

409. F. A. Garcés-Pineda, M. Blasco-Ahicart, D. Nieto-Castro, N. López and J. R. Galán-Mascarós, *Nat. Energy*, 2019, **4**, 519-525.

410. E. Schrödinger, *Phys. Rev.*, 1926, **28**, 1049-1070.

411. M. Born and R. Oppenheimer, *Ann. Phys.*, 1927, **389**, 457-484.

412. A. Szabo and N. S. Ostlund, in *Modern quantum chemistry*, Dover Publications, New York, 1996, ch. 2 and 3, pp. 39-230.

413. D. Hartree, *Math. Proc. Camb. Philos. Soc.*, 1928, **24**, 89-110.

414. D. Hartree, *Math. Proc. Camb. Philos. Soc.*, 1928, **24**, 111-132.

415. D. Hartree, *Math. Proc. Camb. Philos. Soc.*, 1928, **24**, 426-437.

416. V. Fock, *Zeitschrift für Physik*, 1930, **62**, 795-805.

417. J. C. Slater, *Phys. Rev.*, 1929, **34**, 1293-1322.

418. P. O. Lowdin, *Adv. Chem. Phys.*, 1959, **2**, 207-322.

419. F. Jensen, in *Introduction to computational chemistry*, John Wiley & sons, 2 edn., 2007, ch. 4, pp. 133-191.

420. W. Koch and M. C. Holthausen, in *A Chemist's Guide to Density Functional Theory*, Wiley-VCH, Weinheim, 2001, ch. 5, pp. 41-64.

421. P. Hohenberg and W. Kohn, *Phys. Rev. B*, 1964, **136**, B864-B871.

422. W. Kohn and L. J. Sham, *Phys. Rev.*, 1965, **140**, 1133-1138.

423. L. H. Thomas, *Math. Proc. Camb. Philos. Soc.*, 1927, **23**, 542-548.

424. E. Fermi, *Rend. Accad. Naz. Lincei*, 1927, **6**, 602-607.

425. D. M. Ceperley and B. J. Alder, *Phys. Rev. Lett.*, 1980, **45**, 566-569.

426. S. H. Vosko, L. Wilk and M. Nusair, *Can. J. Phys.*, 1980, **58**, 1200-1211.

427. F. Bloch, *Zeitschrift für Physik*, 1929, **52**, 555-600.

428. P. A. M. Dirac, *Math. Proc. Camb. Philos. Soc.*, 1930, **26**, 376-385.

429. W. Koch and M. C. Holthausen, in *A Chemist's Guide to Density Functional Theory*, Wiley-VCH, Weinheim, 2001, ch. 9, pp. 137-176.

430. A. D. Becke, *Phys. Rev. A*, 1988, **38**, 3098-3100.

431. C. T. Lee, W. T. Yang and R. G. Parr, *Phys. Rev. B*, 1988, **37**, 785-789.

432. J. P. Perdew and W. Yue, *Phys. Rev. B*, 1986, **33**, 8800-8802.

433. J. P. Perdew, K. Burke and M. Ernzerhof, *Phys. Rev. Lett.*, 1996, **77**, 3865-3868.

434. J. W. Sun, A. Ruzsinszky and J. P. Perdew, *Phys. Rev. Lett.*, 2015, **115**, 036402.

435. J. W. Sun, R. C. Remsing, Y. B. Zhang, Z. R. Sun, A. Ruzsinszky, H. W. Peng, Z. H. Yang, A. Paul, U. Waghmare, X. F. Wu, M. L. Klein and J. P. Perdew, *Nat. Chem.*, 2016, **8**, 831-836.

436. A. I. Liechtenstein, V. I. Anisimov and J. Zaanen, *Phys. Rev. B*, 1995, **52**, R5467-R5470.

437. S. L. Dudarev, G. A. Botton, S. Y. Savrasov, C. J. Humphreys and A. P. Sutton, *Phys. Rev. B*, 1998, **57**, 1505-1509.

438. A. Rohrbach, J. Hafner and G. Kresse, *Phys. Rev. B*, 2004, **70**, 125426.

439. T. A. Mellan, F. Cora, R. Grau-Crespo and S. Ismail-Beigi, *Phys. Rev. B*, 2015, **92**, 085151.

440. V. I. Anisimov, J. Zaanen and O. K. Andersen, *Phys. Rev. B*, 1991, **44**, 943-954.

441. M. Cococcioni and S. de Gironcoli, *Phys. Rev. B*, 2005, **71**, 035105.

442. T. Koopmans, *Physica*, 1934, **1**, 104-113.

443. S. Lany and A. Zunger, *Phys. Rev. B*, 2009, **80**, 085202.

444. P. R. L. Keating, D. O. Scanlon, B. J. Morgan, N. M. Galea and G. W. Watson, *J. Phys. Chem. C*, 2012, **116**, 2443-2452.

445. I. Timrov, N. Marzari and M. Cococcioni, *Phys. Rev. B*, 2018, **98**, 085127.

446. W. Koch and M. C. Holthausen, in *A Chemist's Guide to Density Functional Theory*, Wiley-VCH, Weinheim, 2001, ch. 6, pp. 65-92.

447. A. D. Becke, *J. Chem. Phys.*, 1993, **98**, 5648-5652.

448. L. A. Curtiss, K. Raghavachari, G. W. Trucks and J. A. Pople, *J. Chem. Phys.*, 1991, **94**, 7221-7230.

449. J. Paier, M. Marsman and G. Kresse, *J. Chem. Phys.*, 2007, **127**, 024103.

450. A. Walsh, J. L. F. Da Silva and S.-H. Wei, *Phys. Rev. Lett.*, 2008, **100**, 256401.

451. C. Adamo and V. Barone, *J. Chem. Phys.*, 1999, **110**, 6158-6170.

452. K. Burke, M. Ernzerhof and J. P. Perdew, *Chem. Phys. Lett.*, 1997, **265**, 115-120.

453. M. G. Medvedev, I. S. Bushmarinov, J. W. Sun, J. P. Perdew and K. A. Lyssenko, *Science*, 2017, **355**, 49-52.

454. J. Heyd, G. E. Scuseria and M. Ernzerhof, *J. Chem. Phys.*, 2003, **118**, 8207-8215.

455. F. Jensen, in *Introduction to computational chemistry*, John Wiley & sons, 2 edn., 2007, ch. 5, pp. 192-231.

456. J. S. Binkley, J. A. Pople and W. J. Hehre, *J. Am. Chem. Soc.*, 1980, **102**, 939-947.

457. M. S. Gordon, J. S. Binkley, J. A. Pople, W. J. Pietro and W. J. Hehre, *J. Am. Chem. Soc.*, 1982, **104**, 2797-2803.

458. W. J. Pietro, M. M. Francl, W. J. Hehre, D. J. Defrees, J. A. Pople and J. S. Binkley, *J. Am. Chem. Soc.*, 1982, **104**, 5039-5048.

459. K. D. Dobbs and W. J. Hehre, *J. Comp. Chem.*, 1986, **7**, 359-378.

460. K. D. Dobbs and W. J. Hehre, *J. Comp. Chem.*, 1987, **8**, 861-879.

461. K. D. Dobbs and W. J. Hehre, *J. Comp. Chem.*, 1987, **8**, 880-893.

462. S. F. Boys and F. Bernardi, *Mol. Phys.*, 1970, **19**, 553-566.

463. E. Wimmer, A. J. Freeman, M. Weinert, H. Krakauer, J. R. Hiskes and A. M. Karo, *Phys. Rev. Lett.*, 1982, **48**, 1128-1131.

464. P. E. Blochl, *Phys. Rev. B*, 1994, **50**, 17953-17979.

465. P. Pulay, *Mol. Phys.*, 1969, **17**, 197-204.

466. F. D. Murnaghan, *Proc. Natl. Acad. Sci. U.S.A.*, 1944, **30**, 244-247.

467. G. H. F. Diercksen and S. Wilson, *Methods in Computational Molecular Physics*, Reidel published in cooperation with NATO Scientific Affairs Division, Dordrecht, 1983.

468. https://gaussian.com/dft/, (accessed 7 July, 2020).

469. R. P. Feynman, *Phys. Rev.*, 1939, **56**, 340-343.

470. V. Bakken, T. Helgaker, W. Klopper and K. Ruud, *Mol. Phys.*, 1999, **96**, 653-671.

471. F. Jensen, in *Introduction to computational chemistry*, John Wiley & sons, 2 edn., 2007, ch. 12, pp. 380-420.

472. R. S. Mulliken, *J. Chem. Phys.*, 1955, **23**, 2343-2346.

473. R. S. Mulliken, *J. Chem. Phys.*, 1955, **23**, 1833-1840.

474. R. S. Mulliken, *J. Chem. Phys.*, 1955, **23**, 1841-1846.

475. R. S. Mulliken, *J. Chem. Phys.*, 1955, **23**, 2338-2342.

476. P. Politzer and R. S. Mulliken, *J. Chem. Phys.*, 1971, **55**, 5135-5136.

477. F. L. Hirshfeld, *Theoret. Chim. Acta*, 1977, **44**, 129-138.

478. J. P. Ritchie, *J. Am. Chem. Soc.*, 1985, **107**, 1829-1837.

479. J. P. Ritchie and S. M. Bachrach, *J. Comp. Chem.*, 1987, **8**, 499-509.

480. P. Bultinck, C. Van Alsenoy, P. W. Ayers and R. Carbó-Dorca, *J. Chem. Phys.*, 2007, **126**, 144111.

481. S. Van Damme, P. Bultinck and S. Fias, *J. Chem. Theory Comput.*, 2009, **5**, 334-340.

482. R. F. W. Bader, in *Atoms in Molecules: a Quantum Theory*, Clarendon Press, Oxford, 1994, ch. 3, pp. 53-109.

483. R. McWeeny, *J. Chem. Phys.*, 1965, **42**, 1717-1725.

484. A. Abragam and B. Bleaney, in *Electron paramagnetic resonance of transition ions*, Oxford : Clarendon press, 1970, ch. 3, pp. 133-216.

485. F. Neese and E. I. Solomon, in *Magnetism: Molecules to Materials IV*, 2002, ch. 9, pp. 345-466.

486. R. Boca, in *Theoretical foundations of molecular magnetism*, Elsevier, Amsterdam; Oxford, 1999, ch. 6, pp. 315-344.

487. W. Heisenberg, *Z. Physik*, 1928, **49**, 619-636.

488. P. A. M. Dirac, *Proc. R. Soc. Lond. A*, 1929, **123**, 714-733.

489. J. H. Vanvleck, *Rev. Mod. Phys.*, 1945, **17**, 27-47.

490. A. P. Ginsberg, *J. Am. Chem. Soc.*, 1980, **102**, 111-117.

491. L. Noodleman, *J. Chem. Phys.*, 1981, **74**, 5737-5743.

492. L. Noodleman, D. A. Case and A. Aizman, *J. Am. Chem. Soc.*, 1988, **110**, 1001-1005.

493. R. Maurice, C. de Graaf and N. Guihery, *Phys. Chem. Chem. Phys.*, 2013, **15**, 18784-18804.

494. K. Yamaguchi, *Chem. Phys. Lett.*, 1975, **33**, 330-335.

495. Y. Kizashi, F. Hiroaki and F. Takayuki, *Chem. Lett.*, 1986, **15**, 625-628.

496. H. Nagao, M. Nishino, Y. Shigeta, T. Soda, Y. Kitagawa, T. Onishi, Y. Yoshioka and K. Yamaguchi, *Coord. Chem. Rev.*, 2000, **198**, 265-295.

497. M. Shoji, K. Koizumi, Y. Kitagawa, T. Kawakami, S. Yamanaka, M. Okumura and K. Yamaguchi, *Chem. Phys. Lett.*, 2006, **432**, 343-347.

498. S. Paul and A. Misra, *J. Phys. Chem. A*, 2010, **114**, 6641-6647.

499. S. Paul and A. Misra, *J. Chem. Theory Comput.*, 2012, **8**, 843-853.

500. M. J. T. Frisch, G. W.; Schlegel, H. B.; Scuseria, G. E.; Robb, M. A.; Cheeseman, J. R.; Scalmani, G.; Barone, V.; Mennucci, B.; Petersson, G. A.; Nakatsuji, H.; Caricato, M.; Li, X.; Hratchian, H. P.; Izmaylov, A. F.; Bloino, J.; Zheng, G.; Sonnenberg, J. L.; Hada, M.; Ehara, M.; Toyota, K.; Fukuda, R.; Hasegawa, J.; Ishida, M.; Nakajima, T.; Honda, Y.; Kitao, O.; Nakai, H.; Vreven, T.; Montgomery, J. A., Jr.; Peralta, J. E.; Ogliaro, F.; Bearpark, M.; Heyd, J. J.; Brothers, E.; Kudin, K. N.; Staroverov, V. N.; Kobayashi, R.; Normand, J.; Raghavachari, K.; Rendell, A.; Burant, J. C.; Iyengar, S. S.; Tomasi, J.; Cossi, M.; Rega, N.; Millam, J. M.; Klene, M.; Knox, J. E.; Cross, J. B.; Bakken, V.; Adamo, C.; Jaramillo, J.; Gomperts, R.; Stratmann, R. E.; Yazyev, O.; Austin, A. J.; Cammi, R.; Pomelli, C.; Ochterski, J. W.; Martin, R. L.; Morokuma, K.; Zakrzewski, V. G.; Voth, G. A.; Salvador, P.; Dannenberg, J. J.; Dapprich, S.; Daniels, A. D.;

Farkas, Ö.; Foresman, J. B.; Ortiz, J. V.; Cioslowski, J.; Fox, D. J. , *Gaussian 09, Revision D.01*, 2009.

501. F. Neese, *WIREs Comput. Mol. Sci.*, 2012, **2**, 73-78.
502. G. Kresse and J. Hafner, *Phys. Rev. B*, 1994, **49**, 14251-14269.
503. G. Kresse and J. Furthmuller, *Comput. Mater. Sci.*, 1996, **6**, 15-50.
504. G. Kresse and J. Furthmuller, *Phys. Rev. B*, 1996, **54**, 11169-11186.
505. Y. Marcus, *Chem. Rev.*, 1988, **88**, 1475-1498.
506. P. L. W. Tregenna-Piggott, H. P. Andres, G. J. McIntyre, S. P. Best, C. C. Wilson and J. A. Cowan, *Inorg. Chem.*, 2003, **42**, 1350-1365.
507. M. Dolg, U. Wedig, H. Stoll and H. Preuss, *J. Chem. Phys.*, 1987, **86**, 866-872.
508. M. M. Francl, W. J. Pietro, W. J. Hehre, J. S. Binkley, M. S. Gordon, D. J. Defrees and J. A. Pople, *J. Chem. Phys.*, 1982, **77**, 3654-3665.
509. H. Stoll, B. Metz and M. Dolg, *J. Comp. Chem.*, 2002, **23**, 767-778.
510. A. K. Wilson, D. E. Woon, K. A. Peterson and T. H. Dunning, *J. Chem. Phys.*, 1999, **110**, 7667-7676.
511. R. C. Binning, Curtiss, L.A., *J. Comp. Chem.*, 1990, **11**, 1206-1216.
512. M. N. Glukhovtsev, A. Pross, M. P. Mcgrath and L. Radom, *J. Chem. Phys.*, 1995, **103**, 1878-1885.
513. H. B. Schlegel, *J. Comp. Chem.*, 1982, **3**, 214-218.
514. E. Ruiz, J. Cano, S. Alvarez and P. Alemany, *J. Comp. Chem.*, 1999, **20**, 1391-1400.
515. R. Bauernschmitt and R. Ahlrichs, *J. Chem. Phys.*, 1996, **104**, 9047-9052.
516. R. K. Dennington, Todd; Millam, John, *GaussView, Version 5*, 2009.
517. J. P. Perdew, A. Ruzsinszky, G. I. Csonka, O. A. Vydrov, G. E. Scuseria, L. A. Constantin, X. L. Zhou and K. Burke, *Phys. Rev. Lett.*, 2008, **100**, 136406.
518. K. Momma and F. Izumi, *J. Appl. Crystallogr.*, 2011, **44**, 1272-1276.
519. M. Yu and D. R. Trinkle, *J. Chem. Phys.*, 2011, **134**, 064111.
520. T. Cauchy, E. Ruiz and S. Alvarez, *J. Am. Chem. Soc.*, 2006, **128**, 15722-15727.
521. E. Ruiz, T. Cauchy, J. Cano, R. Costa, J. Tercero and S. Alvarez, *J. Am. Chem. Soc.*, 2008, **130**, 7420-7426.
522. S. K. Singh, N. K. Tibrewal and G. Rajaraman, *Dalton Trans.*, 2011, **40**, 10897-10906.
523. E. Cremades, J. Cano, E. Ruiz, G. Rajaraman, C. J. Milios and E. K. Brechin, *Inorg. Chem.*, 2009, **48**, 8012-8019.
524. E. Cremades, T. Cauchy, J. Cano and E. Ruiz, *Dalton Trans.*, 2009, 5873-5878.
525. K. R. Vignesh, S. K. Langley, K. S. Murray and G. Rajaraman, *Chem. Eur. J.*, 2015, **21**, 2881-2892.

526. T. Rajeshkumar, H. V. Annadata, M. Evangelisti, S. K. Langley, N. F. Chilton, K. S. Murray and G. Rajaraman, *Inorg. Chem.*, 2015, **54**, 1661-1670.

527. https://github.com/WatsonGroupTCD/EJ_Calc).

528. O. Kahn, *Molecular magnetism*, Wiley-VCH, New York (N.Y.), 1993.

529. N. F. Chilton, R. P. Anderson, L. D. Turner, A. Soncini and K. S. Murray, *J. Comp. Chem.*, 2013, **34**, 1164-1175.

530. https://github.com/WatsonGroupTCD/Suscep).

531. R. Boca, in *Theoretical foundations of molecular magnetism*, Elsevier, Amsterdam; Oxford, 1999, ch. 11, pp. 701-836.

532. E. Libby, J. K. McCusker, E. A. Schmitt, K. Folting, D. N. Hendrickson and G. Christou, *Inorg. Chem.*, 1991, **30**, 3486-3495.

533. E. Libby, K. Folting, C. J. Huffman, J. C. Huffman and G. Christou, *Inorg. Chem.*, 1993, **32**, 2549-2556.

534. E. K. Brechin, R. A. Coxall, A. Parkin, S. Parsons, P. A. Tasker and R. E. P. Winpenny, *Angew. Chem. Int. Ed.*, 2001, **40**, 2700-2703.

535. S. Maheswaran, G. Chastanet, S. J. Teat, T. Mallah, R. Sessoli, W. Wernsdorfer and R. E. P. Winpenny, *Angew. Chem. Int. Ed.*, 2005, **44**, 5044-5048.

536. Y.-S. Ma, Y. Song, Y.-Z. Li and L.-M. Zheng, *Inorg. Chem.*, 2007, **46**, 5459-5461.

537. S. Konar and A. Clearfield, *Inorg. Chem.*, 2008, **47**, 3489-3491.

538. C. J. Milios, C. P. Raptopoulou, A. Terzis, F. Lloret, R. Vicente, S. P. Perlepes and A. Escuer, *Angew. Chem. Int. Ed.*, 2004, **43**, 210-212.

539. A. M. Ako, I. J. Hewitt, V. Mereacre, R. Clérac, W. Wernsdorfer, C. E. Anson and A. K. Powell, *Angew. Chem. Int. Ed.*, 2006, **45**, 4926-4929.

540. H.-C. Yao, Y.-Z. Li, Y. Song, Y.-S. Ma, L.-M. Zheng and Xin, *Inorg. Chem.*, 2006, **45**, 59-65.

541. M. Wang, C. Ma and C. Chen, *Dalton Trans.*, 2008, DOI: 10.1039/B804532A, 4612-4620.

542. L. Zhang, R. Clérac, C. I. Onet, M. Venkatesan, P. Heijboer and W. Schmitt, *Chem.: Eur. J*, 2012, **18**, 13984-13988.

543. L. Zhang, R. Clérac, P. Heijboer and W. Schmitt, *Angew. Chem. Int. Ed.*, 2012, **51**, 3007-3011.

544. L. Zhang, C. I. Onet, R. Clérac, M. Rouzières, B. Marzec, M. Boese, M. Venkatesan and W. Schmitt, *Chem. Commun.*, 2013, **49**, 7400-7402.

545. L. Zhang, B. Marzec, R. Clérac, Y. Chen, H. Zhang and W. Schmitt, *Chem. Commun.*, 2013, **49**, 66-68.

546. J. M. Frost, S. Sanz, T. Rajeshkumar, M. B. Pitak, S. J. Coles, G. Rajaraman, W. Wernsdorfer, J. Schnack, P. J. Lusby and E. K. Brechin, *Dalton Trans.*, 2014, **43**, 10690-10694.

547. E. Chevallot-Beroux, A. M. Ako, W. Schmitt, B. Twamley, J. Moran, B. Corinne, L. Ruhlmann and S. Mameri, *Dalton Trans.*, 2019, **48**, 4830-4836.

548. G. J. Palenik, *Inorg. Chem.*, 1967, **6**, 503-507.

549. B. Morosin, *J. Chem. Phys.*, 1967, **47**, 417-420.

550. E. F. Bertaut, D. Tran Qui, P. Burlet, P. Burlet, M. Thomas and J. M. Moreau, *Acta Crystallogr. B*, 1974, **30**, 2234-2236.

551. E. D. Crozier, N. Alberding and B. R. Sundheim, *Acta Crystallogr. C*, 1983, **39**, 808.

552. J. E. Moore, J. E. Abola and R. A. Butera, *Acta Crystallogr. C*, 1985, **41**, 1284-1286.

553. J. D. Tornero and J. Fayos, *Z. Krist. - Cryst. Mater.*, 1990, **192**, 147.

554. C.-Y. Cheng and S.-L. Wang, *Acta Crystallogr. C*, 1991, **47**, 1734-1736.

555. Y. Yang, H.-G. Schmidt, M. Noltemeyer, J. Pinkas and H. W. Roesky, *J. Chem. Soc., Dalton Trans.*, 1996, DOI: 10.1039/DT9960003609, 3609-3610.

556. M. Wang, D.-Q. Yuan, C.-B. Ma, M.-J. Yuan, M.-Q. Hu, N. Li, H. Chen, C.-N. Chen and Q.-T. Liu, *Dalton Trans.*, 2010, **39**, 7276-7285.

557. V. Chandrasekhar, A. Dey, T. Senapati and E. C. Sañudo, *Dalton Trans.*, 2012, **41**, 799-803.

558. M. Czakler, C. Artner and U. Schubert, *Eur. J. Inorg. Chem.*, 2013, **2013**, 5790-5796.

559. N. Burkovskaya, G. Aleksandrov, E. Ugolkova, N. Efimov, I. Evstifeev, M. Kiskin, Z. Dobrokhotova, V. Minin and I. Eremenko, *New J. Chem.*, 2014, **38**, 1587-1593.

560. J. Goura and V. Chandrasekhar, *Chem. Rev.*, 2015, **115**, 6854-6965.

561. M. Shanmugam, M. Shanmugam, G. Chastanet, R. Sessoli, T. Mallah, W. Wernsdorfer and R. E. P. Winpenny, *J. Mater. Chem.*, 2006, **16**, 2576-2578.

562. M. Wang, C. Ma, H. Wen and C. Chen, *Dalton Trans.*, 2009, DOI: 10.1039/B814794A, 994-1003.

563. T. Albrecht-Schmitt, B. Bujoli, C. Cahill, R. Murugavel, J. Rocha, G. Hix, G. Shimizu, J. Zubieta, J. Zon and E. Brunet, *Metal Phosphonate Chemistry: From Synthesis to Applications*, Royal Society of Chemistry, 2011.

564. M. Wang, C. Ma, D. Yuan, M. Hu, C. Chen and Q. Liu, *New J. Chem.*, 2007, **31**, 2103-2110.

565. T. Cauchy, E. Ruiz and S. Alvarez, *J. Am. Chem. Soc.*, 2006, **128**, 15722-15727.

566. J. Cano, T. Cauchy, E. Ruiz, C. J. Milios, C. C. Stoumpos, T. C. Stamatatos, S. P. Perlepes, G. Christou and E. K. Brechin, *Dalton Trans.*, 2008, 234-240.

567. E. Cremades, J. Cano, E. Ruiz, G. Rajaraman, C. J. Milios and E. K. Brechin, *Inorg. Chem.*, 2009, **48**, 8012-8019.

568. S. K. Singh, N. K. Tibrewal and G. Rajaraman, *Dalton Trans.*, 2011, **40**, 10897-10906.

569. T. Rajeshkumar, H. V. Annadata, M. Evangelisti, S. K. Langley, N. F. Chilton, K. S. Murray and G. Rajaraman, *Inorg. Chem.*, 2015, **54**, 1661-1670.

570. K. R. Vignesh, S. K. Langley, K. S. Murray and G. Rajaraman, *Chem. Eur. J.*, 2015, **21**, 2881-2892.

571. S. Tandon, M. Venkatesan, W. Schmitt and G. W. Watson, *Dalton Trans.*, 2020, **49**, 8086-8095.

572. C. Adamo, M. Cossi and V. Barone, *THEOCHEM*, 1999, **493**, 145-157.

573. E. V. Gorelik, V. I. Ovcharenko and M. Baumgarten, *Eur. J. Inorg. Chem.*, 2008, DOI: 10.1002/ejic.200701305, 2837-2846.

574. B. Miehlich, A. Savin, H. Stoll and H. Preuss, *Chem. Phys. Lett.*, 1989, **157**, 200-206.

575. E. Ruiz, A. Rodriguez-Fortea, J. Cano, S. Alvarez and P. Alemany, *J. Comp. Chem.*, 2003, **24**, 982-989.

576. J. B. Goodenough, *J. Phys. Chem. Solids*, 1958, **6**, 287-297.

577. J. Kanamori, *J. Phys. Chem. Solids*, 1959, **10**, 87-98.

578. M. L. Baker, G. A. Timco, S. Piligkos, J. S. Mathieson, H. Mutka, F. Tuna, P. Kozłowski, M. Antkowiak, T. Guidi, T. Gupta, H. Rath, R. J. Woolfson, G. Kamieniarz, R. G. Pritchard, H. Weihe, L. Cronin, G. Rajaraman, D. Collison, E. J. L. McInnes and R. E. P. Winpenny, *Proc. Natl. Acad. Sci. U.S.A.*, 2012, **109**, 19113-19118.

579. A. B. Shick, J. Kudrnovský and V. Drchal, *Phys. Rev. B*, 2004, **69**, 125207.

580. K. Leung, S. B. Rempe, P. A. Schultz, E. M. Sproviero, V. S. Batista, M. E. Chandross and C. J. Medforth, *J. Am. Chem. Soc.*, 2006, **128**, 3659-3668.

581. Y. Ma, Y. Dai, Z. Zhang, L. Yu and B. Huang, *Appl. Phys. Lett.*, 2012, **101**, 062405.

582. J.-R. Huang and C. Cheng, *J. Appl. Phys.*, 2013, **113**, 033912.

583. T. A. Mellan, K. P. Maenetja, P. E. Ngoepe, S. M. Woodley, C. R. A. Catlow and R. Grau-Crespo, *J. Mater. Chem. A*, 2013, **1**, 14879-14887.

584. T. A. Mellan, F. Corà, R. Grau-Crespo and S. Ismail-Beigi, *Phys. Rev. B*, 2015, **92**, 085151.

585. D. Ghosh, P. Parida and S. K. Pati, *J. Phys. Chem. C*, 2016, **120**, 3625-3634.

586. S. Keshavarz, Y. O. Kvashnin, D. C. M. Rodrigues, M. Pereiro, I. Di Marco, C. Autieri, L. Nordström, I. V. Solovyev, B. Sanyal and O. Eriksson, *Phys. Rev. B*, 2017, **95**, 115120.

587. A. L. Gavin and G. W. Watson, *Solid State Ion.*, 2017, **299**, 13-17.

588. A. L. Gavin and G. W. Watson, *Phys. Chem. Chem. Phys.*, 2017, **19**, 24636-24646.

589. A. L. Gavin and G. W. Watson, *Phys. Chem. Chem. Phys.*, 2018, **20**, 19257-19267.

590. J. E. McGrady and R. Stranger, *Inorg. Chem.*, 1999, **38**, 550-558.

591. C. Lanczos, *J. Res. Natl. Bur. Stand.*, 1950, **45**, 255-282.

592. J. Schnack, P. Hage and H.-J. Schmidt, *J. Comp. Phys.*, 2008, **227**, 4512-4517.

593. S. Alvarez, *Coord. Chem. Rev.*, 2017, **350**, 3-13.

594. J. A. Montgomery, M. J. Frisch, J. W. Ochterski and G. A. Petersson, *J. Chem. Phys.*, 1999, **110**, 2822-2827.

595. J. A. Montgomery, M. J. Frisch, J. W. Ochterski and G. A. Petersson, *J. Chem. Phys.*, 2000, **112**, 6532-6542.

596. P. Gerbier, D. Ruiz-Molina, J. Gómez, K. Wurst and J. Veciana, *Polyhedron*, 2003, **22**, 1951-1955.

597. M. Poyraz, M. Sari, S. Cevik and O. Buyukgungor, *Acta Crystallogr. E*, 2006, **62**, M1442-M1444.

598. T. C. Stamatatos, D. Foguet-Albiol, S. P. Perlepes, C. P. Raptopoulou, A. Terzis, C. S. Patrickios, G. Christou and A. J. Tasiopoulos, *Polyhedron*, 2006, **25**, 1737-1746.

599. I. L. Malaestean, V. C. Kravtsov, M. Speldrich, G. Dulcevscaia, Y. A. Simonov, J. Lipkowski, A. Ellern, S. G. Baca and P. Kögerler, *Inorg. Chem.*, 2010, **49**, 7764-7772.

600. P. Seth and A. Ghosh, *RSC Adv.*, 2013, **3**, 3717-3725.

601. M. Darii, I. G. Filippova, J. Hauser, S. Decurtins, S. X. Liu, V. C. Kravtsov and S. G. Baca, *Crystals*, 2018, **8**, 100.

602. S. Tandon, J. Soriano-López, A. C. Kathalikkattil, G. Jin, P. Wix, M. Venkatesan, R. Lundy, M. A. Morris, G. W. Watson and W. Schmitt, *Sustain. Energy Fuels*, 2020, DOI: 10.1039/D0SE00701C.

603. T. C. Stamatatos, K. M. Poole, K. A. Abboud, W. Wernsdorfer, T. A. O'Brien and G. Christou, *Inorg. Chem.*, 2008, **47**, 5006-5021.

604. C. Lampropoulos, C. Koo, S. O. Hill, K. Abboud and G. Christou, *Inorg. Chem.*, 2008, **47**, 11180-11190.

605. R. A. Coxall, S. G. Harris, D. K. Henderson, S. Parsons, P. A. Tasker and R. E. P. Winpenny, *J. Chem. Soc., Dalton Trans.*, 2000, 2349-2356.

606. M. E. Fleet, *Mineral. Mag.*, 1976, **40**, 531-533.

607. M. Wildner, *Z. Krist.*, 1992, **202**, 51-70.

608. A. Ertl, J. M. Hughes, F. Pertlik, F. F. Foit, S. E. Wright, F. Brandstatter and B. Marler, *Can. Mineral.*, 2002, **40**, 153-162.

609. M. Hazen Robert and T. Downs Robert, *High-Temperature and High Pressure Crystal Chemistry*, De Gruyter, Berlin, Boston, 2018.

610. M. Pinsky and D. Avnir, *Inorg. Chem.*, 1998, **37**, 5575-5582.

611. S. Alvarez, D. Avnir, M. Llunell and M. Pinsky, *New J. Chem.*, 2002, **26**, 996-1009.

612. D. Casanova, J. Cirera, M. Llunell, P. Alemany, D. Avnir and S. Alvarez, *J. Am. Chem. Soc.*, 2004, **126**, 1755-1763.

613. J. Cirera, P. Alemany and S. Alvarez, *Chem.: Eur. J*, 2004, **10**, 190-207.

614. J. Cirera, E. Ruiz and S. Alvarez, *Organometallics*, 2005, **24**, 1556-1562.

615. M. Llunell, D. Casanova, J. Cirera, P. Alemany and S. Alvarez, *SHAPE Version 2.1*, 2013.

616. O. V. Dolomanov, L. J. Bourhis, R. J. Gildea, J. A. K. Howard and H. Puschmann, *J. Appl. Crystallogr.*, 2009, **42**, 339-341.

617. B. Stuart, in *Infrared Spectroscopy: Fundamentals and Applications*, 2004, ch. 4, pp. 71-93.

618. G. B. Deacon and R. J. Phillips, *Coord. Chem. Rev.*, 1980, **33**, 227-250.

619. A. Sharma, S. Kaur, C. G. Mahajan, S. K. Tripathi and G. S. S. Saini, *Mol. Phys.*, 2007, **105**, 117-123.

620. L. Sun, C. H. Hendon and M. Dincă, *Dalton Trans.*, 2018, **47**, 11739-11743.

621. A. Cabeza, M. A. G. Aranda, S. Bruque, D. M. Poojary and A. Clearfield, *Mater. Res. Bull.*, 1998, **33**, 1265-1274.

622. N. Stock and T. Bein, *J. Solid State Chem.*, 2002, **167**, 330-336.

623. N. Stock and T. Bein, *J. Mater. Chem.*, 2005, **15**, 1384-1391.

624. J. Nishida, S. Shigeto, S. Yabumoto and H.-o. Hamaguchi, *J. Chem. Phys.*, 2012, **137**, 234501.

625. M. C. Biesinger, B. P. Payne, A. P. Grosvenor, L. W. M. Lau, A. R. Gerson and R. S. Smart, *Appl. Surf. Sci.*, 2011, **257**, 2717-2730.

626. M. H. Miles, E. A. Klaus, B. P. Gunn, J. R. Locker and W. E. Serafin, *Electrochim. Acta*, 1978, **23**, 521-526.

627. H. J. Shi and G. H. Zhao, *J. Phys. Chem. C*, 2014, **118**, 25939-25946.

628. M. M. Najafpour, N. J. Moghaddam, S. M. Hosseini, S. Madadkhani, M. Hołyńska, S. Mehrabani, R. Bagheri and Z. Song, *Catal. Sci. Technol.*, 2017, **7**, 3499-3510.

629. A. Spek, *Acta Crystallogr. C*, 2015, **71**, 9-18.

630. J. Sienkiewicz-Gromiuk, H. Głuchowska, B. Tarasiuk, L. Mazur and Z. Rzączyńska, *J. Mol. Struct.*, 2014, **1070**, 110-116.

631. M. J. Frisch, J. A. Pople and J. S. Binkley, *J. Chem. Phys.*, 1984, **80**, 3265-3269.

632. M. Blasco-Ahicart, J. Soriano-López, J. J. Carbó, J. M. Poblet and J. R. Galan-Mascaros, *Nat. Chem.*, 2018, **10**, 24-30.

633. M. Gorman, *J. Chem. Educ.*, 1957, **34**, 304.

634. S. Knop, T. L. C. Jansen, J. Lindner and P. Vöhringer, *Phys. Chem. Chem. Phys.*, 2011, **13**, 4641-4650.

635. A. Spek, *Acta Crystallogr. D*, 2009, **65**, 148-155.

636. T. Steiner, *Angew. Chem. Int. Ed.*, 2002, **41**, 48-76.

637. C. R. Groom, I. J. Bruno, M. P. Lightfoot and S. C. Ward, *Acta Crystallogr. B*, 2016, **72**, 171-179.

638. J. Goura, J. P. S. Walsh, F. Tuna and V. Chandrasekhar, *Inorg. Chem.*, 2014, **53**, 3385-3391.

639. I. D. Brown and D. Altermatt, *Acta Crystallogr. B*, 1985, **41**, 244-247.

640. W. Bragg and G. Claringbull, *Crystal Structure of Minerals*, G. Bell, 1965.

641. K. Shinoda, M. Yamakata, T. Nanba, H. Kimura, T. Moriwaki, Y. Kondo, T. Kawamoto, N. Niimi, N. Miyoshi and N. Aikawa, *Phys. Chem. Miner.*, 2002, **29**, 396-402.

642. X. Guo, T. Yoshino, T. Okuchi and N. Tomioka, *Am. Mineral.*, 2013, **98**, 1919-1929.

643. M. Murugesu, M. Habrych, W. Wernsdorfer, K. A. Abboud and G. Christou, *J. Am. Chem. Soc.*, 2004, **126**, 4766-4767.

644. G. N. Newton, S. Yamashita, K. Hasumi, J. Matsuno, N. Yoshida, M. Nihei, T. Shiga, M. Nakano, H. Nojiri, W. Wernsdorfer and H. Oshio, *Angew. Chem. Int. Ed.*, 2011, **50**, 5716-5720.

645. F. A. Mautner, R. C. Fischer, M. Salah El Fallah, S. Speed and R. Vicente, *Polyhedron*, 2012, **36**, 92-96.

646. V. Chandrasekhar, J. Goura, K. Gopal, J. Liu and P. Goddard, *Polyhedron*, 2014, **72**, 35-42.

647. J.-y. Liu, C.-b. Ma, H. Chen and C.-n. Chen, *CrystEngComm*, 2015, **17**, 8736-8745.

648. Bruker, *SADABS, Bruker AXS Inc., Madison, Wisconsin, USA.*, 2001.

649. G. M. Sheldrick, *Acta Crystallogr. A*, 2015, **71**, 3-8.

650. G. M. Sheldrick, *Acta Crystallogr. A*, 2008, **64**, 112-122.

651. Bruker, *DIFFRAC.EVA Version 4.1, Bruker AXS Inc.*, 2015, Karlsruhe, Germany.

12 Appendix

This section includes the equations for the spin projection approach, the details about the calculation of distortion parameters and crystallographic tables for all compounds reported in this thesis.

12.1 Equations for spin projection approach

The following equations were used for calculation of the coupling constants using the spin projection approach in chapter 4.

1. $H^{Ferro} = -96J_{cis} - 24J_{trans}$
2. $H^{1} = -31.99J_{cis} - 7.99J_{trans}$
3. $H^{12} = 0.01J_{cis} + 8.001J_{trans}$
4. $H^{16} = 32.05J_{cis} - 24J_{trans}$
5. $H^{125} = 0.01J_{cis} + 24J_{trans}$
6. $H^{126} = 32.015J_{cis} - 7.99J_{trans}$

12.2 Calculation of extent of distortion

To quantify the extent of distortion from the ideal geometries, bond angle variance and distortion indices have been calculated.[606-609] The bond angle variance (σ^2) for octahedral geometry is defined as:[606-609]

$$\sigma^2 = \frac{1}{11}\sum_{i=1}^{12}(\alpha_i - 90)^2 \quad (12.1)$$

where α_i is the angle between any two centres bound to an octahedrally coordinated Mn centre and lie *cis*- to each other.

For tetrahedral geometry, the bond angle variance is given as:[608]

$$\sigma^2 = \frac{1}{5}\sum_{i=1}^{6}(\alpha_i - 109.47)^2 \quad (12.2)$$

where α_i is the angle between any two centres bound to a tetrahedrally coordinated Mn centre. Similarly, for square pyramidal geometry, the bond angle variance can be calculated as:

$$\sigma^2 = \frac{1}{7}\sum_{i=1}^{8}(\alpha_i - 90)^2 \quad (12.3)$$

where α_i is the angle between any two centres bound to a Mn centre in a square pyramidal coordination environment and lie *cis*- to each other.

The distortion index (DI) for octahedral geometry is defined as:

$$DI = \frac{1}{12\alpha_m}\sum_{i=1}^{12}|\alpha_i - \alpha_m| \quad (12.4)$$

here α_m is the average *cis*- bond angle for the given octahedral system. The DI value lies between 0 and 1 with 0 indicating ideal octahedral geometry and values > 0 indicating angular distortion. For tetrahedral and square pyramidal geometries, the distortion index is calculated using equations 12.5 and 12.6 as follows:

$$DI = \frac{1}{6\alpha_m}\sum_{i=1}^{6}|\alpha_i - \alpha_m| \quad (12.5)$$

$$DI = \frac{1}{8\alpha_m}\sum_{i=1}^{8}|\alpha_i - \alpha_m| \quad (12.6)$$

The limitation of these approaches to quantify the extent of distortion from ideal geometries is that they are limited to the use of bond angles. It still provides a reasonable value as distortion induced by changes in bond lengths are relatively smaller. A more generalised approach for calculating the extent of distortion is provided by continuous shape measure analysis.[610-614] In this approach, the overall structure of the system under investigation is compared with its ideal analogue for determining the extent of distortion. If P_i and Q_i represent the position vectors of the reference polyhedron and the system under study respectively, with Q_0 being the position vector of the geometrical centre, the continuous shape measure value (S) can be determined as follows:

$$S = min\frac{\sum_{i=1}^{N}|Q_i - P_i|^2}{\sum_{i=1}^{N}|Q_i - Q_0|^2} \times 100 \quad (12.7)$$

S varies between 0 and 100 with larger values indicating greater distortions. The use of continuous shape measures also provides a way to assign the correct shape to a system in cases where the structure is close to two or more different polyhedrons. The continuous shape measure analysis, in this work, has been carried out using SHAPE V2.1 code.[615]

12.3 Crystallographic tables

Compounds **6.1**-**6.3**

Identification code	**Compound_6.1**	**Compound_6.2**	**Compound_6.3**
Empirical formula	$C_{65}H_{125.67}Mn_6N_5O_{27.33}$	$C_{170}H_{306}Cl_6K_4Mn_{16}N_4O_{76}$	$C_{208}H_{152}Mn_{12}O_{48}$
Formula weight	1744.33	4870.31	4078.57
Temperature/K	100(2)	99.99	100.15
Crystal system	monoclinic	monoclinic	monoclinic
Space group	Cc	$P2_1/n$	Cc
a/Å	24.8031(10)	19.040(2)	29.0406(17)
b/Å	14.1011(5)	15.7109(17)	29.0343(16)
c/Å	26.7382(11)	20.192(2)	35.023(2)
α/°	90	90	90
β/°	113.6240(10)	100.691(2)	114.478(2)
γ/°	90	90	90
Volume/Å^3	8568.0(6)	5935.3(11)	26876(3)
Z	4	1	4
ρ_{calc}g/cm^3	1.352	1.363	1.008
μ/mm^{-1}	0.931	1.033	0.600
F(000)	3677.0	2540.0	8336.0
Crystal size/mm^3	0.2 × 0.2 × 0.2	0.26 × 0.18 × 0.05	? × ? × ?
Radiation	MoKα (λ = 0.71073)	MoKα (λ = 0.71073)	MoKα (λ = 0.71073)
2Θ range for data collection/°	5.778 to 55.25	3.306 to 53.514	4.752 to 45
Index ranges	-32 ≤ h ≤ 32, -18 ≤ k ≤ 18, -34 ≤ l ≤ 34	-24 ≤ h ≤ 24, -19 ≤ k ≤ 19, -25 ≤ l ≤ 25	-31 ≤ h ≤ 31, -31 ≤ k ≤ 31, -37 ≤ l ≤ 37
Reflections collected	65360	190941	132205
Independent reflections	19778 [R_{int} = 0.0265, R_{sigma} = 0.0309]	12589 [R_{int} = 0.0683, R_{sigma} = 0.0274]	34395 [R_{int} = 0.1715, R_{sigma} = 0.1688]
Data/restraints/parameters	19778/566/1145	12589/103/749	34395/1569/2034
Goodness-of-fit on F^2	1.037	1.063	0.955
Final R indexes [I>=2σ (I)]	R_1 = 0.0237, wR_2 = 0.0584	R_1 = 0.0439, wR_2 = 0.1096	R_1 = 0.0898, wR_2 = 0.2177
Final R indexes [all data]	R_1 = 0.0264, wR_2 = 0.0596	R_1 = 0.0641, wR_2 = 0.1214	R_1 = 0.1844, wR_2 = 0.2812
Largest diff. peak/hole / e Å^{-3}	0.62/-0.53	1.02/-1.30	0.76/-0.49
Flack parameter	0.132(8)		0.07(4)

Compounds **7.1**-**7.3**

Identification code	**Compound_7.1**	**Compound_7.2**	**Compound_7.3**
Empirical formula	$C_{96}H_{168}Mn_{12}O_{46}P_4S_6$	$C_{109}H_{183}Mn_{15}O_{59}P_6$	$C_{94.45}H_{152.9}Mn_{15}O_{59}P_6$
Formula weight	3033.81	3447.48	3242.38
Temperature/K	100.01	100.01	100(2)
Crystal system	trigonal	trigonal	trigonal
Space group	R-3c	R-3	R3
a/Å	35.9770(10)	26.6412(10)	48.387(3)
b/Å	35.9770(10)	26.6412(10)	48.387(3)
c/Å	88.049(3)	36.1302(17)	17.8264(10)
α/°	90	90	90
β/°	90	90	90
γ/°	120	120	120
Volume/Å^3	98697(6)	22208(2)	36146(4)
Z	18	5.99994	9
ρ_{calc}g/cm^3	0.919	1.547	1.341
μ/mm^{-1}	6.625	11.351	1.266
F(000)	28224.0	10644.0	14909.0
Crystal size/mm^3	0.264 × 0.162 × 0.109	0.06 × 0.06 × 0.05	0.43 × 0.09 × 0.08
Radiation	CuKα (λ = 1.54178)	CuKα (λ = 1.54178)	MoKα (λ = 0.71073)
2Θ range for data collection/°	5.762 to 122.374	4.544 to 112.164	5.052 to 52.344
Index ranges	-40 ≤ h ≤ 34, -38 ≤ k ≤ 33, -99 ≤ l ≤ 95	-28 ≤ h ≤ 28, -28 ≤ k ≤ 28, -38 ≤ l ≤ 38	-59 ≤ h ≤ 59, -60 ≤ k ≤ 57, -22 ≤ l ≤ 22
Reflections collected	99748	48719	152549
Independent reflections	16601 [R_{int} = 0.1161, R_{sigma} = 0.0972]	6429 [R_{int} = 0.1709, R_{sigma} = 0.1126]	31014 [R_{int} = 0.1254, R_{sigma} = 0.1012]
Data/restraints/parameters	16601/181/845	6429/283/738	31014/2460/2187
Goodness-of-fit on F^2	0.912	1.014	0.970
Final R indexes [I>=2σ (I)]	R_1 = 0.0630, wR_2 = 0.1763	R_1 = 0.0744, wR_2 = 0.1684	R_1 = 0.0609, wR_2 = 0.1418
Final R indexes [all data]	R_1 = 0.1019, wR_2 = 0.1912	R_1 = 0.1432, wR_2 = 0.2041	R_1 = 0.1112, wR_2 = 0.1683
Largest diff. peak/hole / e Å^{-3}	0.80/-0.58	0.56/-0.59	0.76/-0.73
			-0.007(8)

Compounds **7.4**-**7.5**

Identification code	**Compound_7.4**	**Compound_7.5**
Empirical formula	$C_{84.68}H_{153.02}Mn_{14}O_{54}P_3$	$C_{83.94}H_{142.34}Mn_{13}N_{0.58}O_{48.78}P_4$
Formula weight	2897.26	2778.15
Temperature/K	100.15	100.15
Crystal system	triclinic	triclinic
Space group	P-1	P-1
a/Å	16.8387(8)	15.6787(7)
b/Å	17.5125(9)	18.4538(8)
c/Å	24.2245(13)	23.4553(10)
α/°	71.548(4)	99.277(3)
β/°	80.665(4)	93.245(3)
γ/°	69.798(3)	112.715(3)
Volume/Å^3	6348.1(6)	6125.2(5)
Z	2	2
ρ_{calc}g/cm^3	1.516	1.506
μ/mm^{-1}	11.977	11.686
F(000)	2976.0	2850.0
Crystal size/mm^3	0.182 × 0.036 × 0.022	0.18 × 0.08 × 0.06
Radiation	CuKα (λ = 1.54178)	CuKα (λ = 1.54178)
2Θ range for data collection/°	3.852 to 118.396	3.85 to 126.386
Index ranges	-18 ≤ h ≤ 18, -19 ≤ k ≤ 17, -26 ≤ l ≤ 26	-18 ≤ h ≤ 18, -21 ≤ k ≤ 15, -26 ≤ l ≤ 27
Reflections collected	55345	62111
Independent reflections	18219 [R_{int} = 0.1000, R_{sigma} = 0.1323]	19514 [R_{int} = 0.1018, R_{sigma} = 0.1133]
Data/restraints/parameters	18219/858/1706	19514/519/1542
Goodness-of-fit on F^2	1.018	1.014
Final R indexes [I>=2σ (I)]	R_1 = 0.0731, wR_2 = 0.1811	R_1 = 0.0685, wR_2 = 0.1644
Final R indexes [all data]	R_1 = 0.1342, wR_2 = 0.2187	R_1 = 0.1341, wR_2 = 0.2024
Largest diff. peak/hole / e Å^{-3}	0.88/-0.54	0.79/-0.60

Compounds **8.1**-**8.3**

Identification code	**Compound_8.1**	**Compound_8.2**	**Compound_8.3**
Empirical formula	$C_{46}H_{91}BrMn_6N_5O_{25}P_6$	$C_{146}H_{291.6}Mn_{26}N_8Na_{0.4}O_{92}P_{22}$	$C_{57}H_{139}KMn_{13}O_{51}P_{11}$
Formula weight	1709.60	5750.43	2734.66
Temperature/K	100.01	100(2)	100.01
Crystal system	triclinic	triclinic	triclinic
Space group	P-1	P-1	P-1
a/Å	12.6480(8)	16.772(3)	15.766(2)
b/Å	15.7206(9)	18.558(3)	16.047(2)
c/Å	19.3918(11)	20.026(3)	22.047(3)
α/°	92.405(2)	94.613(5)	90.046(2)
β/°	93.354(2)	98.296(4)	94.385(2)
γ/°	102.354(2)	91.378(5)	96.007(3)
Volume/Å^3	3754.1(4)	6143.8(16)	5530.4(12)
Z	2	1	2
ρ_{calc}g/cm^3	1.512	1.554	1.642
μ/mm^{-1}	1.709	1.507	1.708
F(000)	1754.0	2944.0	2796.0
Crystal size/mm^3	0.09 × 0.08 × 0.05	0.464 × 0.157 × 0.042	0.14 × 0.13 × 0.08
Radiation	MoKα (λ = 0.71073)	MoKα (λ = 0.71073)	MoKα (λ = 0.71073)
2Θ range for data collection/°	3.298 to 51.474	4.84 to 53.936	1.852 to 54.36
Index ranges	-15 ≤ h ≤ 15, -19 ≤ k ≤ 19, -23 ≤ l ≤ 23	-21 ≤ h ≤ 21, -23 ≤ k ≤ 23, -25 ≤ l ≤ 25	-20 ≤ h ≤ 20, -20 ≤ k ≤ 20, -28 ≤ l ≤ 28
Reflections collected	87008	129759	236619
Independent reflections	14323 [R_{int} = 0.1481, R_{sigma} = 0.1193]	26500 [R_{int} = 0.0835, R_{sigma} = 0.0613]	24521 [R_{int} = 0.0703, R_{sigma} = 0.0408]
Data/restraints/parameters	14323/7/800	26500/921/1648	24521/65/1278
Goodness-of-fit on F^2	1.015	1.044	1.031
Final R indexes [I>=2σ (I)]	R_1 = 0.0625, wR_2 = 0.1301	R_1 = 0.0692, wR_2 = 0.1807	R_1 = 0.0475, wR_2 = 0.1192
Final R indexes [all data]	R_1 = 0.1379, wR_2 = 0.1597	R_1 = 0.1109, wR_2 = 0.2077	R_1 = 0.0786, wR_2 = 0.1353
Largest diff. peak/hole / e Å^{-3}	2.48/-1.11	2.17/-1.67	1.85/-1.11

Compounds **8.4**-**8.5**

Identification code	**Compound_8.4**	**Compound_8.5**
Empirical formula	$C_{85.7}H_{164.3}Ca_2Mn_{13}N_{1.7}O_{54.3}P_{12}$	$C_{90}H_{168}Ca_2Mn_{15}O_{58}P_{10}$
Formula weight	3253.50	3392.19
Temperature/K	100.0	100.15
Crystal system	triclinic	monoclinic
Space group	P-1	$P2_1/c$
a/Å	14.7883(6)	18.6161(8)
b/Å	16.5903(7)	26.5973(10)
c/Å	16.6969(7)	17.7786(7)
α/°	72.567(3)	90
β/°	85.567(3)	117.532(2)
γ/°	63.836(3)	90
Volume/Å^3	3500.6(3)	7806.0(6)
Z	1	2
ρ_{calc}g/cm^3	1.543	1.443
μ/mm^{-1}	11.814	11.689
F(000)	1670.0	3474.0
Crystal size/mm^3	0.22 × 0.08 × 0.03	0.11 × 0.09 × 0.09
Radiation	CuKα (λ = 1.54178)	CuKα (λ = 1.54178)
2Θ range for data collection/°	5.558 to 137.082	5.354 to 136.808
Index ranges	-17 ≤ h ≤ 17, -19 ≤ k ≤ 20, -19 ≤ l ≤ 20	-22 ≤ h ≤ 22, -31 ≤ k ≤ 32, -21 ≤ l ≤ 21
Reflections collected	51359	62901
Independent reflections	12770 [R_{int} = 0.1396, R_{sigma} = 0.1560]	14166 [R_{int} = 0.1276, R_{sigma} = 0.1194]
Data/restraints/parameters	12770/84/798	14166/0/815
Goodness-of-fit on F^2	1.071	0.968
Final R indexes [I>=2σ (I)]	R_1 = 0.0991, wR_2 = 0.2672	R_1 = 0.0667, wR_2 = 0.1633
Final R indexes [all data]	R_1 = 0.1462, wR_2 = 0.3098	R_1 = 0.1240, wR_2 = 0.1965
Largest diff. peak/hole / e Å^{-3}	0.95/-1.05	0.86/-0.59